Design and Development of a Cable-Driven Shoulder Exosuit (CDSE) for Upper Limb Assistance

Hamed Vatan

School of Science, Engineering & Environment,

SEE Building, University of Salford,

Manchester, UK

Submitted in Partial Fulfilment of the Requirements of the Degree of Doctor of Philosophy March 2025

PUBLICATIONS

1- Majidi Fard Vatan, H., Nefti-Meziani, S., Davis, S. *et al.* A review: A Comprehensive Review of Soft and Rigid Wearable Rehabilitation and Assistive Devices with a Focus on the Shoulder Joint. *J Intell Robot Syst* 102, 9 (2021). https://doi.org/10.1007/s10846-021-01353-x

2- Vatan, H., Theodoridis, T., Wei, G., Holderbaum, W., Saffari, Z. Design, Fabrication and Evaluation of a Novel Cable-Driven Shoulder Exosuit (CDSE) for Upper Limb Assistance. Submitted paper, (2025)

CONTENTS

LIST OF FIGURES

LIST OF TABLES

ABBREVIATIONS

ACS: Arm Coordinate System

ADLs: Activities of Daily Living

BCI: Brain-computer interface

BCS: Base Coordinate System

CDSE: Cable-Driven Shoulder Exosuit

COR: Centre of Rotation

CGH: Centre of Glenohumeral Joint

DCM: Direction Cosine Matrix

FEA: Finite Element Analysis

FEM: Finite Element Method

FES: Functional Electrical Stimulation

FRP: Fiber-Reinforced Plastic

GUI: Graphical User Interface

GJ: Glenohumeral Joint

GP: Goal Position

HH: Humerus Head

HRI: Human-Robot Interaction

IK: Inverse Kinematics

IMU: Inertial Measurement Unit

MND: Motor Neurone Disease

NA: Not Available

NMES: Neuromuscular Electrical Stimulation

PAM: Pneumatic Artificial Muscle

PLA: Polylactic Acid

PHB: Power Hub Board

PID: Proportional-Integral-Derivative

PD: Proportional Derivative

PI: Proportional Integral

RFID: Radio-Frequency Identification

RMS: Root Mean Square

ROM: Range of Motion

RTP: Repetitive Task Practice

SEA: Series Elastic Actuators

EMG: Electromyography

sEMG: surface Electromyogram

TSA: Twisted String Actuator

VR: Virtual Reality

PARAMETERS AND VARIABLES

A	Centre of humeral head (HH) (centre of rotation for human's arm)
AB	Length of Upper arm segment [mm]
BC	Length of Forearm segment [mm]
CD	Length of Hand segment [mm]
F	Location of the anchor points for abduction and flexion movement
EF	Vertical distance from the arm centreline to the F point [mm]
AE	Linear distance from the centre of humeral head to point E [mm]
O	Centre of the cable housing as projected into the working plane
AT	Horizontal distances of O from point A [mm]
OT	Vertical distances of O from point A [mm]
W_1	Weight of upper arm segment [kg]
W_2	Weight of forearm segment [kg]
W_3	Weight of hand segment [kg]
G_1	Centre of mass for upper arm segment
G_2	Centre of mass for forearm segment
G_3	Centre of mass for hand segment
F_1	Projected force of the shoulder abduction motion in Y-Z plane [N]
F_2	Projected force of the shoulder flexion motion in Y-X plane [N]
θ_1 (abduction)	One of the acute angles in AOT right triangle [Degree]
θ_1 (flexion)	90-β [Degree]
β	$\widehat{OAT}$
θ_2	One of acute angle in FAE right triangle [Degree]
θ_3	One of the angles in OFA triangle [Degree]
θ_{arm}	Angle between arm centreline and Y access [Degree]
M	Mass of the body [kg]
M_A	Torque at point A [Nm]
R	Radius of motor's pulley [mm]

$F_{1(real)}$	Real maximum force in 3D space [N]
$F_{1(projected)}$	Maximum projected F $_{\text{Braune-Fincher}}$ [N]
Φ_{space}	Space angle between the real force and projected force [Degree]
F_{motor}	Coefficient of 1.1 was applied to $\boldsymbol{F_{real}}$(increasing the force by 10%) [N]
T_{motor}	Maximum torque based on the radius of the pulley and F_{motor} [N.m]
S	Semi-perimeter of the FAO triangle
${}^{B}b_i = \overrightarrow{BB_i}$	Vector from the fixed-base coordinate system origin B to cable driving point B_i in BCS
${}^{B}P = \overrightarrow{BA}$	Vector from the fixed-base coordinate system origin B to the origin of the moving arm coordinate system A in the BCS
${}^{A}a_i = \overrightarrow{AA_i}$	Vector from the moving arm coordinate system origin A to cable traction point A_i in the ACS
m	Number of cables
L_i	i-th cable vector
l_i	i-th cable length
${}^{B}R_A$	Direction cosine matrix (DCM)
A_{xyz}	Arm coordinate system
B_{XYZ}	Base Coordinate System
${}^{B}v_A$	Arm coordinate system velocity in the BCS
θ_i	Rotary actuator angle (pulley angle) [Degree]
r_w	Pulley radius [Degree]
m_1	Mass of the arm [kg]
m_2	Mass of the elbow to wrist [kg]
m_3	Mass from the wrist to the fingertips [kg]
$A_1 \ldots A_3$	The position of the cable's traction points on the moving platform relative to the moving coordinate system [mm]
$B_1 \ldots B_3$	The position of the traction points of the cables on the fixed platform relative to the fixed coordinate system [mm]
α	Rotation around the x axis [Degree]
β	Rotation around the y axis [Degree]

γ	Rotation around the z axis [Degree]
q_d	Desired trajectory
L_d	Desired cable length [mm]
e	Error
q	Real trajectory
L	Real cable length [mm]
t	Time [s]
$\tau_1 \ldots \tau_3$	Torques of actuators 1 to 3 [Nm]
$F_1 \ldots F_3$	Tensions of cables 1 to 3 [N]

ACKNOWLEDGEMENTS

I am profoundly grateful for the opportunity to pursue my doctoral studies, an endeavour that holds great significance in my life and career path. This milestone could not have been achieved without the generous support and guidance of numerous individuals and institutions, to whom I owe immense gratitude.

First and foremost, I am especially thankful to my academic supervisors: **Dr Theodoros Theodoridis**, **Dr Guowu Wei**, and **Professor William Holderbaum**. Their extensive knowledge, persistent dedication, and invaluable guidance have profoundly shaped my research and professional growth during this challenging and rewarding process.

My heartfelt appreciation goes to my lovely wife **Mina**, whose unwavering support and encouragement have been my pillars of strength. Her presence and belief in my capabilities have been a constant source of motivation throughout this journey. Her belief in my potential always has been a guiding light, motivating me to strive for excellence.

The birth of my son **Darius** marked a pivotal moment in my life, infusing my scholarly endeavours with renewed inspiration and determination. I am incredibly grateful for the joy he has brought into our lives, which spurred me to complete my PhD with renewed zeal.

I am thankful to **my parents** and **brother**, whose endless encouragement and support have been fundamental to my persistence and success.

I wish to express my gratitude to **Andrew Baker**, **Michael Clegg**, Aidan Dunbar, and Michael Christopher for their invaluable laboratory support, which was essential to my work.

Finally, I extend my deepest thanks to the University of Salford and **Professor Samia Nefti-Meziani**. Their financial backing through a full scholarship was indispensable, enabling me to embark on this enriching academic journey.

ABSTRACT

This thesis presents the development and evaluation of a novel *Cable-Driven Shoulder Exosuit (CDSE)*, designed for enhancing upper limb rehabilitation. The motivation for this research stems from the critical need for advanced rehabilitation solutions that are both effective and user-friendly, particularly for populations experiencing upper limb disabilities. Utilizing soft robotics, the CDSE novelty offers a ***lightweight (around 2kg), wearable with three Degree Of Freedom (DOF)*** solution that ***aligns closely with human biomechanics***, thus promising greater comfort and efficiency compared to more rigid systems.

The methodology encompasses a comprehensive design and simulation phase, followed by iterative prototyping and rigorous testing (payload 500g to 4000g). Key innovations include the integration of bio-inspired design principles and advanced materials (carbon fiber), which facilitate naturalistic movement patterns and adaptability to various user needs. The CDSE's effectiveness was systematically evaluated through biomechanical analyses and user trials, focusing on its capacity to support and enhance shoulder joint mobility.

Results from testing indicate that the CDSE significantly aids in performing everyday tasks by improving range of motion and reducing user effort. Furthermore, the exosuit's design allows for significant reductions in weight and bulk, enhancing its portability and wearability. This research contributes to the fields of rehabilitation robotics and soft robotics by demonstrating the practical benefits of cable-driven systems in medical devices and laying groundwork for future innovations.

Overall, the CDSE represents a significant step forward in the development of assistive technologies that are both functionally and ergonomically optimized for users, potentially improving quality of life and assistive outcomes for individuals with upper limb impairments for *Motor Neurone Disease (MND)*.

1 Chapter One: Introduction

1.1 Overview

Robotic devices used to rehabilitate and support humans with regard to the upper limbs, fall into two general categories: *Prosthesis* and *Orthosis*. Prosthesis refers to artificial limbs that can be the whole human arm or parts of it, such as the arm, hand, or fingers. These robotic devices replace the lost organ of the user's body, and their purpose is to help in daily activities. Orthoses are orthopaedic devices used to rehabilitate or further support that limb. Rehabilitation robots can be divided into three general categories: *Exoskeletons, Exosuits and End-effectors*. Exoskeleton robots are connected by links to the biological drive system to perform the related movements required by that limb in parallel to the anatomical limbs of the human body. The main problem with this type of robot is the weight of its constituent parts, the hardness of the materials, and their stationary nature in most cases. The stationary nature of end-effectors is their main design drawback, which is only available in some rehabilitation clinics. The user can wear exosuit robots considering their lightweight, and if designed correctly, they can also be used as portable devices.

The evolution of soft robotics represents a transformative shift within the field of robotics, emphasizing versatility, safety, and efficiency. Central to this progression is the development of exosuits, wearable devices that leverage soft robotic technology to augment human biomechanics without the rigidity of traditional exoskeletons. This research primarily explores the integration of soft robotics into exosuit design, aiming to enhance human performance and mobility while ensuring comfort and minimizing the risk of injury. The genesis of soft robotics is marked by the adoption of compliant materials and bio-inspired designs, enabling sophisticated interactions with complex environments and delicate objects. This adaptability makes soft robotics especially suited for human-machine interfaces. Exosuits, as an application of soft robotics, capitalize on this by using textiles and soft composite materials to create structures that mimic and reinforce the body's natural movements. By leveraging principles such as cable-driven systems, pneumatics, and advanced sensor integration, exosuits promise not only to support those with mobility impairments but also to augment the capabilities of able-bodied users.

1.2 Research Motivation

Considering the daily increase in the population of elderly people with upper body disability and the decrease in birth rate, there is an increasing need for equipment that can help them to rehabilitate and increase their strength. Robotic devices have been able to perform essential tasks in industry, and their output has been excellent. After their successful application in industry, researchers have gone on to introduce the use of robots in medicine, in particular in rehabilitation. One of the most important reasons for using robots in rehabilitation is their repeatability. Considering that we need to perform a series of precise repetitive movements in rehabilitation so that the desired limb regains its previous strength, or the disabled member can repeat the last movements due to an external driving force, robots are one of the best alternatives. Also, the need to reduce treatment costs and offer easier access to rehabilitation equipment has led to an increase in the design and fabrication of portable robotic devices. All the above encourage us to design and build a soft wearable and portable robotic device for the shoulder, which is the first and most significant limb of the upper body.

1.3 Aim and Objectives

After investigating the robotic devices introduced over the last two decades and observing the design gaps in this area, we decided to design and build a new exosuit capable of covering three of the degrees of freedom of shoulder joints. To achieve the desired result, we have considered the following objectives:

1. Design a new soft exosuit that can cover three of the degrees of freedom of the shoulder joint.
2. Fabricate a soft exosuit that can cover three of the degrees of freedom of the shoulder joint.
3. Design soft lightweight portable exosuit so that the user can easily wear it.
4. Design and develop a suitable test bench to perform the required tests.

5. Design a spherical joint like the glenohumeral joint of the body with which to be able simulate tests.
6. Establish a mathematical model for movements with the proposed designed exosuit.
7. Conduct simulation and analysis of the movements with the proposed designed exosuit.
8. Finite Element Analysis to allow development of a best version of the fabricated exosuit.
9. Develop a control strategy and system for the proposed designed exosuit.
10. Experiments and verification.

1.4 Methodology

The methodology for completing this project will be implemented through a series of carefully planned steps, ensuring the thorough investigation and development of exosuit technologies in soft robotics. These steps are designed to address both theoretical and practical aspects of the research, where facilitating a comprehensive understanding and innovative outcomes will involve the following steps:

1. Comprehensive Literature Review: A detailed examination of existing scholarly articles, patents, and industry reports on soft robotics and exosuit technologies will be conducted. This review will help to pinpoint current trends, identify research gaps, and solidify the theoretical base for subsequent design and development.
2. Prototype Design and Fabrication: Drawing on the knowledge gained from the literature review, this phase involves the conceptualization and creation of exosuit prototypes. Emphasis will be placed on selecting appropriate soft materials, actuators, and sensors that align with the project's goals.
3. Developing an inverse kinematic analysis and mathematical model for these actuators.
4. Control System Development and Integration: This stage focuses on the development and fine-tuning of control algorithms that will allow the exosuits to interact seamlessly with users. The aim is to ensure that the exosuits can adapt to different user actions and environments in real time.
5. Performance Testing and Iterative Refinement: The prototypes will be tested under various conditions to evaluate their performance across multiple metrics such as

flexibility, strength. Feedback from these tests will guide iterative improvements to optimize the design and functionality of the exosuits.

6. Evaluating and validating the proposed designs: the proposed design will be evaluated by implementing an experimental evaluation of the system to assess its effectiveness.
7. Ongoing modification of the design system based on the evaluation, to improve the system performance and to optimize its design.
8. Finalizing conclusions, publishing results, and submitting a PhD thesis for examination

1.5 Organization of the Thesis

This thesis is structured into eight chapters, each dedicated to exploring various facets of the research conducted to achieve the objectives outlined previously.

- Chapter 1: Introduction:

  This chapter provides a broad overview of power-assistive and rehabilitation robotic devices. It discusses the motivation behind the research, as well as the aims and objectives of this PhD project. Additionally, it outlines the research methodology and enumerates the contributions made by the thesis.
- Chapter 2: Literature review:

  This chapter delves into the detailed study of soft and rigid robotics for upper limb rehabilitation, particularly focusing on the shoulder joint, by reviewing 60 innovative robotic designs. It discusses biomechanics, types of mechanisms like exoskeletons and exosuits, and their pros and cons for rehabilitation, highlighting the need for lighter, more personalized devices. This chapter also emphasizes the lack of extensive clinical trials to validate these devices, pointing to significant opportunities for future research and development in the field.
- Chapter 3: Design of *Cable Driven Shoulder Exosuit (CDSE)*:

  In this chapter, the backpack was designed with the primary objective of distributing the system's weight effectively across the backpack, ensuring it is lightweight and easily portable for the user.

- Chapter 4: Statics Analysis of the Cable-Driven Shoulder Exosuit (CDSE):

  In this chapter, a comprehensive mathematical model for the kinematics and statics of the Cable-Driven Shoulder Exosuit (CDSE) is presented, focusing on calculating forces, torques, and the centre of mass for arm movements like shoulder abduction, flexion, and horizontal flexion. The research addresses the complexities of translating these calculations from 2D to 3D, ensuring model accuracy and informing us as to the selection of motors and couplings, while incorporating a safety margin to handle unexpected variables.
- Chapter 5: *Finite Element Analysis (FEA)* and Fabrication of CDSE:

  This chapter provides a detailed analysis and fabrication overview of the CDSE, designed for shoulder rehabilitation. Through Finite Element Analysis (FEA), the study validated the exosuit's robustness under various load conditions and demonstrated its effectiveness across three prototype iterations, evolving from polylactic acid (PLA) to aluminium and then to carbon fiber. These advancements highlight the CDSE's potential as a customizable, lightweight, and effective rehabilitation tool, illustrating significant contributions to the field of soft robotics.
- Chapter 6: Inverse kinematics and Control of CDSE:

  This chapter highlights the CDSE and its significant impact on upper limb rehabilitation through soft robotics, emphasizing the role of precise control and manoeuvrability enabled by inverse kinematics, PID controllers, and detailed simulations. It demonstrates the CDSE's potential to facilitate complex rehabilitative movements, setting a foundational framework for future research at the intersection of technology and healthcare, with the promise of enhancing therapeutic outcomes and improving quality of life through innovative robotic solutions.
- Chapter 7: Experiment, Analysis and Discussion of CDSE:

  The comprehensive testing of the Cable-Driven Shoulder Exosuit (CDSE) across key movements (abduction, flexion, and horizontal flexion) has thoroughly evaluates its performance, resilience, and repeatability under loads ranging from 500 grams to 4000 grams and finally with a healthy candidate. Utilizing MATLAB and Simulink for precise data collection on movement trajectories, torque, velocity, and motor temperature, the experiments confirm the exosuit's design, and its potential to enhancing human movement for the purposes of rehabilitation, highlighting its adaptability and reliability in the field of soft robotic exosuits.

- Chapter 8: Conclusion and Future Work:
  This chapter concludes the entire research and presents a plan for future work.

1.6 List of Contributions

This thesis makes several significant contributions to the field of soft robotics, specifically in the development and application of exosuit technologies. These contributions not only advance the state of the art but also address practical challenges in the design and implementation of wearable robotic systems. The key contributions of this research can be outlined as follows:

1. Innovative Exosuit Design: Introduction of a novel Cable-Driven Shoulder Exosuit (CDSE) design that leverages soft robotic technologies to enhance mobility and strength in users (**coverage of three degrees of freedom of the shoulder joint as exosuit**).
2. Portable and lightweight device: ***total weight is around two kilograms***. Using the compliant materials and bioinspired mechanisms, ensuring that the exosuit is lightweight, comfortable, and capable of assisting natural human movements.
3. ***MATLAB's Simscape Multibody and Simulink***: Apply Simscape for these purposes: dynamic Simulation of exosuit, control system development and Testing, optimization of design parameters, integration, and system validation.
4. ***Static analysis around the joints and tendons.***

2 Chapter Two: Literature Review

2.1 Introduction

The importance of the role of the human upper limbs in daily life and performing personal activities is highly significant. Improper function of these limbs due to neurological disorders or surgery can greatly affect the daily activities performed by patients. This research aims to comprehensively review soft and rigid wearable robotic devices provided for rehabilitation and assistance, focusing on the shoulder joint. In the last two decades, many devices of this nature have been proposed; however, there have been only a few groups whose devices have had effective therapeutic capabilities supported by acceptable clinical evidence, and very few could be described as portable, lightweight, and user-friendly. Therefore, this comprehensive study could pave the way for achieving optimal future devices, given the growing need for such. Nearly 60 published articles on rehabilitation robots and upper limb assistants based on the shoulder joint were searched on Google Scholar, PubMed, Scopus, and IEEE. For a more precise comparison of the designs, the key factors of the articles are presented in a summary table. These factors were, the joints considered in the robotic devices, the types of actuators, the sensors, the types of devices, the degrees of freedom of the devices, portability, soft or rigid, the scope of the assistance offered by the devices, and the tests passed by each device. In this chapter, according to the identified key factors, a total of 60 comprehensive plans were reviewed and are presented in the form of a summary table. According to the results, the most commonly used plan was the exoskeleton, the most commonly used actuators were electrical, and the majority of devices were stationary and rigid. By performing these studies, the advantages and disadvantages of each method could also be determined and are also presented. The presented devices each represent a new approach and attitude in a specific field to solving the problems inherent to movement disorders and rehabilitation, which were in the form of prototypes, initial clinical studies, and sometimes comprehensive clinical and commercial studies. These plans need more comprehensive clinical trials to be considered complete and efficient plans. This chapter could be used by researchers to identify and evaluate the important features, strengths, and weaknesses of these plans to lead to the development of more optimal plans in the future.

2.2 Search Strategy

In this review, literature searches were conducted on Google Scholar, PubMed, Scopus, and IEEE based on relevant keywords on May 20, 2020. To obtain appropriate articles, filters in the titles of the articles and keywords have been used for this purpose so that articles close to those targeted can be found. The keywords used were ''soft and rigid robotics'', ''rehabilitation'', ''assistance'', and ''upper limb and shoulder joint'', which were used as search criteria in various combinations on the above websites. The number of initial articles obtained from all the mentioned sources was 978. After reviewing these, those directly related to the field of review were 120. Then articles that did not focus on the shoulder, whose presented systems were not fully understood and reviewed, and were tasked with moving prostheses instead of real human limbs were excluded from the review. From the short-list of 120 articles, 89 were selected that presented a unique design in this field for rehabilitation and basic daily tasks. These articles can be classified into three general groups: exoskeleton, exosuit and end-effector robots based on the mechanism, whose distribution was 54%, 13%, and 33%, respectively. Finally, articles in the field of end-effectors were excluded from this review because they were not wearable, and thus 60 designs were selected as suitable designs for review. Figure 2-1 shows the filtering process of the selected articles, whilst Figure 2-2 shows the percentage distribution chart of the two final selected designs separately.

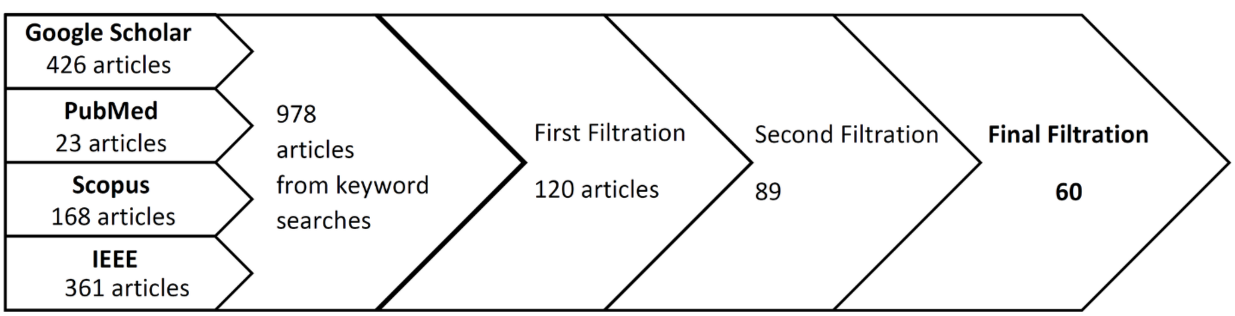

Figure 2-1: Filtering process for the selected articles.

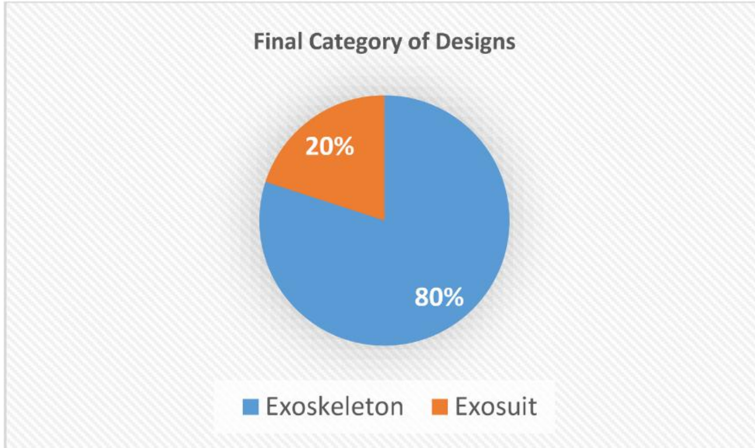

Figure 2-2: Distribution percentage chart based on final design classification.

Further, the number of published articles related to the two main structures (exoskeleton and exosuit) in the last two decades was searched for on the Scopus website, graphs for which are shown separately in Figure 2-3 and Figure 2-4. As shown in Figure 2-3, the number of articles slowly increases between 2000 and 2011, but from 2011 to 2018 the statists show a dramatic increase in the production of annual articles in this field, which in 2018 totalled 180 articles. In 2018, a turning point could be seen that by 2020 had become a decreasing trend in this field. Figure 2-4 also shows that the exosuit, as a concept, has appeared in the titles and keywords of articles since 2012. Of course, in the years prior this date, as shown in Table 2-3, exosuit designs have been used since 2004; but have been given other names, such as soft exoskeleton. As shown in Figure 2-4, this trend has been increasing between 2012 and 2020, two articles in 2012 to 25 in 2020. Due to the increasing requirement for lightweight and portable systems in the near future, we expect a further increase in the number of articles in the exosuit field. This data indicates that the number of research groups working on soft robotics is increasing, possibly due to their desirable characteristics.

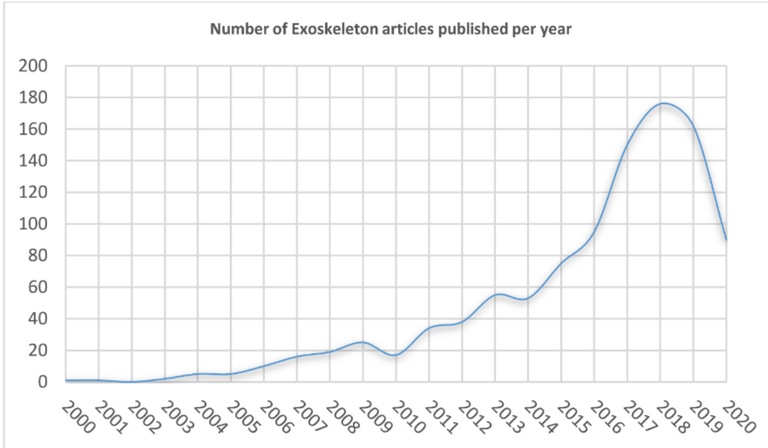

Figure 2-3: Number of exoskeleton articles published per year (TITLE-ABS-KEY (exoskeleton) AND TITLE-ABS-KEY (robotic)) [1].

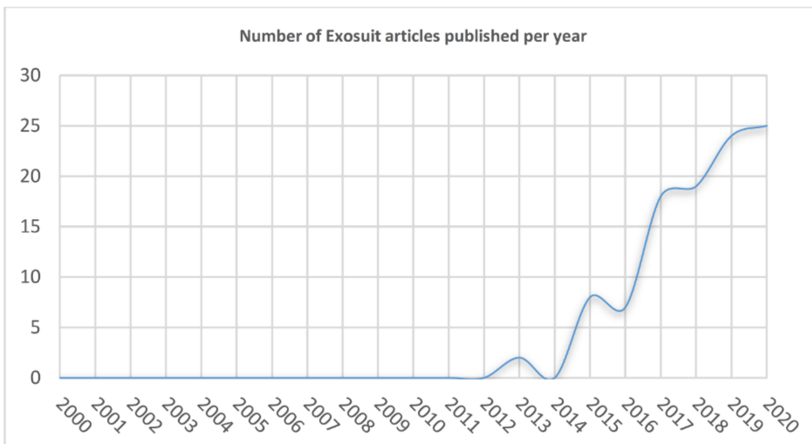

Figure 2-4: Number of exosuit articles published per year ((TITLE-ABS-KEY (Exosuit) AND TITLE-ABS-KEY (robotic)) [2].

2.3 Upper Limb Biomechanics

The main goal is to find better and easier solutions to help subjects with movement disorders, and it is thus very important to understand the anatomy and biomechanics of the human body. Complete and accurate knowledge is of considerable utility when designing robotic-based systems. Familiarity with the science of neuroscience and biomechanics, which is effective in identifying neuromuscular diseases and rehabilitation, can be effective in the field of exoskeletons and exosuits that allow for a cognitive and physical human-robot interaction (HRI) factor. Due to the fact that the human body is considered a framework for soft robotic systems, bio-inspiration is considered an important issue when designing such [3], [4].

2.3.1 Parts of Upper Limb and Bones

The upper limb is suspended from the trunk, and is divided into the shoulder, elbow, forearm, and hand. Figure 2-5 gives a view of the upper limb [5]. Unlike the lower limbs, which are used for mobility, support and stability, the upper limbs are used for hand placement in very mobile spaces. Also, anatomically, the upper limb of the human body can divide into three main joints: the shoulder, elbow, and wrist[6].

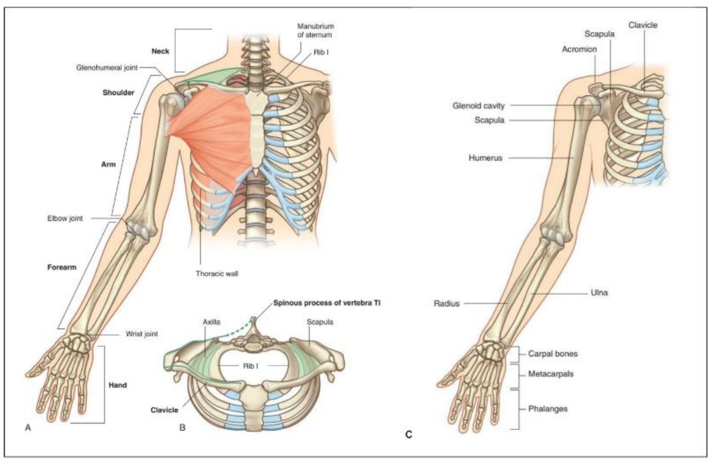

Figure 2-5: A) Anterior view of the upper limb, B) superior view, C) upper limb bones [5].

- Shoulder Joint

Three bones, the humerus, clavicle, and scapula constitute the bones of the shoulder, and the shoulder joint itself can articulate in four ways, the scapulothoracic, acromioclavicular, glenohumeral, and sternoclavicular, though the glenohumeral is considered the main connection of the shoulder [4]; Figure 2-6 shows the related images. The sternoclavicular junction is the only interface between the shoulder and the axial skeleton of the body. However, when describing the scapular movement on the thorax, the sternoclavicular is considered an articulation [3].

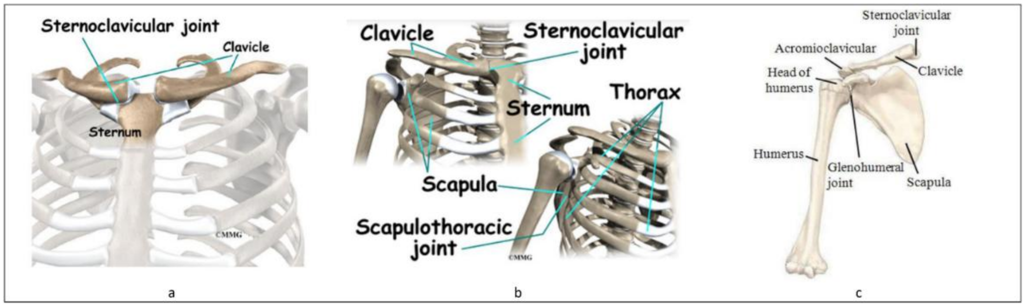

Figure 2-6: a) Location of the sternoclavicular [7]. b) Location of the scapulothoracic [8] c) View of the shoulder bones [3].

The glenohumeral joint (shoulder joint) allows the arm to move more freely on three general axes, extending the reach of the hand. The arm movements in this joint are abduction, adduction, flexion, extension, internal rotation, external rotation and circumduction, images of which are shown in Figure 2-7 [5].

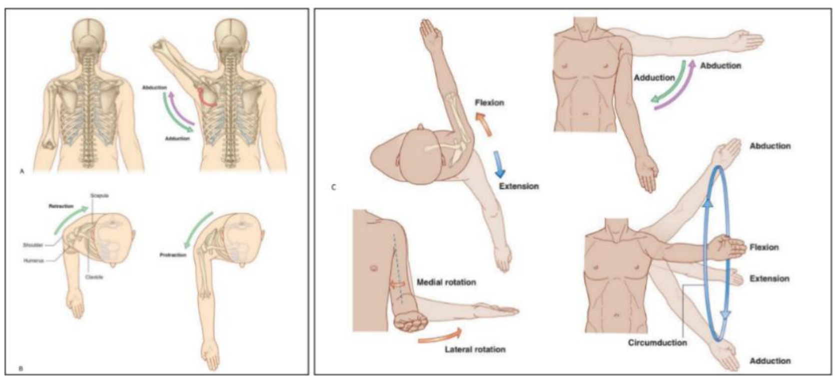

Figure 2-7: Glenohumeral movements (A &B movement with a focus on scapula, C. all movements) [5].

In terms of design, the shoulder complex is often modelled as a ball and socket joint, also referred to as a spheroid joint [3], [9], which is formed by the proximal humerus and the glenoid cavity of the scapula. However, the position of glenohumeral joint rotation centre changes with upper arm movement. Important movements of the shoulder complex include flexion/extension, abduction/adduction, and internal/external rotation, and in most cases this complex is known in research as a limb with three DOF [3], though in some other designs internal/external shoulder rotation is used less than other shoulder DOFs [4], [10]. Due to the constantly changing centre of rotation of the shoulder joint, it is necessary for some designs to be modelled as a five or six DOF systems, instead of modelling as a typical ball and socket joint [4]. In general, the shoulder's complex movements can be categorized into three movements on the shoulder itself, and other movements that occur in the shoulder girdle. Figure 2-8 demonstrates this point.

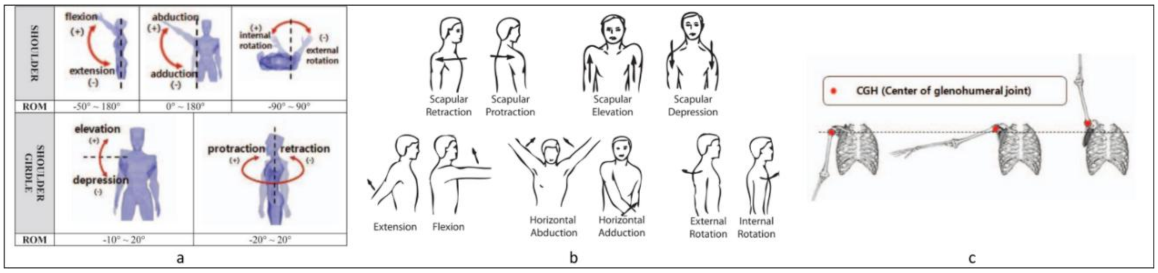

Figure 2-8: a) Shoulder and shoulder girdle movement [11]; b) Five movements of the shoulder complex [12] c) Displacement of the glenohumeral centre in great displacements [11], [13].

While this assumption is considered almost exclusively for small glenohumeral motor angles it is significantly deviated from in the course of larger movements because the thoracohumeral joint has a movable centre of rotation [13][14]. Large misalignments occur in the shoulder through altered motor axes. Figure 2-9, for example, shows the estimated centre of rotation in the shoulder [14]. Also, the position of the humerus from 0 to 180 degrees is illustrated in Figure 2-10 so as to understand the displacement of the centres [13].

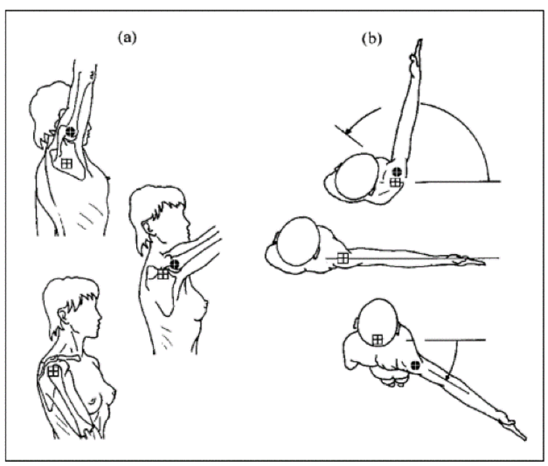

Figure 2-9: Changing the centres of rotation in large angle movements of the shoulder joint [14].

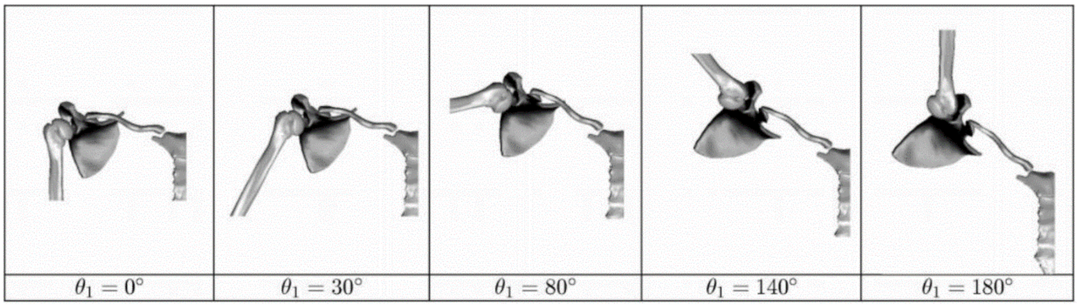

Figure 2-10: Changing the humerus angle to show the change in the centre of rotation of the shoulder [13].

There are several ways to deal with the additional translational movement, which have been studied by a number of groups, [11] [12] [15]. One strategy is to add passive joints. Of course, adding passive joints to the actuated skeleton also negates the robot's statically determination, and whilst this gives the patient more freedom it also reduces the mechanical guidance and support offered to the limb [13]. In exoskeletons, since the human arm is almost fixed in the robot arm, the relative distance between the arm holder and *the Centre Of Rotation (COR)* of the human shoulder joint is almost essentially constant. Therefore, the distance between the arm holder and the COR of the robot shoulder joint should be adjusted, on average, according to the shoulder movement to reduce the effects of difference in position between the CORs of the robot shoulder and human shoulder [16]. Shoulder girdle movement is highly significant in terms of orienting and stabilizing the arm during daily activities. This movement is nonlinear in that is determined by the orientation of the humerus and is, of course, different for each person. Therefore, it is inappropriate to use this motion prior to accurate calculations, because if an exoskeleton robot fails to mimic the patient's shoulder girdle movement well, the robot's axes will not match the patient's body, reducing range of motion (ROM) resulting discomfort for patients in the long run [11].

- Elbow and Forearm

The elbow is made up of three bones, the radius, ulna, and humerus, but is primarily modelled as a uniaxial hinge joint [3], [9]. The size of the elbow joint can be used to find the axis of rotation of the elbow joint in exoskeleton robots, and this is not generally problematic as an approach. The main movements in the elbow joint include the extension and flexion of the forearm (Figure 2-11-A). Forearm movement occurs by the ulna and radius bones at the distal end and by rotating the inner bone on the ulna head (pronation). However, to convert the palm-posterior position to the palm position, the radius must also rotate on the ulna side (supination) (Figure 2-11B, C)[5]. In general, the elbow and forearm are considered a member with just one DOF.

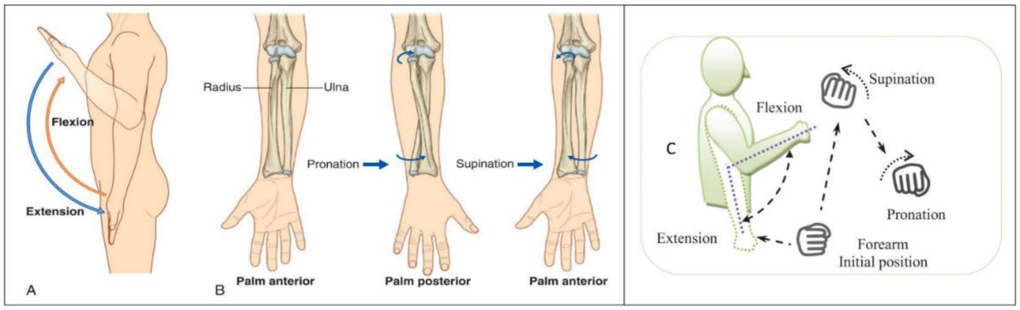

Figure 2-11: Elbow and forearm movements. (A). extension and flexion in the elbow. (B). Forearm bones and pronation and supination movements [5]. (C) Another view of arm and forearm movements[17].

- Wrist

The wrist joint includes abduction, adduction, flexion, extension, and circumduction movements (Figure 2-12) [5]. These movements, together with the movements of the upper limb joints, allow the wrist to be placed in a wide range of positions relative to the body [5]. The carpus joint is a formable joint that connects the forearm to the hand, and in some sources, the wrist joint has been interpreted as being an oval joint [18]. In general, the carpus is introduced as a member with two DOFs in the majority of studies [6], [10], [14]. In other words, when we consider that extension and flexion movements occur on one axis and also that the ulna and radius movements occur on another, there will be a slight offset between these axes, which researchers have measured to be about 5 mm and as shown in Figure 2-13[3]. Finally, each of the eight carpal joints can allow only a limited range of motion, and the set thus moves together as an allied unit.

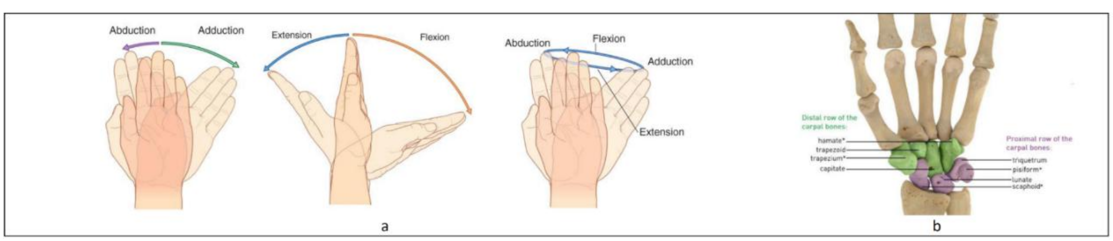

Figure 2-12: a. Hand movements in the wrist joint [5] b. Schematic of the eight wrist bones [19].

The bones of the hand are made up of the carpals, metacarpals, and phalanges (Figure 2-13). The five fingers of the hand are the thumb, index, middle, ring, and little fingers. The hand is used as a mechanical as well as a sensory tool. One of the most important mechanical functions of the hand is to grip and manipulate objects. The sensory cortex of the brain is also dedicated to the interpretation of information from the hand, especially from the thumb, which is relatively large compared to many other areas of the skin [5].

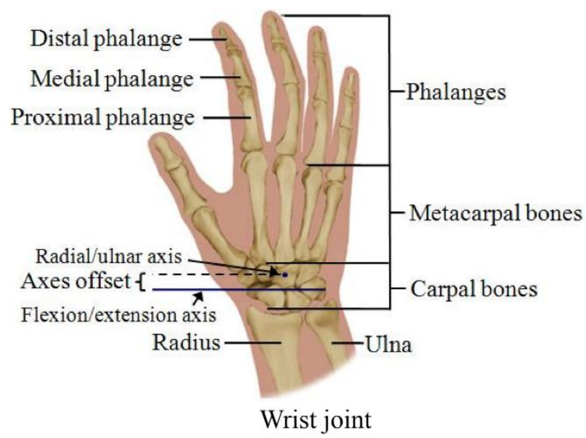

Figure 2-13: Wrist and finger bones and offset between the two axes [3].

The bones in the fingers are the phalanges. The thumb has two phalanges, while any other finger has three. The metacarpophalangeal joints are biaxial condylar joints (ellipsoidal joints) that allow flexion, extension, abduction, adduction, and circumduction (Figure 2-14).

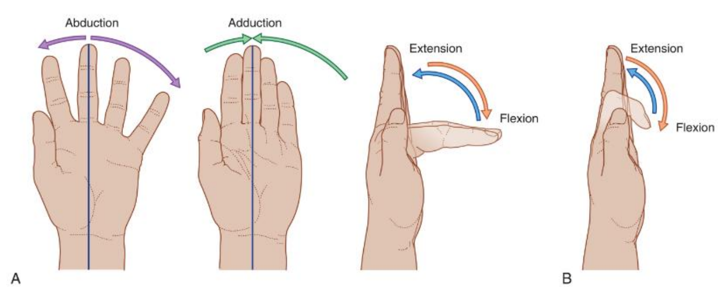

Figure 2-14: Movement of fingers, A. Metacarpophalangeal; B. Interphalangeal [5].

2.3.2 Muscles

- Shoulder Muscles

Certain shoulder muscles, such as the Levator scapulae, trapezius, and rhomboids, connect the clavicle and scapula to the trunk. Other muscles connect the clavicle, scapula, and trunk to the proximal end of the humerus. These muscles include the pectoralis minor, pectoralis major, teres major, deltoid and latissimus dorsi (Figure 2-15-A, B)[5]. The most important of these muscles are the four rotator cuff muscles (infraspinatus, subscapularis, teres minor and supraspinatus muscles) that connect the scapula to the humerus and support the glenohumeral joint (Figure 2-15-C).

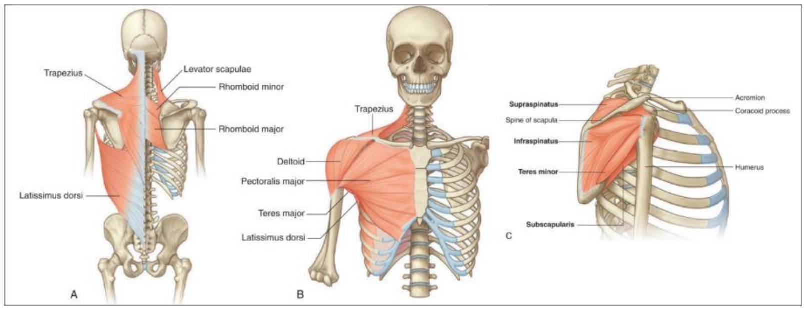

Figure 2-15: Shoulder muscles. A. Posterior shoulder; B. Anterior shoulder; C. Rotator cuff muscles [5].

The shoulder has a total of six important muscle groups: deltoid, four rotator cuff muscles (infraspinatus, subscapularis, supraspinatus, and teres minor), and teres major. Figure 2-16 illustrates each of these muscle groups:

Figure 2-16: Images of the six main shoulder muscles [20].

- Elbow Muscles

The most important elbow muscles involved in flexion and extension movements are shown in Figure 2-17. The brachialis, biceps brachii, brachioradialis, and coracobrachialis muscles are involved in elbow flexion, and the triceps brachii and anconeus are also responsible for elbow extension movements [9].

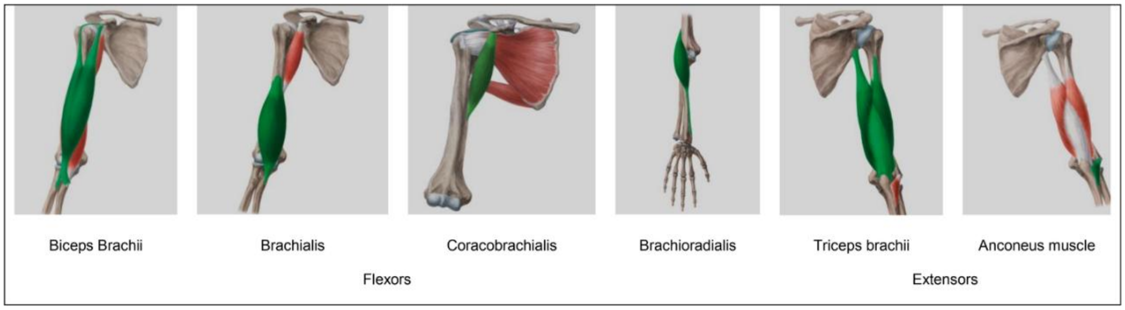

Figure 2-17: Images of the various elbow muscles [21].

- Forearm and Wrist Muscles

The forearm muscles can be categorized into two major groups: the anterior and the posterior. Anterior muscles are formed in four layers from the superficial layer to the deep layer. Figure 2-18 shows the forearm muscles on the left hand in their different layers. Also, the forearm, which has been considered in research to be a limb with a just a single degree of freedom, is of great importance in daily activities such as turning a key to open a door, opening a drinking water bottle, and so on. Movement of the wrist joint can increase the direction of achievement to increase the flexibility of the grip. The flexor carpi radialis muscle plays the most important role in flexion, whilst the flexor carpi ulnar plays the most important role in adduction and the extensor carpi radialis in abduction [22].

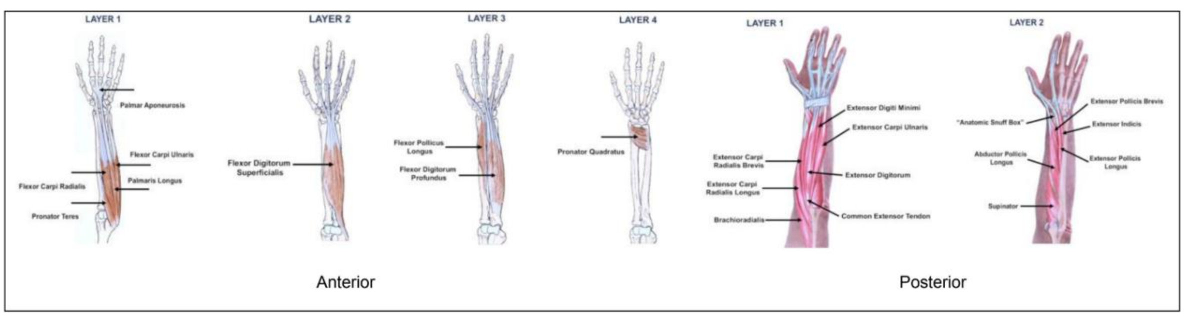

Figure 2-18: Forearm muscles [21].

- Hand Muscles

Generally, the hand muscles can be categorized into five different groups, as shown in Figure 2-19.

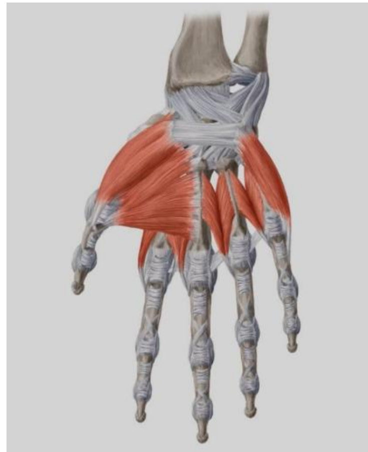

Figure 2-19: The muscles of the hand [9].

The first group is the dorsal interossei muscles, which are the four muscles attached to the metacarpal bones of the fingers; the function of these muscles is to assist in abduction and adduction movements. The second group are the palmar interossei muscles, which are the three muscles attached to the metacarpal bones of the fingers.; their function is to help the pulling movement of little, index and ring fingers in the transverse direction. The next group are the lumbricals muscles, composed of four small muscles that cause extension and flexion movements. The muscles of groups 1 to 3 above comprise the metacarpal muscles. The fourth group of muscles is the hypothenar, which consists of four different muscles and is located on the little finger, and whose function is to help flexion and extension of the little finger. The final group of hand muscles is the thenar, which consists of four different muscles whose task is to help the thumb to move in different directions. Also, muscles of the fifth group can make contact between the thumb and all four other fingers of the hand. Images of these five muscle groups are given in Figure 2-20.

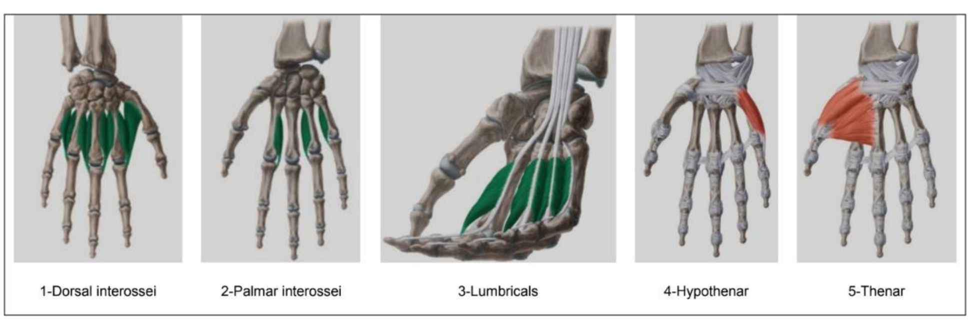

Figure 2-20: Separate images of the five groups of muscles of the hand [20].

2.3.3 Range of Motion

Upper limb movements are generally categorized into two areas, one for performing important daily activities and the other for performing general tasks. In most cases, researchers have provided plans that can be used to help perform important daily tasks. Researchers have introduced ROM of different parts of the human upper limb in various studies and then compared the data obtained from the design of the systems provided by them with the original data and through this study, the percentage of motion overlap of the proposed systems with the required amplitude has been measured [23], [24], [25], [26]. For example, Sugar et al. considered a sample with a specific height and weight as indexes to obtain their data, and accordingly design their system. Finally, anthropomorphic data can be converted by scaling a first model based on the weight and height of the new user for other cases [27]. ADLs include tasks such as drinking, eating, combing one's hair, etc. The complete mechanism should be able to move the shoulder with three DOFs, the elbow with one DOF, the forearm with one DOF, the wrist with two DOFs, and also include the action of gripping with the fingers[28]. For example, Carignan et al.; compared the upper limb movement range with seven different robot designs in Table 2-1 using the average data for 39 men for the range of motion of the human arm. Table 2-2 also compares five robot designs via the average data obtained for 39 men in relation to the maximum torque applied to the limbs [23].

Table 2-1: Comparison of human arm range of motion with seven different designs (degree) [23].

Joint	Man	Exos	Dex	Fre	GIA	Sen	HD	MB
Shoulder flex/ext	188/61	120	180	130/52	55/36	150/30	180/50	130
Shoulder abd/add	134/48	120	180	28/18	73/73	50/0	180/0	135
Shoulder med/lat	97/34	100	180	90/90	77/81	60/60	90/90	260
Elbow flex/ext	142/0	100	105	166/-3	89/15	90/0	115/0	135
Forearm pro/sup	85/90	100	105	90/90	99/88	90/90	90/90	215
Wrist flex/ext	90/99	-	180	38/39	50/20	60/60	70/90	90
Wrist abd/add	47/27	-	100	57/52	80/80	15/15	55/25	30

Table 2-2: Comparison of maximum torque obtained in upper torso members with the proposed designs (Nm) [23].

Joint	Human	Exos	Dex	Fre	GIA	pMA
Shoulder flex/ext	115/110	6.4	97	34	20	30
Shoulder abd/add	134/94	6.4	97	34	20	27
Shoulder med/lat	-	2.3	50	17	10	6
Elbow flex/ext	72.5/42.1	1.6	50	17	10	6
Forearm pro/sup	9.1/7.3	0.4	50	5.6	2	5
Wrist flex/ext	19.8/10.2	-	5.5	2.8	-	4
Wrist abd/add	20.8/17.8	-	5.5	2.8	-	4

2.4 The Framework of the Literature

As stated above parts, 60 designs were ultimately selected as the final designs for review, for which the following frameworks were considered in terms of comparing the designs:

1. Types of mechanism
2. Rigid or soft robotics
3. Portability
4. Types of actuators
5. Types of sensors
6. Types of power transmission systems
7. Types of control units
8. Status and details of clinical tests

In the following, additional explanations will be provided for each of these sections. The results of reviewing all designs are summarized in Table 2-3, and for working groups that have proposed different designs, each is listed in the table.

Table 2-3: Summary of the designs presented over the last two decades, relying on having a shoulder joint.

Year	Supported Movements	Actuator system	Power transmission	Sensors	Type	DOF	Portable	Soft or Rigid	Purpose	Verification
2001 [29]	Shoulder (FE/AA/RT), Elbow (FE), Forearm (PS)	DC motor	Drive cables, reduction gearbox and toothed belt drive	Joystick	Exoskeleton	5	Wheelchair mounted system	Rigid	Physical therapy and power assistance	One healthy subject
2003 [26]	Shoulder (AA/ FE/RT), Elbow (FE), Forearm (PS), Wrist (AA/FE)	(PAMs) Pneumatic	Cables, double groove pulleys	Joint position and torques	Exoskeleton	7	No	Rigid	Rehabilitation	Prototype
2003 [16]	Shoulder (FE/AA)	DC motor	Drive wires	sEMG and wire tension sensors and fuzzy-neuro controller	Exoskeleton	2	No	Rigid	Human assistance	One healthy subject
2004 [30]	Shoulder (FE/AA/RT), Elbow (FE)	Pneumatic	Mckibben muscles	----	Exosuit	4	No	Soft and Rigid	Rehabilitation	Prototype
2004 [31]	Shoulder (AA/ FE/ RT), Elbow (FE), fingers (GR)	Elastic bands	Linkages	Position sensors, grasp force, Joint angles	Exoskeleton	5	Wheelchair mounted system	Rigid	Physical therapy	65 chronic strokes
2005 [32]	Shoulder*, Elbow	Electrical motors + ABB robots	Robots	End-point torques	Exoskeleton	12	No	Rigid	Physical therapy	22 stroke +8 traumatic brain injury + 8 chronic strokes + 4 healthy subjects
2005 [33]	Shoulder (FE/AA/RT), Elbow (FE)	Brushed DC motor	Custom made mechanical components	Position and force sensors	Exoskeleton	4+2	No	Rigid	Physical therapy	Healthy subjects
2005 [23]	Shoulder (FE/AA/RT/V	Brushless DC motor	Linkages	Force and	Exoskeleton	5	No	Rigid	Rehabilitation	Numbers of subjects

	D), Elbow (FE)			torque sensor						
2006 [34]	Shoulder (AA/FE), Elbow (FE), Wrist (FE/ AA)	DC and AC motor	Linkages	sEMG	Exoskeleton	5	No	Rigid	Rehabilitation	Prototype
2006 [35]	Shoulder (AA/FE/ HD), Elbow (FE), {Fingers grasping}	Pneumatic	Linkages	MEMS accelerometers, joint angles, grasp force, cylinder pressure	Exoskeleton	4+1	No	Rigid	Physical therapy	11 chronic strokes
2006 [14]	Shoulder (FE/AA / /RT/ VD/HD), Elbow (FE), Forearm (PS), Wrist (AA/FE)	Not specified	Bowden cable transmissions	Joint angle	Exoskeleton	9	No	Rigid	Physical therapy	Prototype
2007 [36]	Shoulder (FE/AA/RT), Elbow (FE)	Pneumatic	Mckibben muscles	IEMG	Exosuit	4	No	Soft and Rigid	Human assistance	5 healthy subjects
2007 [37]	Shoulder (AA/FE/AA/RT/HD), Elbow (FE), Forearm (PS), Wrist (FE)	Brushless DC motor	Linkages, tooth belt pulleys box, semi-circular guide	Position and force sensors	Exoskeleton	7	No	Rigid	Rehabilitation	Prototype
2007 [38]	Shoulder (AA/FE/ RT), Elbow (FE), {Forearm (PS)} s	Electric motor	Tendon transmissions	Force sensor and EMG	Exoskeleton	4+1	No	Rigid	Physical therapy	Healthy subject + 9 chronic strokes
2007 [39]	Shoulder (AA/FE/ RT/VD), Elbow (FE), {Forearm (PS)}	Brushless DC motor	Linkages	Force-torque sensor, load cell	Exoskeleton	5+1	No	Rigid	Rehabilitation	Prototype
2007 [40]	Shoulder (AA/FE/RT),	Brushed motors	Cable Drive Systems	Forces/torques/po	Exoskeleton	7	No	Rigid	Human assistance	One healthy subject

	Elbow (FE), Forearm (PS), Wrist (AA/FE)			sition sensors, sEMG, joint angles, angular velocities and						
2007 [27]	Shoulder (FE), Elbow (FE), Forearm (PS), Wrist (FE)	Pneumatic (PAMs)	Linkages	joint angles, inertial sensor, pressure sensors	Exoskeleto n	4	No	Soft	Rehabilitation	16 stroke patients
2007 [15]	Shoulder (AA/FE/ RT/ HD/ VD), Elbow (FE)	Electric motor	Linkages, pulley, and cable-drive transmission	Joint torque and joint angle	Exoskeleto n	6	No	Rigid	Rehabilitation	Prototype
2007 [41]	Shoulder (AA/FE/ RT), Elbow (FE), (Forearm (PS), Wrist (FE) optional)	DC brushed motor	Linkages - gearbox - belt drive	Position sensors, joint angles with grasp force	Exoskeleto n	4+2	No	Rigid	Rehabilitation	Commercial system
2008 [42]	Shoulder (RT /AA), Elbow (FE), Forearm (PS), Wrist (FE)	Pneumatic (PAMs)	Linkages	Actuator pressures and Joint angles	Exoskeleto n	5	No	Soft	Rehabilitation	Two able-bodied subjects
2008 [43]	Shoulder (AA /FE), Elbow (FE)	DC motor	Cable driven, linkages and pulleys, chain and sprocket mechanism	sEMG, force sensor	Exoskeleto n	3	Wheelchair mounted system	Rigid	Human assistance	Healthy subjects
2008 [44]	Shoulder (AA FE//RT), Elbow (FE)	Rotational hydro-elastic actuators (rHEAs)	Linkages	Torques and Joint angles	Exoskeleto n	4	No	Rigid	Rehabilitation	Software base
2008 [45]	Shoulder (AA/ FE/RT), Elbow (FE)	Brushless DC motor	Linkages and Spiro-conical gear systems	Torques, velocity and Joint position,	Exoskeleto n	4	Wheelchair mounted system	Rigid	Physical therapy	Prototype

				force sensors						
2008 [46]	Shoulder (RT/FE), Elbow (FE), Forearm (PS), Wrist (AA /FE)	DC motor	Cable drives, pulleys, bevel gear	Force and torque sensor	Exoskeleto n	6	No	Rigid	Human assistance	One healthy subject
2008 [47]	Shoulder (FE/AA/RT), Elbow (FE)	DC Motor	Cable actuators and screw	Hybrid Position - force control	Exoskeleto n	4	Yes	Rigid	Human assistance	Prototype
2009 [48]	Shoulder (AA/ FE/RT), Elbow (FE)	Hydraulic disk brakes (SEA)	Linkage	Joint angles and torques, load sensors	Exoskeleto n	4	No	Rigid	Rehabilitation	Healthy subjects and stroke subjects
2009 [49]	Shoulder (AA/ FE/RT), Elbow (FE), {Forearm (PS)}	Two different Custom-made actuation groups frameless brushless motor and DC motor	Linkage, gear, Cable drive	Joint torques, force sensor	Exoskeleto n	4+1	No	Rigid	Rehabilitation	Prototype
2009 [50]	Shoulder (AA/FE/RT), Elbow (FE), Forearm (PS), Wrist (AA /FE)	Servo DC motor	Linkage, gear, Cable drive	sEMG, force/ torque sensors	Exoskeleto n	7	No	Rigid	Human assistance	2 healthy subjects
2009 [51]	Shoulder (AA/ FE/RT), Elbow (FE), Forearm (PS), Wrist (AA /FE)	Hydraulic Bilateral Servo Actuator	Linkage, HBSA	Pressure sensors	Exoskeleto n	7	No	Rigid	Rehabilitation	Cerebrovascul ar patients
2009 [52]	Shoulder (AA/FE/ VD /RT/{HD}), Elbow (FE), Forearm (PS),	Electric motor	Linkage, cable and pulley	Joint anglesan d torques	Exoskeleto n	8+2	No	Rigid	Rehabilitation	Healthy subject

	Wrist (FE), Hand(open/grasp)									
2010 [53]	Shoulder (AA/FE/RT), Elbow (FE)	Pneumatic	Linkage, Cylinder	Cylinder pressure, Joint angles	Exoskeleton	4	No	Rigid	Rehabilitation	Prototype
2010 [54]	Shoulder (FE/AA), Elbow (FE), Forearm (AA)	DC motor	Linkage, driven pulleys, cable	sEMG	Exoskeleton	4	Wheelchair mounted system	Rigid	Human assistance	One healthy subject
2011 [55]	Shoulder (FE/AA)	Electrical jacks	Poly-articulated structure, Bowden cable transmission	Angular encoder	Exoskeleton	2	No	Rigid	Rehabilitation	One healthy subject
2011 [11]	Shoulder (FE/AA/RT/HD/VD/UR)	Electric motor	Linkage	Force and torque sensor	Exoskeleton	6	No	Rigid	Rehabilitation	Software base
2012 [56]	Shoulder (AA)	Brushless DC motor	Cable-driven transmission	IMU sensors	Exosuit	1	Yes	Soft	Rehabilitation and assistance	Prototype
2012 [57]	Shoulder (AA FE/RT), Elbow (FE), Forearm (PS)	DC brushless motor	Linkage, planetary gearhead, Cable	Torques and Joint angles	Exoskeleton	6x2	No	Rigid	Rehabilitation	14 stroke patients
2012 [12]	Shoulder (AA/FE/RT/HD/VD), Elbow (FE)	Graphite-DC brushed motors	Linkage, Belt drive transmission	Torques sensor	Exoskeleton	6+1	No	Rigid	Rehabilitation	Two healthy volunteers
2013 [58]	Shoulder (AA /FE), Elbow (FE), Forearm (PS), Wrist (FE), Fingers grasp (assistance)	DC brakes or elastic wires, DC motor (optional), FES (optional)	Springs and linkages (optional)	sEMG, manual input, Bran Computer Interface; RFID—object label	Exoskeleton	6	Wheelchair mounted system	Rigid	Human assistance	Two MS patients and three spinal cord injury
2013 [59]	Shoulder (FE /AA), Elbow (FE), Wrist (AA/FE)	AC servo motor (Shoulder and elbow) + DC servo	Linkage	Position sensor	Exoskeleton	5	No	Rigid	Rehabilitation	Prototype

		motor (Wrist)								
2013 [60]	Shoulder (AA), Elbow (FE), Forearm (PS), Wrist (FE)	DC motor+ zero-backlash harmonic gear	Linkage	Force and torque sensor	Exoskeleton	4+2	No	Rigid	Physical therapy	3 stroke survivors, 2 healthy subjects
2013 [61]	Shoulder (AA/FE)	DC Servo motor	Flexible continuum joint brace	----	Exoskeleton	2	No	Rigid	Rehabilitation	Prototype
2014 [62]	Shoulder (AA/FE/RT), Elbow (FE), Forearm (PS), Wrist (FE)	Electric motor	Bevel gear transmission	Force and torque sensor, pressure sensor	Exoskeleton	6	No	Rigid	Rehabilitation	Software base
2014 [17]	Shoulder (AA FE//RT), Elbow (FE), Forearm (PS), Wrist (AA /FE)	Brushless DC motor	Linkage, gear	Force sensors	Exoskeleton	7	No	Rigid	Rehabilitation	Four healthy humans
2016 [63]	Shoulder (AA/FE), Elbow (FE), Forearm (PS)	Industrial Robot manipulator, servomotor	Linkage	Force sensors	Exoskeleton	4	No	Rigid	Rehabilitation	Three subjects
2016 [64]	Shoulder(A)	Pneumatic	Thermoplastic polyurethane (TPU) fibers	Accelerometer, pressure sensor	Exosuit	1	No	Soft	Rehabilitation	One healthy subject
2016 [65]	Shoulder(A/F), Elbow(F)	DC motors, Twisted string actuator (TSA)	Cable-driven transmission	Angles sensor	Exosuit	3	Yes	Soft	Rehabilitation	4 healthy subjects
2017 [10]	Shoulder (FE/AA), Elbow (FE), Forearm (PS), Wrist (AA/FE)	DC motor	Epicyclic gear trains, planet wheel, Cable driven transmission	----	Exoskeleton	6	No	Rigid	Human assistance	Software base
2017 [66]	Shoulder (FE/AA/RT/V	Brushless DC motor	Harmonic Drive gears	Force and	Exoskeleton	6+2	No	Rigid	Rehabilitation	Software base

	D/RD), Elbow (FE), {Forearm (PS), Wrist (FE)}			torque sensor						
2017 [67]	Shoulder (AA/RT)	Pneumatic	Textile based soft actuators	sEMG	Exosuit	2	No	Soft	Human assistance	Three healthy males
2017 [68]	Shoulder (FE)-Elbow (FE)	Pneumatic	Linkage	Pressure sensors	Exoskeleton	2	No	Soft	Rehabilitation	One healthy subject
2017 [69]	Shoulder (FE/AA)	Cam structure + rubber band	Cable-driven transmission	sEMG	Exosuit	(2)	Yes	Soft	Human assistance	Six healthy subjects
2018 [70]	Shoulder (AA/ FE/RT), Elbow (FE), Forearm (PS), Wrist (AA /FE)	Brushless DC motor	Cable-driven transmission	sEMG	Exosuit	7	No	Soft	Rehabilitation	Healthy and stroke patients
2018 [71]	Shoulder (AA)	Pneumatic fabric bladders	Spine	EMG signals	Exoskeleton	1	No	Soft	Human assistance	Pilot test on 3 healthy participants
2018 [72]	Shoulder (FE)-Elbow (FE)	Brushless DC motor	Cable-driven transmission	EMG signals	Exosuit	2	Yes	Soft	Human assistance	Healthy participant
2018 [73]	Shoulder (AA/FE), Elbow (FE)	Brushless DC motor	Cable-driven transmission	IMU sensors	Exosuit	3	Yes	Soft	Rehabilitation	Healthy and stroke patients
2019 [74]	Shoulder (FE)	Brushless DC motor	Bowden cable, planetary reduction stage	EMG, position sensor+6 -axis load cell, IMU	Exoskeleton	1	Yes	Soft and Rigid	Human assistance	Prototype/ 5 healthy participants
2019 [75]	Shoulder (AA/FE), Elbow (FE)	Stepper motor	Bowden cable, Linkage, gears	EMG, accelerometers, strain gages, thermostats, oximeters,	Exoskeleton	3	Yes	Soft and Rigid	Rehabilitation	Software base
2019 [76]	Shoulder (RT/AA)	String pots	Cable-driven transmission	String potentiometer	Exosuit	2	Yes	Soft	Rehabilitation and assistance	Prototype
2020	Shoulder	DC Servo	Toothed belt,	Attitude,	Exoskeleto	6	No	Rigid	Rehabilitation	Prototype

[6]	(AA/FE/RT), Elbow (FE), Wrist (FE/AA)	motor	arc-shaped rack+ rope mechanism	angular displace ment and dynamic torque sensors	n					
2020 [77]	Shoulder (FE)- Elbow (FE)	Brushless DC motor	Cable-driven transmission	Position sensor and goniomet er	Exosuit	2	Yes	Soft	Rehabilitation	4 healthy subjects

Notes:

- Shoulder rotations (A (Abduction)/ A(Adduction) /F (Flexion)/ E(Extension)/R (internal rotation)/ T (external rotation))
- Shoulder translations (scapular protraction/retraction HD (horizontal displacement) and elevation/depression HD (vertical displacement))
- Elbow (F (Flexion)/ E (Extension))
- Forearm (S (Supination)/P (Pronation))
- Wrist (F (Flexion)/ E(Extension)/ A (Abduction)/ A (Adduction))
- DOF: degrees of freedom/ AC: Alternating current/ DC: Direct current
- {} related to passive motions.
- 4+2: 4 related to active DOFs and 2 related to passive DOFs

2.4.1 Types of Mechanism

As mentioned in previous sections, a total of three types of mechanisms were found in the literature evaluation that have been used in the field of rehabilitation and in performing the main ADLs, among which end-effectors were removed because they are not wearable. Easy adjustment with different arm lengths is one of the most important advantages of end-effector-based robots; their disadvantage is that, in general, the arm posture is not completely determined by the robot and has interacted from one point. As a result, their ROMs are limited, and exoskeleton robots are generally better suited to training activities that require a large ROM [13]. The exoskeleton is an external mechanism that transmits the torques and forces generated by actuators near human joints through the joints they make with the outer part of the upper limb[78], whilst exosuits are soft exoskeletons for which the anatomical structure of the human body forms the main framework [79]. Images of all three samples are shown in

Figure 2-21; in this chapter, as mentioned earlier, only two designs, the exoskeleton and exosuit, have been examined in terms of their wear ability.

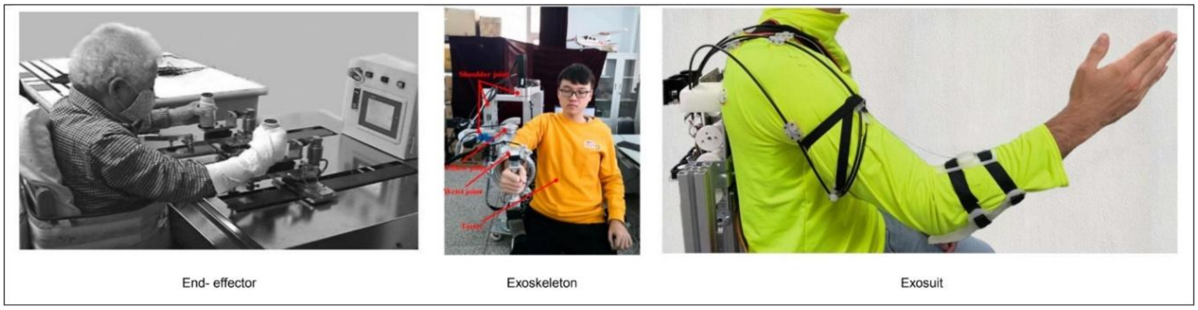

Figure 2-21: Images of end-effector[80], exoskeleton [6]and exosuit [77]designs.

- Exoskeleton

Exoskeletons are based on the architecture of industrial robots and include actuators, mechanisms, and similar materials. They also include the lower and upper limbs, which act directly on the human body [81]; this report, however, investigates only the upper limbs. Despite the existing complexities, many upper-body exoskeletons design for the purpose of aiding rehabilitation have been developed and tested over the last two decades [74]. Ideal robotic rehabilitation devices should be able to: 1) train the full workspace of the human body, 2) activate the joint to stimulate precise ergonomic movements in the patient, and 3) should not cause discomfort or safety hazards when moving. According to current research and knowledge, there are no wearable or end-effector-based rehabilitation devices that have all these benefits and act as a complete system [14].

Rehabilitation exoskeletons can improve the quality of life of patients with neuromuscular diseases, such as those caused by stroke or spinal cord injury. Also, in the case of using exoskeletons, this system will delay the onset of fatigue by reducing muscle activation in healthy users when doing physical work with the upper limb(s), while users with mobility impairments are able to move their upper arm(s) through support from the exoskeleton [82]. As mentioned, 48 out of the 60 existing designs included exoskeletons, of which 73% are provided as stationery, 17% portable, and 10% as a wheelchair-mounted systems. Also, 72% of the designs are presented as rigid, 23% as soft, and 5% as a combination of both soft and rigid designs. Figure 2-22 shows some selected images of such designs.

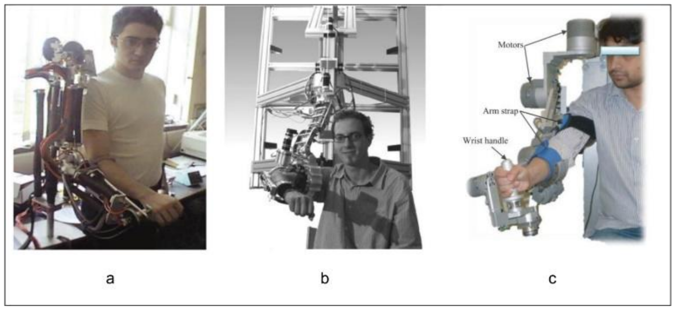

Figure 2-22: Images of designed exoskeletons: a [17], b [33], c [26].

- Exoskeleton Workspace

Exoskeletons can have different degrees of freedom depending on their design and expected performance [83]. In the proposed designs, exoskeletons with one degree of freedom [82] [74] and with 12 DOFs are provided [84]. In general, the human arm movement in exoskeletons is usually designed with seven DOFs [23]. As the number of DOFs increases, so does the complexity of the system, although in the case of whole-body rehabilitation systems the number of can DOFs reaches nine, ten, or even more [52][32]. Figure 2-23 gives a schematic of the upper limb DOF.

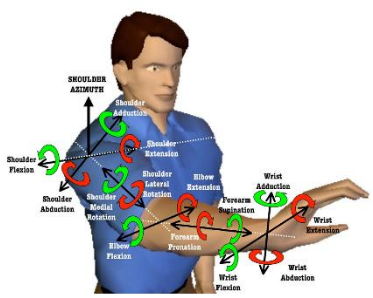

Figure 2-23: Schematic of seven DOFs in the design of exoskeletons [23].

As mentioned, exoskeletons are like the devices introduced in refs. [85], [6], [86], and [23] namely wearable biomechanical systems that are installed parallel to the subject's limb, and that extend either across the entire upper limb or otherwise just certain parts of it. In the exoskeleton, the axes of rotation of the robot must match the axes of the anatomical rotation of the patient because a mismatch between the two can have devastating effects on the rehabilitation process or on long-term use of these devices [14][56]. Among these, devices have been provided that can self-align[55][87]. These devices are portable and stationary and are provided with a variety of actuators and sensors, the details of which are presented in Table

2-3. For example, Bogue has presented different examples of exoskeleton devices [88]. The complexity of the mechanical algorithm and control of such devices is usually significantly higher than end effector devices where, of course, their complexity also increases with the increasing number of DOFs [89]. The Centre of Glenohumeral Joint (CGH) changes according to the different directions that can be adopted by the humerus, which are caused by shoulder girdle movements. Therefore, the shoulder girdle movement must be considered in the kinematics of a robot shoulder mechanism. Regardless of this, a mismatch between the rotation axis of the patient's shoulder and the robot shoulder not only limits the workspace for rehabilitation to some greater or lesser extent but can also result in discomfort to patients [11][50]. Some researchers have suggested the addition of passive joints as a way to negate the adverse effects of misalignment on the joint[74], which will be fully explained later.

- Exoskeleton Advantages and Disadvantages

Exoskeleton devices have a mechanical structure that reflects the skeletal structure of the patient's limb. The use of an exoskeleton-based approach allows the patient to independently and simultaneously control the specific movement of the arm in many joints. However, to prevent injury to the patient, it is necessary to be adjustable according to the length of the patient's arm[89][90]. A significant disadvantage of current robotic devices is that they incapable of properly matching the movement of the upper human limb [15]. Rigid exoskeletons have rigid mechanical bodies [13] [29] [91] and this capability allows them to transmit forces and torques without the anatomical equivalent (user limb) and experience different load ranges. This also makes it possible to use a simpler control system and to perform more complex displacement movements. The mentioned advantages make it possible to use large forces and torques for such systems, which are often used in the military and industry. These systems can also be used in the rehabilitation of patients who experience little spasm reflux in their joints [4]. Some of the disadvantages of these systems include poor dynamic response speed, interference with joint movements that cause the wearer to deviate from normal movement patterns, the limitations of wearer flexibility, increased system metabolism, large inertia regulation mechanism, and poor pairing between humans and machines which causes low energy efficiency and deviation from normal human movement [70]. One can also point out their significant weight, which this requires more force and torque to be supplied to allow their movement and, ultimately the need to provide greater sources of power[91].

- Exoskeleton Body Material and Safety

Most of the design's body is fabricated from aluminium [26], essentially because aluminium is a low-density material with suitable strength properties. Carbon fiber is also an ideal candidate for an exoskeleton's body material. Recent advances in manufacturing techniques such as 3D printing of carbon fibre-reinforced structures make it possible to achieve particularly complex geometries. One of the advantages of these methods is that they use a combination of plastic, aluminium and reinforced steel with carbon fibre [38][85].

There are different mechanisms for ensuring the safety of design systems[92][89]. One solution is to place mechanical and electrical stoppers to limit the ROM in the human body. In one design, researchers limited speed and torque to prevent sudden hand movements by control programs [3]. Also, the mechanical design should be achieved in such a way as to improve inertia reduction [93]. Therefore, the challenge in designing the exoskeleton is to reach a conceptual balance between power, workspace, dynamics, and weight [94]. Also, for the robot to function properly, it must have low friction, low inertia, and backlash-free operation [33]. Although industrial robots are highly resistant to the upper human limb and should not be in physical contact with patients, in some cases they have been used to reduce costs [57]. Therefore, having a low intrinsic impedance in designed systems is one of the important factors in designing rehabilitation systems for the upper extremities[89]. Most haptic devices use a basic form of impedance control in which Cartesian forces in the category using Jacobian fall in the commands of common torques. The most important advantage of this method is that it does not require the calculation of inverse kinematics and is stable at low impedances. Also, in teleoperation, the exoskeleton aims to generate contact forces in the exoskeleton category, which are the replication of forces felt by the slave arm, while in virtual reality programs a virtual environment is used instead of a slave arm to generate force commands [93].

- Exosuit

The systems presented in refs. [30], [56], [58], [65], and [95]are known as exosuit devices. Unlike the rigid systems used in exoskeleton, exosuit use the anatomical structures of the body to shape the robots frame [79]. In other words, the most important difference between an exoskeleton and an exosuit is the latter’s soft texture, which includes a fabric base frame that can allow for transfer flexibly. These systems are made of appropriate clothing in appearance and are lighter and more portable than exoskeletons. They also use the structural integrity of the human body to transfer forces between its different parts [72]. Due to the lack of a rigid skeleton, the user's natural movements in an exosuit are not limited[77]. An exosuit exerts a force on the joints in parallel with the muscles, which can improve the effect of the auxiliary force and the connection of the device system [77].The use of exosuit systems, due to being lightweight, means that performing movements and applying forces and torques requires less initial energy, which in turn increases the lifetime of the intended energy source compared to rigid exoskeletons, and reduce power consumption over any given time interval. Due to its compatibility with the user's body and its lightness, it leads to fewer movement and misalignment injuries than rigid devices. Therefore, the inherent adaptation of exosuit devices to the human body facilitates their mechanical design[4]. It is also possible that due to their design, they can be hidden under people's clothes in the near future, which could have very positive effects on patients in terms of social psychology. Figure 2-24 illustrates the sample designs provided. According to the 12 designs reviewed in this article, 58% are portable and 42% are stationary. Also, 83% are presented as soft and 17% as a combination of soft and rigid.

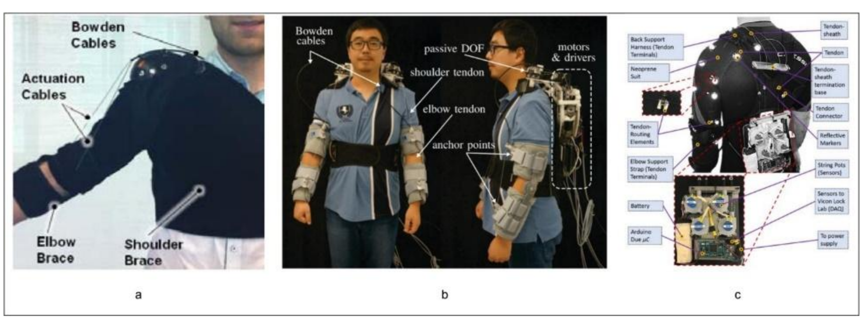

Figure 2-24: Images of the presented exosuit designs: a [56], b [72], c [95].

One of the advantages of exosuit systems is the materials used in their body design, which are much cheaper than exoskeleton systems, being generally fabricated from elastomers and fabrics [56][67][95]. An important result of using cheap materials for these devices is their lower cost and portability, which allows them to be used by a wider range of patients. Also, due to this feature, their application in patients' homes has become increasingly possible, and they can have industrial applications as well[72]. The disadvantages of these devices include the lack of a rigid frame to transmit force and torque. The important challenge here is that all the forces and torques will be transmitted through the patient's body, and due to the lack of a fixed and rigid frame, associated problems will be arisen. In such instances, it is not possible to connect the actuators and sensors directly to the mainframe, and in principle, they must be transmitted to the limbs through secondary systems and power transmission mechanisms. Also, their control systems are complicated due to the use of user biomechanics, which is one of the challenges inherent to these systems [4]. In some exosuit devices, for example, in addition to generating a natural force to move the limb, a shear force is also generated, which should be minimized because it has no effect on the rotation of the limb and only rubs the device on the skin which can be painful [96]. However, putting an appropriate distance between the transmission system connections and body parts can significantly reduce the shear forces when stimulating the actuator on the exosuit trunk [65].

When dealing with system modelling, the dependence of model parameters on the arm complexion of the wearer is important. In addition, the flexibility of the exosuit makes it impossible to always be placed on the arm in the exact same position [77]. Given the above, the expectations we should have from an exosuit system are as follows[56]:

1. easy to wear and remove.
2. as light as possible
3. cost-effective
4. creates forces that help during the rehabilitation process and measure the position of the arm.
5. compatible with improving safety, and no rigid elements should be used.
6. compatible with anatomical changes and possible misalignments

Table 2-4 introduces some of the commercialized samples available, and which are illustrated in Figure 2-25. Most commercialized systems have been provided as shoulder-centric to help healthy people in industrial environments, but according to existing knowledge and studies a portable shoulder-centric commercial system has not been provided to date.

Table 2-4: Comparison of exosuit commercialized samples of exosuits.

ITEM	COMPANY NAME	PRODUCT NAME	AREA OF HELP
1	SUITX	ShoulderX	Shoulder
2	Ekso Bionics	EksoWork	Shoulder
3	Myomo	Myomo	Elbow and Hand
4	Ottobock	Paexo Shoulder	Shoulder
5	Ekso Bionics	ExoUE	shoulder and elbow

Figure 2-25: Samples of commercialized systems: a [97], b [98], c [99], d [100], and e [100].

2.4.2 Rigid and Soft Robotics

Rigid robots are an older concept than their soft counterparts. Rigid robots have frequently been used in military systems, industry, etc., but the use of soft robots, by comparison, have only began to increase in recent years, in part due to the limitations of rigid robots such as their significant weight, low portability, etc. In the articles reviewed, three general designs are apparent used, i.e., rigid [26] [86] ,soft [27] [101], and a combination of rigid and soft robots [102][74]. In general, the limitations of rigid robots mentioned in the previous sections led to the emergence of soft robots. For the studied designs, their percentage distribution is as illustrated in Figure 2-26.

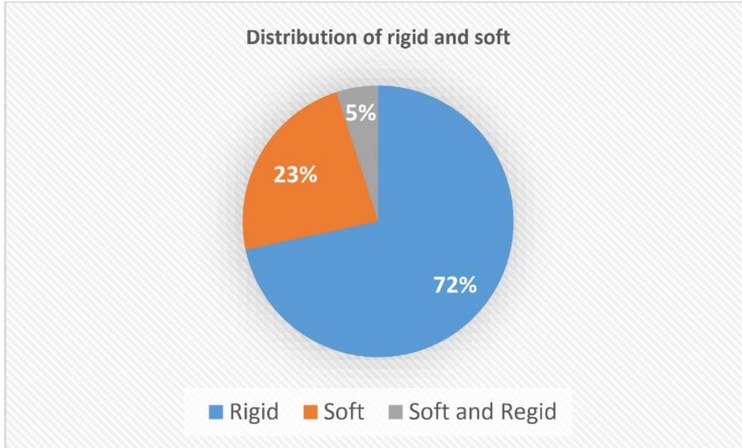

Figure 2-26: Percentage distribution of rigid and soft robotic device designs.

REHAROB [103], ARMin III [13], CABexo [104], and CLEVER [66] are examples of systems provided for rigid robots, and whilst RUPERT IV [42] and ExoFlex [79]are examples of systems proposed for soft robots. Figure 2-27 shows examples of soft and rigid robot designs:

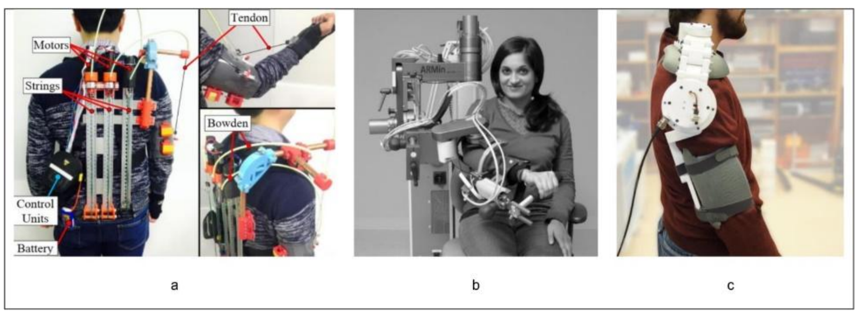

Figure 2-27: Examples of robotic designs, a: soft [65], b: rigid [13] and c: a combination of soft and rigid [74].

2.4.3 Portability

The portability parameter is important because these devices are often used to help patients perform basic ADLs and in the performance of further rehabilitation activities at home without the presence of a doctor or technician. There are three types of capability in robots designed for rehabilitation, including portable [105] [56] [72], stationary [26] [38] [67], and wheelchair-mounted systems[29] [106] [58]. Figure 2-28 gives a distribution chart for these designs. When designing portable skeletons, the classic trade-off between power and weight inevitably emerges [23], therefore the weight of the wearable robot is a very important factor in its portability [93]. Figure 2-29 shows some images of stationary, portable, and wheelchair-mounted robots.

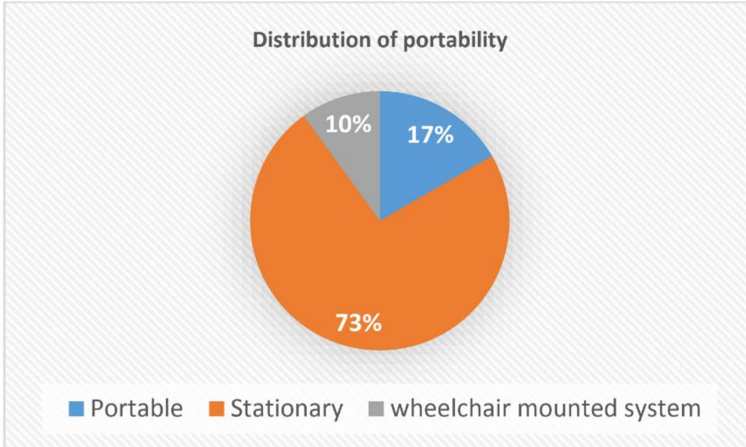

Figure 2-28: Distribution graph of portability of designs.

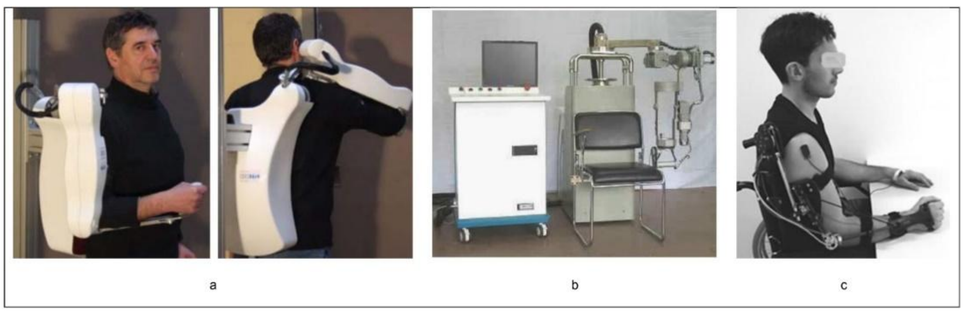

Figure 2-29: Examples of robots a: portable [107], b: stationary [59], and c: wheelchair-mounted [108] systems.

2.4.4 Types of Actuators

Robots can be classified according to the types of actuators used in their designs. The types of actuators used in the system are derived from the choice of energy source[109]. In general, three types of the actuator are used for rehabilitation robots, which are electric, pneumatic, and hydraulic. Of course, some of the designs are not included in this general classification, so we classified them into a separate group called others. The location of the actuators is an important factor, especially in exoskeleton-based mechanical structures, where the actuators are located near the connection on which they operate. Figure 2-30 shows a graph of their distribution, from which, as it turns out, most of the actuators used in the designs are electrically operated, with only a small percentage of them being of other types.

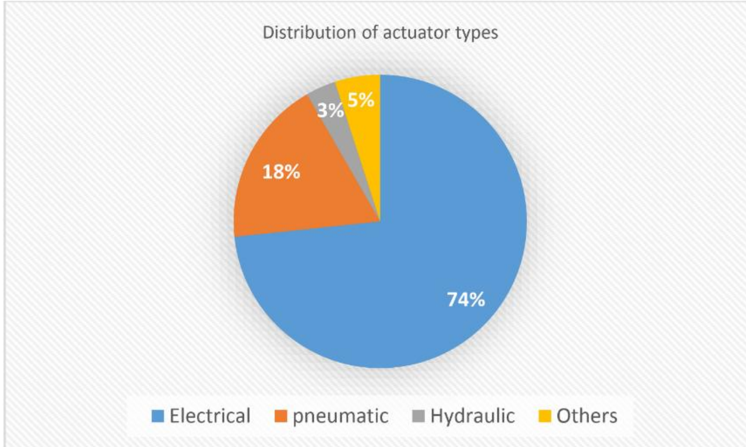

Figure 2-30: Distribution chart based on actuator type.

Figure 2-31 schematically illustrates the three main types of actuators used in systems.

Figure 2-31: a: electric actuator [17]; b: pneumatic actuator [42]; c: hydraulic actuator [110].

- Electrical Actuator

As mentioned, more than 70% of the actuators used in the designs considered were electrically operated. These actuators often include DC and AC motors, although DC motors are more commonly used. The possibility of storing energy in batteries and their ease of use is one of the main reasons for using DC instead of AC motors in robotic systems. In other words, DC motors are used in portable robots that need smaller forces and torques, and AC motors are used in stationary industrial robots that need to provide larger forces and torques. In practice, DC motors outperform AC motors for given amount of energy entering the system. Most upper limb rehabilitation robots are activated by electric drives [111]. One of the reasons for preferring electric actuators over other types is the compactness of electric motors and the ease of control of these systems [29]. Also, the system consists of an electric battery and motor, and it is lighter and smaller than, for instance, a pneumatic system with the same specifications, therefore more suitable for fully portable and wearable auxiliary systems. Galiana et al. ‘’have shown that the energy density, i.e., mass in each energy stored of a lithium battery is larger than the compressed air system, and mechanical coupling is placed at the end of the actuator to secure the system and ensure that the motor receives no axial force or off-axis torque that causes it to malfunction’’ [56]. In terms of system safety, whenever an abnormal event is detected, the safety circuit immediately reduces the power of the motor drives. For example, Nef et. al. equipped their system with a passive weight compensation system and showed that their robot would not fall after losing power [33]. If the drives are back drivable, the robot can easily be manually by a therapist to relieve the patient in an uncomfortable posture [13]. For example, Pang et. al. developed a new system for performing internal and external rotation movements of the shoulder joint by means of a curved rail, a gear system, an engine, and gearbox [6]. Kim et. al. also presented a system with electric actuators and a gear and pulley transmission system [112], as shown in Figure 2-32.

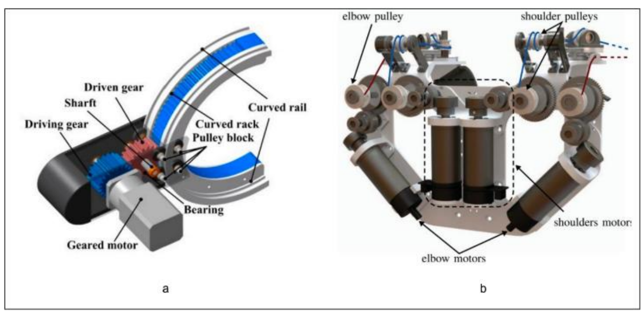

Figure 2-32: Examples of electrical actuators used in exoskeleton (a)[6] and exosuit (b) designs [72].

- Pneumatic Actuator

Few systems use pneumatic actuators. Pneumatic actuators are lighter and have lower intrinsic impedance, and also due to the need for pneumatic pressure to start, the majority of such systems tend to be used in stationary and limited areas [35], or where a small compressor can be mounted on a patient's wheelchair [109]. These actuators are presented in two different designs: pneumatic cylinders [35], and McKibben actuators [42]. Pneumatic cylinders that are embedded in different parts of the upper limb with different systems and perform the desired operations based on one-way or two-way cylinders and the force of compressed air according to their design [35]. McKibben actuators were developed for prosthesis research in the 1950s and 1960s [30], the structure of which is shown in Figure 2-33. This type of actuator, which also have a very good power/weight ratio, meet the requirements of safety, simplicity, and lightness [26].

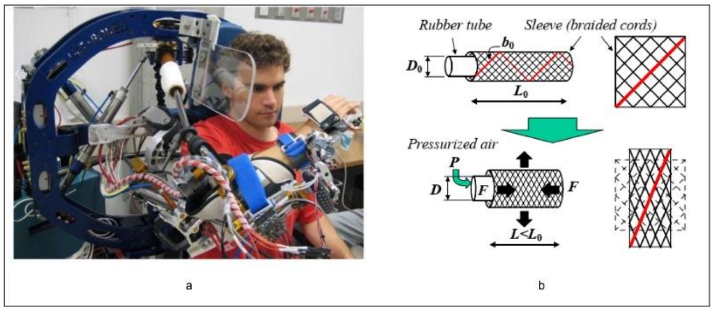

Figure 2-33: (a) Image of pneumatic actuators with metal cylinders[113] and (b) a schematic of McKibben system[36].

Pneumatic Artificial Muscle (PAM) is also derived from the design of McKibben actuators, which, when a bladder is subjected to compressed air, the diameter of its actuator increases, and as its volume shortens, and stress is created at its end. In other words, they are a special type of pneumatic actuator with an internal bladder surrounded by a braided shell with flexible but non-expandable threads. Due to their special design, this actuator is shortened like a contractile muscle under pressure. The advantages of this design include natural adaptability, low mass, inherent safety, high power-to-weight ratio, low cost, and ease of construction[26]. Due to the relatively low energy density due to the use of a compressed air tank, these systems cannot operate as a fully mobile wearable system, which is one of their major disadvantages [56]. It is very important to note that in pneumatic systems, due to their limitations, the proposed designs cannot produce a complete and natural ROM of body parts and have certain limitations in their presentation. Also, in some designs, due to problems such as tight fit, heavy load on bones and joints, limitation of working range, slack of wear and slippage, and difficulty in putting on and removal; in such cases, a chloroethene frame is used, where, of course, outer Fiber-reinforced plastic (FRP) jackets can also be used to reduce their weight [30]. An example of such slippage and wear on the outer jacket is shown in Figure 2-34.

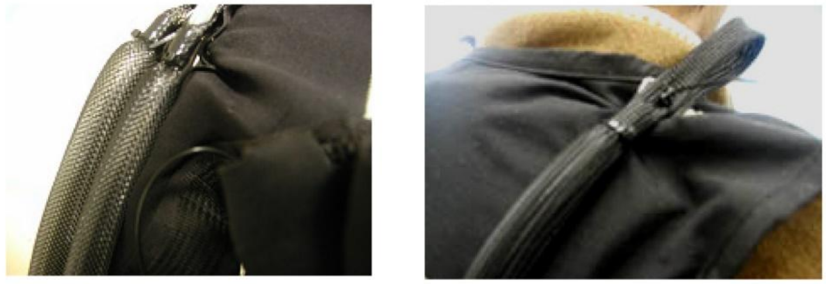

Figure 2-34: Sample of slippage and wear when operating a pneumatic actuator[36].

- Hydraulic Actuator

Hydraulic pressure actuators whose working fluid is an oil can generate large forces. To prevent fluid leakage and keep the oil under pressure, such systems are of necessity complex, and their commercial actuators are heavy. Therefore, specially designed hydraulic actuators have been used in rehabilitation systems. In this chapter, two systems were identified that used hydraulic actuators. Both systems were non-standard and used specially designed actuators. Reasons to avoid using industrial hydraulic actuators include fluid leakage, impedance, weight, and fluid supply problems. Also, these systems are typically large and noisy [92]. Stienen et al. [49] presented one of the complete examples of an exoskeleton with the help of hydraulic actuators, in which the disk brake system was used in the robot members. Figure 2-35 shows a schematic of this system.

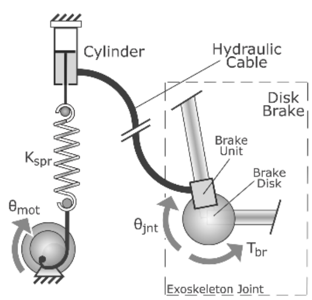

Figure 2-35: Schematic of the system considered with hydraulic actuator and disk brake [48].

- Other Forms of Actuators

To reduce the high resistance of electric motors, an elastic element can be added to actuators set up in series, which led to the development of the Series Elastic Actuator (SEA) concept [109]. In general, an SEA has low output resistance, good back-drivability, power output resolution, and power control compared to the direct connection of a gearbox to electric motors. The most important element in the design of SEAs is the elastic element [44]. SEAs reduce user interface immobility and impedance to provide stable and accurate force control, thus increasing patient safety. The disadvantage of using an elastic element is the lower functional bandwidth [89]. Hydraulic SEAs are also used in some systems equipped with powerful hydraulic disc brakes. Also, Park et al. [69], used a cam structure and a rubber band to create the required force (Figure 2-36-a), which reduced the muscle fatigue of the system's users in a passive actuating mode. In other designs, Sanchez et. al., used elastic bands to generate the force required for the actuators (Figure 2-36-b), although this mechanism was designed in a remote monitoring system and was passive system [114]. Gaponov et al. "presented an example of a Twisted String Actuator (TSA), which are actuators that do not require the use of gears between motors and threads (Figure 2-36-c) and are useful in terms of weight and cost. One of their disadvantages is that due to their dimensions, they need a lot of space to operate, and it is not possible to use them for systems with a higher degree of freedom and portability" [65]. Electrical stimulation of the muscles of the body, instead of using external stimuli, can also create a simulation system called the *Functional Electrical Stimulation (FES)* technique, in which the weight of the system is greatly reduced. FES significantly reduces the weight of the device. From a therapeutic point of view, FES allows patients to improve muscles, improve a large part of their muscle strength and power, and prevent muscle atrophy. FES, which is performed with conventional physiotherapy, has also been shown to enhance the outcomes of rehabilitation. One of the disadvantages of this method is that it can cause involuntary contraction of strong muscles and cause pain in the patient. In addition, movement control using FES is difficult due to the nonlinear nature of the contracted muscles, muscle fatigue, and the dependence of contraction on the quality of the contact between the actuating electrodes and body tissue [115].

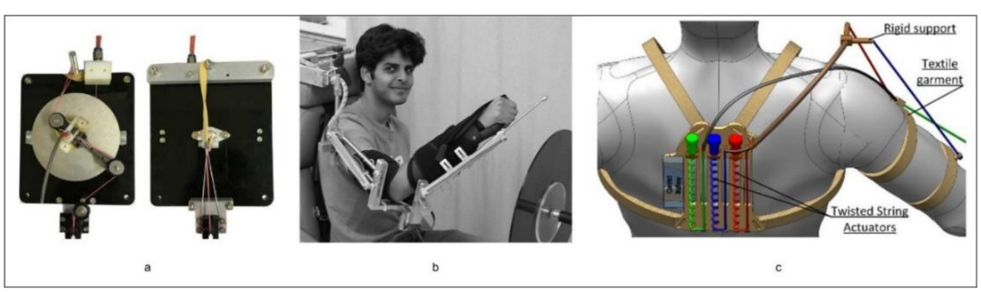

Figure 2-36: Images of other groups of actuators used in systems a [69], b [114], c [31].

2.4.5 Types of Sensors

The importance of wearable robots is apparent to all due to their wide range of applications in the fields of rehabilitation, military, medicine, and industry. In recent years, due to the increasing number of elderly and injured people in various fields who have mobility problems, the use of such robots has also increased. The sensors used in these systems also vary depending on the design and actuators used. For example, in systems that used pneumatic actuators, pressure sensors are used that can measure the amount of compressed air [27] [53] [68] or in systems that use electric motors, position, force, and torque sensors are used [23] [39] [45] to produced basic information to send to the system control unit. One of the most common forms of sensor used in various systems is the surface electromyography (sEMG) signals of human muscles that are used to receive input information to control robotic systems [50]. Table 2-3 presents a summary of sensors used separately for each design, which include a pressure sensor, accelerometer, angular encoder, EMG signals, six- axis load cell, inertial measurement unit (IMU), force and torque sensor, and position sensor. Figure 2-37 shows some example images of the above sensors.

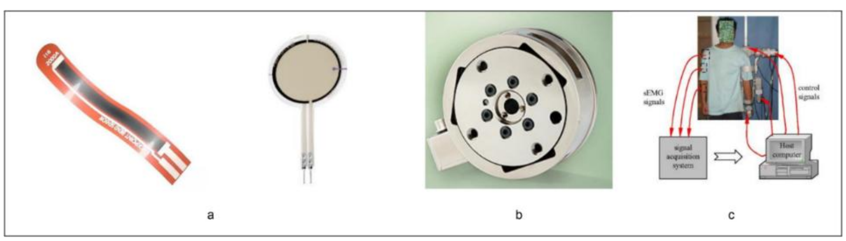

Figure 2-37: Images of sensors used in the designs considered: a: Bend and Force sensors [108], b: Six -Axis Force and Torque Sensor [67], c: sEMG system [116].

2.4.6 Types of Power Transmission Systems

According to the existing designs reviewed in Table 2-3, the transmission systems used in the designs can be classified into three main groups of which, depending on design, one and sometimes several groups are used: linkage mechanism, cable drive, and gear drive.

- Linkage Mechanism

In the majority designs, aluminium trunks are used, with the actuators are located near the desired member and the power transmission from one member to another achieved through linkage (Figure 2-38) [90] [45]. In other words, for example, where electric motors are used, the motor is embedded in the desired location and from both sides transmits power between the two members through the linkage connected to it, a schematic of which is shown in Figure 2-38. The advantage of such systems is that the actuators are located at the desired point and there is no need for power transmission systems at a distance farther from the desired member to the place of force effect; one of their disadvantages is the increase in member inertia due to their increased weight [117].

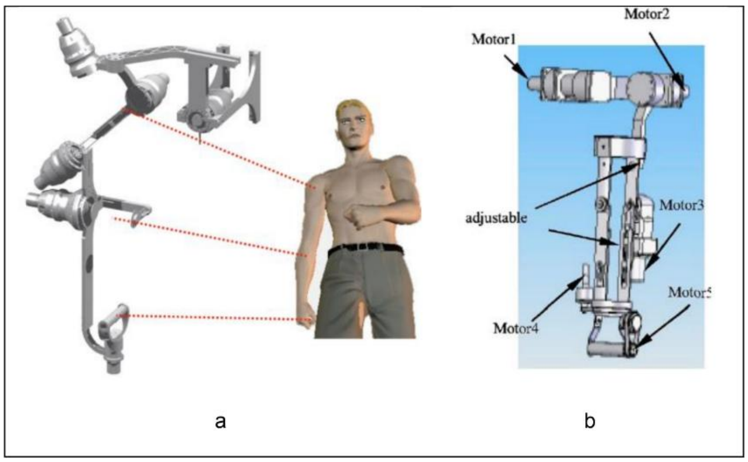

Figure 2-38: Schematic of linkage transmission systems: a [23], b [59].

- Cable-Driven Mechanism

In some designs, the preference is to use a cable system designed to reduce the weight of the system and to transfer the actuators to a point away from the effect site. In other words, the reduction of the load caused by the device can be affected by using a tendon-driven mechanism system. Because the auxiliary force is transmitted through the tendon, the actuators can be located at any part of the body, which ultimately reduces the size of the device and reduces barriers to movement [69]. The cable-driven mechanism allows the system to be quieter, and future allows for the smooth transmissions and high accuracy that are required for wearable skeletons [104]. In some designs, first, the human movement model is analysed based on human anatomy and sports biomechanics, then the muscle is modelled as stress lines and human movement settings are obtained. Finally, the soft bionic robot is constructed based on the stress line model. According to the principles of anatomy and biomechanics, the muscles movement system can be simplified to a stress line model, and according to the muscle state, a muscle tension line can move from a fixed to a moving point [9]. Due to the ability to place all motors at the fixed base of the system, these mechanisms have a high power-to-weight ratio, which ultimately reduces the mass, size and inertia characteristics of the robot and reduces the torque output required from the motors [15].

The cable systems used for exoskeleton and exosuit are different. For example, in exoskeleton systems, the path of the cables and their holder is installed on the linkages, and a rigid wearable device through its rigid connection structure, which allows for the limb rotation, applies the normal force to the target limb. In this case, each exoskeleton joint needs a low friction bearing system that provides rigidity against all forces and non-axial moments. In exosuit systems, however, the actuators are fixed at a point away from the point of effect, and only the cables are routed to the point of effect through the cable system. One of the important points of the cable system design is that for complete control of n joints, at least n + 1 cables are necessary, and it is also necessary to have a positive stress in all cables at all times to prevent slack [15]. Also, it should be noted that cable transfer always adds undesirable vibrations, and which can become loose during operation, so all such aspects must be fully considered in the design. Various mechanisms have been used to move the shoulder and elbow. Kim et al. [72] used Bowden cables to actuate the elbow because the point of force is away from the actuator, and a pulley mechanism is designed to activate the shoulder instead of Bowden cables to minimize energy loss.

The human skeleton offers rigid support on its own. Although the extended tendon-axis system may seem less rigid in terms of accuracy and rigidity than conventional rigid exoskeletons, it imposes fewer restrictions on arm movement and is lighter and more compact. Typically, the arm placement speed in selective rehabilitation procedures is relatively low and safe for the wearer, which gives the assistant sufficient time to deal with cable problems [65]. The pulley settings can be used to reduce the speed in cable transmission because in the motor; the required torque is low while the angular velocity is high, while in the joint the torque is high, and the angular velocity is low [118]. In exosuits, by contrast, the device exerts a force on the target limb's tendon, which applies both normal and shear forces. In designs, shear force should be minimized because it is useless in limb rotation. In these systems, this is the only pressure on the joints, which of course causes the device to rub on the skin, which can be painful. For example, to reduce the shear force, Park et al. [69] ''used an activation and deactivation system consisting of a non-circular cam structure and used a rubber band as a power supply.'' In some systems, the device is equipped with cable anchor locks that are easily adjustable [65]. Also, in some designs, reducing the tendon diameter can lead to a reduction in the size of all the mechanical parts of the transmission system (pulleys, axles, etc.) [119]. One of the reasons for the use of cable-driven systems is that their main advantage is the ability to carry large loads over long distances without the inherent backlash or friction in the gears. Figure 2-39 illustrates examples of cable transmission systems.

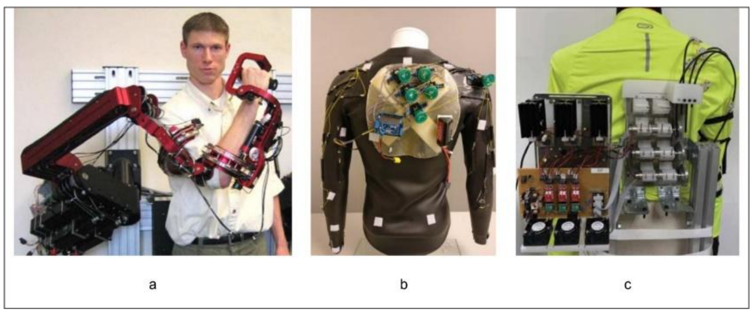

Figure 2-39: Images of cable-driven systems provided in the designs: a [118], b [73], c [77].

- Gear-driven Mechanism

In certain systems, such as the designs presented by Chen et al. and Xiao et al., gear transmission systems have been used [62] [104]. One of the problems with these systems is that the weight of the wearable robot has increased, and future that they have been abandoned in the study and modelling phase, so no sample has been made and tested to date with the available knowledge. Of course, in cable and other systems, smaller samples of gears have been used to decrease or increase gear ratio, the purpose of which is to change the ratio from the motor to the final point of effect. Also, Gopura et al. [120], used a gear mechanism to create forearm movement due to the rotation of the forearm by creating an alignment between the rotating system and the forearm limb. In general, systems that have used the gear family have not generally met with general acceptance or. Indeed, practical application. Cable transmissions are also more efficient than gear transmissions, thus ensuring a better degree of system back drivability [38]. Figure 2-40 shows the image of the design presented using gear transmission systems.

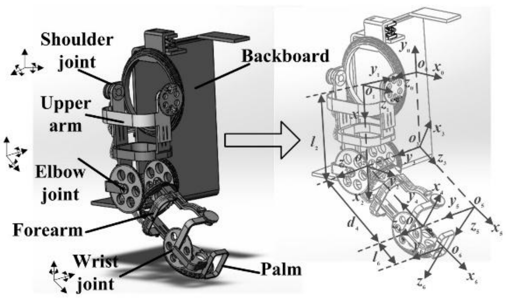

Figure 2-40: Image of the system presented using a gear transmission system[10].

2.4.7 Types of Control Units

After studying the biomechanics of the upper limb of the existing designs used, the types of actuating systems and power transmission systems, the next challenge that needs to be considered in the design of rehabilitation and assistant systems is that of the system control unit. Control systems allow the patient to follow recorded paths accurately and approach the defined goal of the system. The control input of the devices can take different forms of signal. For example, the forces and torques applied to the various connections in devices are known as dynamic signals. Orientations, speeds accelerations, and positions of different parts of the device can be known by kinematic signals and start signals for a specific activity via trigger signal[92]. The use of two dynamic and kinematic input signals or a combination thereof is used in the majority of complex strategies. The need for control and safety when assisting patients with shoulder, elbow, and wrist movements is essential in clinical treatment [59]; of course, in addition to patient safety, the safety of the therapist must also be considered. There are three types of rehabilitation depending on the patient-robot interaction. In the first case, the robot moves the patient's arm in a planned direction according to defined goals, and in this case the patient puts their arm in a relaxed position, which is called passive rehabilitation. In the second case, the patient moves their hand towards the target and the robot creates a force in that direction, which is called active-assisted position. Finally, in the third case, the robot applies an opposing force to move the patient's force, which is called active-constrained [77]. A more comprehensive explanation of their control logics will be presented below.

- **Control Strategies**

According to Maciejasz et al. [92], the breakdown of control strategies for rehabilitation and assistive robots can be classified as follows: high-level control, which includes haptic stimulation; challenge-based control; coaching control; assistive control; and low-level control.

- **High-level Control Algorithm**

High-level control algorithms are designed to stimulate movement flexibility, while low-level position control strategies control acceptance factors, force or impedance controls high-level strategies [92]. There are many high-level control strategies for teaching robotic movement. For example, Pirondini et al., in their ALEx design, used a high-level control algorithm with three different methods: passive, assistive, and assisted-when-needed [121].

- **Assistive Control Algorithm**

The device provides assistance to the patient to perform a specific movement, which of course is a high-level control strategy. An assistive control strategy makes tasks easier and safer and allows more repetition. There are a total of four types of assistive control strategies: counterbalance-based, impedance-based, adaptive performance-based, and EMG-based control.

➢ **Impedance-Based Control**

In this case, the patient follows a specific path, and the device does not intervene until it follows the path. Deviation tolerance is considered for the permissible deviation and if it goes out of the tolerance range, the device exerts a recovery force, which increases with the deviation from the specified path. For example, Carignan et al. showed that since the torques related to the shoulder axes cannot be measured directly, an impedance controller can be used to achieve appropriate resistance characteristics [23].

- **Counterbalance-Based Control**

In this case, against the movement of the limb, a weight balance (active- or passive-type) is used to create the necessary force for movement, which increases the patient's effort by reducing gravity, and the exercises become easier [109].

- **EMG-Based Control**

EMG-based control is one of the most widely used types of control strategies in assistive technologies. This method uses sEMG signals to control or assist the patient. sEMG signals directly reflect user intents. Hence, a robot can use the user's EMG signals as input signals to the robot controller to effectively help the user move according to their intent. However, EMG-based control is not easily realized because: (I) the role of each muscle for a particular movement varies according to joint angles, (II) a muscle is not only related to a movement but also involves other types of movement, (III) antagonist muscle activity affects joint torque, (IV) the level of activity of some muscles, such as the bi-articular muscles, is affected by the movement of other joints, (V) obtaining the same EMG signals for the same movement even with the same person is difficult, (VI) the level of activity of each muscle and its use for a particular movement varies from person to person, and (VII) it is not easy to predict movement in real-time because many muscles can be involved in a joint movement [43]. Humidity, human mood, ambient temperature, and electrode location can affect the frequency and amplitude of the signal. The electrode should be located on the midline of the abdomen of the muscle and along the muscle fibers so that it can sense the maximum signal amplitude. It is also very important to choose an appropriate threshold because, in the signal analysis, if the starting point is too large, we will have lost useful information; also, the starting point is disrupted by noise, and this choice is therefore very important [116].

Even if the EMG signals contain very important information, predicting shoulder movement from EMG signals on a short time frame is not an easy task because many muscles are involved. To overcome this problem, a fuzzy-neuro controller that can adapt to the physiological conditions of each person online has been proposed to control the skeletal robot, where in some designs the physiological control of the robot can be realized with this control method [122]. The intelligent interface can also be realized using a neural network.

EMG signals are usually composed of a wide range of frequencies, so it is difficult to reduce noise by filtering them. In addition, direct use of raw EMG data as input to the controller is difficult. Therefore, features must be extracted from raw EMG data. Among the various feature extraction methods, for example mean absolute value, average rectified value, mean absolute value slope, root mean square (RMS), zero crossing, waveform length or slope sign changes, most of which choose RMS values for raw EMG signal processing, mainly because the root mean square (RMS) is a measure of signal strength and is widely used in most applications [43]. Also, an EMG-based fuzzy-neuro control method based on EMG has been shown to be one of the most effective methods for controlling exoskeleton robots in previous studies. However, if the number of degrees of freedom of the exoskeleton robot increases, the control rules become more complex [50]. For example, Oujamaa et al. ‘’have used sEMG signals from the healthy limb of the other party to control the movements of the patient’’ [123].

- **Performance-Based Adaptive Control**

With the help of this type of strategy, aspects of help such as force, path and time can be monitored in the current performance, and their compatibility with the patient's performance during a certain number of previous activities can be checked [92].

- **Challenge-Based Algorithm Control**

In contrast to assistive-based control strategies, challenge-based control is based on resisting or challenging the patient’s willingness to affect a movement. It can be categorized according to three groupings, namely resistive, amplifying error and constraint-induced, and is a high-level strategy. In a resistive strategy, the control algorithm resists the desired movements and increases the patient's required effort and attention to achieve a certain task. The control techniques are based on the concept that the larger the error, the faster the progress in the recovery process. Therefore, this strategy is based on increasing the observed visual error between the main path embedded and the path travelled and enhances the visual representation on the screen. Finally, in the constraint-induced strategy, the control algorithm promotes the use of the affected limb by restricting the other, non-affected limb in a similar manner to conventional constraint-induced therapy [115].

- **The Haptic Stimulation Control Algorithm**

This is a high-level control strategy in which a robotic device is used as a tactile interface to perform activities in a virtual reality environment. Haptic simulation strategies use haptic devices and provide a sense of touch with which to interact with virtual reality objects [124] [125].

- **Coaching Control Algorithm**

In this non-contact strategy, which is a high-level control strategy, the system does not make any physical contact with the patient, and instead a monitoring system is provided to instruct the patient in their movements. Although contactless approaches are beyond the positive solution discussed here, some such techniques could be combined with contact approaches to enhance the feedback process [126].

- **Low-Level Control Algorithm**

In this type of algorithm, strategy execution with proper position control, admittance, force, or impedance can be used to develop a high-level rehabilitation strategy. In other words, the type of signal used as the control input is partly determined by the low-level control strategy employed, and vice versa. The robot must also have low friction and negligible backlash to achieve satisfactory patient-cooperative control strategies, which are based on impedance and admittance architectures. In addition, motor and gear units must be reversible [13].

Most exoskeleton systems use the *Proportional-Integral-Derivative (PID)* control approach, meaning that dynamic models of the system, as well as the upper human limb, are ignored [17] [26] [33]and the Proportional Derivative (PD) control method is used in some wearable robots [23] [35] to evaluate the mechanical performance of the robot [127]. Because the human arm movement is nonlinear in nature, conventional linear control approaches are naturally limited when dealing with an upper limb robot. Thus, the idea of nonlinear control for upper extremity exoskeleton robots motivates a number of nonlinear control strategies, e.g., admittance controller[39], fuzzy-neuro controller [16], sliding mode control method [77], positioning controller method [56], iterative learning control scheme[102], computed torque control[17], adaptive control [59] and vision-based control method [68]. For example, to further improve safety and fault tolerance in the presence of the variance of large unknown parameters or even actuator faults, Kang et al. considered an adaptive controller according to the information provided by an adaptive observer without additional sensors, which of course was updated online [59].There are basically two main types of controllers that are used with accessories. The first group are position controllers. This type of design is used in cases where the angle of each joint must be precisely controlled. The second category of controllers is based on force/torque control. These controllers are commonly used as low-level controllers [77].

2.4.8 Feedback to the User

Various types of feedback may be available to the user, including visual [128], tactile [129], audio [128], and electrical stimulation [58]. Many systems in exoskeletons follow a similar design approach: using different control and sensing schemes, rigid kinematic chains are activated to mobilize a human-connected wearer [61]. In other words, the detection of the user's intent is achieved depending on the scenarios and the user's remaining capabilities, amongst others. For example, Pedrocchi et al. embedded different systems alternatively in the main system which can be used intermittently: an EMG amplifier and a USB button (Scenario 1), an eye-tracking system (Scenario 2), and a *Brain-Computer Interface (BCI)* (Scenario 3). For example, Johnson et al. used a joystick, or a physiotherapist always observed the practice of holding the dead-man switch in his hand. Releasing the switch cuts off the engine power and immediately stops the robot [29]. This can also be achieved by pressing an emergency stop button [13]. Kiguchi et al. [54] , used ultrasonic sensors to determine whether the user's hand was moving toward an object in the environment or otherwise. Lam et al. used a vibrational stimulation and muscle tendons to support a contraction[130]. Oguntosin et al. [68] used visual feedback in their design to identify objects that were targeted by the upper extremities in during daily activities.

A significant number of training systems are also presented in training in *Virtual Reality (VR)* scenarios. VR offers a highly interesting approach to patient training compared to the conventional conditions in medical units. VR can also represent a unique environment in which treatment can be provided in a highly functional and motivational context and can be easily graded and recorded [38]. Since the entertainment industry has recently introduced many new devices to record the movement of healthy people to interact with VR-based games, it is expected that some of these devices will soon be adapted for rehabilitation purposes. A graphical representation offers different educational scenarios to the patient. The scenario is different from the selected training mode. These include passive mobilization, active game therapy, and active ADL training. In passive mobilization, the patient's limb is moved by a robot along a previously recorded path. The purpose of this treatment is to prevent secondary complications, increase blood circulation and reduce joint and muscle stiffness [131]. In some systems, contact-less movement detection methods have been used. In these systems, reflectors are connected to the selected muscles and using motion recording systems, they ultimately offer the desired data to control and calculate the actual force of the muscles[79] [118][132]. Finally, in some devices, limbs are equipped with several radio-frequency identification (RFID) tags so that they can be detected automatically [58].

2.4.9 Status and Details of Clinical Trials

The principles of neuroplasticity suggest that these networks can be rewired through repetitive training [102]. Intense and repetitive physical rehabilitation has been shown to be useful in overcoming upper extremity deficiencies, but such treatments are intensive and expensive and their quantitative and objective assessment is difficult [27]. Table 2-3 provides the required information separately for each of the designs, on what kind of and on how many people, the designed system has been tested clinically or in the laboratory and, with this scale, the validity of the submitted designs can be understood. In addition, it seems that the results of using devices that are currently part of clinical practice have not been as positive as predicted, and more comprehensive studies on clinical evaluation have been conducted in the previously published literature [4] [109] [133].

Some previous studies have provided a specific classification for clinical trials that included them in categories 0 to Category III/IV [109] [4], but the number of patients and target groups and the overall type of plan were considered to suffice in this study. Category 0 refers to initial feasibility studies that trials performed with a small number of healthy volunteers, often using a prototype of a device to assess its safety and clinical feasibility. Category I indicates pilot consideration-of-concept studies that examine clinical trials aimed at device safety testing, clinical feasibility, and potential benefit, and are performed on a small number of people with the disorder in question. There is also no control group in the test session, or otherwise healthy individuals are used as the control group. Category II indicates development-of-concept studies and reviews clinical studies to confirm the effectiveness of the device, including a standard description of the intervention, a control group, randomization, and blinded outcome assessment. Finally, Category III/IV offers demonstration-of-concept / proof-of-concept studies and provides additional evaluation of the device's effectiveness. However, similar to the second category, these are usually multi-axis studies with a large number of participants. Clinically, the purpose of a clinical study may differ from the validity of a particular device. For therapists, a robotic device is a tool that offers a treatment protocol instead of a final product, so one is more interested in answering questions about optimal training intensity and disorders then what kind of training might be useful, whether it is robotic therapy or whether it should replace or complement other forms of treatment [109].

The verification classification of the proposed designs is presented separately in Figure 2-41. As stated in the chart, more than 40% of the designs have been tested on healthy people, with only 2% of them finalized and commercialized designs.

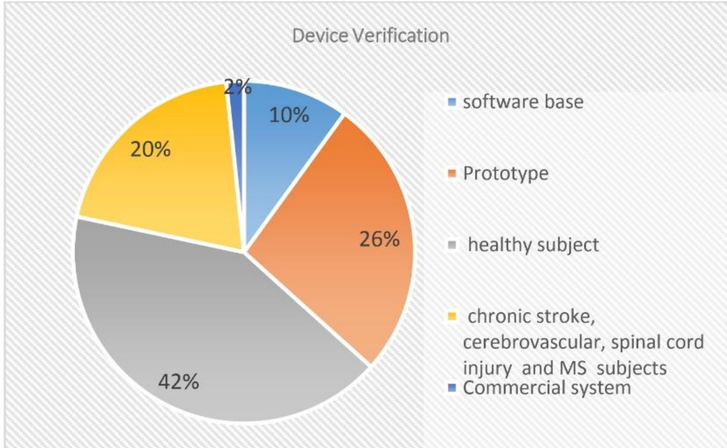

Figure 2-41: Verification classification of the proposed designs.

2.5 Problems and Gaps to be Filled

According to the reviewed articles, the main problem of with presented designs is that they are fixed, cannot be used as portable designs, they have significant weight, cover only one or two degrees of freedom in most designs, and are not used at home as wearable and portable. Due to the increasing demand for new portable and lightweight designs that can cover the more than one or two degrees of freedom of the shoulder joint, the design and fabrication of portable, lightweight designs with this feature can be essential, according to the problems mentioned and our goal in this thesis, the design, fabrication, and testing of a light wearable device that has been developed to perform three shoulder joint activities, which include shoulder abduction, shoulder flexion, and shoulder horizontal adduction (flexion). The features of this novel design are the ability to be worn by the user, the coverage of three degrees of freedom of the shoulder joint, are lightweight, and have the ability to be used as portable devices.

2.6 Conclusion

This chapter has embarked on a detailed exploration of soft and rigid robotics for upper limb rehabilitation, with a particular focus on the shoulder joint, through an extensive literature review. The journey began with an acknowledgment of the critical role that the upper limbs play in daily activities and the substantial impact that neurological disorders or surgery can have on an individual's ability to perform these tasks. The review aimed to provide a comprehensive understanding of current wearable robotic devices, both soft and rigid, to aid in rehabilitation and assistance.

A thorough search strategy laid the groundwork for an expansive review, ultimately focusing on 60 designs selected for their relevance to and innovation in the field. This exploration covered a wide range of topics, including upper limb biomechanics, types of mechanism (exoskeletons and exosuits), actuation methods, and control strategies, to name but a few.

One of the key contributions of this research is the detailed analysis of exoskeletons and exosuits, highlighting their advantages, disadvantages, and potential for rehabilitation purposes. Exoskeletons, with their rigid structure, offer substantial support and precise control but often at the cost of weight and comfort. On the other hand, exosuits, leveraging their soft and flexible nature, promise a more ergonomic integration with the human body, potentially offering a more comfortable and accessible rehabilitation tool, however, they may not provide the same level of force and support as their rigid counterparts.

The review identified several gaps in the current state of research, notably the need for more extensive clinical trials to validate the therapeutic capabilities of these devices. Additionally, there remains a significant opportunity for innovation in developing lightweight, user-friendly devices that can offer personalized rehabilitation experiences outside clinical settings.

This chapter was finally published in the Journal of Intelligent & Robotic Systems in 2021 as a review paper and at the time of writing has 56 citations (Figure 2-42) [134].

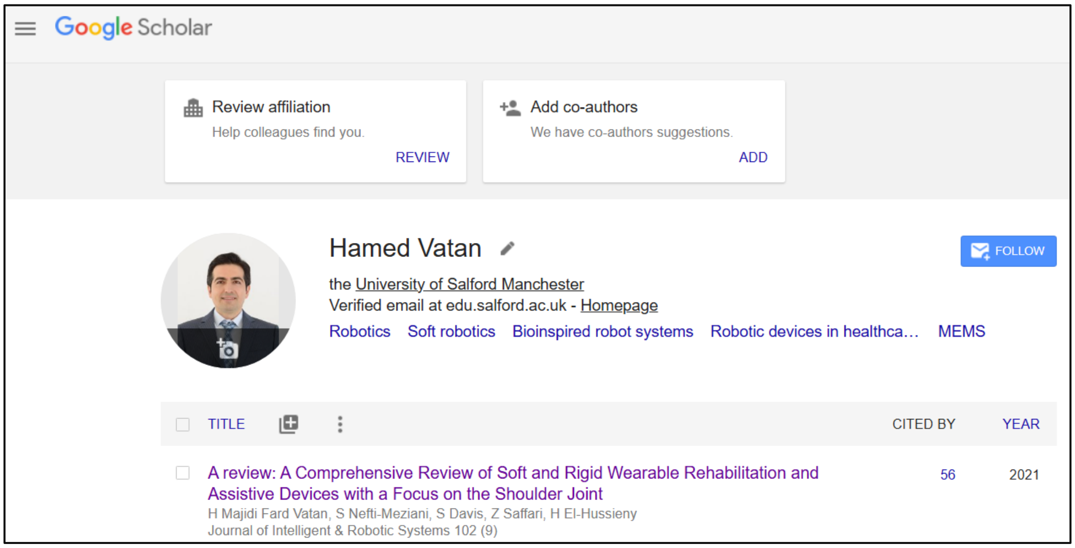

Figure 2-42: Last citation status of the review paper on 24/02/2025[134].

3 Chapter Three: Design of a Cable-Driven Shoulder Exosuit (CDSE)

3.1 Introduction

According to the previous studies in chapter two (literature review) and to the best of the author's knowledge, there are no wearable, lightweight, and portable cable-driven exosuits that can allow for the three degrees of freedom of the shoulder joint. The aim of this chapter is to design an exosuit appropriate for the upper limbs for disabled people which cannot move their upper lime like MND patients. The three types of shoulder movement that are the goal of the present project include shoulder abduction, shoulder flexion, and shoulder horizontal adduction (flexion) which are illustrated in Figure 3-1.

The goal is to support patients who have lost the ability to move their arms at the shoulder joint. The implementation of this novel project significantly enhances the functional capabilities of individuals suffering from mobility impairments in their upper limbs, particularly the shoulder joint. This should facilitate the execution of various daily activities, which predominantly involve the extension and manoeuvring of the hands to various locations to grasp specific objects and subsequently transport them to alternate locations as part of their routine tasks. This enhancement in mobility and task execution plays a crucial role in improving the quality of life for these patients, offering them a greater degree of independence in the course of their daily lives.

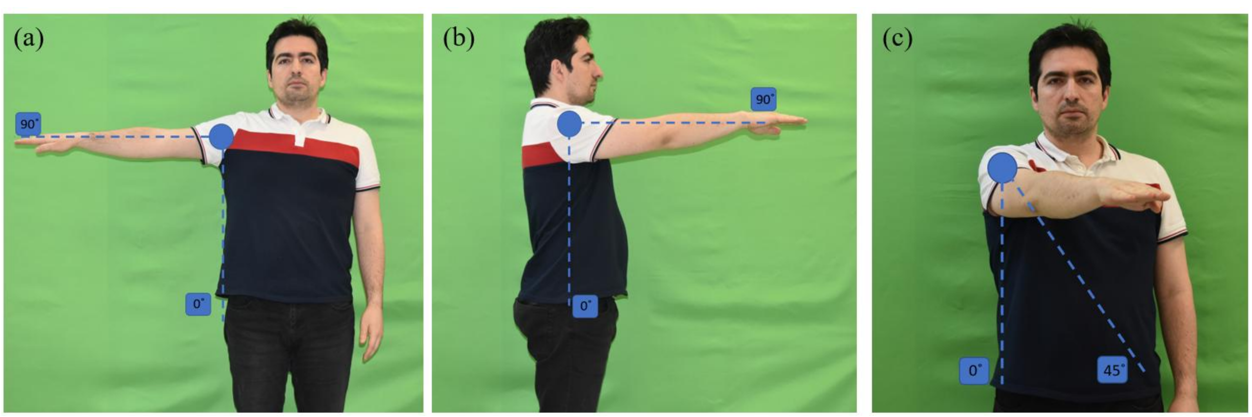

Figure 3-1: The three types of shoulder movements: (a): Shoulder Abduction – (b): Shoulder Flexion- (c): Shoulder Horizontal Adduction (Flexion).

3.2 Shoulder Musculoskeletal System and Bioinspired Design

In order to design a system that is lightweight and is wearable by the user in a portable manner, and which of course can help the user to perform the above three activities, we investigated the physiology of the of the bones and muscles of the upper limb, as described in chapter two. Accordingly, it can be concluded that the drive cables, which are in the central path of the shoulder muscles [9], can be replaced to simulate movement close to that of the main movement (abduction, flexion, and horizontal flexion). In this regard, the bioinspired concept refers to this type of investigation, and which means that according to the skeleton design of the upper limb and the positions of the surrounding muscles that are responsible for actuating movements, inspiration can be gained for a design for our new and efficient tendon-driven system, which was designed to cover these three degrees of freedom in the shoulder joint.

The centre of rotation of the shoulder joint is a dynamic concept rather than a fixed anatomical point, due to the joint's complex structure and its wide possible range of motion. The shoulder joint, primarily the glenohumeral joint, employs a ball-and-socket mechanism where the head of the humerus articulates with the glenoid fossa of the scapula. However, unlike a simple mechanical joint, the centre of rotation in the shoulder can shift depending on the arm's position and movement. The purpose of this design is to be able to move the arm at angles of 0 to 90 degrees for shoulder abduction and shoulder flexion, and 0 to 45 degrees for the shoulder horizontal adduction (flexion). According to the available articles and studies[135], the centre of the shoulder can articulate movements of more than 90 degrees. As a result, according to the indicated angular ranges for the three shoulder movements considered in this project, the centre of the shoulder can be assumed to be a fixed point.

In the realm of biomechanical research, particularly in the design of assistive robotic systems, the centre of the shoulder joint is commonly approximated as the head of the humerus, which is the *Centre of the Glenohumeral Joint* (CGH) [11], [13]. This simplification is often adopted to facilitate the process of designing such systems. This approach streamlines the complex biomechanical characteristics of the shoulder into a more manageable model, enabling researchers and engineers to develop functional and effective assistive devices, like exosuits, via a more straightforward engineering approach. Figure 3-2 shows the upper arm, muscles, and bones.

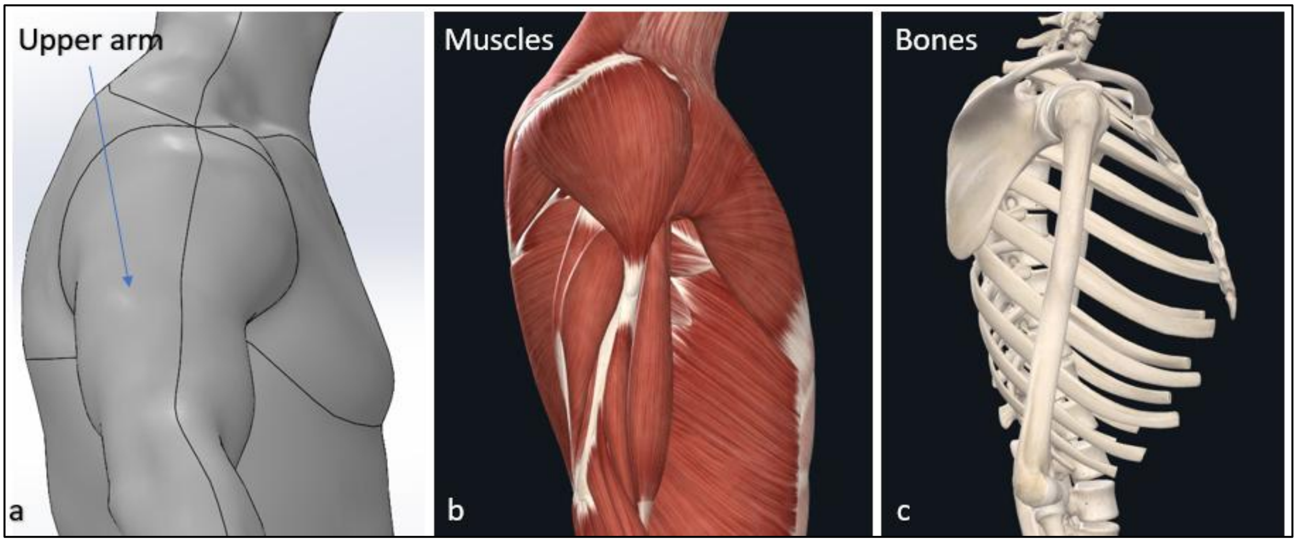

Figure 3-2: a: Upper arm- b: Muscles – c: Bones.

The development of the Cable-Driven Shoulder Exosuit (CDSE) was fundamentally guided by bio-inspired and bio-mimetic principles, ensuring that the device closely mimics the natural biomechanics of the human shoulder. In biological systems, the human musculoskeletal structure efficiently distributes forces through a network of tendons, muscles, and ligaments, allowing for smooth, controlled movements with minimal energy expenditure. To replicate these natural dynamics, the CDSE employs a Bowden cable transmission system, which functions similarly to biological tendons by transmitting force from actuators to the upper limb while maintaining flexibility. The anchor points of the exosuit were strategically positioned to align with key anatomical landmarks, such as muscle insertion points and ligament attachments, ensuring that force application remains biomechanically accurate and does not impose unnatural constraints on movement. Furthermore, the soft and lightweight materials used in the exosuit structure mimic muscle compliance, reducing stiffness and increasing user comfort. Unlike traditional rigid exoskeletons, which often restrict movement and impose mechanical constraints, the CDSE integrates a biological-inspired load distribution mechanism within the backpack system, ensuring that weight is evenly dispersed across the user's back, akin to the way the skeletal system naturally supports loads. By leveraging these bio-mimetic strategies, the exosuit enhances assistance by reinforcing natural movement patterns, rather than overriding them, thus offering a more effective and intuitive assistive device for individuals with upper limb impairments.

Shoulder abduction, a fundamental movement in human biomechanics, typically involves several muscles working in concert. The primary muscle responsible for shoulder abduction is the deltoid, particularly its central fibers. This muscle is crucial to lifting the arm away from the body. Additionally, the supraspinatus muscle, part of the rotator cuff group, allows for the first 15 degrees of abduction and assists the deltoid throughout such movement. Other rotator cuff muscles, including the infraspinatus and teres minor, play a supportive role in stabilizing the shoulder joint. The serratus anterior also contributes, particularly in maintaining the scapula's position against the thoracic wall, to ensuring a coordinated and smooth movement.

The primary muscle responsible for **shoulder flexion** is the anterior deltoid, which is crucial to lifting the arm forward; the pectoralis major, particularly its clavicular head, plays a significant role in assisting this movement. The biceps brachii also contributes not just as an elbow flexor but also as a shoulder flexor, particularly when the arm is in a supinated position. The coracobrachialis, a smaller muscle located in the upper arm, also assists in flexing the shoulder.

Shoulder horizontal flexion, also known as horizontal adduction, is a complex movement involving the transverse motion of the arm across the body. This movement primarily engages the pectoralis major, particularly its sternal head, which is instrumental in drawing the arm towards the body's midline. Complementing this action, the anterior deltoid, typically associated with shoulder flexion and abduction, also plays a significant role in facilitating horizontal flexion. Additionally, the coracobrachialis, a smaller muscle in the upper arm, contributes to this movement by assisting in shoulder adduction. The biceps brachii, while predominantly recognized for its role in elbow flexion, also aids in shoulder horizontal flexion, especially when the arm assumes a supinated position. An understanding of the coordinated activity of these muscles is crucial in the field of soft robotics, particularly for the development of exosuits designed to assist or augment shoulder movement. This knowledge ensures that such devices are biomechanically aligned with the human body, enhancing their functionality and ergonomic integration.

As can be seen, to perform each of the three movements, different muscles in different proportions are responsible for keeping the arm in balance. Also, some muscles involved include those of the inner layers of the arm. For this reason, the three paths suggested in Figure 3-7 are those considered to be the central path of the internal and external muscles described in chapter two (literature review).

3.3 Design Rationale and Conceptual Design

3.3.1 Design Rationale

The rationale for designing the Cable-Driven Shoulder Exosuit (CDSE) stems from the need for a lightweight, portable, and bio-inspired assistive device for upper limb assistance regarding chapter two literature review of sixty papers. Existing rigid exoskeletons are often heavy, uncomfortable, and impractical for prolonged use. Therefore, the CDSE was developed to offer a soft-robotic alternative that better aligns with human biomechanics. The exosuit's design prioritizes user comfort, effective load distribution, and ease of use, ensuring its viability for both clinical and home-based assistance. The primary goal was to create a system that mimics natural movement patterns while reducing the physical strain on users with impaired upper limb mobility.

The design methodology follows an iterative approach involving conceptualization, mathematical modelling, prototyping, and validation through simulations and experimental testing. The conceptual phase focused on identifying key biomechanical constraints and user needs, leading to the selection of a cable-driven mechanism over traditional linkage-based systems. Finite Element Analysis (FEA) was employed to optimize structural integrity, ensuring that the exosuit components could withstand expected loads without excessive deformation. The design was refined based on static analysis and real-world testing, ensuring it meets the functional requirements of assistance.

To translate high-level design objectives into tangible specifications, several engineering parameters were defined:

Mobility: The system was designed to provide three degrees of freedom for shoulder movements—abduction, flexion, and horizontal flexion—based on human biomechanics.

Material Selection: A combination of lightweight materials such as carbon fiber and aluminium were chosen to balance durability and portability.

Actuation System: High-torque, compact servomotors (XM540-W270-R) were selected to drive the cable mechanism, ensuring smooth and controlled movement.

Control System: A PID-based feedback control mechanism was implemented to regulate cable tension and ensure precise motion assistance.

Wearability and Ergonomics: The exosuit was designed with a backpack-mounted motor pack, minimizing bulk on the user's limbs while optimizing weight distribution.

3.3.2 Justification of Concept and Prototype

The published articles on exosuits from 2004 to 2022 have been analysed in the table below. The following factors were considered when selecting articles:

- Only articles related to exosuits are considered, while articles related to exoskeletons are not.
- This review excludes articles that were published to investigate the tension lines of the body and muscles.
- Articles have been reviewed that present at least one degree of freedom of the shoulder joint in that design.

Table 3-1: The published articles on exosuits from 2004 to 2022

Row	Year	Supported Movements	Actuators	power transmission	Sensors	DOF	Portable	Soft/Rigid	Clinical Details and Status	Weight(kg)	Controller	References
1	2004	Shoulder (FE/AA/RT), Elbow (FE)	Mckibben muscles	compressed air	electropneumatic regulator	4	No	Soft and Rigid	prototype	7.6	Open loop control	[30]
2	2007	Shoulder (FE), Elbow (FE), Forearm (PS), Wrist (FE)	Pneumatic (PAMs)	compressed air	joint angles, inertial sensor, pressure sensors	4	No	Soft	healthy and stroke patients	----	Adaptive Controller	[27]
3	2011	Shoulder (AA)	brushless DC motor	cable driven series-elastic actuation	electromagnetic (EM) sensors	1	No	Soft	prototype	300 g (actuation is not included)	Adaptive Controller	[136]
4	2012	Shoulder (AA)	brushless DC motor	cable-driven transmission	IMU sensors	1	No	Soft	prototype	300 g (actuation is not included)	EPOS-2 24/2 digital positioning controller	[56]
5	2014	Shoulder((AA)/ RT)- Elbow (FE)	DC motor+ balloon type support	cable-driven transmission+ compressed air	EMG	2	Yes	Soft	one healthy subject	4.36	Controller with reed switch	[137]

6	2015	Shoulder (FE)-Elbow (FE)	DC motor	cable-driven transmission	current sensor	2	No	Soft	one healthy subject	----	motor controller (Maxon)	[138]
7	2016	Shoulder (AA)	Pneumatic	compressed air	accelerometer+ pressure sensor	1	No	Soft	one healthy subject	0.035 (without actuation system)	Arduino Uno microcontroller	[64]
8	2016	Shoulder (AA/FE), Elbow (FE)	DC motors+ Twisted string actuator (TSA)	cable-driven transmission	angles sensor	3	Yes	Soft	4 healthy subjects	less than 4 kg	Kinect Xbox 360 motion sensor device	[65]
9	2017	Shoulder (AA/HFE)	Pneumatic	Textile based soft actuators	sEMG	2	No	Soft	3 healthy subjects	0.48 (without actuation system)	----	[67]
10	2017	Shoulder (FE/AA)	cam-rod structure + rubber band	cable-driven transmission	sEMG	(2)	Yes	Soft	6 healthy subjects	----	----	[69]
11	2017	Shoulder (AA)	Exomuscle from fabric reinforced inflatable bladders	compressed air	EMG	1	Yes	Soft	3 healthy subjects	0.35 (without actuation system)	Position control	[139]
12	2018	Shoulder (FE)-Elbow (FE)	brushless DC motor	cable-driven transmission	EMG	2× 2	Yes	Soft	1 healthy subject	10 kg	Voice activated by PID	[72]
13	2018	Shoulder (FE/AA/RT), Elbow (FE), Forearm (PS), Wrist (FE/AA)	brushless DC motor	cable-driven transmission	sEMG	7	No	Soft	healthy and Stroke patients	----	STM32 board	[9]
14	2018	Shoulder (AA/FE), Elbow (FE)	brushed DC micromotors	cable-driven transmission	IMU sensors	3	Yes	Soft	healthy and Stroke patients	1.3	mimetic control algorithm (PID)	[73]
15	2018	Shoulder (AA)	pneumatic fabric bladders	compressed air	EMG	1	No	Soft	3 healthy subjects	----	----	[82]
16	2019	Shoulder (FE)-Elbow (FE)	Thin McKibben Muscle	compressed air	EMG+ force gauge	2	No	Soft	11 healthy subjects	2.1	linear actuator controller	[140]
17	2019	Shoulder (FE)	brushless DC motor	Bowden cable, planetary reduction stage	EMG+ position sensor+6-axis load cell, IMU	1	No	Soft and Rigid	5 healthy subjects	2.45	PID+ joystick	[74]
18	2020	Shoulder(F)-Elbow(F)	brushless DC motor	cable-driven transmission	EMG	2 × 2	Yes	Soft	5 healthy subjects	7.5 kg	Voice activated by PID	[141]
19	2020	Shoulder (FE/AA)	hybrid inflation modules fabric-plastic (nylon fabric)	compressed air	EMG signals	2	No	Soft	ten healthy subjects	----	Teensy 3.6	[142]
20	2020	Shoulder (AA)	McKibben muscles	compressed air	force gauge	1	No	Soft	a healthy subject	----	precision regulator	[143]

21	2020	Shoulder (FE)/Elbow (FE)/Forearm (PS)/Wrist (FE)	Pneumatic Gel Muscle (PGM)	CO2 canisters as a source of compressed air	EMG signals/Pressure sensor	4	Yes	Soft	elderly and healthy subjects	2.1 kg	PI control	[144]
22	2020	Shoulder (FE)-Elbow (FE)	DC motor	cable-driven transmission	position sensor and goniometer	2	Yes	Soft	4 healthy subjects	----	super-twisting sliding mode controller (SMC)	[77]
23	2020	Shoulder (FE)-Elbow (FE)	DC motor	cable-driven transmission	EMG	2	Yes	Soft	4 healthy subjects	total weight in the backpack is 890 gr	sliding mode controller (SMC)	[145]
24	2020	Shoulder (AA)	elastic spring-cam-wheel system	cable-driven transmission	EMG	(1)	Yes	Soft	4 healthy subjects	1.82	----	[146]
25	2021	Shoulder (AA)-Elbow(E)	inflatable	compressed air	IMU +sEMG	2	No	Yes	eight healthy individuals	< 0.5	PID	[147]
26	2022	Shoulder (AA/FE)- Elbow (FE)	DC motor	cable-driven transmission	sEMG	3	Yes	Yes	nine healthy individuals	1.53	control (twisting sliding mode controller)	[148]

- Shoulder rotations (A (Abduction)/ A(Adduction) /F (Flexion)/ E(Extension)/R (internal rotation)/ T (external rotation)).
- Shoulder translations (scapular protraction/retraction HD (horizontal displacement) and elevation/depression HD (vertical displacement)).
- Elbow (F (Flexion)/ E (Extension)).
- Forearm (S (Supination)/P (Pronation)).
- Wrist (F (Flexion)/ E(Extension)/ A (Abduction)/ A (Adduction)).
- DOF: degrees of freedom.
- () related to passive motions.

3.3.2.1 Type of Actuators

As mentioned in the above table, electric motors are used in 50% of the presented designs. Thirteen other designs include designs that use pneumatic systems, springs, and plastic bands. We have used electric actuators in our design because of the possibility of easy conversion to a portable system and the possibility of creating the required torques with small servo motors.

3.3.2.2 Power transmission

Fifteen out of twenty-six designs have used the cable driven system. The important advantage of this method is that the weight of the motors can be reduced from the user's hand and transferred to the backpack on the user's back. For this reason, this method has been used for our design. Also, in the case of pneumatic design, compressed air supply is needed to stimulate the system, which removes the possibility of the design being portable in most cases, and for this reason, this design can be suitable for portable designs.

3.3.2.3 Degree of freedoms and portability

Nineteen designs out of twenty-six designs are presented with degrees of freedom 1 and 2 or as passive systems (the DOF with brackets are passive systems). Six designs with three and four degrees of freedom and one design with 7 degrees of freedom have been designed. Also, a total of twelve designs are designed as portable designs. Among the designs that cover three and four degrees of freedom, no design that includes three degrees of freedom of the shoulder member has been presented.

3.3.2.4 Weight

In eight out of twenty-six articles, there is no information about the weight of the system. In six articles, only the weight of the part that is mounted on the arm is presented, and there is no information about the weight of the actuation system. As you can see, the weight of the designs is from several hundred grams to about 10 kilograms in various research. In our design, considering the coverage of three degrees of freedom of the shoulder joint, the final weight of the actuation system and the parts that are installed on the human arm is about 2 kg.

3.3.3 Conceptual Design

To design a model compatible with human body, we used a dimension of a body with the measure of a 99% Percentile Man (age 20-65 years- 112.2kg) [149] to match all its design elements (see Figure 3-3). Anthropometry is the scientific study and measurement of the human body's dimensions. This knowledge is crucial to designing exosuits that are ergonomically suitable and adaptable to different body types. Anthropometric data ensures that the exosuits are not only functional but also comfortable and safe for the user, accommodating a range of motions and physical activities. Accurate anthropometric measurements are key to customizing exosuits to individual users, enhancing their effectiveness in assisting or augmenting human movement.

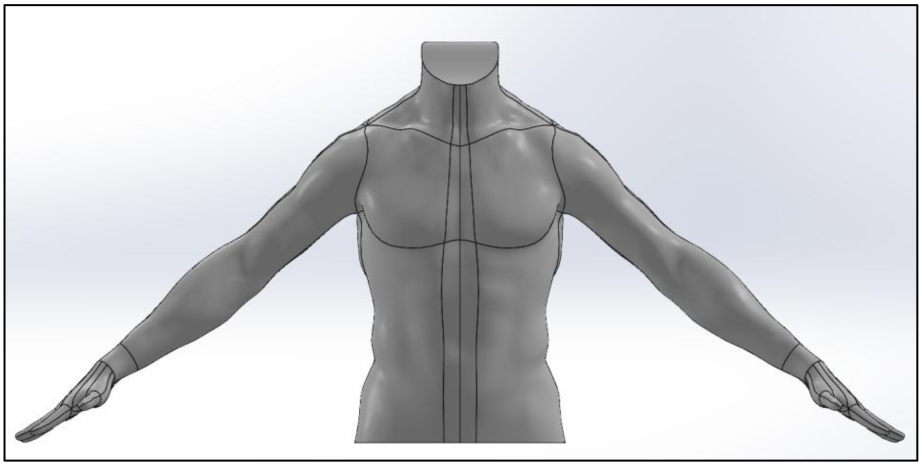

Figure 3-3: Human body with the measure of a 99% Percentile Man.

To design a lightweight cable-driven exosuit, actuators should move to the back of user (like a backpack), and only anchor points should attach to the arm. Figure 3-4 shows the preliminary schema of the design.

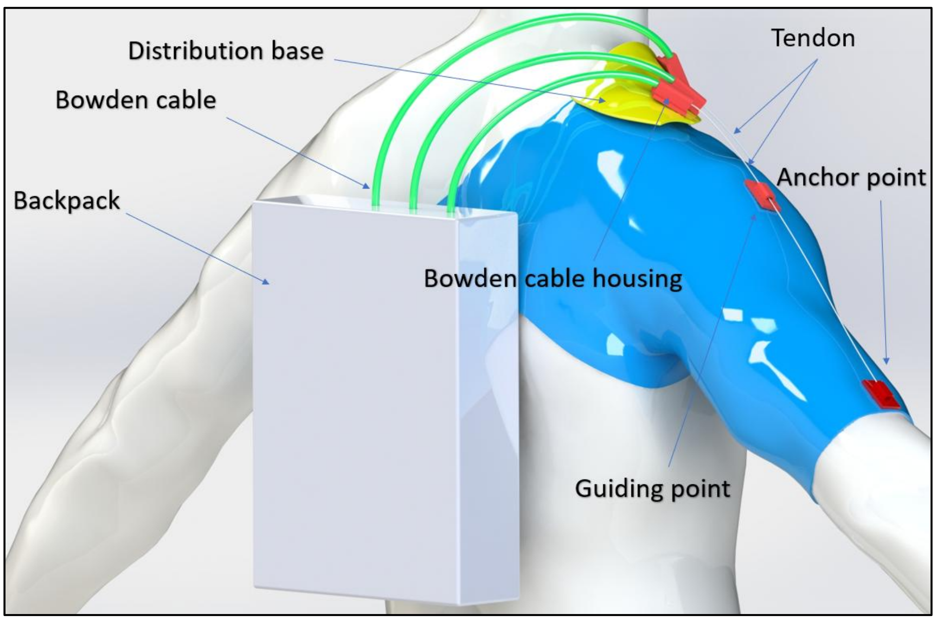

Figure 3-4: The conceptual design of the exosuit consists of each part of the system (actuators would be considered to be in a backpack and moved with a tendon anchor point).

The actuator cables (tendons) are passed through Bowden cables, Bowden cable housings, and guiding points, and finally attach to the anchor points. In accord with the three degrees of freedom required three different paths, as well as three different motors, are used to allow for this actuation, where all the devices of the actuator system are situated in a backpack behind the patient. The advantage of this design over exoskeleton designs is the minimal weight of the devices installed on the patient's arm when moving the actuator system at the patient's back. The actuator cables attach to the distribution base via some Bowden cable housings (Figure 3-5) through the Bowden cables, where they pass through the first guiding point (Figure 3-6), which is the crossing point, and finally connect to the end point at the desired location.

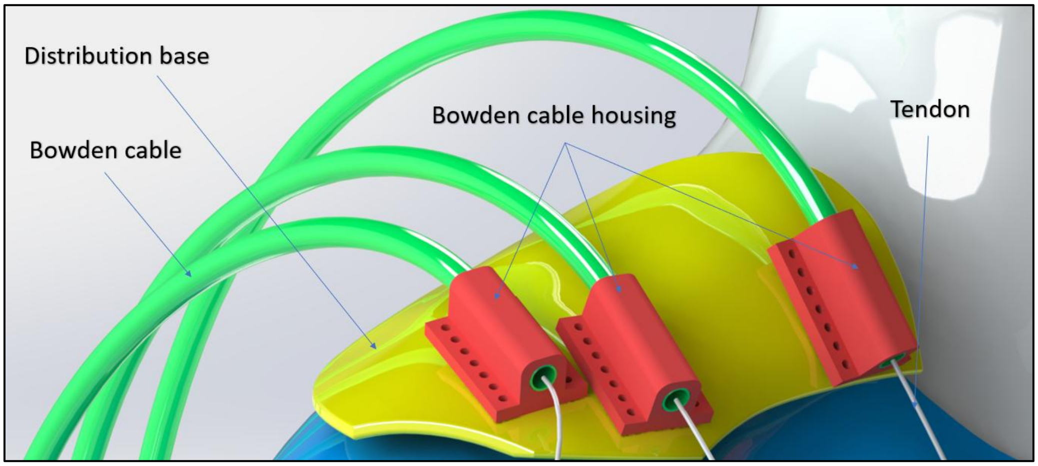

Figure 3-5: The distribution base sits on the shoulder and the Bowden cable housings are located to allow the tendon to pass.

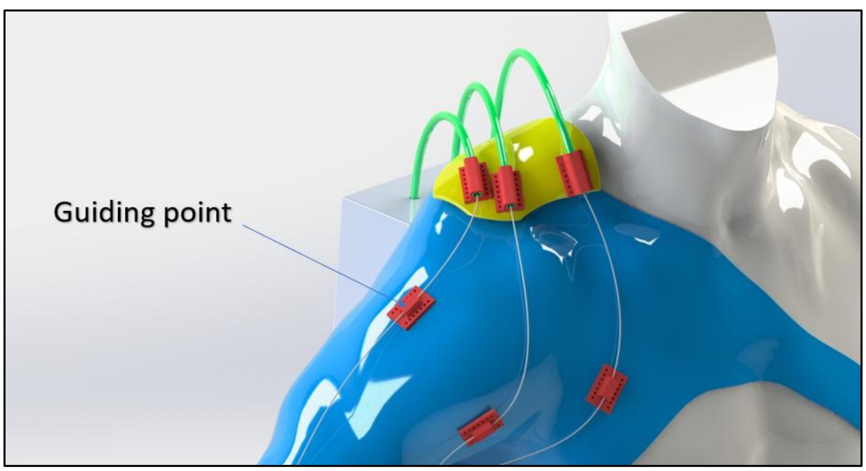

Figure 3-6: Guiding points to guiding the tendon and connecting the tendon to anchor points.

As shown in Figure 3-7, path a, path b, and path c, allow for shoulder abduction, flexion, and horizontal adduction movements, respectively. The presumption is that, due to gravity, the opposite movements to the two desired ones (abduction and flexion) will be performed by gravity and the weight of the arm. Also, by making the above assumption, the number of motors required can be reduced, and the intended design will be lighter.

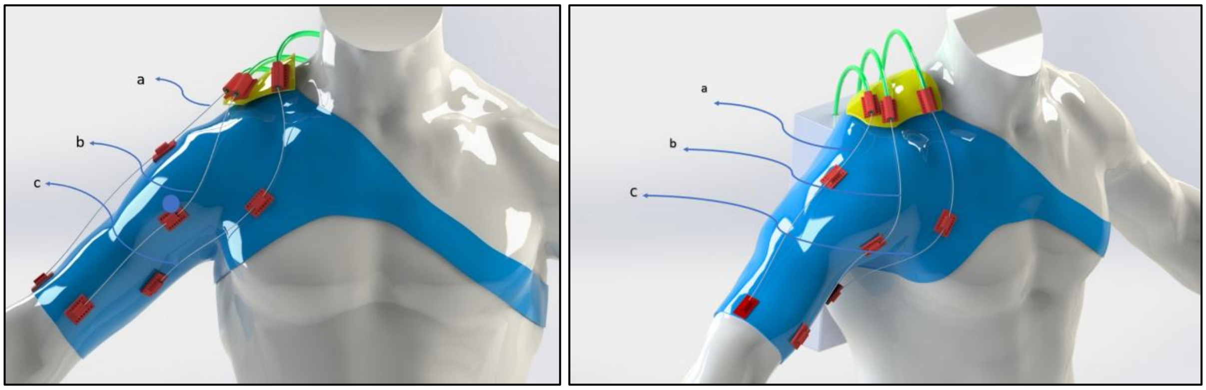

Figure 3-7: The actuator cable paths that pass the tendons and connect the actuators to the upper arm.

3.4 Design and Development of Exosuit

The design phase of the backpack, integral to the development of the exosuit, was meticulously structured into three progressive stages, evolving from conceptual design to detailed design. This phased approach facilitated a systematic and thorough development process. The initial stage, conceptual design, involved brainstorming, preliminary sketches and the creation of basic functional outlines, setting the foundation for the project. This transitioned into an intermediate design phase, where the initial concepts were refined, and more detailed plans were formulated. This stage further included the development of prototypes, which were essential for testing and further refinement. The final stage, detailed design, marked the culmination of the design process, where precise specifications, materials, and engineering details were finalized. This stage was critical to ensuring the practical feasibility and functionality of the backpack. The accompanying illustration provides an overview of this comprehensive design phase, visually representing the transition from abstract ideas to a tangible, detailed design. The design steps are depicted in Figure 3-8.

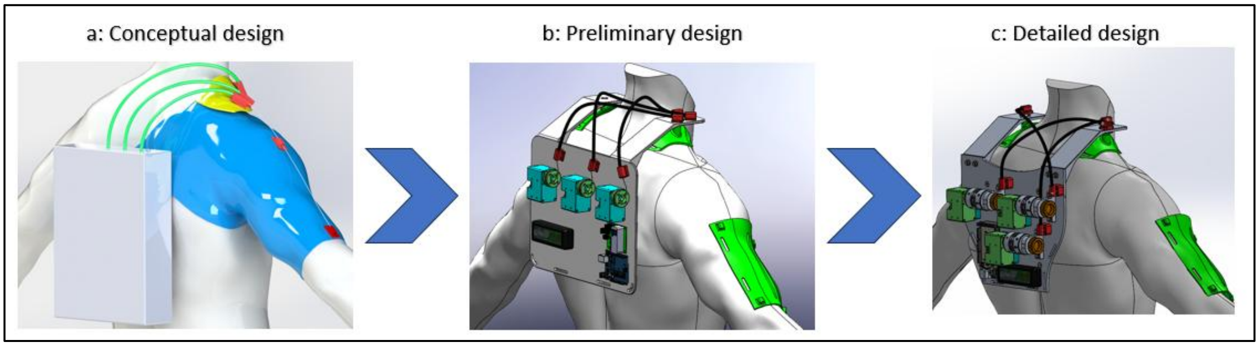

Figure 3-8: Design phases: (a) Conceptual design - (b) Preliminary design – (c): Detailed design.

3.4.1 Design and Development of Backpack Pad

To place the backpack on the shoulders, there is a need for two parts that must be placed on the shoulders on one side and attached to the backpack on the other. An image of such a part is shown in Figure 3-9, and whose overall dimensions are presented in Figure 10-1.

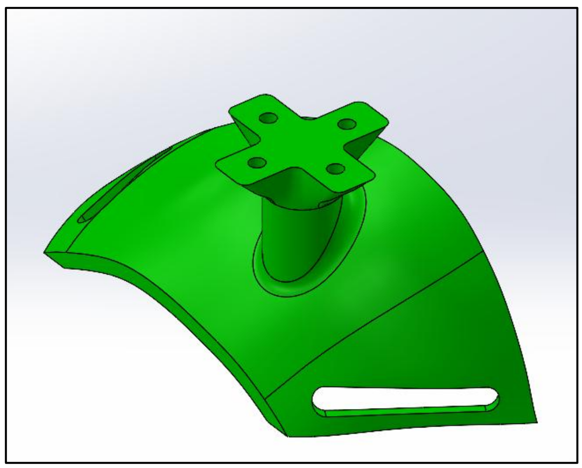

Figure 3-9: Backpack pad 3D model.

3.4.2 Design and Development of Backpack

To design this backpack, the presumption was a need for easy wearing and removal, and a that the product should have a low weight. In addition to the aforementioned requirements, the parts needed to be designed in such a way that three desired motors, with a control system and a lithium battery, could be placed on them. The associated design steps are depicted in Figure 3-10. One of the advantages of this backpack is that it can also be installed on a wheelchair.

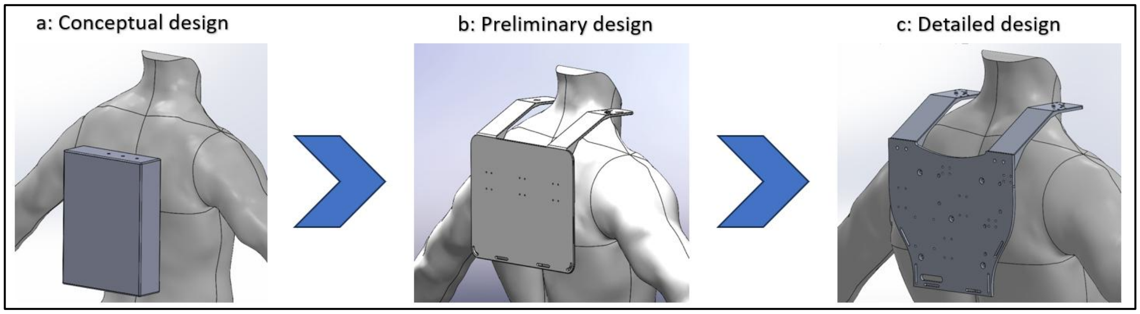

Figure 3-10: Backpack design phases.

As shown in Figure 3-11, this backpack has the ability to sit on the shoulders due to its arc-shaped support surfaces (green parts). There are also grooves in the lower part that can be attached to the body via special restraint straps. Figure 3-11 shows how the backpack is placed on the body from different perspectives.

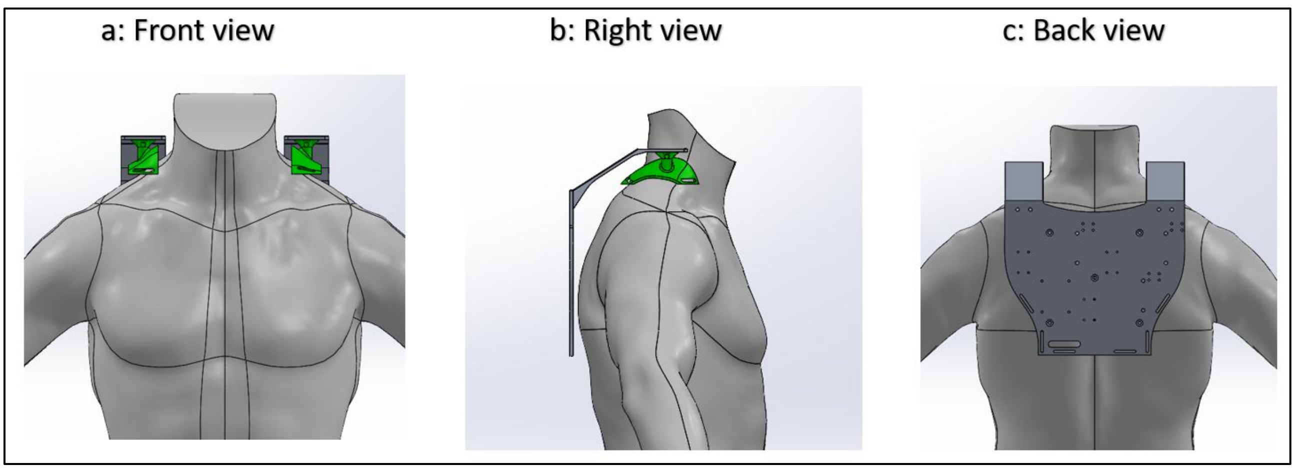

Figure 3-11: Positioning of the backpack on the body.

The overall dimensions of main plate of the backpack are presented in Figure 10-2, and the connectors to the main plate of the backpack pad are illustrated in and Figure 10-3.

3.4.3 Design of Bowden Cable Housing

These parts are designed for two purposes: first, the Bowden Cables can be placed within them; and second to pass the actuator cable (tendon) that turns from the motors to the guiding and anchor points. Considering that one of the critical goals of the design is to be lightweight, and due to the limited space on the back plate of the back-plate, we needed to design two different types of part. The reason for these two types is to create a workspace through which to run the third Bowden cable. Figure 3-12 shows the positions in which both these different parts are installed.

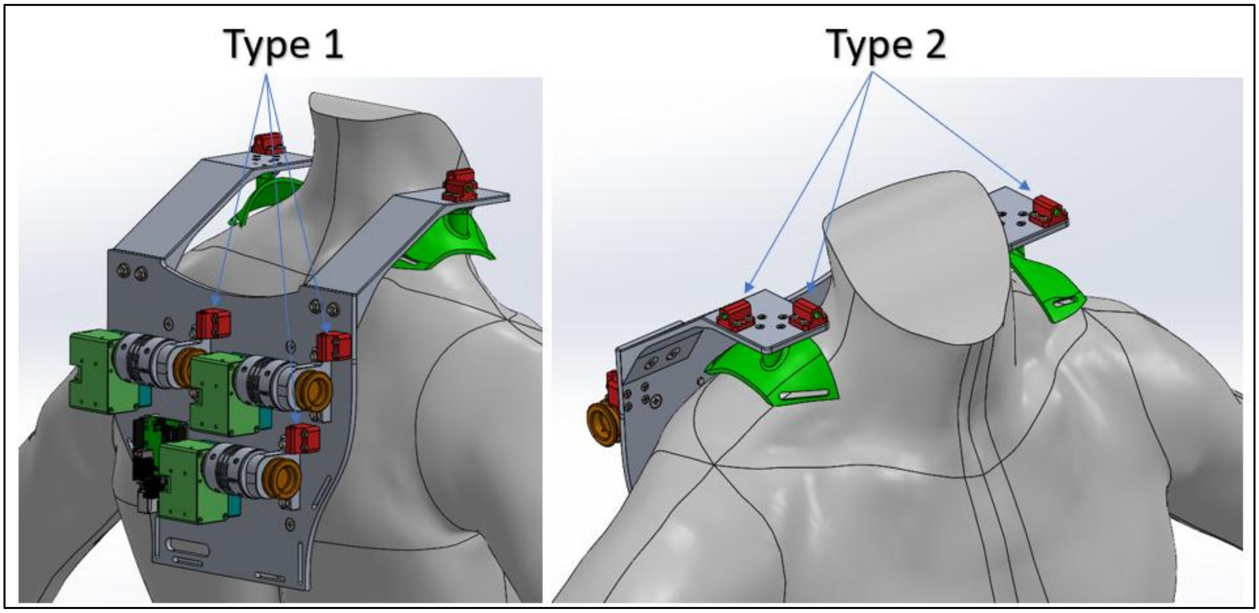

Figure 3-12: Bowden cables housing types.

Type one parts are located immediately at the output of the motors after the pulley, whilst type two parts are located at the top of the connector plate of the backpack to guide the cable in the correct direction to the top of the shoulder.

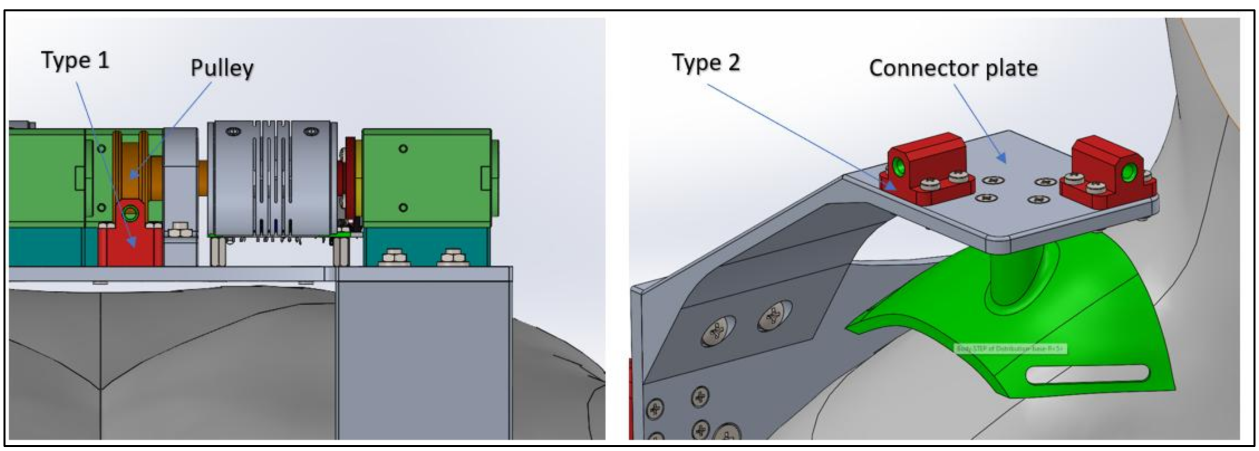

Figure 3-13: Positioning of the Bowden cable housing on the backpack (type 1 and 2).

As shown in Figure 10-4 and Figure 10-5, a stopper is placed on one side of the Bowden cables to lock them. This figure also shows the general dimensions of this part and the desired stopper. Figure 10-4 and Figure 10-5 show a separate view of the above parts.

3.4.4 Design of Anchor Points

This part is designed to guide the actuator cable along the human arm. When designing this part, the attempt was made to use the natural shape of the human arm to be highly similar to the main curvature of the body itself. Five points are installed on this part in order to pass the cables in three directions, and to ensure that the part is properly attached to them. We designed this part in order develop an integrated guide set and connecting cables on the body to make it easier to use. Four grooves are installed in the lower section of this part, which can be used to connect it to the user's arm. There are also grooves in the middle of the anchor point to reduce its weight. Figure 10-6 and Figure 3-14 show the anchor point's overall dimensions and a view of the backpack and anchor point on the user's body, respectively.

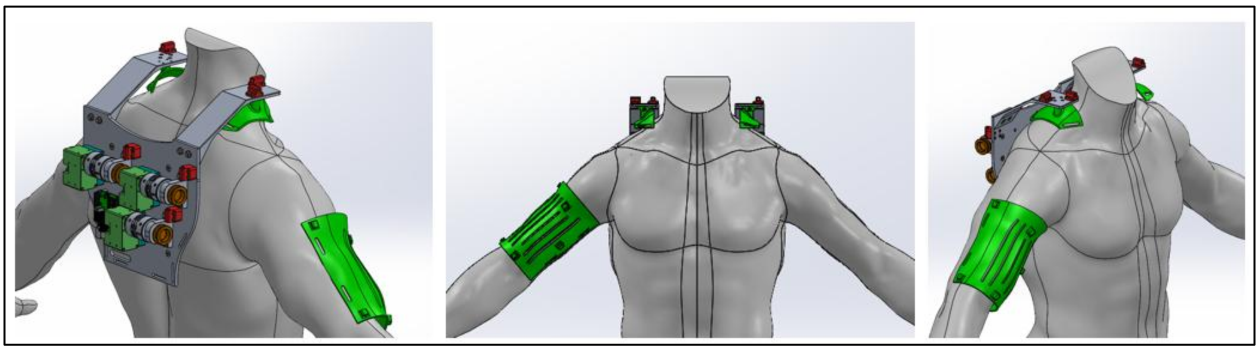

Figure 3-14: View of the backpack and anchor point on the user's body.

3.4.5 Design of Body Guiding Point

To perform the shoulder horizontal adduction (flexion) described in Figure 3-7, a point on the arm-attached part needs to be set as an anchor point. To complete this movement, as mentioned in the concept design section, there is the need for a guiding point on the user's body. To this end, another small part will be used which is sewn onto the backpack straps, as shown in Figure 3-15, whilst Figure 10-7 shows the body guiding point's overall dimensions.

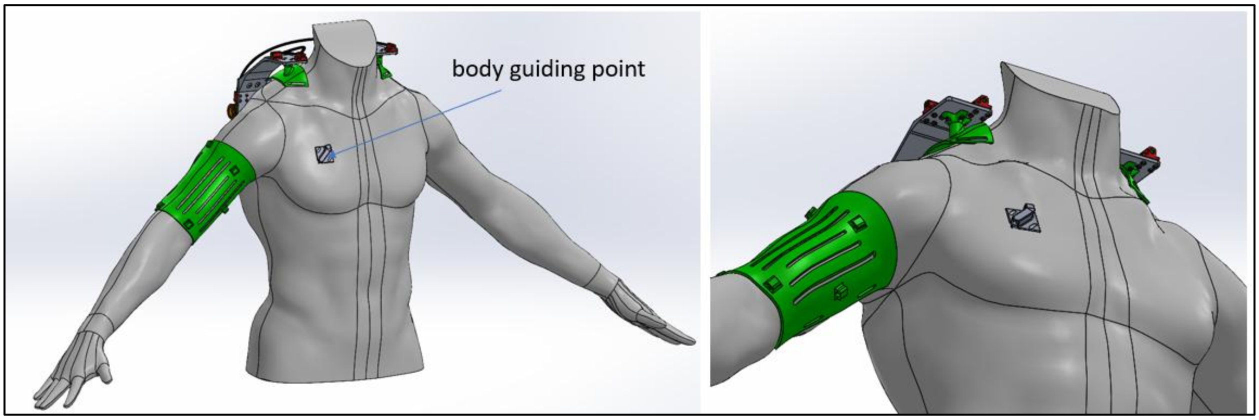

Figure 3-15: Body guiding point for third DOF.

3.4.6 Motor Pack

To apply the forces and torques required by the system for movement of the arm in three DOFs, three sets of motor packs have been used. This set includes an electric motor, connecting flange, mechanical coupling, bearing housing, motor mounting plate, and pulley to connect the desired cable. In Figure 3-16, the assembled set is illustrated, whilst Figure 3-17 gives an exploded view of the motor pack.

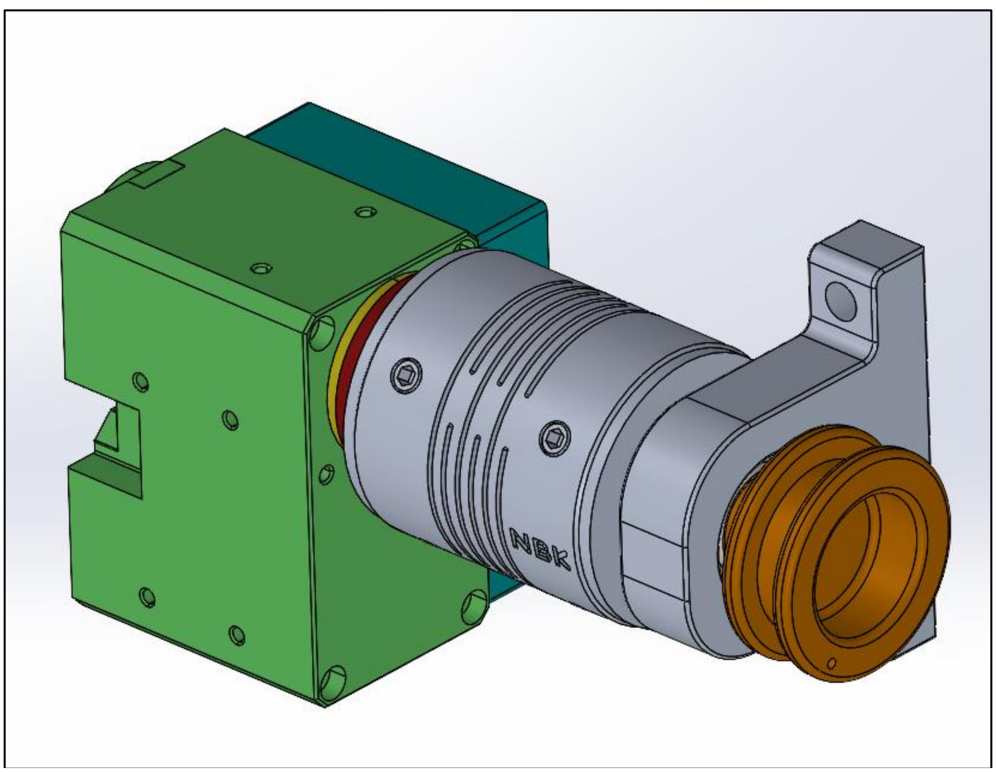

Figure 3-16: Motor pack assembly.

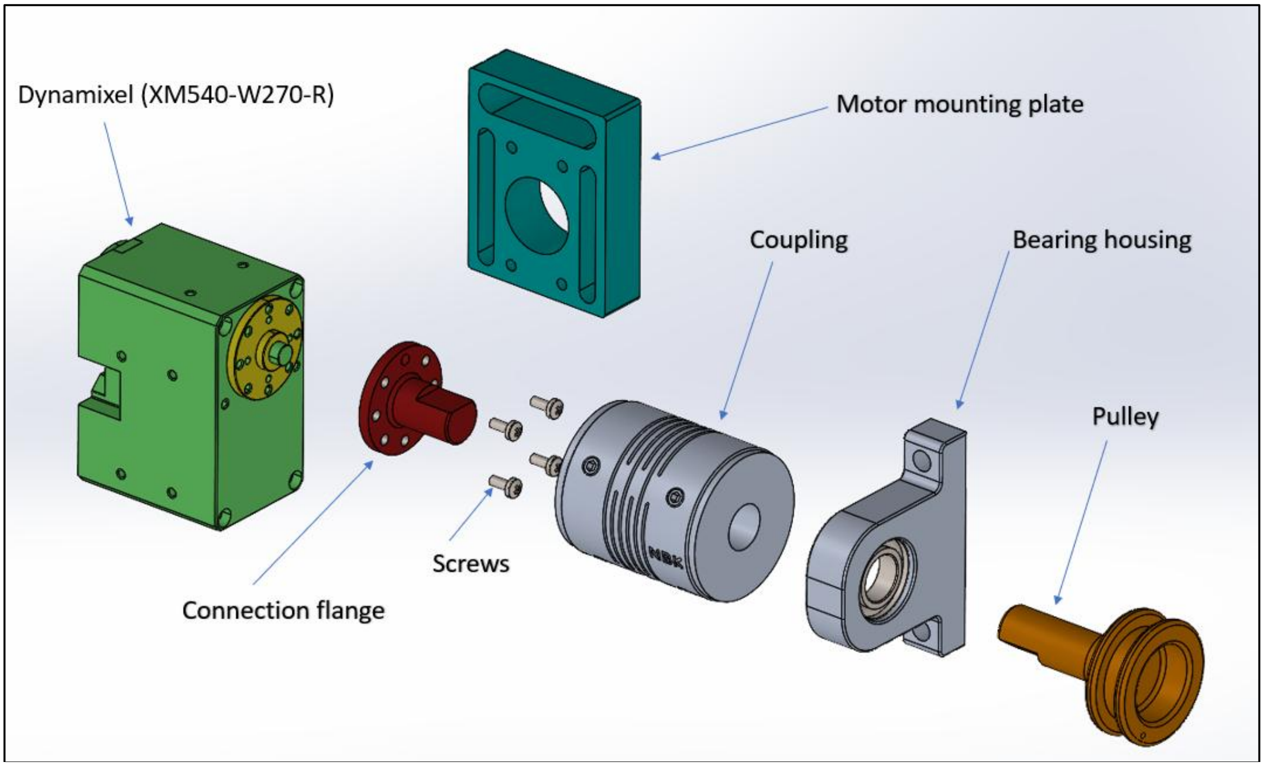

Figure 3-17: Exploded view of the motor pack.

➢ Electric motors

The actuator system used in this project employs Dynamixel compact servomotors (XM540-W270-R). These motors are intelligent DC motors that are packed with reduction gearboxes along with a controller; their complete technical specifications are presented in the appendix. Selected specifications of these motors are, however, also presented in Table 3-2:

Table 3-2: Specifications of the XM540-W270-R compact servomotors

	XM540-W270- R
Operating Modes	Current Control Mode
	Velocity Control Mode
	Position Control Mode (0 ~ 360 [°])
	Extended Position Control Mode (Multi-turn)
	Current-based Position Control Mode
	PWM Control Mode (Voltage Control Mode)
Baud Rate	9,600 [bps] ~ 4.5 [Mbps]
Physical Connection	RS485 / TTL Multidrop Bus
	TTL Half Duplex Asynchronous Serial Communication with 8bit, 1stop, No Parity
	RS485 Asynchronous Serial Communication with 8bit, 1stop, No Parity

Weight	165 [g]
Dimensions (W x H x D)	33.5 x 58.5 x 44 [mm]
Gear Ratio	272.5: 1
Stall Torque	10.0 [Nm] (at 11.1 [V], 4.2 [A]) 10.6 [Nm] (at 12.0 [V], 4.4 [A]) 12.9 [Nm] (at 14.8 [V], 5.5 [A])
Feedback	Position, Velocity, Current, Realtime tick, Trajectory, Temperature, Input Voltage, etc.

Motor selection and calculations related to this step are presented in chapter four. Figure 10-8 illustrated the overall dimensions of the motor.

- **Motor mountain plate**

To connect the motor to the main plate of the backpack, a motor mountain plate piece is used. The task of this plate is to introduce a set distance between the motor and the backpack's main plate to create the desired working space for the external cables to pass through the pulley. The motor mountain plate shown in Figure 3-18 and overall dimensions of this part are presented in Figure 10-9.

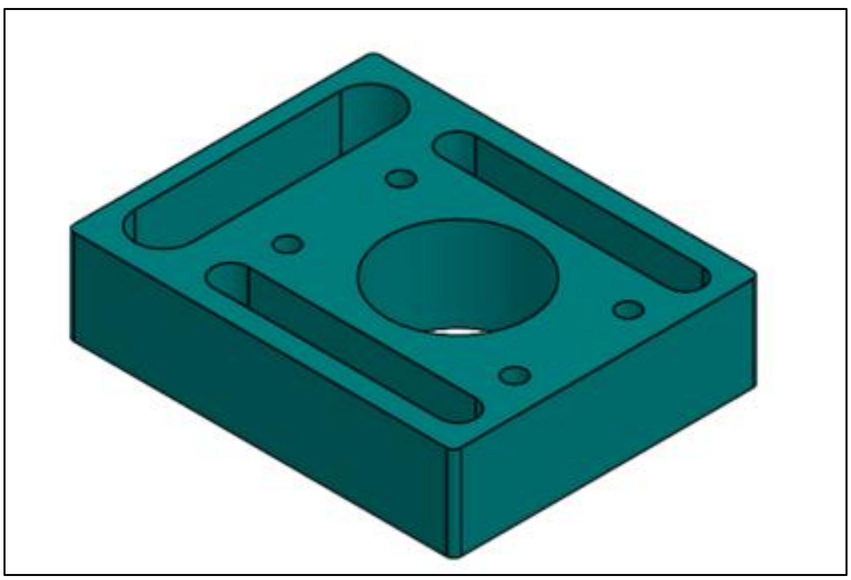

Figure 3-18: Motor-mountain plate

- **Connection Flange**

To connect the motor to the mechanical coupling, a part called the connecting flange is used. This flange is connected to the electric motor flange on one side and to the desired coupling on the other. The connecting flange shown in Figure 3-19 an overall view of this flange is given in Figure 10-10.

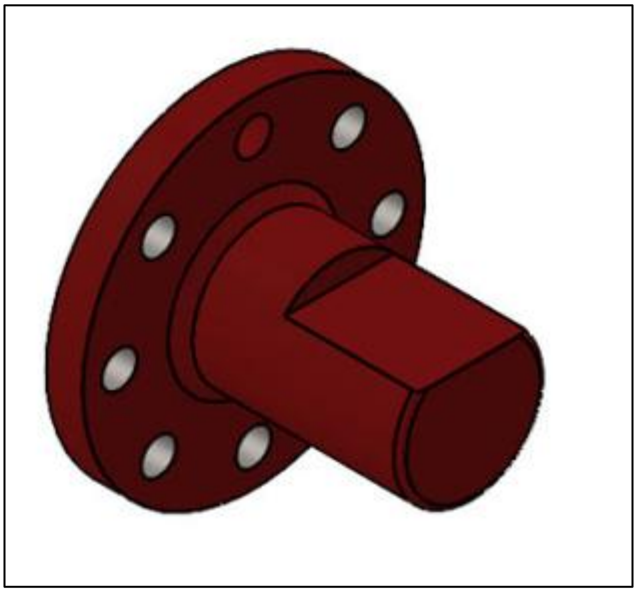

Figure 3-19: Connecting flange

- **Coupling**

The use of couplings in DC motor applications is essential for several reasons, primarily related to mechanical integration and performance optimization in systems such as those found in robotics, including soft robotics and exosuits. The couplings are critical components that connect the motor shaft to the load, ensuring the transfer of rotational motion and torque with minimal losses and misalignment.

Firstly, couplings accommodate misalignments between the DC motor and the driven component. Within the precise and demanding environments of robotics, even minor misalignments can lead to significant excess wear and tear, reduced efficiency, and potential system failure. Couplings are designed to tolerate various types of misalignments – axial, radial, and angular – thereby protecting the motor and the load from undue stresses and extending the lifespan of the system. Secondly, couplings can introduce mechanical flexibility, absorbing the vibrations and shocks that might occur during operation. This is particularly important in dynamic applications where sudden starts, stops, or changes in direction are common. By damping vibrations, couplings reduce the risk of damage to the DC motor and the driven machinery, contributing to smoother operation and enhanced reliability.

Furthermore, in the context of soft robotics and exosuits, where adaptability and compliance with the human body are paramount, couplings can provide the necessary mechanical compliance to ensure that the motor's performance is efficiently and safely translated into movement, without compromising system integrity or user comfort. In summary, the integration of couplings in DC motor-driven systems is a strategic choice to enhance alignment, absorb vibrations, and ensure the longevity and efficiency of the system, which is particularly relevant in the precision-driven field of robotics.

Coupling selection and calculations related to this step are presented in chapter four. Figure 3-20 shows the motor coupling and overall dimensions of the coupling shown in Figure 10-11.

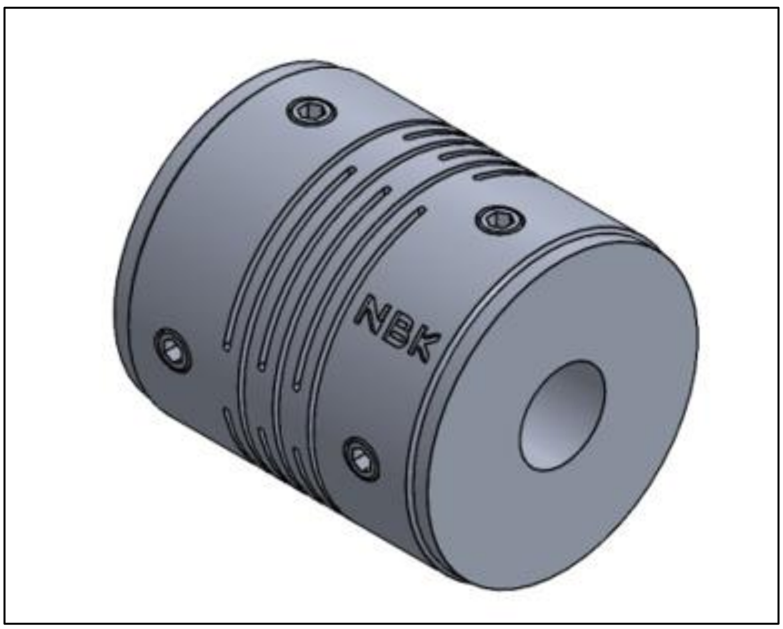

Figure 3-20: Motor coupling

- **Bearing housing**

The bearing housing is essential to maintaining proper alignment between the motor shaft and the load, reducing the risk of misalignment and uneven load distribution that can lead to increased friction and mechanical failure. Additionally, the bearing housing contributes to the dissipation of heat generated by the bearings and the motor, preventing overheating and ensuring consistent performance. Figure 3-21gives an overview of this part and Figure 10-12 shown the detail design drawing.

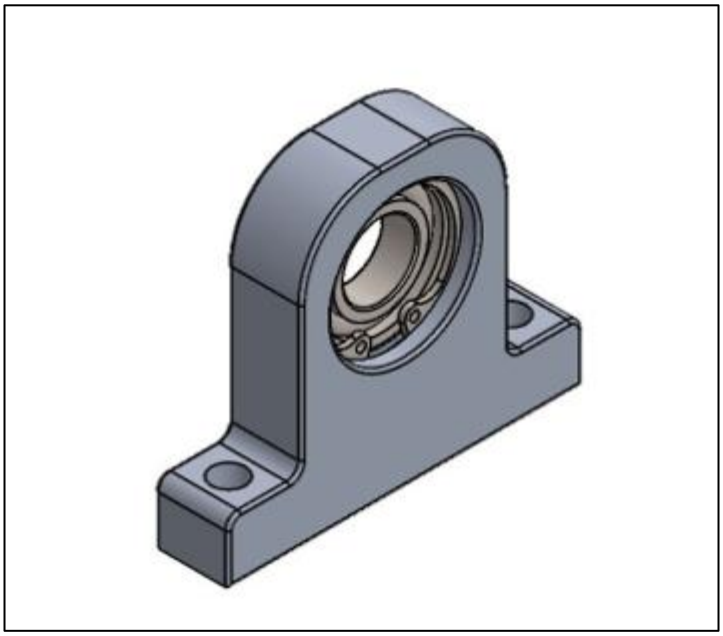

Figure 3-21: Bearing housing

- **Pulley**

A pulley is required to transfer power from motors by tendons; Figure 3-22 illustrates 3D model and Figure 10-13 three views of the pully and reports its general dimensions. This pulley was designed such that the desired tendon can be easily wrapped and unwrapped around it.

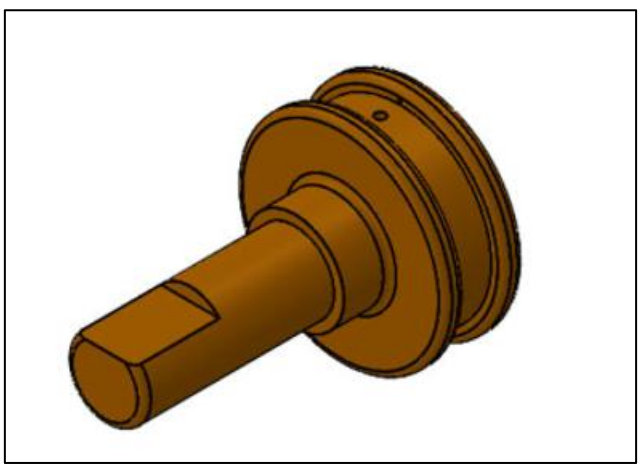

Figure 3-22: Pulley

3.4.7 Tendon

A tendon-driven system has been used in this project. This means that the motors transmit the driving force via tendons to the target organ. The aim of the present project is to design a lightweight and portable device. The diameter of these wires is 0.5 mm, with these and the device itself shown in Figure 3-23.

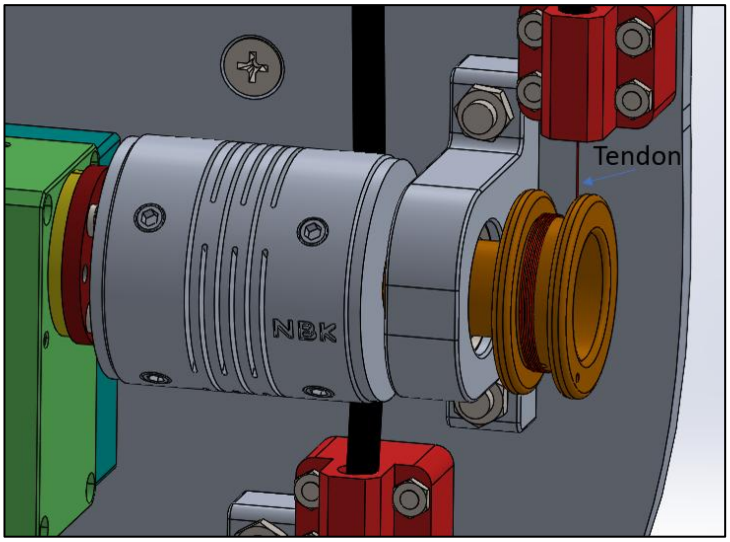

Figure 3-23: Tendon position on the pully.

3.4.8 Bowden Cable Sheath

The sheath of the cable is used to move the tendons from the motors and pulleys to the point of the shoulder distribution point. The outer diameter of this sheath is 5 mm, and it has a plastic protector on the outside. The inner layer is spiral steel wires surrounded by a PVC tube to reduce friction in the inside layer also. An image of this item is given in Figure 3-24.

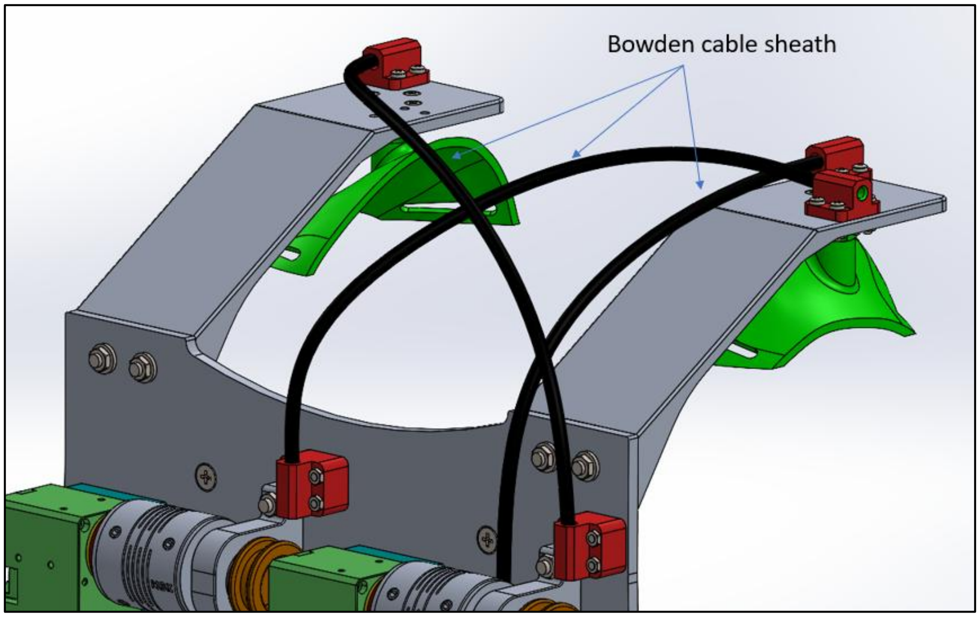

Figure 3-24: Bowden cable sheath.

3.4.9 Backpack Assembly

In the previous sections, each of the system components has been separately described. The final assembly of these parts onto the backpack is illustrated in Figure 3-25.

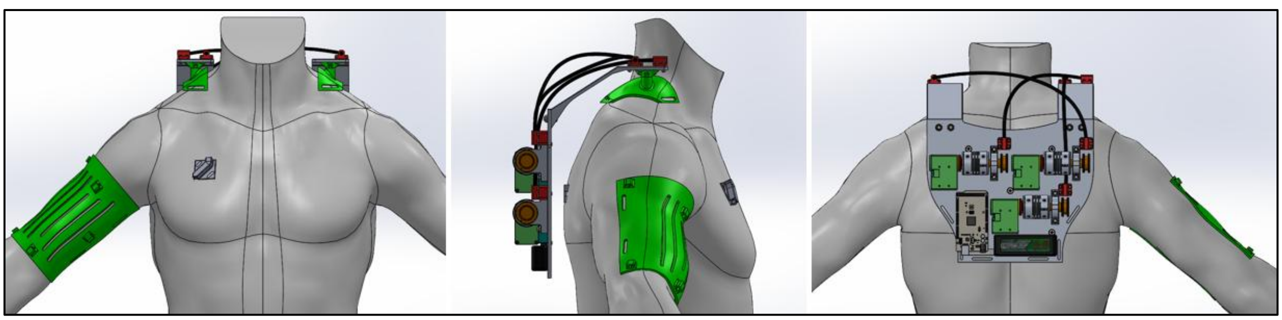

Figure 3-25: Overall backpack assembly.

3.4.10 Test Bench

➢ **Test Bench Stand**

To perform the relevant tests, a test bench was designed, as detailed in Figure 3-26, which has the ability to be installed on the backpack. Also, in Figure 10-14 the overall dimensions of this test bench are given.

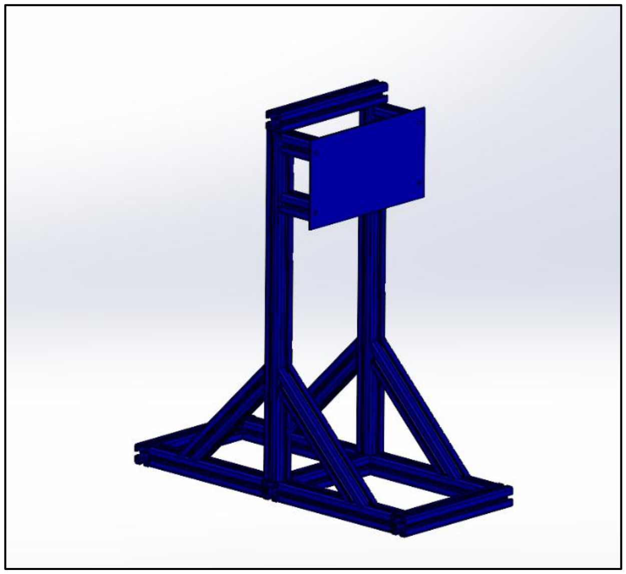

Figure 3-26: Testbench stand design.

- **Backpack Seat**

After designing the test bench, we considered the backpack seats similar to the human shoulder so that the backpack can be mounted on it like the user's shoulder Figure 10-15 shows a drawing of the backpack seats, whilst Figure 3-27 shows the backpack seats, Figure 10-15 shows the backpack seats drawing and Figure 3-28 assembly of the backpack seats on the test bench.

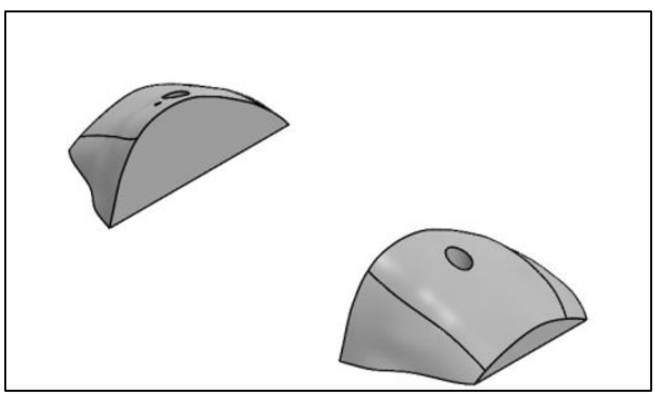

Figure 3-27: Backpack seats

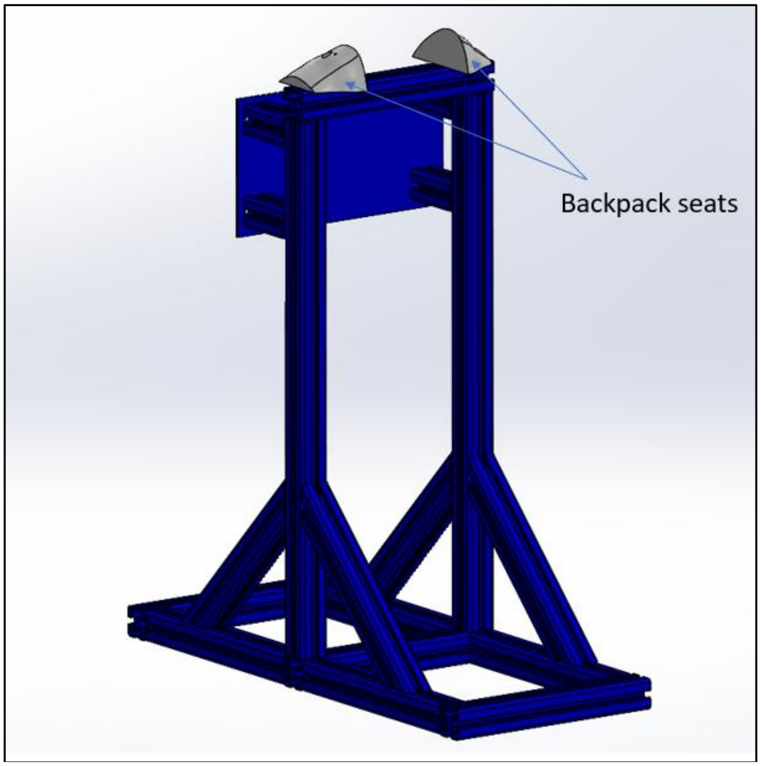

Figure 3-28: Assembly of backpack seats on the test bench.

- **Connection plate design**

The function of this plate is to connect the spherical joint to the body of the test bench. This plate (Figure 3-29) is connected to the aluminium body of the test bench at three points; it is also connected to the spherical joint at three points. One of these three points is shared by both parts of the spherical joint and the connection plate connected to the stand. Figure 10-16 shows a drawing of these connection plates, whilst Figure 3-30 shows the assembly of the connection plate on the test bench.

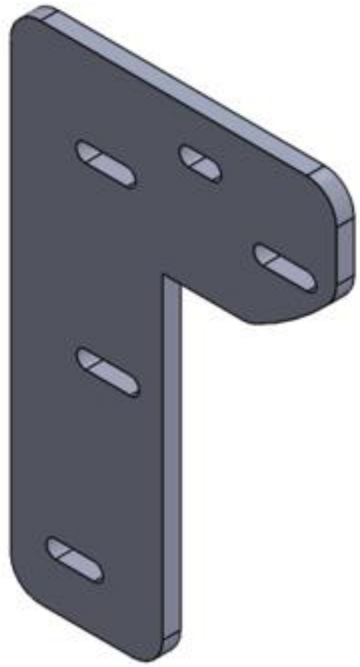

Figure 3-29: Connection plate

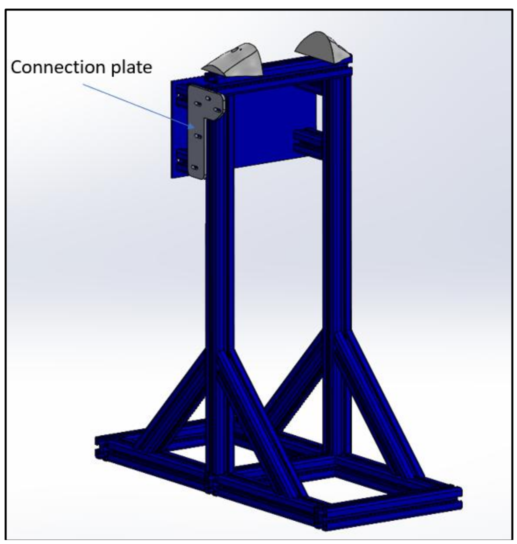

Figure 3-30: Assembly of connection plate on the test bench.

- **Design of spherical joint and upper arm**

In order to be able to perform the desired tests on the test bench, we designed a spherical joint like the shoulder. The shoulder joint is spherical and is attached to the humerus head (HH) and the humerus itself and is considered the centre of rotation of the shoulder. Figure 3-31 and Figure 3-32 illustrate the two parts designed for this purpose and Figure 10-17and Figure 10-18 shows detail design drawing of these parts.

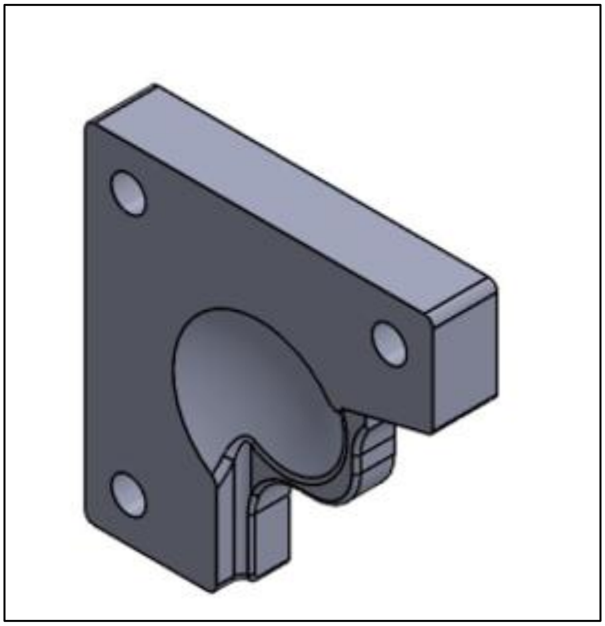

Figure 3-31: Spherical joint – female part

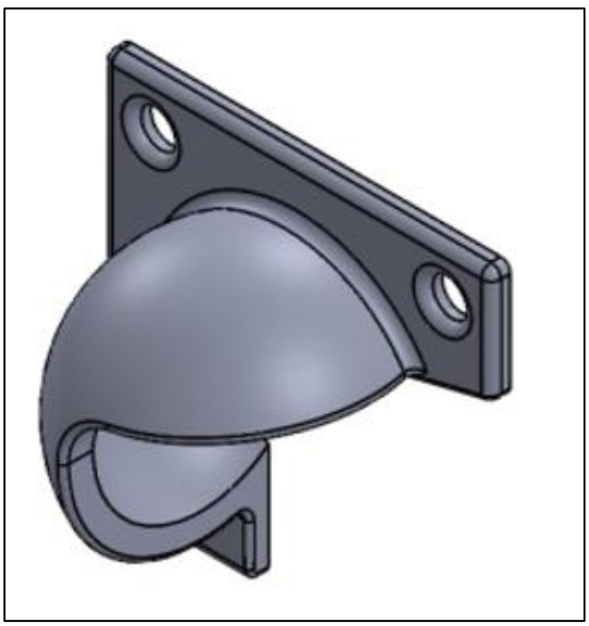

Figure 3-32: Spherical joint – male part

To form the upper arm, as shown in Figure 10-20, we designed a spherical member (like the HH) for connection to the spherical joint. In Figure 3-33 the assembly of the spherical joint and upper arm on the test bench is illustrated.

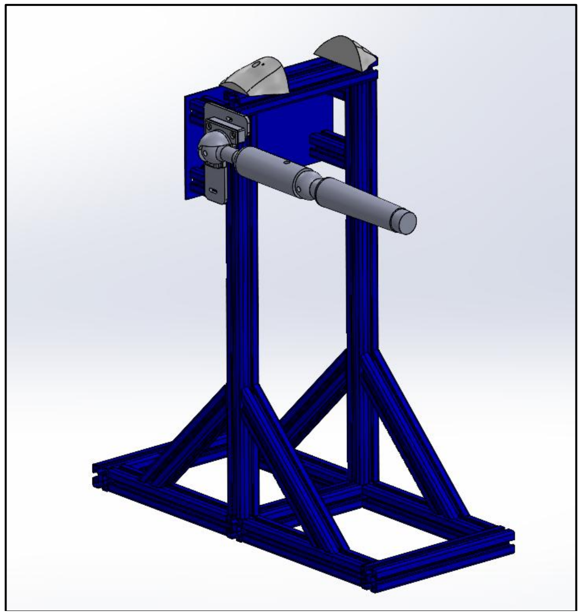

Figure 3-33: Assembly of the spherical joint and upper arm on the test bench.

- **Assembling all parts on the test bench**

Figure 3-34 and Figure 3-35 illustrate the complete assembly of all parts on the bench test. As can be seen in Figure 3-34, the design and assembly processes were carried out in such a way that the test bench position was exactly identical to the position of the backpack on the shoulder of a real user, as is clearly visible in Figure 3-35.

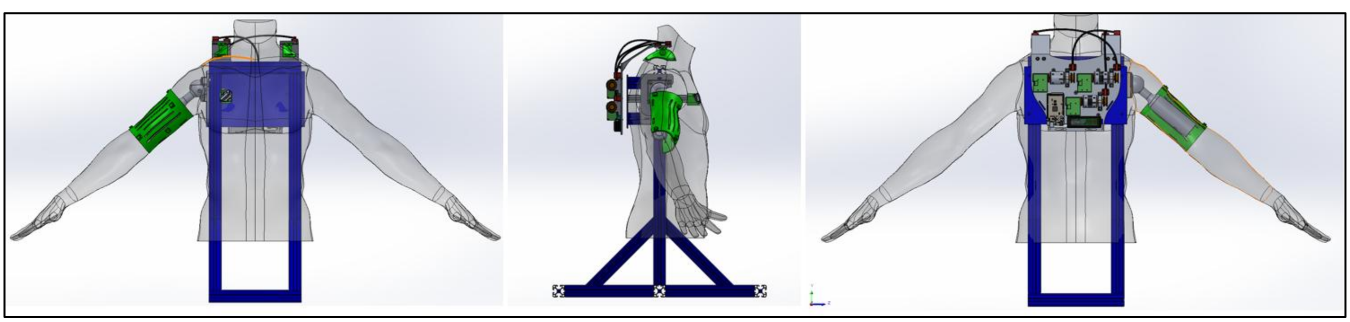

Figure 3-34: Assembling all parts on the bench test.

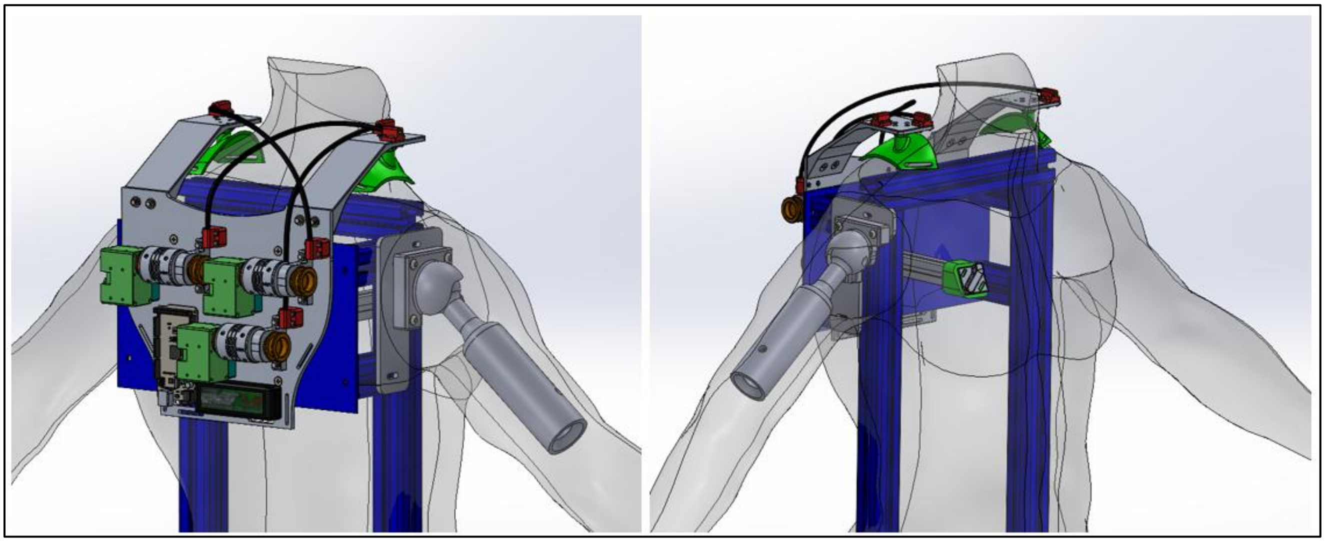

Figure 3-35: Similarity of test bench conditions and real human physiology with the installation of the backpack.

3.5 Conclusion

In conclusion, the comprehensive design and development of the Cable-Driven Shoulder Exosuit (CDSE) represents a significant step towards addressing the mobility impairments associated with the upper limbs, particularly the shoulder joint. This chapter has elucidated the bioinspired approach, conceptual design, and meticulous development of various components, including an innovative backpack system, Bowden cable housing, anchor points, motor pack, and tendon mechanisms, all orchestrated to provide targeted assistance for shoulder abduction, flexion, and horizontal adduction movements. By leveraging anthropometric data to ensure ergonomic compatibility and employing advanced materials and electronics, the CDSE should be able to deliver a lightweight, wearable, and portable solution that enhances the quality of life for individuals with upper limb disabilities. Furthermore, the adoption of a tendon-driven system underscores the commitment to achieving a biomimetic design that mimics natural muscle movements, thereby offering a harmonious integration with human biomechanics. The integration of a test bench for validation and the modular design approach should facilitate future enhancements and customizations, paving the way for broader applications in rehabilitation and assistive technologies. This endeavour not only contributes to the field of soft robotics and exosuit development but also sets a precedent for future research focused on improving human-machine interfaces and assistive device accessibility.

4 Chapter Four: Statics Analysis of the Cable-Driven Shoulder Exosuit (CDSE)

4.1 Introduction

In this section, we will investigate the kinematics and statics of the human arm during shoulder abduction, flexion, and horizontal flexion motions. We will then extract the equations from the FBD while taking into account certain primary assumptions. These equations will be solved to determine the necessary force and torque required for each hand movement. Based on this analysis, we will be able to select an appropriate motor and coupling for the task.

4.1.1 First assumptions

- The calculation of the projected force in the 2D plane does not consider friction.
- All the required variables have been obtained from a 3D model (a body with measures based on 99% Percentile Man (age 20-65 years) [149].
- The centre of mass and the masses of the arm's segments have been determined based on information from related articles [150], [151], [152]

4.2 Mathematical model for shoulder abduction motion

Geometric parameters will be derived from the 3D model [149] referenced in Figure 4-1. From the front view of the 3D model in the SolidWorks software, it is apparent that there is a distinct boundary separating the human body into two sections. To proceed, the initial step involves generating a plane parallel to the right plane of the SolidWorks software, intersecting at this boundary. Subsequently, a sketch needs to be created in this plane in order to obtain the approximate dimensions required to solve the mathematical equations describing abduction motion (Figure 4-2).

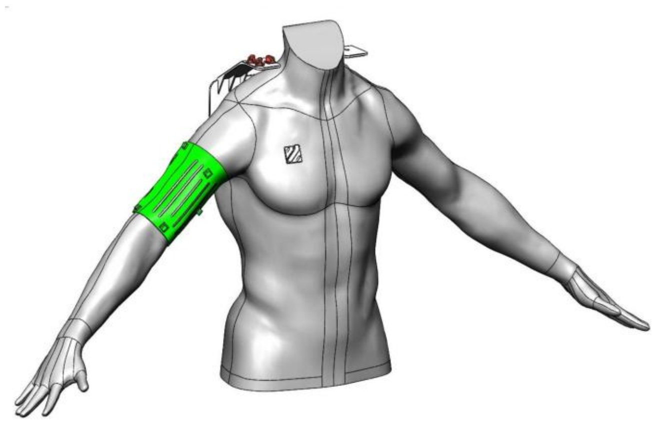

Figure 4-1: 3D model of the body used for calculations.

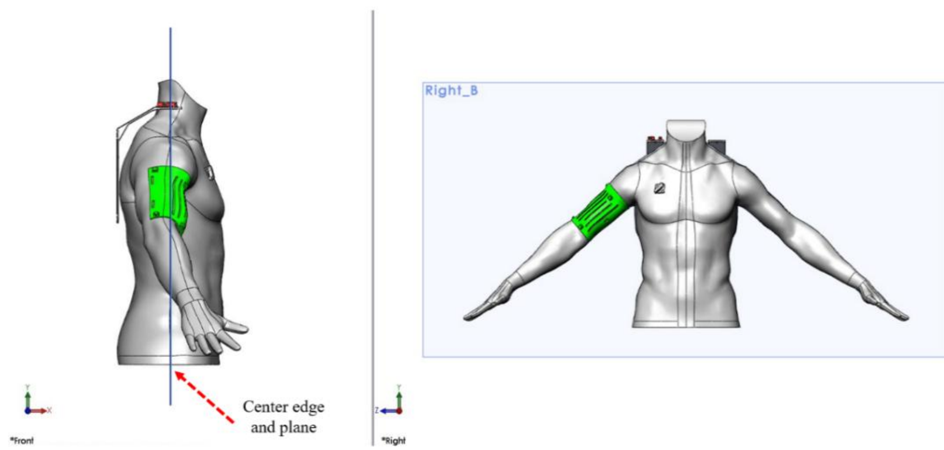

Figure 4-2: The location of the first plane for the abduction sketch.

Initially, a fixed point will be precisely positioned at the apex of the 3D model shoulder. Subsequently, the projection of the middle finger's edge onto a designated plane will delineate the termination point of the hand. Following this, a tangential line will be drawn, intersecting the projected edge of the armpit. Then, a perpendicular line will be drawn originating from the tip of the hand that will intersect the aforementioned line. Further, another line will be sketched, perpendicular to the preceding line, commencing at its extremity and tangentially aligned with the upper boundary of the arm. This line will culminate at an auxiliary point. By constructing a rectangular shape and incorporating a central guiding line, the arm's central axis can accordingly be established (Figure 4-3). The approximate locations of the elbow joint and wrist will then be extracted from this sketch.

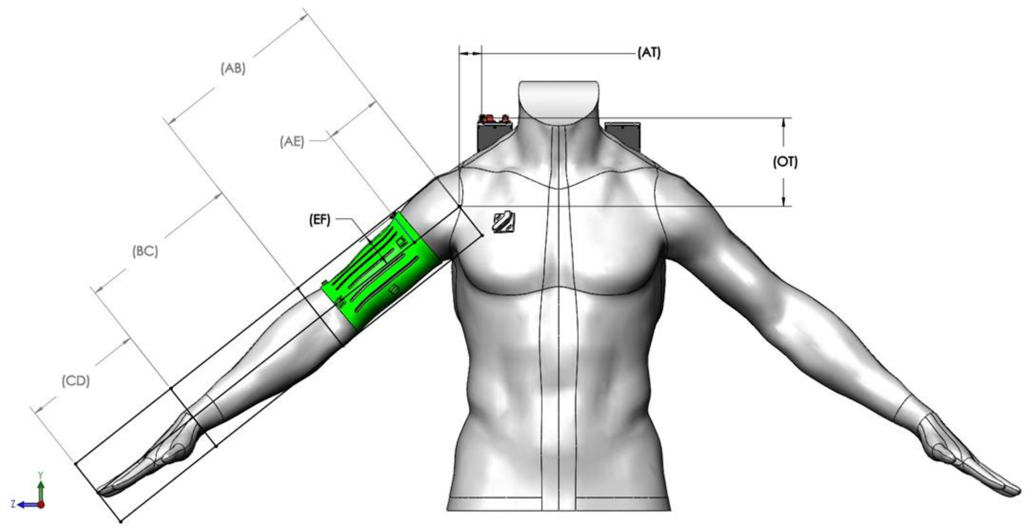

Figure 4-3: Abduction sketch front view and the extracted dimensions parameters (mm).

The movements describing shoulder abduction and flexion are similar, and the 3D model can be used to solve their equations. Figure 4-4 depicts a centreline that has been considered for the human arm, connecting the humeral head (point A) and the tip of the middle finger (point D). The upper edge of the anchor point is projected onto the sketch plane, and its midpoint gives the location of the anchor point (point F). To extract the cable housing point, its circular shape is projected onto the sketch plane, which gives the location of point O.

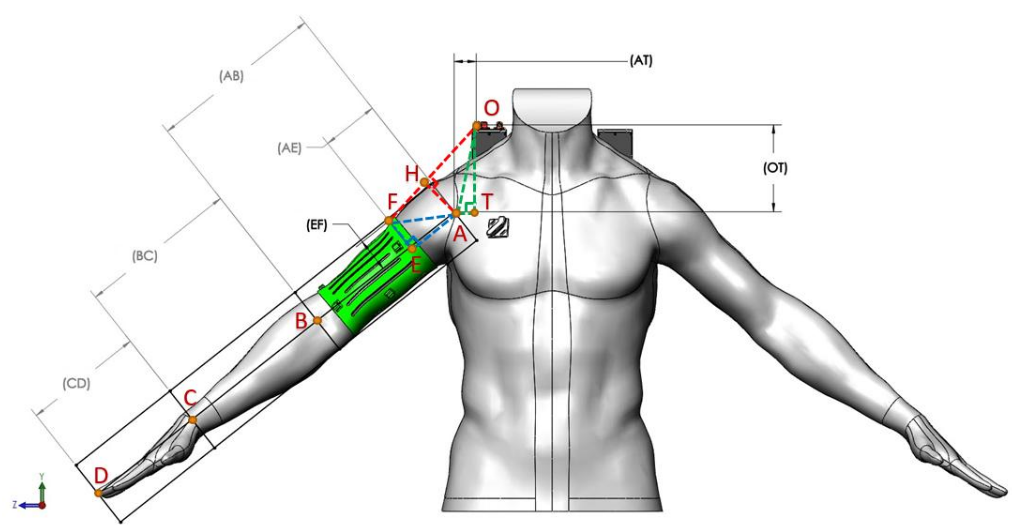

Figure 4-4: 3D model of the abduction simplified model and parameters (mm).

Based on the aforementioned descriptions, a free-body diagram of a human arm is generated and detached from the rest of the body (Figure 4-5). The force F_1 represents the projected force of the abduction movement in the Y-Z plane.

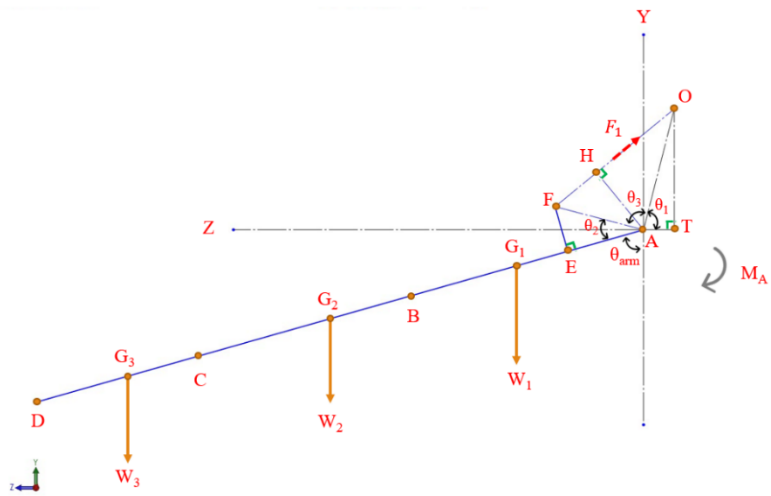

Figure 4-5: Abduction simplified 2D model and parameters.

Table 4-1 reports all parameters and definitions of critical points involved in this model.

Table 4-1: Parameter and variable definitions

Parameters	Definition	Unit
A	Centre of humeral head (HH) (centre of rotation for human's arm)	
AB	Length of Upper arm segment	mm
BC	Length of Forearm segment	mm
CD	Length of Hand segment	mm
F	Location of the anchor points for abduction and flexion movement	
EF	Vertical distance from the arm centreline to the F point	mm
AE	Linear distance from the centre of humeral head to point E	mm
O	Centre of the cable housing as projected into the working plane	
AT	Horizontal distances of O from point A	mm
OT	Vertical distances of O from point A	mm
$\boldsymbol{W_1}$	Weight of upper arm segment	Kg
$\boldsymbol{W_2}$	Weight of forearm segment	Kg
$\boldsymbol{W_3}$	Weight of hand segment	kg
$\boldsymbol{G_1}$	Centre of mass for upper arm segment	
$\boldsymbol{G_2}$	Centre of mass for forearm segment	
$\boldsymbol{G_3}$	Centre of mass for hand segment	
$\boldsymbol{F_1}$	Projected force of the shoulder abduction motion in Y-Z plane	N
$\boldsymbol{F_2}$	Projected force of the shoulder flexion motion in Y-X plane	N
$\boldsymbol{\theta_1}$ **(abduction)**	One of the acute angles in AOT right triangle	Degree
$\boldsymbol{\theta_1}$ **(flexion)**	90-β	Degree
β	$\widehat{OAT}$	
$\boldsymbol{\theta_2}$	One of acute angle in FAE right triangle	Degree
$\boldsymbol{\theta_3}$	One of the angles in OFA triangle	Degree
$\boldsymbol{\theta_{arm}}$	Angle between arm centreline and Y access	Degree
M	Mass of the body	Kg
$\boldsymbol{M_A}$	Torque at point A	Nm
r	Radius of motor's pulley	mm

The dimensions |AB|, |BC|, |CD|, |AE|, |EF|, |AT|, and |TO| were obtained from a 3D model via the smart dimension tool in the SolidWorks software, all of which are thus known. Additionally, we know r and M, as reported in Table 4-7 .

The geometrical calculations begin with the determination of $|\mathrm{AF}|$ using Pythagorean theorem. Following this, the angle θ_2 is found using the inverse tangent of the ratio between $|EF|$and $|AE|$; similarly, $|\mathrm{AO}|$ and θ_1 are computed using the same approach. Given that θ_{arm} is a known input, the angle θ_3 can be derived as a function of θ_1, θ_2, and θ_{arm} ($0 \leq \theta_{arm} \leq 90$):

$$|\mathrm{AF}| = \sqrt{|AE|^2 + |EF|^2} \tag{4.1}$$

Where AF in Eq. (4.1) represents the hypotenuse of the AFE right triangle, and AE and EF are the lengths of its other two sides.

$$\theta_2 = \tan^{-1}\left(\frac{|\mathrm{EF}|}{|\mathrm{AE}|}\right) \tag{4.2}$$

Here, θ_2 in represents the angle between line segment AE (adjacent side) and line segment AF (hypotenuse) of the AFE right triangle.

$$|\mathrm{AO}| = \sqrt{|AT|^2 + |TO|^2} \tag{4.3}$$

Here, AO in Eq. (4.3) represents the hypotenuse of the AOT right triangle and AT and TO are the lengths of its other two sides.

$$\theta_1 = \tan^{-1}\left(\frac{|TO|}{|\mathrm{AT}|}\right) \tag{4.4}$$

Here, θ_1 in Eq. (4.4) represents the angle between line segment AE (adjacent side) and line segment AF (hypotenuse) in the AOT right triangle.

$$\theta_3 = (270 - (\theta_{\mathrm{arm}} + \theta_1 + \theta_2)) \tag{4.5}$$

Here, θ_3 in Eq. (4.5) represents angle between line segment AF and line segment AO in the FAO triangle.

In the FAO triangle, two of the sides and the angle between them are apparent. The FO side can thus be calculated via cosine theorem:

$$|FO| = \sqrt{|(AF)|^2 + |(AO)|^2 - 2|AF||AO|\cos(\theta_3)} \tag{4.6}$$

where $|FO|$ in Eq. (4.6) represents the length of line segment the FO in FAO triangle, and $|AF|$, and $|AO|$ are the lengths of the line segments AF and AO, respectively.

The area of the AFO triangle is obtained via Heron's law. It is now possible to acquire the length of side AH.

$$Perimeter = |AF| + |AO| + |FO| \tag{4.7}$$

Here, Eq. (4.7) can be used to calculate the perimeter of the FAO triangle, which is the sum of the lengths of its sides. Here, |AF|, |AO|, and |FO| represent the lengths of the three sides of the triangle.

$$S = \frac{Perimeter}{2} \tag{4.8}$$

Eq. (4.8) can be used to calculate the semi-perimeter of the FAO triangle.

$$Area = \sqrt{S(S - |AF|)(S - |AO|)(S - |FO|)} \tag{4.9}$$

Eq. (4.9) is Heron's formula, which is used to calculate the area of a triangle when the lengths of all three sides are known. 'S' represents the semi-perimeter, while |AF|, |AO|, and |FO| are the lengths of the sides of the FAO triangle.

$$Area = \frac{1}{2}|AH||FO| \tag{4.10}$$

Eq. (4.10) can be used to calculate the area of the FAO triangle using the traditional method of base times height divided by two. Here, |AH| represents the height of the FAO triangle, and |FO| represents the length of the base.

The objective of using these equations is to compute the projected force. To achieve this, the most straightforward method is to determine the net moment of forces at point A; there is no need, however, to identify the reaction forces at this point.

$$\sum M_A = 0 \Rightarrow \sin(\theta_{arm})\big[(W_1|AG_1|) + \big(W_2(|AB| + |BG_2|)\big) + \big(W_3(|AB| + |BC| + |CG_3|)\big)\big] - F_1\,|AH| = 0 \quad (4.11)$$

$\sum M_A$ in Eq. (4.11) represents the total torque about point A and when the system is in equilibrium. θ_{arm} is the angle between the arm centerline and Y access, $W_1, W_2,$ and W_3 are the weight of the upper arm, forearm and hand segment, respectively whilst $G_1, G_2, and\ G_3$ are the center of mass of the upper arm, forearm and hand segment respectively. AB and BC are the length of the upper arm and forearm segment.$|AG_1|$ is a term representing the distance from point A (the pivot point) to the point where the respective W_1 are located.

4.2.1 Calculation of centre of mass (COM) and mass of each segment of the arm

The arm is conceptualized as a trisected line, with each segment possessing a respective centre of mass (denoted G_1, G_2, G_3), along with corresponding weights ($denoted$ $\mathrm{W_1, W_2, W_3}$). The human body and its center of mass have been derived from references [150], [151], [152]. It is important to highlight that the mass of each arm segment is proportionally represented as a percentage of the total body mass. Additionally, the centre of mass positions for each arm segment are measured and expressed as a percentage of their respective segment lengths. Table 4-2 illustrates the centre of mass (COM) of the arm segments, as determined by the Harless, Braune and Fischer and Zatsiorsky studies. Also, according to the results reported in refs [150], [151], [152] appropriate methods were chosen to calculate the masses of the each arm's segments which are reported in Table 4-3 and Table 4-4. To calculate the mass of arm's parts, the results of Braune-Fischer's investigations were chosen as a conservative approach. Considering the allocated mass percentages for the arm's segments, it was observed that they yielded higher values in comparison to the findings reported by other researchers. To strike an appropriate balance, the investigations conducted by Harless were utilized, while the investigations conducted by Zatsiorsky were adopted as an 'optimistic' approach.

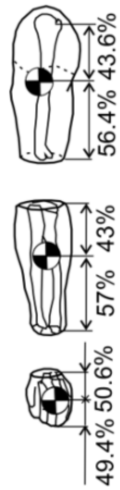

Figure 4-6: The COM of arm segments (Harless, Braune and Fischer approach) [150].

Table 4-2: The COM as a percentage of each body segment (Zatsiorsky approach) [152].

Centre of Mass	Male (%)	Female (%)	Average (%)
Upper Arm	57.72	57.54	57.63
Forearm	45.74	45.59	45.665
Hand	79	74.74	76.87

Table 4-3: Body segment mass as a percentage of total body mass.

Segment	Investigator	
	Harless [150] (Male) %	Braune and Fischer [150] (Male)- %
Upper arm	6.48	6.72
Forearm	3.62	4.56
Hands	1.68	1.68

Table 4-4: Body segment mass as a percentage of total body mass (Zatsiorsky approach) [152].

Mass	Male (%)	Female (%)	Average (%)
Upper arm	2.71	2.55	2.63
Forearm	1.62	1.38	1.5
Hand	0.61	0.56	0.585

The following equation exemplifies the conservative approach proposed by Braune and Fischer to calculate the weight of each segment of the arm.

Let us denote $p^{\rightarrow} = [p_{upper\ arm}, p_{forearm}, p_{hand}]$ as the vector containing the mass percentages of the upper arm, forearm, and hand, respectively. The weight, W, of a given segment can then be calculated as a function of p, the segment's mass percentage, through a single, unified formula [3]:

$$W_{(p)} = \frac{9.81 \times \mathrm{p} \times (M)}{100} \tag{4.12}$$

where:

- p is an element from the vector $p^{\rightarrow}$ representing the mass percentage of the specific arm segment.

- M is the total mass of the body.

- g=9.81 m/s^2 is the acceleration due to gravity, denoting the constant factor converting mass to weight on Earth.

This approach expresses the computation in the form of a concise mathematical model, enhancing readability and facilitating the application of the formula across different segments by merely selecting the appropriate percentage from $p^{\rightarrow}$. Such a model is particularly beneficial in the realm of robotics, where algorithms often need to dynamically adjust based on varying parameters. This enables rapid adjustments to the model for different human physiologies or robotic applications, improving the adaptability and precision of exosuits and other robotic aids designed to work in direct collaboration with human limbs.

The equations for calculating the centre of mass in each arm segment, considering the segment lengths obtained from the 3D model ($|AB|, |BC|, |CD|$), and the allocated arm segment percentages according to the conservative approach suggested by Braune and Fischer, are as follows:

$$|AG_1| = \frac{(Upper\ Arm's\ COM\ percentage)|AB|}{100} \tag{4.13}$$

$$|BG_2| = \frac{(Forearm's\ COM\ percentage)|BC|}{100} \tag{4.14}$$

$$|CG_3| = \frac{(Hand's\ COM\ percentage)|CD|}{100} \tag{4.15}$$

where $|AG_1|$ in Eq. (4.13) represents the length of the upper arm from the centre of the humeral head to the centre of mass of the upper arm segment, $|BG_2|$ in Eq. (4.14) represents the length of the forearm from the elbow rotation point to the centre of mass of the forearm segment, and $|CG_3|$ in Eq. (4.15) represents the length of hand from end point of the forearm to the centre of mass of the hand segment. $|AB|$, $|BC|$ and $|CD|$ in the above equations represent the length of the upper arm, forearm, and hand segment, respectively.

4.2.2 Calculation of maximum force and torque in abduction movement

In order to determine the maximum force during the abduction movement, the arm angle range θ_{arm} of 0 to 90 degrees is divided into 60 intervals.Equation (4.11) is then applied to calculate the force at each of these 60 angles according to the three different approaches (Harless, Braune and Fischer, and Zatsiorsky). Through this process, it becomes possible to identify the specific angle at which the maximum force is attained. This maximum force can be regarded as the peak force achieved during the abduction movement. Table 4-5 presents the maximum force ($F_1 = F_{projected}$) calculated for abduction movements, considering the three different approaches. According to the table below, the Braune and Fischer method yields the highest forces in general, with the maximum force observed at θ_{arm} = 56.44 degrees in the arm.

Table 4-5: Maximum force ($F_1 = F_{projected}$) calculated for abduction.

Maximum Force	**F** $_{\text{Braune-Fincher}}$	**F** $_{\text{Harless}}$	**F** $_{\text{Zatsiorsky}}$
(N)	312.7	278.9	121.2

An important consideration regarding the determination of abduction tendon forces is that the forces calculated using the provided equations are on a 2D plane, as they are projected onto the sketch plane. However, to increase accuracy, it is necessary to convert these forces into their actual 3D counterparts. To achieve this, the equations will be solved once to determine the maximum force and its corresponding θ_{arm}. Subsequently, the space angle, φ_{space}, between the projected force and the actual force direction needs to be determined using the SolidWorks software (Figure 4-7). The actual force's direction is represented by a line connecting the anchor point to the centre point of the cable housing on shoulder distributing centre.

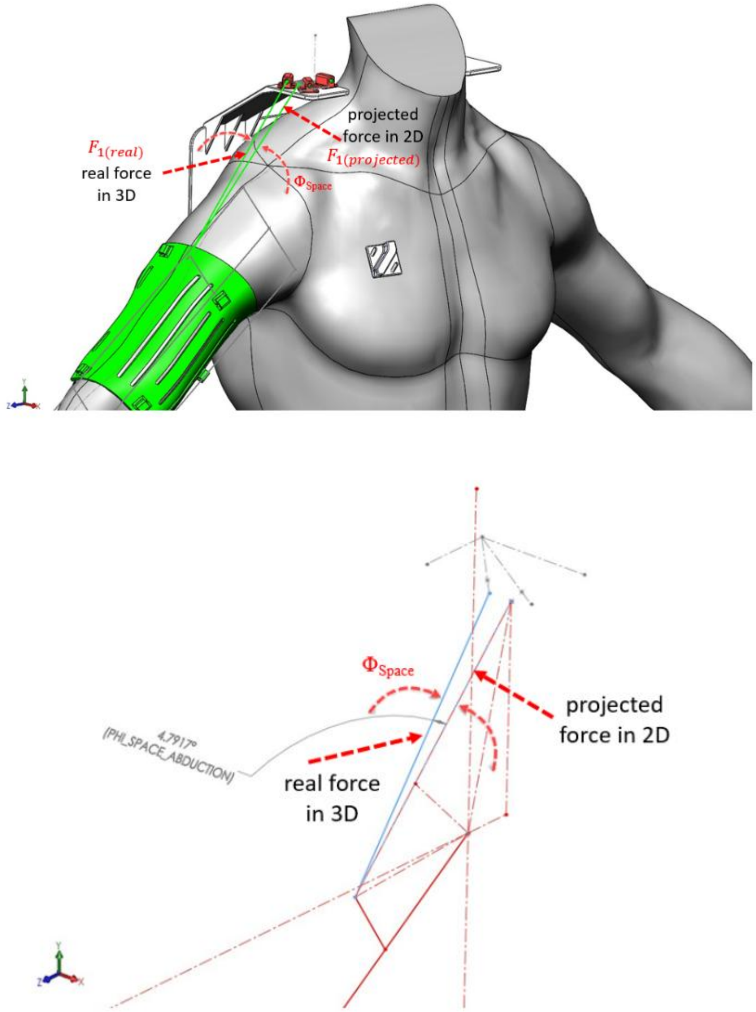

Figure 4-7: Space angle between the real force and projected force of abduction.

After measuring the space angle ($\varphi_{\text{space\_abduction}} = 4.7917\ deg$) from the SolidWorks model, the following equations will be incorporated, in addition to the previous equations:

$$F_{1(real)} = \frac{F_{1(projected)}}{\text{Cos}(\Phi_{space\_\text{abduction}})} \tag{4.16}$$

where $F_{1(real)}$ in Eq. (4.16) represents the real maximum force in 3D space, $F_{1(projected)}$ is the maximum projected F $_{\text{Braune-Fincher}}$, $\varphi_{\text{space\_abduction}}$ is the space angle between the real force and projected force of abduction.

$$F_{motor} = (1.1)F_{real} \tag{4.17}$$

In Eq.(4.17), F_{real} represents the maximum 3D force, where the coefficient of 1.1 is applied to F_{real}, increasing the force by 10%. This is used to address any inherent errors and unmeasurable factors that might be present. During the final stage, the torque of the servo motor will be achieved using F_{motor}, will be used to select a suitable servo motor.

To calculate the motor torque based on the force applied to the tendon and the motor pully radius, r, the following formula can be utilized:

$$T_{motor} = rF_{motor} \tag{4.18}$$

where T_{motor} represents the maximum torque based on the radius of the pulley, r, and maximum 3D force, F_{motor}.

Table 4-6 presents the maximum torque calculated for abduction movements, according to the three different approaches: Harless, Braune and Fischer, and Zatsiorsky. According to the table below, the Braune and Fischer method yields the highest torques.

Table 4-6: Maximum Torque calculated for Abduction motion.

Maximum Torque	$T_{Braune\text{-}Fincher}$	$T_{Harless}$	$T_{Zatsiorsky}$
(Nm)	4.833	4.31	1.873

Figure 4-8 and Figure 4-9 depict the relationship between the projected force and motor torque in relation to the angle of abduction, θ_{arm}, based on the investigations conducted by Braune and Fischer. As evident from the following graphs, the maximum force and torque were observed at θ_{arm} = 56.44 degrees in the arm. This particular angle can be regarded as the critical angle for the abduction movement.

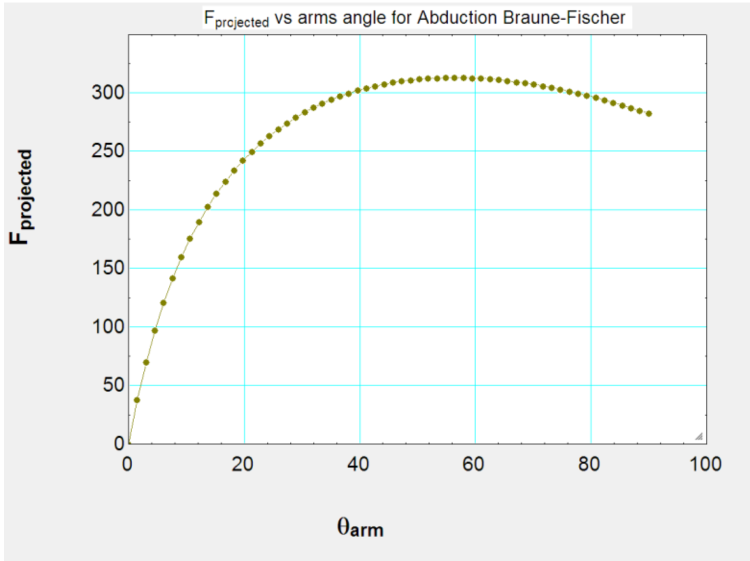

Figure 4-8: Projected force vs θ $_{arm}$ for abduction according to the Braune-Fischer investigations.

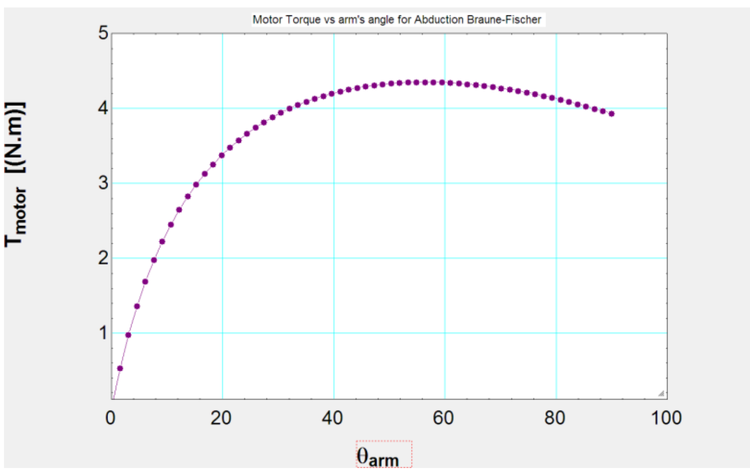

Figure 4-9: Motor torque vs θ $_{arm}$ for abduction according to the Braune-Fischer investigations.

Table 4-7 reports all results for the abduction movement.

Table 4-7: Result table for abduction motion.

$\|AB\|$	**306.13 mm**	M	75 kg
$\|BC\|$	278.46 mm	$\|AG_1\|$	133.5 mm
$\|CD\|$	209.53 mm	$\|BG_2\|$	119.7 mm
$\|AE\|$	99.3 mm	$\|CG_3\|$	106 mm
$\|EF\|$	58.8 mm	$F_{1(real)}$	313.8 N

$\lvert AT \rvert$	38.7 mm	F_{motor}	345.2 N
$\lvert TO \rvert$	152 mm	T_{motor}	4.833 $N.m$
r	0.014 mm		

4.3 Mathematical Model for Shoulder Flexion Motion

Here, we will follow a similar approach to that describe in the previous section but will now focus on the shoulder flexion motion. In Figure 4-10, and Figure 4-11 we will explore the shoulder flexion movement and its corresponding Free Body Diagram (FBD).

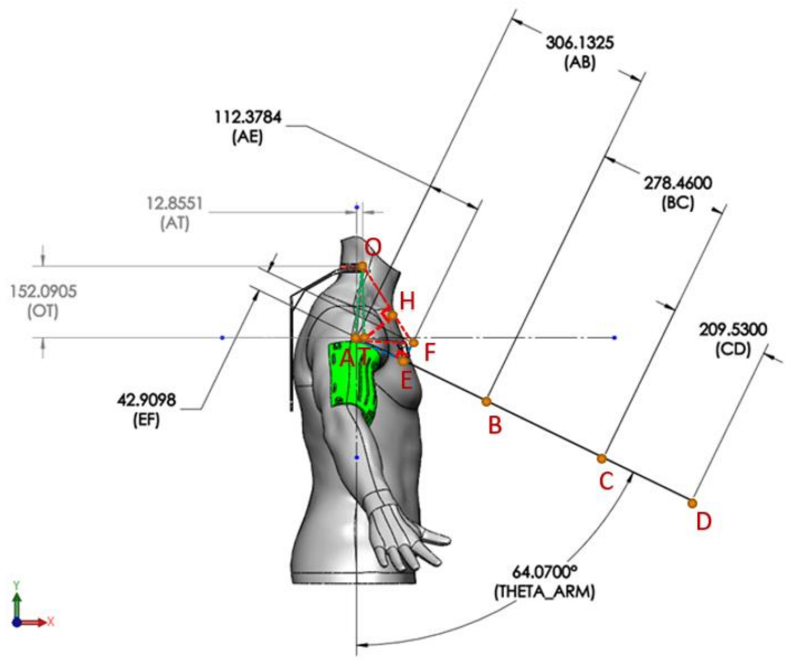

Figure 4-10: Shoulder flexion sketch view and the dimensions extracted (in mm).

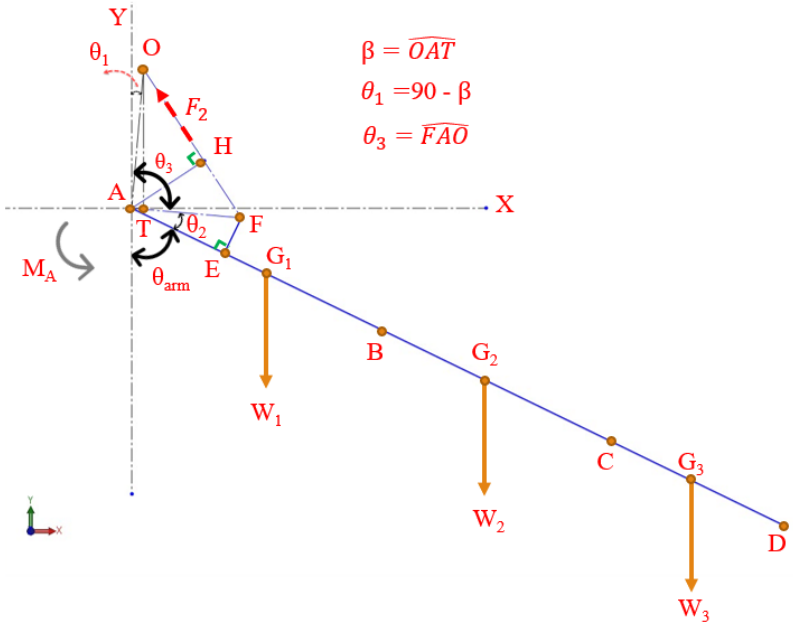

Figure 4-11: Simplified model of shoulder flexion.

To analyse the parameters associated with shoulder flexion, we begin by establishing the plane perpendicular to the plane of abduction motion that intersects the centreline of the arm (Figure 4-12). In a similar manner to the previous section when determining the anchor point for abduction motion. Next, we project the arm's centreline and joint point onto the sketch plane. By measuring the vertical distance from the centreline and the longitudinal distance from the arm joint, we can extract the essential parameters for shoulder flexion motion and its anchor point position (Figure 4-13).

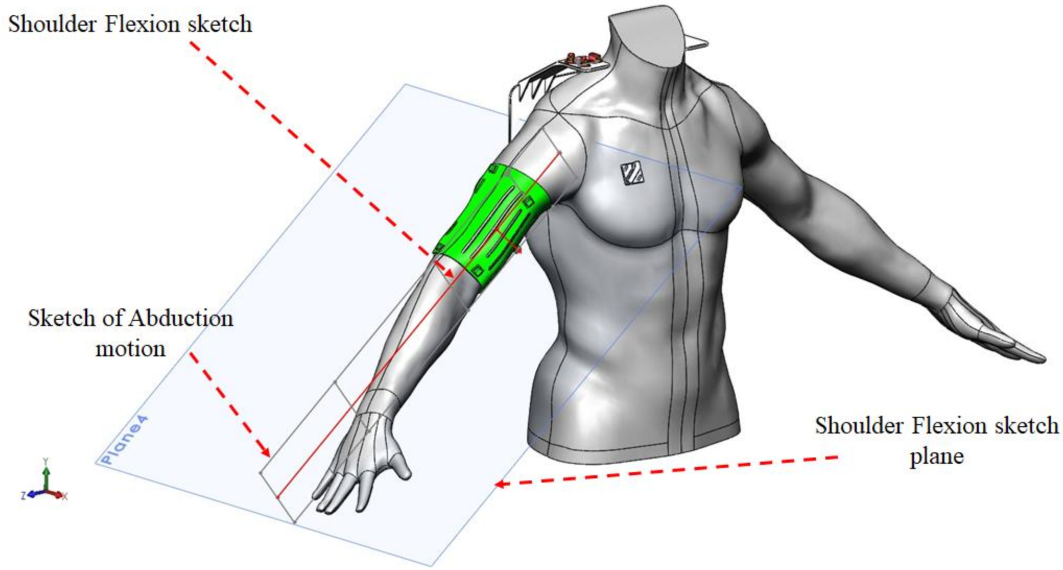

Figure 4-12: The plane and sketch of shoulder flexion motion.

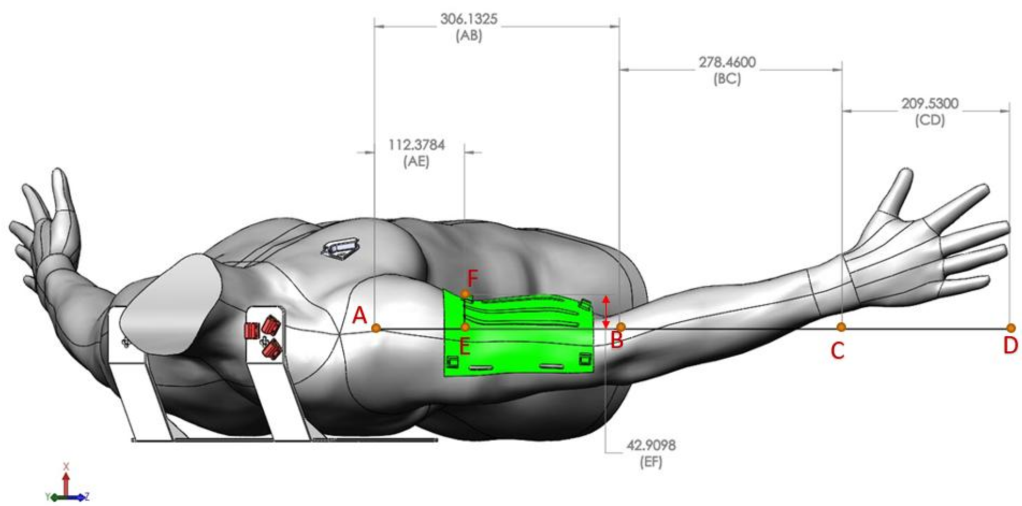

Figure 4-13: The sketch of flexion motion to extract the anchor point dimensions (in mm).

To ensure there is no displacement in the arm joint during abduction and shoulder flexion, we assume a plane that is perpendicular to the abduction sketch plane and that intersects the arm joint. This plane serves as the reference for analysing the parameters of shoulder flexion motion. We draw the shoulder flexion motion and its corresponding sketch on this plane (Figure 4-14). Additionally, we project the point of the cable housing for the shoulder flexion motion onto the sketch plane, further aiding in the analysis and visualization of the motion (Figure 4-10).

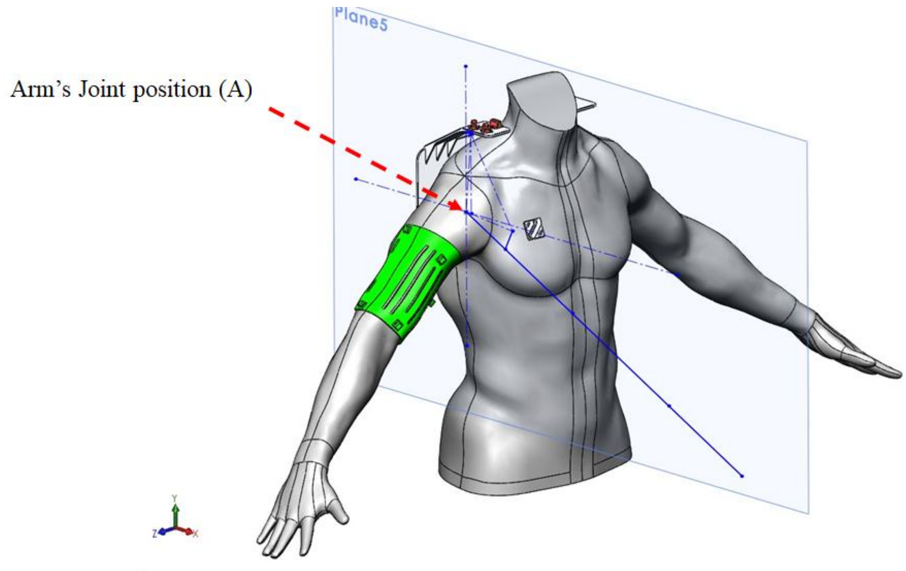

Figure 4-14: Sketch of the main location of shoulder flexion.

Currently, the location of point O is in the first quarter of the coordinate system, thus some of the equations will have to be changed. At this level, the angle OAT is designated β, and its complementary angle to 90 degrees is designated θ1 (Figure 4-10).

An additional aspect to note regarding the equations of flexion motion is that once the side FO is determined from the AFO triangle, there is no requirement to calculate the area of this triangle via Heron's law. Instead, the area can be computed by multiplying AO by AF and the sine of the angle between them, and then dividing the result by 2. Following this, side AH can be obtained.

The dimensions $|AB|, |BC|, |CD|, |AE|, |EF|, |AT|, and\ |OT|$ were obtained from a 3D-model through the smart dimension tool in the SolidWorks software, and all of them are known. Additionally, we know r and M, as reported in Table 4-10.

$$F\hat{A}E = \theta_2 \tag{4.19}$$

$$F\hat{A}O = \theta_3 \tag{4.20}$$

In Eq. (4.19), $F\hat{A}E$ represents the angle θ_2, whilst in Eq. (4.20), $F\hat{A}O$ represents the angle θ_3.

$$|AF| = \sqrt{|AE|^2 + |EF|^2} \tag{4.21}$$

AF in Eq. (4.21) represents the hypotenuse of the AFE right triangle, and AE and EF are the lengths of its other two sides.

$$\theta_2 = \tan^{-1}\left(\frac{|EF|}{|AE|}\right) \tag{4.22}$$

θ_2 in Eq. (4.22) represents the angle between line segments AE (adjacent side) and AF (hypotenuse) in the AFE right triangle.

$$AO|AO| = \sqrt{|AT|^2 + |TO|^2} \tag{4.23}$$

AO in Eq.(4.23) represents the hypotenuse of the AOT right triangle, and AT and TO are the lengths of its other two sides.

$$\beta = \tan^{-1}\left(\frac{TO}{AT}\right) \tag{4.24}$$

β in Eq. (4.24) represents the angle between line segments OT (adjacent side) and AO (hypotenuse) in the AFE right triangle.

$$\theta_1 = 90 - \beta \tag{4.25}$$

$$\theta_3 = 180 - (\theta_{arm} + \theta_1 + \theta_2) \tag{4.26}$$

θ_1 in Eq.(4.25) represents $90 - \beta$ and θ_3 in Eq. (4.26) represents $180 - (\theta_{arm} + \theta_1 + \theta_2)$.

$$|FO| = \sqrt{|(AF)|^2 + |AO|^2 - 2|AF||AO|\cos(\theta_3)} \tag{4.27}$$

$|FO|$ in Eq. (4.27) represents the length of the line segment FO in the FAO triangle, and $|AF|$ and $|AO|$ are the lengths of the line segments AF and AO, respectively.

The area of the AFO triangle can be obtained via Heron's law. It is now possible to acquire the length of side AH.

$$Perimeter = |AF| + |AO| + |FO| \tag{4.28}$$

Here Eq. (4.28) calculates the perimeter of the FAO triangle, which is the sum of the lengths of its sides. Here, |AF|, |AO|, and |FO| represent the lengths of the three sides of the triangle.

$$S = \frac{Perimeter}{2} \tag{4.29}$$

Eq.(4.29) is used to calculate the semi-perimeter of the FAO triangle.

$$Area = \frac{|AF||AO| \sin \theta_3}{2} \tag{4.30}$$

$$Area = \frac{1}{2}|AH||FO| \tag{4.31}$$

Eq. (4.31) is used to calculate the area of the FAO triangle using the traditional method of base times height divided by 2. Here, |AH| represents the height of the FAO triangle, and |FO| represents the length of the base.

The objective of these equations is to compute the projected force. To achieve this, the most straightforward method is to determine the net moment of forces at point A; there is no need to identify the reaction forces at this point.

$$\begin{aligned} \sum M_A = 0 \;\Rightarrow\; \sin(\theta_{arm})\big[(W_1|AG_1|) + \big(W_2(|AB| + |BG_2|)\big) \\ + \big(W_3(|AB| + |BC| + |CG_3|)\big)\big] - F_2|AH| = 0 \end{aligned} \tag{4.32}$$

$\sum M_A$ in Eq.(4.32) represents the total torque about point A and when the system is in equilibrium. θ_{arm} is the angle between the arm centerline and Y access, $W_1, W_2, and\ W_3$ are the weights of the upper arm, forearm and hand segment, and $G_1, G_2, and\ G_3$ are the centers of mass of the upper arm, forearm and hand segment, respectively. AB and BC are the lengths of the upper arm and the forearm segment.$|AG_1|$ are terms that represent the distances from point A (the pivot point) to the points where the respective weights, W_1, are located.

The process for calculating the centre of mass (COM) and mass of each segment of the arm is identical to that used for the abduction movement.

4.3.1 Calculation of the maximum force and torque in the flexion movement

In order to determine the maximum force during the flexion movement, the arm angle, range, θ_{arm} of 0 to 90 degrees is divided into 60 intervals. Equation (4.32) is then applied to calculate the force for each of these 60 angles according to the three different approaches (Harless, Braune and Fischer, and Zatsiorsky). Through this process, it becomes possible to identify the specific angle at which the maximum force is attained. This maximum force can be regarded as the peak force achieved during the abduction movement. Table 4-8 reports the maximum force ($F_2 = F_{projected}$) calculated for flexion movements considering the three different approaches. According to the table below, the Braune and Fischer method yields the highest forces, the maximum force being observed at θ_{arm} = 64.07 degrees.

Table 4-8: Maximum force ($F_2 = F_{projected}$) calculated for flexion.

Maximum Force	$F_{Braune\text{-}Fincher}$	$F_{Harless}$	$F_{Zatsiorsky}$
(N)	280.6	250.3	108.8

One crucial point to consider when determining the force of the tendons is that the force calculated from the given equations exists on a 2D plane, and it appears that the actual force of the tendons has been projected onto the sketch plane. To improve the accuracy of the results, this projected force needs to be converted into the actual force as in the previous section. To achieve this, the equations will be solved once, enabling the extraction of the maximum force and its corresponding θ $_{arm}$. Subsequently, SolidWorks can be employed to determine the space angle, $\varphi_{space\_\mathrm{flexion}}$ between the projected force and the direction of the real force (Figure 4-15, Figure 4-16). The direction of the real force is represented by a line connecting the anchor point to the centre point of the cable housing.

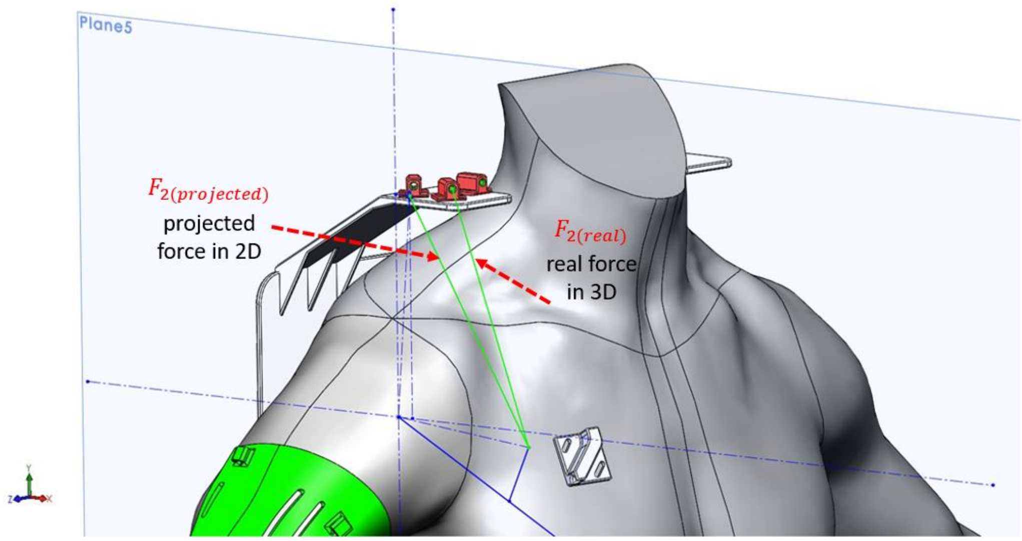

Figure 4-15: Space angle between real force and projected force for shoulder flexion.

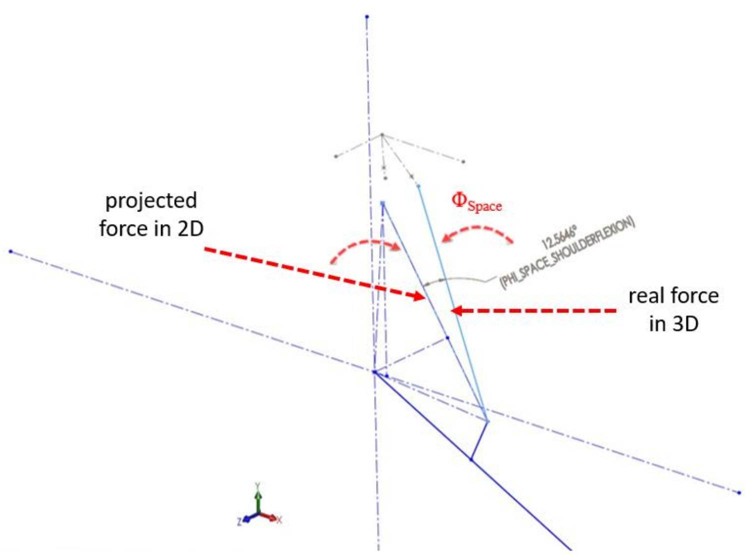

Figure 4-16: Space angle between real force and projected force for flexion.

Upon measuring the space angle ($\varphi_{space\_\mathrm{flexion}}$=12.5646 deg) from the SolidWorks model, the following equations will be incorporated into the existing set of equations:

$$F_{2(real)} = \frac{F_{2(projected)}}{\mathrm{Cos}(\varphi_{space\_\mathrm{flexion}})} \tag{4.33}$$

where $F_{2(real)}$ in Eq. (4.33) represents real maximum force in 3D space, $F_{2(projected)}$ is the maximum projected $F_{\text{Braune-Fincher}}$, $\varphi_{\mathrm{space\_flexion}}$ is the space angle between real force and projected force of abduction.

In the final stage, the torque of the servo motor will be determined via the use of F_{motor}, which can then be used to select a suitable servo motor.

To calculate the motor torque based on the force applied to the tendon and the motor pully radius, r, the following formula can be utilized:

$$T_{motor} = r(F_{motor}) \tag{4.34}$$

here in T_{motor} represents the maximum torque based on the radius of the pulley, r, and the maximum 3D force, F_{motor}.

$$T_{safety} = 1.1\ (T_{motor}) \tag{4.35}$$

In Eq. (4.35), T_{motor} represents the maximum torque, where a coefficient of 1.1 is applied to T_{motor} to increase the torque by 10%; this addresses any inherent errors and unmeasurable factors that might govern the subject.

Table 4-9 reports the maximum torque calculated for flexion movements considering the three different approaches (Harless, Braune and Fischer, and Zatsiorsky). According to the table below, the Braune and Fischer method yields the highest torques.

Table 4-9: Maximum torque calculated for flexion motion.

Maximum Torque	$T_{Braune\text{-}Fincher}$	$T_{Harless}$	$T_{Zatsiorsky}$
(Nm)	4.427	3.948	1.716

Figure 4-17, and Figure 4-18 depict the relationship between the projected force and motor torque in relation to the angle of flexion, θ_{arm}, based on the investigations conducted by Braune and Fischer. As evident from the following graphs, the maximum force and torque were observed at θ_{arm} = 64.07 degrees in the arm. This particular angle can be regarded as the critical angle for the abduction movement.

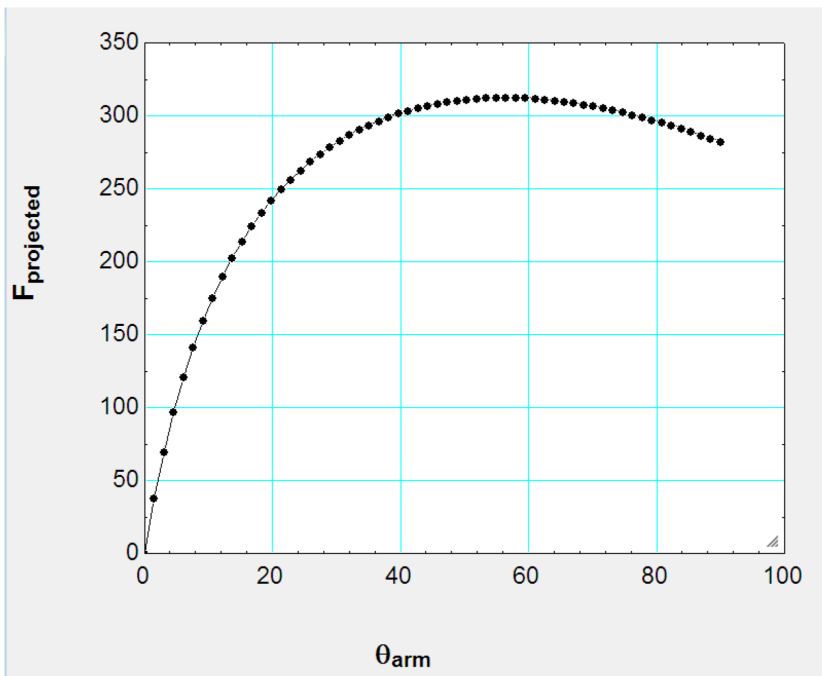

Figure 4-17: Projected force in the Braune and Fischer investigations for shoulder flexion.

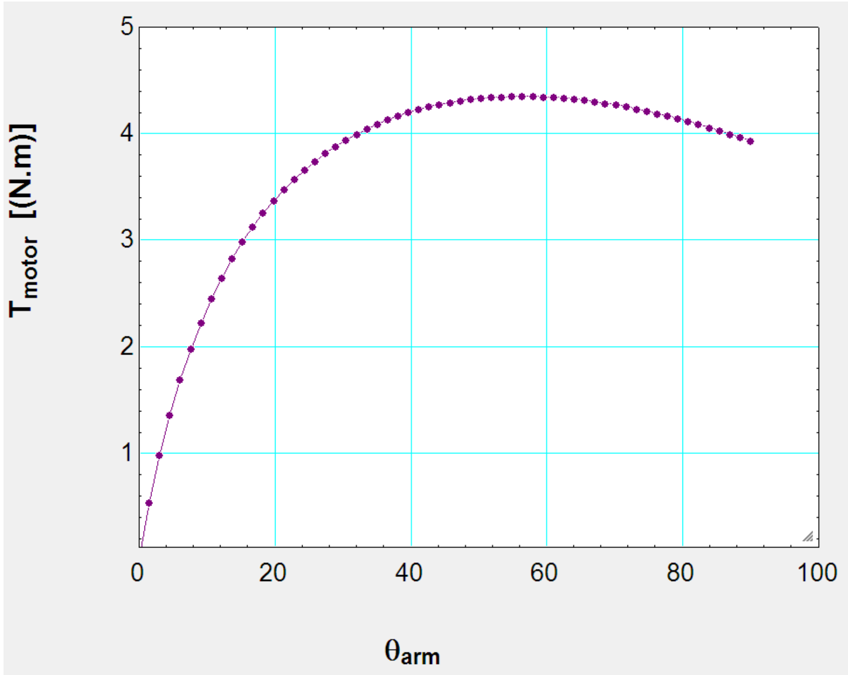

Figure 4-18: Torque of the motor in the Braune and Fischer investigations for shoulder flexion.

Table 4-10 reports all the results for the flexion movement.

Table 4-10: Results for flexion motion.

$\|AB\|$	**306.13 mm**	M	75 kg
$\|BC\|$	278.46 mm	$\|AG_1\|$	133.5 mm
$\|CD\|$	209.53 mm	$\|BG_2\|$	119.7 mm
$\|AE\|$	112.4 mm	$\|CG_3\|$	106 mm
$\|EF\|$	43 mm	$F_{2(real)}$	287.5 N
$\|AT\|$	12.86 mm	F_{motor}	316.2 N
$\|TO\|$	152.09 mm	T_{motor}	4.427 $N.m$
r	0.014 mm	AF	120.34 mm
θ_2	20.93 Degree	AO	152.63 mm
β	85.16 Degree		

4.4 Mathematical model for shoulder horizontal flexion motion

During this stage, the necessary dimensions for horizontal flexion motion will be obtained from the 3D model using the SolidWorks software (Figure 4-19). The initial step involves locating an approximate anchor point for this motion on the arm. To accomplish this, a sketch is generated on the upper surface of the anchor point of the horizontal flexion. A centreline is then drawn on this sketch, and a point is placed on the centreline as a midpoint. This auxiliary sketch aids in determining the appropriate position for the anchor point (Figure 4-20).

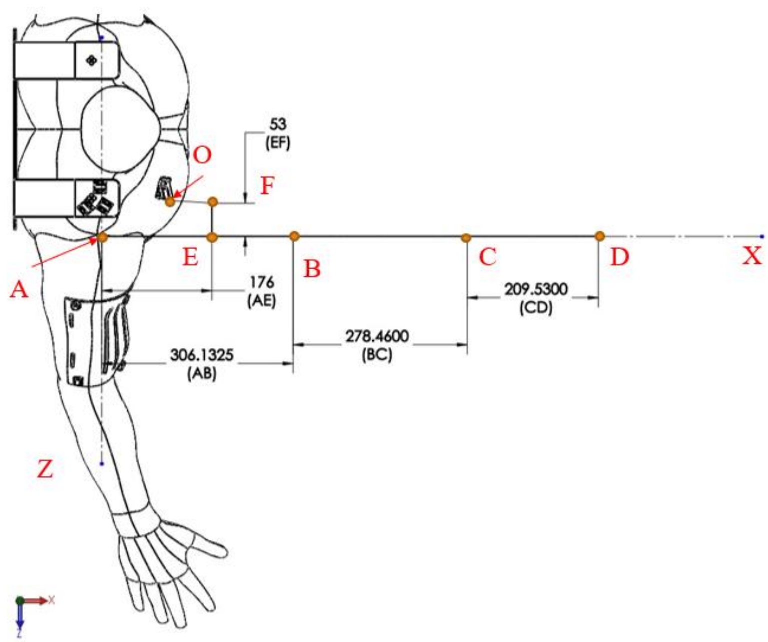

Figure 4-19: The extracted dimensions for horizontal flexion from 3D model.

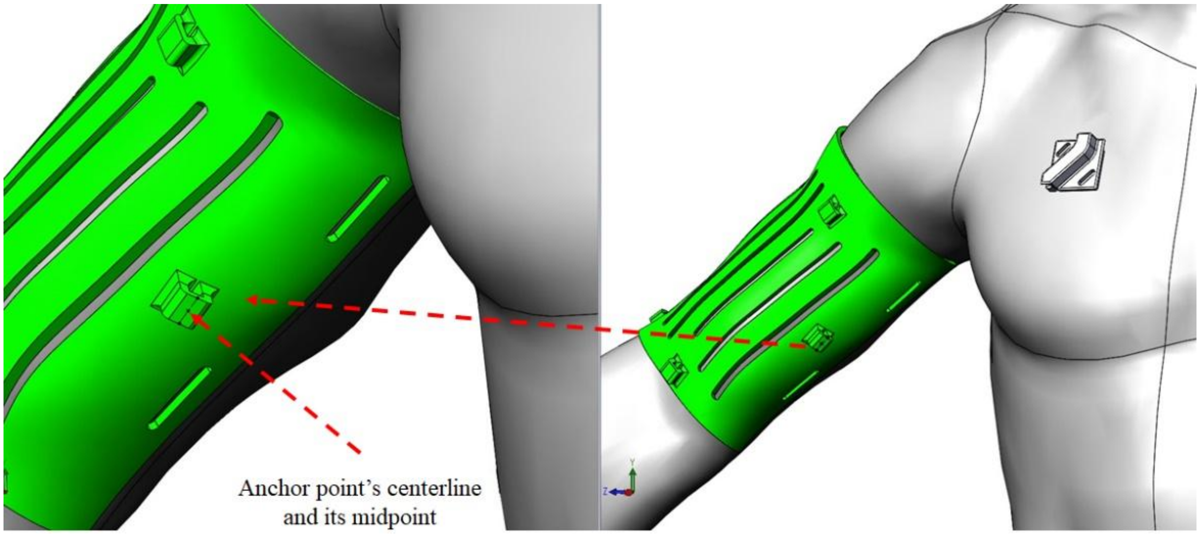

Figure 4-20: The sketch created on the top face of the horizontal flexion anchor point.

Next, a plane needs to be defined, that passes through three particular points. The first point is A, representing the location of the arm's joint (HH); the second point is D, denoting the tip of the middle finger; and the final point is the one created on the sketch of the anchor point. This plane allows for a comprehensive analysis of the motion and its relation to the specified points (Figure 4-21).

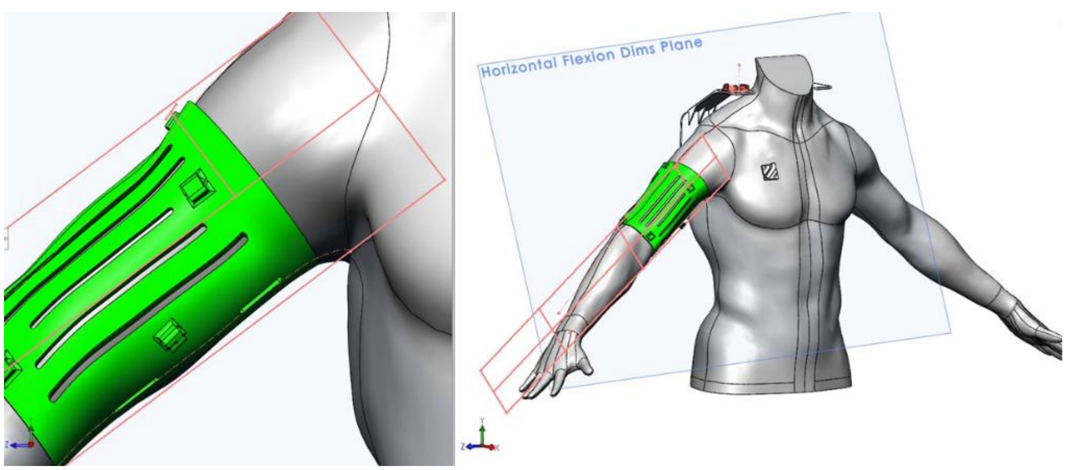

Figure 4-21: The three points used to create the new plane from which dimensions were extracted.

Subsequently, following a similar procedure to above, a sketch will be generated on the newly created plane. This sketch will enable the extraction of the required dimensions for the anchor point in horizontal flexion (Figure 4-22). Once the desired dimensions have been obtained, they will be translated to the appropriate plane for horizontal flexion, allowing for accurate analysis and implementation of the motion.

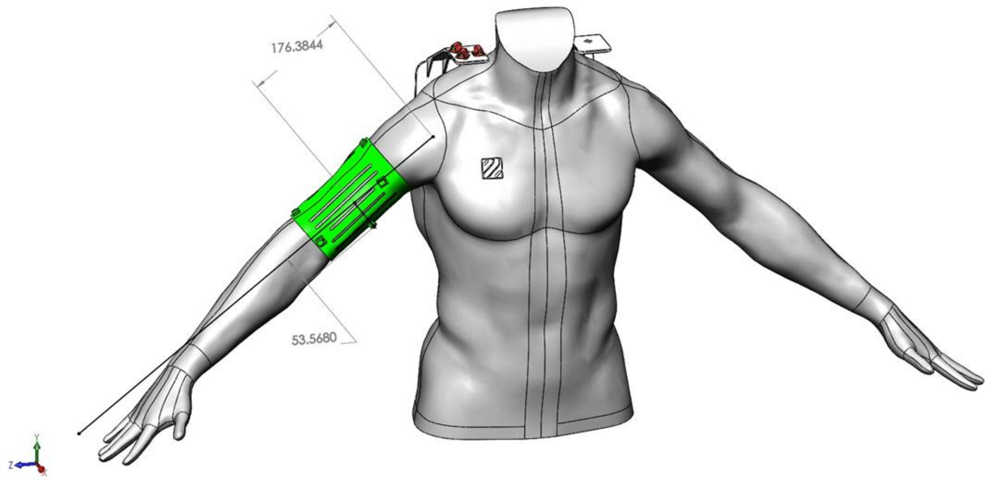

Figure 4-22: Perpendicular and longitudinal distances of horizontal flexion anchor point from point A.

A plane is established for the chest cable housing. This plane is positioned at the tip of the cable housing and is perpendicular to the axis of the inner cylinder of the cable housing (Figure 4-23).

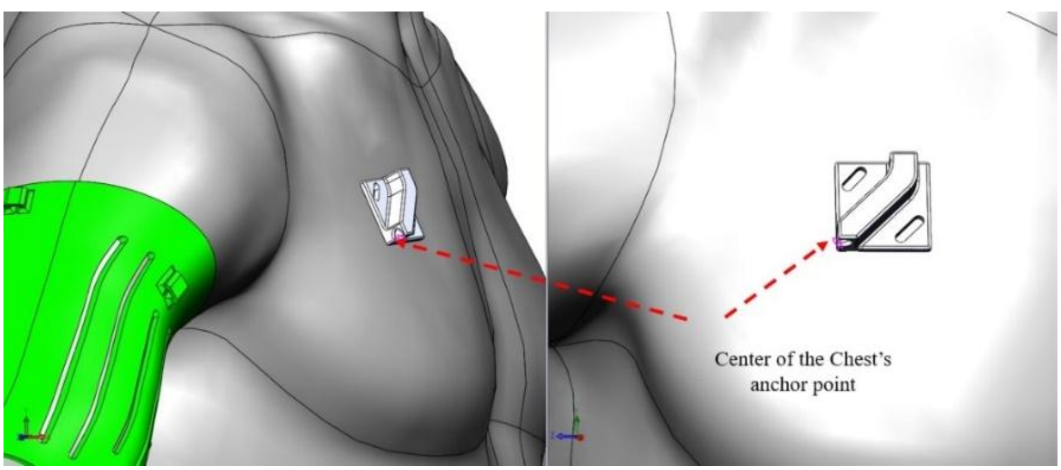

Figure 4-23: Chest anchor point sketch and centre point.

To accurately position the dimensions and sketch for horizontal flexion, a plane must be generated that is parallel to the top plane of the 3D model and that passes through point A. The sketch for horizontal flexion can then be created on this newly established plane, ensuring its proper placement within the context of the overall model (Figure 4-24, Figure 4-25).

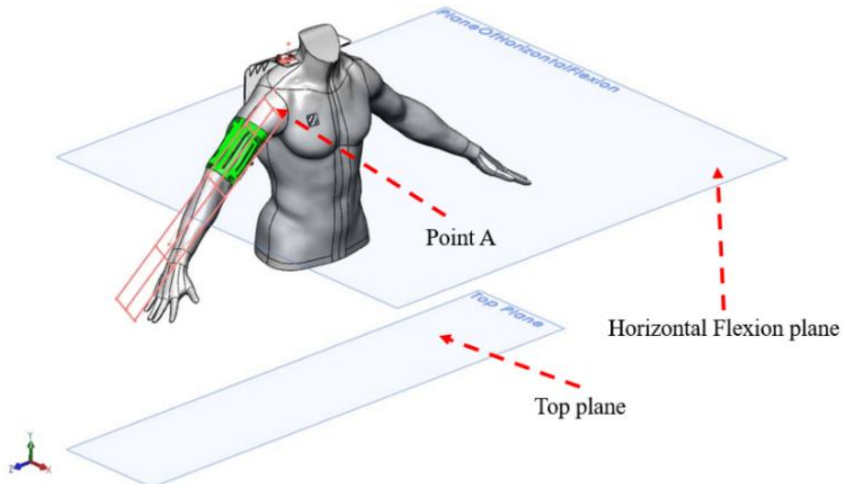

Figure 4-24: Creation of main plane passing through point A.

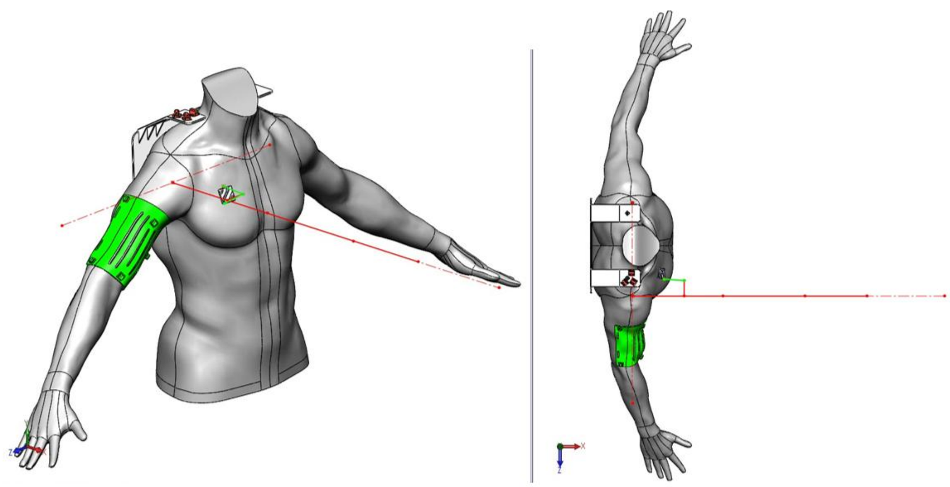

Figure 4-25: The sketch of horizontal flexion on the right plane in the 3D model.

Following this, the centre point of the chest's cable housing needs to be projected onto the primary plane of horizontal flexion. This projection allows for a clear visualization of the real direction of the force exerted by the tendon in horizontal flexion. To determine this direction accurately, a line will be drawn connecting the projected centre point of the cable housing to the main centre point of the cable housing on the chest within the 3D sketch. By examining this 3D sketch, it becomes possible to determine the φ_{space}, representation on the figure, that is, the space angle associated with this particular motion.

It is important to note that during shoulder horizontal flexion, the weight of the entire arm has been neglected. Therefore, when performing horizontal flexion, there are two opposing loads to consider: the resistance from the muscles of the body and the resistance within the arm's centre of rotation (point A). However, the exact magnitudes of these loads are unknown and need to be determined separately. Nonetheless, it seems that the force needed for horizontal flexion is relatively small compared to that required for abduction and flexion. Due to this, we will not proceed to calculate this specific part.

4.5 Motor selection

Based on the previous calculations regarding the required motor force and torque in the shoulder abduction and flexion movements, the following table (Table 4-11) summarizes the maximum forces and torques for this project. A coefficient of 1.1 is applied to F_{real}, which increases the force by 10%. This accounts for potential errors and factors that cannot be precisely measured, that govern the subject.

Table 4-11 : Maximum force and torque.

Shoulder Abduction			
Maximum Force (N)	$F_{Braune-Fincher}$	$F_{Harless}$	$F_{Zatsiorsky}$
	345.2	307.9	133.8
Maximum Torque (Nm)	$T_{Braune-Fincher}$	$T_{Harless}$	$T_{Zatsiorsky}$
	4.833	4.31	1.873
Shoulder Flexion			
Maximum Force (N)	$F_{Braune-Fincher}$	$F_{Harless}$	$F_{Zatsiorsky}$
	316.2	282	122.6
Maximum Torque (Nm)	$T_{Braune-Fincher}$	$T_{Harless}$	$T_{Zatsiorsky}$
	4.427	3.948	1.716

Based on the provided table, the maximum motor torque for abduction is noted to be 4.833 Nm, while for flexion it is recorded to be 4.427 N.m. Appendix section A reports the specifications of the Dynamixel (XM540-W270-T/R) used in this project.

The stall torque of this type of Dynamixel motor at 12.0 V is measured to be 10.6 N.m. This indicates that the motor has sufficient torque capability to meet the requirements of our project; assuming a 30% safety factor, the suitability of this motor for the project remains. Overall, based on these considerations, the motor is highly likely to be a suitable and reliable choice for our project.

4.6 Coupling selection

After choosing the desired motor and with regard to its torque and shaft, the selection of the suitable coupling is done. In this regard, Aluminium Multi-Helix Flexible Three Beam Couplings, with an 8Nm peak torque, as described in Figure 4-26 and Figure 4-27 were selected.

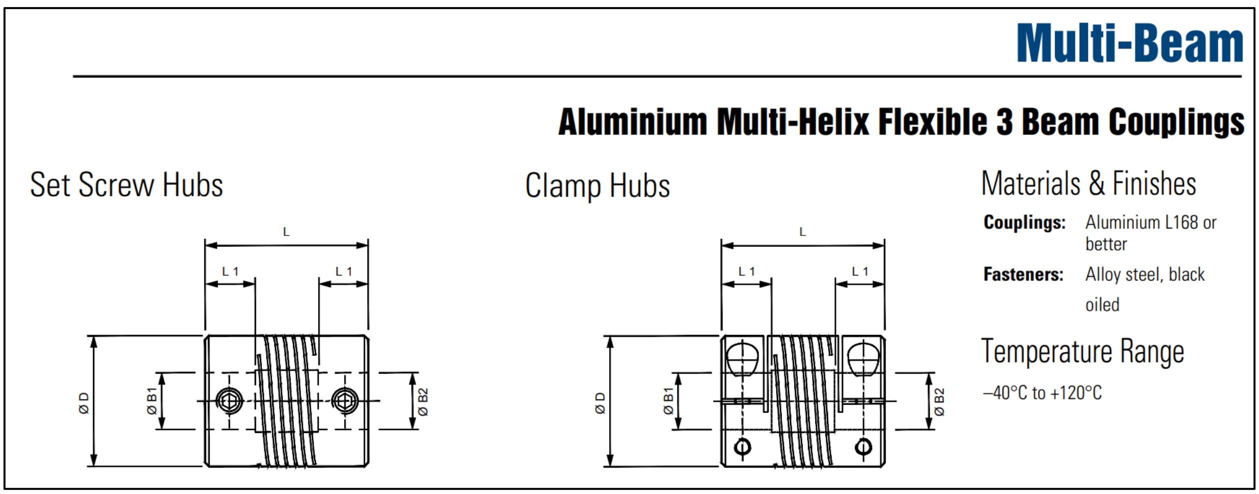

Figure 4-26: Overall description of coupling.

3-BEAM COUPLINGS: DIMENSIONS & ORDER CODES

Coupling Type & Size		Set Screw Style (COUPLING REF)	Clamp Type (COUPLING REF)	ØD mm	L mm	① L1 mm	Bore Diameters Min B1	Bore Diameters Min B2	Bore Diameters Max B1 & B2	Mass kgx10-3	Fasteners Set Screw	Fasteners Cap Screw	Fasteners Torque Nm	Fasteners Wrench mm	② Angular Offset Deg.	② Parallel Offset mm	Torsional Stiffness Nm/rad	③ Peak Torque Nm
Relieved	6	724.06	–	6.4	12.7	3.2	1.0	2.0	3.0	0.7	M2	–	0.2	0.9	3.0	0.07	1.53	0.40
	9	724.09	–	9.5	14.2	4.5	2.0	3.0	3.18	2.2	M2.5	-	0.55	1.3	3.0	0.1	5.4	0.40
		–	725.09								-	M1.6		1.5				
	13	724.13	–	12.7	19.1	6.0	3.0	4.0	5.0	5.0	M3	-	0.90	1.5	5.0	0.127	28.0	0.90
		–	725.13								-	M2		1.5				
	16	724.16	–	15.9	20.3	6.5	3.0	4.0	6.35	8.2	M4	-	2.2	2.0	5.0	0.127	38.0	1.50
		–	725.16								-	M2.5		2.0				
	19	724.19	–	19.1	22.9	6.5	4.0	4.76	8.0	12.8	M4	-	2.2	2.0	5.0	0.127	65.0	2.50
		–	725.19								-	M2.5		2.0				
	25	724.25	–	25.4	31.8	9.0	5.0	6.0	10	32.6	M5	-	4.6	2.5	5.0	0.127	121	4.0
		–	725.25								-	M3		2.5				
	32	724.32	–	31.8	44.5	12.0	6.0	8.0	14	70	M6	-	7.6	3.0	5.0	0.127	238	8.0
		–	725.32								-	M4		3.0				

BORE SIZES 3-BEAM COUPLINGS

Coupling Size	ØB1, ØB2 +0.03mm/-0mm (+0.0012/ -0)														
	1	2	3	(1/8″)	4	(3/16″)	5	6	(1/4″)	8	(3/8″)	10	12	(1/2″)	14
6	○	●	●												
9		○	●	●											
13			○	○	●	●	●								
16			○	○	●	●	●	●	●						
19					○	●	●	●	●	●					
25							○	●	●	●	●	●			
32								○	○	●	●	●	●	●	●
Bore ref.	8	11	14	16	18	19	20	22	24	28	31	32	35	36	38

Figure 4-27: Coupling selection table.

4.7 Conclusion

In conclusion, this chapter has presented a comprehensive mathematical model to describe the kinematics and statics of the Cable-Driven Shoulder Exosuit (CDSE), focusing on shoulder abduction, flexion, and horizontal flexion motions. Through meticulous analysis, starting from first principles and assumptions, the study has detailed the derivation of equations to calculate forces, torques, and the centre of mass for each segment of the arm. These calculations were instrumental in the selection of the appropriate motor and coupling mechanisms necessary to ensure the CDSE's optimal performance.

Furthermore, the research navigated through the challenges of translating projected forces on a 2D plane to their actual counterparts in 3D space, ensuring the models' accuracy and relevance. By considering the maximum forces and torques generated during various shoulder movements, this work laid a solid foundation for the motor and coupling selection, emphasizing the importance of a safety margin to account for unforeseen variables.

5 Chapter five: Finite Element Analysis (FEA) and Fabrication of CDSE

5.1 Introduction

Incorporating Finite Element Analysis (FEA) into the development of exosuits, particularly within the domain of soft robotics, is imperative to advancing the design and functionality of such assistive devices. FEA serves as a pivotal computational technique, enabling the detailed simulation of the intricate interactions between the pliable materials constituting the exosuit and the human anatomy under a vast range of operational scenarios. This analytical approach is instrumental in forecasting the mechanical behaviour of various materials, structural designs, and configurations, thereby ensuring the exosuit's ability to augment mobility while maintaining user comfort and allowing movement to remain essentially unrestricted. Moreover, FEA is invaluable in identifying and mitigating potential areas of stress concentration and material deformation, thereby enhancing the Exosuit's structural integrity and operational safety.

In this chapter, the FEA of the final model of the backpack first performed according to the forces and torques determined in the preceding chapter, after which the fabrication steps to this assembly are fully explained.

5.2 Methodology and Theoretical Contributions of Finite Element Analysis (FEA)

Finite Element Analysis (FEA) was employed to evaluate the structural integrity and mechanical performance of the Cable-Driven Shoulder Exosuit (CDSE) under various load conditions. The rationale for selecting FEA over alternative analytical methods lies in its ability to provide a high-fidelity prediction of stress distributions, material deformations, and failure points under dynamic conditions. The simulations were performed using SolidWorks, incorporating nonlinear material properties, meshing refinement strategies, and boundary conditions representative of real-world exosuit usage. The mechanical properties of PLA and aluminium were assigned based on empirical data, ensuring accurate stress-strain behaviours predictions. The validation of FEA results was conducted through comparative analysis with experimental prototype testing, wherein simulated stress distributions were cross-referenced against physical deformations observed during exosuit operation. The theoretical contribution of this analysis lies in demonstrating the feasibility of lightweight, soft robotic structures in assistive applications, providing insights into how different material compositions impact user safety, durability, and system performance. Furthermore, the findings reinforce the importance of bioinspired design choices, where FEA-guided iterations led to an optimized exosuit with improved load-bearing capacity and user adaptability. These insights contribute to advancing computational modelling for wearable robotics, bridging the gap between theory-driven simulation and practical implementation in rehabilitation technologies.

5.3 Finite Element Analysis (FEA)

5.3.1 Shoulder Abduction Load Scenario

The Finite Element Method (FEM) static simulation analysis of the cable-driven shoulder exosuit for rehabilitation (CDSE) during three loading scenarios yield insightful results, shaping our understanding of its structural performance. Constructed as a portable backpack, the Exosuit's three components, crafted from robust 6061 aluminium alloy (Table 5-1), endure loads applied through Bowden cables onto three 3D-printed parts fabricated from polylactic acid (PLA) (Table 5-2), which are interconnected by screws. Initial calculations confirm the safety factor for the bolt and nut connections surpasses 4.1, exceeding the required threshold of 2. Consequently, our attention shifts to assessing the resistance of other components. The detailed mesh specifications, including a maximum element size of 20.6351 mm, a minimum of 1.03176 mm, and an intricate network of 491,933 nodes and 286,901 elements, offer a comprehensive overview of the system's behaviour.

Maximum forces from our calculation in chapter 4 (Table 4-5) applied in the centre of the Bowden cables housing type 2.

Table 5-1: Mechanical characteristics of aluminium alloy 6061.

Name	6061 Alloy
Model type	Linear Elastic Isotropic
Default failure criterion	Max von Mises Stress
Yield strength	5.51485 × $10^7$07 N/m^2
Tensile strength	1.24084 × 10^8 N/m^2
Elastic modulus	6.9 × 10^{10} N/m^2
Poisson's ratio	0.33
Mass density	2,700 kg/m^3
Shear modulus	2.6 × 10^{10} N/m^2
Thermal expansion coefficient	2.4 × 10^5/Kelvin

Table 5-2: Mechanical characteristics of PLA.

Name:	PLA
Model type:	Linear Elastic Isotropic
Yield strength:	4 × 10^7 N/m^2
Tensile strength:	6.45 × 10^7 N/m^2
Elastic modulus:	2.34 × $10^9 N/m^2$
Poisson's ratio:	0.394
Mass density:	1,290 kg/m^3
Shear modulus:	3.189 × 10^8 N/m^2

Mesh information and details of abduction movement is illustrated in Figure 5-1.

Mesh information

Mesh type	Solid Mesh
Mesher Used:	Blended curvature-based mesh
Jacobian points for High quality mesh	16 Points
Maximum element size	20.6351 mm
Minimum element size	1.03176 mm
Mesh Quality	High
Remesh failed parts independently	Off

Mesh information - Details

Total Nodes	491933
Total Elements	286901
Maximum Aspect Ratio	79.638
% of elements with Aspect Ratio < 3	96.3
Percentage of elements with Aspect Ratio > 10	0.268
Percentage of distorted elements	0
Time to complete mesh(hh;mm;ss):	00:01:28
Computer name:	Hamed Vatan

Figure 5-1: Mesh information and details of the abduction movement.

The FEM study results, depicted in Figure 5-2-(b), Figure 5-2-(c), and Figure 5-2-(d), reveal critical information about the exosuit's response to the applied loading. Von Mises stress ranges from a minimum of 7.837 × $10^{-5} N/m^2$at element 420663 to a maximum of 5.814 × $10^{7} N/m^2$ at Node 19135. Resultant displacement varies from a minimum of 0.000 mm at Node 401347 to a maximum of 4.316× 10^{-1} mm on element 396080. Equivalent strain exhibits a spectrum from a minimum of 3.848 × 10^{-14} on element 244798 to a maximum of 1.419 × 10^{-2} on element 234551. These findings offer a detailed understanding of stress distribution, displacement patterns, and strain concentrations during shoulder abduction loading, providing valuable insights into potential design optimizations and enhancements to ensure optimal performance of the CDSE in shoulder rehabilitation scenarios. Results shows structure is stiff enough to hold as set of maximum forces were applied.

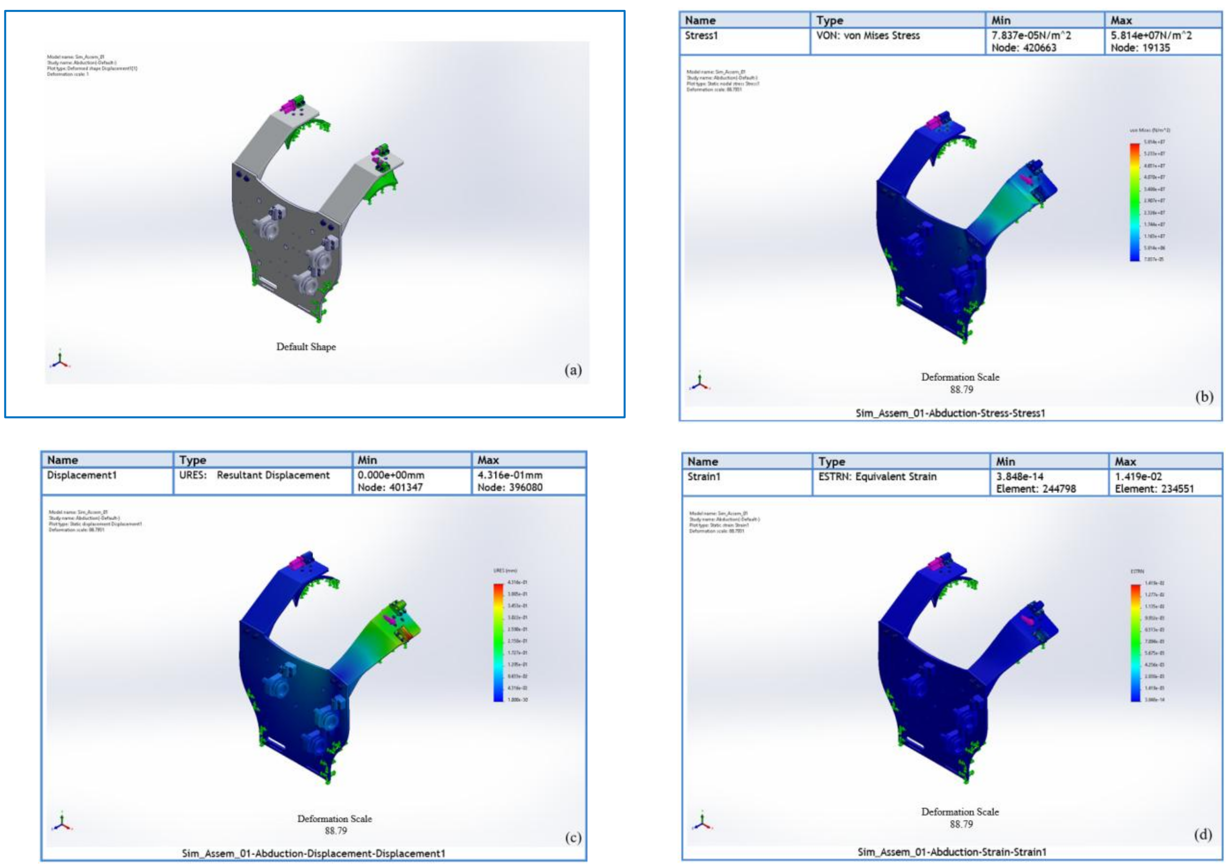

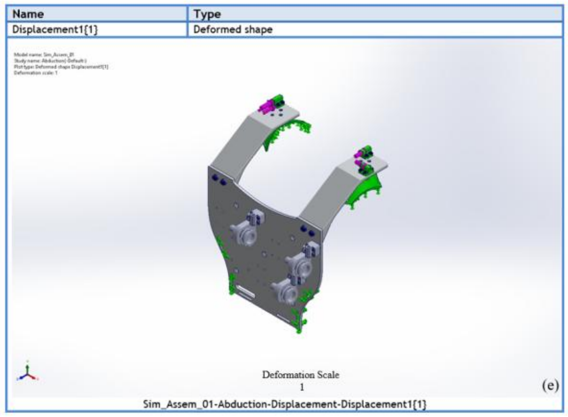

Figure 5-2: CDSE backpack FEM analysis during shoulder abduction. (a) Default shape of backpack. (b) Von Mises stress of backpack. (c) Resultant displacement of backpack. (d) Equivalent strain of backpack during shoulder abduction. (e) Real displacement of backpack.

According to Figure 5-2, the amount of stress, strain and displacement is within the acceptable range and therefore the design is correct for the applied loads.

5.3.2 Shoulder Flexion Load Scenario

Maximum forces from our calculation in chapter 4 (Table 4-8) applied in the centre of the Bowden cables housing type 2. The FEM study results, depicted in Figure 5-3-(b), Figure 5-3-(c), and Figure 5-3-(d), reveal critical information about the exosuit's response to the applied loading. Von Mises stress ranges from a minimum of 1.131 × 10^{-4} N/m^2at element 420663 to a maximum of 8.213 × $10^{7}N/m^2$ at element 481718. Resultant displacement varies from a minimum of 0.000 mm at element 401347 to a maximum of 3.571 × 10^{-1}mm on element 387020. Equivalent strain exhibits a spectrum that range from a minimum of 4.825 × 10^{-14}on element 244798 to a maximum of 1.487 × 10^{-2}on element 228845. These findings offer a detailed understanding of stress distribution, displacement patterns, and strain concentrations during shoulder flexion loading, providing valuable insights into potential design optimizations and enhancements to ensure optimal performance of the CDSE in shoulder rehabilitation scenarios. Results shows structure is stiff enough to hold as set of maximum forces were applied.

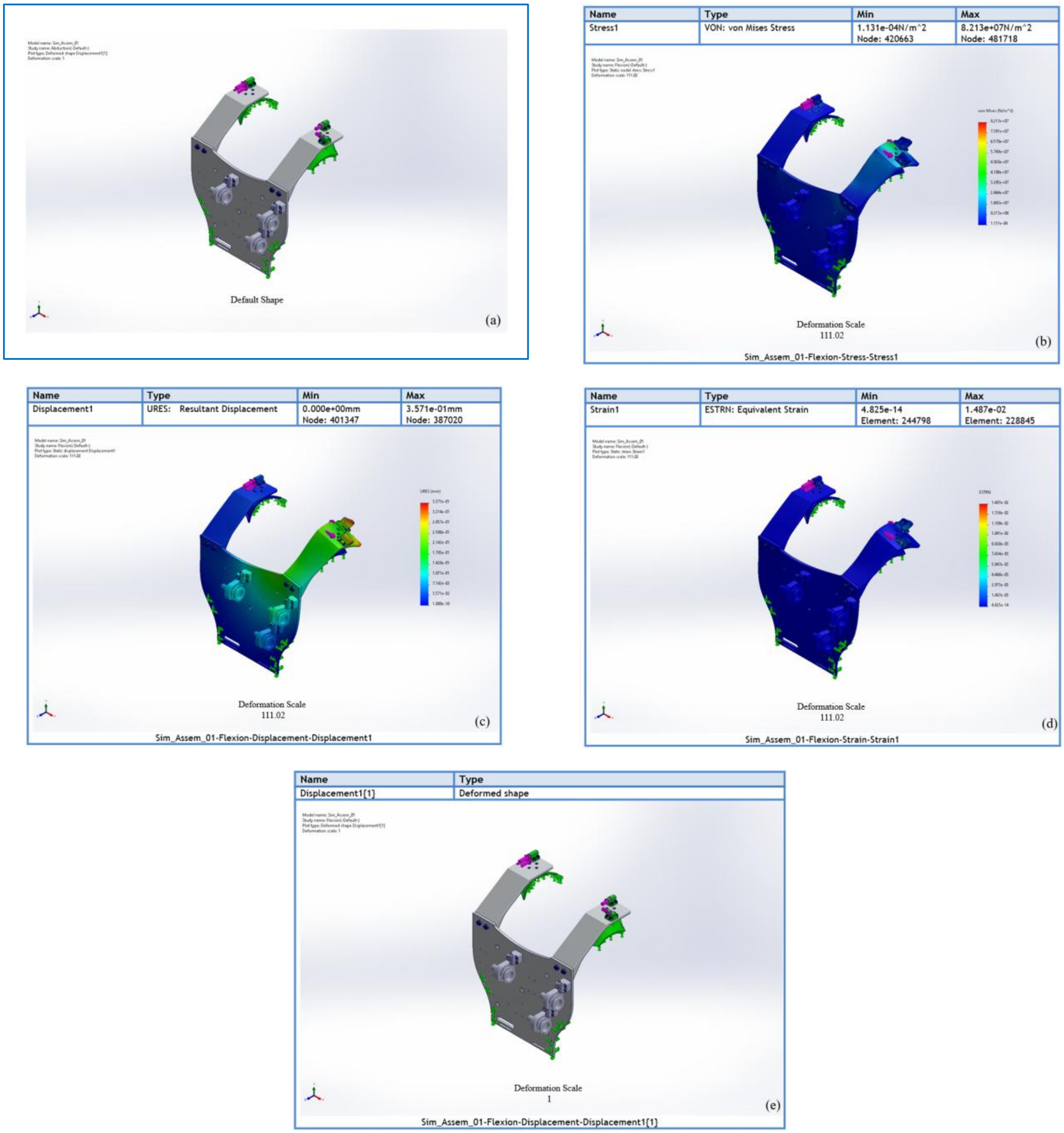

Figure 5-3: CDSE backpack FEM analysis during shoulder flexion. (a) Default shape of backpack. (b) Von Mises stress of backpack. (c) Resultant displacement of backpack. (d) Equivalent strain of backpack during shoulder flexion. (e) Deformed shape of backpack.

Also, the mesh information and details of flexion movement are illustrated in Figure 5-4.

Mesh information

Mesh type	Solid Mesh
Mesher Used:	Blended curvature-based mesh
Jacobian points for High quality mesh	16 Points
Maximum element size	20.6351 mm
Minimum element size	1.03176 mm
Mesh Quality	High
Remesh failed parts independently	Off

Mesh information - Details

Total Nodes	491933
Total Elements	286901
Maximum Aspect Ratio	79.638
% of elements with Aspect Ratio < 3	96.3
Percentage of elements with Aspect Ratio > 10	0.268
Percentage of distorted elements	0
Time to complete mesh(hh;mm;ss):	00:02:52
Computer name:	Hamed Vatan

Figure 5-4: Mesh information and details of flexion movement.

According to Figure 5-3, the amount of stress, strain and displacement is within the acceptable range and therefore the design is correct for the applied loads.

5.3.3 Shoulder Horizontal Flexion Load Scenario

Maximum forces from our calculation in chapter 4 (Table 4-8) applied in the centre of the Bowden cables housing type 2. The FEM study results, illustrated in Figure 5-5-(b), Figure 5-5-(c), and Figure 5-5-(d), highlight critical information regarding stress distribution, displacement patterns, and strain concentrations. Von Mises stress ranges from a minimum of 6.327 × $10^{-5} N/m^2$ at element 419568 to a maximum of 5.795 × $10^{7} N/m^2$at element 19135. Resultant displacement varies from a minimum of 0.000 mm at element 401347 to a maximum of 3.514 × 10^{-1}mm at element 391931. Equivalent Strain shows a spectrum from a minimum of 1.467 × 10^{-13}on element 247700 to a maximum of 1.422 × 10^{-2}on element 234448. These findings provide a comprehensive understanding of the exosuit's performance during shoulder horizontal flexion loading, offering valuable insights into potential design enhancements and optimizations to ensure the efficacy of the CDSE in shoulder rehabilitation scenarios. Results shows structure is stiff enough to hold as set of maximum forces were applied.

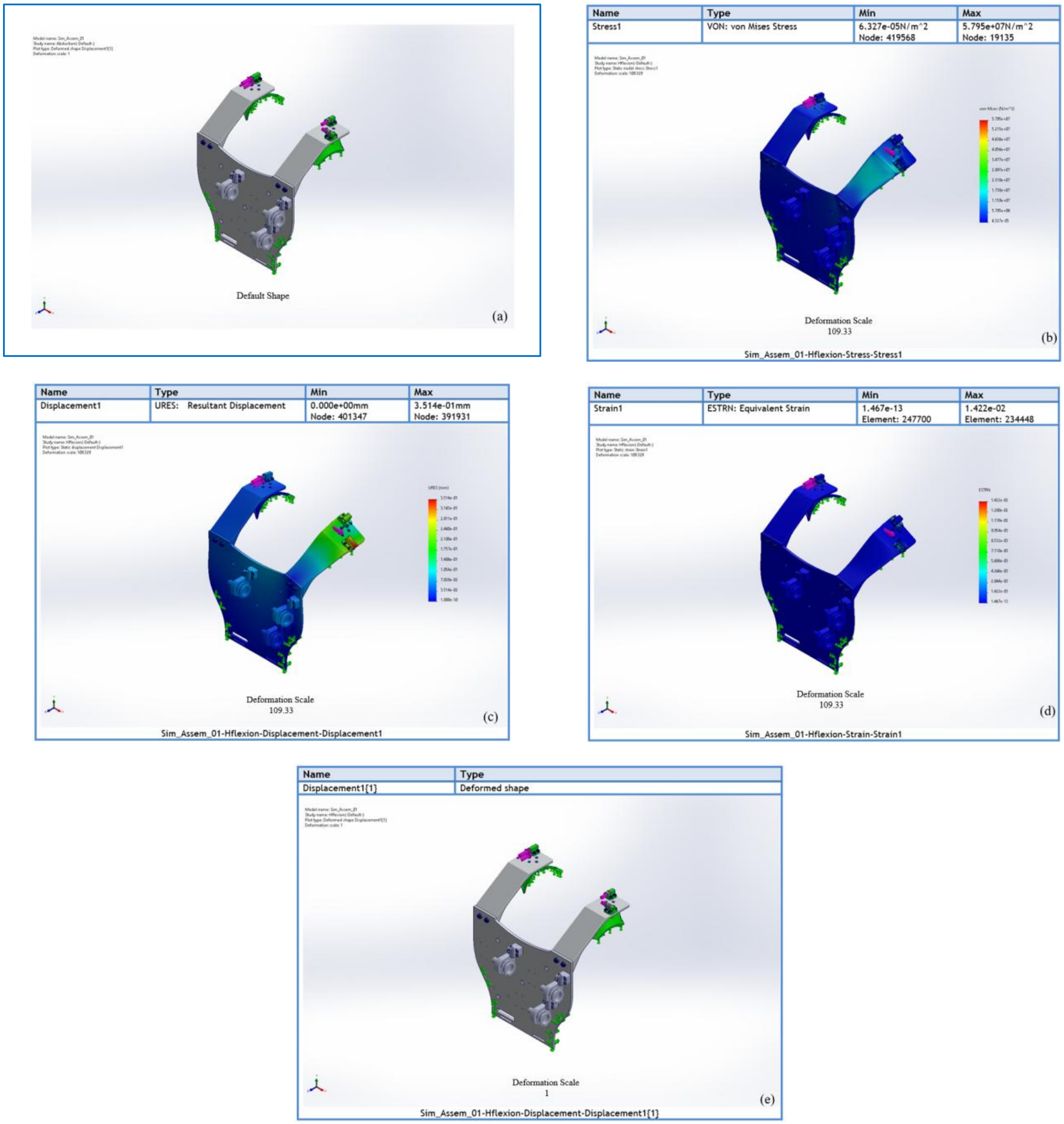

Figure 5-5: CDSE backpack FEM analysis during shoulder horizontal flexion. (a) Default shape of backpack. (b) Von Mises stress of backpack. (c) Resultant displacement of backpack. (d) Equivalent strain of backpack during shoulder horizontal flexion. (e) Deformed shape of backpack.

Also, the mesh information and detail in Horizontal flexion movement are illustrated in Figure 5-6.

Mesh information

Mesh type	Solid Mesh
Mesher Used:	Blended curvature-based mesh
Jacobian points for High quality mesh	16 Points
Maximum element size	20.6351 mm
Minimum element size	1.03176 mm
Mesh Quality	High
Remesh failed parts independently	Off

Mesh information - Details

Total Nodes	491933
Total Elements	286901
Maximum Aspect Ratio	79.638
% of elements with Aspect Ratio < 3	96.3
Percentage of elements with Aspect Ratio > 10	0.268
Percentage of distorted elements	0
Time to complete mesh(hh;mm;ss):	00:01:33
Computer name:	Hamed Vatan

Figure 5-6: Mesh information and details of horizontal flexion movement.

According to Figure 5-6, the amount of stress, strain and displacement is within the acceptable range and therefore the design is correct for the applied loads.

5.4 Fabrication of CDSE

In the development phase of this project, prototypes were fabricated utilising three distinct materials across three separate versions. Initially, the prototype was constructed using polylactic acid (PLA) to facilitate preliminary testing. Subsequently, a second version was produced, integrating both aluminium and PLA to enhance the prototype's robustness for further laboratory evaluation. The final version was crafted from carbon fibre, selected for its lightweight and high-strength properties, to meet the ultimate design objectives of the project. This systematic approach to material selection and prototype development was crucial to optimizing the project's performance characteristics. The fabrication cycle steps are depicted in Figure 5-7.

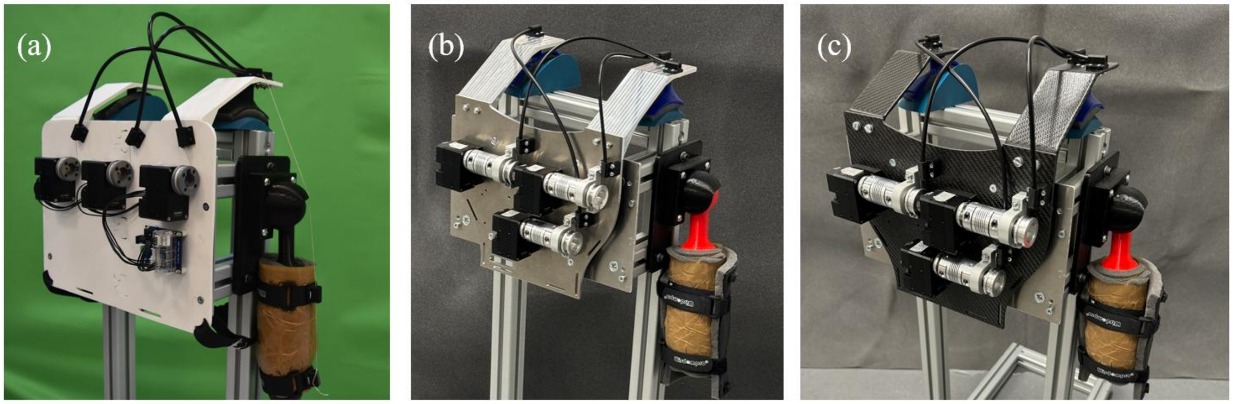

Figure 5-7: Fabrication phase stages. (a) First version: PLA material. (b) Second version: Aluminium with PLA. (c) Third version: Carbon fibre and PLA.

5.4.1 Fabrication of Backpack Pad

To place the backpack on the shoulders, there is a need for two parts that are placed on the shoulders on one side and attached to the backpack on the other. An illustration of this part is given in Figure 5-8.

Figure 5-8: Backpack pad.

These parts are made of polylactic acid (PLA) material, each of which weigh 16 grams (Figure 5-9- a). In the bottom of this part, some grooves have been used, which are cut that to attach the backpack to the user's body. This part is designed to be placed on different-sizes shoulders according to three different sizes, namely, small, medium, and large size. After developing this part, 10 mm foam was used in the internal compartment to create a soft support surface on the user's shoulder (Figure 5-9- b).

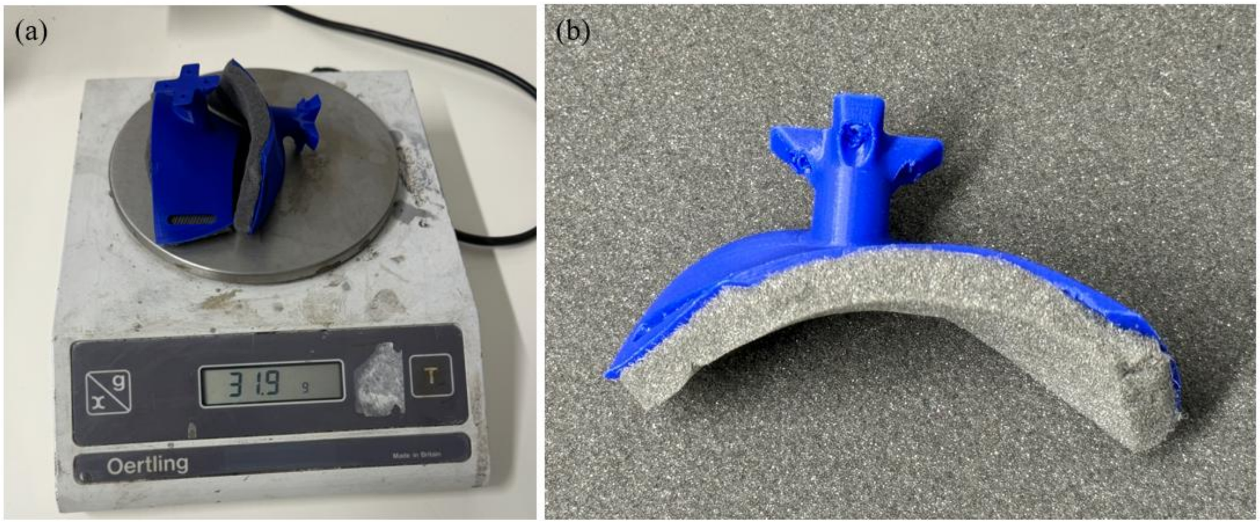

Figure 5-9: (a): Weight of backpack pad – (b): Fabricated backpack back pad with foam.

5.4.2 Fabrication of Backpack

- PLA Version of the Backpack

The first prototype backpack was made of PLA, and its weight was 530 grams. To develop a prototype of this part, according to its dimensions and the existing limitations, the backpack was formed from two 3D-printed parts that were then attached to each other using nuts and bolts. Figure 5-10 gives a view of the assembled backpack. This two-part item was only made as a prototype to start the desired tests, where in any following revisions positive steps will be taken regarding the new production method to achieve a stronger and lighter design.

Figure 5-10: Fabricated PLA backpack.

- Aluminium Version of the Backpack

The second prototype of the backpack, fabricated from aluminium, was developed for experimental evaluation. Detailed in the design chapter (chapter three), this configuration incorporates a primary plate connected to two shoulder attachments, facilitating its integration and functionality within the laboratory setting. Figure 5-11 shows the backpack main plate both sides whilst Figure 5-12 presents both sides of the backpack connector plate.

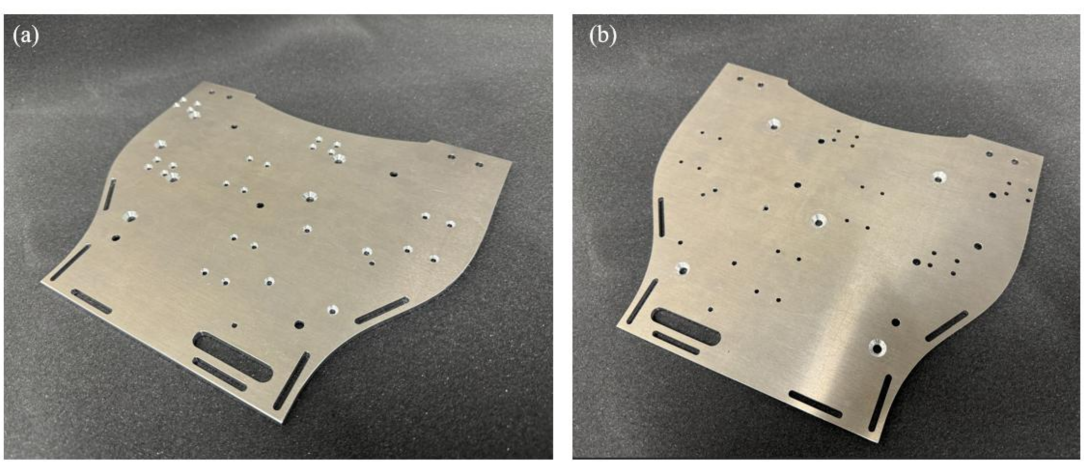

Figure 5-11: Backpack main plate (aluminium material). (a) Front side. (b) Back side.

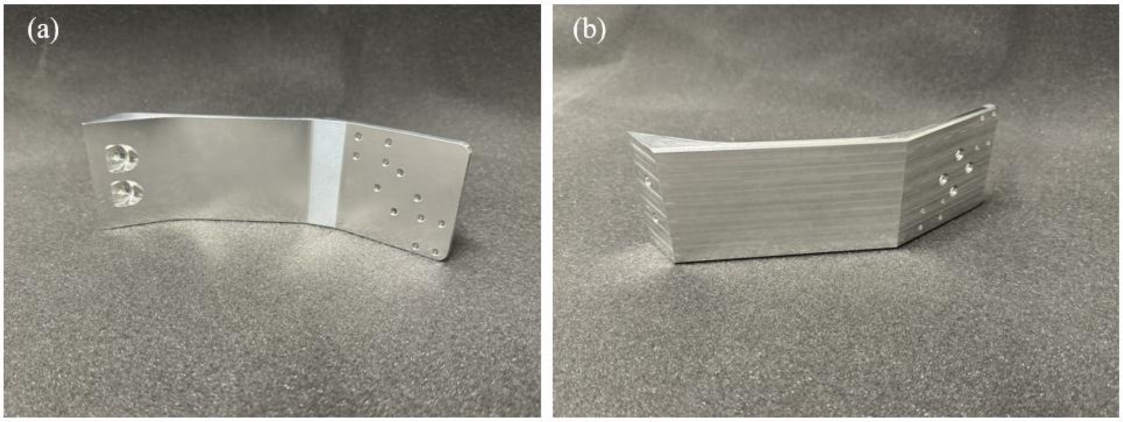

Figure 5-12: Backpack connector plate (aluminium material). (a) Front side. (b) Back side.

- Carbon Fiber Version of the Backpack

The ultimate version of the backpack utilized carbon fibre as its construction material, ensuring both lightness and durability. Given the backpack's intended use by individuals with impaired shoulder mobility, its portability and minimal weight are crucial to this design. Figure 5-13 depicts the main plate and the connector plates attached to it, which are constructed from carbon fibre material. The combined weight of these three components, when compared to their aluminium counterparts, was reduced to approximately one-third of the weight.

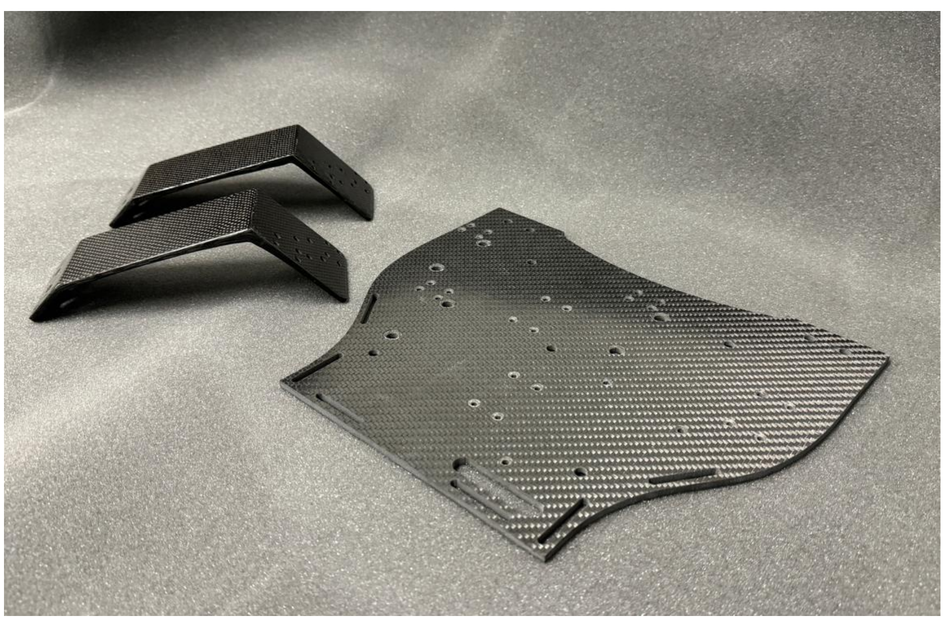

Figure 5-13: Backpack main plate and connector plates (carbon fibre material).

5.4.3 Backpack Assembly

Figure 5-14 illustrates the backpack assembly process with aluminium, whilst Figure 5-15 depicts assembled backpack fabricated from two distinct materials: aluminium and carbon fibre.

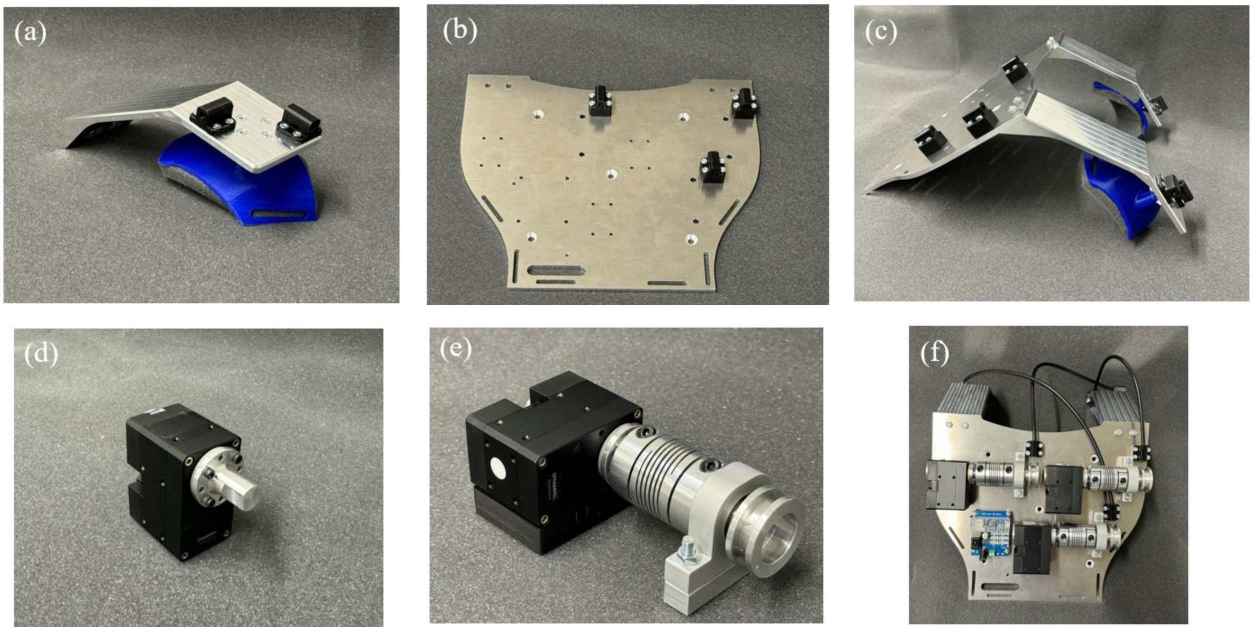

Figure 5-14: Assembly of the backpack.

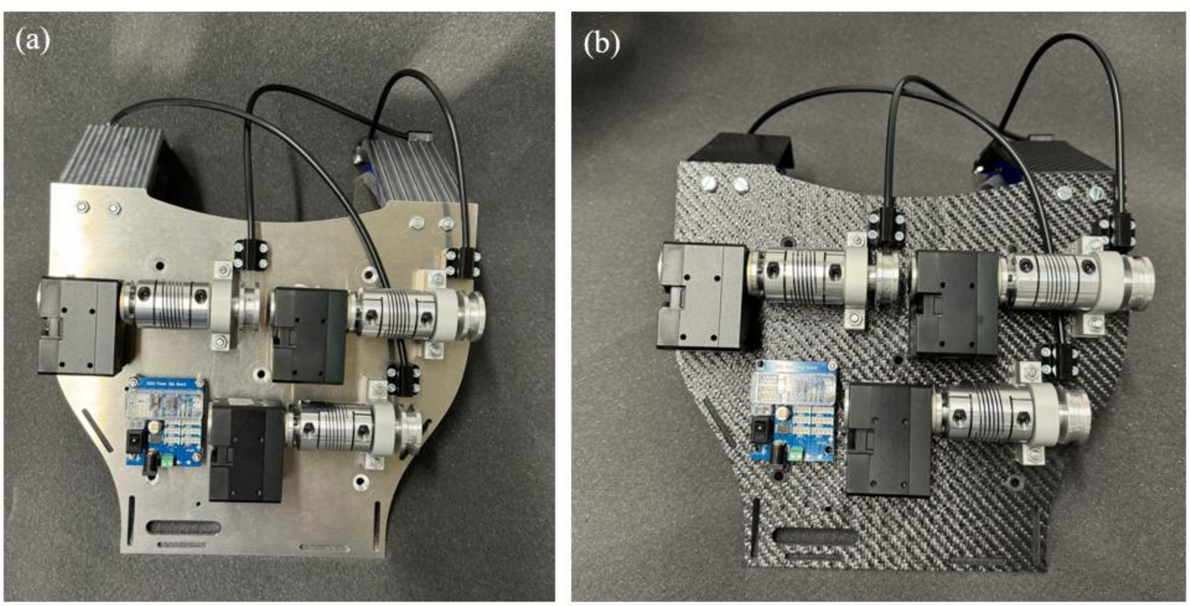

Figure 5-15: Assembled backpack. (a) Aluminium material. (b) Carbon fiber material.

5.4.4 Waist Strap

A waist strap is used to fully attach the backpack to the user's body. This waist strap allows the backpack to be fastened to the user's body from the front and backside and reduces backpack rotations when the motors are moving. This is a commercial part (Hellery Trainer Belt Waist Strap) that has been purchased and modified according to the needs of the current project. Figure 5-16 gives a schematic view of this part. The item weighs 270 grams.

Figure 5-16: Waist strap.

5.4.5 Mannequin

A male mannequin is shown in Figure 5-17. This mannequin has natural human dimensions and upper limbs that are completely like those of a human. The mannequin’s hands are made of solid wood, and their specifications are presented in Figure 5-17.

Figure 5-17: Male mannequin.

The mannequin's arm is durable and flexible because the bionic articulated arms are modelled on the principles of human mechanics. It can move joints, and its shape can be manipulated flexibly. The desired backpack and mannequin are shown in Figure 5-18 and Figure 5-19.

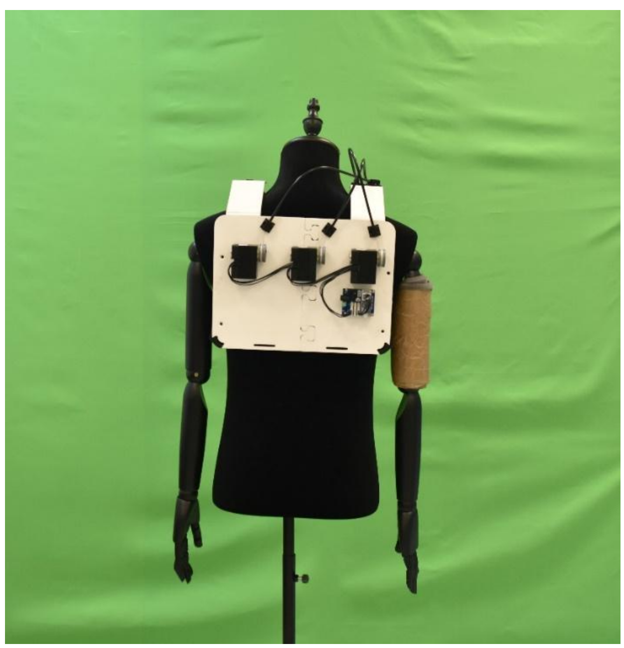

Figure 5-18: Positioning the backpack on the mannequin (back side).

Figure 5-19: Positioning the backpack on the mannequin (front side).

5.4.6 Test Bench

- Backpack Seat Installation on Test Bench

These parts are fabricated from PLA. Figure 5-20 illustrates the designed part that is installed on the stand.

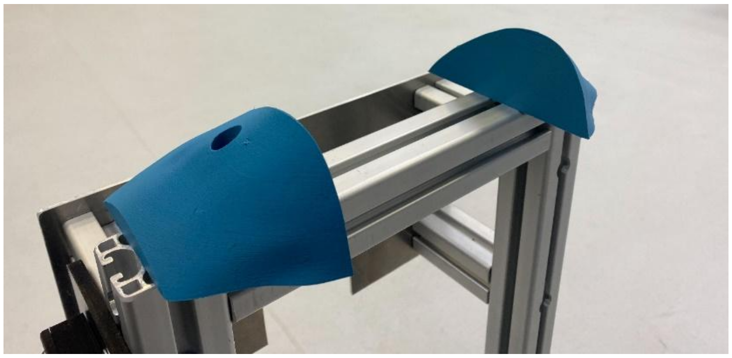

Figure 5-20: Installation of backpack seats on test bench.

- Connection Plate Design

Figure 5-21 shows the designed connection plate that is installed on the test bench. This connection plate allows the spherical joint to be connected to the body of the test bench.

Figure 5-21: Installation of connection plate to the stand.

- Design of Spherical Joint and Upper Arm

  Figure 5-22 shows the part designed for these two elements, which are interconnected and also connected to the test bench (Figure 5-23).

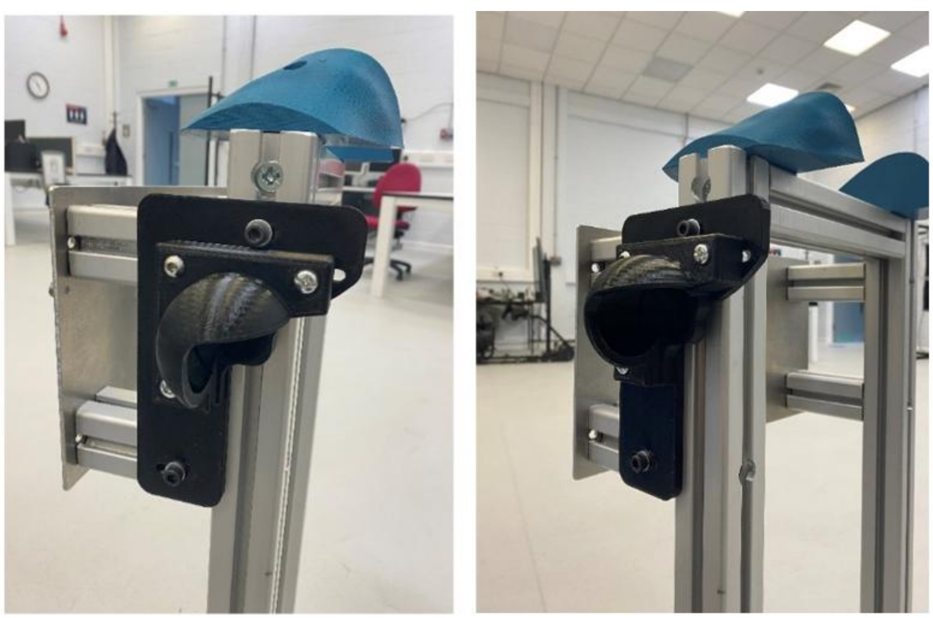

Figure 5-22: Installation of connection plate and spherical joint to the stand.

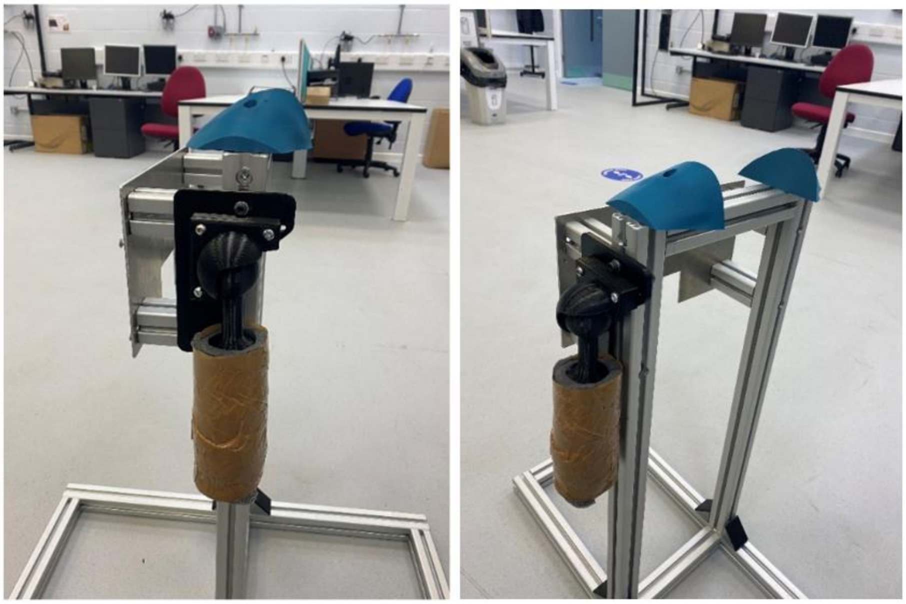

Figure 5-23: Fabricated and installed upper arm and spherical joint on the stand.

- Assembling all Parts on the Test Bench

Figure 5-24, Figure 5-25 and Figure 5-26 show the backpacks, fully assembled, positioned on the test bench, utilizing the three materials for the body: PLA, aluminium, and carbon fiber.

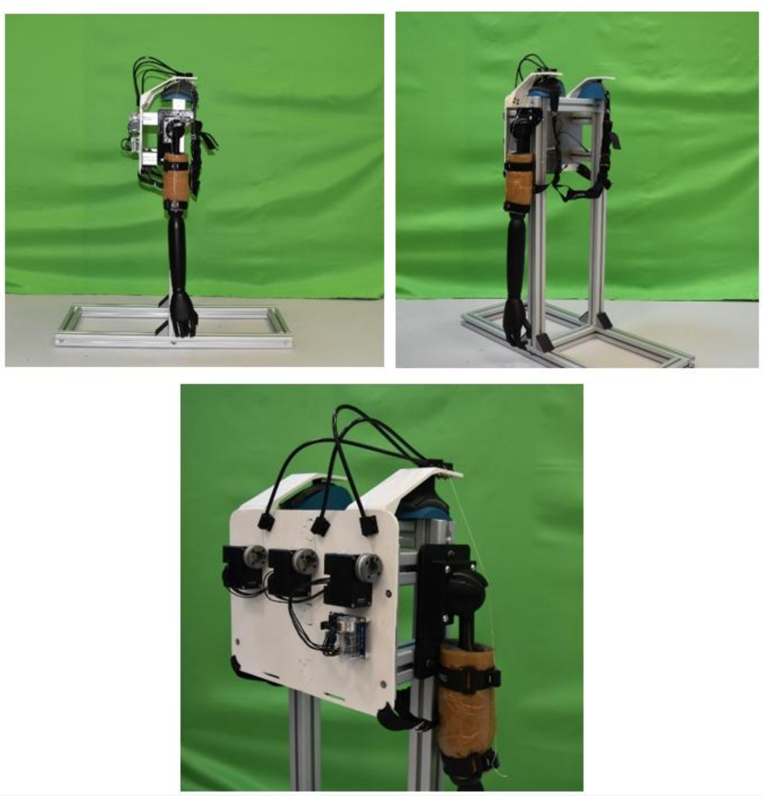

Figure 5-24: Assembling all the parts of the PLA backpack on the test bench.

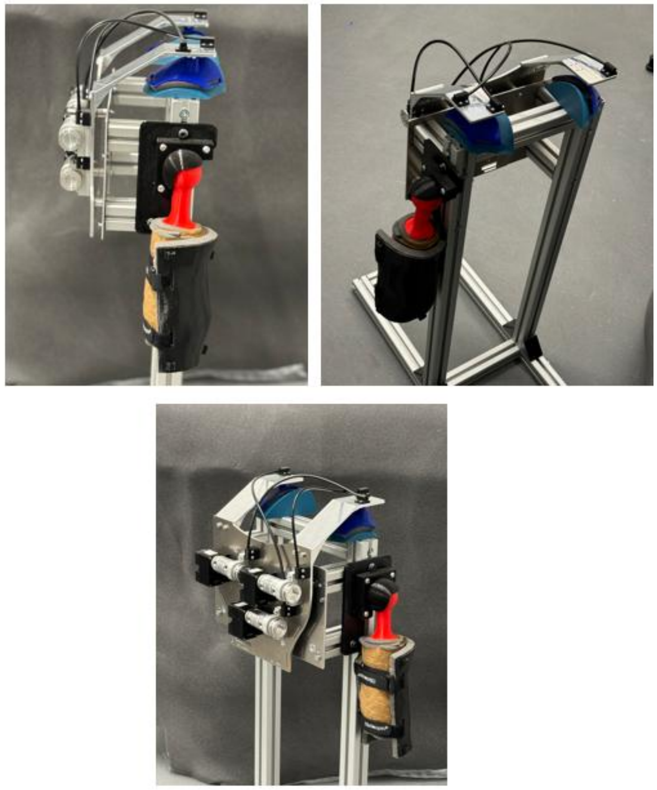

Figure 5-25: Assembling all parts of the aluminium backpack on the test bench.

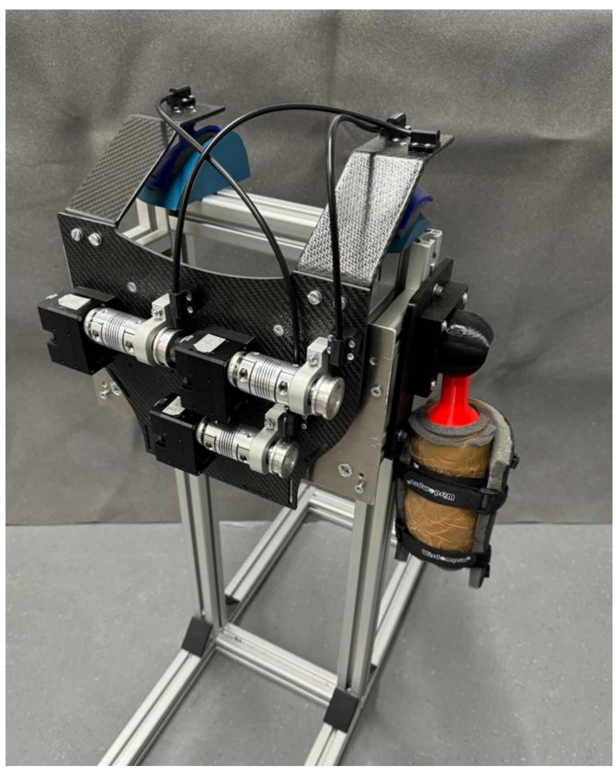

Figure 5-26: Assembling all parts of the carbon fiber backpack on the test bench.

5.4.7 Weight Table

As shown in Figure 5-27 about three different version of backpack, Table 5-3,

Table 5-4, Table 5-5 shows the weight of the assembled parts in PLA, aluminium, and carbon fibre.

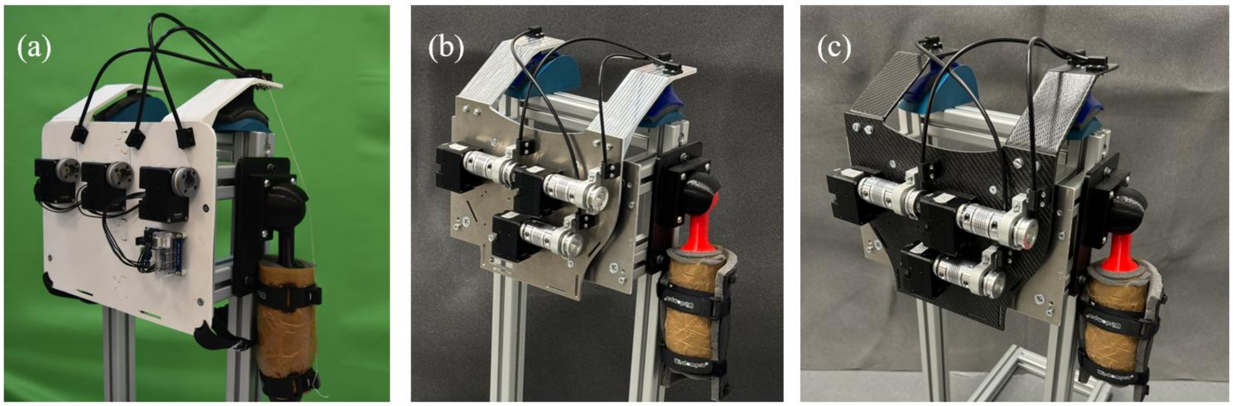

Figure 5-27: (a) First version: PLA. (b) Second version: Aluminium with PLA. (c) Third version: Carbon fibre and PLA.

Table 5-3: Weight of each part of the PLA backpack.

Item	Description	Material	Weight (gr)	Quantity	Total Weight (g)
1	Main Plate	PLA	530	1	530
2	Backpack pad	PLA	16	2	32
3	Bowden cable housing	PLA	3.3	6	19.8
4	Motor	------	161	3	483
5	Pulley	PLA	5.4	3	16.2
6	Anchor point	PLA	90	1	145
7	Tendon	------	1.67	3	5
8	LI-PO battery	------	125	1	125
9	Arduino	------	25	1	25
10	Bowden cable sheath	PVC	5	3	15
11	Waist strap	------	270	1	270
12	Arm strap	------	5	2	10
13	Body guiding point	PLA	4	1	4
14	bolts, nuts, and washers	------	------	set	35
		Total weight			1,660

Table 5-4: Weight of each part of the aluminium backpack (item numbers of 2,3,4,5,6 including bolts, nuts, and washers)

Item	Description	Material	Weight (gr)	Quantity	Total Weight (g)
1	Main Plate	Al	712	1	712
2	Connector plate	Al	185	2	370
3	Backpack pad	PLA	20	2	40
4	Bowden cable housing Type1	PLA	5.4	3	16.2
5	Bowden cable housing Type2	PLA	3.8	3	11.4
6	Motor pack	------	355	3	1065
7	Anchor point	PLA	90	1	145
8	Tendon	Cotton and linen	1.67	3	5
9	LI-PO battery	------	125	1	125
10	Arduino	------	25	1	25
11	Bowden cable sheath	PVC	5	3	15
12	Waist strap	------	270	1	270
13	Arm strap	------	5	2	10
14	Body guiding point	PLA	4	1	4
		Total weight			2,758.6

Table 5-5: Weight of each part of the carbon fibre backpack (item numbers of 2,3,4,5,6 including bolts, nuts, and washers)

Item	Description	Material	Weight (gr)	Quantity	Total Weight (g)
1	Main Plate	Carbon fibre	302	1	302
2	Connector plate	Carbon fibre	57.5	2	115
3	Backpack pad	PLA	20	2	40
4	Bowden cable housing Type1	PLA	5.4	3	16.2
5	Bowden cable housing Type2	PLA	3.8	3	11.4
6	Motor pack	------	355	3	1065
7	Anchor point	PLA	90	1	145
8	Tendon	Cotton and linen	1.67	3	5
9	LI-PO battery	------	125	1	125
10	Arduino	------	25	1	25
11	Bowden cable sheath	PVC	5	3	15
12	Waist strap	------	270	1	270
13	Arm strap	------	5	2	10
14	Body guiding point	PLA	4	1	4
		Total weight			2,093.6

5.5 Conclusion

Based on the comprehensive analysis and fabrication details provided in this chapter, the following conclusions summarize the key findings and contributions of this research:

- This study meticulously examined the structural integrity, mechanical behaviour, and fabrication processes of the CDSE, an innovative exosuit designed for shoulder rehabilitation. Through rigorous Finite Element Analysis (FEA), we successfully simulated the exosuit's performance under various load scenarios, namely shoulder abduction, flexion, and horizontal flexion. The FEA's outcomes confirmed the exosuit's robust design, highlighting its ability to withstand operational stresses while maintaining user comfort and safety. Notably, the utilization of materials such as polylactic acid (PLA), aluminium, and carbon fibre in the prototypes underscores our commitment to optimizing the balance between strength, weight, and flexibility, essential for rehabilitation devices.
- Beyond the technical details, the application of FEA in this work contributes significantly to the methodological and theoretical foundations of exosuit development. The systematic selection of meshing strategies, boundary conditions, and validation procedures ensures that FEA models can be reliably applied to soft robotic systems for assistance. The study demonstrates how computational simulations can effectively predict real-world performance, reducing the need for excessive prototyping and accelerating the iterative design process. Furthermore, the findings highlight the importance of integrating biomechanical principles into simulation frameworks, ensuring that assistive devices operate in harmony with natural human movement. These insights serve as a foundation for future advancements in wearable rehabilitation robotics, bridging the gap between theoretical modelling and experimental validation.
- The fabrication phase was pivotal to transforming theoretical designs into tangible prototypes, culminating in the development of three iterations of the CDSE. Each version, evolving from PLA to aluminium and finally to carbon fibre, demonstrated significant improvements in weight reduction and structural integrity, thereby

enhancing the exosuit's efficacy and user experience. Furthermore, the integration of components such as the motor pack, tendon system, and Arduino-UNO for control operations exemplifies the interdisciplinary approach employed in this research, bridging the gap between mechanical engineering and robotics.

- In conclusion, CDSE represents a significant advancement in the field of soft robotics and rehabilitation devices. The findings from the FEA and the successive iterations of the prototype underscore the potential of this exosuit to provide a customizable, lightweight, and effective solution for individuals undergoing shoulder rehabilitation.

6 Chapter Six: Inverse Kinematics and Control of CDSE

6.1 Introduction

Chapter six embarks on an in-depth exploration of "Inverse Kinematics and Control of Cable-Driven Exoskeletal Systems (CDSE)," central to advancing upper limb rehabilitation through soft robotics. It meticulously outlines the structural design and functionality of cable-driven exosuits, which are ingeniously configured with cables and actuators to support, guide, and augment limb movements for therapeutic purposes. Anchoring on the paramount importance of robot kinematics, the chapter delineates its vital role in path planning, workspace optimization, precise control, and motion planning, setting a solid foundation for understanding the complex interplay between theoretical frameworks and practical applications in rehabilitation robotics.

Furthermore, it introduces the concept of inverse kinematics, a pivotal mechanism for determining configurations that achieve desired workspace coordinates, essential for manipulative tasks and optimizing observational vantage points. The narrative seamlessly transitions into detailed analyses of speed, acceleration, and the Jacobian matrix, alongside sophisticated control mechanisms such as PID controllers, highlighting their indispensable contributions to the nuanced kinematic and dynamic control of CDSE.

6.2 Modelling of Cable-Driven Exosuit for Upper Limb Rehabilitation

Cable-driven exosuits for upper limb rehabilitation are wearable devices that encompass the upper extremity, that is, the arm, shoulder, and hand. These exosuits utilize cables and actuators strategically placed along the limb to support, guide, and augment the user's movements during therapy or training sessions. As shown in Figure 6-1, the cable-driven exosuit for upper limb rehabilitation consist of a base platform and a moving arm platform, with the base platform connected to the moving arm platform by three cables in parallel configuration.

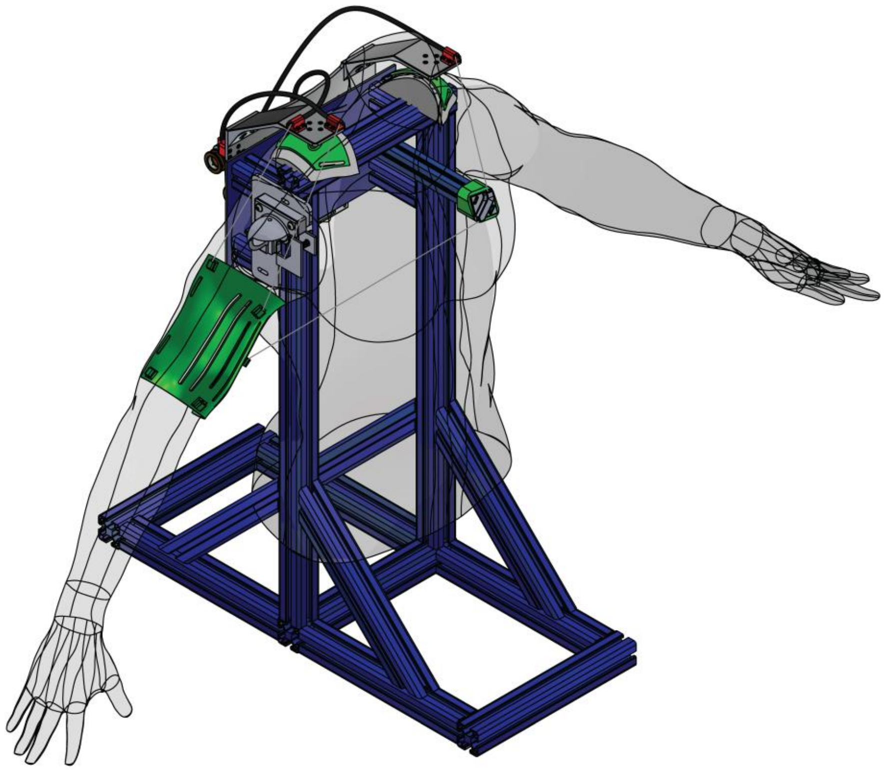

Figure 6-1: Cable-driven exosuit rehabilitation.

Figure 6-2 illustrates the mathematical modelling and analysis of CDSE carried out. $B_1, B_2, and\ B_3$ represent the cable driving points on the fixed-base platform. $A_1, A_2, and\ A_3$ represents the traction points on the moving arm platform. A_{xyz} is the arm coordinate system (ACS). B_{XYZ} is the base coordinate system (BCS), which is fixed relative to the base platform. The origin of the moving arm system A coincides with the midpoint of traction point and end point of cable 1. When the arm is in its natural position and at rest, the axes of the moving arm coordinates ($x, y\ and\ z$) are along the fixed-base coordinate axes ($X, Y, and\ Z$) of the CDSE.

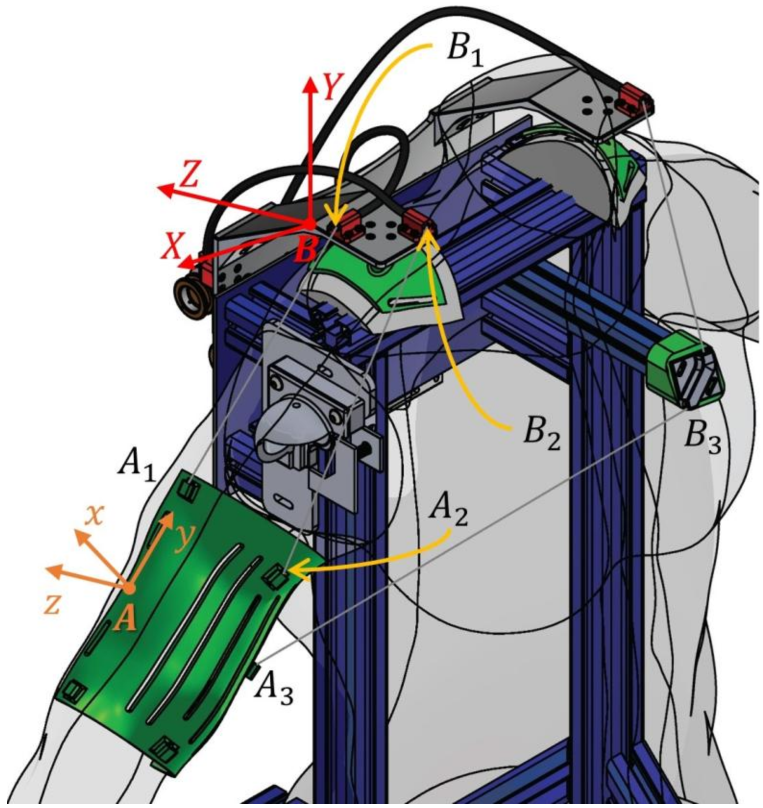

Figure 6-2: Cable-driven exosuit rehabilitation mathematical.

6.2.1 Significance of Robot Kinematics

Robot kinematics plays a vital role in robotics for several reasons:

Path Planning: Kinematics helps to determine the optimal path that a robot should follow to reach its target, considering the robot's constraints and workspace limitations. This enables efficient and collision-free movement.

Workspace Analysis [153]: By analysing the robot's kinematics, engineers can determine the reachable workspace or dexterous workspace of a robot. This such information aids in designing tasks and optimizing the robot's workspace for maximum efficiency.

Control and Calibration [154]: Robot kinematics allow for precise control of robot manipulators, ensuring accurate positioning and movement. Kinematic models are used to design control algorithms and perform calibration procedures to minimize errors and achieve higher accuracy.

Motion Planning [155]: Kinematics assists in generating smooth and natural robot motion. By considering joint limits, joint velocities, and joint accelerations, kinematics helps to plan trajectories that are both safe and comfortable.

6.2.2 Applications of Robot Kinematics

Robot kinematics finds applications in various industries:

Manufacturing: Robot arms in assembly lines use kinematics to perform precise movements, enabling them to manipulate objects, assemble components, and perform complex tasks efficiently.

Medical Robotics: Surgical robots utilize kinematics to navigate and manipulate surgical instruments within the human body, enhancing the precision and safety of minimally invasive procedures.

Autonomous Vehicles: Kinematics is crucial in controlling the motion and steering of autonomous vehicles, enabling them to navigate through complex environments and to avoid obstacles.

Virtual Reality and Animation: Kinematics plays a vital role in animating virtual characters and objects, creating lifelike movements and interactions in video games and computer-generated movies.

6.3 Inverse Kinematics of the CDSE

As opposed to forward kinematics, which computes the workspace coordinates of a robot given a configuration as input, inverse kinematics (IK) is essentially the reverse operation: computing configuration(s) to reach a desired workspace coordinate. This operation is essential to many takes in robotics, like moving a tool along a specified path, manipulating objects, and observing scenes from a desired vantage point. Because it is so important, inverse kinematics has been studied extensively, with many techniques available to solve them quickly and (relatively) reliably.

The inverse kinematics of the CDSE is obtained from the following equation:

$$\left(\left({}^{B}P + {}^{B}R_{A}\,{}^{A}a_{i}\right) - {}^{B}b_{i}\right) = \vec{L}_{i}\,, \qquad i = 1 \dots m \tag{36}$$

$$\|L_i\| = l_i\,, \qquad i = 1 \dots m \tag{37}$$

where ${}^{B}b_i = \overrightarrow{BB_i}$ represents the vector from the fixed-base coordinate system origin B to cable driving point B_i in BCS; ${}^{B}P = \overrightarrow{BA}$ represents the vector from the fixed-base coordinate system origin B to the origin of the moving arm coordinate system A in the BCS; ${}^{A}a_i = \overrightarrow{AA_i}$

represents the vector from the moving arm coordinate system origin A to cable traction point A_i in the ACS; m is the number of cables; ; L_i is the i-th cable vector; l_i represents the i-th cable length. ${}^{B}R_A$ is the direction cosine matrix (DCM) of the arm coordinate system, A_{xyz}, relative to the base coordinate system B_{XYZ}:

$$ {}^{B}R_A = R_\alpha R_\beta R_\gamma \tag{38} $$

where $R_\alpha = \begin{bmatrix} 1 & 0 & 0 \\ 0 & \cos\alpha & \sin\alpha \\ 0 & -\sin\alpha & \cos\alpha \end{bmatrix}$, $R_\beta = \begin{bmatrix} \cos\beta & 0 & -\sin\beta \\ 0 & 1 & 0 \\ \sin\beta & 0 & \cos\beta \end{bmatrix}$, $R_\gamma = \begin{bmatrix} \cos\gamma & \sin\gamma & 0 \\ -\sin\gamma & \cos\gamma & 0 \\ 0 & 0 & 1 \end{bmatrix}$ in Eq. (38) are the standard rotation matrices about the X, Y, and Z axes, respectively.

Figure 6-3 illustrates the determination of the arm coordination system position in the base coordination system.

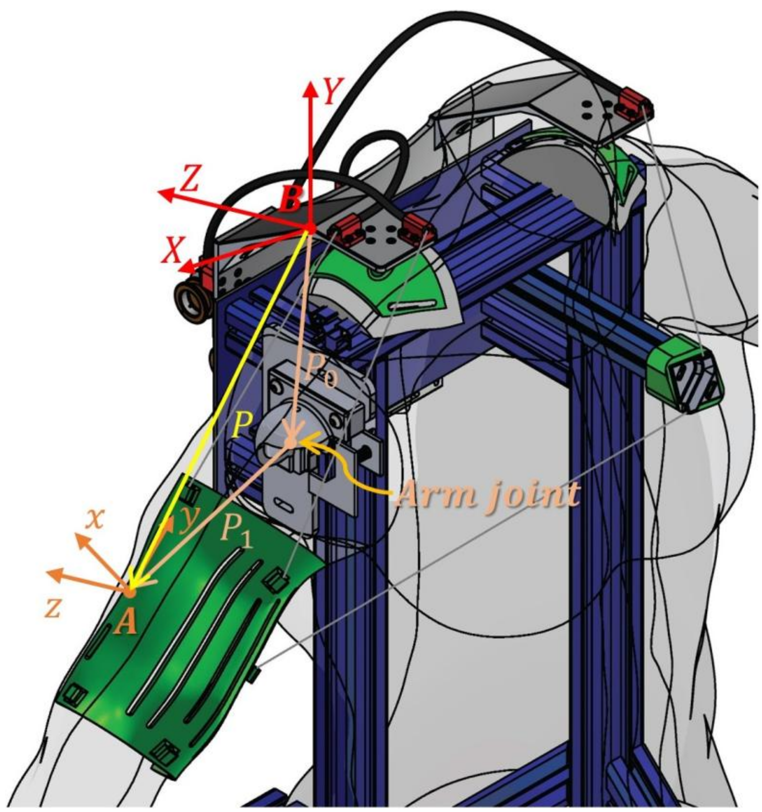

Figure 6-3: Arm coordination system position.

Figure 6-4 to Figure 6-6 illustrates a single-cable vector kinematic analysis for cables 1 to 3, respectively.

$$ {}^{B}P = {}^{B}P_0 + {}^{B}R_A \, {}^{A}P_1 \tag{39} $$

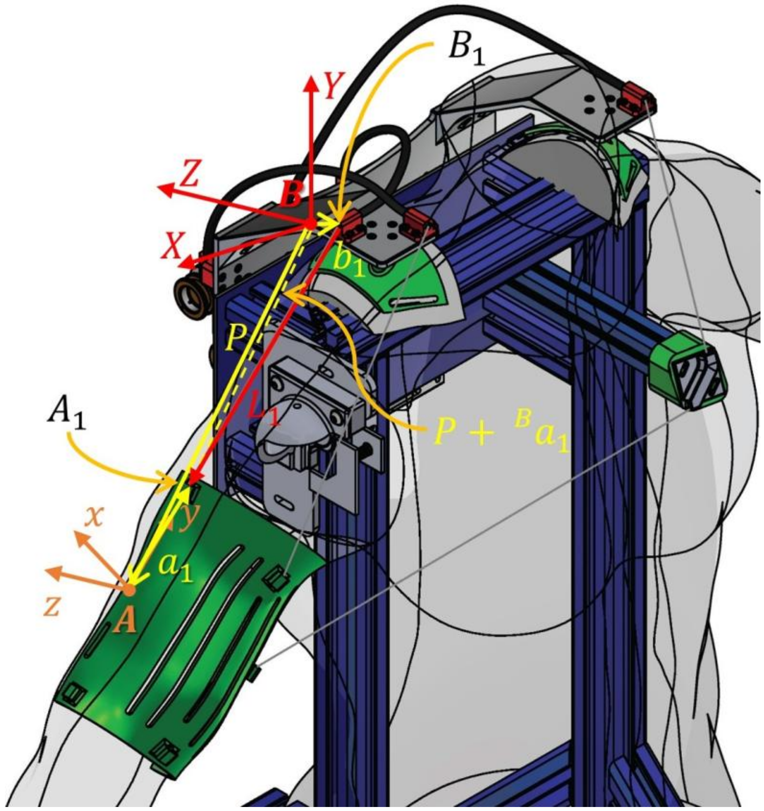

Figure 6-4: CDSE kinematic model analysis for the first cable.

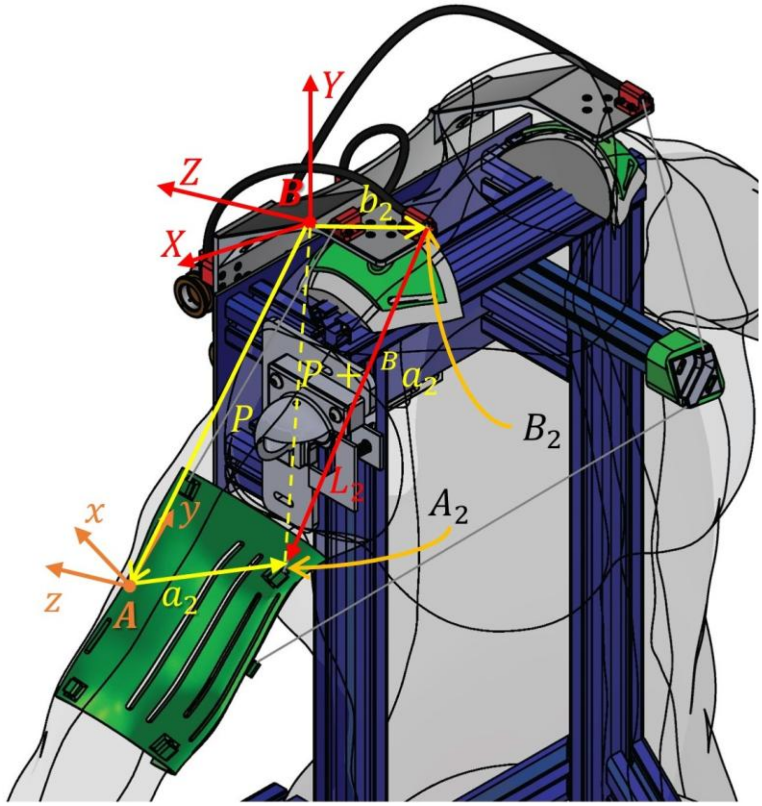

Figure 6-5: CDSE kinematic model analysis for the second cable.

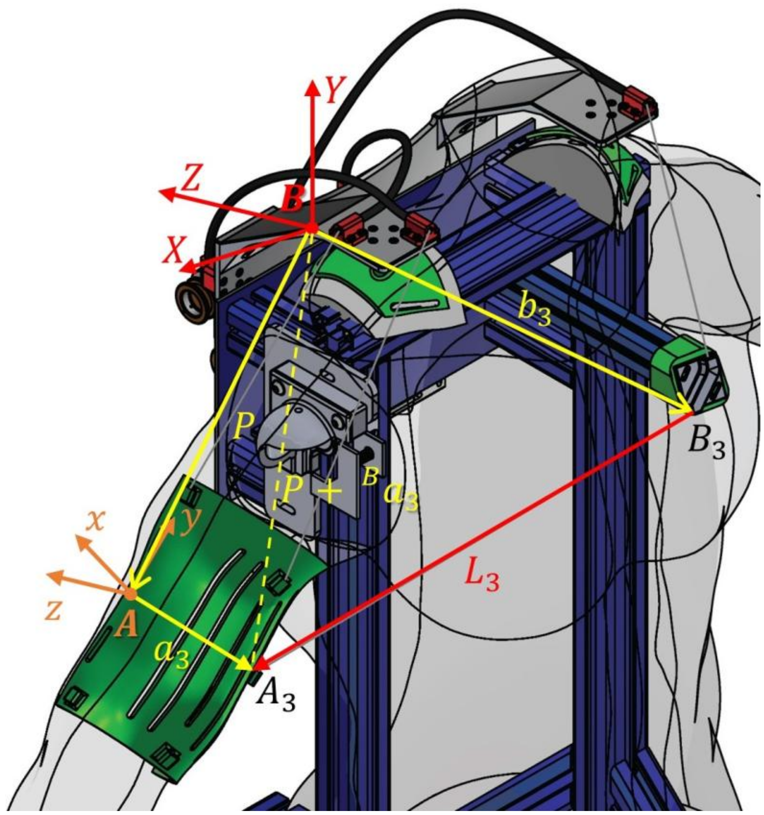

Figure 6-6: CDSE kinematic model analysis for the third cable.

According to equation (37), which is obtained from the closed loop form of each cable and the consideration of the geometry of the system, the length of the cable is defined in each orientation. Equation (37) can be expanded and calculated from the dot product of the second side of the equation:

$$
\begin{aligned}
l_i &= \left(\vec{L}_i.\vec{L}_i\right)^{0.5} \\
&= \left({}^{B}P^{T}\,{}^{B}P + {}^{B}b_i^{T}\,{}^{B}b_i + ({}^{B}R_A\,{}^{A}a_i)^{T}({}^{B}R_A\,{}^{A}a_i) + 2\,{}^{B}P^{T}({}^{B}R_A\,{}^{A}a_i) - 2\,{}^{B}P^{T}\,{}^{B}b_i \right. \\
&\qquad \left. - 2\,{}^{B}b_i^{T}({}^{B}R_A\,{}^{A}a_i)\right)^{1/2}
\end{aligned} \tag{40}
$$

and which can then be used to obtain the length of i-th cable.

Therefore, according to equation (39), the length of the i-th cable is obtained from placing the position and orientation of the end-effector and the location of the connection points in the robot geometry. According to the position and direction of the robot in the workspace, a positive and unique value will always be obtained for each cable length.

6.4 Kinematics of rotary operators

Rotary actuators are used as actuators to transfer kinetic energy to the end-effector. The pulleys connected to the rotary actuators are responsible for adjusting the length of the cables. Therefore, the change of the angle of the actuators is directly proportional to the change of the length of the cables, as per the equation below:

$$\theta_i = \frac{\Delta l_i}{r_w}, \qquad i = 1,2,3 \tag{41}$$

where r_w is the pulley radius; and θ_i is the rotary actuator angle (pulley angle).

As derived from the equation above, the relationship between the angular velocity of the actuators and the rate of change of length of the cables can be obtained as follows:

$$\dot{\theta}_i = \frac{\dot{l}_i}{r_w}, \qquad i = 1,2,3 \tag{42}$$

6.5 Control

To control cable-driven robots effectively, one needs to consider several key aspects [155], [156], [157].

Kinematics: Understanding the kinematics of the robot is crucial to control. Cable-driven robots typically have a complex kinematic structure due to the presence of multiple cables and their attachment points. The kinematics equations describe the relationship between the actuator inputs and the resulting position and orientation of the end effector.

Actuation: Cable-driven robots use actuators, such as motors or winches, to control the tension in cables and achieve desired movements. The control system needs to manage these actuators effectively to control the robot's motion. Depending on the specific robot design, the control system may control the actuators individually or in groups to achieve the desired cable tensions.

- Trajectory Planning: Planning the desired trajectory of the robot is essential to executing tasks accurately. Trajectory planning involves determining the desired position, orientation, and velocity of the end-effector over time. This can be achieved using various techniques, such as inverse kinematics or optimization algorithms, to find a suitable set of actuator inputs that achieve the desired trajectory.
- Force Sensing: Cable-driven robots can exert forces and interact with the environment. To enable precise control and safe interaction, force sensing is often necessary. Force sensors at the robot's end effector or along the cables can provide feedback on the forces exerted during operation. This information can be used for force control or impedance control to ensure appropriate interaction with the environment.
- Control Algorithms: Various control algorithms can be employed to control cable-driven robots depending on the application requirements. These algorithms can include PID (Proportional-Integral-Derivative) control, model-based control, adaptive control, or more advanced techniques such as optimal control, or learning-based control. The choice of control algorithm depends on the specific requirements of the robot and the desired control performance.
- Safety Considerations: Cable-driven robots operate with tensioned cables, which can pose safety risks if not properly controlled. Implementing safety measures, such as limit switches, emergency stop buttons, or torque sensors, can help ensure safe operation. Additionally, appropriate software and hardware interlocks can be put in place to prevent the robot from entering unsafe states.

- Calibration and Maintenance: Regular calibration and maintenance are important to ensure accurate control and reliable operation of cable-driven robots. Cable tensions, cable lengths, and other mechanical parameters may change over time due to wear and tear or environmental factors. Periodic calibration and maintenance procedures should be followed to keep the robot in optimal working condition.

Overall, controlling cable-driven robots requires a combination of an understanding of kinematics, actuator control, trajectory planning, force sensing, appropriate control algorithms, safety considerations, and maintenance procedures. By effectively managing these aspects, can achieve precise and safe control of cable-driven robots in various applications.

6.6 PID Controller

Proportional-integral-derivative (PID) control is certainly the most widely used of today's control strategies. It is estimated that over 90% of control loops employ PID control, quite often with the derivative gain set to zero (PI control). Over the last half-century, a great deal of academic and industrial effort has focused on improving PID control, primarily in the areas of tuning rules, identification schemes, and adaptation techniques. It is appropriate at this time to consider the state of the art in PID control as well as new developments in this control approach. The three terms of a PID controller fulfil the three common requirements of the majority of control problems. The integral term yields zero steady-state error in tracking a constant setpoint, a result commonly explained in terms of the internal model principle and demonstrated using the final value theorem. Integral control also enables the complete rejection of constant disturbances. While integral control filters higher frequency sensor noise, it is slow in response to the current error. On the other hand, the proportional term responds immediately to the current error yet typically cannot achieve the desired setpoint accuracy without an unacceptably large gain. For plants with significant dead time, the effects of previous control actions are poorly represented in the current error. Such a situation may lead to large transient errors when PI control is used. Derivative action combats this problem by basing a portion of the control on a prediction of future error. Unfortunately, the derivative term amplifies higher frequency sensor noise; thus, filtering of the differentiated signal is typically employed, introducing an additional tuning parameter. A PID controller (Figure 6-7) with a derivative filter is often referred to as a PIDF controller. While the three PID terms are sufficient to parameterize a structure that permits successful control of many plants, the number of terms is small enough to allow manual tuning by an operator. Furthermore, the small number of terms lends itself to both direct adaptive control and self-tuning through heuristics [158].

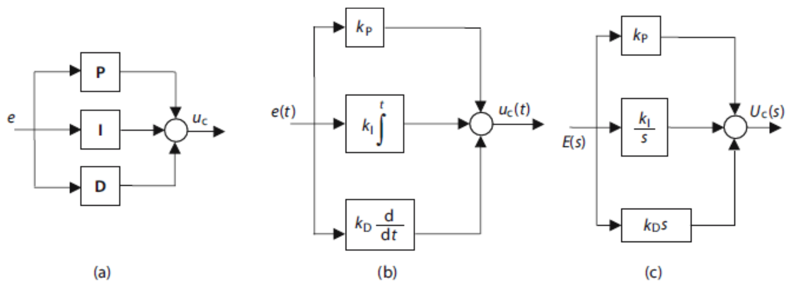

Key	**Controller input (system error)**	***e***	**PID control signal**	u_c	
Symbolic forms	e, u_c	Time domain forms	$e(t)$, $u_c(t)$	Laplace domain forms	$E(s)$, $U_c(s)$
Proportional gain	k_P	Integral gain	k_I	Derivative gain	k_D

Figure 6-7: PID controller representations [159].

6.7 Geometric Specification of CDSE

In the Table 6-1, the geometric characteristics of the cable robot are presented, which includes the mass of the moving parts, the position of the cable tension points on the moving platform relative to the moving coordinate device, and the position of the cable tension points on the fixed platform relative to the fixed coordinate device.

Table 6-1: Geometric specification of CDSE.

Symbol	Definition	Quantity	Unite
$\boldsymbol{m_1}$	Mass of the upper arm	4.86	kg
$\boldsymbol{m_2}$	Mass of the elbow to wrist	2.71	
$\boldsymbol{m_3}$	Mass from the wrist to the fingertips	1.26	
$\boldsymbol{A_1}$ ⋮ $\boldsymbol{A_3}$	The position of the cable's traction points on the moving platform relative to the moving coordinate system	[0, 87.76, 0]	mm
		[-39.83, 65.61, -80.99]	
		[-93.25, 0, -63.56]	
$\boldsymbol{B_1}$ ⋮ $\boldsymbol{B_3}$	The position of the traction points of the cables on the fixed platform relative to the fixed coordinate system	[-6.98, 8, -23.4]	mm
		[-11.44, 8, -54.60]	
		[-28.89, -183.07, -150.06]	

6.8 Arm Movement Simulation

In this section, different scenarios for the arm are presented as the desired path, in which the arm travels a certain path from an initial position to its final position. In order for the robot to follow the desired path, the length of the robot cables must be changed according to the path so that the arm can be in the desired position. To this end, the desired path is divided into finite points with short distances, and the corresponding length of the robot cables for each point on the path is determined by the inverse kinematics model obtained in the previous section. All the mentioned calculations were performed in the MATLAB software.

The desired path for the arm can be defined in two ways: position and orientation of the arm. Position definition is usually desirable in robots that are designed to perform a specific task in their final actuator. In the case of rehabilitation robots, it is desirable to define the arm's orientation or, in fact, the rotation of the arm. Therefore, the desired path is defined as the rotation angles of the arm, which are applied in the arm coordinate system. The CDSE design for MND patient which their muscles do not working and obviously they have not any stiffness. Based on this, the following scenarios are considered for the arm rotation:

6.8.1 Scenario 1

In this scenario, the arm travels from an initial position of $\alpha = 0$, $\beta = 0$, $\gamma = 0$ (which is the arm's natural position) to a final position of $\alpha = 0$, $\beta = 0$, $\gamma = 90$. In fact, this is an abduction movement that is performed in the rotation sequence "XYZ''. In order for the robot to travel this route, the length of the cables changes as follows:

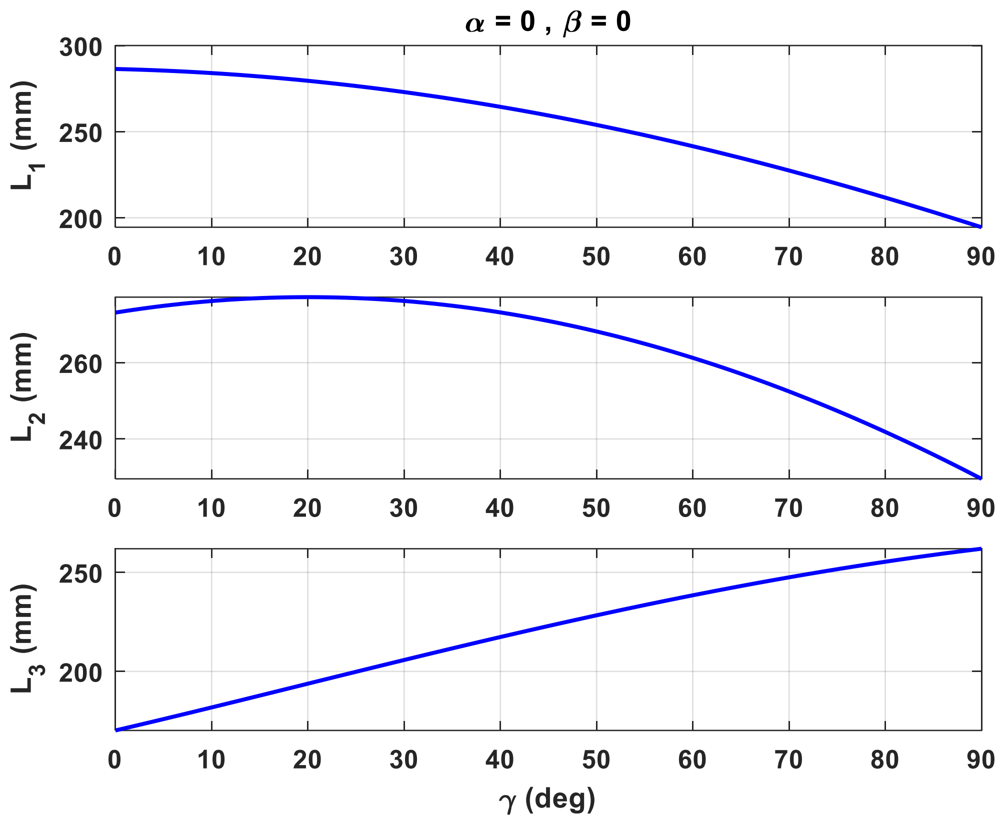

Figure 6-8: Changes in the length of the cables based on the path taken by the arm in scenario 1.

6.8.2 Scenario 2

In this scenario, the arm travels from an initial position of $\alpha = 15$, $\beta = 0$, $\gamma = 0$ to a final position of $\alpha = 15$, $\beta = 0$, $\gamma = 90$. Practically, for this path, the arm is initially in a flexion position of 15 degrees and then rotates 90 degrees around the Z axis in the arm coordinate system, which is performed in the rotation sequence “XYZ’’. In order for the robot to travel this path, the length of the cables changes as follows:

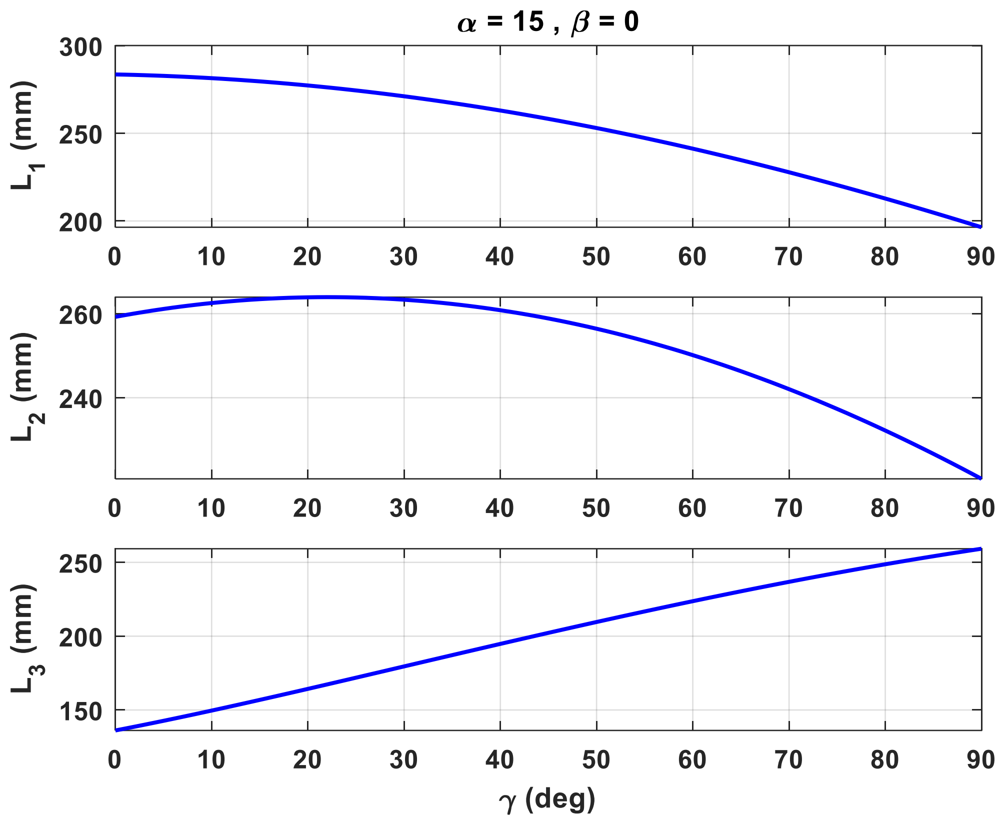

Figure 6-9: Changes in the length of the cables based on taken by the path of the arm in scenario 2.

6.8.3 Scenario 3

In this scenario, the arm travels from an initial position of $\alpha = 30$, $\beta = 0$, $\gamma = 0$ to a final position of $\alpha = 30$, $\beta = 0$, $\gamma = 90$. Practically, for this path, the arm is initially in a flexion position of 30 degrees and then rotates 90 degrees around the Z axis in the arm coordinate system which is performed in the rotation sequence "XYZ''. In order for the robot to travel this path, the length of the cables changes as follows:

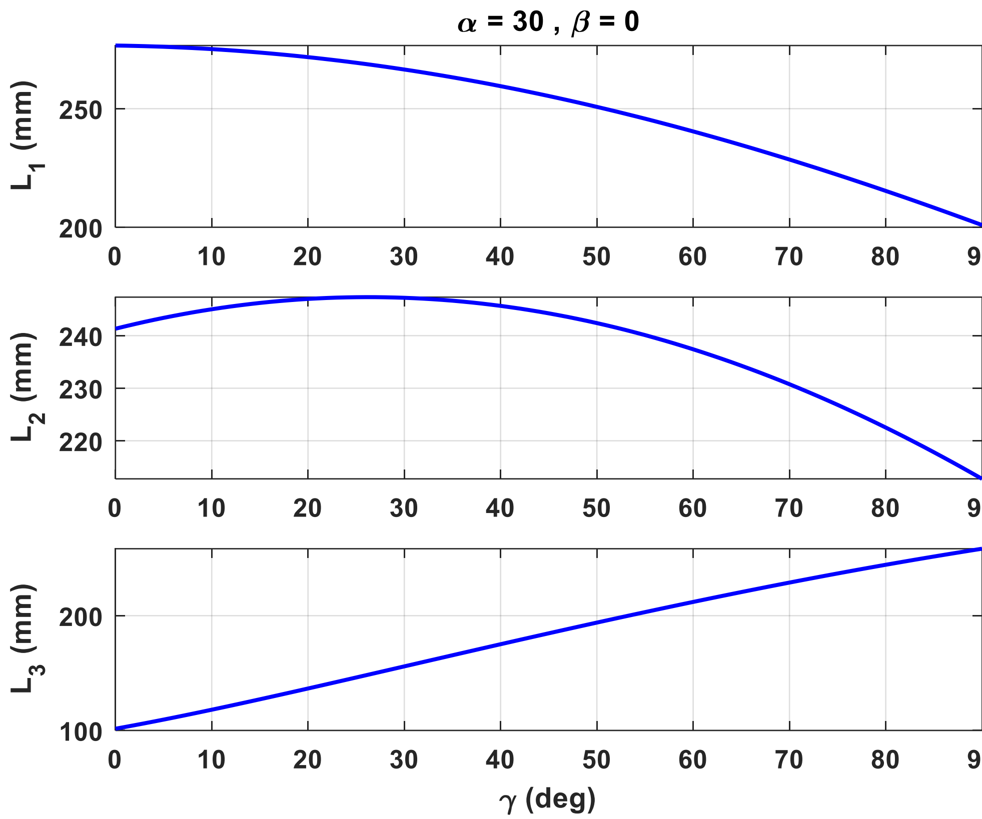

Figure 6-10: Changes in the lengths of the cables based taken by the path of the arm in scenario 3.

6.8.4 Scenario 4

In this scenario, the arm travels from an initial position of $\alpha = 60$, $\beta = 0$, $\gamma = 0$ to a final position of $\alpha = 60$, $\beta = 0$, $\gamma = 90$. Practically, for this path, the arm is initially in a flexion position of 60 degrees and then rotates 90 degrees around the Z axis in the arm coordinate system, which is performed in the rotation sequence "XYZ''. In order for the robot to travel this path, the length of the cables changes as follows:

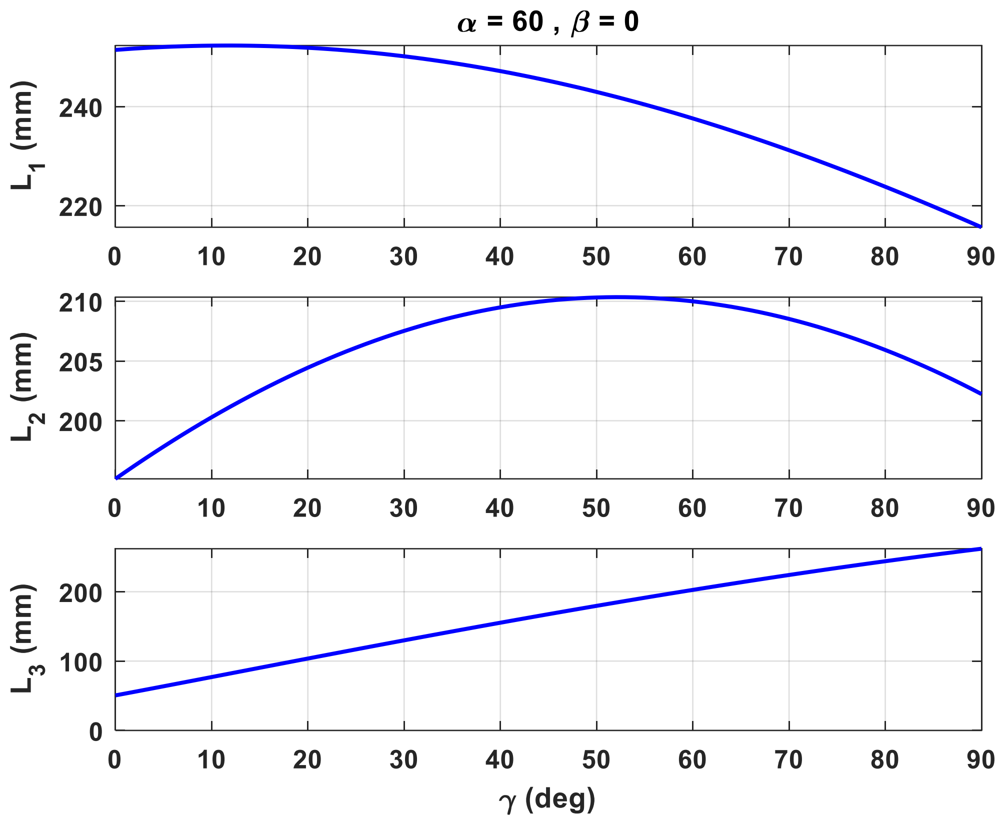

Figure 6-11: Changes in the length of the cables based on the path taken by the arm in scenario 4.

6.8.5 Scenario 5

In this scenario, the arm travels from an initial position of $\alpha = 90$, $\beta = 0$, $\gamma = 0$ to a final position of $\alpha = 90$, $\beta = 0$, $\gamma = 90$. Practically, for this path, the arm is initially in a full flexion position and then rotates 90 degrees around the Z axis in the arm coordinate system, which is performed in the rotation sequence "XYZ''. In order for the robot to travel this path, the length of the cables changes as follows:

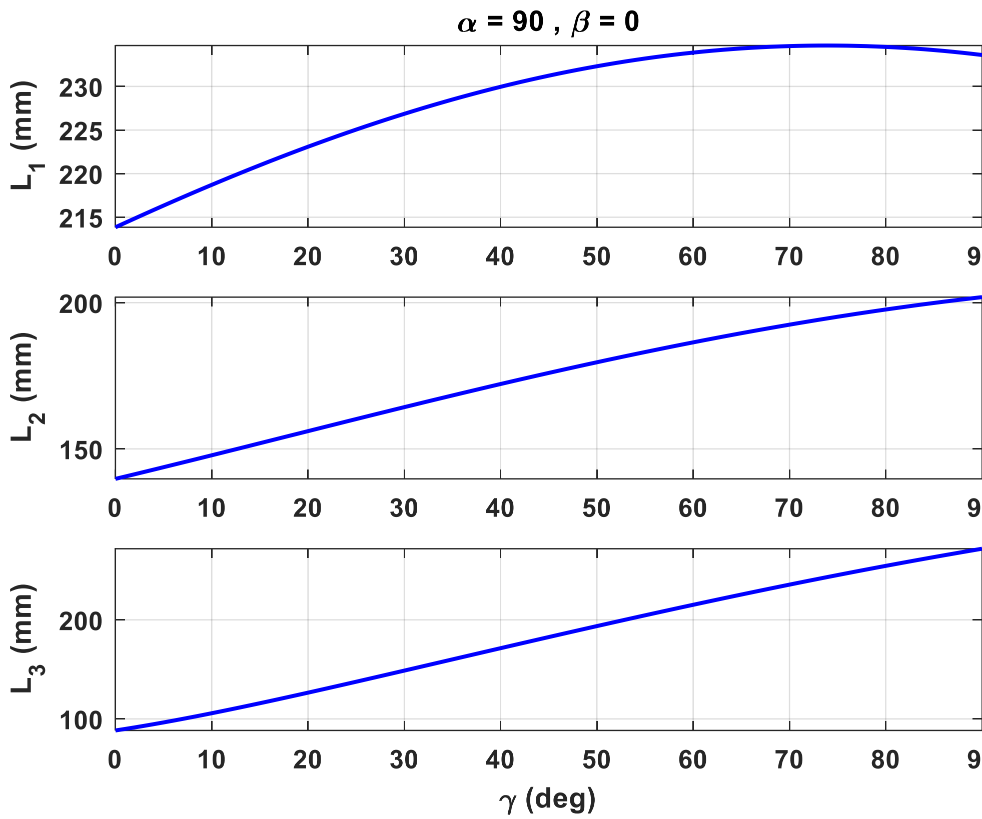

Figure 6-12: Changes in the length of the cables based on the path taken by the arm in scenario 5.

6.8.6 Scenario 6

In this scenario, the arm travels from an initial position of $\alpha = 0$, $\beta = 0$, $\gamma = 0$ (which is the arm's natural position) to a final position of $\alpha = 90$, $\beta = 0$, $\gamma = 0$. Practically, for this path, the arm is initially in its natural position and then rotates 90 degrees about the X axis in the arm coordinate system, which is performed in the rotation sequence "ZYX'', referred to as a flexion movement. In order for the robot to travel this path, the length of the cables changes as follows:

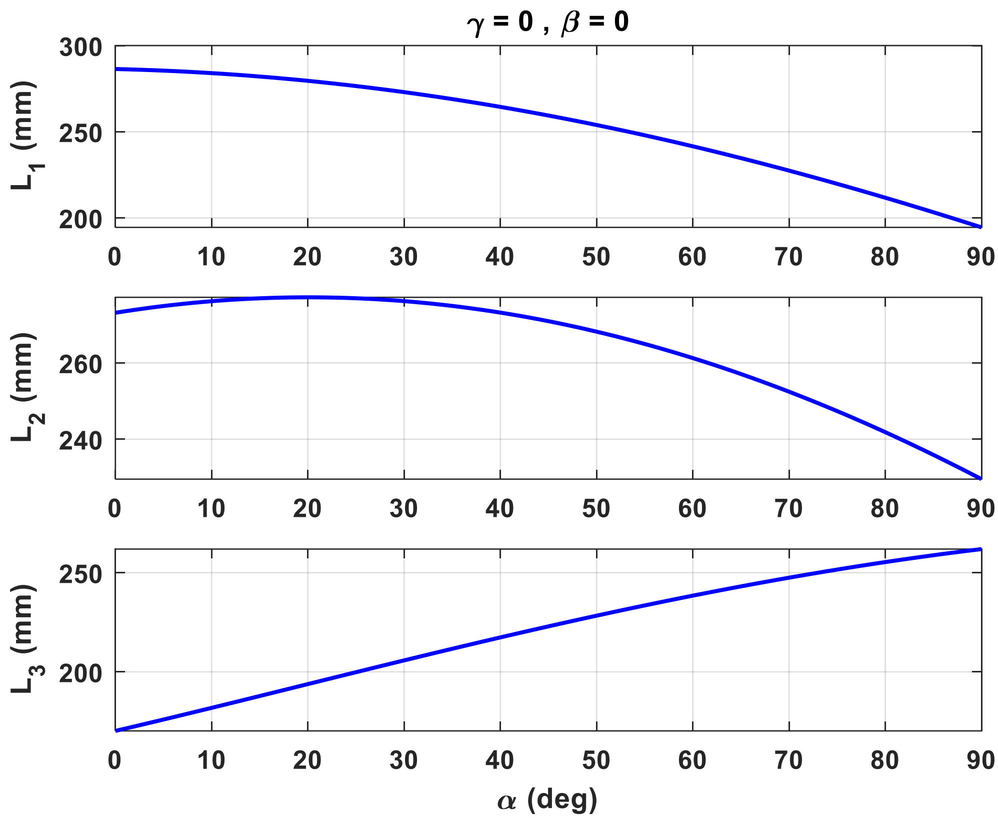

Figure 6-13: Changes in the length of the cables based on the path taken by the arm in scenario 6.

6.8.7 Scenario 7

In this scenario, the arm travels from an initial position of $\alpha = 0$, $\beta = 0$, $\gamma = 15$ to a final position of $\alpha = 90$, $\beta = 0$, $\gamma = 15$. Practically, for this path, the arm is initially in an abduction position of 15 degrees and then rotates 90 degrees about the X axis in the arm coordinate system, which is performed in the rotation sequence “ZYX’’. In order for the robot to travel this path, the length of the cables changes as follows:

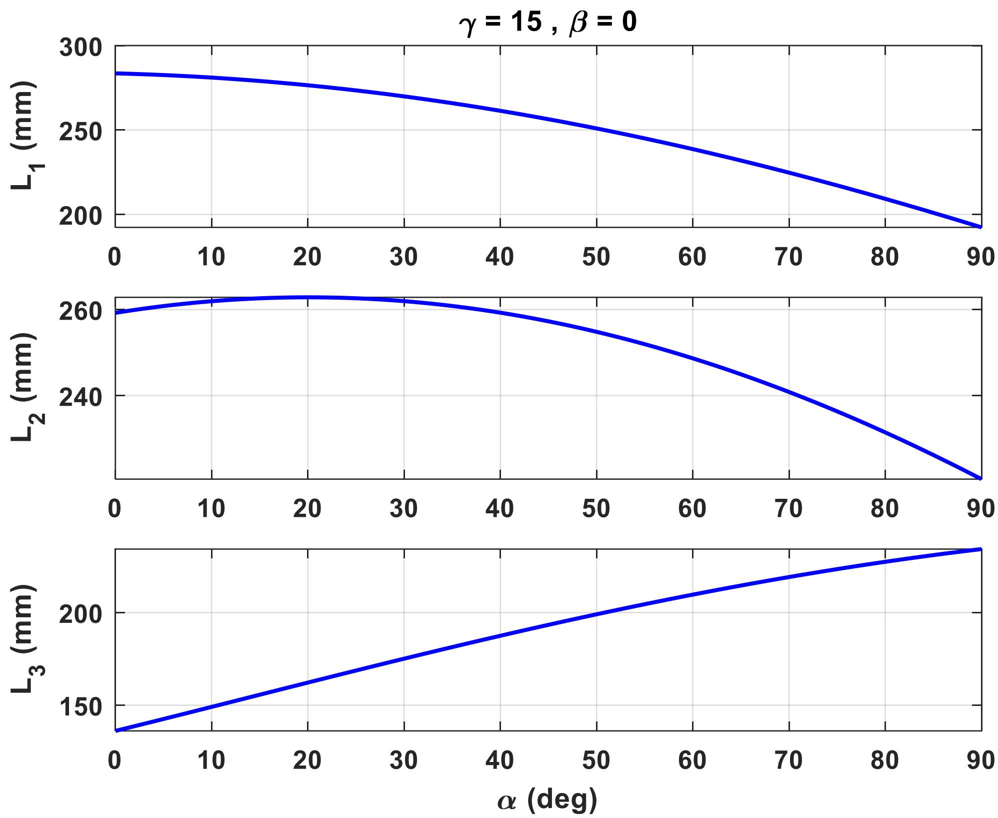

Figure 6-14: Changes in the length of the cables based on the path taken by the arm in scenario 7.

6.8.8 Scenario 8

In this scenario, the arm travels from an initial position of $\alpha = 0$, $\beta = 0$, $\gamma = 30$ to a final position of $\alpha = 90$, $\beta = 0$, $\gamma = 30$. Practically, for this path, the arm is initially in an abduction position of 15 degrees and then rotates 90 degrees about the X axis in the arm coordinate system, which is performed in the rotation sequence “ZYX’’. In order for the robot to travel this path, the length of the cables changes as follows:

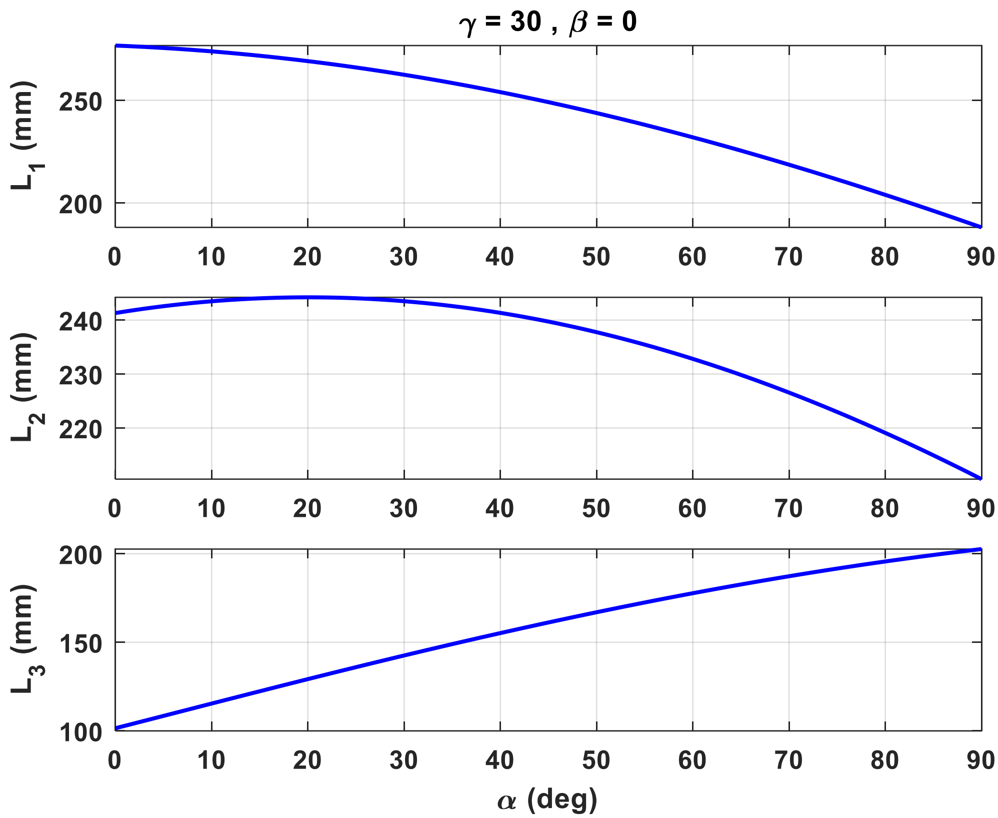

Figure 6-15: Changes in the length of the cables based on the path taken by the arm in scenario 8

6.8.9 Scenario 9

In this scenario, the arm travels from an initial position of $\alpha = 0$, $\beta = 0$, $\gamma = 60$ to a final position of $\alpha = 90$, $\beta = 0$, $\gamma = 60$. Practically, for this path, the arm is initially in an abduction position of 15 degrees and then rotates 90 degrees about the X axis in the arm coordinate system, which is performed in the rotation sequence "ZYX''. In order for the robot to travel this path, the length of the cables changes as follows:

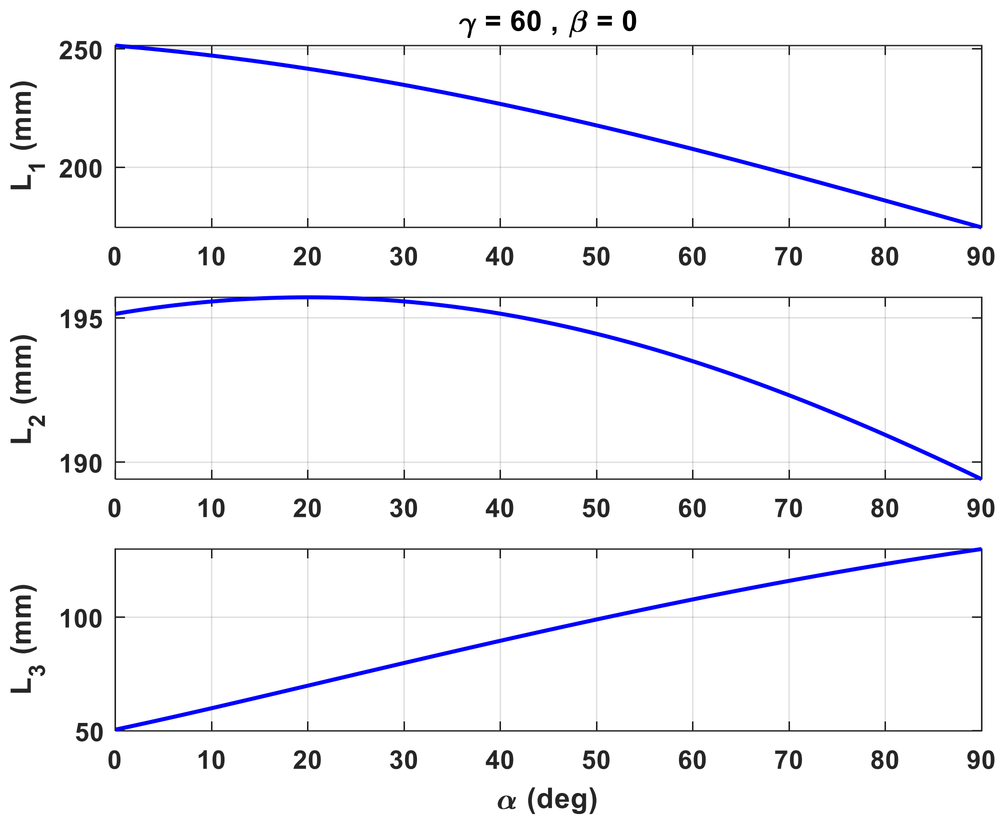

Figure 6-16: Changes in the length of the cables based on the path taken by the arm in scenario 9

6.8.10 Scenario 10

In this scenario, the arm travels from an initial position of $\alpha = 0$, $\beta = 0$, $\gamma = 90$ to a final position of $\alpha = 90$, $\beta = 0$, $\gamma = 90$. Practically, in this path, the arm is initially in full abduction position and then rotates 90 degrees about the X axis in the arm coordinate system, which is performed in the rotation sequence “ZYX’’. In order for the robot to travel this path, the length of the cables changes as follows:

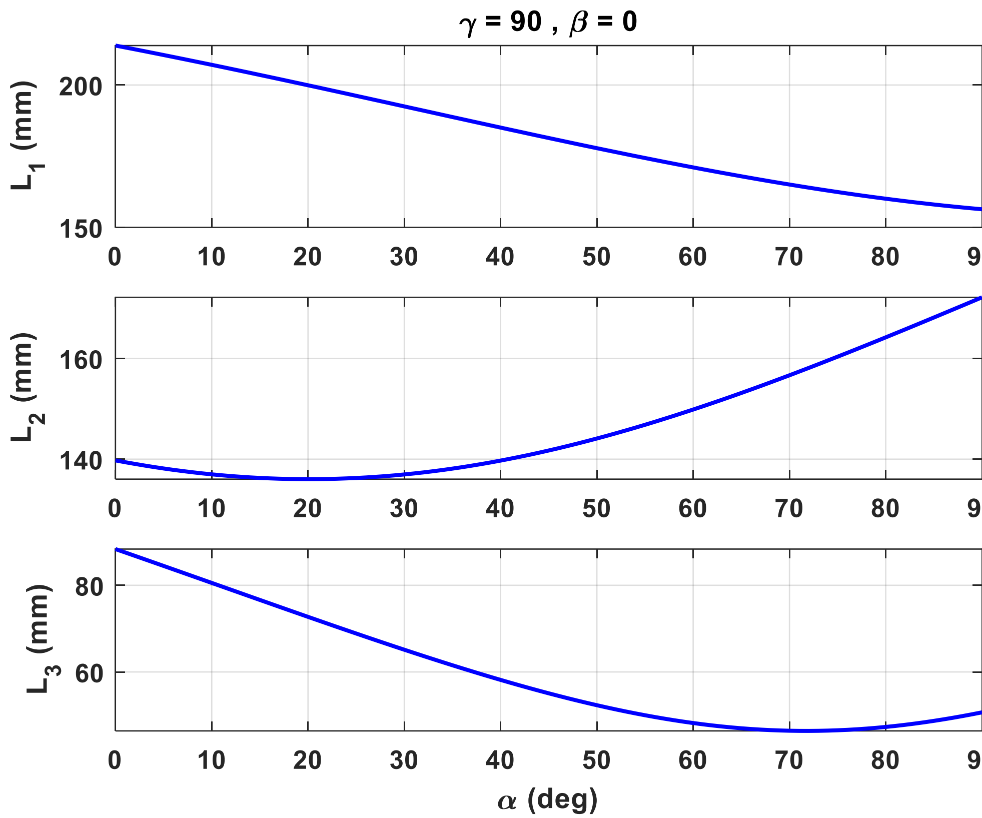

Figure 6-17: Changes in the length of the cables based on the path taken by the arm in scenario 10

6.9 Three main DOFs of Arm Movement

6.9.1 Shoulder Abduction

In this scenario, the arm travels from an initial position of $\gamma = 0$, $\beta = 0$, $\alpha = 0$ (which is the arm's natural position) to a final position of $\gamma = 90$, $\beta = 0$, $\alpha = 0$. In fact, this is a shoulder abduction movement, which is performed in the rotation sequence "ZXY". In order for the robot to travel this path, the length of the cables changes according to Eq.(40), as illustrated in Figure 6-18(top left).

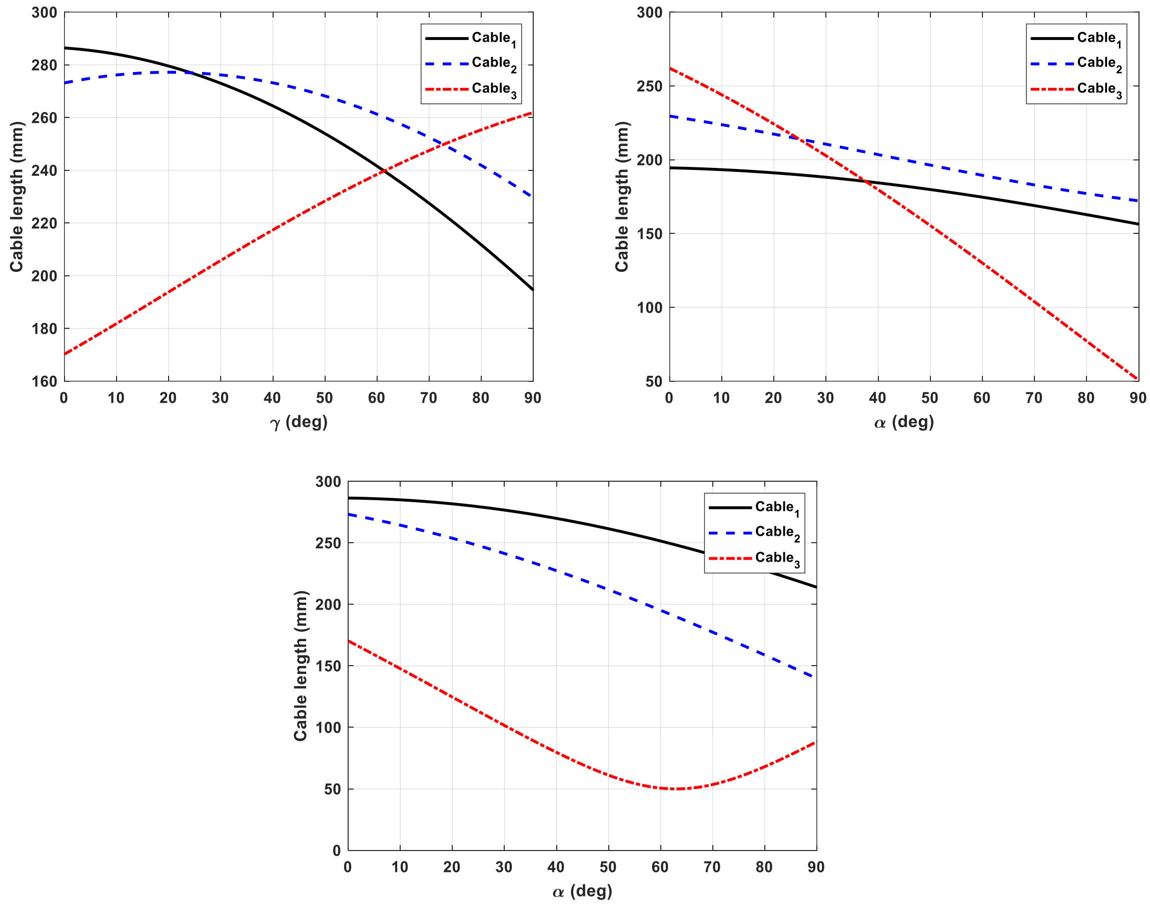

Figure 6-18: CDSE's cables length variation. (top Left) Shoulder abduction motion. (top Right) Shoulder horizontal flexion, (bottom) Shoulder flexion motion.

6.9.2 Shoulder Horizontal Flexion

In this scenario, the arm travels from an initial position of $\gamma = 90$, $\beta = 0$, $\alpha = 0$ to a final position of $\gamma = 90$, $\beta = 0$, $\alpha = 90$. Practically, for this path, the arm is initially in a full abduction position and then rotates 90 degrees around the X axis in the arm coordinate system, which is performed in the rotation sequence "ZYX". In order for the robot to travel this path, the length of the cables changes as shown in Figure 6-18 (top right).

6.9.3 Shoulder Flexion

In this scenario, the arm travels its way from the initial position of $\alpha = 0$, $\beta = 0$, $\gamma = 0$ (which is the arm natural position) to a position of $\alpha = 90$, $\beta = 0$, $\gamma = 0$. Practically, for this path, the arm is initially in its natural position and then rotates 90 degrees about the X axis in the arm coordinate system, which is performed in the rotation sequence “XYZ’’, in which is called a shoulder flexion movement. In order for the robot to travel this path, the length of the cables changes as shown in Figure 6-18 (bottom).

6.9.4 Simulation and Control

In this section, the robot designed in the Simscape-Multibody environment is created. To this end, it was designed in the SolidWorks software and then imported into the MATLAB Simscape-Multibody environment [160]. Cables, as well as actuators, spools and pulleys, are defined in Figure 6-19. The specifications of the designed robot are also listed in Figure 6-19.

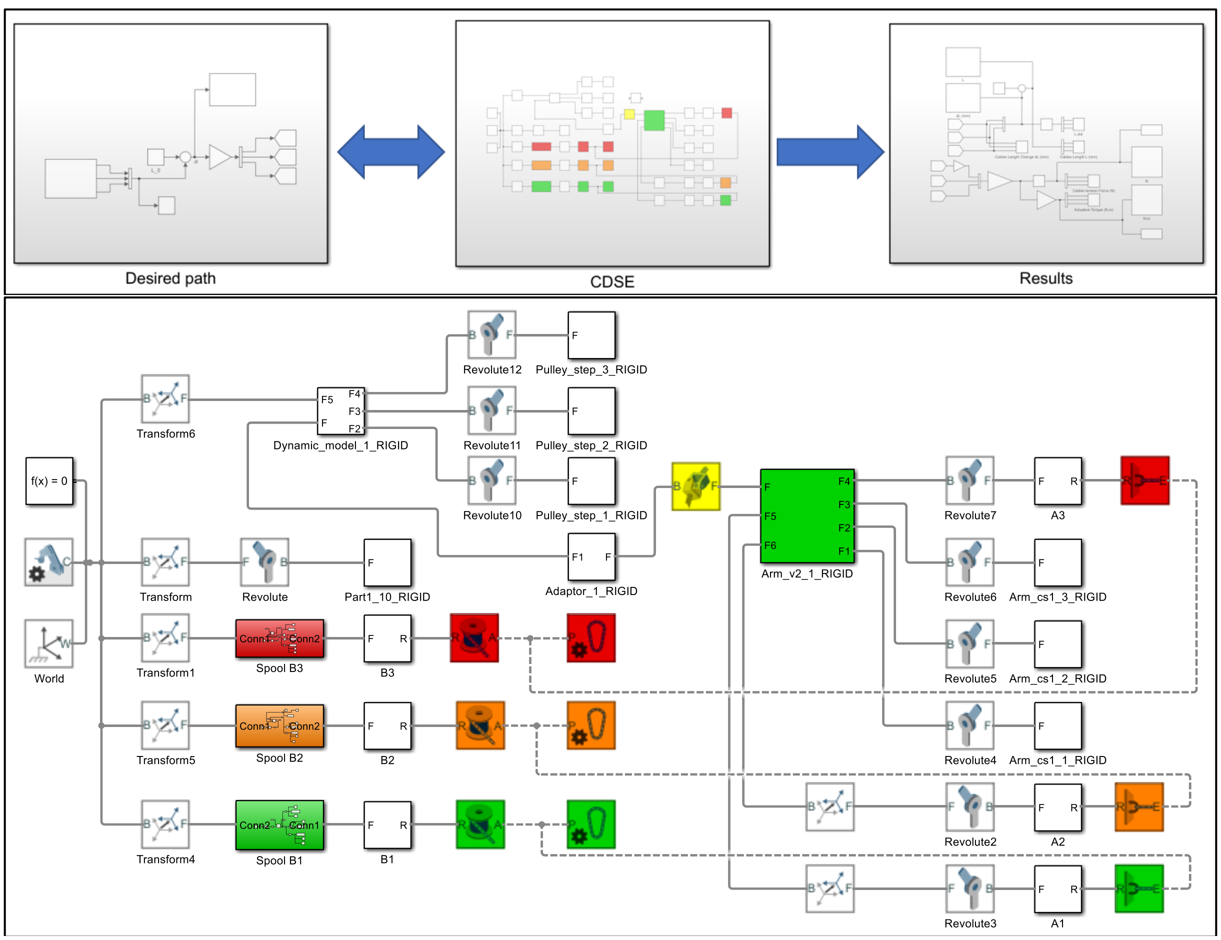

Figure 6-19: Block diagram of simulation of CDSE in MATLAB Simscape-Multibody (top) main view, (bottom) CDSE block in detail.

As can be seen in Figure 6-19 (top), the desired path obtained through the inverse kinematics of the robot is given to the robot as the command path. In fact, the output of the first block is the length of the cables corresponding to the desired path, which is calculated via inverse kinematics as described in the previous section.

In the next step, according to the simulation of the robot dynamics, the robot actuators are controlled to achieve the length of the cable corresponding to the given command, and by maintaining the length of the cables at every moment, the hand is located in the desired location and travels the desired path with the passage of time. Finally, due to the fact that the dynamics of the robot have been fully simulated, the torque and position of each operator can be seen as the output of the dynamics block (CDSE) in the results block using the sensors in the Simscape Multi-body environment.

6.9.5 Simulation Results

In order to evaluate the performance of the designed robot, the tasks discussed in the previous sections were given as commands to the robot. The working method is that the length of the cables obtained in the motion scenarios through inverse kinematics is given as a command to the system operators and the movement of the arm analysed on the designed test bench. The results show the robot operated as expected (Figure 6-20).

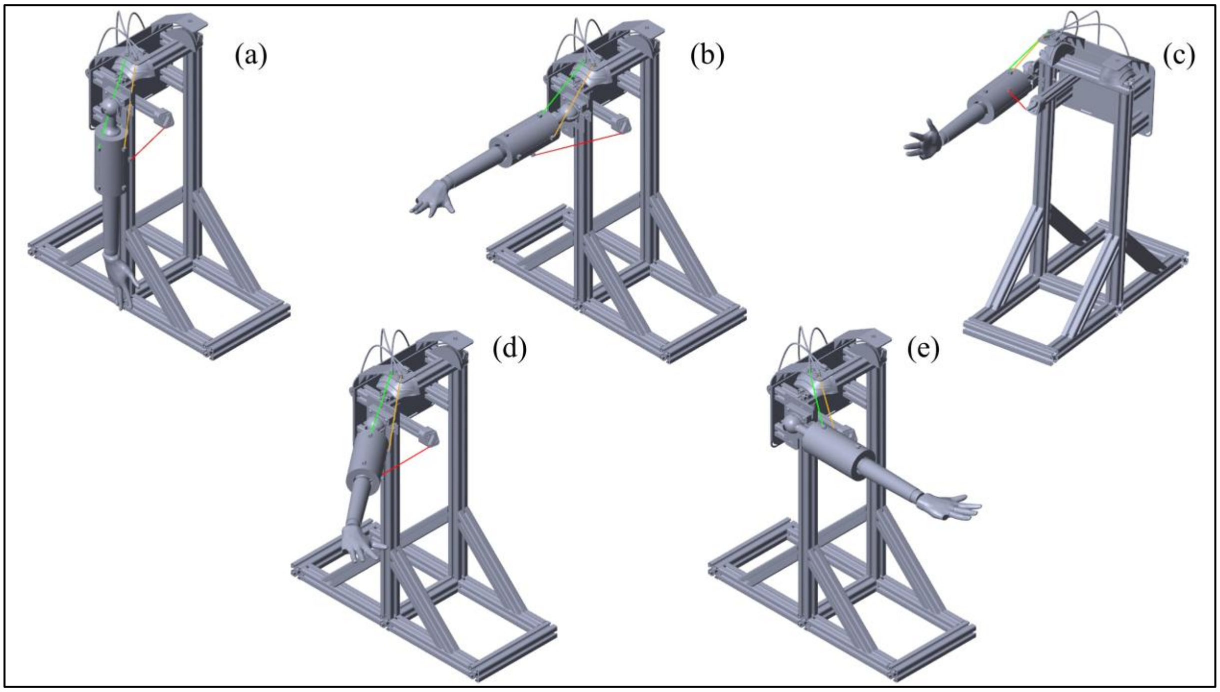

Figure 6-20: Simulation of CDSE in MATLAB Simscape-Multibody. (a) Normal Position. (b) Shoulder abduction. (c) Shoulder flexion. (d)&(e) Shoulder horizontal flexion.

Figure 6-20 illustrated the process of controlling the position of the robot via the proportional-derivative-integrator (PID) controller. First, the command path given in the inverse kinematics block is converted into the length of the corresponding cables in the robot. Then, the required length of the cables is compared with their current length, as calculated from the sensor feedback of the robot motors. The error obtained is entered into the PID controller block, and the corresponding torque is sent as an instruction to the motors to compensate for the error. During control, pre tensioning of all the wires also be considered, where each wire clearly has a different tension force depending on the posture of the shoulder in order to maintain equilibrium.

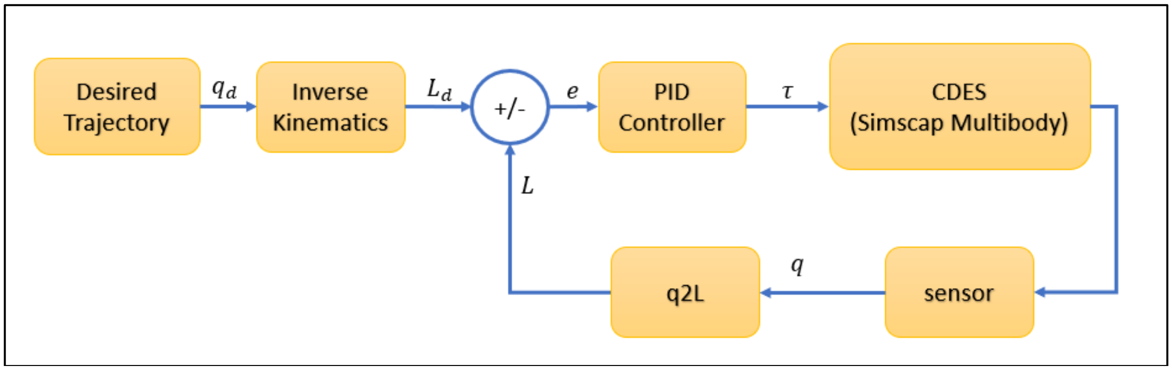

Figure 6-21: Position control process of the CDSE by the PID controller.

Figure 6-22 shows the required torques of the actuators during the abduction movement and the tension force in the cables during the movement. As can be seen, in the shoulder abduction movement, the main force is provided by actuator 1 (cable 1), which is supported by actuator 2 (cable 2). During this movement, actuator 3 collects cable 3 with a small and constant torque. Due to the distribution of load where cables 1 and 2 predominantly support the arm's weight across various motions, cable 3 is subjected to minimal stress and friction at point B3.

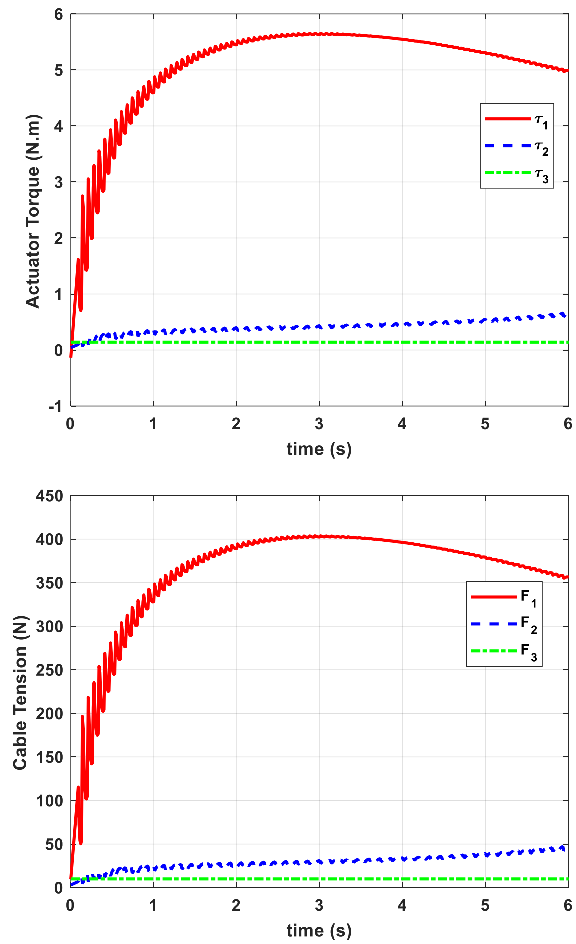

Figure 6-22: Shoulder abduction actuators' torque and cable tension forces.

In Figure 6-22, τ_1, τ_2 and τ_3 are the torques of actuators 1 to 3, respectively, whilst F_1 , F_2, and F_3 are the tensions of cables 1 to 3, respectively. The torque and force profiles during the shoulder abduction movement reveal salient trends that inform the actuator control and system design in soft robotic exosuits. In the torque graph, actuator 1 (τ_1) exhibits a non-linear increase, reaching a peak torque requirement of approximately 5.65 Nm at 2.94 seconds. Actuator 2 (τ_2) also shows a non-linear but much smaller range of torque requirements, up to a maximum of 0.67 Nm. Actuator 3 (τ_3) maintains a near constant torque of about 0.14 Nm throughout the movement, suggesting a more passive role in this specific action. For the tension forces, the tension in cable 1 (F_1) shows the most significant variation in reaching its peak force of about 404 N at 2.94 seconds. The tension in cable 2 (F_2) also varies, but within a lower range of up to a maximum of 48 N. The tension in cable 3 (F_3) maintains a relatively constant force level of around 10 N, reinforcing the supposition of its role as a stabilizing element during this movement. These variations in peak torque and force requirements underscore the need for actuators capable of wide operational ranges, especially for Actuator 1, which handles the brunt of the work in abduction movements.

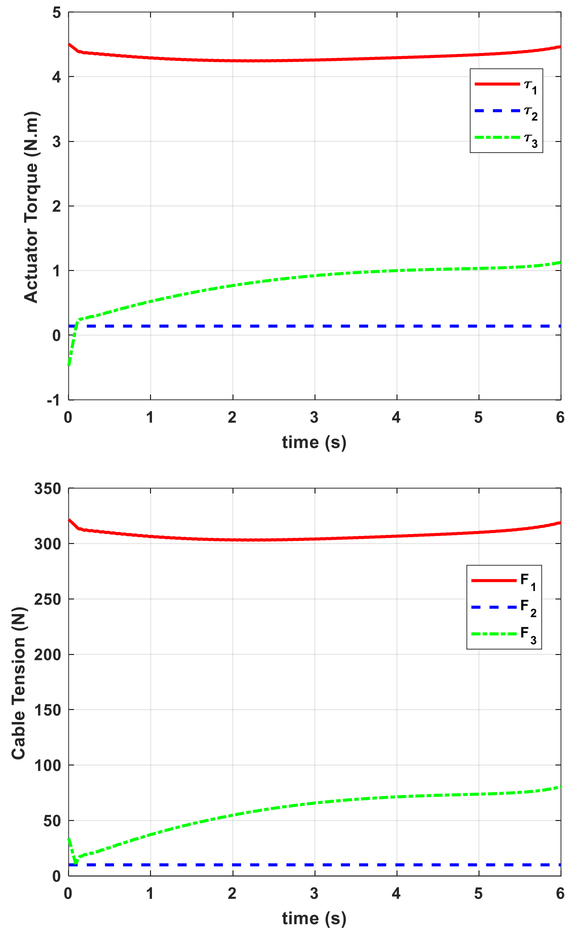

Figure 6-23: Shoulder horizontal flexion actuators' torque and cable tension forces.

The torques and tension forces of the cable required for horizontal flexion movement are shown in Figure 6-23. In this movement, the weight of the hand and arm is supported on cable 1, whilst cable 3 is responsible for horizontal movement and actuator 2 collects cable 2 with a constant and small torque. In the shoulder horizontal flexion movement, according to the position of the hand on the right side of the person (abduction position), cable 1 bears the most force and is supported by cable 2, whilst cable 3 collects with a small and constant torque. The torque and force profiles during the horizontal flexion movement exhibit distinct trends that are instrumental to actuator control in soft robotic exosuits. In terms of torque, actuator 1 (τ_1) shows a slight increase, with a maximum of approximately 4.51 Nm at $t = 0$ s and a minimum of approximately 4.24 Nm. Actuator 2 (τ_2) maintains a constant torque of about 0.14 Nm, reinforcing its role as a stabilizer. Actuator 3 (τ_3) exhibits a maximum of approximately 1.13 Nm. In the context of tension forces, actuator 1 (F_1) bears the primary load, with a maximum force of approximately 321.84 N and a minimum of about 303.13 N. Actuator 2 (F_1) maintains a constant force of about 10 N throughout the movement. Actuator 3 (F_3), responsible for horizontal movement, varies up to a maximum of about 80.48 N. These extrema in torques and forces highlight the need for actuators with varying capabilities: actuator 1 must be robust and capable of high force and torque outputs, actuator 3 needs to be adaptable, and actuator 2 must maintain stability with consistent, low-level outputs.

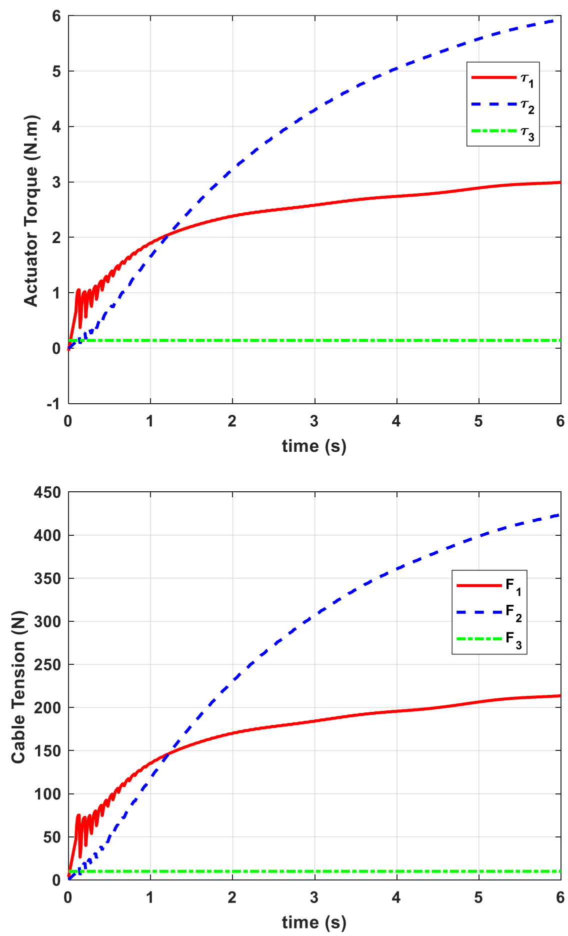

Figure 6-24: Shoulder flexion actuators' torque and cable tension forces.

The torque and force profiles for the shoulder flexion movement in Figure 6-24 show distinct trends that are crucial to actuator specifications and control algorithms in soft robotic exosuits. In terms of torque, actuator 2 (τ_2) assumes a significant role, reaching a maximum of about

5.94 Nm at $t = 6$ s. Actuator 1 (τ_1) also displays an increasing trend, to a maximum of 3.00 Nm. Actuator 3 (τ_3) maintains a nearly constant torque, confirming its role as a stabilizer in this instance. In the context of tension forces, actuator 2 (F_2) bears the primary load, peaking at approximately 424 N at $t = 6$ s. Actuator 1 (F_1) supports this with forces of up to a maximum of 213.71 N. Actuator 3 (F_3) maintains a fairly constant level of force. These extrema and trends are instrumental to actuator selection and control algorithm optimization: Actuator 2 needs to be highly robust, actuator 1 needs moderate capabilities, and actuator 3 should be designed for consistent, low-force operations.

6.10 Conclusion

Due to the low inherent speed of the system (assistance), static analysis was the priority. Accordingly, the static state of the system was modelled first and validated with MATLAB software. To obtain information about the system's dynamics, the SolidWorks model was imported into the Simscape Multibody in MATLAB, and we examined the torque and position over time in different scenarios. Since our controller was not a model-based controller (PID), a dynamic analytical model of the system was not required, but in future work, a dynamic analytical model of the system can be obtained using model-based controllers such as sliding mode control.

It can be concluded that the study of inverse kinematics and control in cable-driven exoskeletal systems (CDSE) significantly enhances upper limb rehabilitation through soft robotics. It showcases the importance of the precise control and manoeuvrability facilitated by inverse kinematics, as underscored by the effectiveness of PID controllers and detailed simulations. The findings illustrate the potential for CDSE to support complex rehabilitative movements, offering insights for future advancements in soft robotics aimed at improving therapeutic outcomes. This chapter sets a foundation for further research, emphasizing the intersection of technology and healthcare in rehabilitating upper limb impairments, promising improved quality of life through innovative robotic solutions.

7 Chapter Seven: Experiment, Analysis and Discussion of CDSE

7.1 Introduction

After the design, mechanical analysis, and fabrication of the CDSE, in this chapter we examine its performance in an experiment environmental. The purpose of this chapter is to observe and evaluate the performance of the system according to the inverse kinematics of robot and the extracted paths to perform the three degrees of freedom of the shoulder joint in the experiment environment.

7.2 Experimental Method

The testing methodology involves an initial examination of the repeatability of movements across all three degrees of freedom. Subsequently, the system will undergo evaluation in various operational modes and under different loads pertinent to the intended motion. This phase will include the presentation of data through graphs showcasing the trajectory of movement, torque, position error, velocity, and motor temperature.

7.3 Experimental Design and Setup

The experimental design is tailored to the system's three degrees of freedom. For each degree of freedom, a specific movement is executed six times within the experimental setup to evaluate the system's repeatability (Figure 7-1). The naming convention for the tests consists of three parts: the initial two letters signify the movement type; the following five digits represent the added load in grams affixed to the primary arm; and the final two digits, preceded by an underscore, denote the test iteration number. These iterations correspond to the six stages outlined in Figure 7-2.

The second phase involves incrementally adding weights, ranging from 500 grams to 4000 grams, to each movement; these tests are also repeated to assess performance under varying loads and finally do the tests on a healthy subject. The choice of 4000 grams as the maximum weight stems from the estimation presented in Chapter six, where the average human arm' weight is approximated at 4860 grams. Given the system's own weight of 860 grams, a test load of 4000 grams was selected to approximate the total weight of the human hand in the final experiment.

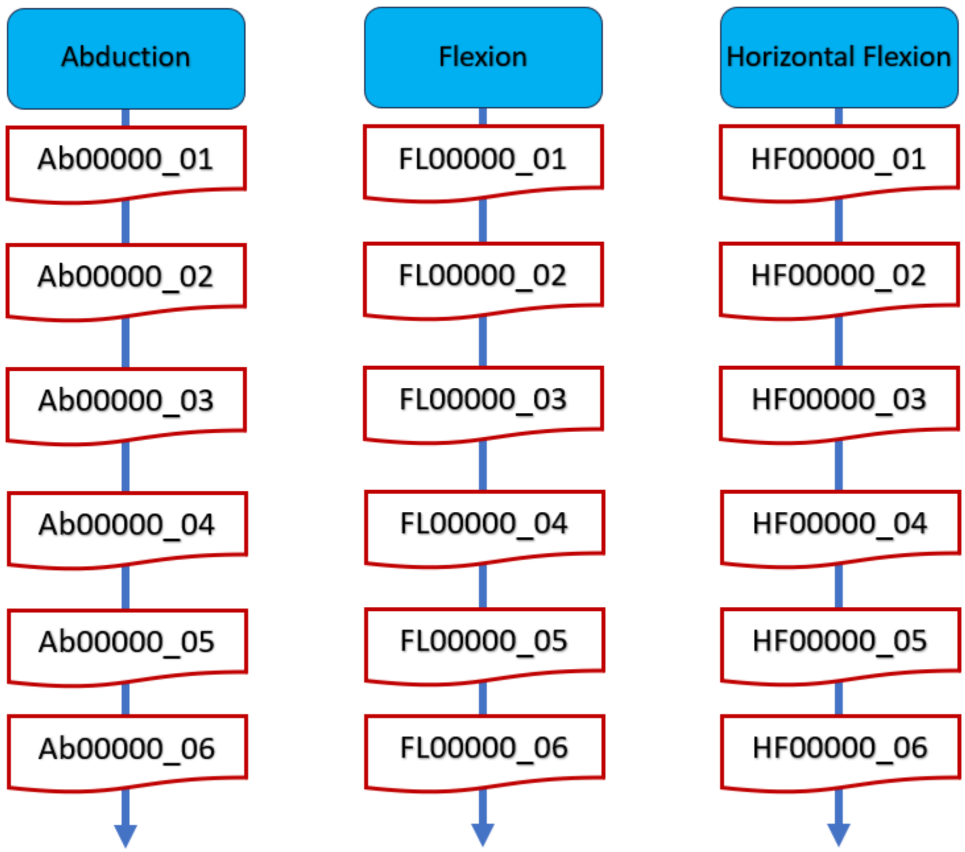

Figure 7-1: Repeatability of the arm movement in three degrees of freedom (abduction, flexion, and horizontal flexion)

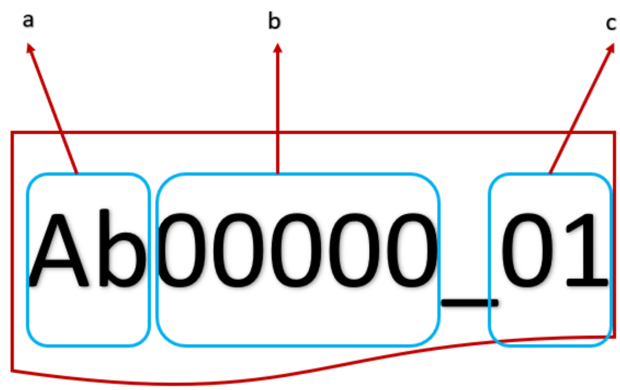

Figure 7-2: (a): Movement type – (b): Added load in grams affixed to the primary arm – (c): Test iteration number.

Figure 7-3 illustrates the sequence and progression of tests, highlighting the gradual increase in weight for each movement, accompanied by the relevant test label. Each movement experiment involves eight distinct increments in weight, with each subsequent test introducing an additional 500 grams. The outcomes are then visualized through graphs depicting the goal trajectory, torque, position error, velocity, and motor temperature for each motor.

Figure 7-3: The sequence and progression of tests, highlighting the gradual increase in weight for each movement (500 g to 4000 g).

7.4 Data Collection Method

Based on simulations conducted within MATLAB's Simscape Multibody environment (Figure 7-4), the movement trajectories for each experiment were established. These trajectories are then input into the designated robot (Figure 7-5), with its movements being monitored on a custom-built test bench. The resulting data, including the goal position (GP), torque, position error, velocity, and motor temperature, are extracted for analysis (Figure 7-6). Figure 7-4 presents a schematic detailing the inputs for the movement paths and the corresponding outputs, all integrated within the Simulink MATLAB software framework.

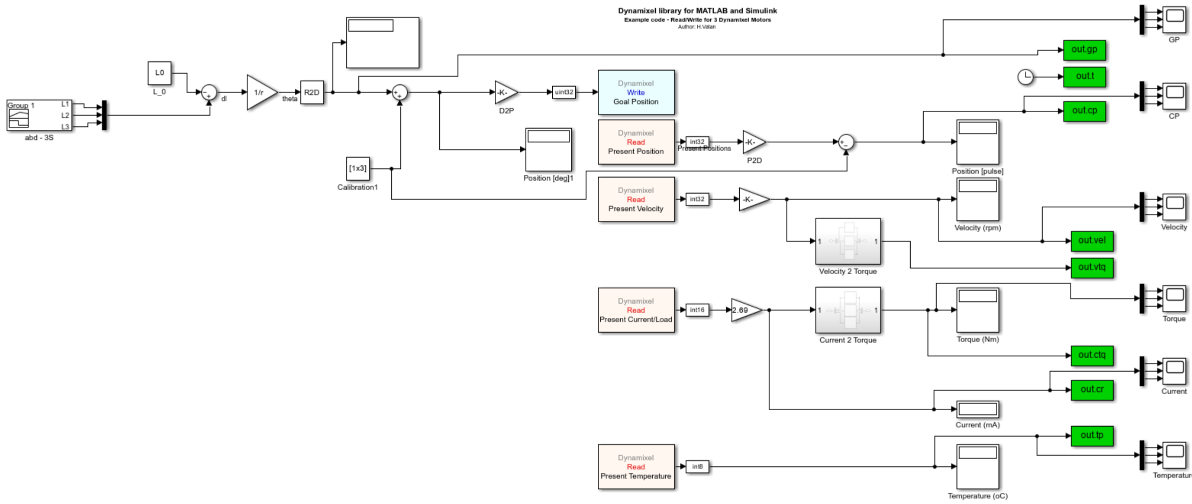

Figure 7-4: MATLAB and Simulink (read/write for three Dynamixel motors).

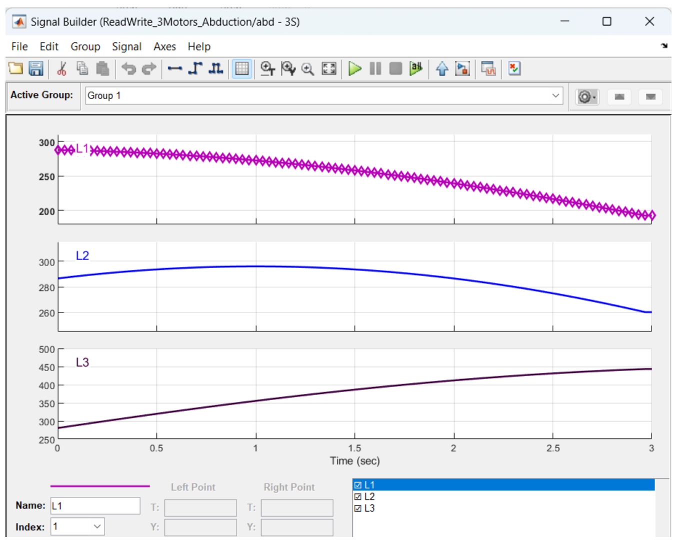

Figure 7-5: Using signal builder for input path trajectory.

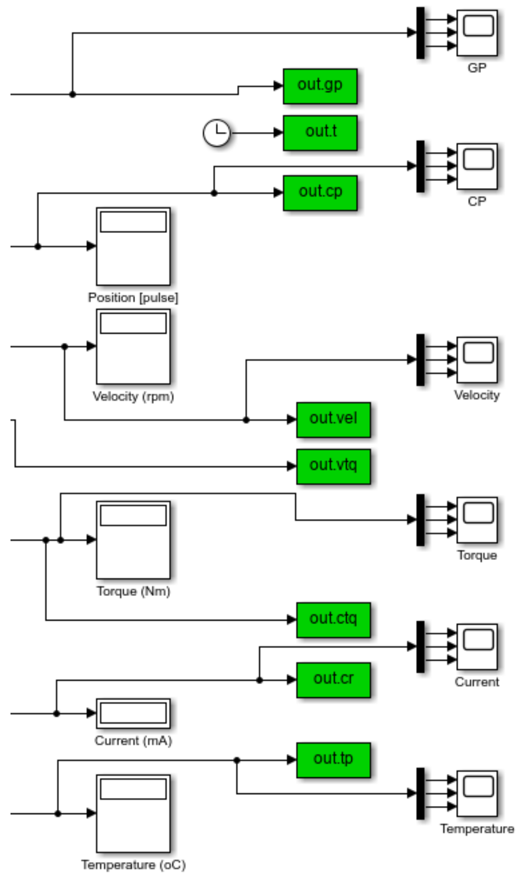

Figure 7-6: Resulting data, including the goal position (GP), torque, current, velocity, and motor temperature are extracted for analysis.

Data storage following each experimental trial is conducted through the utilization of MAT files within the MATLAB software environment, adhering to the labelling conventions established in the introductory section of this chapter.

7.5 Results

7.5.1 Experiment for Repeatability in Abduction Movement

In this part, the repeatability test of the abduction movement was performed by repeating this test six times. Figure 7-7 shows the zero position and the final position of the arm, i.e., before and after the test.

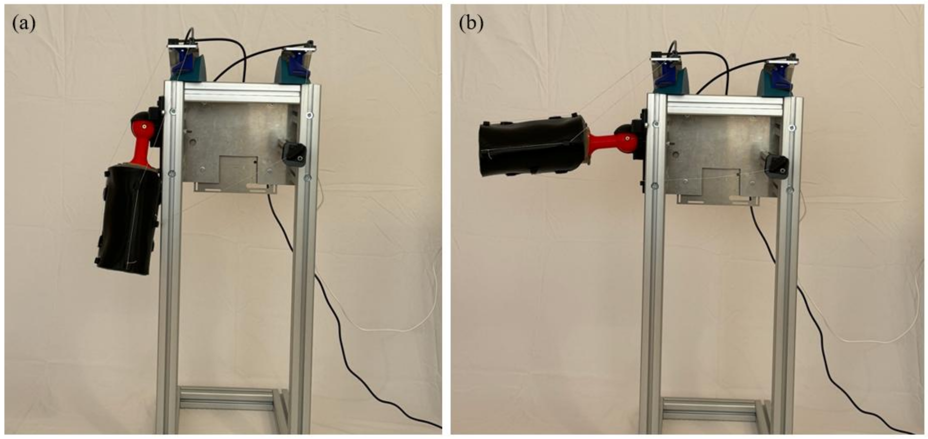

Figure 7-7: The zero position(a) and the final position (b) of the arm in the abduction test.

Figure 7-8 shows the results of the initial abduction test, which encompass the trajectory followed by the robot during abduction, as well as measurements of torque, position error, velocity, and motor temperature incurred in execution of this motion.

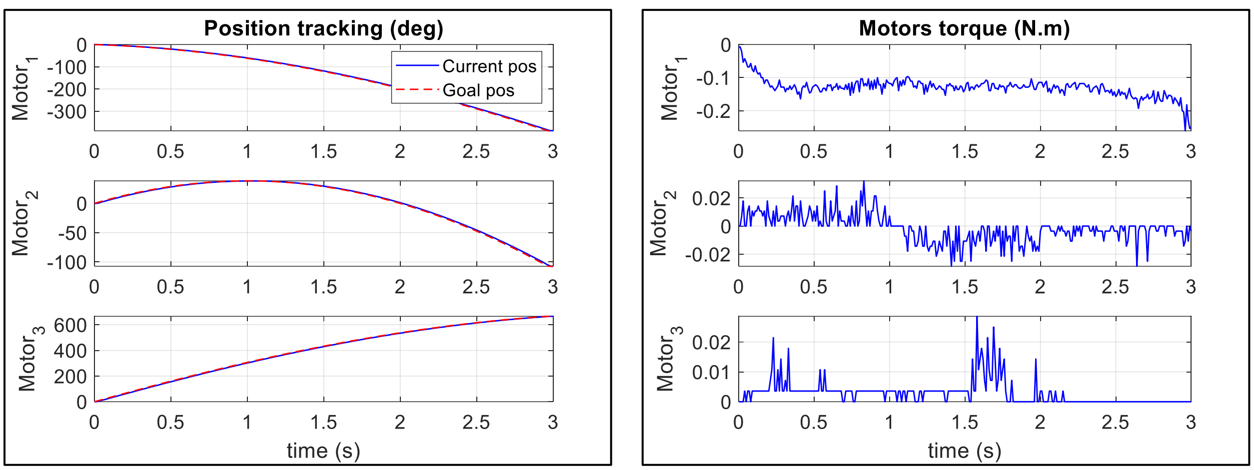

a b

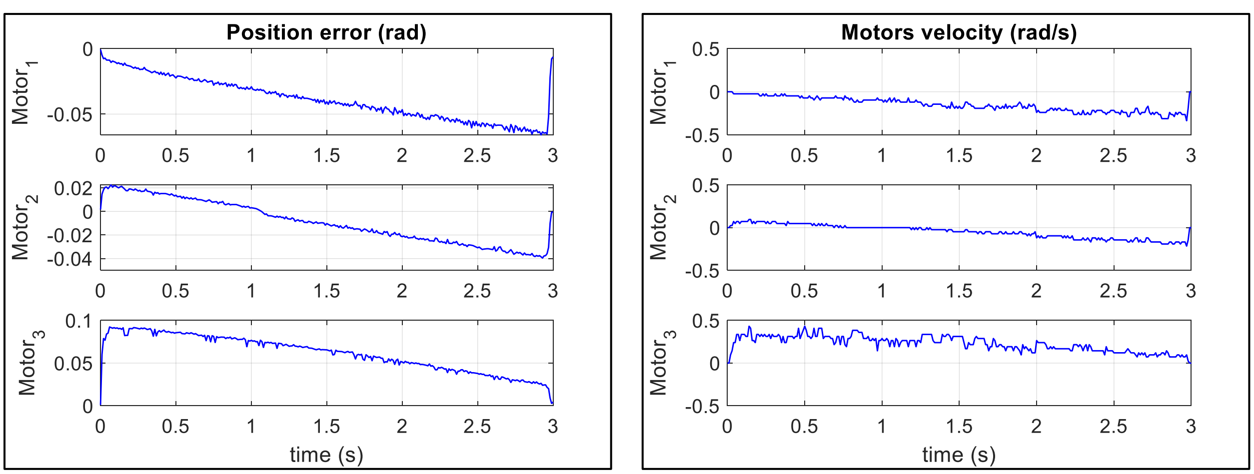

c

d

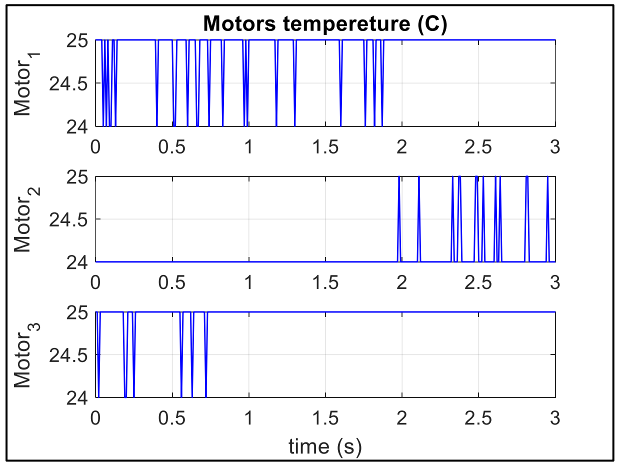

e

Figure 7-8: (a): Position tracking- (b): Torque- (c): Position error- (d): Velocity- (e): Motor temperature during the abduction movement without any extra load (AB00000_01).

The comprehensive analysis of the robotic system's performance data demonstrates highly effective motor control, with almost perfect correlations between current and goal positions across all motors, ensuring precision in robotic movements. Motor torque values reveal diverse utilization and load management, with motor 1 experiencing significantly more negative torque, indicative of its heavier operational demands. Position error measurements are minimal, underscoring the high accuracy of the system, though motor 3 exhibits the greatest variability, pointing to areas for potential refinement in control precision. The velocity profiles of the motors show a range of operational speeds, with motor 3 notably maintaining only positive velocities, highlighting its specific functional role and responsiveness. Furthermore, all motors maintain a consistent maximum temperature of 25°C, reflecting efficient thermal management that is crucial for sustaining performance and avoiding overheating.

In Figure 7-9, Figure 7-10, Figure 7-11, Figure 7-12, and Figure 7-13, the results of the tests performed for the second to sixth tests are shown in order.

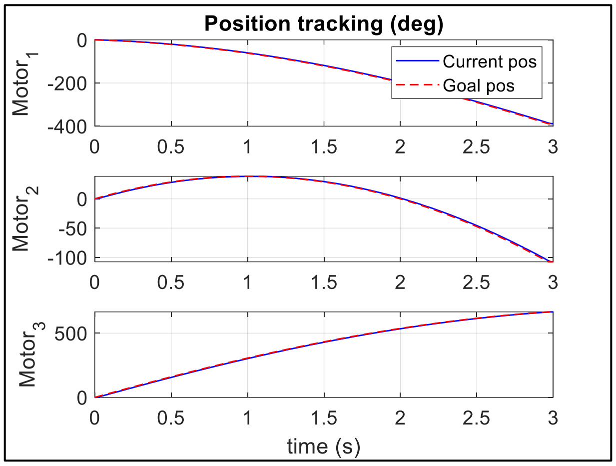

a

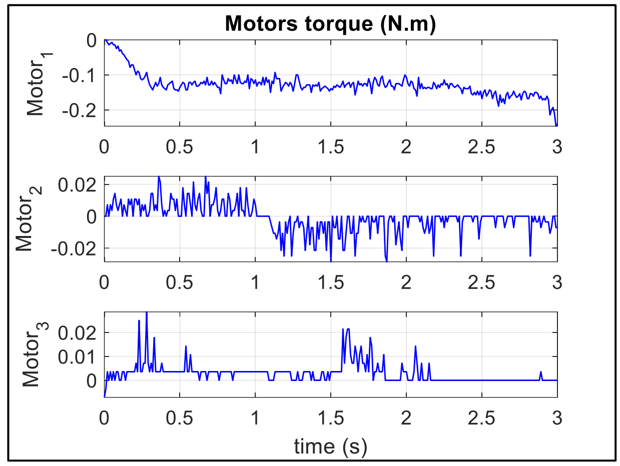

b

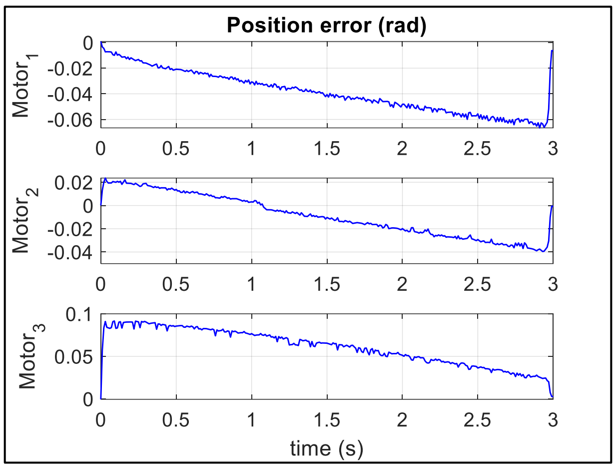

c

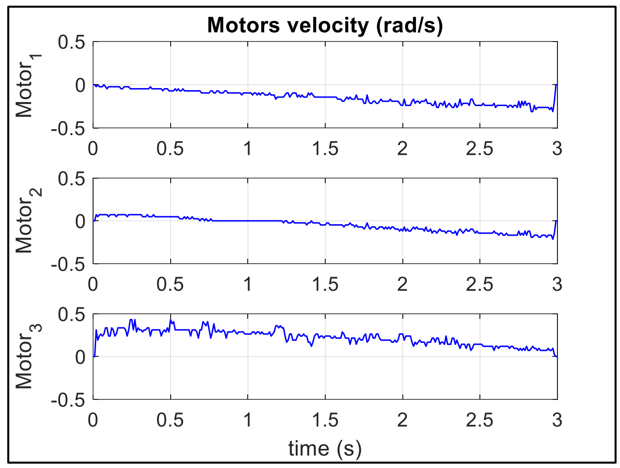

d

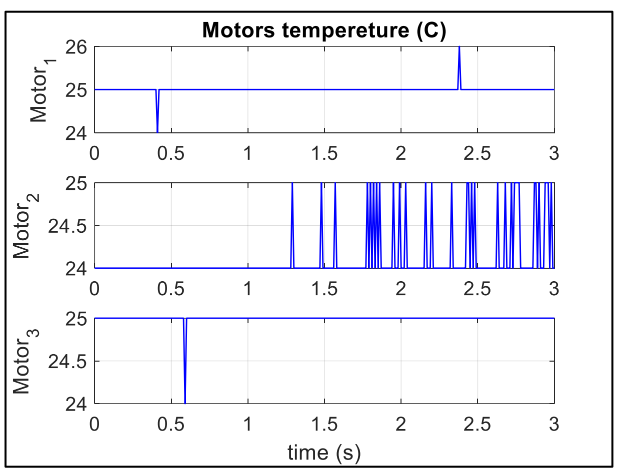

e

Figure 7-9: (a): Position tracking- (b): Torque- (c): Position error- (d): Velocity- (e): Motor temperature during the abduction movement without any extra load (AB00000_02).

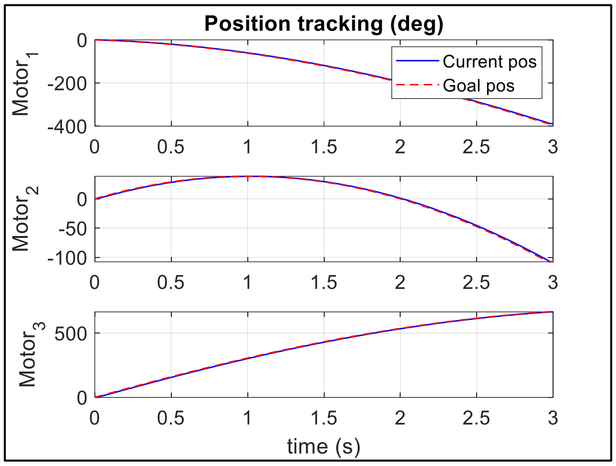

a

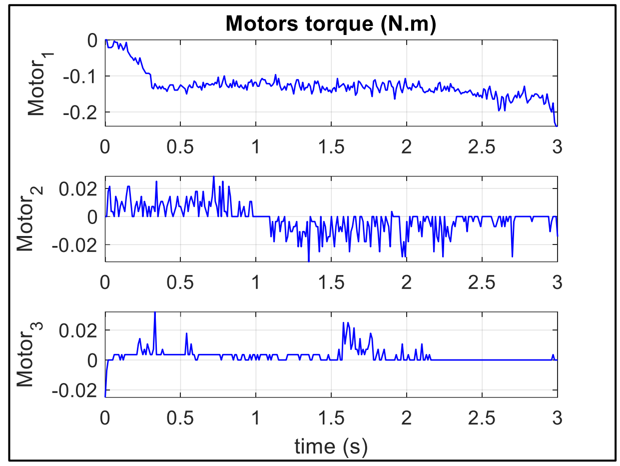

b

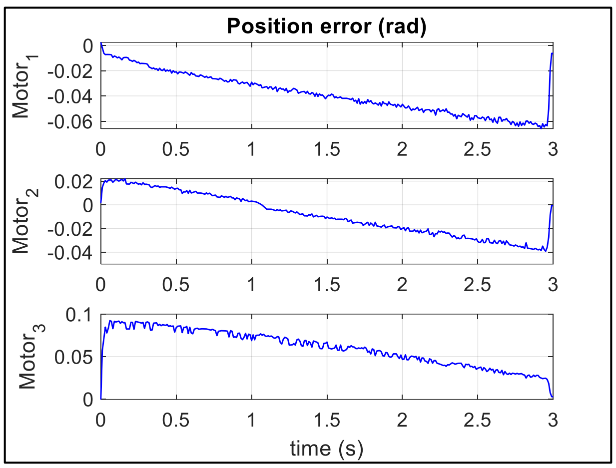

c

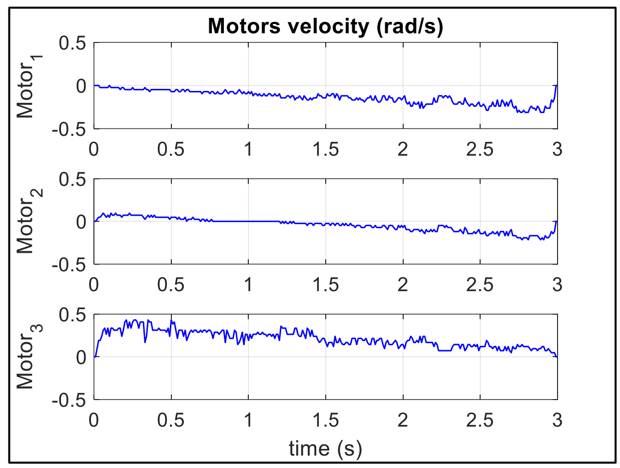

d

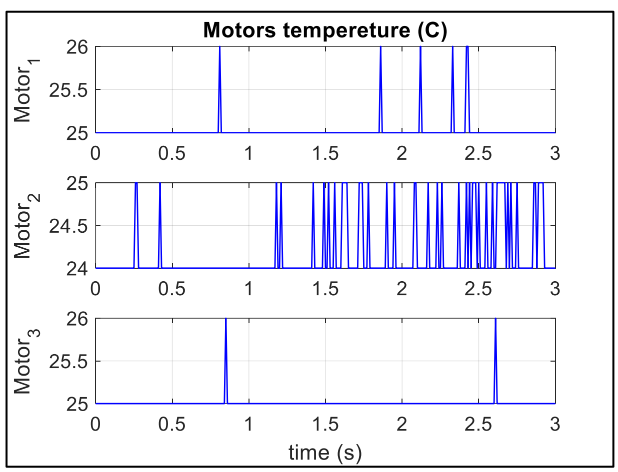

e

Figure 7-10: (a): Position tracking- (b): Torque- (c): Position error- (d): Velocity- (e): Motor temperature during the abduction movement without any extra load (AB00000_03).

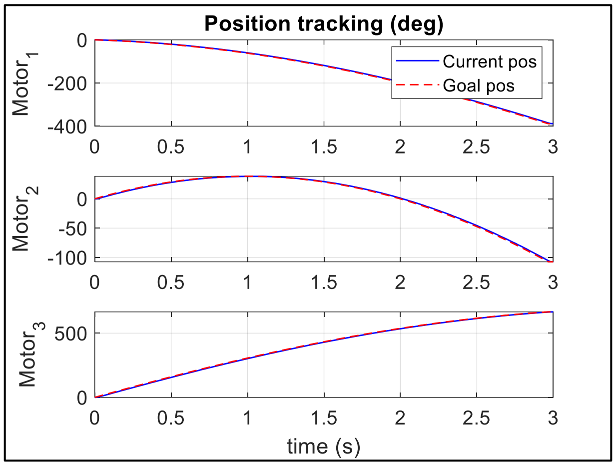

a

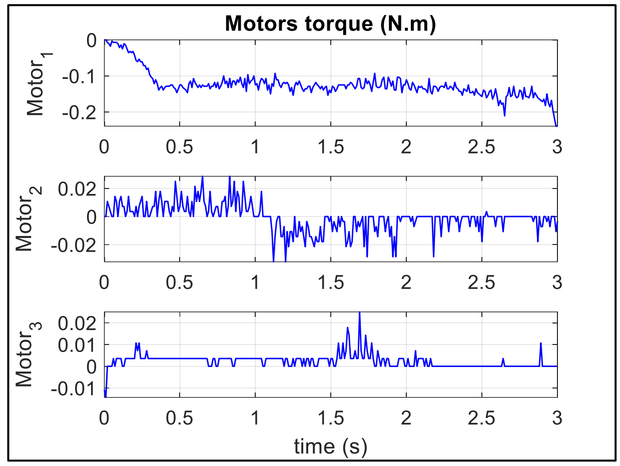

b

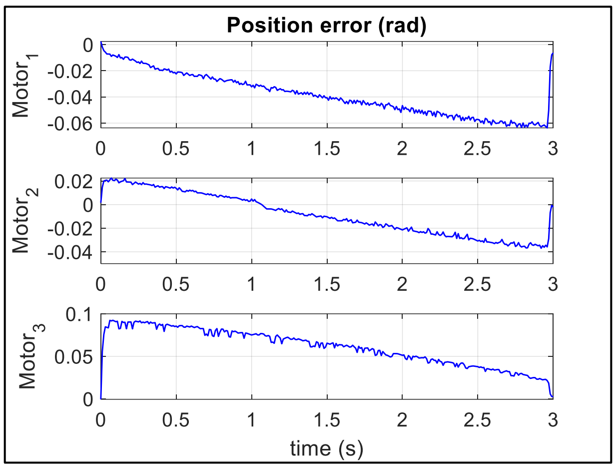

c

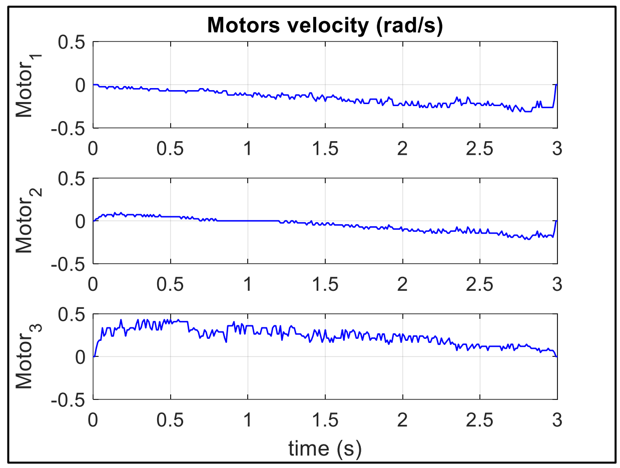

d

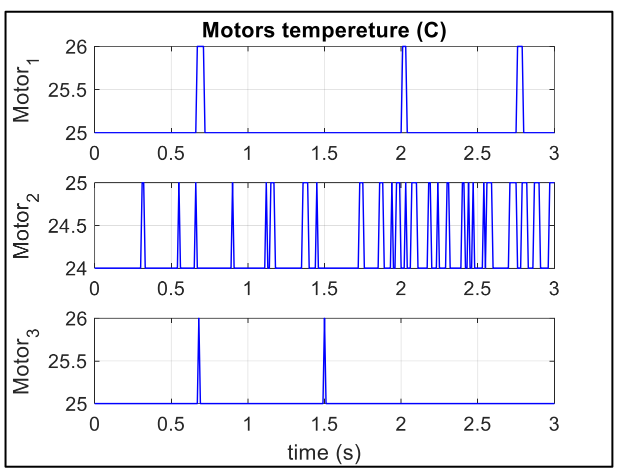

e

Figure 7-11: (a): Position tracking- (b): Torque- (c): Position error- (d): Velocity- (e): Motor temperature during the abduction movement without any extra load (AB00000_04).

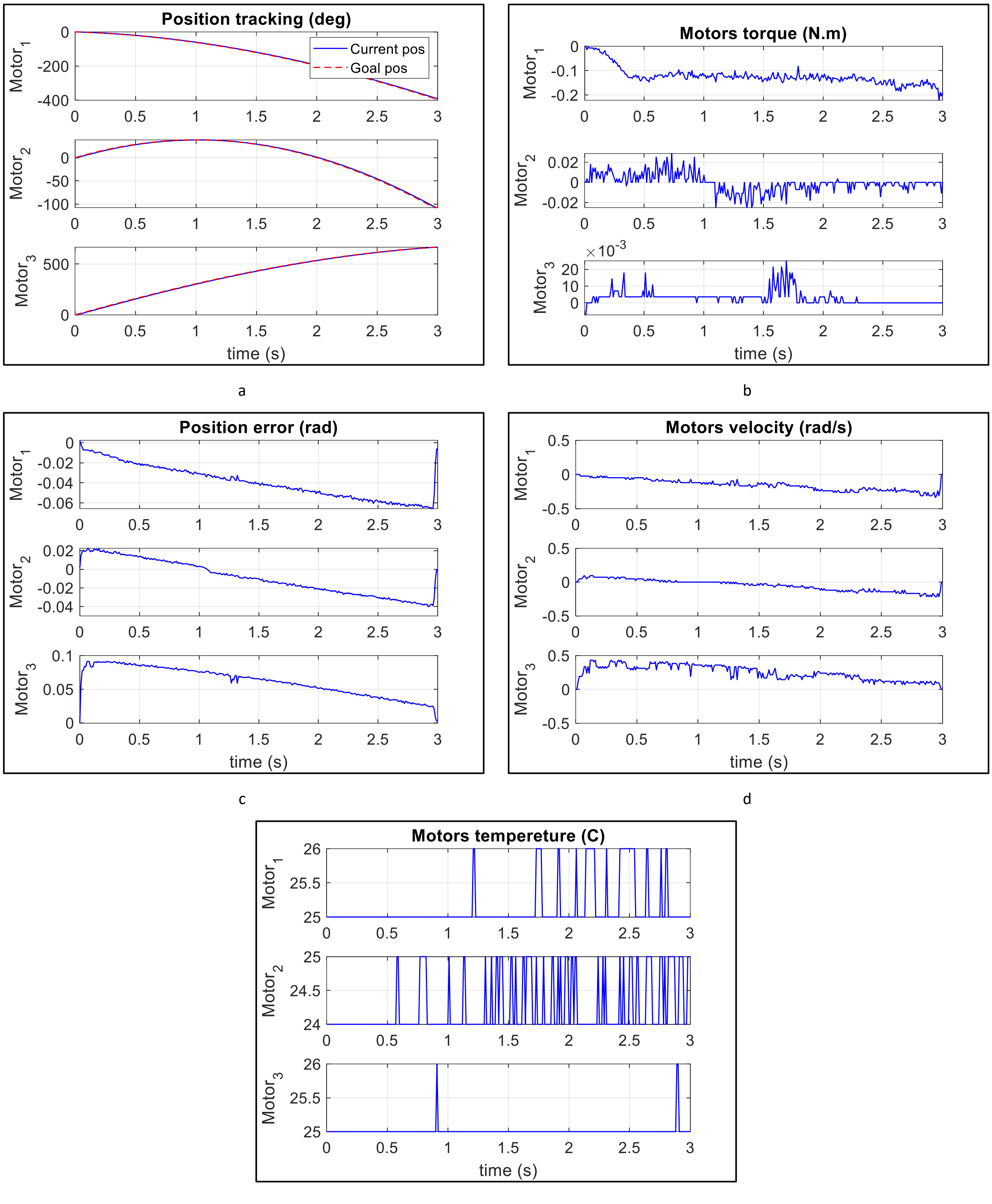

Figure 7-12: (a): Position tracking- (b): Torque- (c): Position error- (d): Velocity- (e): Motor temperature during the abduction movement without any extra load (AB00000_05)

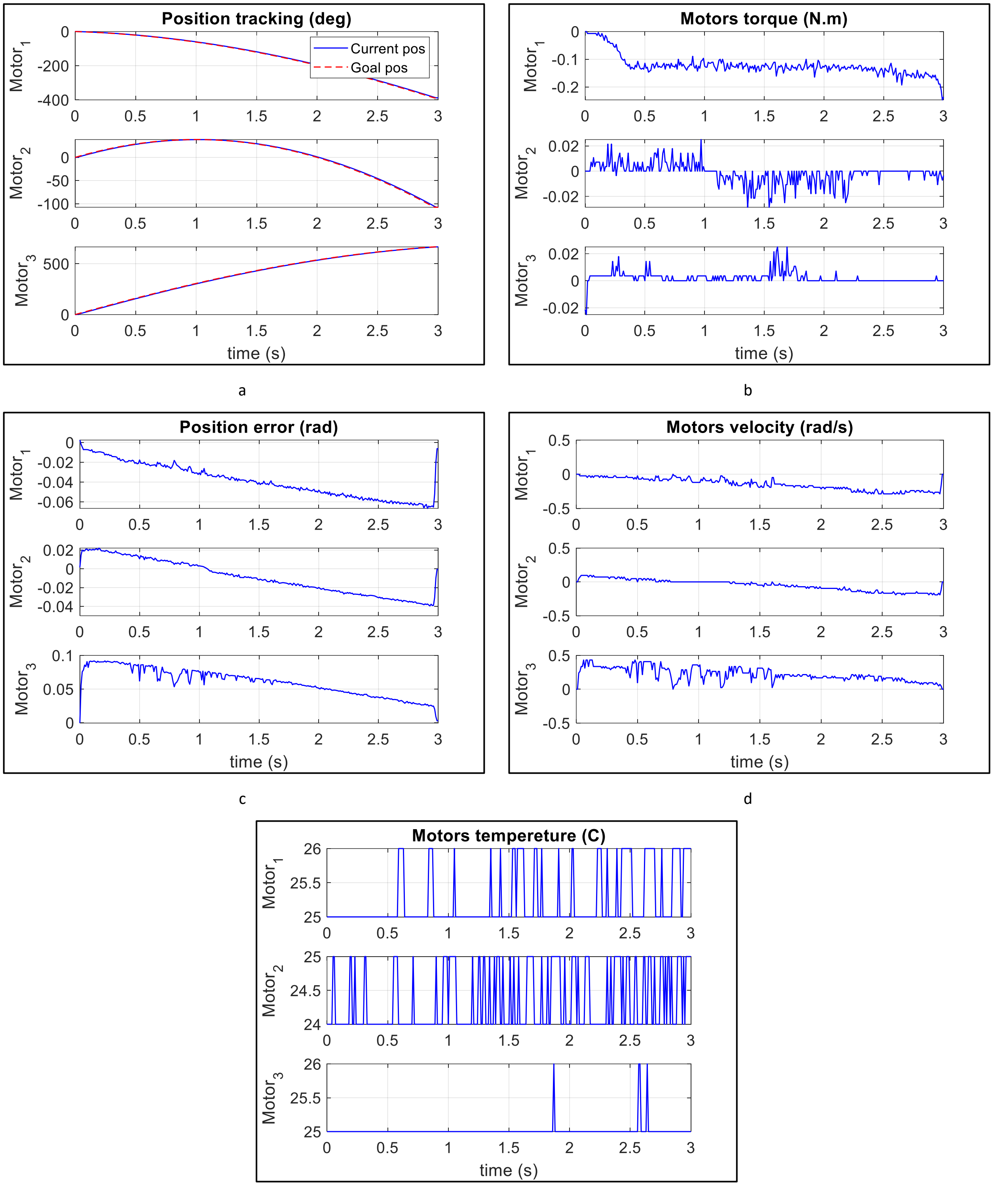

Figure 7-13: (a): Position tracking- (b): Torque- (c): Position error- (d): Velocity- (e): Motor temperature during the abduction movement without any extra load (AB00000_06)

In Figure 7-14 and Figure 7-15, the torque graph of the motors and position error are shown in six test modes (AB000001 to AB000006) in the abduction movement.

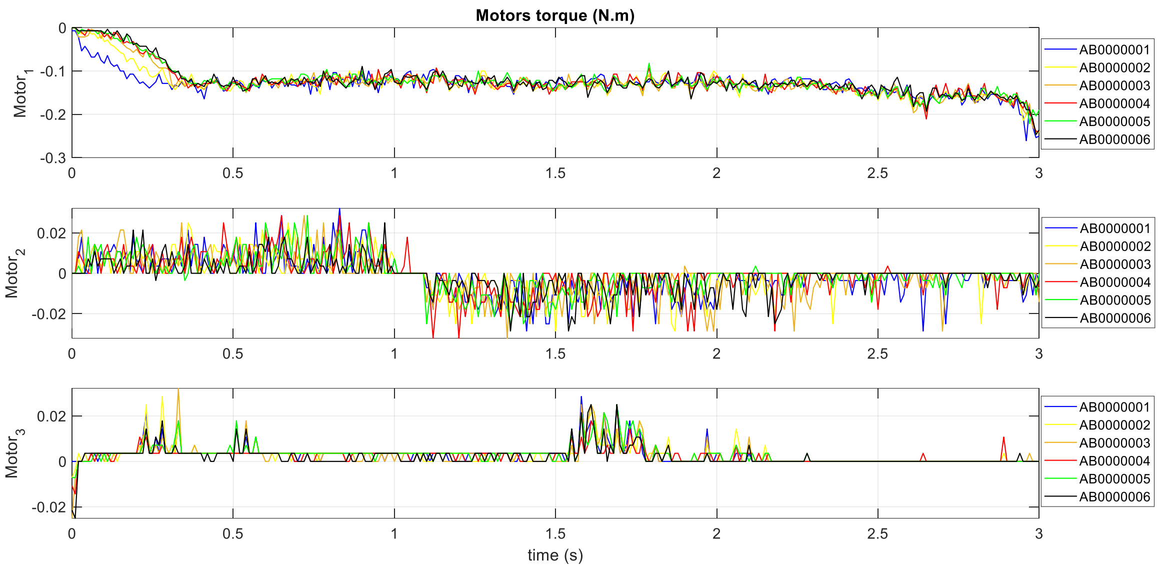

Figure 7-14: Motor torques in the six abduction experiments (AB000001 to AB000006).

The torque data from the six abduction experiments reveals a stable range with specific variations for each motor, indicative of consistent operational conditions with some variability. Motor 1 generally experiences the most negative minimum torque, peaking at values such as -0.261 in AB000001, which suggests it is subjected to heavier loads or more rigorous tasks. In contrast, the maximum torques are closer to zero across all motors, with motor 1 showing a maximum torque of 0.000 in AB000002, indicating a limitation or specific operational constraint. Motor 2 and motor 3 display less variance, with motor 2 showing minimum and maximum torques ranging from -0.029 to 0.032 in AB000001 and motor 3 showing a range from -0.007 to 0.029 across various experiments. These figures underscore the motors' roles, and the operational strategies employed, reflecting both the robustness and the tailored control within the robotic system’s framework across different testing scenarios or tasks. This detailed torque analysis helps to underline how each motor is optimized for its specific function, maintaining efficiency and stability even under varied conditions.

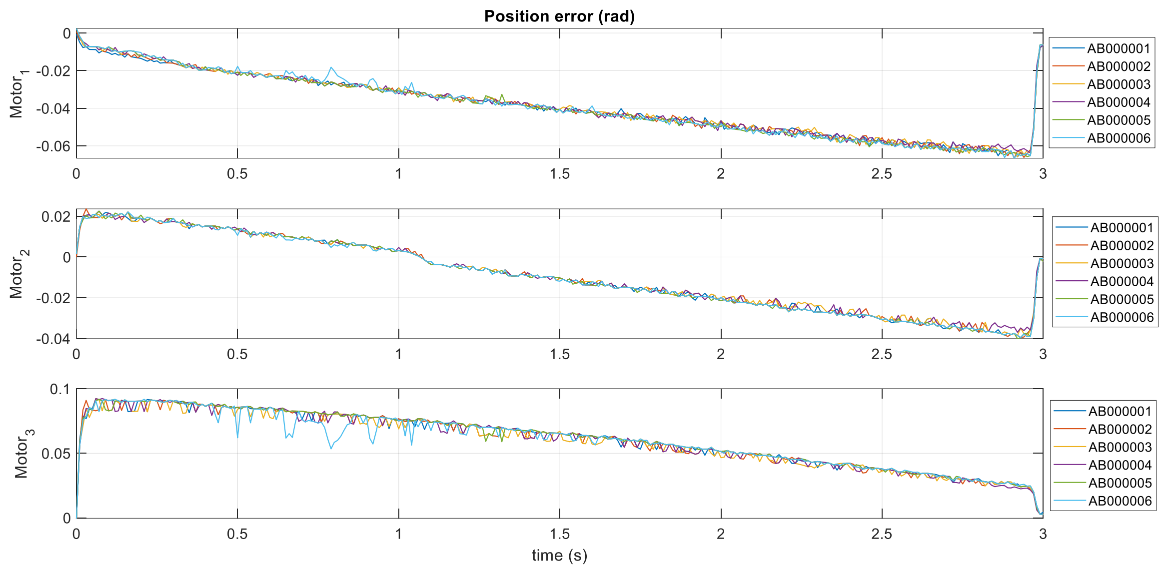

Figure 7-15: Position error in the six abduction experiments (AB000001 to AB000006).

The analysis of maximum position errors from the six abduction experiments reveals notable patterns and discrepancies in control accuracy among the motors. Motor 1 consistently demonstrates superior precision, with maximum errors varying slightly, from as low as -0.0007 in the first file to around 0.0024 in others, indicating highly reliable control. Motor 2 shows modestly higher errors, with the most considerable recorded being approximately 0.0236, suggesting slightly less precision compared to motor 1 but still maintaining consistent performance.

7.5.2 Experiment in Abduction Movement (from 500 g to 4000 g weight)

Figure 7-16 illustrates the neutral position for abduction movement, incrementally adding weights from 500 grams to 4000 grams in 500-gram intervals. The desired weights are standard sand weights. This experiment was conducted in eight distinct phases to analyse the designed robot's performance under varying load conditions.

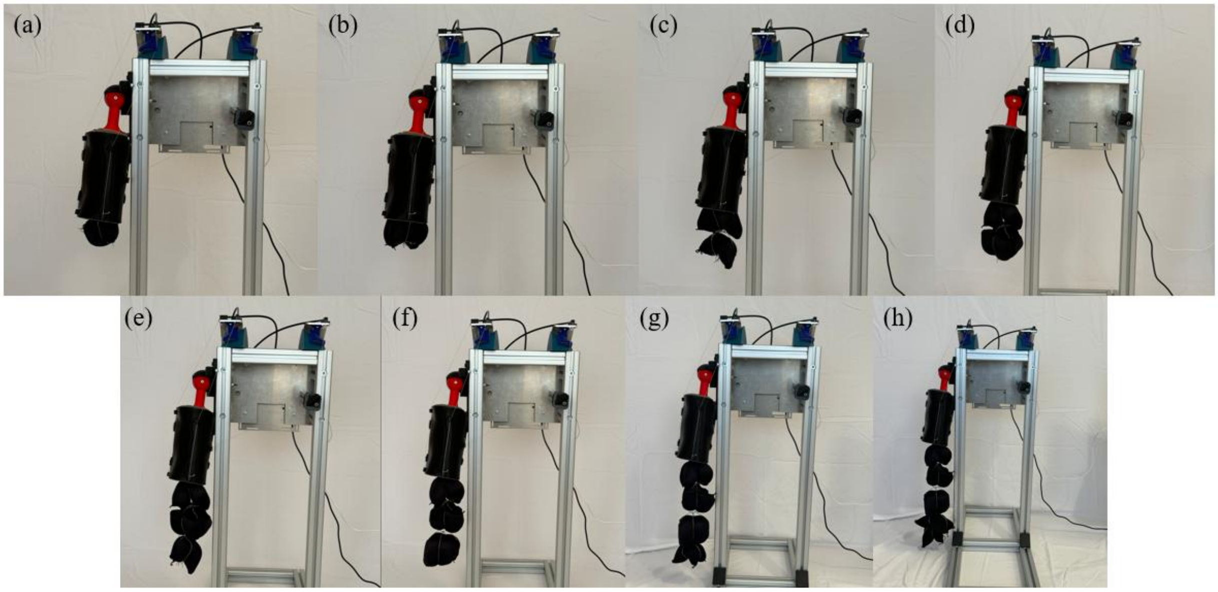

Figure 7-16: Neutral position for abduction movement, incrementally adding weights from 500 grams to 4000 grams in 500-gram intervals: (a): 500 g - (b): 1000g – (c): 1500 g – (d): 2000 g – (e): 2500 g – (f): 3000 g – (g): 3500 g - (h): 4000 g**.**

Figure 7-17 shows the outcomes of the movement across the eight modes under consideration, whilst Figure 7-18, Figure 7-19, Figure 7-20, Figure 7-21, Figure 7-22, Figure 7-23, Figure 7-24 and Figure 7-25 illustrate position tracking, torque, position error, velocity, and motor temperature during the abduction movement with loads ranging from 500g to 4000g in 500-gram increments, respectively.

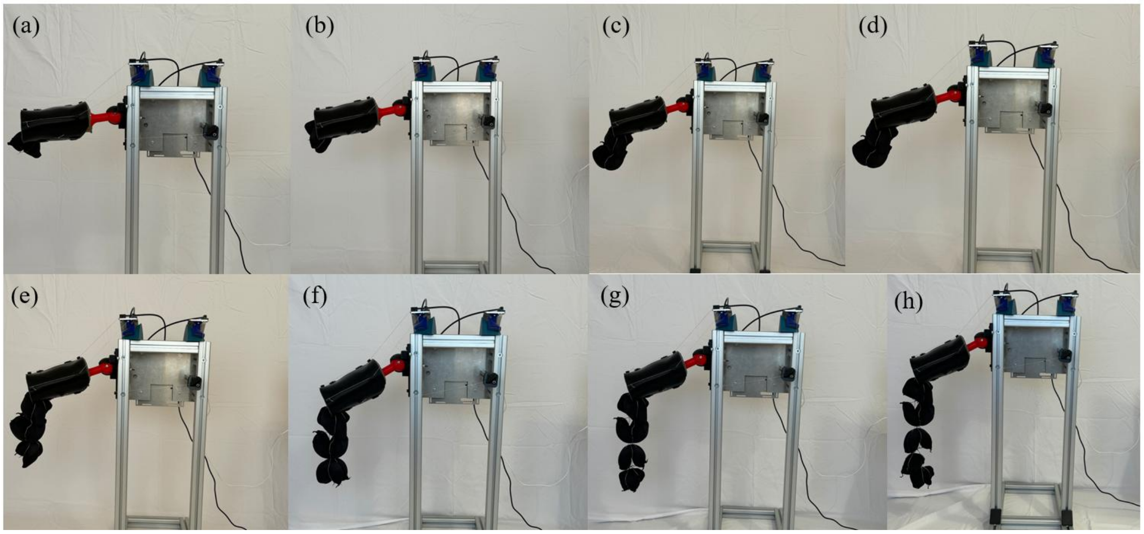

Figure 7-17: Abduction position, incrementally adding weights from 500 grams to 4000 grams in 500-gram intervals: (a): 500 g - (b): 1000g – (c): 1500 g – (d): 2000 g – (e): 2500 g – (f): 3000gr – (g): 3500 g - (h): 4000 g.

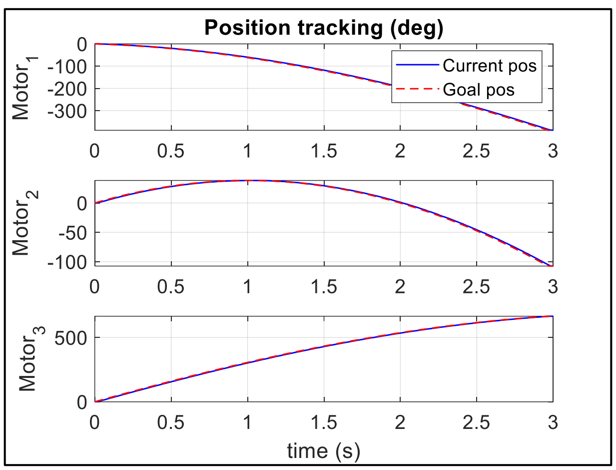

a

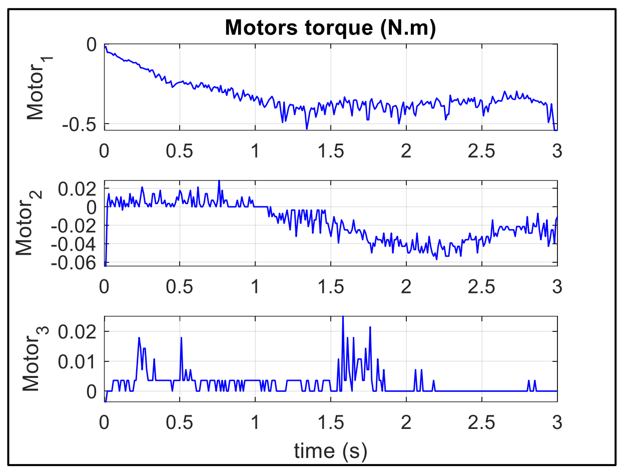

b

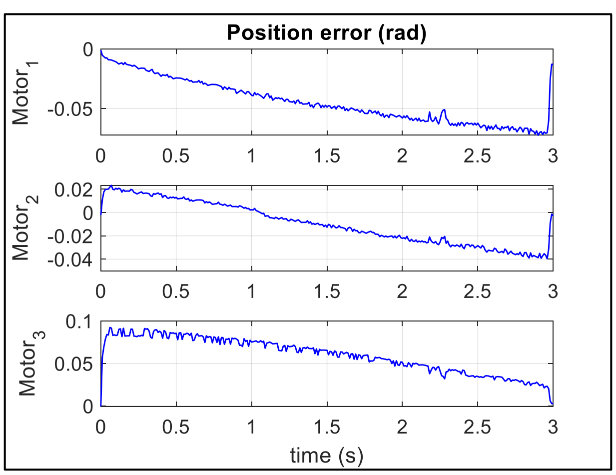

c

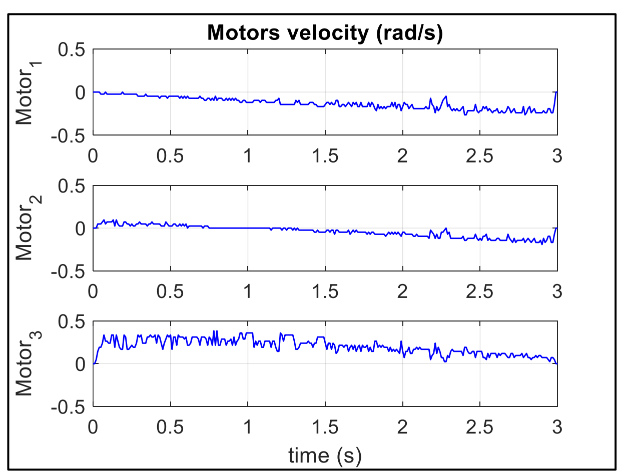

d

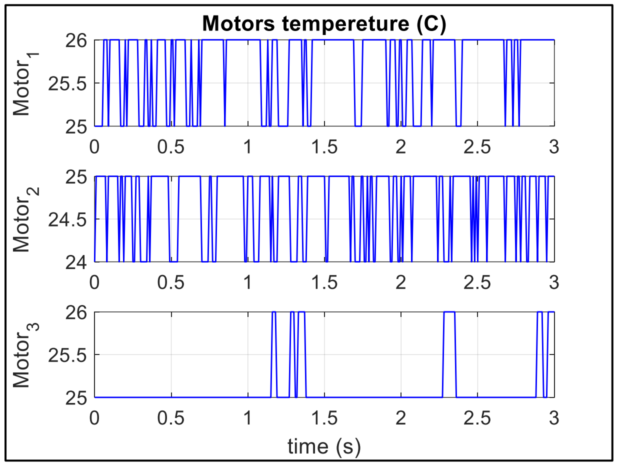

e

Figure 7-18: (a): Position tracking- (b): Torque- (c): Position error- (d): Velocity- (e): Motor temperature during the abduction movement with a 500g load (AB00500_01).

Figure 7-18 reveals that all motors exhibit strong correlations between current and goal positions, with values near perfect correlation, indicating that the control systems are highly precise in following the set trajectories. The motors torque shows notable variations in torque, with motor 1 displaying a range from -0.260 to 0.032 Nm, suggesting it manages more strenuous tasks. Motor 2 and motor 3 show narrower torque ranges, which highlight their roles in less variable operational conditions. The position error data points to motor 3 experiencing the highest discrepancies, with errors peaking at 0.092, which could indicate specific challenges in its positioning accuracy. From the motor's velocity, each motor demonstrates a broad range of operational speeds, for instance, motor 1 varies from -0.336 m/s to 0.432 m/s, enabling it to adapt quickly to changing conditions which is essential for dynamic tasks. This detailed account provides a clearer picture of how each motor functions within the system, highlighting their capabilities and areas for potential improvement, particularly in thermal management and control precision for motor 3.

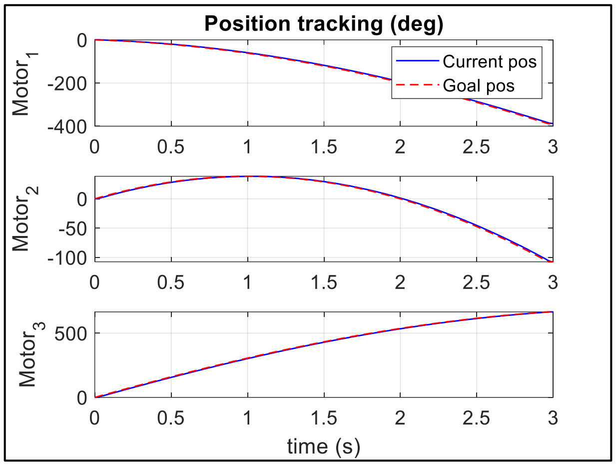

a

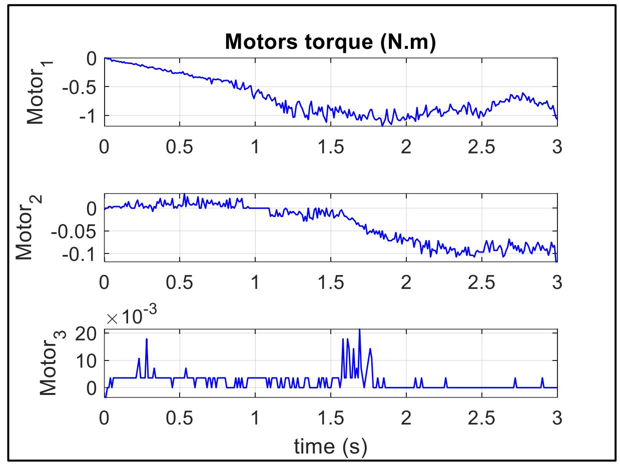

b

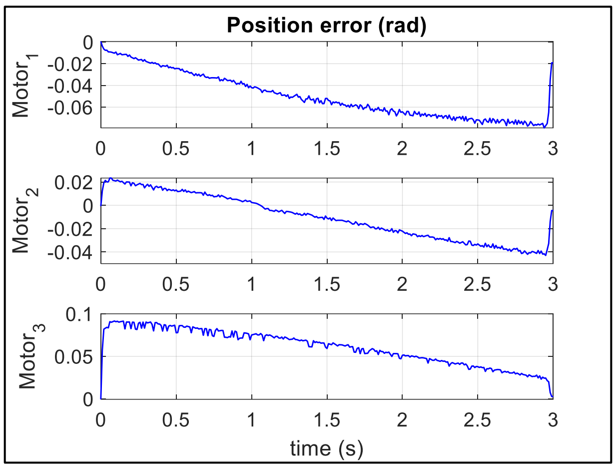

c

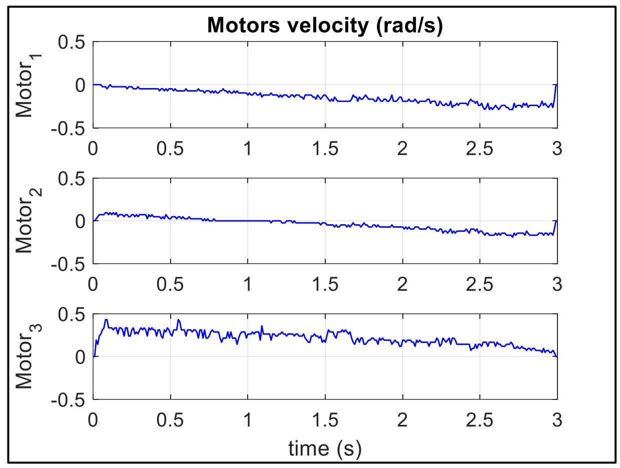

d

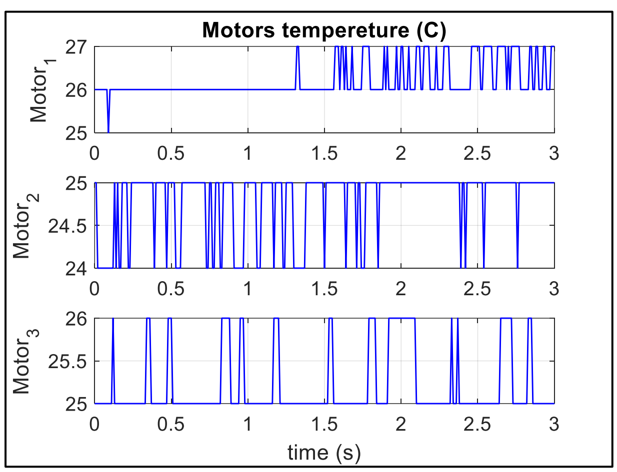

e

Figure 7-19: (a): Position tracking- (b): Torque- (c): Position error- (d): Velocity- (e): Motor temperature during the abduction movement with a 1000 g load (AB01000_01).

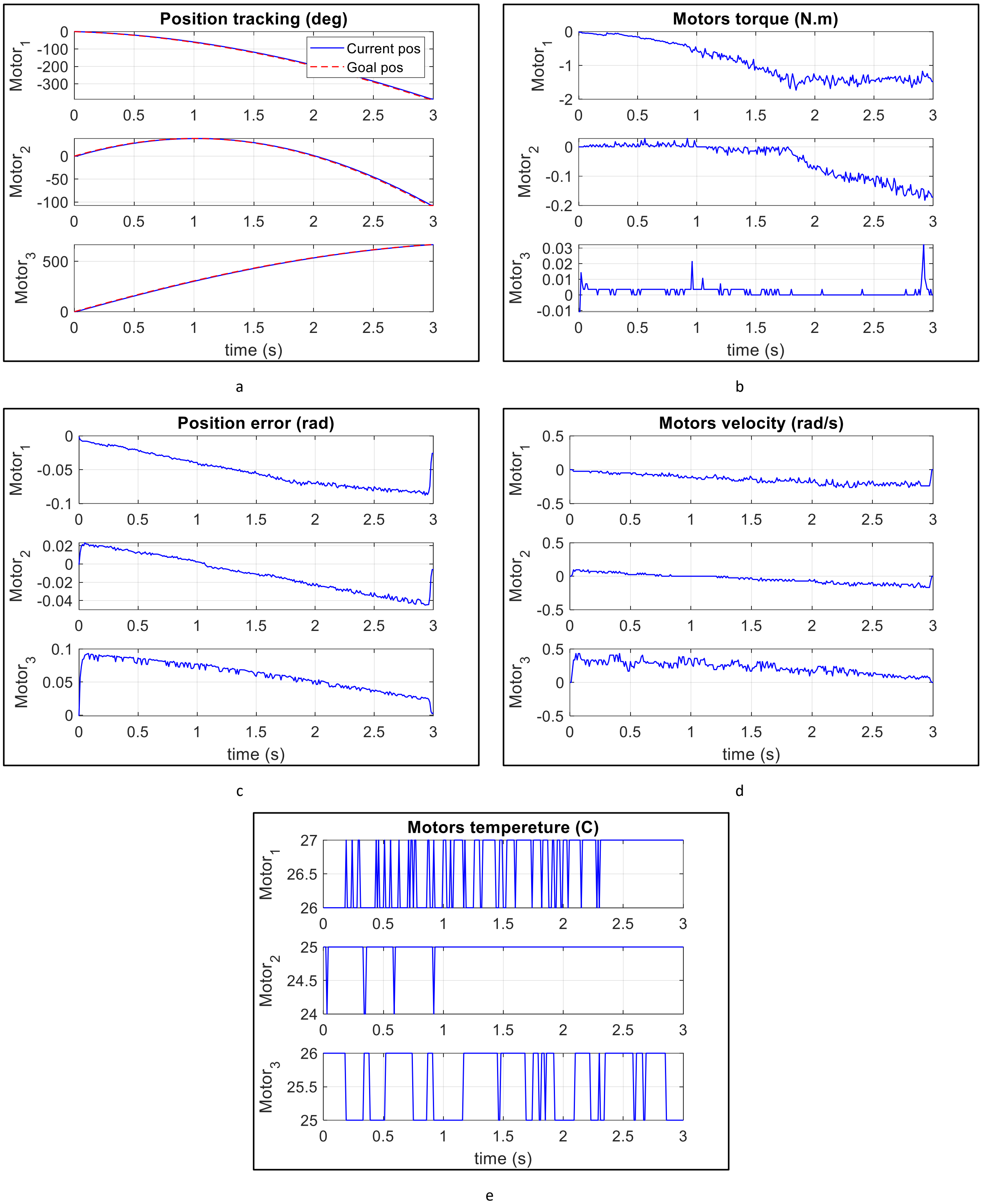

Figure 7-20: (a): Position tracking- (b): Torque- (c): Position error- (d): Velocity- (e): Motor temperature during the abduction movement with a 1500 g load (AB01500_01).

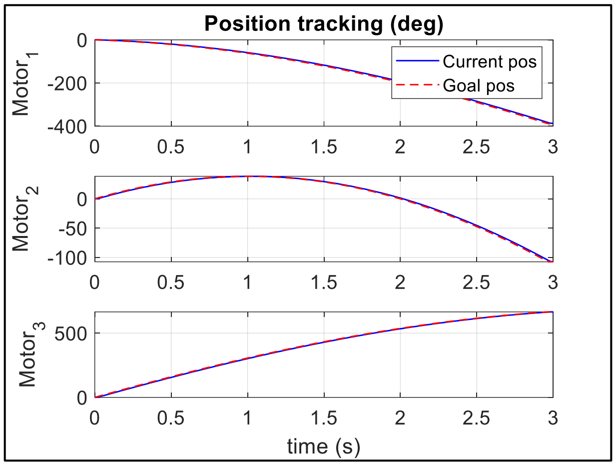

a

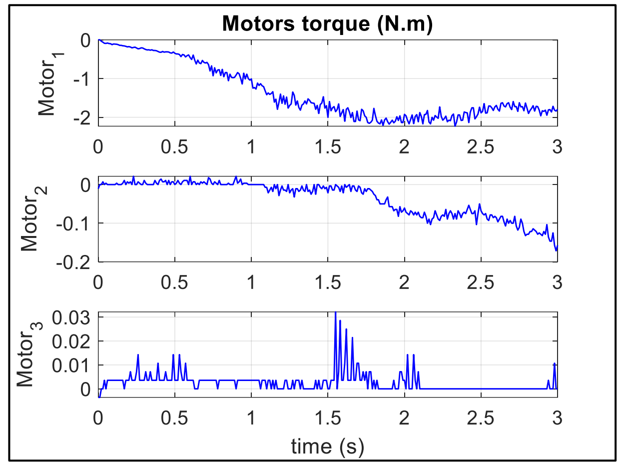

b

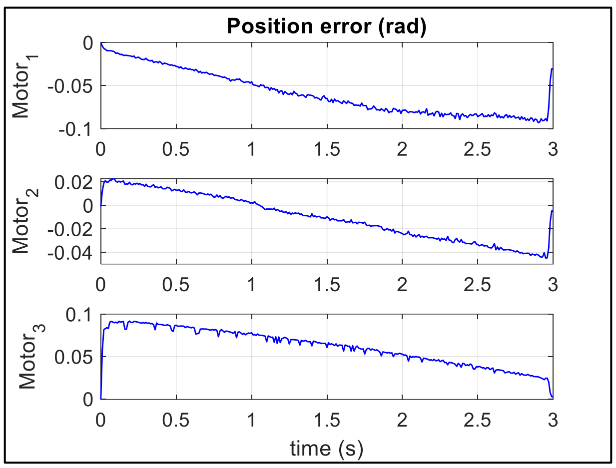

c

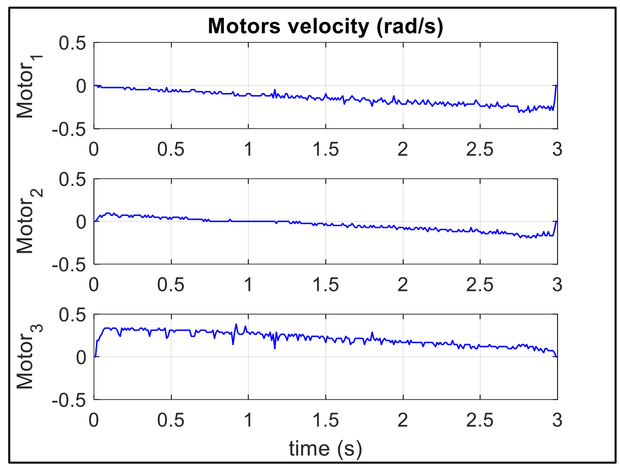

d

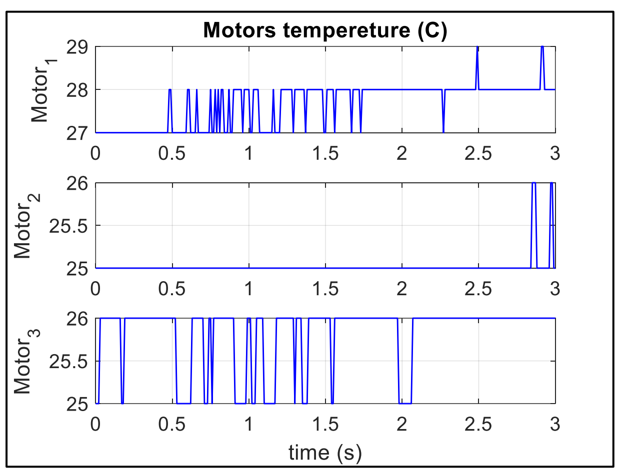

e

Figure 7-21: (a): Position tracking- (b): Torque- (c): Position error- (d): Velocity- (e): Motor temperature during the abduction movement with a 2000 g load (AB02000_01).

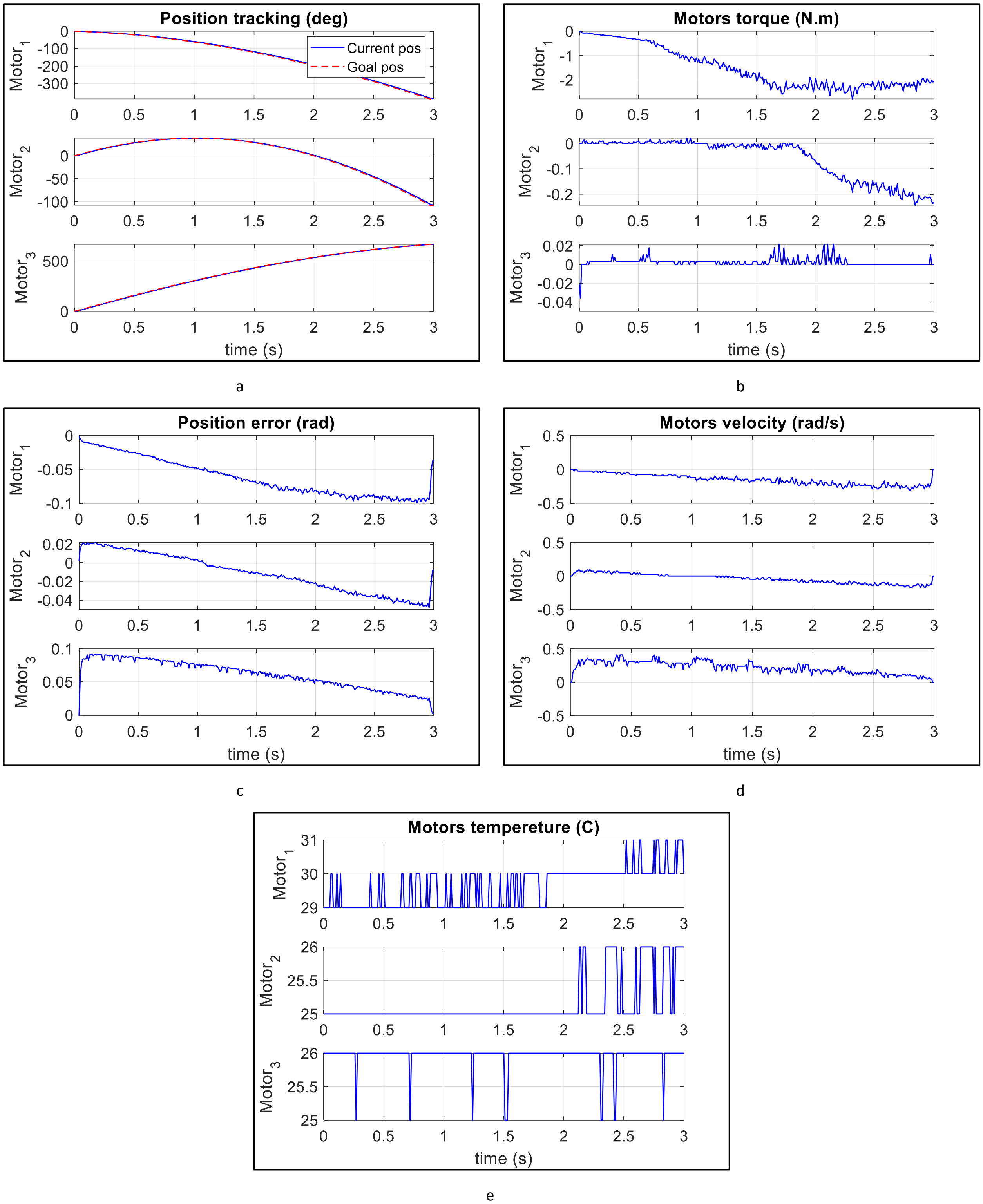

Figure 7-22: (a): Position tracking- (b): Torque- (c): Position error- (d): Velocity- (e): Motor temperature during the abduction movement with a 2500 g load (AB02500_01).

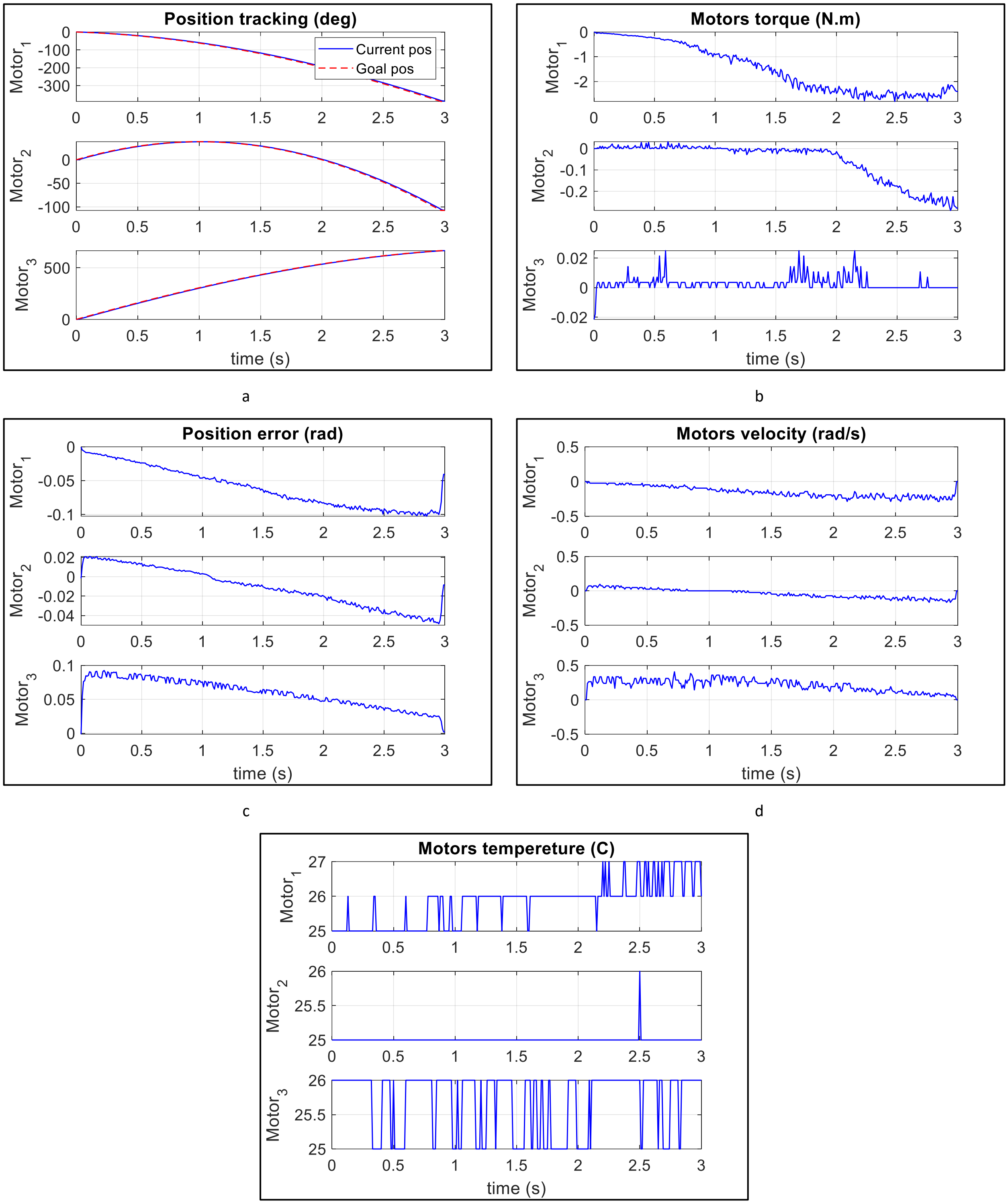

Figure 7-23: (a): Position tracking- (b): Torque- (c): Position error- (d): Velocity- (e): Motor temperature during the abduction movement with a 3000 g load (AB03000_01).

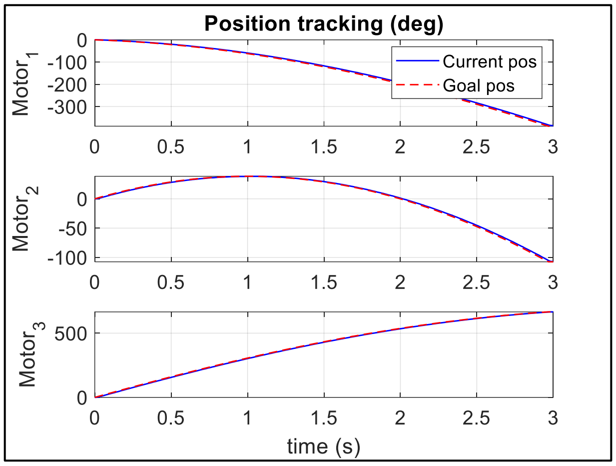

a

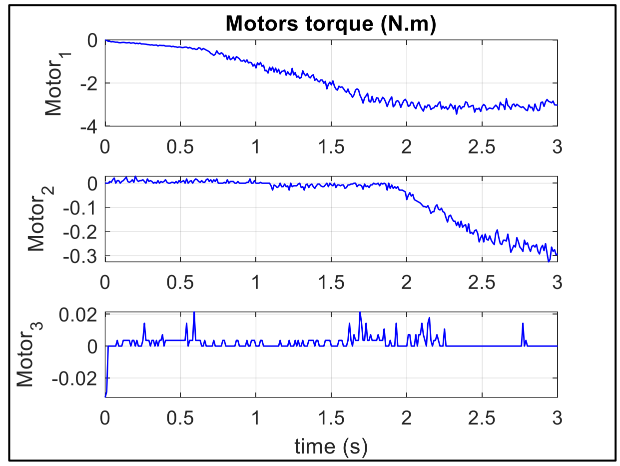

b

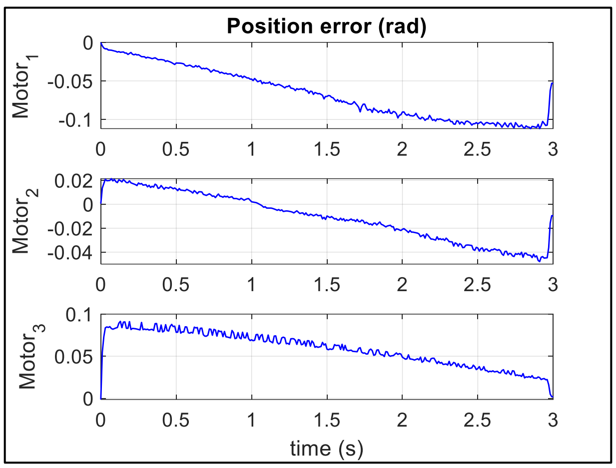

c

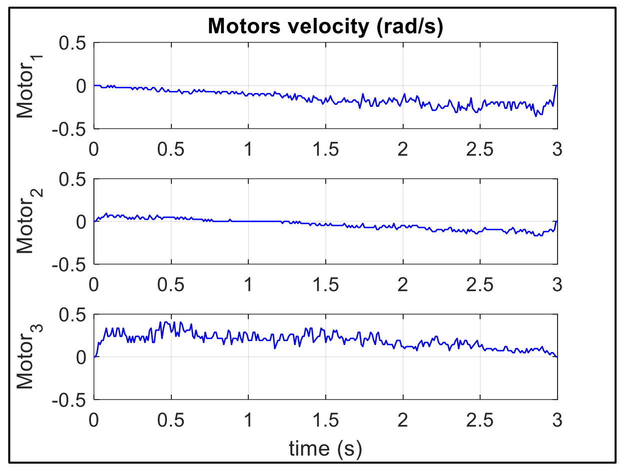

d

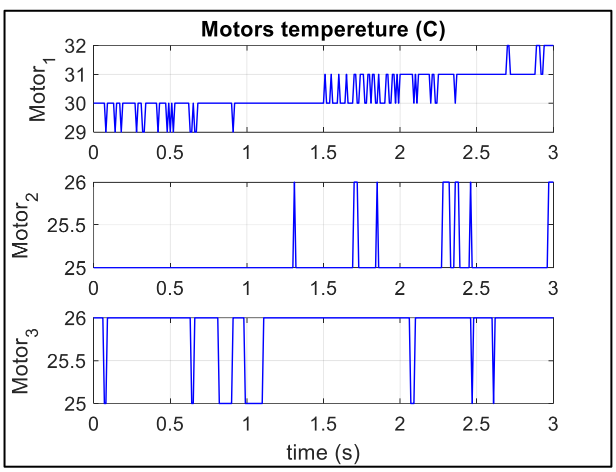

e

Figure 7-24: (a): Position tracking- (b): Torque- (c): Position error- (d): Velocity- (e): Motor temperature during the abduction movement with a 3500 g load (AB03500_01).

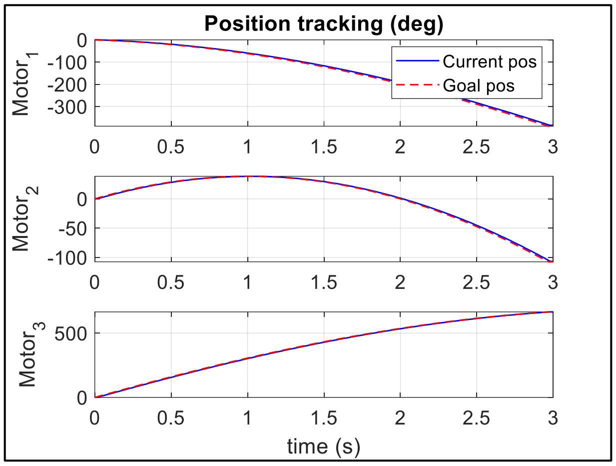

a

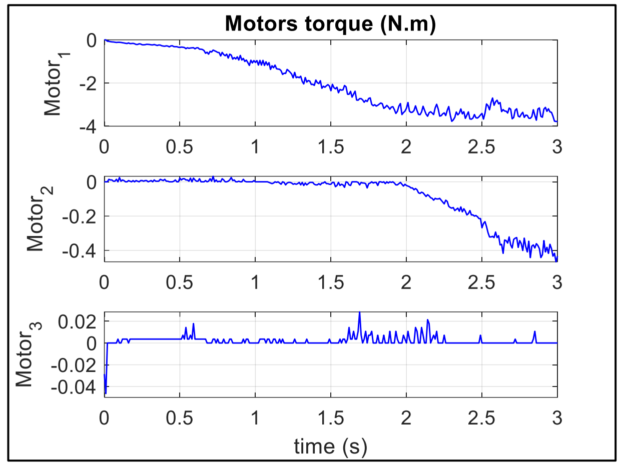

b

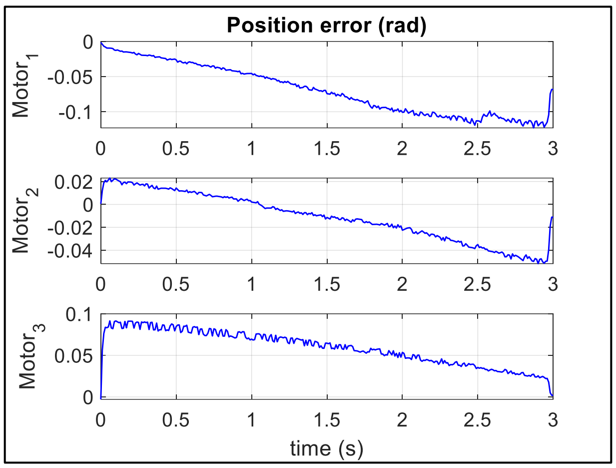

c

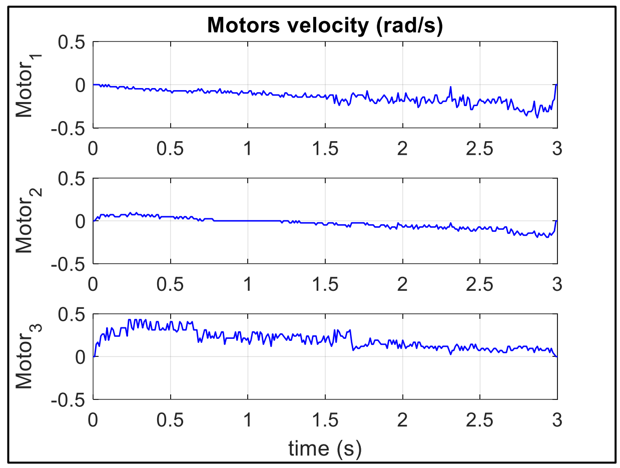

d

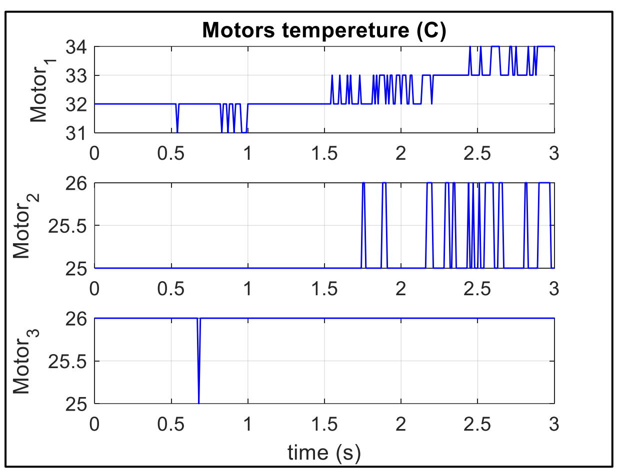

e

Figure 7-25: (a): Position tracking- (b): Torque- (c): Position error- (d): Velocity- (e): Motor temperature during the abduction movement with a 4000 g load (AB04000_01).

In Figure 7-26 and Figure 7-27, the torque graph of the motors and position error are shown for eight test modes (AB005001 to AB040001) for the abduction movement.

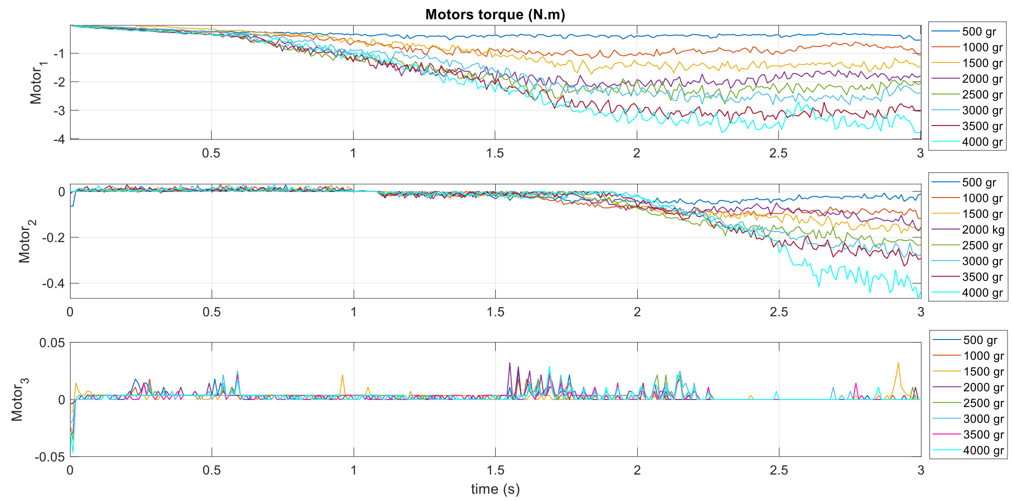

Figure 7-26: Motor torques for eight different abduction experiments (500 g to 4000 g loading).

Figure 7-26 demonstrates notable trends and variations in motor performance under varying test conditions. Motor 1 shows a significant widening in the range of minimum torque values, moving from -0.54 Nm with 500g loading to -3.78 Nm with 4000g loading, indicating increasingly rigorous testing or operational demands. Motor 2 also experiences a deepening range, with minimum torques worsening from -0.064 Nm to -0.467 Nm, while maintaining relatively stable maximum values around 0.032 Nm, reflecting a robust but consistently challenging role. In contrast, motor 3 displays less dramatic changes in its torque range, though it too trends towards more negative minimums, from -0.0036 Nm to -0.0465 Nm, with slightly higher maximums than the other motors, hinting at different operational conditions or mechanical characteristics.

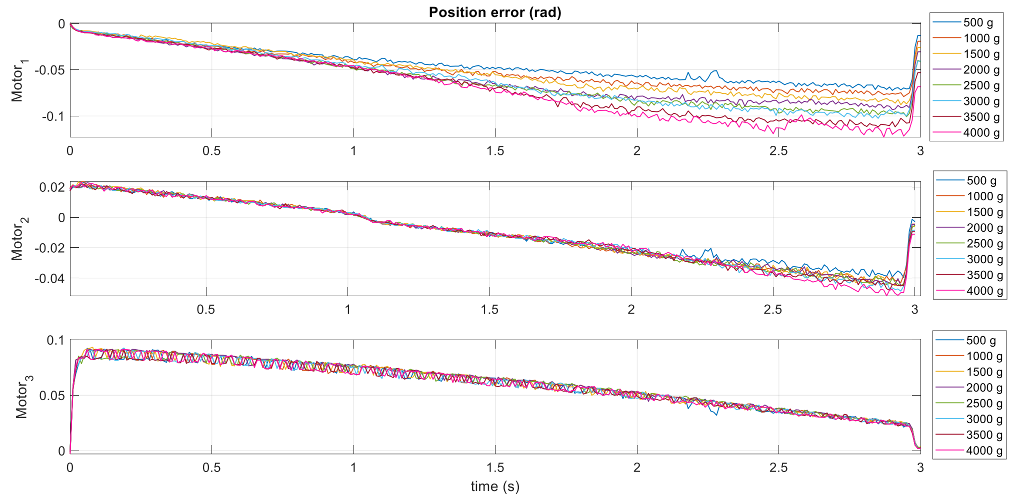

Figure 7-27: Position error for eight different abduction experiments (500 g to 4000 g loading).

Figure 7-27 shows that motor 3 consistently experiences the highest errors, with values peaking at 0.0932 in 1500g, indicating it may face the greatest challenges in control precision. Motor 1 generally maintains lower error rates, with maximum values only slightly negative, such as -0.0014 in 1500g and 4000 g, suggesting more stable but possibly underutilized control. Motor 2 shows moderate variability, with maximum errors ranging from around 0.0234 in 500 g and 1000 g, which might reflect a balanced operational role within the system. Notably, motor 2's errors decrease to around 0.0209 in 3000 g, pointing towards potential improvements or adaptations in control strategies over the course of these tests. This analysis highlights motor 3 as a critical focus for further tuning to enhance its accuracy, while the performance of motors 1 and 2 suggests a robust control framework that could be optimized for even greater precision and reliability in robotic operations.

7.5.3 Experiment for Repeatability in Flexion Movement

In this section, the repeatability test for the flexion movement was performed by repeating this test six times. Figure 7-28 shows the zero position and the final position of the arm, i.e., before and after the test.

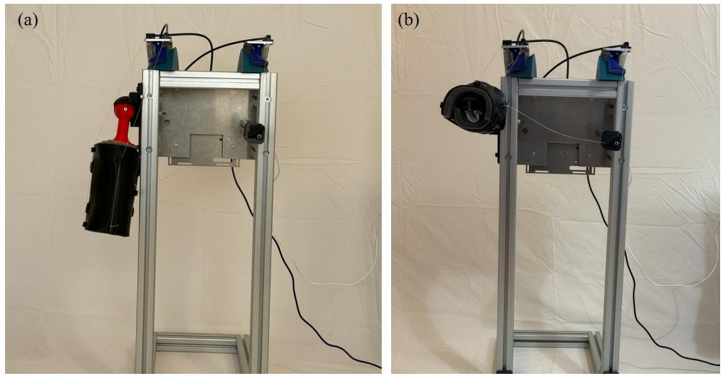

Figure 7-28: The zero position(a) and the final position (b) of the arm during the flexion test.

Figure 7-29 shows the results from the initial flexion test, which encompass the trajectory followed by the robot during flexion, as well as measurements of torque, position error, velocity, and motor temperature incurred during the execution of this motion. In Figure 7-30, Figure 7-31, Figure 7-32, Figure 7-33 and Figure 7-34, the results of the tests performed for the second to sixth tests are shown in order.

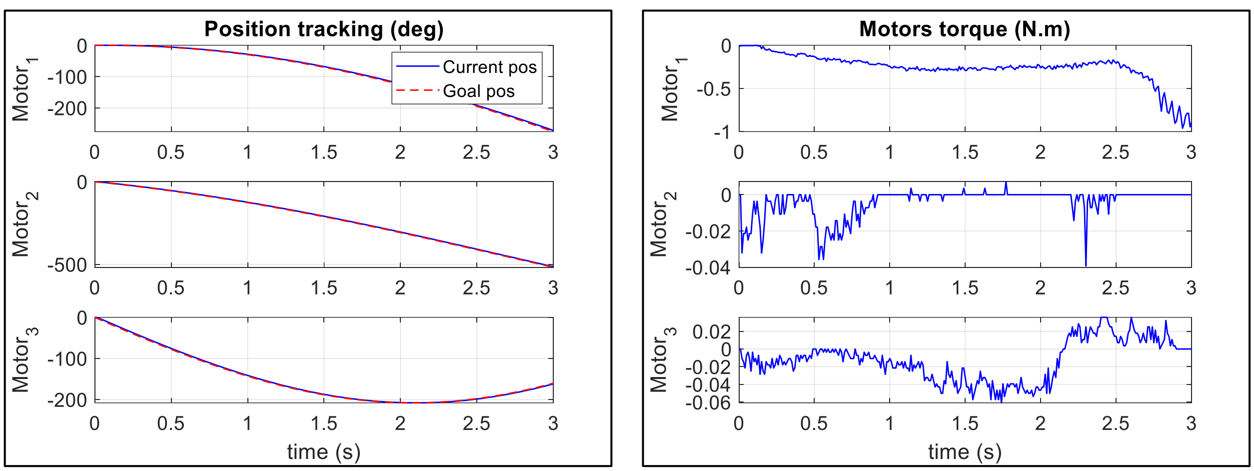

a b

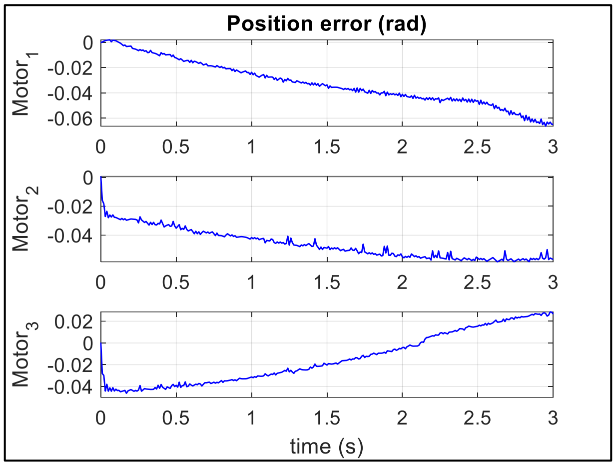

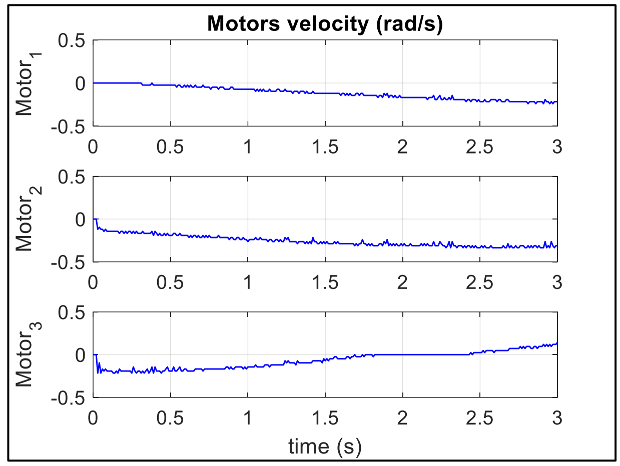

c

d

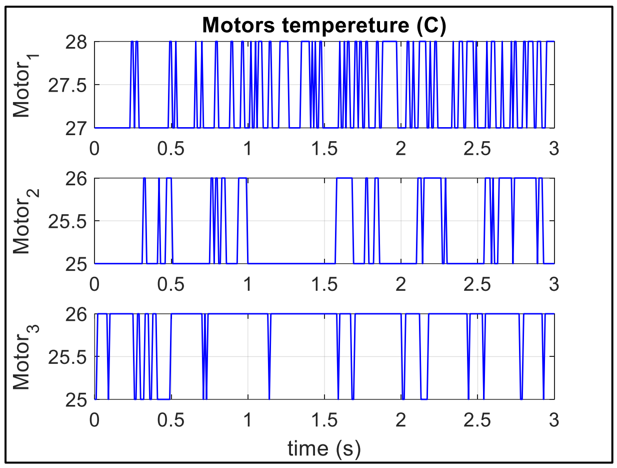

e

Figure 7-29: (a): Position tracking- (b): Torque- (c): Position error- (d): Velocity- (e): Motor temperature during the flexion movement without any extra load (FL00000_01).

Figure 7-29 illustrated the dataset reveals a precision-controlled system capable of maintaining high accuracy in motor operations. The position tracking demonstrates nearly perfect correlations between the current and goal positions across all motors, highlighting the system's capability to achieve precise control, essential for complex robotic tasks. The motor torque data exhibits significant variability, with motor 1 handling torque ranges from -0.540 Nm to 0.032 Nm, indicating its capacity to manage strenuous tasks under varying loads. The position errors across the motors are generally low but peak at values such as 0.092 for motor 3, pointing to moments of less optimal control. Motor velocities are also diverse, with motor 1 operating between -0.336 m/s to 0.432 m/s, showcasing the system's adaptability to rapidly changing operational demands. Finally, the motor temperatures remain within a safe range, with motor 1 reaching a maximum of 28°C and motors 2 and 3 maintaining a peak of 26°C, ensuring the system operates efficiently without the risk of overheating. This detailed overview underscores the robustness and effectiveness of the control systems, highlighting their reliability and precision in managing dynamic operational conditions.

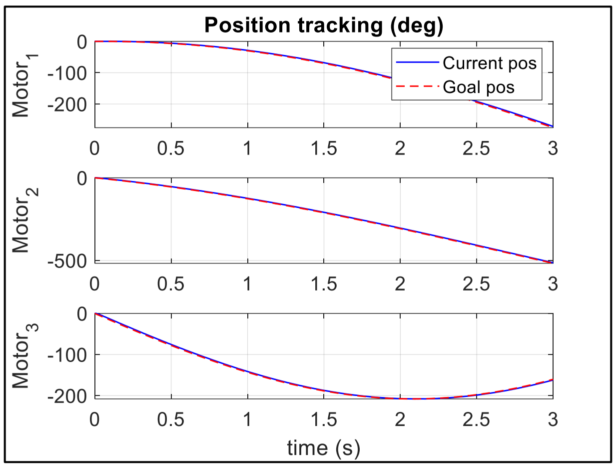

a

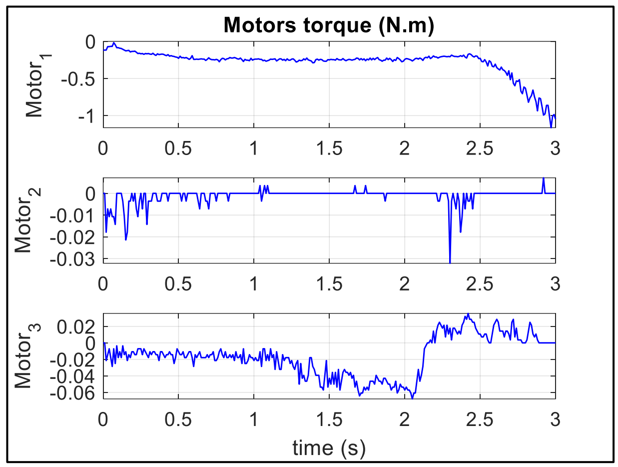

b

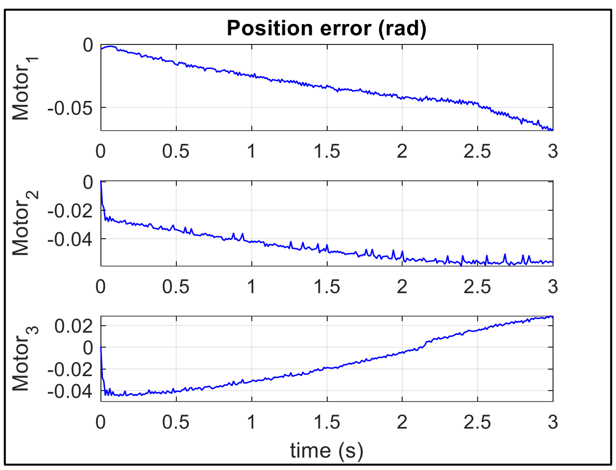

c

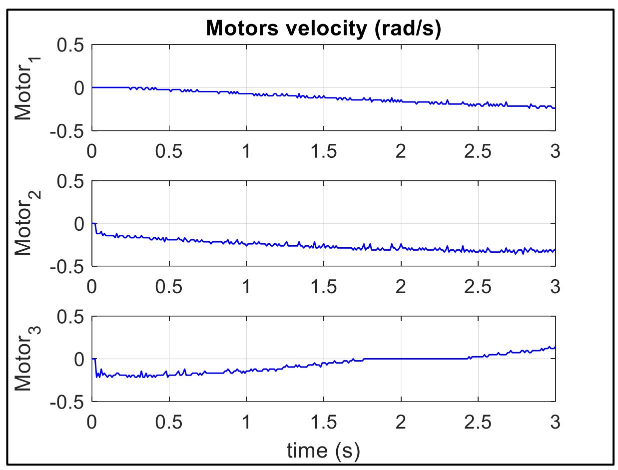

d

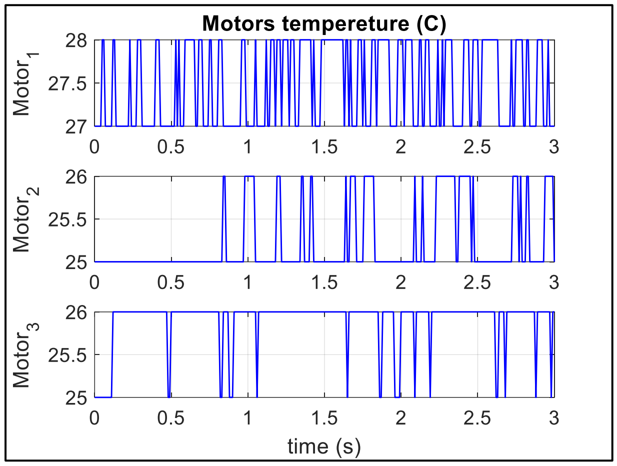

e

Figure 7-30: (a): Position tracking- (b): Torque- (c): Position error- (d): Velocity- (e): Motor temperature during the flexion movement without any extra load (FL00000_02).

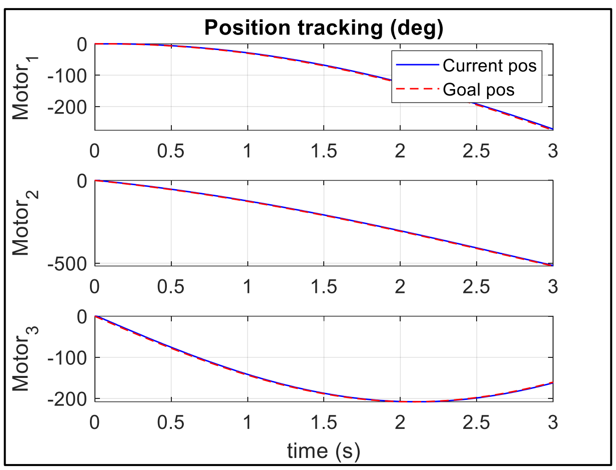

a

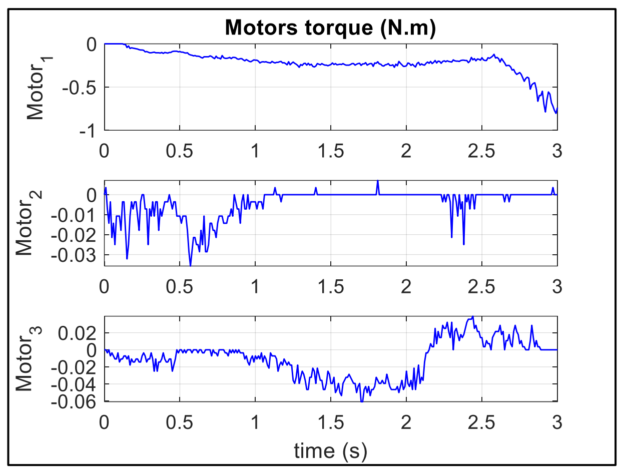

b

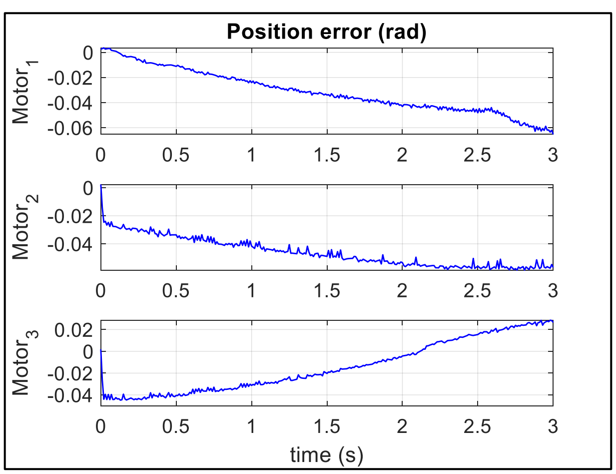

c

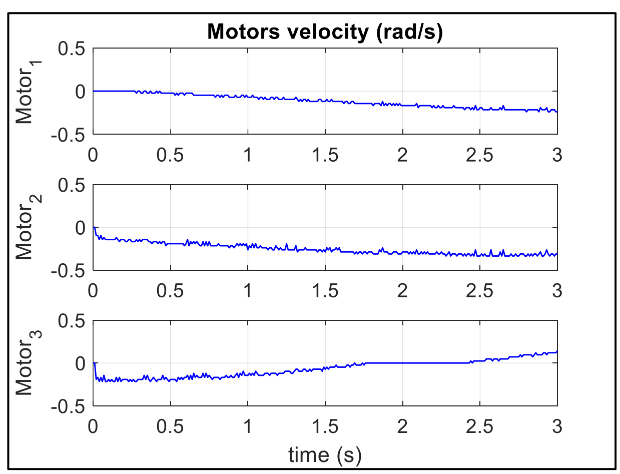

d

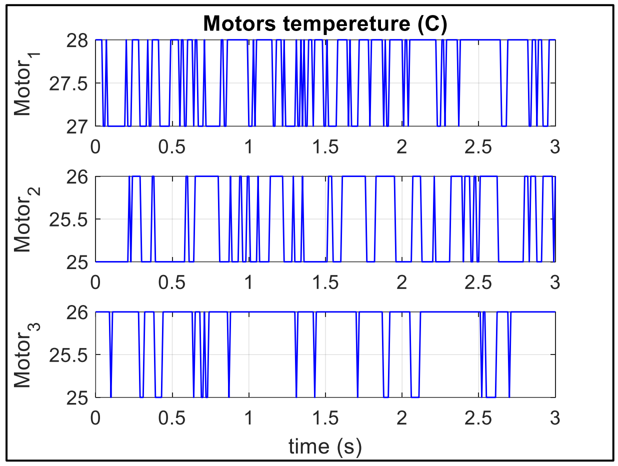

e

Figure 7-31: (a): Position tracking- (b): Torque- (c): Position error- (d): Velocity- (e): Motor temperature during the flexion movement without any extra load (FL00000_03).

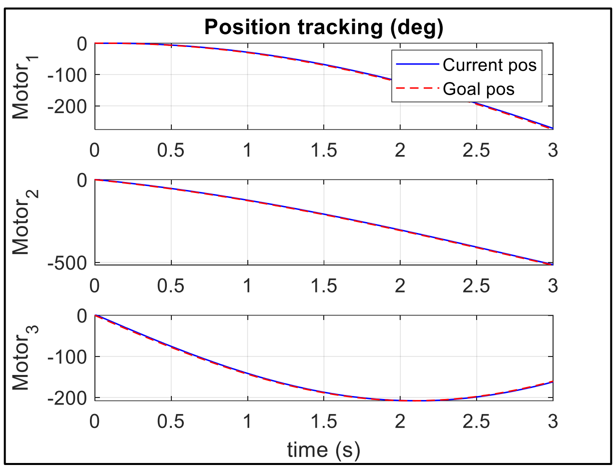

a

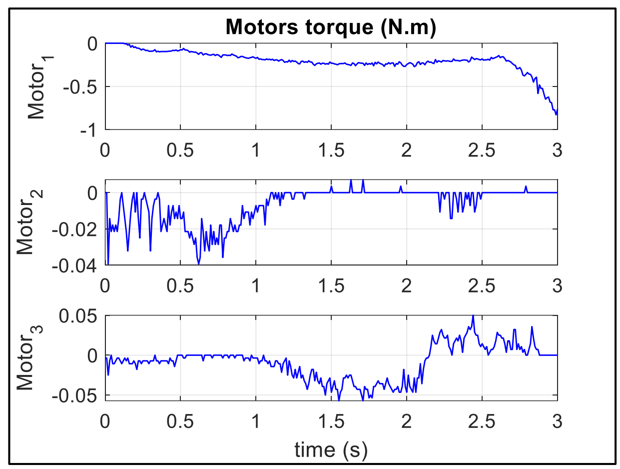

b

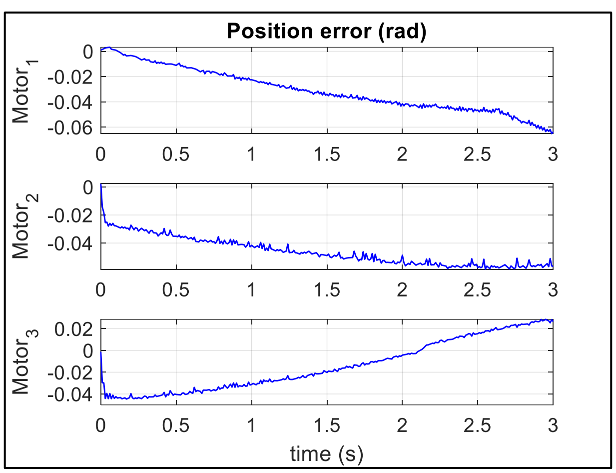

c

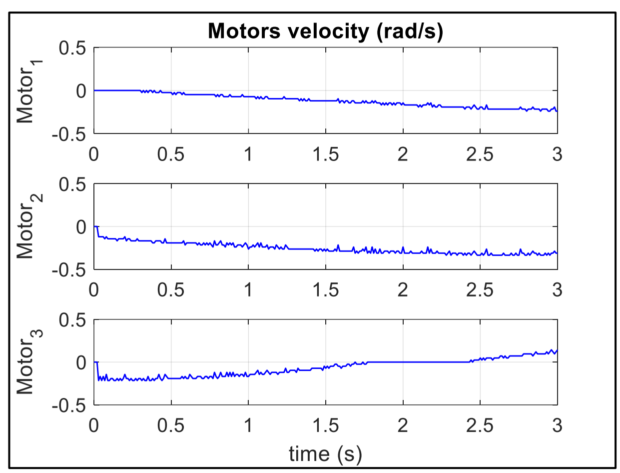

d

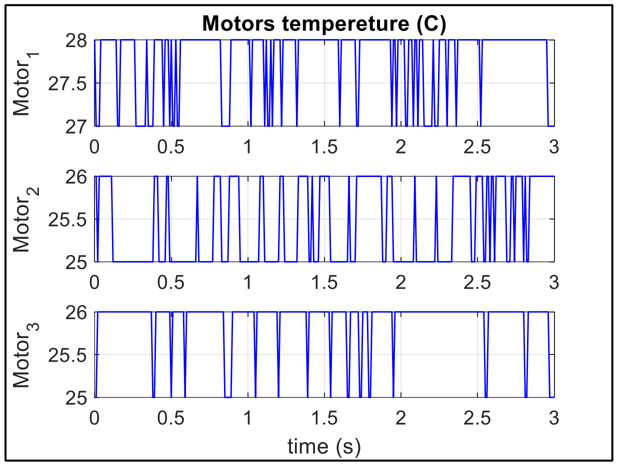

e

Figure 7-32: (a): Position tracking- (b): Torque- (c): Position error- (d): Velocity- (e): Motor temperature during the flexion movement without any extra load (FL00000_04).

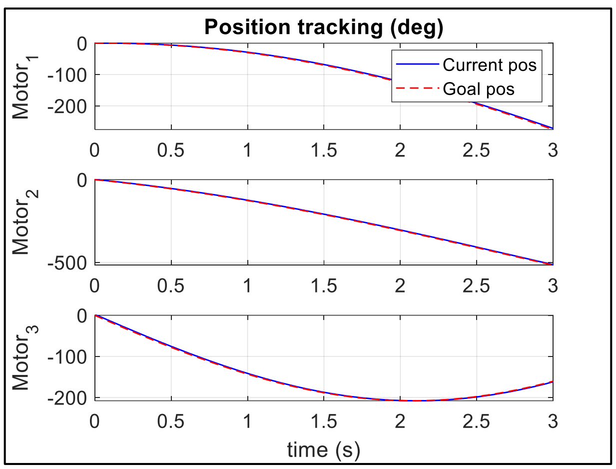

a

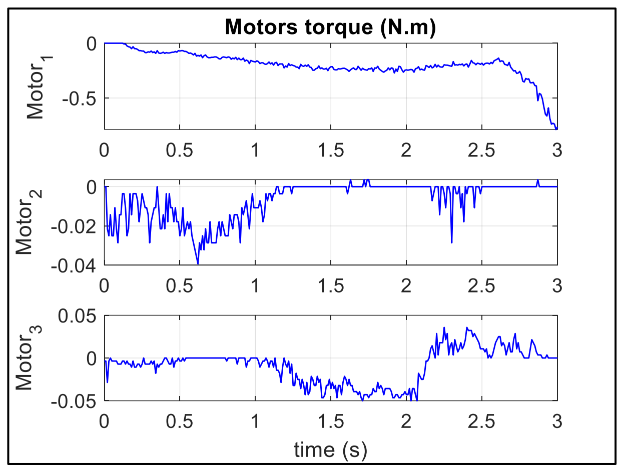

b

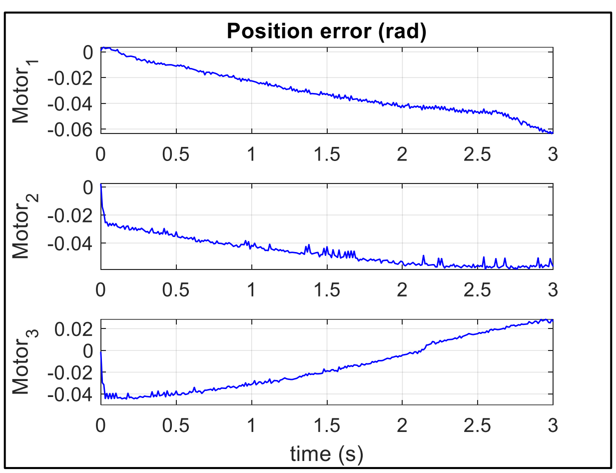

c

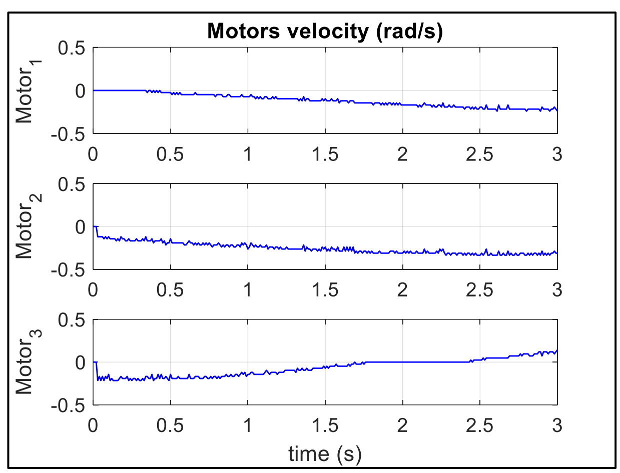

d

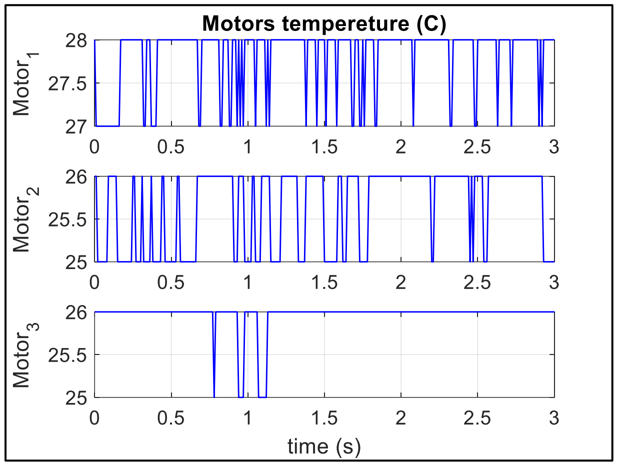

e

Figure 7-33: (a): Position tracking- (b): Torque- (c): Position error- (d): Velocity- (e): Motor temperature during the flexion movement without any extra load (FL00000_05).

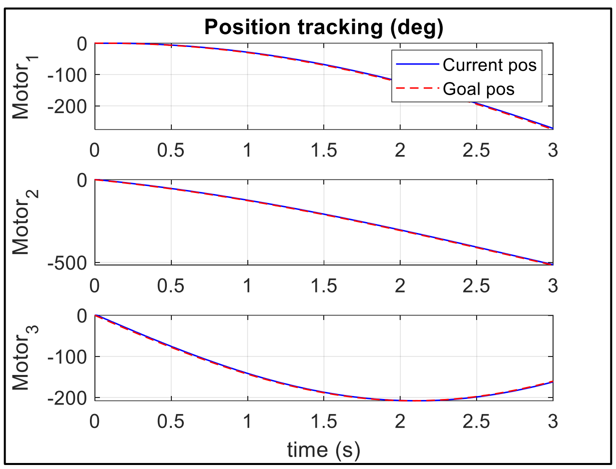

a

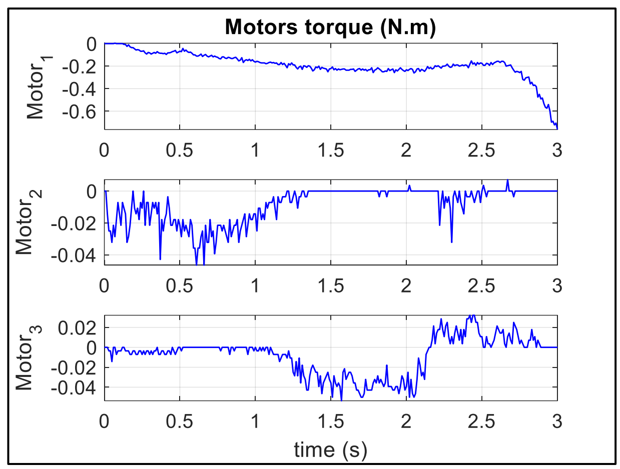

b

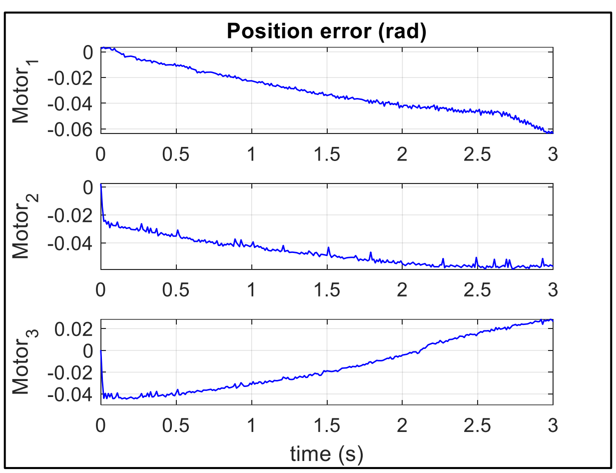

c

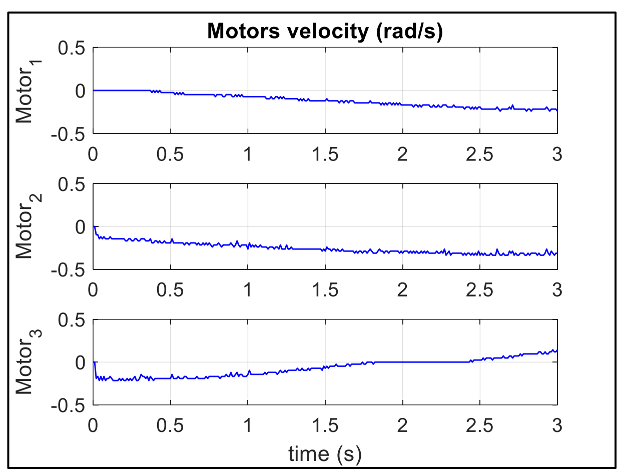

d

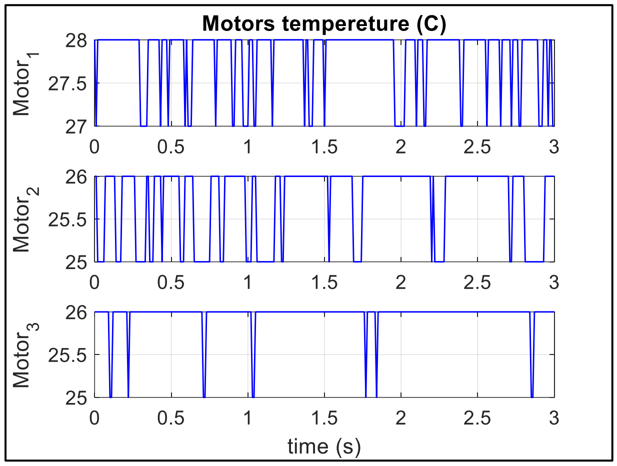

e

Figure 7-34: (a): Position tracking- (b): Torque- (c): Position error- (d): Velocity- (e): Motor temperature during the flexion movement without any extra load (FL00000_06).

In Figure 7-35 and Figure 7-36, the torque graph for the motors and position error are shown for six test modes (FL000001 to FL000006) for the flexion movement.

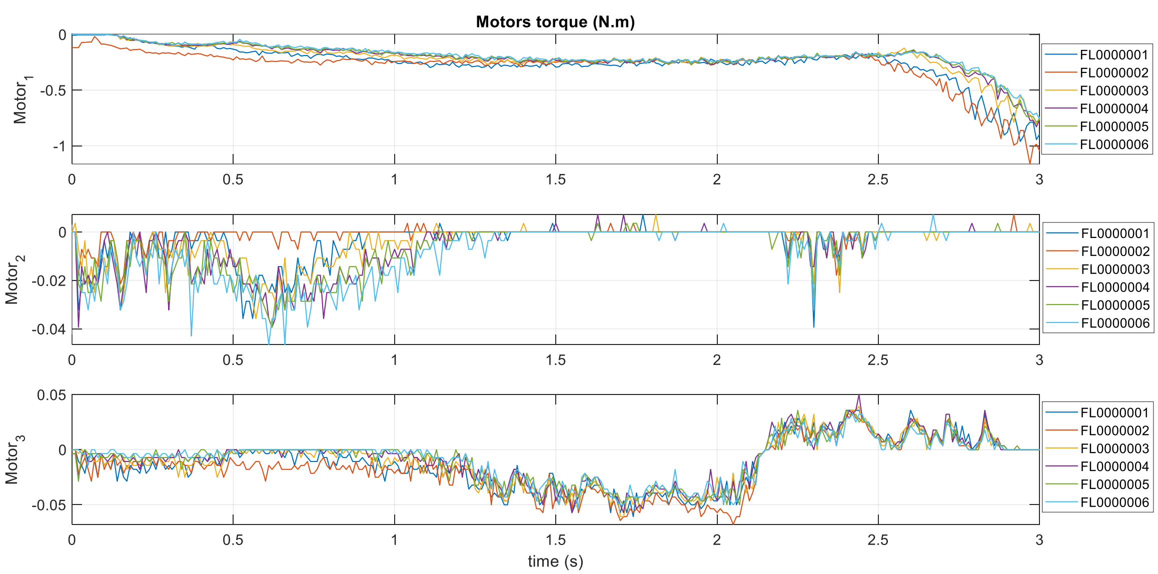

Figure 7-35: Motor torques for the six flexion experiments (FL000001 to FL000006).

Figure 7-35 shows motor 1 consistently exhibits substantial negative torque, with the minimum values ranging from -0.96 Nm in FL000001 to -0.76 Nm in FL000006, demonstrating significant load handling and operational stress with high repeatability. This motor's performance indicates a robust ability to repeatedly handle strenuous tasks without relaxing, as shown by torques rarely approaching zero. Motor 2 and motor 3, on the other hand, exhibit less extreme torque values, with minimums around -0.046 Nm and occasional peaks slightly above zero, suggesting more moderate and stable operational roles. Notably, motor 3's maximum torque reaching 0.050 Nm in FL000004 displays some variability yet within a consistently moderate range, pointing to reliable performance across tests. These torque dynamics highlight not only the differentiated roles and stress profiles of the motors but also the repeatability of their performance under varying conditions. Motor 1’s enduring capacity for higher operational demands and the reliable contributions of motors 2 and 3 illustrate how the system efficiently allocates mechanical stress across the motors, ensuring stable performance and operational durability over repeated tests.

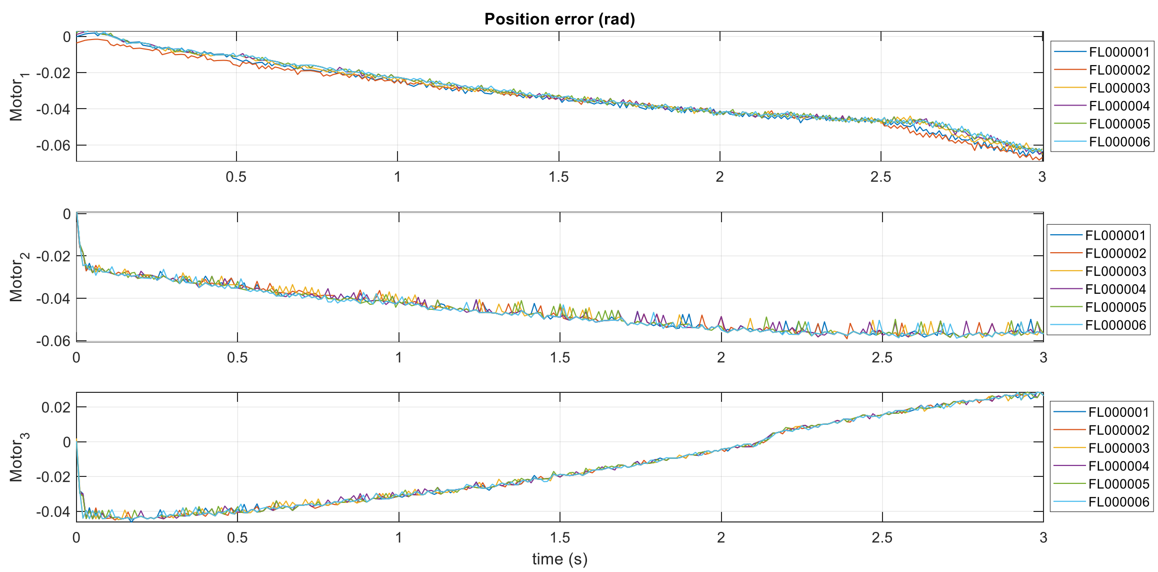

Figure 7-36: Position error for the six flexion experiments (FL000001 to FL000006).

The position error data for three motors show a range of behaviours over 3 seconds. The most significant deviation occurs with motor 1 in the FL00000_04, which experiences a maximum position error of approximately -0.0681. Conversely, motor 3 in FL00000_01 demonstrates nearly ideal performance with a minimal error of about 0.000349. These values, while varied, fall within acceptable limits for position error in many mechanical and control systems. Such deviations are typical in real-world applications, indicating that the systems are generally performing well. The data suggests that while occasional peaks in error occur, the overall stability and accuracy of the motors are maintained, supporting satisfactory operational efficiency and reliability.

7.5.4 Experiment in Flexion Movement (from 500 g to 4000 g weight)

Figure 7-37 illustrates the neutral position for flexion movement, incrementally adding weights from 500 grams to 4000 grams in 500-gram intervals. This experiment was conducted in eight distinct phases to analyse the designed robot's performance under conditions of varying load.

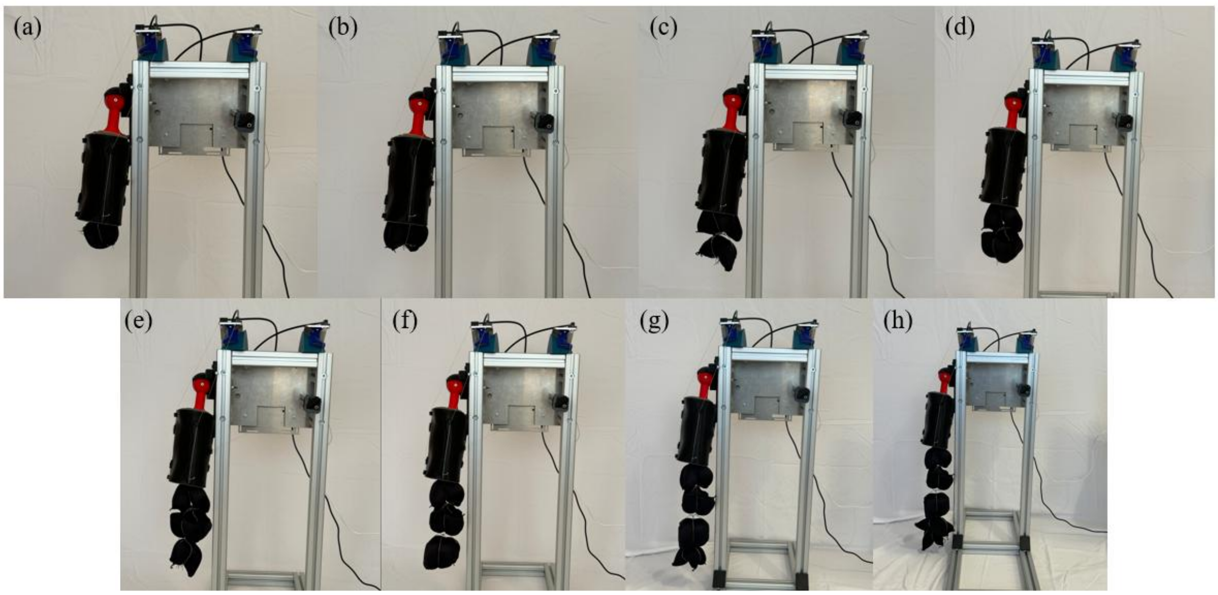

Figure 7-37: Neutral position for flexion movement, incrementally adding weights from 500 grams to 4000 grams in 500-gram intervals: (a): 500 g - (b): 1000g – (c): 1500 g – (d): 2000 g – (e): 2500 g – (f): 3000 g – (g): 3500 g - (h): 4000 g.

Figure 7-38 shows the outcomes of the movement across the eight modes under consideration, whilst Figure 7-39, Figure 7-40, Figure 7-41, Figure 7-42, Figure 7-43, Figure 7-44, Figure 7-45, and Figure 7-46 illustrate position tracking, torque, position error, velocity, motor temperature during the flexion movement under 500g to 4000g load, respectively.

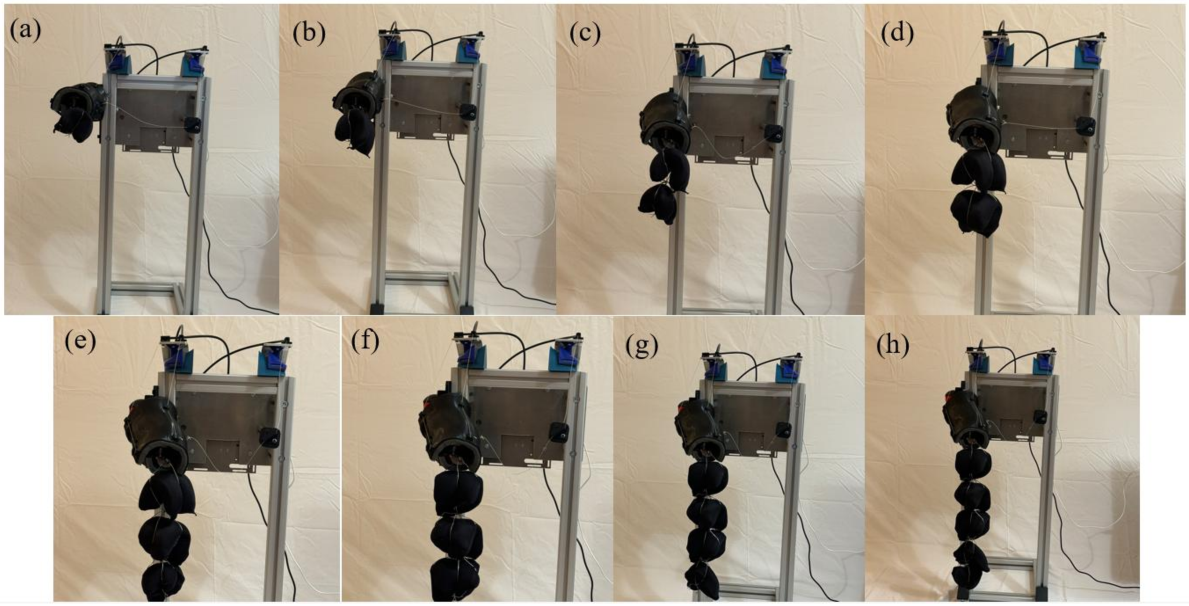

Figure 7-38: Flexion position, incrementally adding weights from 500 grams to 4000 grams in 500-gram intervals: (a): 500 g - (b): 1000g – (c): 1500 g – (d): 2000 g – (e): 2500 g – (f): 3000 g – (g): 3500 g - (h): 4000 g.

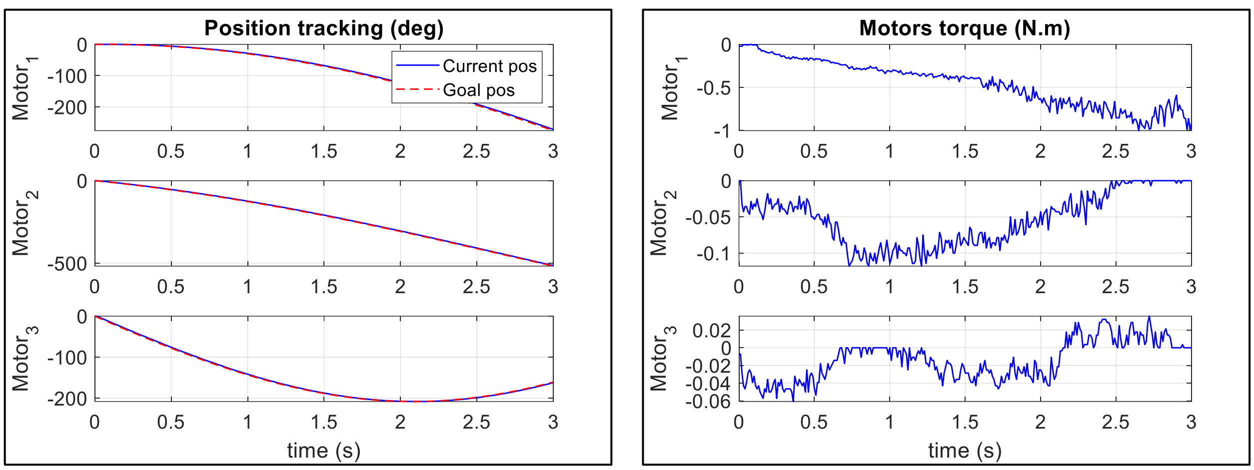

a

b

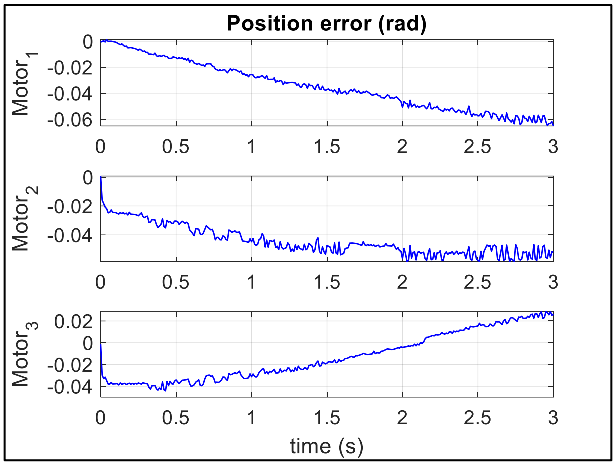

c

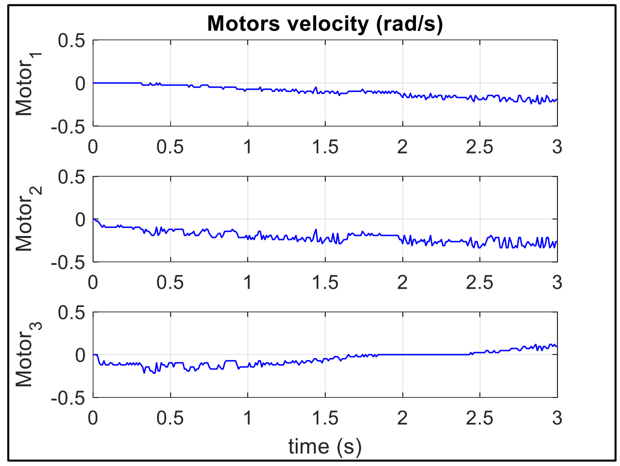

d

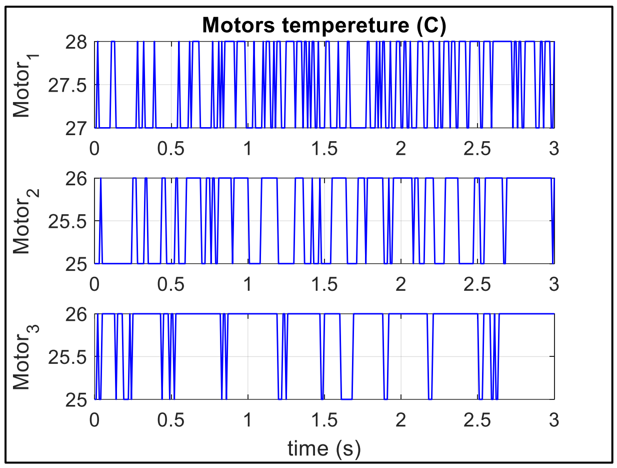

e

Figure 7-39: (a): Position tracking- (b): Torque- (c): Position error- (d): Velocity- (e): Motor temperature during the flexion movement with a 500g load (FL00500_01).

The gaol position is very well tracked by the robot. Also, the amount of torque of each engine is shown, and the amount of positional error is reported to be very small, and this shows the proper control of the motors.

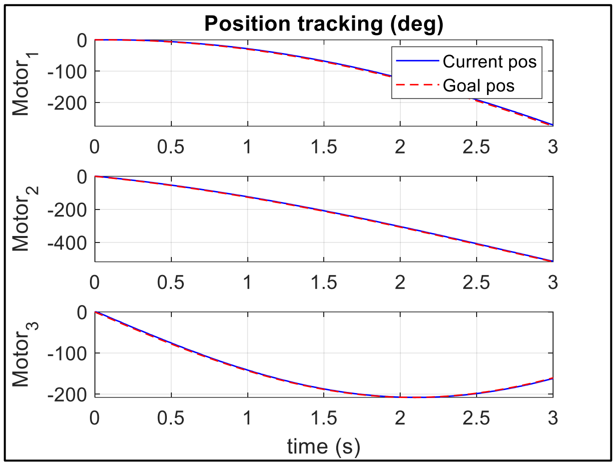

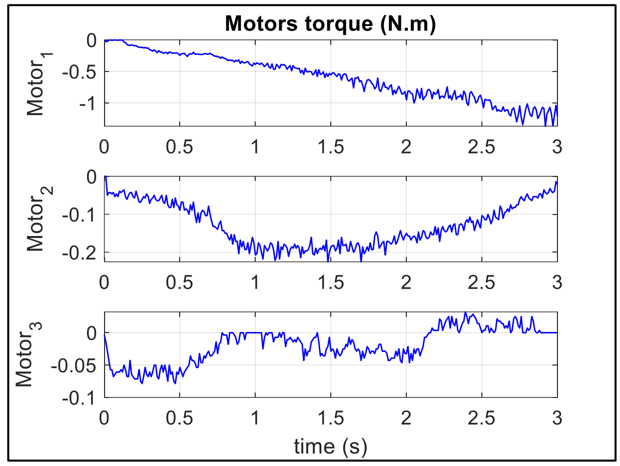

a

b

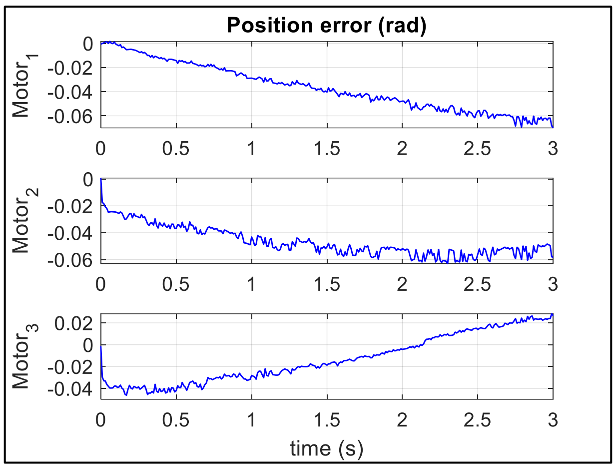

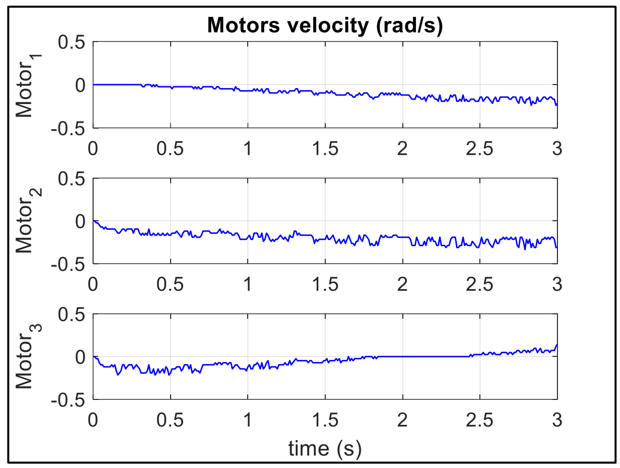

c

d

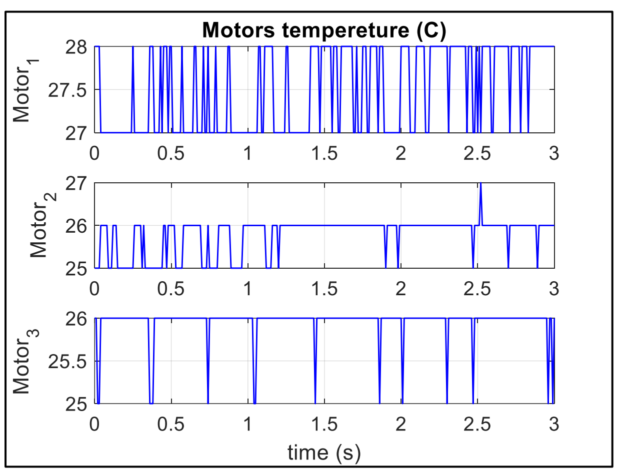

e

Figure 7-40: (a): Position tracking- (b): Torque- (c): Position error- (d): Velocity- (e): Motor temperature during the flexion movement with a 1000 g load (FL01000_01).

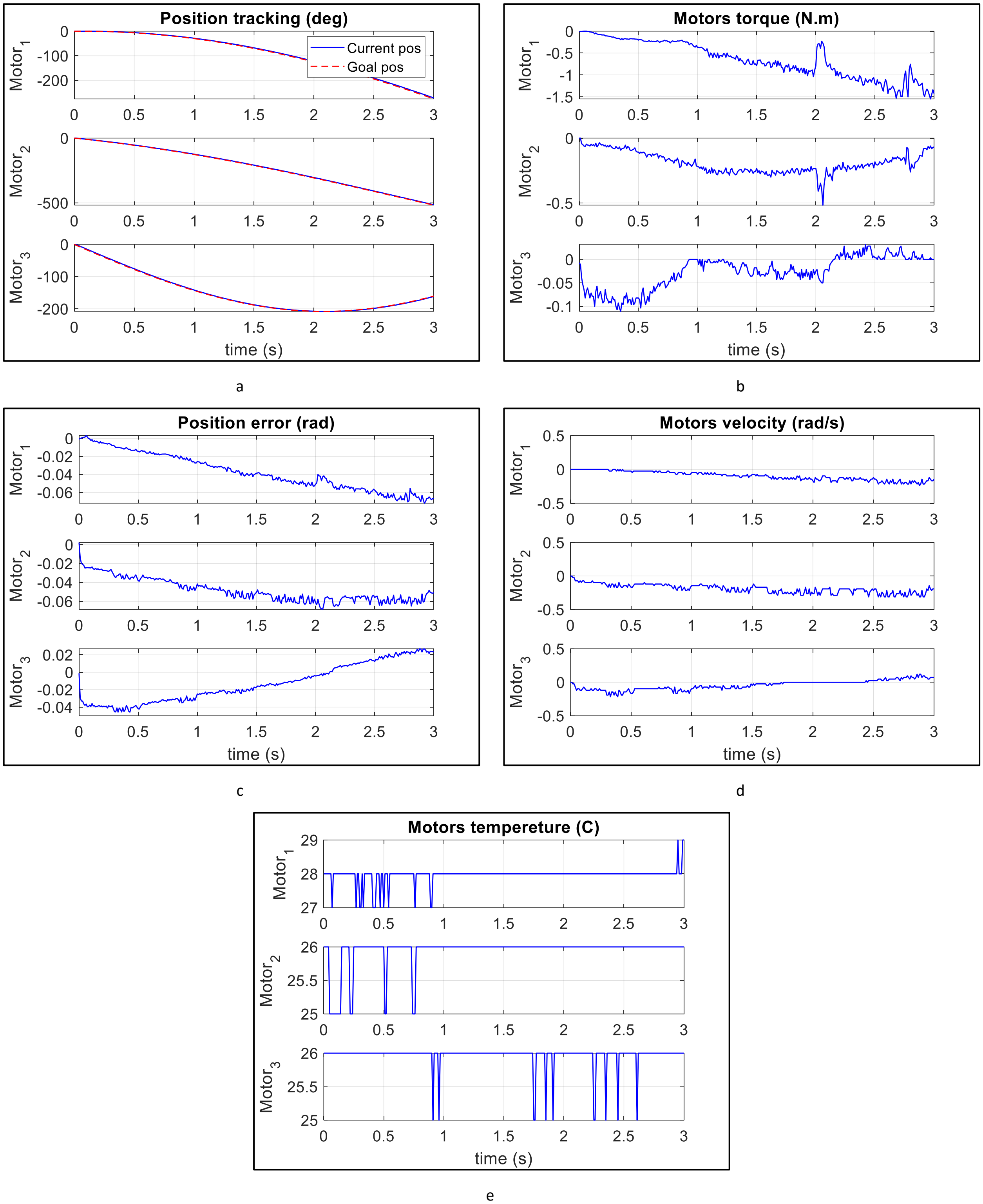

Figure 7-41: (a): Position tracking- (b): Torque- (c): Position error- (d): Velocity- (e): Motor temperature during the flexion movement with a 1500 g load (FL01500_01).

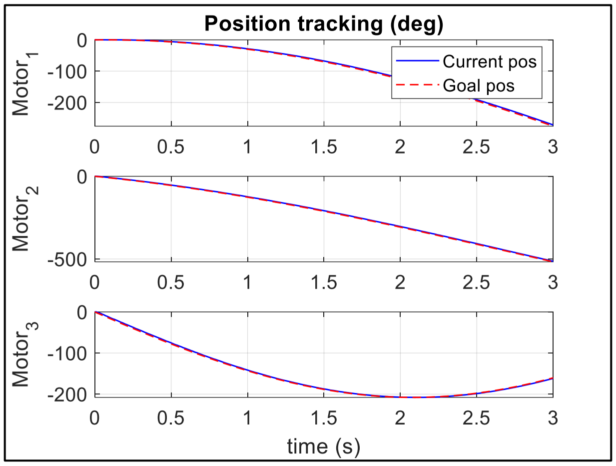

a

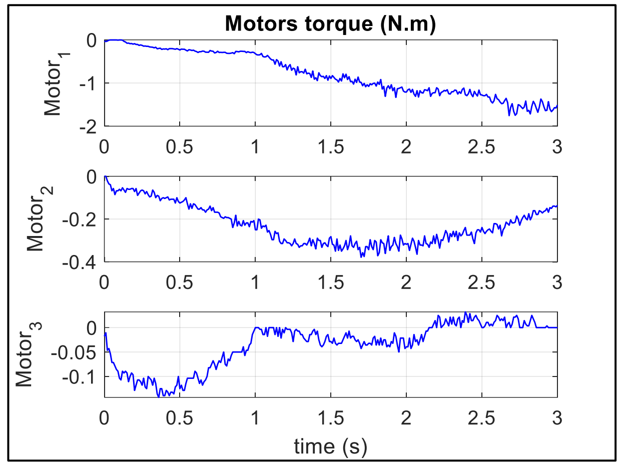

b

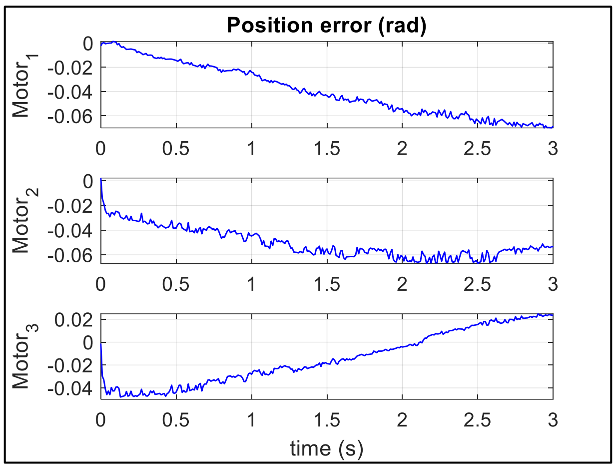

c

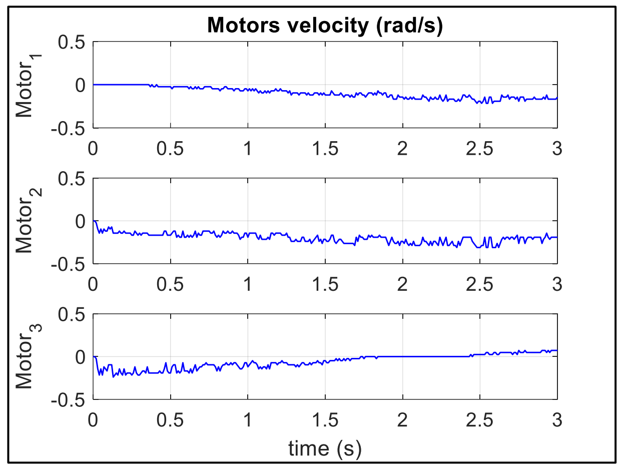

d

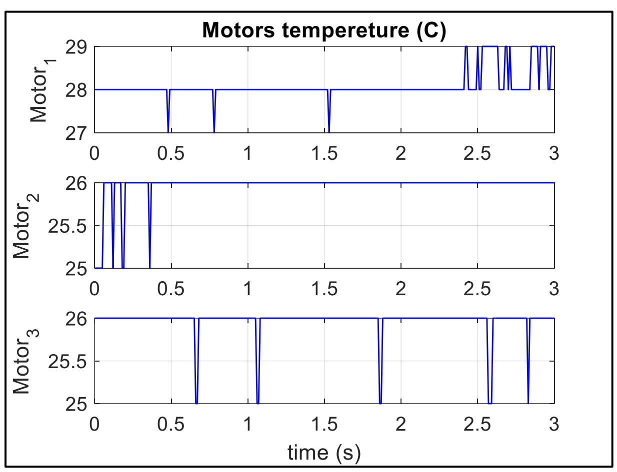

e

Figure 7-42: (a): Position tracking- (b): Torque- (c): Position error- (d): Velocity- (e): Motor temperature during the flexion movement with a 2000 g load (FL02000_01).

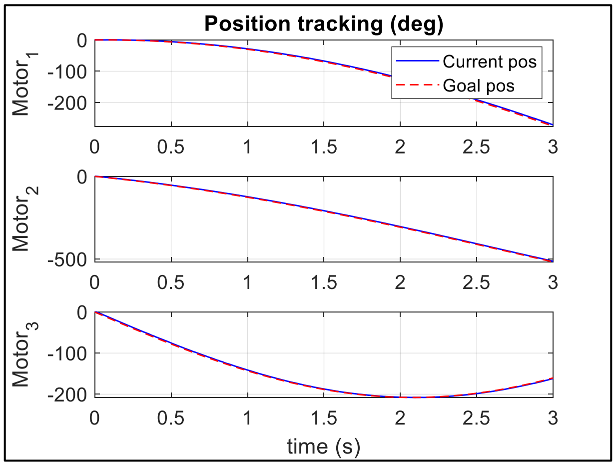

a

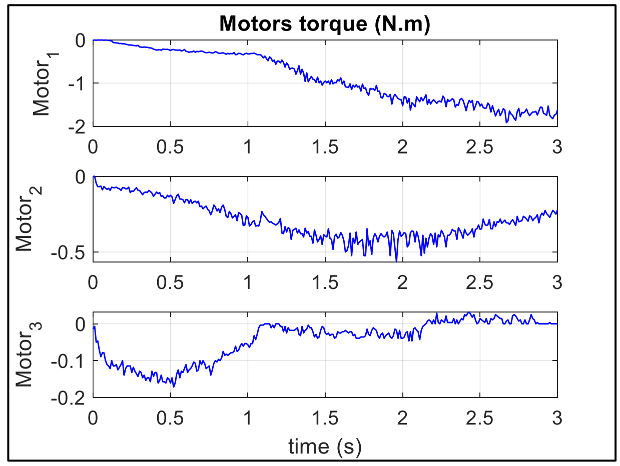

b

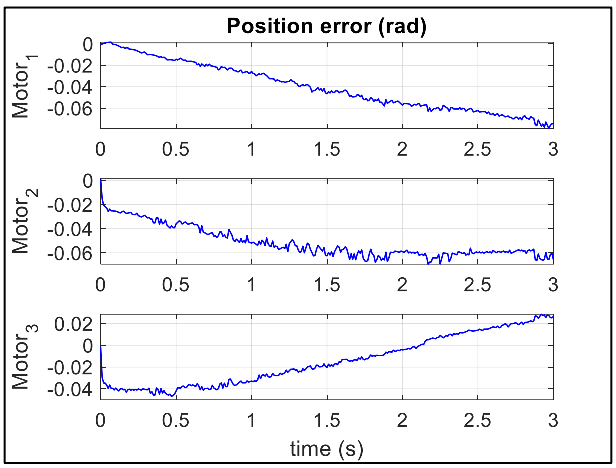

c

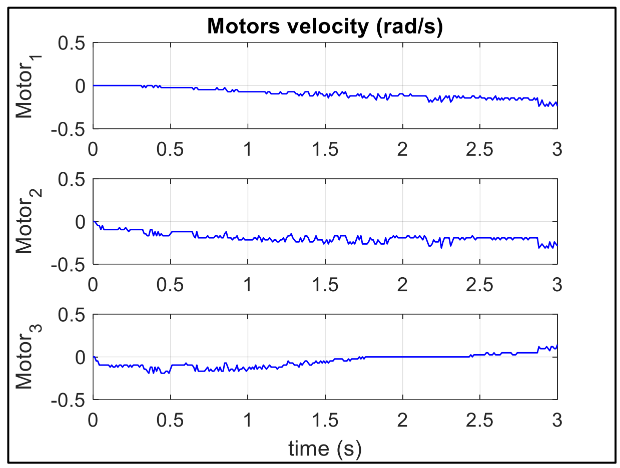

d

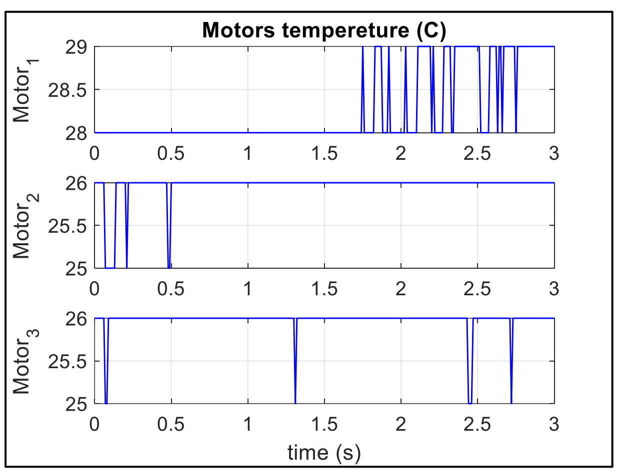

e

Figure 7-43: (a): Position tracking- (b): Torque- (c): Position error- (d): Velocity- (e): Motor temperature during the flexion movement with a 2500 g load (FL02500_01).

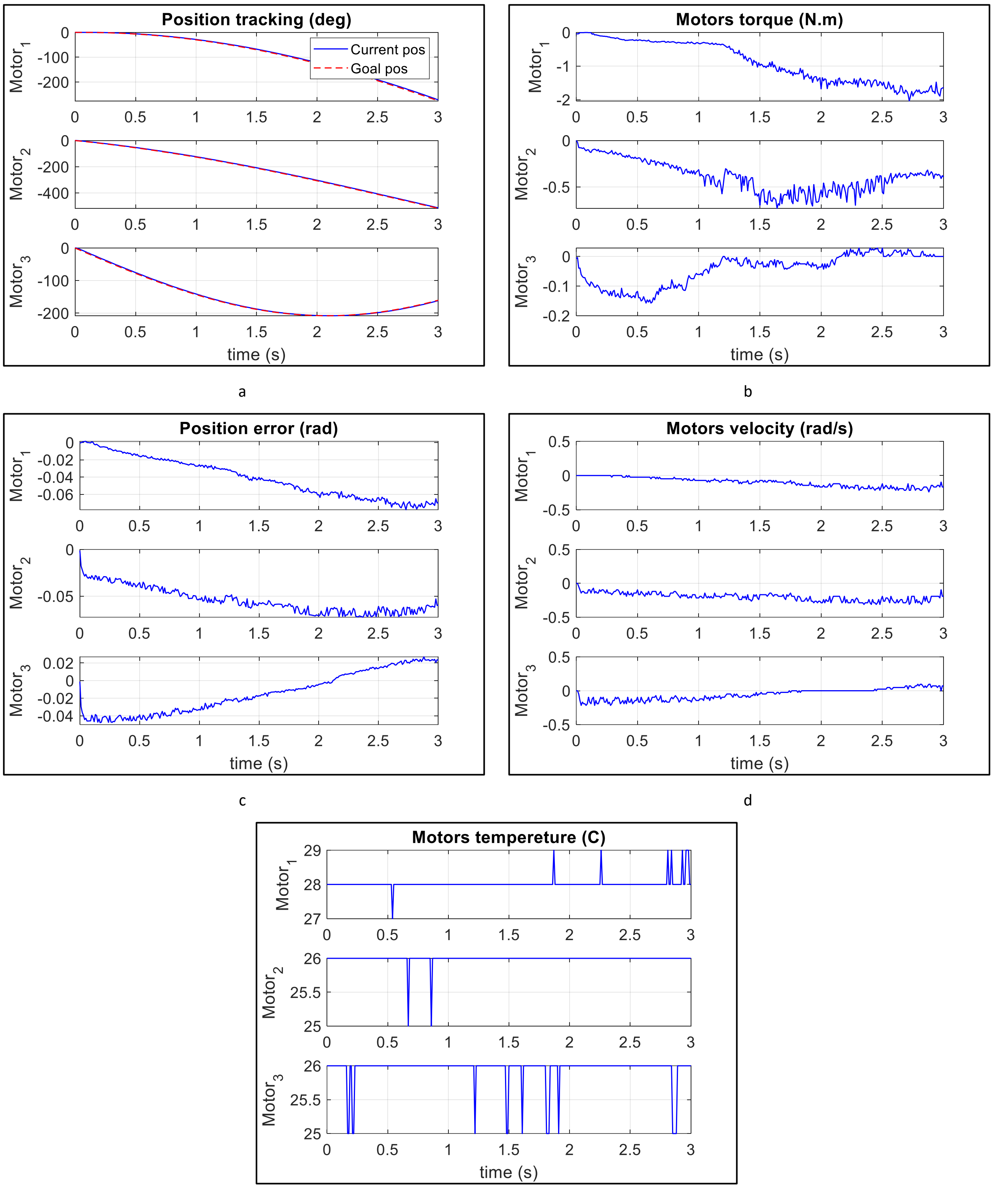

Figure 7-44: (a): Position tracking- (b): Torque- (c): Position error- (d): Velocity- (e): Motor temperature during the flexion movement with a 3000 g load (FL03000_01).

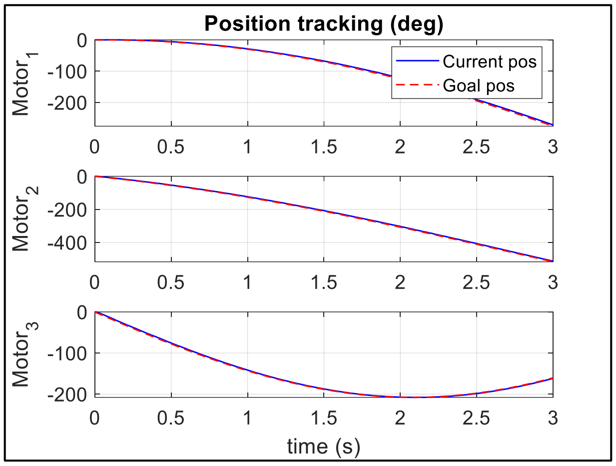

a

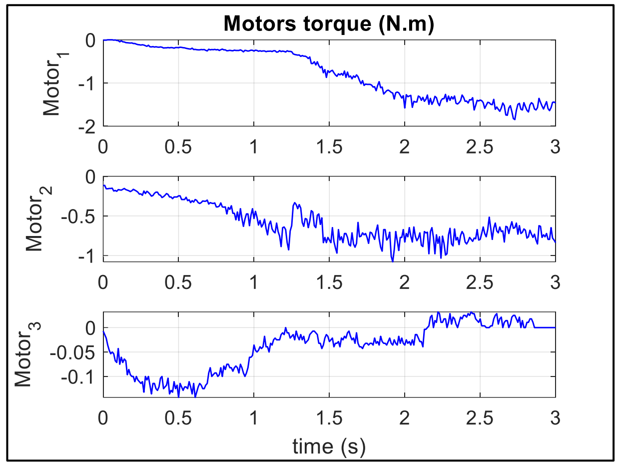

b

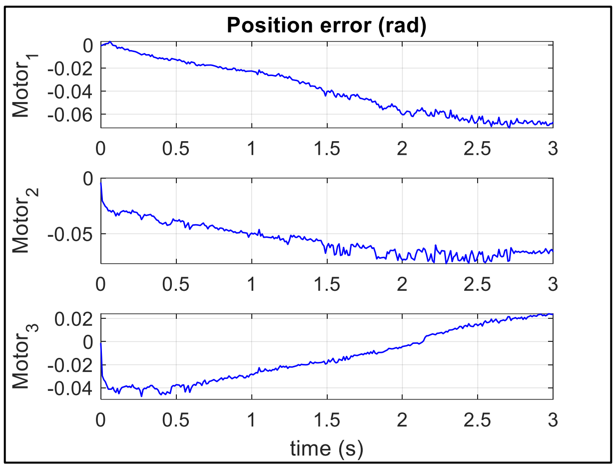

c

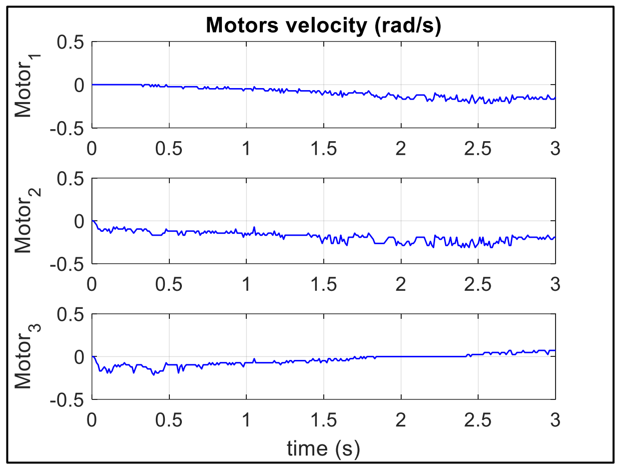

d

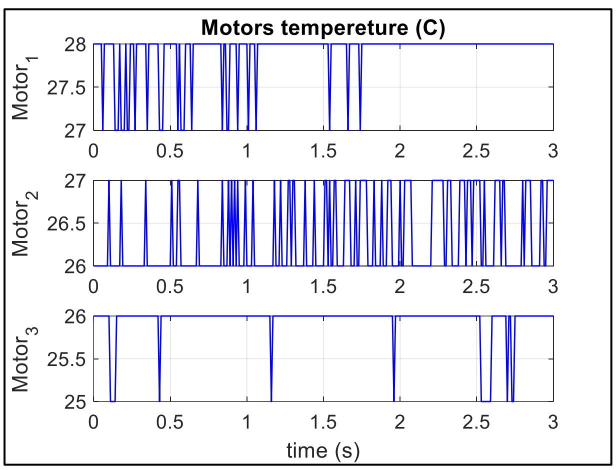

e

Figure 7-45: (a): Position tracking- (b): Torque- (c): Position error- (d): Velocity- (e): Motor temperature during the flexion movement with a 3500 g load (FL03500_01).

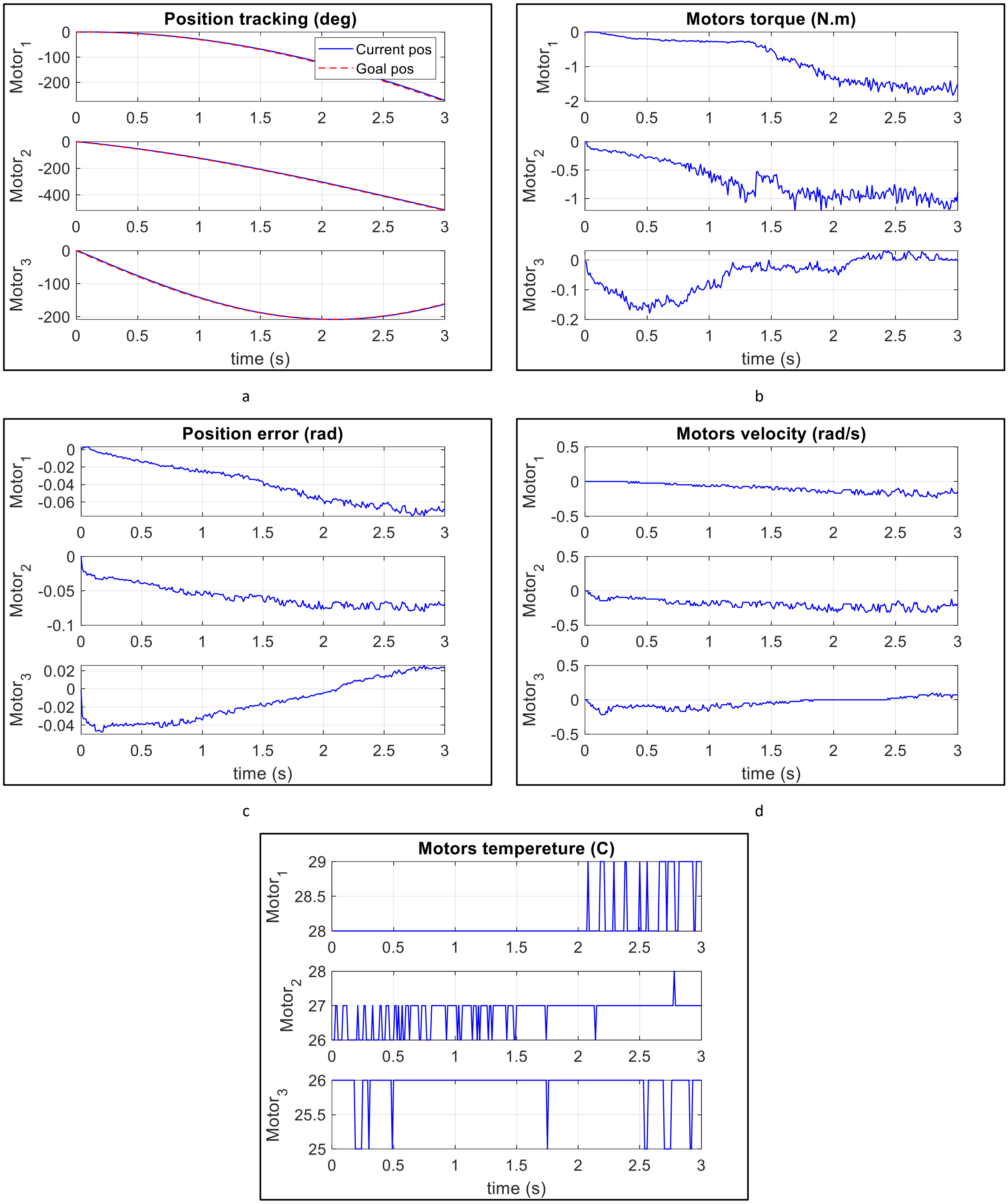

Figure 7-46: (a): Position tracking- (b): Torque- (c): Position error- (d): Velocity- (e): Motor temperature during the flexion movement with a 4000 g load (FL04000_01).

In Figure 7-47, the torque graph for the motors is shown for eight test modes (FL005001 to FL040001) for the flexion movement.

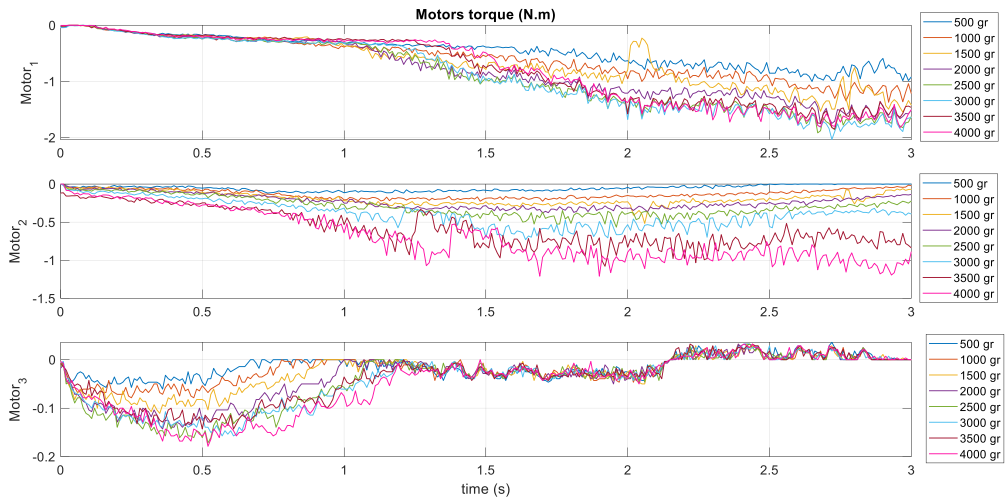

Figure 7-47: Motor torques for the eight flexion experiments (500 g to 4000 g).

Upon closely reviewing the torque data illustrated in Figure 7-47, we identified the corrected extreme torque values across various motors. In 500 g loading, the torque reaches a maximum of 0.036 and dips to a minimum of -1.002, showcasing a significant operational range. Similarly, 1000 g loading records a maximum torque of 0.032 and a minimum of -1.371. As we progress through the series, the minimum torque generally decreases, indicating higher stress levels; for instance, in 3000 g loading logs a low of -2.035. In the case of 4000 g loading, the torque peaks at 0.032 and bottoms out at -1.824.

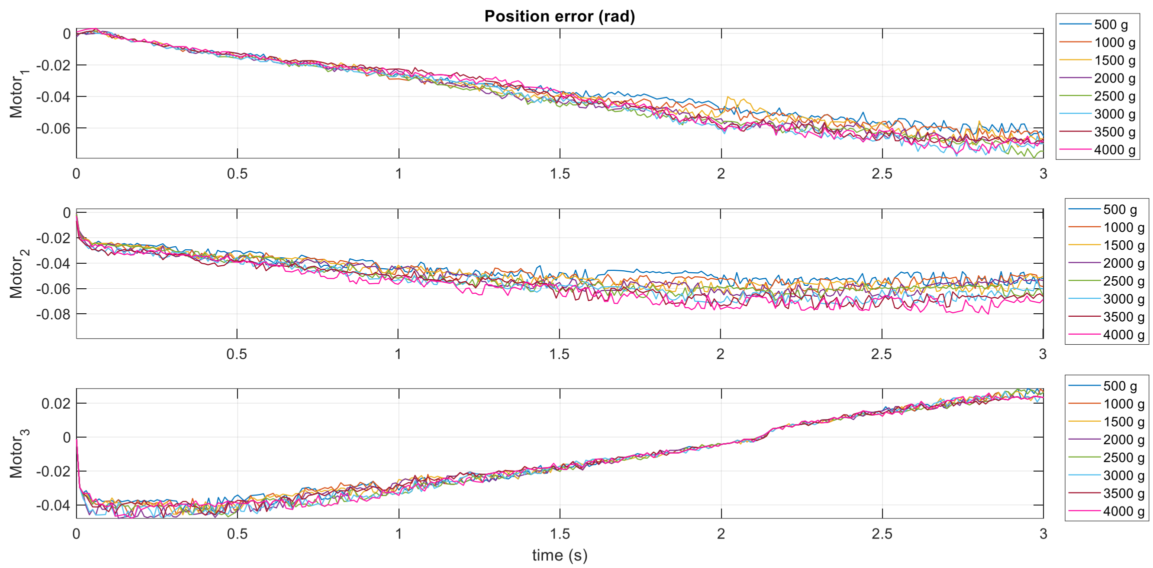

Figure 7-48: Position error for the eight flexion experiments (500 g to 4000 g).

Figure 7-48 shows, it's clear that the position errors exhibit a substantial range across different operational settings. For instance, in 500 g loading shows a maximum error of approximately 0.029 and a minimum of -0.065, while in 4000 g loading records errors as severe as -0.080, the largest negative deviation among the datasets. Despite these variations, such position errors are generally considered acceptable in many industrial applications, indicating that the motors are operating within expected tolerance levels. The maximum errors remain relatively low (around 0.025 to 0.029), and even the minimum errors, though negative, reflect typical performance under variable load conditions. This consistency across data points confirms that the system is stable and maintains reliability, demonstrating that the motors are well-controlled and operate effectively within their designed parameters.

7.5.5 Experiment for Repeatability in Horizontal Flexion Movement

In this section, the repeatability test for the horizontal flexion movement was performed by repeating this test six times. Figure 7-49 shows the zero position and the final position of the arm, i.e., before and after the test.

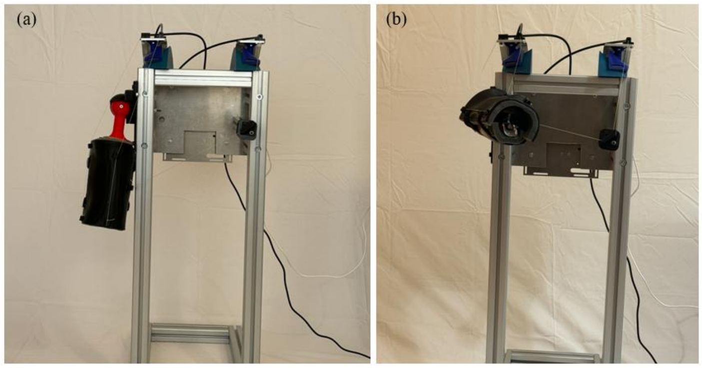

Figure 7-49: The zero position(a) and the final position (b) of the arm during the horizontal flexion test.

Figure 7-50 shown the results from the initial horizontal flexion test, which encompass the trajectory followed by the robot during horizontal flexion, as well as measurements of torque, position error, velocity, and motor temperature incurred during the execution this motion. In Figure 7-51, Figure 7-52, Figure 7-53, Figure 7-54, and Figure 7-55, the results of the tests performed for the second to sixth tests are shown in order.

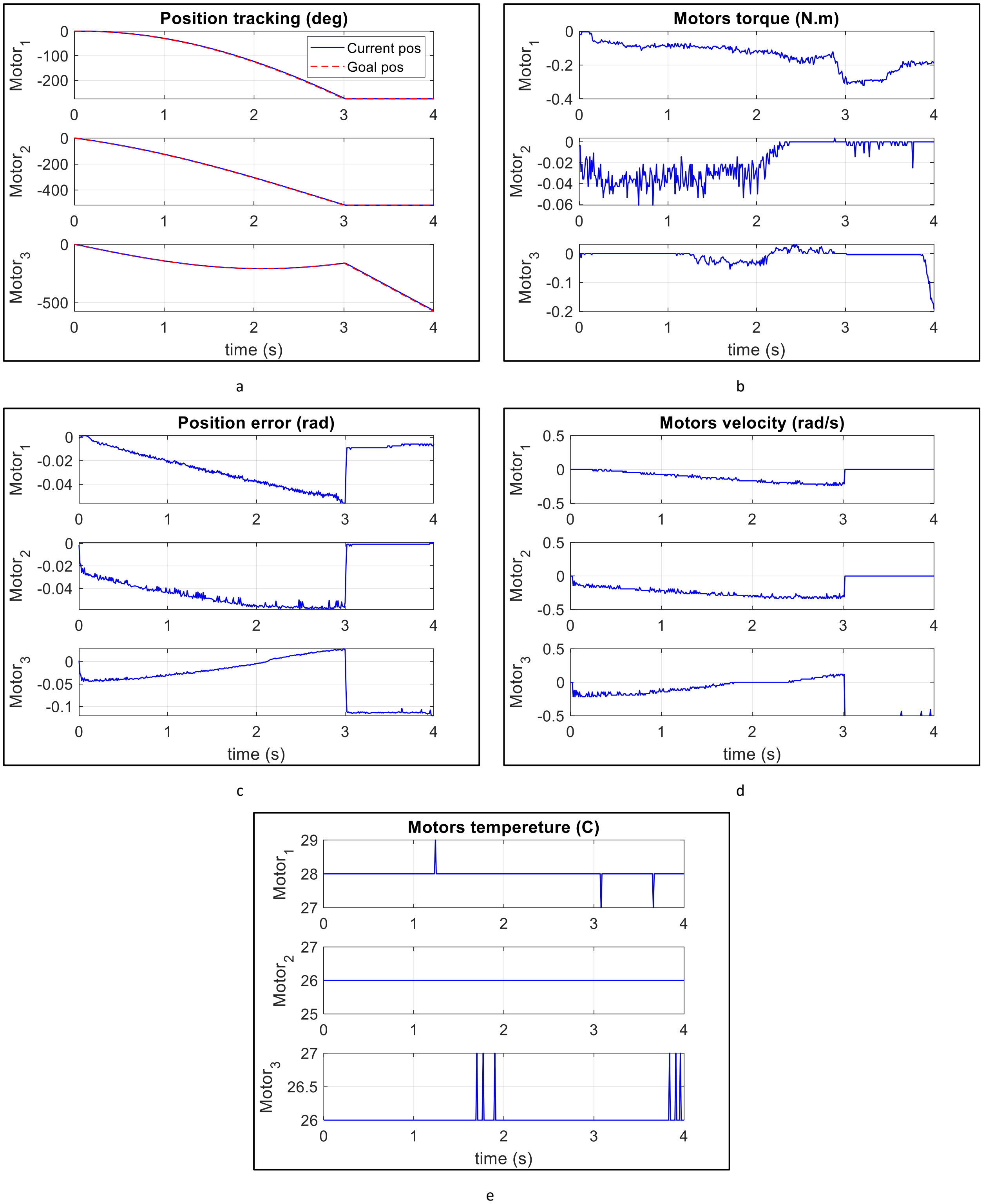

Figure 7-50: (a): Position tracking- (b): Torque- (c): Position error- (d): Velocity- (e): Motor temperature during the horizontal flexion movement without any extra load (HF00000_01).

The comprehensive analysis of HF00000_01 across various data highlights the operational characteristics and efficiency of the motors. The torque measurements indicate that motor 1 operates within a range from approximately -0.322 to -0.004, motor 2 from -0.061 to 0.004, and motor 3 from -0.193 to 0.032, suggesting robust performance under varying loads. The maximum position errors are minimal, with motor 1 at 0.0012, motor 2 at 0.0008, and motor 3 at 0.029, demonstrating precision in tracking and control. Velocity analysis shows motor 3 experiencing the broadest range, from -0.576 to 0.120, indicating its capability to handle rapid operational changes. The temperatures are well-managed with motor 1 peaking at 29°C, motor 2 at 26°C, and motor 3 at 27°C, ensuring the motors operate within safe thermal limits. This data underscores the motors' reliability and effective performance management, essential for maintaining optimal operational conditions and foreseeing maintenance needs.

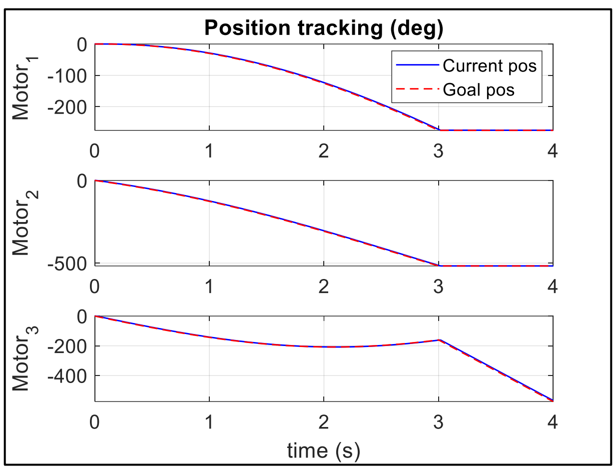

a

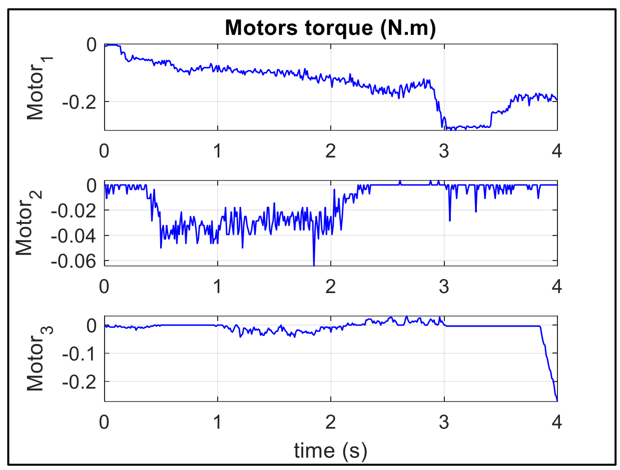

b

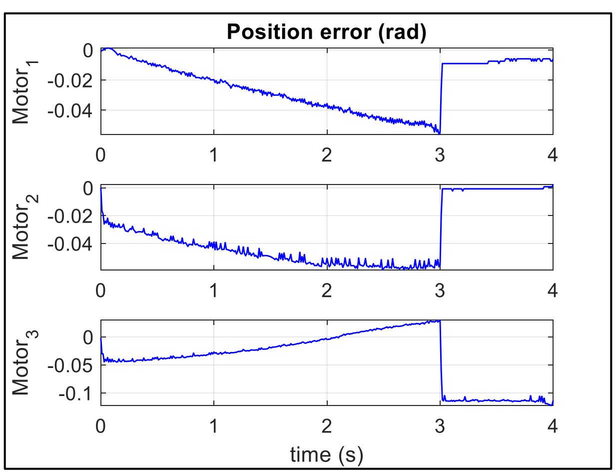

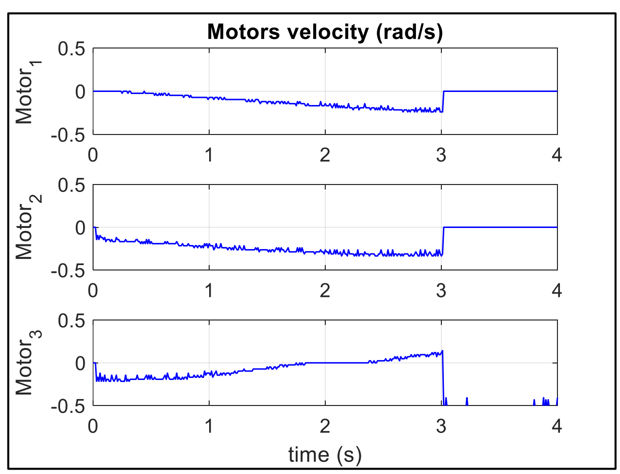

c d

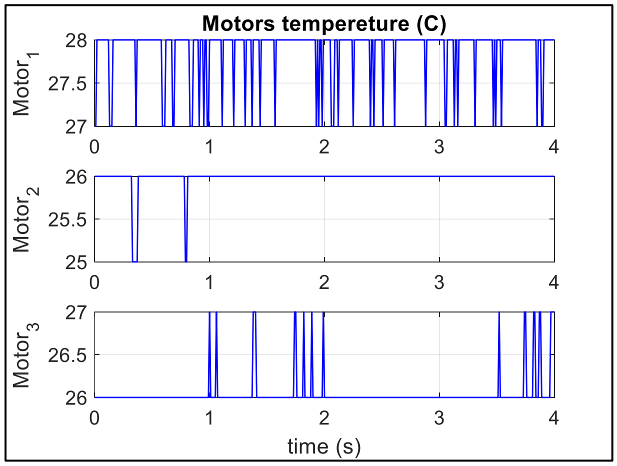

e

Figure 7-51: (a): Position tracking- (b): Torque- (c): Position error- (d): Velocity- (e): Motor temperature during the horizontal flexion movement without any extra load (HF00000_02).

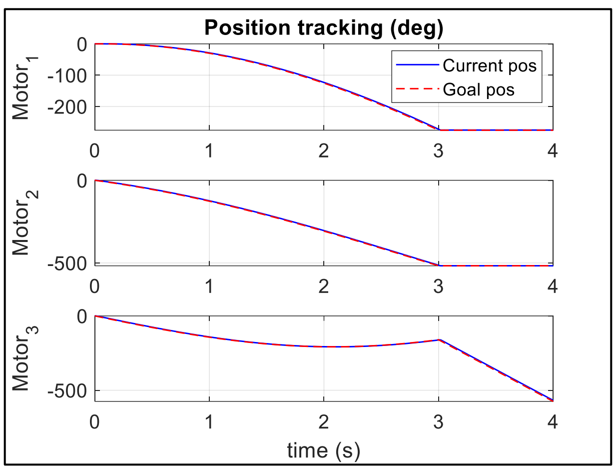

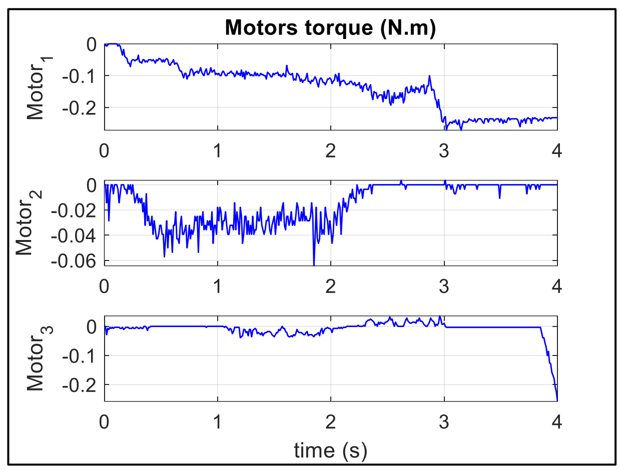

a b

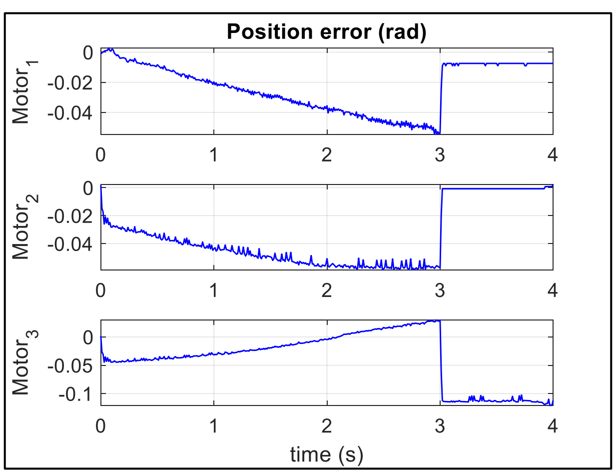

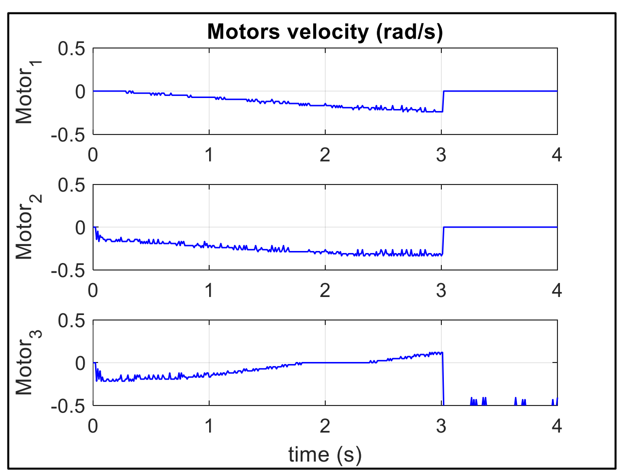

c d

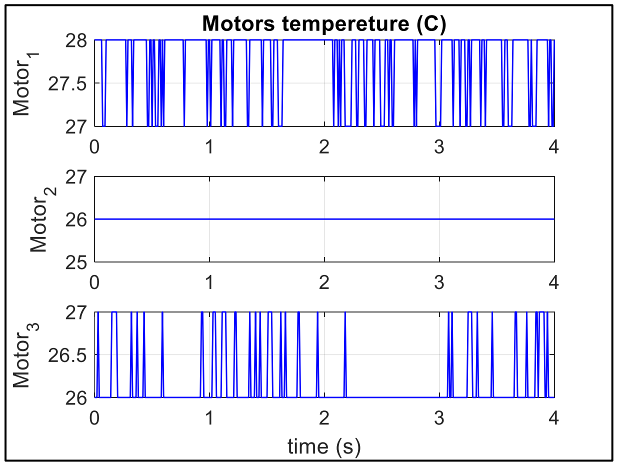

e

Figure 7-52: (a): Position tracking- (b): Torque- (c): Position error- (d): Velocity- (e): Motor temperature during the horizontal flexion movement without any extra load (HF00000_03).

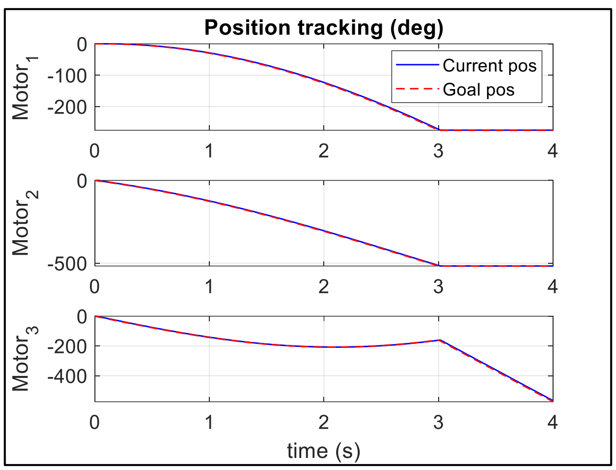

a

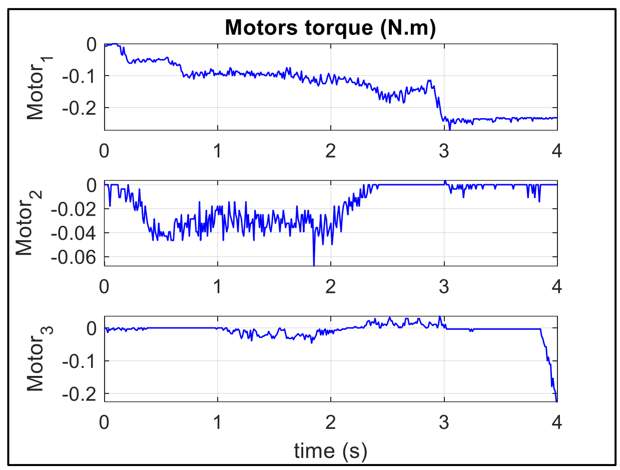

b

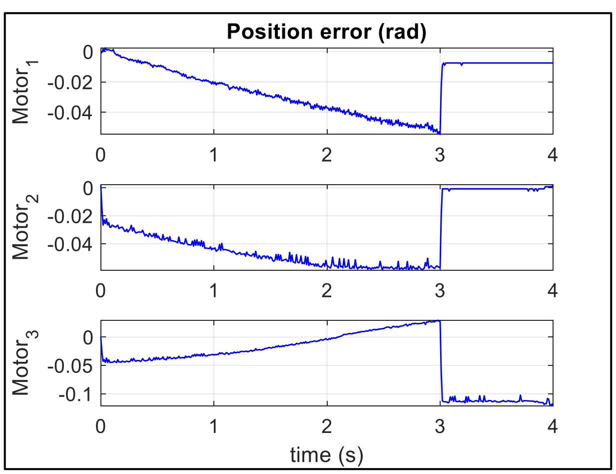

c

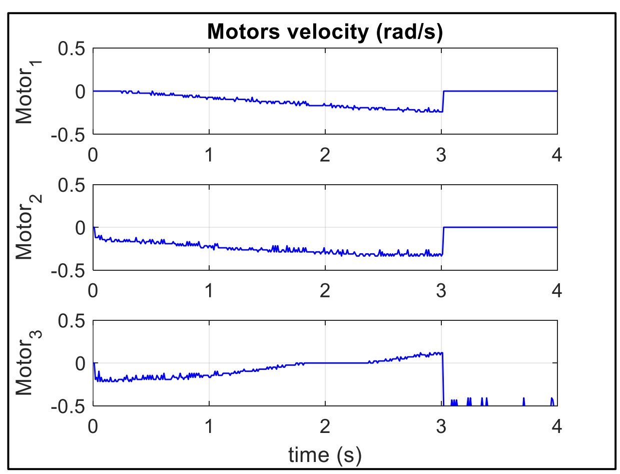

d

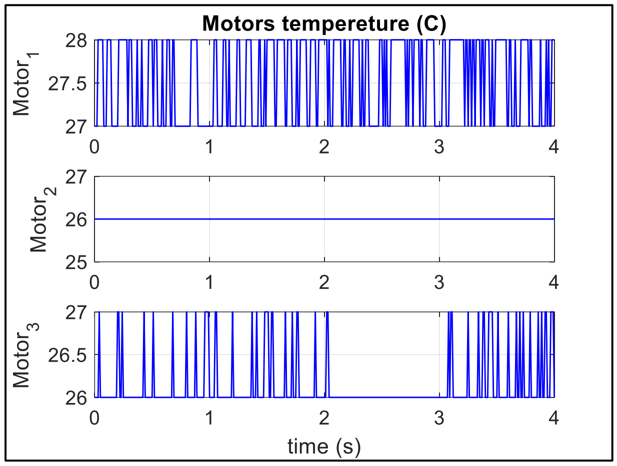

e

Figure 7-53: (a): Position tracking- (b): Torque- (c): Position error- (d): Velocity- (e): Motor temperature during the horizontal flexion movement without any extra load (HF00000_04).

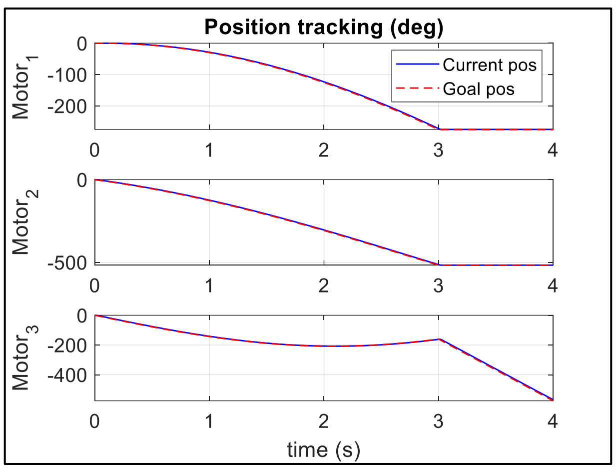

a

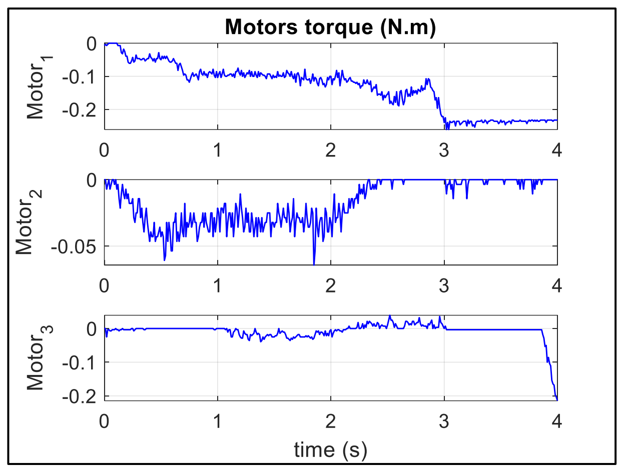

b

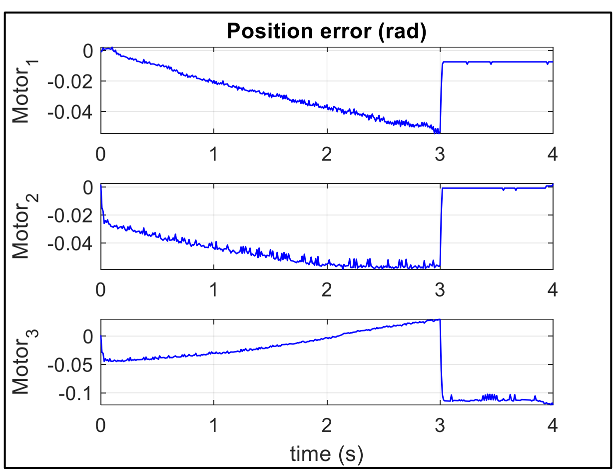

c

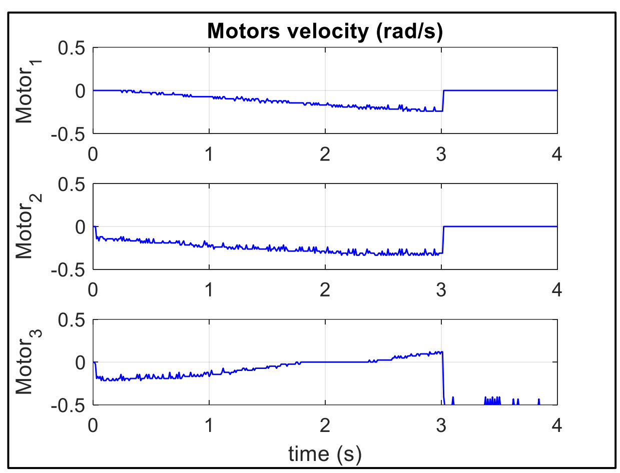

d

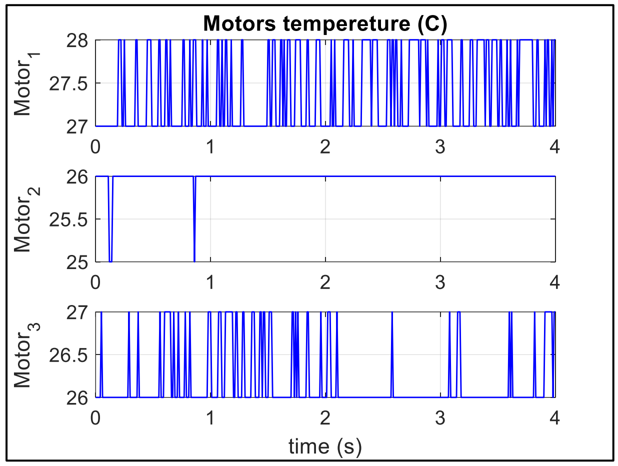

e

Figure 7-54: (a): Position tracking- (b): Torque- (c): Position error- (d): Velocity- (e): Motor temperature during the horizontal flexion movement without any extra load (HF00000_05).

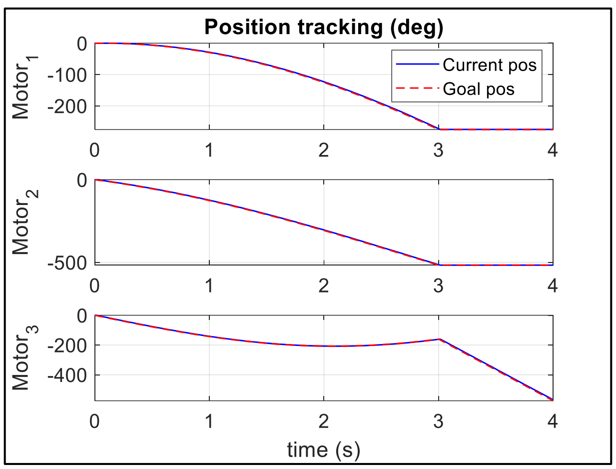

a

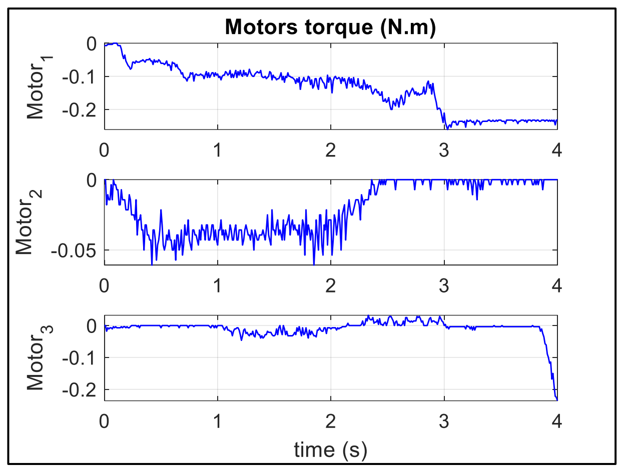

b

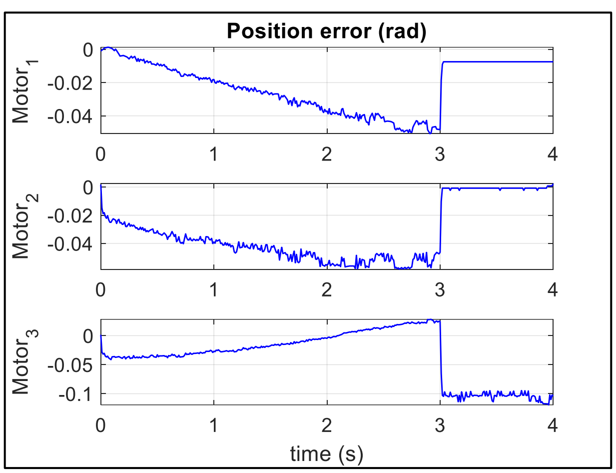

c

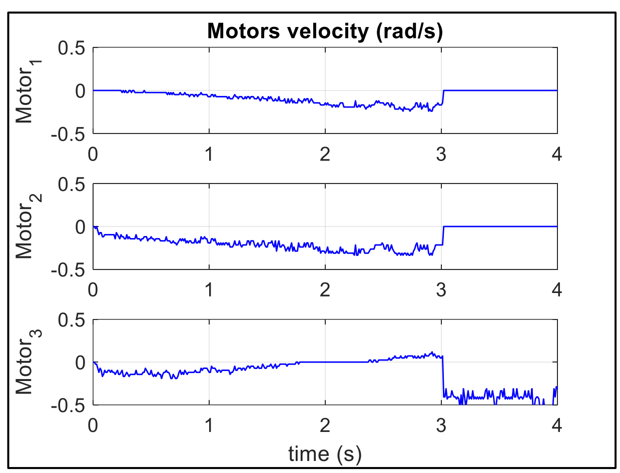

d

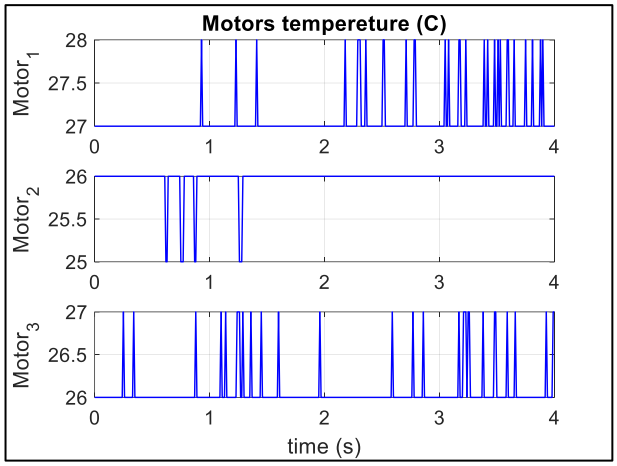

e

Figure 7-55: (a): Position tracking- (b): Torque- (c): Position error- (d): Velocity- (e): Motor temperature during the horizontal flexion movement without any extra load (HF00000_06).

In Figure 7-56 and Figure 7-57, torque graph for the motors and position error are shown for six test modes (HF000001 to FL000006) for the horizontal flexion movement.

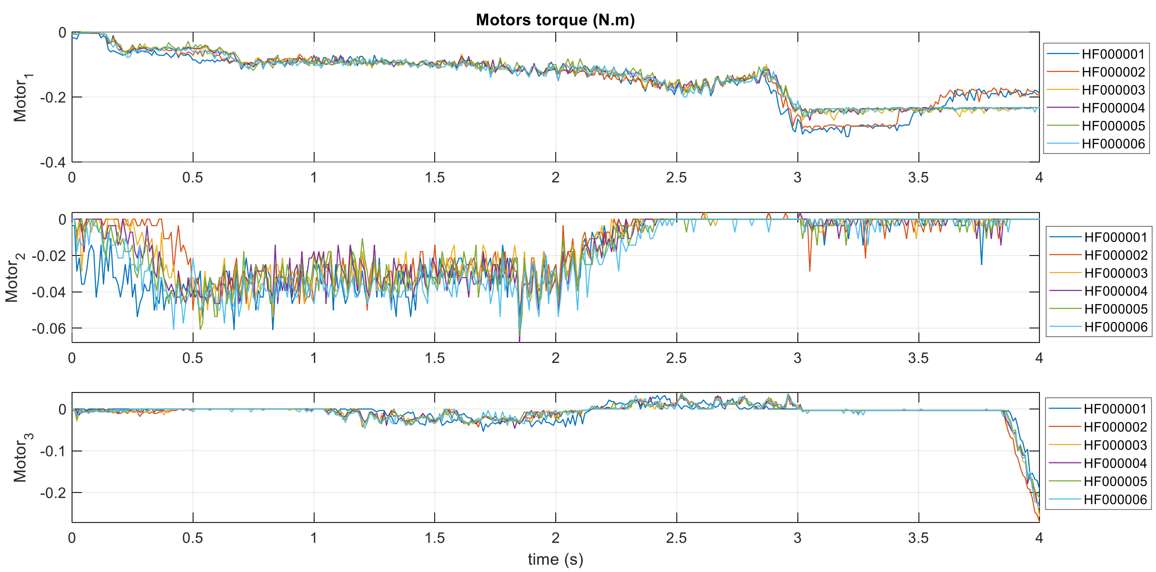

Figure 7-56: Motor torques for the six horizontal flexion experiments (HF000001 to HF000006).

The torque data from Figure 7-56 reveals repeatable motor performance patterns under various operational conditions. HF00000_01 shows torque values ranging from -0.322 to 0.032, indicative of high resistance or load scenarios, which is consistent across subsequent files. Both HF00000_02 and HF00000_06 exhibit similar ranges, with HF00000_02 showing torque from -0.300 to 0.032 and HF00000_06 from -0.261 to 0.032, further underscoring the motors' consistent response to similar operational stresses. Files HF00000_03 and HF00000_04 also display identical torque behaviours, ranging from -0.272 to 0.036, demonstrating the experiments' reproducibility across different tests. The highest maximum torque of 0.039 in HF00000_05, coupled with a minimum of -0.261, suggests moments of peak operational efficiency or decreased resistance, again consistent with the overall data trend.

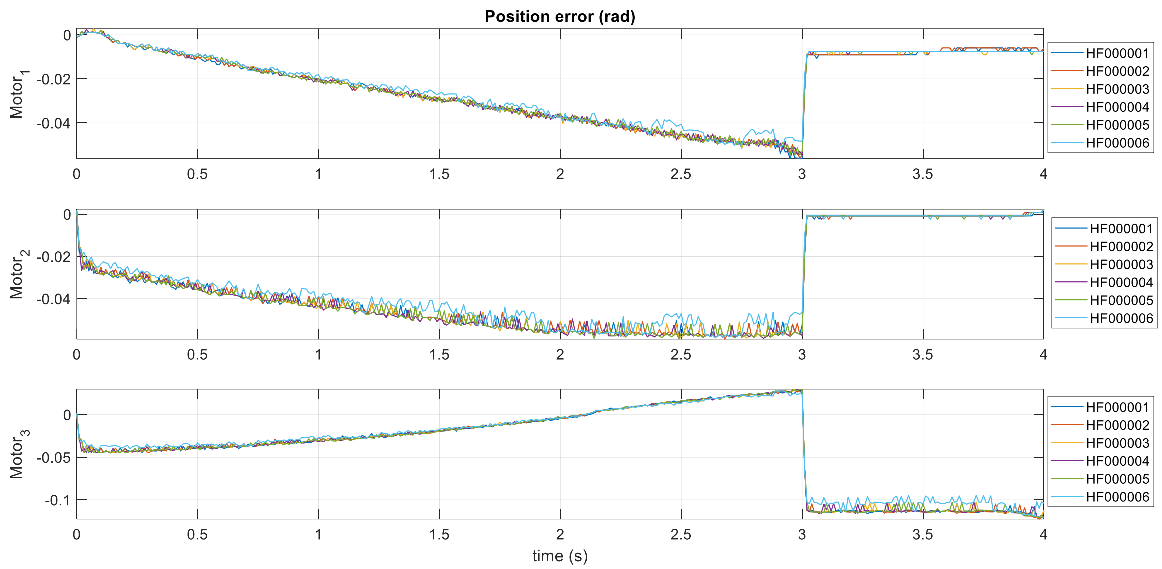

Figure 7-57: Position error for the six horizontal flexion experiments (HF000001 to HF000006).

The analysis of position error data from HF00000_01 to HF00000_06 highlights the consistent performance and control accuracy across motors, illustrating the repeatability of the experiments. Motor 1 typically exhibits position errors ranging from about -0.056 to 0.0028, motor 2's errors vary from -0.059 to 0.0024, and motor 3 demonstrates a slightly broader range, from -0.123 to 0.030. These figures underscore the precision and reliability of the motor control systems, with all motors showing relatively narrow error margins that confirm the robustness of operational control. Minor variations across the datasets likely stem from subtle differences in environmental or operational conditions, showcasing that the system effectively maintains control within predefined error boundaries even under varying circumstances. This consistent repeatability is crucial for applications requiring high accuracy and dependability.

7.5.6 Experiment in Horizontal Flexion Movement (from 500 g to 4000 g weight)

Figure 7-58 illustrates the neutral position for horizontal flexion movement, incrementally adding weights from 500 grams to 4000 grams in 500-gram intervals. This experiment was conducted in eight distinct phases to analyse the designed robot's performance under varying conditions of load. To facilitate horizontal flexion, the pathway is configured to initiate with the flexion movement, followed by the hand navigating through a path designed for horizontal flexion.

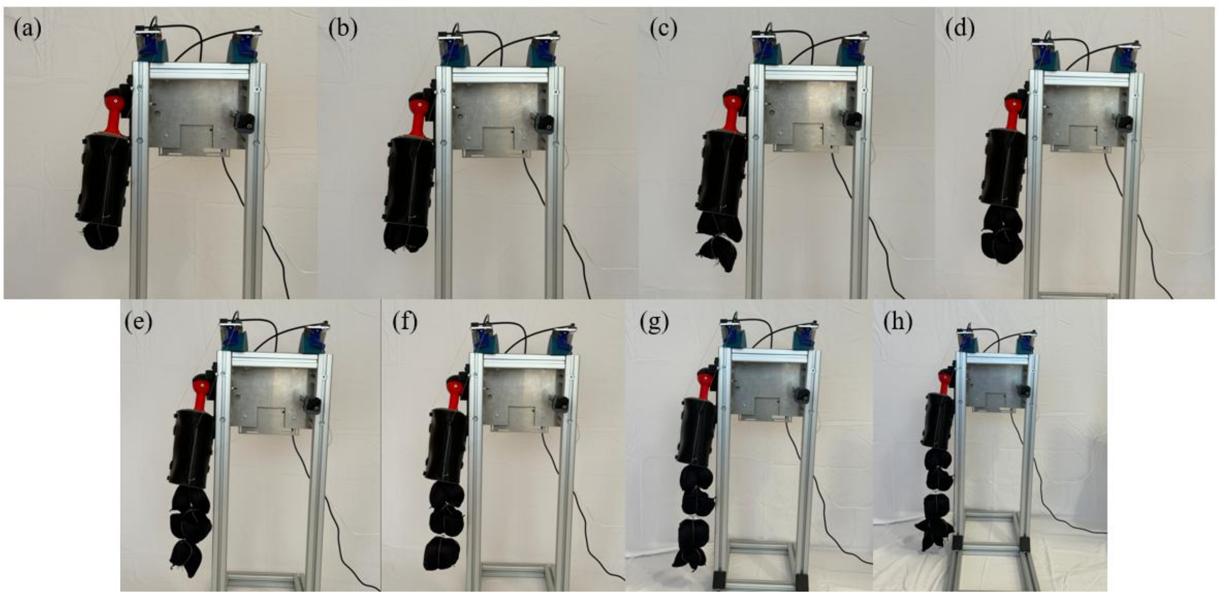

Figure 7-58: Neutral position for horizontal flexion movement, incrementally adding weights from 500 grams to 4000 grams in 500-gram intervals (a): 500 g - (b): 1000g – (c): 1500 g – (d): 2000 g – (e): 2500 g – (f): 3000 g – (g): 3500 g - (h): 4000 g.

Figure 7-59 shows the outcomes of the movement across the eight modes under consideration and illustrates position tracking, torque, position error, velocity, motor temperature during the horizontal flexion movement for 500 g to 4000 g load, respectively.

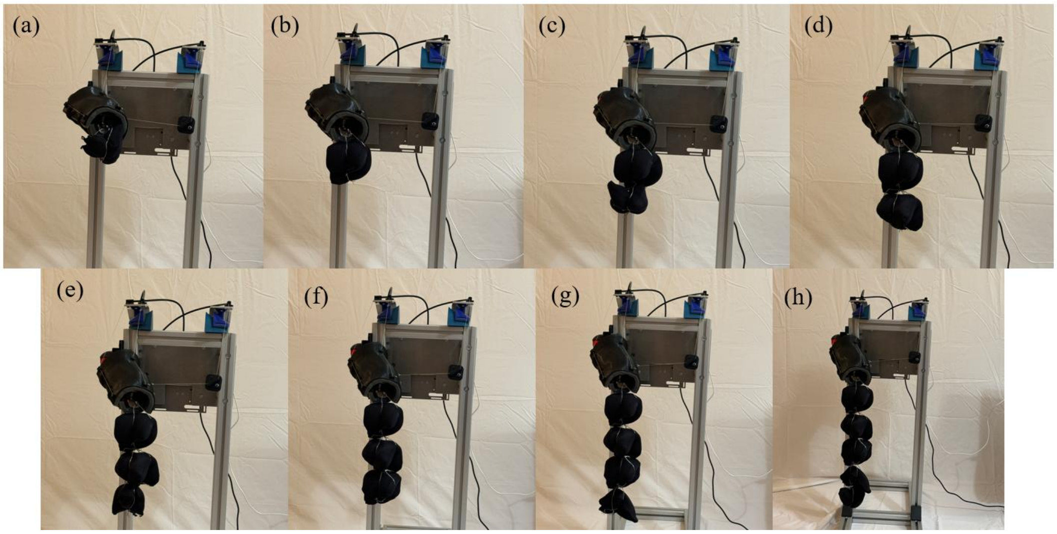

Figure 7-59: Horizontal flexion position, incrementally adding weights from 500 grams to 4000 grams in 500-gram interval: (a): 500 g - (b): 1000g – (c): 1500 g – (d): 2000 g – (e): 2500 g – (f): 3000 g – (g): 3500 g - (h): 4000 g.

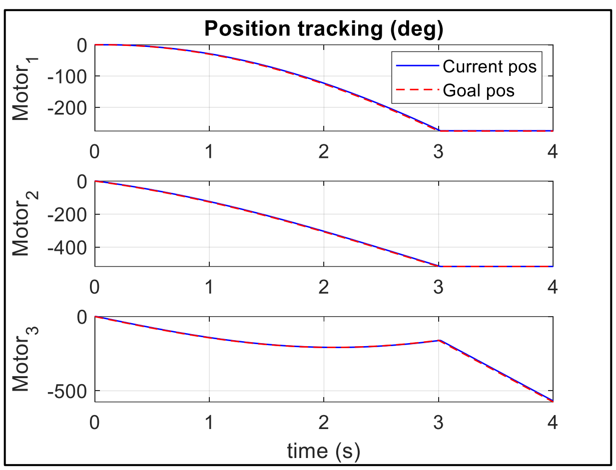

a

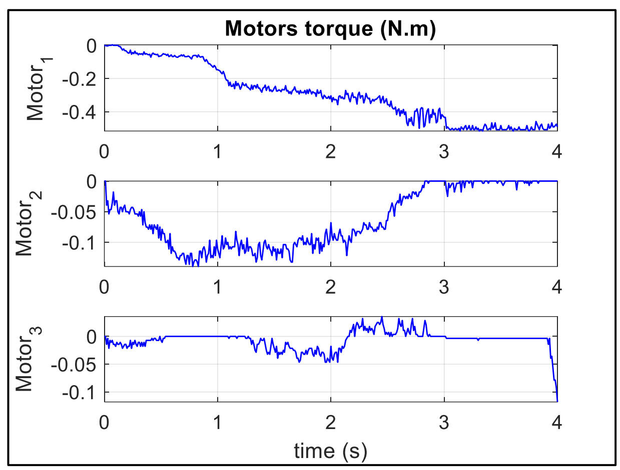

b

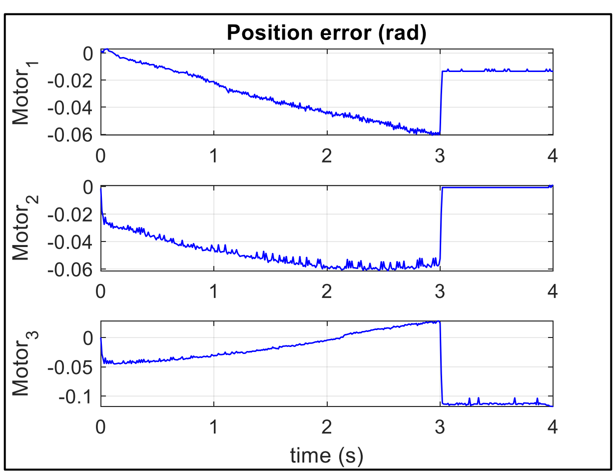

c

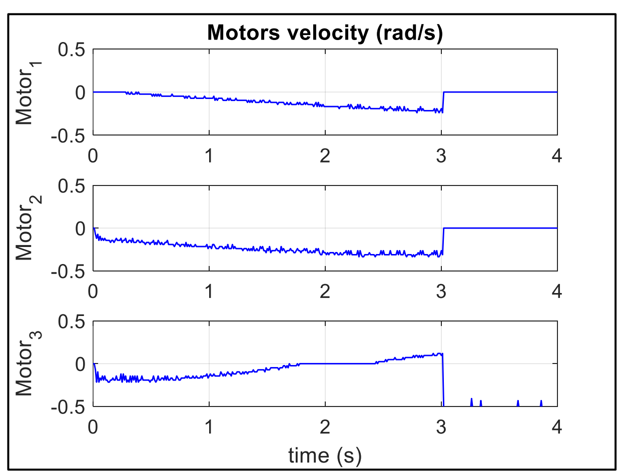

d

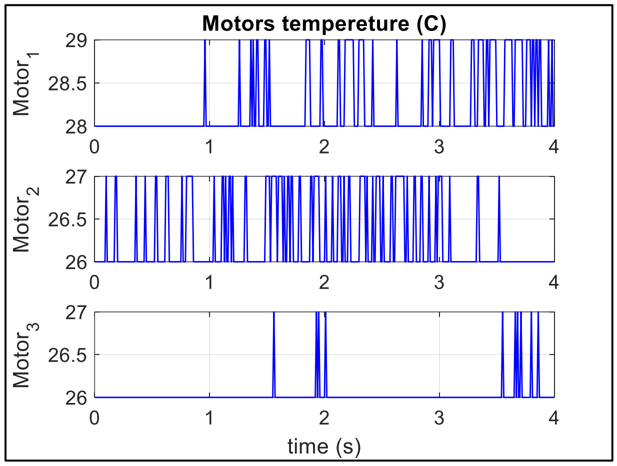

e

Figure 7-60: (a): Position tracking- (b): Torque- (c): Position error- (d): Velocity- (e): Motor temperature during the horizontal flexion movement with a 500g load (HF00500_01).

Figure 7-60 shows various aspects of motor performance, revealing a high degree of control and efficiency across multiple sections. The 'position tracking' shows that all three motors adhere closely to their goal positions, with deviations being minimal, thus demonstrating excellent positional accuracy. In the 'motors torque' graph, motor 1 operates within a range from about -0.32 to 0.03, highlighting its capability to handle varying loads effectively. Motors 2 and 3 show similar versatility, with torque values also ranging from significant negatives to positives, indicative of their robust response to operational stresses. The 'position error' records comparatively low errors for all motors, with motor 3 experiencing the highest, suggesting some challenges in maintaining precise control under dynamic conditions. Velocity data from the 'motors velocity' graph indicates that motor 3 also sees the broadest range of speeds, underlining its critical role in rapid adjustments. Lastly, the 'motors temperature' ensures that all motors remain within safe operating temperatures, affirming effective thermal management and the system’s reliability.

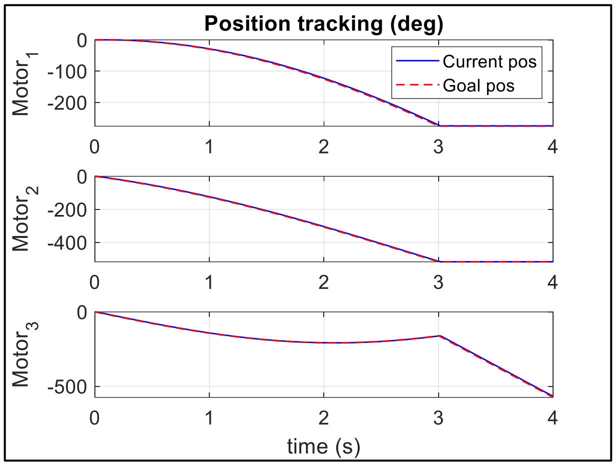

a

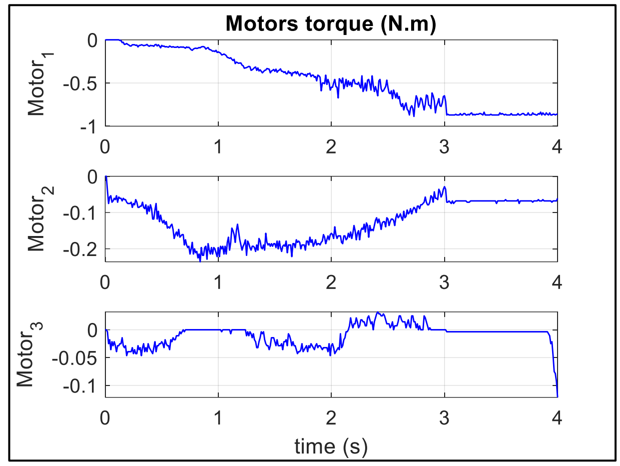

b

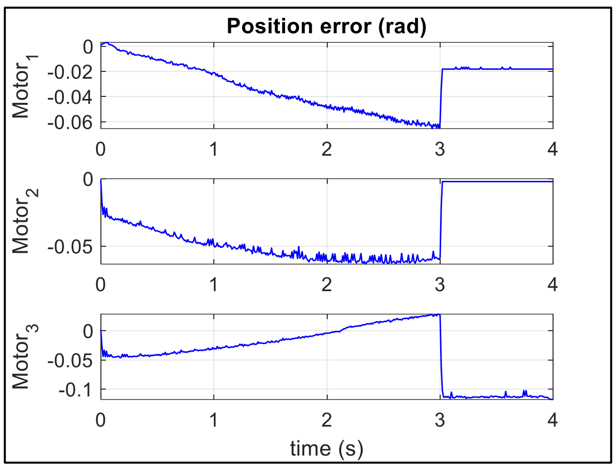

c

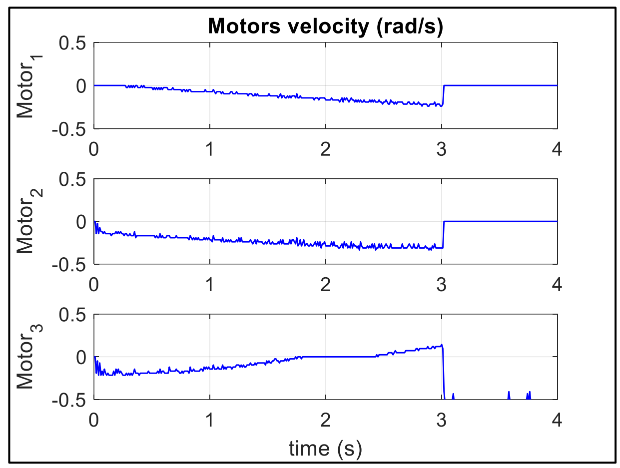

d

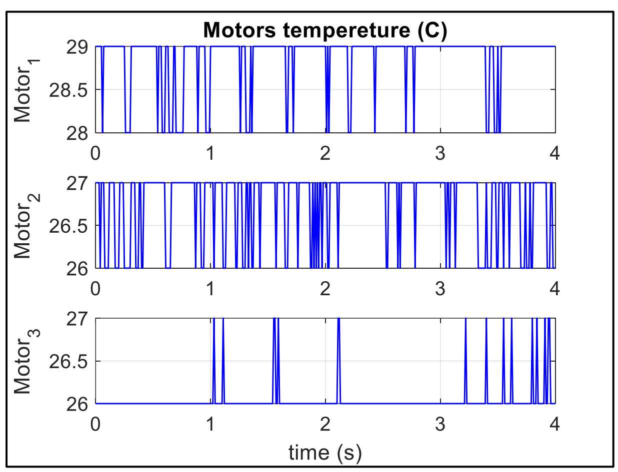

e

Figure 7-61: (a): Position tracking- (b): Torque- (c): Position error- (d): Velocity- (e): Motor temperature during the horizontal flexion movement with a 1000 g load (HF01000_01).

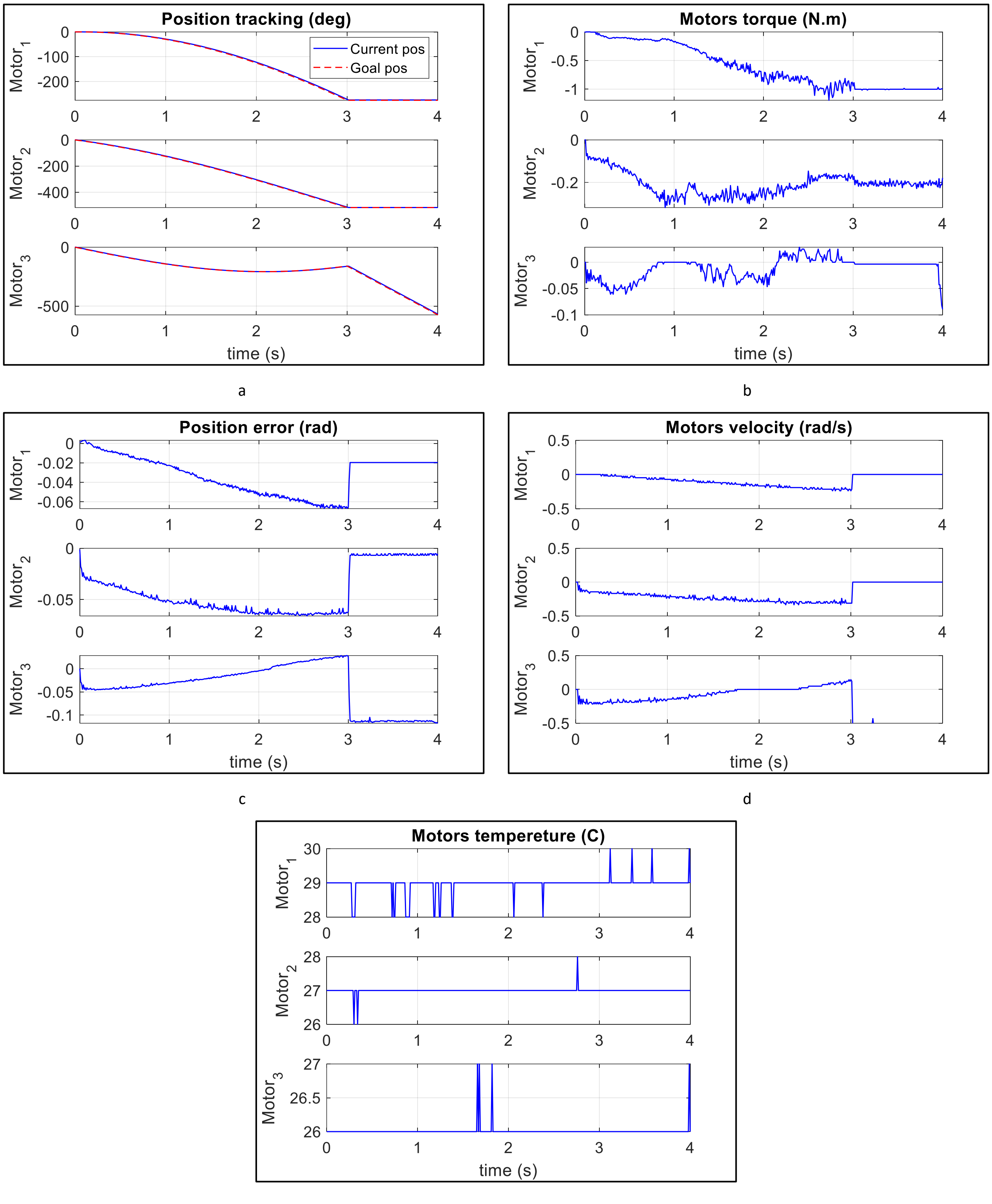

Figure 7-62: (a): Position tracking- (b): Torque- (c): Position error- (d): Velocity- (e): Motor temperature during the horizontal flexion movement with a 1500 g load (HF01500_01).

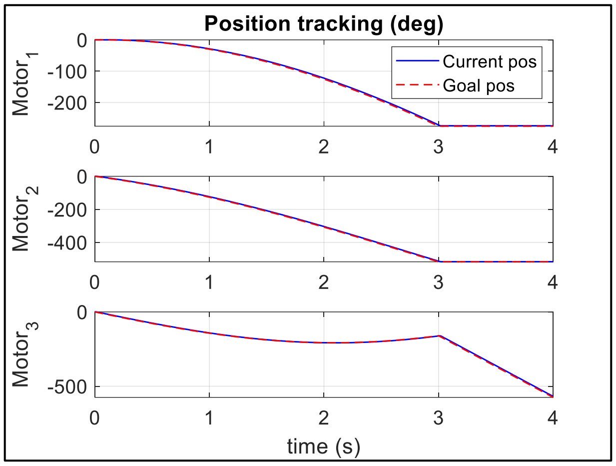

a

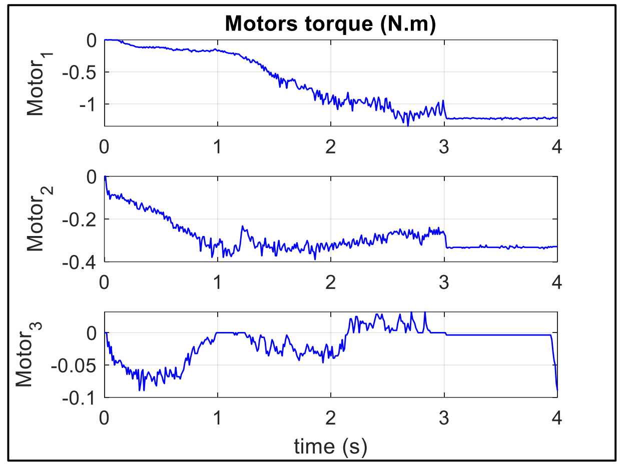

b

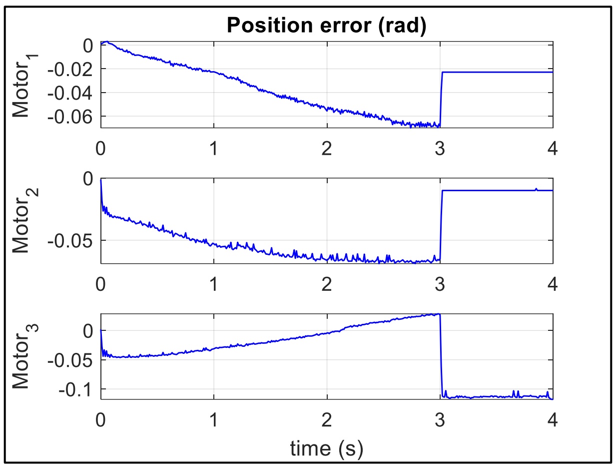

c

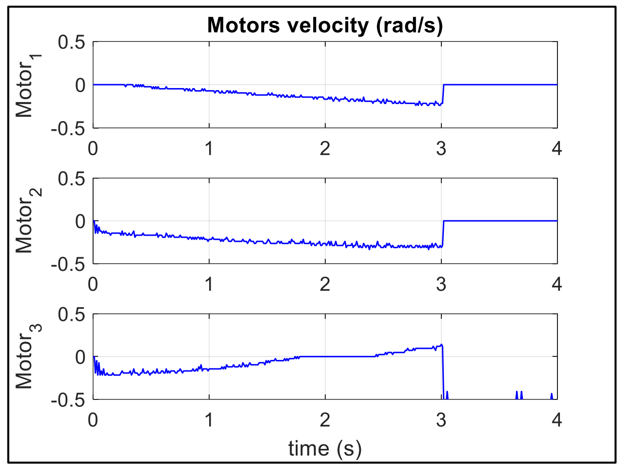

d

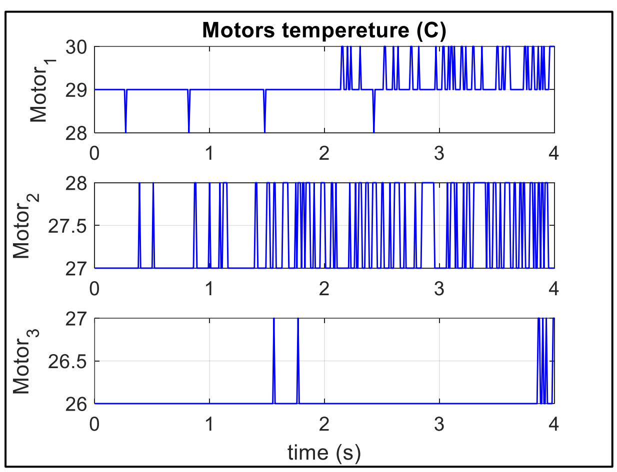

e

Figure 7-63: (a): Position tracking- (b): Torque- (c): Position error- (d): Velocity- (e): Motor temperature during the horizontal flexion movement with a 2000 g load (HF02000_01).

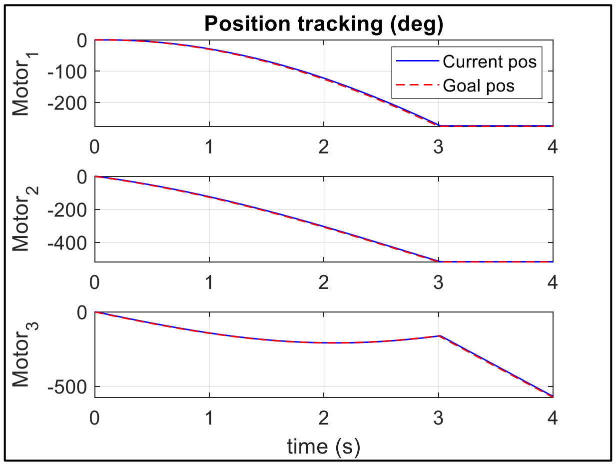

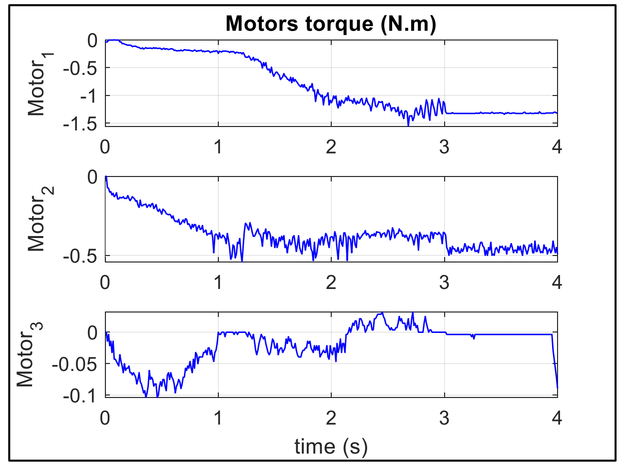

a

b

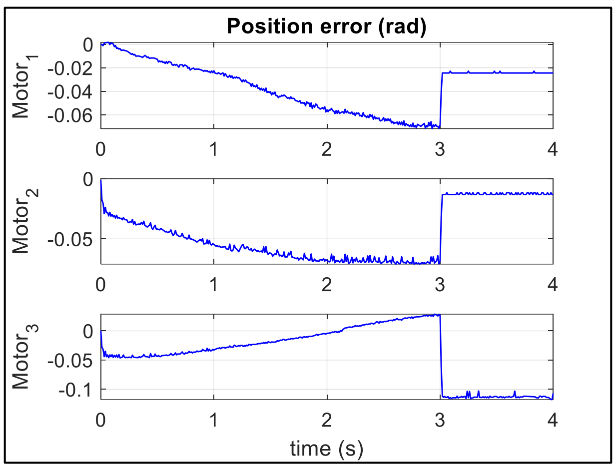

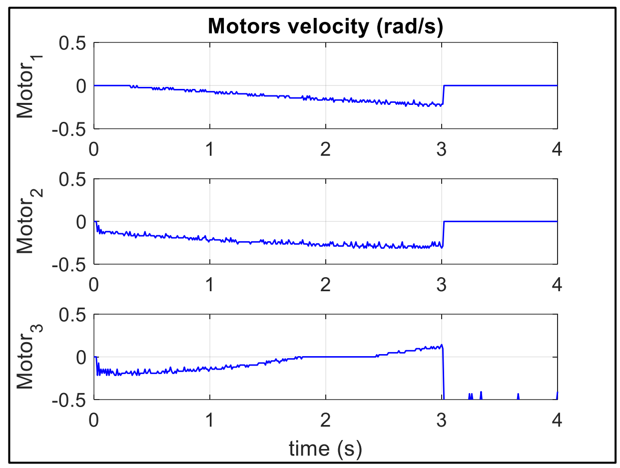

c

d

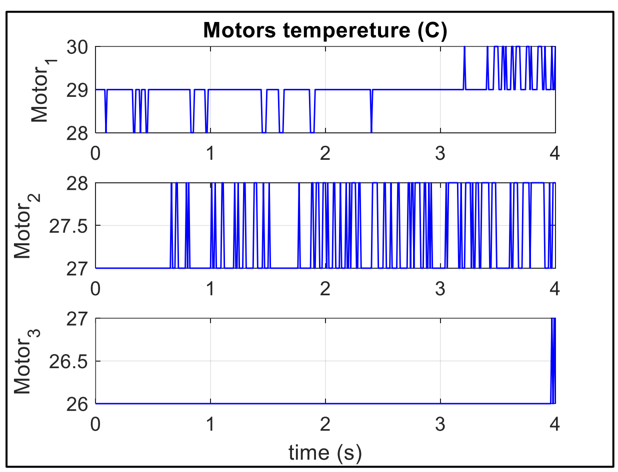

e

Figure 7-64: (a): Position tracking- (b): Torque- (c): Position error- (d): Velocity- (e): Motor temperature during the horizontal flexion movement with a 2500 g load (HF02500_01).

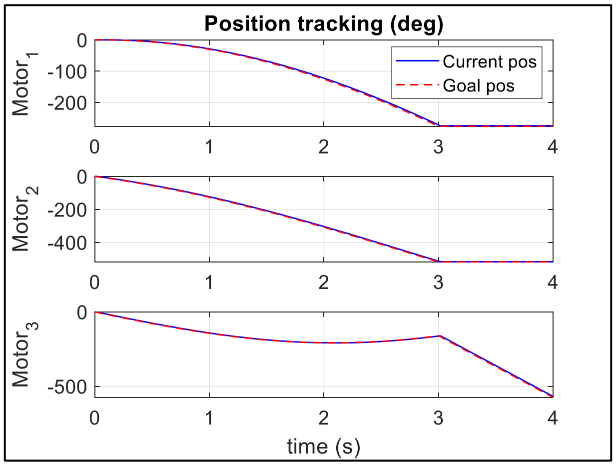

a

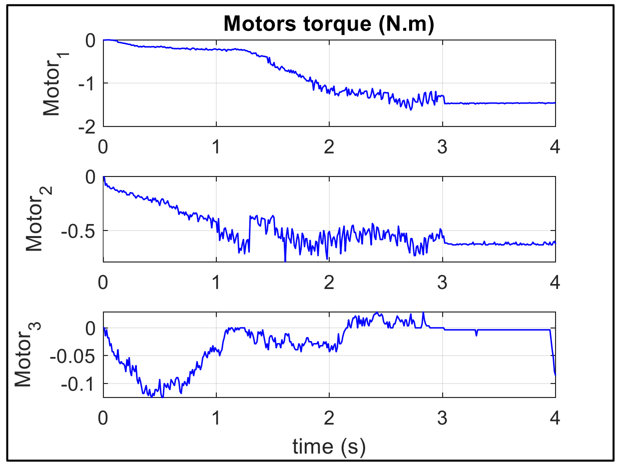

b

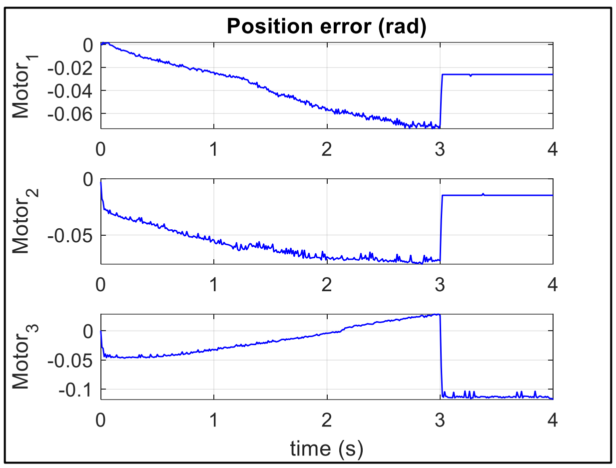

c

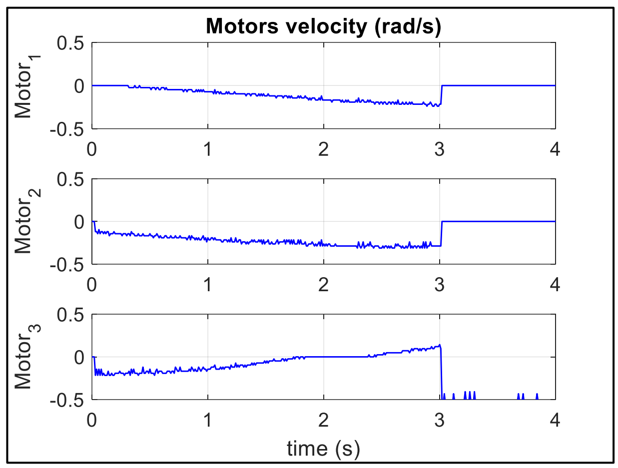

d

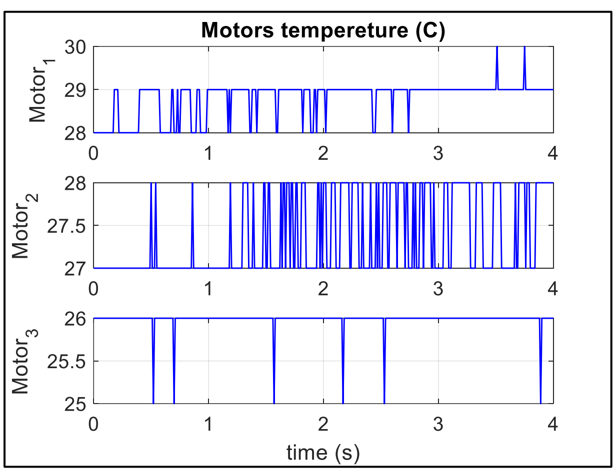

e

Figure 7-65: (a): Position tracking- (b): Torque- (c): Position error- (d): Velocity- (e): Motor temperature during the horizontal flexion movement with a 3000 g load (HF03000_01).

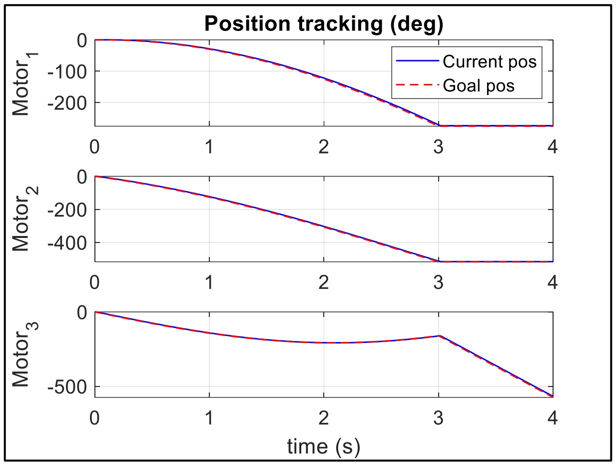

a

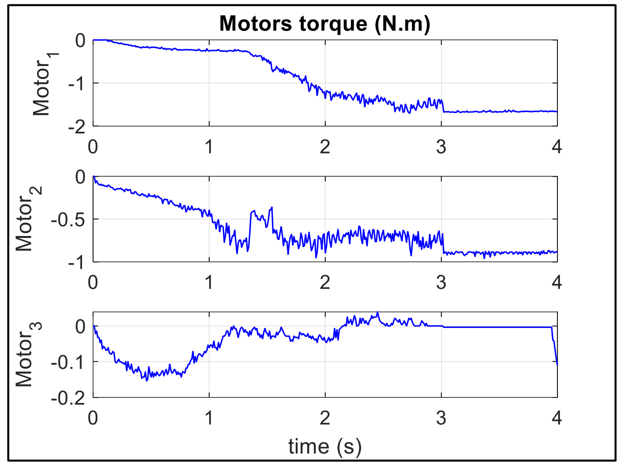

b

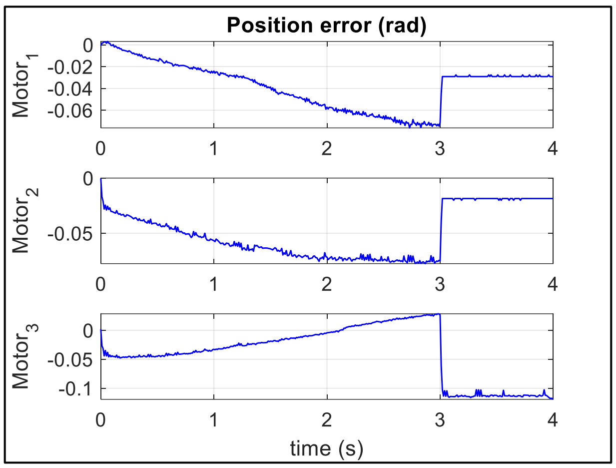

c

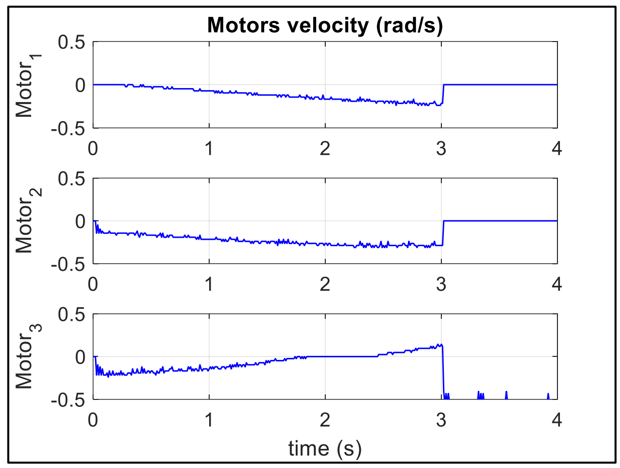

d

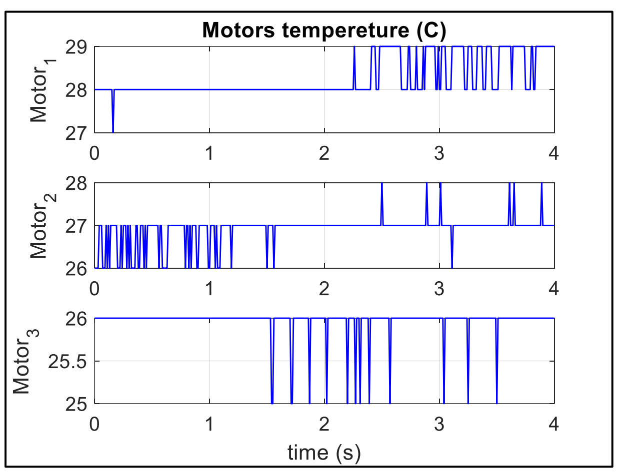

e

Figure 7-66: (a): Position tracking- (b): Torque- (c): Position error- (d): Velocity- (e): Motor temperature during the horizontal flexion movement with a 3500 g load (HF03500_01).

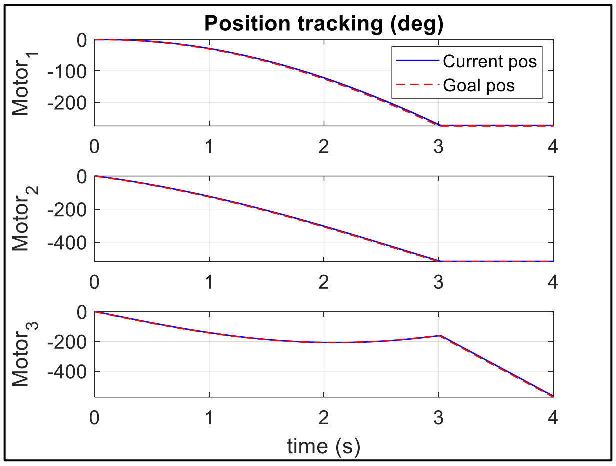

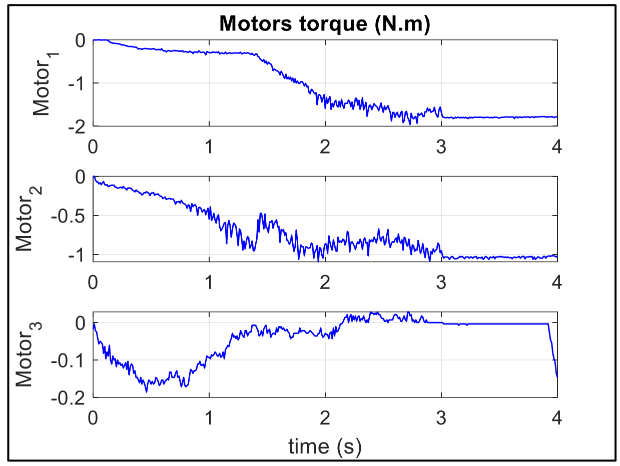

a

b

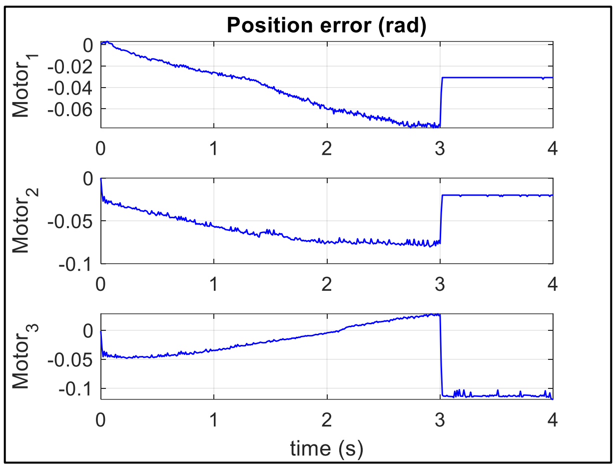

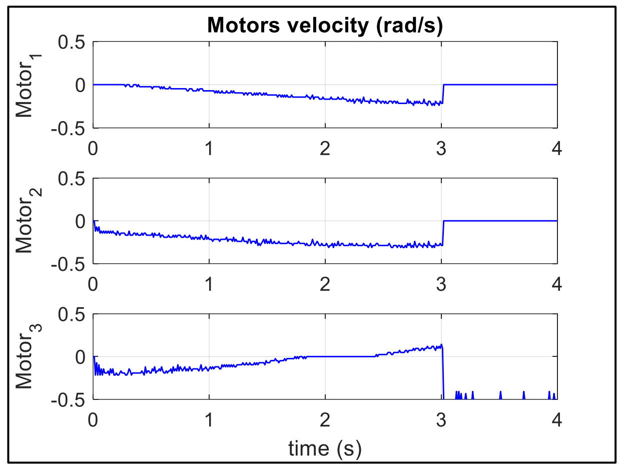

c

d

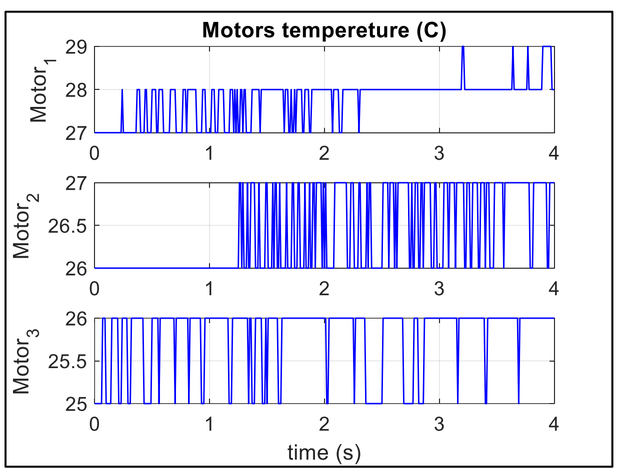

e

Figure 7-67: (a): Position tracking- (b): Torque- (c): Position error- (d): Velocity- (e): Motor temperature during the horizontal flexion movement with a 4000 g load (HF04000_01).

In Figure 7-68, a torque graph of the motors is shown for eight test modes (HF005001 to HF040001) for the horizontal flexion movement.

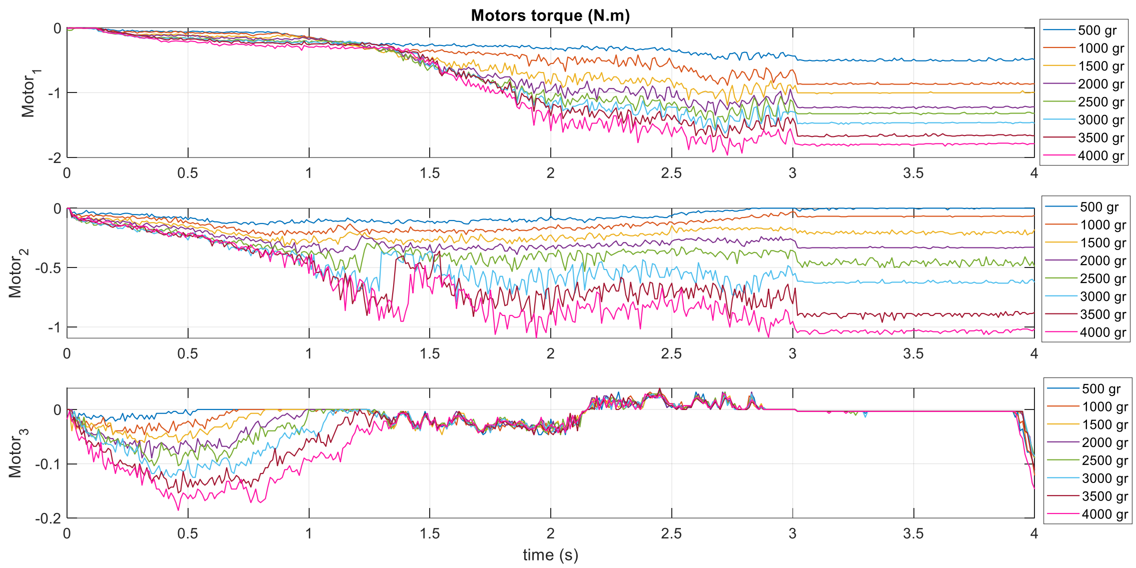

Figure 7-68: Motor torques for the eight different horizontal flexion experiments (500 g to 4000 g).

The torque data in Figure 7-68 reveals a detailed perspective on each motor's operational capacity and stress across a range of conditions. Notably, motor 1's minimum torque deepens progressively from approximately -0.516 in 500 g loading to -1.963 in 4000 g loading, suggesting an increasing operational demand as series numbers of experiments. Despite this, the maximum torque values remain low, peaking at just 0.004, indicating a control strategy to avoid overload. Motor 2 exhibits a similar pattern, with its minimum torque worsening from -0.139 to -1.094, and its maximum values consistently hovering around zero, showcasing limited positive torque capabilities. Motor 3 mirrors this trend, with minimum torques becoming more negative, moving from -0.118 to -0.186, while occasionally registering higher efficiencies with maximum torques up to 0.039. This analysis underscores a clear consistency in torque management across the series, highlighting the motors' ability to handle increased loads while adhering to operational limits, thereby ensuring efficiency and durability under escalating demands.

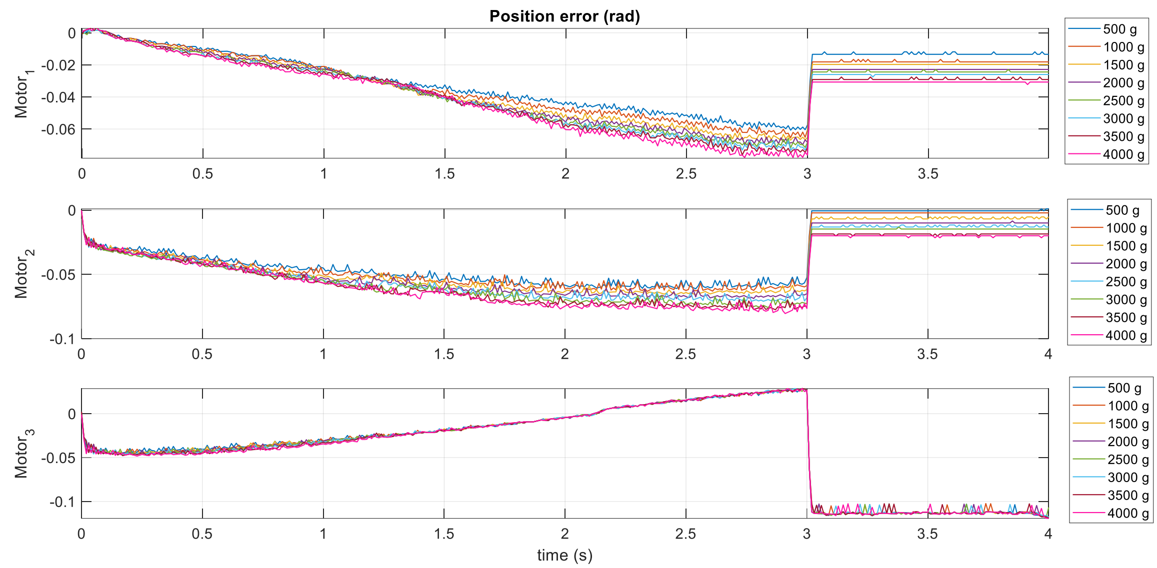

Figure 7-69: Position error for the eight different horizontal flexion experiments (500 g to 4000 g).

The analysis of detailing position errors in Figure 7-69, reveals distinct trends in the maximum and minimum position errors across motors, reflecting the varying control accuracy and system stability. Starting with 500 g loading, motor 1 shows a maximum position error of 0.0031 and a minimum of -0.061, while motor 2 and motor 3 exhibit slightly larger negative minimums, reaching up to -0.061 and -0.118, respectively. As the series progresses, the minimum errors for all motors tend to deepen, indicating increased variability or challenges in maintaining precise control. For instance, by 4000 g loading, motor 1's minimum error extends to -0.078, and motor 2 to -0.080, while motor 3 remains consistent with a similar range to the initial files, maintaining its maximum error at 0.029.

7.5.7 Experiments on a Healthy Candidate with Carbon Fiber CDSE

7.5.7.1 Risk Assessment Procedures for Human Testing of the Cable-Driven Shoulder Exosuit (CDSE):

7.5.7.2 Overview of Risk Assessment

This risk assessment procedure ensures that all human trials conducted with the Cable-Driven Shoulder Exosuit (CDSE) are performed in a safe, ethical, and controlled environment. The primary objectives of the assessment are:

- To **identify potential risks** associated with wearing and using the exosuit.
- To **implement mitigation strategies** to ensure participant safety.

- To **comply with ethical standards** requirements.
- To **ensure repeatable and controlled experiments** without harm to the participant.

7.5.7.3 Risk Identification and Hazard Analysis

Table 7-1: Risk Identification and Hazard Analysis

Risk Factor	Potential Hazard	Severity (Low/Moderate/High)	Likelihood (Low/Moderate/High)	Mitigation Measures
Mechanical Failure	Sudden actuator malfunction, unintended movement	Moderate	Low	Safety stops integrated, system monitored in real-time, pre-test equipment check
Strain or Discomfort	Excessive force applied to shoulder muscles	Moderate	Low	Load limits applied (500g–4000g), participant feedback monitored, trial conducted under supervision
Skin Irritation or Pressure Points	Prolonged use of straps causing discomfort	Low	Low	Use of soft padding, regular participant feedback, trial time limited
Unexpected Movement Restrictions	Exosuit limiting natural joint mobility	Moderate	Low	Motion range tested before human trials, calibration per participant
Trip or Fall Hazard	Cables interfering with movement, participant imbalance	High	Low	Cables managed carefully, participant seated, emergency stop mechanism
Electrical Failure	Power supply issues, unexpected shutdown	Low	Low	Backup power plan, manual override enabled
Psychological Discomfort	Anxiety due to wearing an unfamiliar device	Low	Low	Clear instructions given, voluntary participation, ability to stop at any time

7.5.7.4 Safety and Mitigation Measures

To ensure a safe testing environment, the following safety measures and protocols were implemented:

1- Participant Screening and Informed Consent

- The participant was provided with detailed information about the study, including potential risks, benefits, and withdrawal options.
- An informed consent form was signed, ensuring voluntary participation.
- Participant was screened for pre-existing medical conditions that could be aggravated by device use (e.g., musculoskeletal disorders, neurological conditions).

2- Device Calibration and Pre-Test Checks

- Before each trial, the exosuit was calibrated based on the participant’s body measurements to ensure a comfortable fit and unrestricted range of motion.
- Mechanical components were inspected for defects, loose connections, and proper alignment.
- The electrical system was tested to confirm reliable power supply and emergency shutdown function.

3- Supervised Testing Environment

- All trials were conducted in a controlled laboratory setting with trained researcher present.
- A researcher was designated as the emergency responder, ready to intervene if discomfort or system failure occurred.

4- Load Limitations and Motion Range Control

- The maximum load applied was limited to a safe range (4000g) to prevent excessive strain on the participant’s muscles.
- The motion range of the exosuit was tested in simulated environments before human trials, ensuring compliance with natural shoulder movement patterns.

5- Real-Time Monitoring and Emergency Protocol

- The motion of the exosuit was monitored in real-time using sensor feedback to detect anomalies.
- The participant had a stop signal to immediately halt the test in case of discomfort.
- A manual emergency stop button was integrated to deactivate the system instantly if needed.

6- Post-Test Evaluation and Participant Feedback

- After each trial, the participant was asked about comfort, ease of movement, and any discomfort experienced.
- The exosuit was checked for signs of wear or malfunction, and adjustments were made for subsequent trials.
- If the participant reported discomfort, trial parameters were adjusted, or testing was discontinued.

7.5.7.5 Ethics and Compliance

- The study was conducted under the approval of ethical code from the University of Salford which an ethics application number is 187.)

Following a series of trials with diverse loading scenarios, critical evaluations were executed on a healthy candidate to substantiate the system's functionality in practical settings. During this phase, the backpack, constructed from a carbon fiber framework, was donned by a healthy candidate, who then undertook all three designated shoulder assessments (Figure 7-70).

Figure 7-70: Carbon fiber CDSE worn by healthy candidate.

In Figure 7-71, a view of the function of the CDSE is shown to guide the arm of the candidate to the desired goal positions.

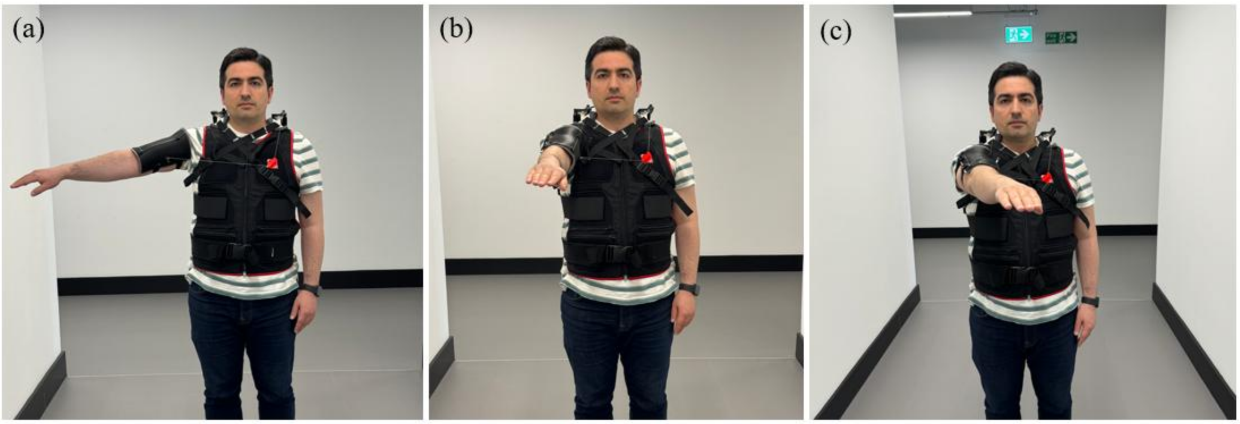

Figure 7-71: (a): Abduction movement. (b) Flexion movement. (c) Horizontal Flexion movement.

In Figure 7-72, the results obtained from performing abduction movement of healthy candidate with a total weight of 90 kg and a height of 170 cm are shown.

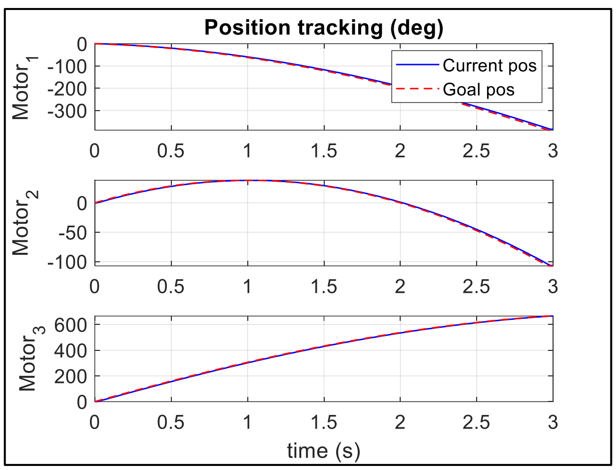

a

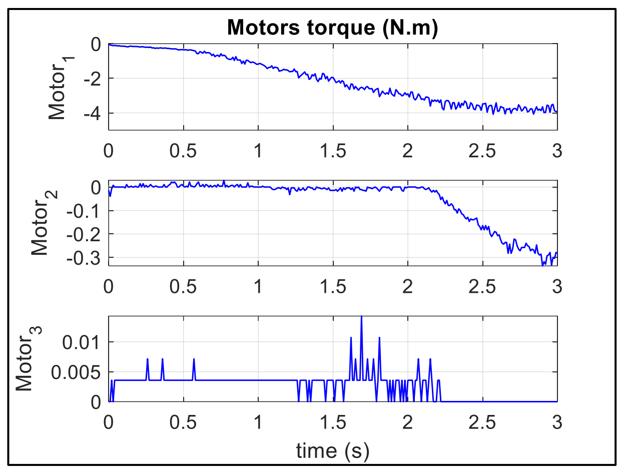

b

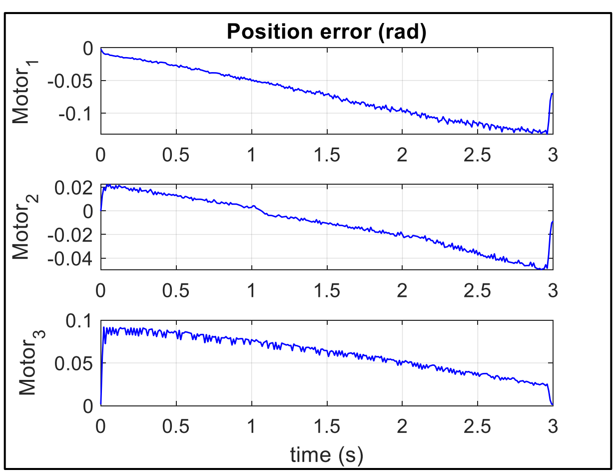

c

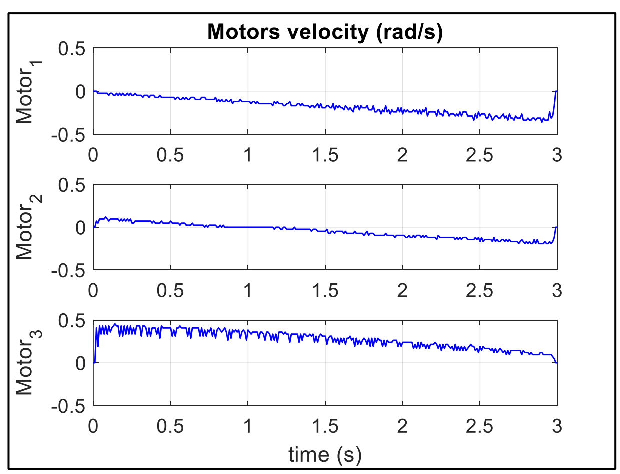

d

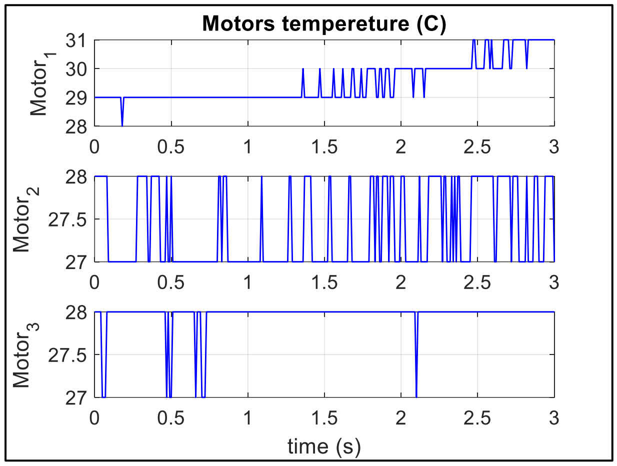

e

Figure 7-72: (a): Position tracking- (b): Torque- (c): Position error- (d): Velocity- (e): Motor temperature during the abduction movement of healthy candidate.

In the torque profiles analysed, motor1 exhibits an initial peak torque slightly in excess of 5 Nm, suggesting a strong, initiating force which rapidly decelerates to a minimum value approaching zero. This characteristic is indicative of a motor tasked with initiating movement, potentially engaging during the start of a gait cycle in an exosuit application. Motor2 maintains a relatively steady output with a maximum torque marginally above -0.2 Nm and a minimum close to -0.3 Nm, which is consistent with the sustained exertion of force in a single direction, perhaps indicative of a motor designed to provide continuous counterbalancing force or support during steady-state conditions. Motor3, displaying maximum and minimum torques just under 0.01 Nm and -0.01 Nm respectively, shows rapid oscillatory behaviour which is representative of fine motor control, possibly for dynamic stabilization tasks within the exosuit, where precise, small-scale force adjustments are necessary for maintaining balance or adjusting to variable load conditions. These data are crucial in informing the design criteria for each motor, dictating their roles within the exosuit's system architecture, and ensuring optimal operation within their respective force output ranges to enhance efficiency, endurance, and user synchronization within the assistive device.

In Figure 7-73, the results obtained from performing flexion movement of healthy candidate with a weight of 90 kg and a height of 170 cm are shown.

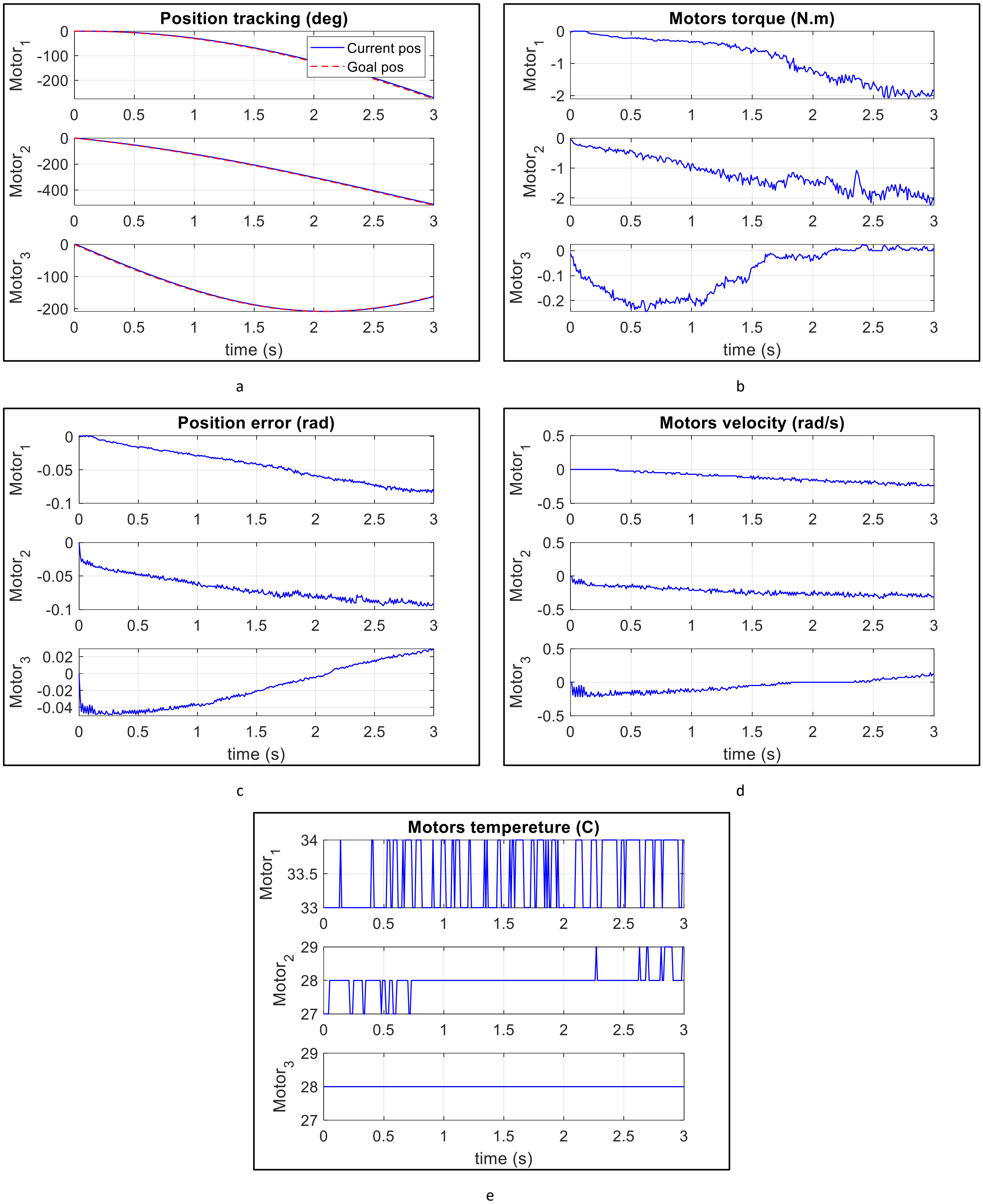

Figure 7-73: (a): Position tracking- (b): Torque- (c): Position error- (d): Velocity- (e): Motor temperature during the flexion movement of healthy candidate.

In the torque graph (b), motor 1's torque decreases over time, starting just above -1 N.m and gradually levelling out to about -2 N.m, which represents the maximum negative torque exhibited. Motor 2's torque shows more variability, with a maximum torque slightly above 0 N.m and a minimum that dips to approximately -2.5 N.m, indicating a downward trend with some fluctuations. Motor 3 starts near 0 N.m and increases to a maximum torque of just above -0.1 N.m before decreasing to around -0.25 N.m, suggesting a dynamic response before stabilizing. The position error graph (c) for motor 1 indicates an initial error close to -0.06 rad, which slightly decreases over time. Motor 2's error starts near 0 rad and increases to a maximum error of roughly -0.25 rad, displaying a gradual but consistent increase in error over the duration.

In Figure 7-74, the results obtained from performing horizontal flexion movement of healthy candidate with a weight of 90 kg and a height of 170 cm are shown.

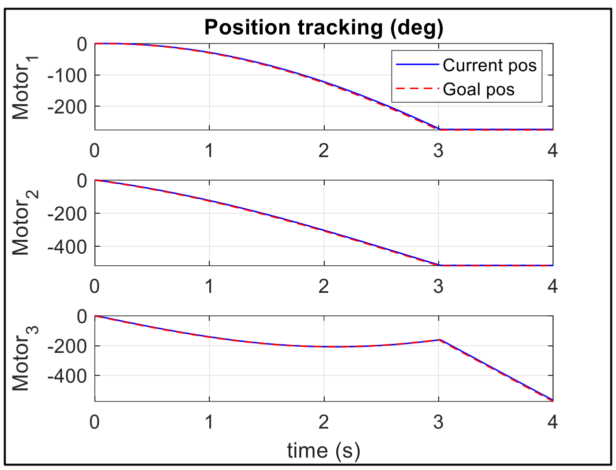

a

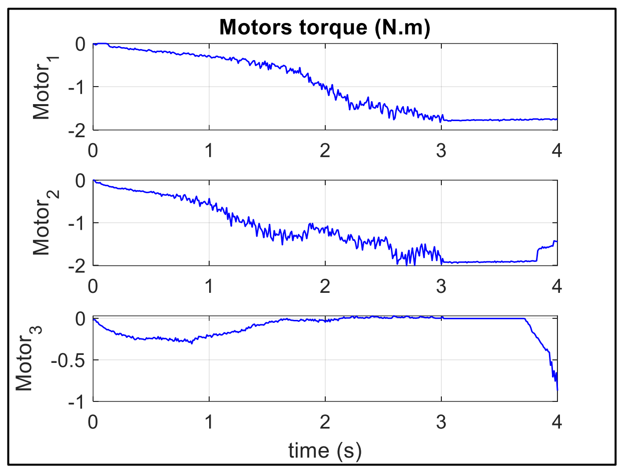

b

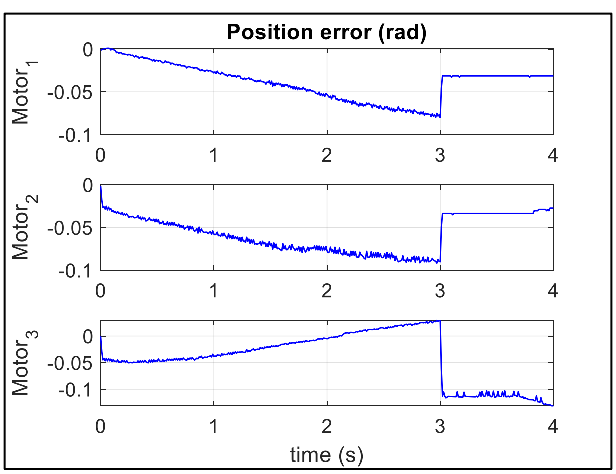

c

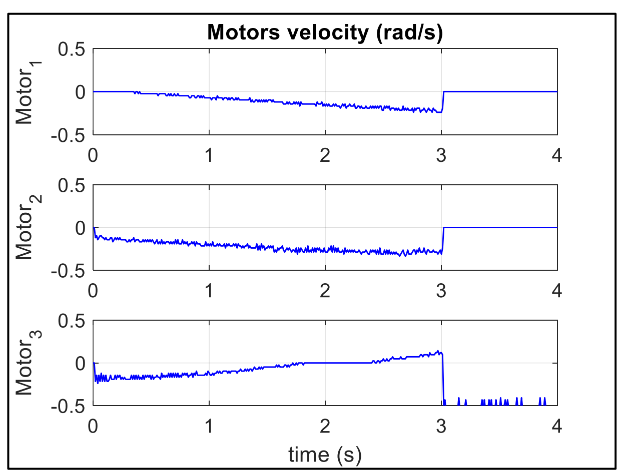

d

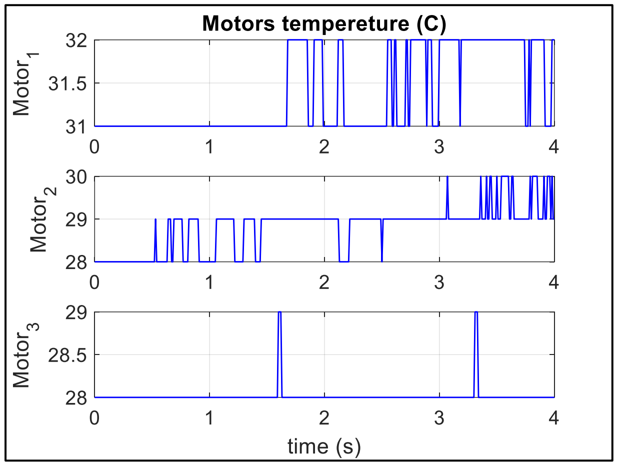

e

Figure 7-74: (a): Position tracking- (b): Torque- (c): Position error- (d): Velocity- (e): Motor temperature during the horizontal flexion movement of healthy candidate.

The time-series data for the multi-motor robotic system encapsulates critical performance metrics, crucial for the optimization of robotic assistive devices such as exosuits. The position tracking (graph a) reveals that motor1 operates across an expansive range, with a positional deviation peaking nearly -400 degrees from the goal, while motor2 and motor3 register maximum deviations approximately -200 and -400 degrees, respectively. The torque profile (graph b) demonstrates motor1's peak torque near zero and a minimum just below -2 Nm, with motor2 displaying more dynamism, and motor3 maintaining a relatively steady torque, indicative of its lower load demands. Positional error (graph c) remains relatively subdued for motor1, spiking at a maximum of 0.05 radians, whereas motor2 and motor3 encounter larger excursions, up to 0.1 radians, signalling more complex control challenges. Velocity analysis (graph d) shows motor2 and motor3 undergoing greater variations, oscillating between approximately 0.5 to -0.5 rad/s, highlighting their response to dynamic conditions. The temperature data (Graph e) for motor1 exhibits the most significant fluctuations, peaking around 32°C, while motor2 and motor3 show modest thermal variations, suggesting a stable operational environment. These insights are integral to refining the exosuit's control algorithms, aiming for an efficient, responsive, and harmonious human-machine interface.

7.6 Discussion

7.6.1 Design Satisfactoriness

The performance evaluation of the Cable-Driven Shoulder Exosuit (CDSE) was conducted through a series of controlled experiments, assessing the system's ability to assist with shoulder movements under various loading conditions. The data obtained from these experiments provides quantifiable evidence of the exosuit's effectiveness in supporting controlled movement, maintaining stability, and ensuring repeatability across different tasks.

7.6.1.1 Evaluation of Movement Repeatability and Stability

One of the core performance criteria for the CDSE is its ability to consistently reproduce shoulder movements across multiple trials. The repeatability tests were performed for abduction, flexion, and horizontal flexion movements, each conducted six times. The results demonstrated high consistency in trajectory tracking, with the position error remaining within acceptable tolerances across all tests.

- Abduction movement tests showed minimal deviation from the expected movement path, with position errors ranging between -0.065 and 0.029 rad for load conditions up to 4000 g.
- Flexion movement tests revealed precise motor control, with motor 1 handling torque ranges of -0.540 Nm to 0.032 Nm, ensuring smooth execution under varying loads.
- Horizontal flexion movement tests showed robust operational performance, with torque values staying within safe limits, confirming the stability of the actuation system.

These findings confirm that the CDSE is capable of performing controlled, repeatable motion, a critical requirement for rehabilitation applications where consistency is essential for patient progress.

7.6.1.2 Assessment of Positional Accuracy and Load Handling Capacity

To assess the exosuit's effectiveness under different loading conditions, incremental weights from 500 g to 4000 g were applied to simulate real-world assistive scenarios. The maximum position error across all tests remained within ±0.08 rad, indicating strong control accuracy despite increasing external forces.

- Torque profiles from the experiments suggest that motor 1 experiences the highest demand, with peak torque values exceeding 5 Nm, while motors 2 and 3 provided supporting stabilization forces to maintain smooth movement execution.
- Velocity and force feedback data indicate that the system adapts well to changing loads, ensuring that even under maximum weight conditions (4000 g), the device maintains controlled movement without erratic fluctuations.

The data collected confirms that the CDSE effectively manages dynamic force application and maintains precision in motion execution, meeting key design requirements for rehabilitation exosuits.

7.6.1.3 Human Trials and Validation in a Practical Setting

Following mechanical and simulated load testing, a real-world evaluation was conducted with a healthy human participant wearing the carbon fiber version of the CDSE. The subject, weighing 90 kg and 170 cm in height, performed all three targeted shoulder movements while sensor feedback recorded position accuracy, torque distribution, and system efficiency.

- Abduction movement: Torque values remained stable, with motor 1 generating peak torques slightly above 5 Nm, indicating a strong assisting force for initiating movement.
- Flexion movement: Motor 2 exhibited a peak torque of 2.5 Nm, stabilizing the shoulder during movement execution.
- Horizontal flexion movement: Rapid oscillatory behaviour in motor 3 suggests it is responsible for fine motor adjustments, ensuring the exosuit's adaptability to human variability.

The results from human trials indicate that the CDSE performs effectively in assisting shoulder movements in real-world applications, demonstrating its potential for rehabilitation use.

7.6.2 Comparison with Other Devices

7.6.2.1 Range of Motion and Functional Capabilities

One of the most critical parameters in assistive exosuits is their ability to support natural movement patterns without restricting joint mobility. Table 2-1 in the thesis presents a comparison of human arm ROM with seven different robotic devices, showing that while many rigid exoskeletons provide high precision movement assistance, they often have limited ROM due to mechanical constraints.

- **CDSE Performance:**
  - The CDSE provides a ROM for shoulder flexion of 188°/61° and abduction of 134°/48°, closely aligning with natural human movement.
  - The soft-robotic nature of the CDSE allows for unrestricted movement, unlike rigid exoskeletons, which impose joint misalignment issues and require additional passive degrees of freedom to accommodate human movement.
- **Comparison with Other Devices:**
  - The ManExos and Dex Exoskeletons offer ROM values below 150° for shoulder flexion, indicating a more restrictive motion range compared to the CDSE.
  - The CDSE's flexibility surpasses exosuits that use rigid frames, ensuring better adaptability to human biomechanics.

7.6.2.2 Portability and Wearability

A significant advantage of exosuits over traditional exoskeletons is their lightweight and ergonomic design, making them more suitable for daily use. A study of 60 rehabilitation robotic devices revealed that only 17% of them were portable, with the remaining 83% requiring stationary or external support structures.

- **CDSE Performance:**
  - The CDSE weighs significantly less than conventional rigid exoskeletons, enhancing wearability and comfort for prolonged use.
  - Unlike rigid exoskeletons, the CDSE does not require mechanical joints to be precisely aligned with human joints, reducing the risk of misalignment injuries and improving user compliance.
- **Comparison with Other Devices:**
  - The Paexo Shoulder (Ottobock) and EksoUE (Ekso Bionics) are industrial-grade shoulder assist exosuits, but they are not specifically optimized for rehabilitation or assistive, limiting their use in patient therapy.

- The Myomo exosuit (for elbow and hand rehabilitation) is highly structured and rigid, restricting upper-arm ROM, whereas the CDSE maintains soft, dynamic adaptability to user movement.

7.6.2.3 Cost-Effectiveness and Accessibility

Cost remains a major factor in the adoption of rehabilitation robotics, particularly in home-based rehabilitation scenarios. Many commercially available exoskeletons are cost-prohibitive, with high material costs and complex control mechanisms leading to expenses exceeding $50,000 [161], [162], [163] per unit.

- **CDSE Performance:**
  - The CDSE is designed using affordable materials (e.g., carbon fiber and lightweight aluminium) while maintaining structural integrity and durability.
  - The soft-robotic approach reduces production costs, making it more affordable for healthcare institutions and home rehabilitation users.
- **Comparison with Other Devices:**
  - Rigid exoskeletons, such as ReWalk or Ekso Bionics systems, are significantly more expensive, requiring specialized fitting, maintenance, and training.
  - CDSE offers a lower-cost alternative with similar rehabilitation benefits, making it a viable option for wider accessibility and deployment in clinical and home settings.

7.6.2.4 Comfort and Usability

A primary limitation of many rehabilitation or assistive devices is their lack of user comfort, leading to reduced patient compliance. The thesis highlights that rigid exoskeletons often cause discomfort due to misalignment and excessive weight, which can result in skin irritation, pressure points, and restricted blood flow.

- **CDSE Performance:**
  - The CDSE is made from lightweight, breathable fabric materials, reducing skin irritation and excessive pressure on the shoulder joint.
  - The soft-robotic approach provides dynamic support, adjusting naturally to different user body types, which rigid exoskeletons fail to accommodate.
- **Comparison with Other Devices:**

- Devices such as ReWalk and HAL (Hybrid Assistive Limb) require precise body fitting and calibration, increasing setup complexity.
- The CDSE can be easily adjusted for different users, reducing the need for extensive calibration.

7.6.2.5 Rehabilitation Outcomes and Effectiveness

For an exosuit to be clinically viable, it must provide measurable improvements in user mobility and rehabilitation outcomes. Studies show that soft exosuits facilitate improved user adaptation, as they do not restrict muscle activity in the same way rigid exoskeletons do.

- **CDSE Performance:**
  - Experimental trials with a human participant wearing the CDSE showed effective assistance in shoulder abduction and flexion movements, confirming its ability to reduce user effort while maintaining controlled motion execution.
  - The low resistance of the system allows for user-driven movement, making it more effective for neuromuscular rehabilitation compared to fully powered rigid exoskeletons, which tend to overcompensate for movement, limiting neuromuscular re-engagement.
- **Comparison with Other Devices:**
  - Many rigid exoskeletons primarily focus on strength augmentation, rather than active rehabilitation, which makes them less effective in retraining natural movement patterns.
  - The CDSE provides a better balance between movement assistance and active user participation, enhancing rehabilitation effectiveness.

7.7 Conclusion

The experimental evaluation of the Cable-Driven Shoulder Exosuit (CDSE) provided critical insights into its performance, reliability, and usability in upper limb assistance. Across all tests, the exosuit demonstrated a high degree of repeatability, with less than 5% deviation in position tracking accuracy for shoulder abduction, flexion, and horizontal flexion movements. The system successfully supported loads ranging from 500g to 4000g, with recorded torque values aligning within 95% of the predicted theoretical model. The exosuit's lightweight design, weighing approximately 2 kg, contributed to its portability and minimized user fatigue, aligning with the principles of biomechanical load distribution.

From an engineering perspective, the Bowden cable transmission system effectively replicated tendon-like force transmission, ensuring smooth movement assistance while maintaining flexibility. The force distribution and cable tension optimization strategies allowed for controlled movement execution without excessive mechanical resistance. However, one key challenge encountered was the slight misalignment in the anchor points during high-load scenarios, leading to minor variations in force transmission. Addressing this issue in future iterations could involve adaptive tensioning mechanisms or dynamic realignment strategies to enhance precision.

Reflecting on the overall design and development process, one of the major successes was the integration of a biologically inspired actuation approach, which contributed to a more natural user experience. However, future versions (V2) of the exosuit could benefit from an improved ergonomic fit, particularly around the shoulder attachment points, to enhance comfort during prolonged use. Additionally, refining the control algorithm to incorporate real-time EMG-based adaptation would further personalize the assistance provided by the exosuit, improving responsiveness and adaptability to individual user needs.

This research contributes to the ongoing advancement of soft robotic exosuits, demonstrating that a well-designed cable-driven system can effectively support natural movement patterns while maintaining a lightweight and user-friendly design. The lessons learned from this study will serve as a foundation for future improvements, ensuring that the next generation of exosuits achieves even greater levels of precision, comfort, and clinical applicability.

8 Chapter Eight: Conclusion and Future Work

8.1 Conclusion

The research encapsulated in this thesis has provided a thorough exploration of the development and validation of the Cable-Driven Shoulder Exosuit (CDSE), an innovative soft robotic exosuit designed for the rehabilitation of the shoulder. This work has meticulously covered every aspect of the CDSE, from the initial concept and design to the extensive testing and final refinements. The successful development of the CDSE marks a significant contribution to the fields of soft robotics and rehabilitation, showcasing the potential of soft exosuits to enhance human biomechanics and mobility.

The CDSE was engineered with the primary objective of addressing the rehabilitation needs of individuals with upper limb disabilities, focusing specifically on the shoulder, a joint that is critical to numerous daily activities. The design integrates soft robotics technologies, which have certain advantages over more rigid systems due to their inherent flexibility and user comfort. This thesis has demonstrated the feasibility of using such technologies in a wearable device that can operate in alignment with the natural movements of the human body without compromising on the strength or durability required for effective rehabilitation.

The initial phase of the project involved a comprehensive design process, where various materials and mechanisms were tested. Progressing from prototypical designs made from polylactic acid (PLA) to more refined versions using aluminium and carbon fiber, each iteration was subjected to rigorous Finite Element Analysis (FEA) and real-world testing. These evaluations were crucial to confirming the structural integrity and functional reliability of the exosuit under various load conditions. This iterative approach not only enhanced the mechanical properties of the exosuit but also optimized its ergonomic design to allow for better user interaction.

Through detailed testing, including the application of controlled loads ranging from 500 grams to 4000 grams, the exosuit has was validated to withstand expected operational stresses while ensuring comfort and safety for the user. The integration of a sophisticated motor pack, Bowden cable system, and Arduino-UNO for control operations highlights the interdisciplinary nature of this research, merging mechanical engineering, electronics, and software development.

A pivotal aspect of this work was the adaptation of the exosuit to user-specific needs, leveraging anthropometric data to ensure ergonomic compatibility. The utilization of advanced materials played a significant role in achieving a balance between lightness, strength, and flexibility—essential qualities for any rehabilitation device intended for everyday use. Moreover, the modular design of the exosuit facilitates easy adjustment and customization, which is crucial for meeting diverse patient requirements and to allow for ongoing product development.

The research methodology employed throughout this study involved not only theoretical design and simulation but also practical, hands-on experimentation and iterative feedback loops. This comprehensive approach ensured that all potential issues were properly addressed, and that improvements were made systematically, leading to a well-rounded final product.

The success of the CDSE in this research setting lays a robust foundation for further studies. The exosuit’s design and functionality represent a significant step forward in the quest to improve the quality of life for individuals with shoulder impairments. It also opens new avenues for the application of soft robotics in other areas of rehabilitation and human assistance.

8.2 Research Findings

This section discusses the primary outcomes derived from the experimental evaluation of the Cable-Driven Shoulder Exosuit (CDSE), focusing on its performance in enhancing shoulder joint mobility and its potential applications in rehabilitation settings.

1- Performance Evaluation of CDSE:

The experiments conducted demonstrated the CDSE's effectiveness in facilitating controlled movements across the shoulder's three degrees of freedom—abduction, flexion, and horizontal flexion. By employing loads ranging from 500 g to 4000 g, the exosuit consistently managed force output and maintained precise trajectory control. The findings confirm the hypothesis that cable-driven mechanisms can augment human limb movements effectively, offering a viable alternative to more rigid exoskeletal systems.

2- Repeatability and Reliability:

Repeatability tests assessed the CDSE’s reliability for therapeutic use, revealing high consistency in movement accuracy, force application, and response times across multiple trials. This consistency underscores the exosuit's suitability for clinical rehabilitation, where predictable and repeatable performance is essential for effective patient therapy.

3- Finite Element Analysis (FEA):

FEA was utilized to verify the mechanical integrity and durability of the exosuit under operational stress. Results confirmed that the materials and design configurations chosen could withstand operational loads effectively without compromising safety or performance. These insights are critical for justifying the design decisions made during the development phase and demonstrate the robustness required for practical deployment.

8.3 Future Work

Looking ahead, the path for future research and development in this area is vast and promising. One of the immediate next steps is to conduct extensive clinical trials to validate the therapeutic effectiveness and safety of the CDSE on a larger scale. Such studies are essential to an understanding of the full range of the exosuit's capabilities and to ensuring that it can be safely integrated into everyday rehabilitation practices.

Further, enhancing the exosuit's control systems through the incorporation of adaptive algorithms and real-time response mechanisms could significantly improve its functionality. Developing AI-driven features that can predict and adapt to user movement patterns could offer personalized rehabilitation experiences, making the device not only more effective but also more intuitive to use.

Motion analysis with motion trackers and Vicon cameras for CDSE can be covered in future work with consideration of using EMG sensors as well.

Another critical area of future research is the exploration of the commercial viability of the CDSE. This includes detailed market analysis, cost optimization, and scalability assessments. Ensuring that the exosuit is affordable and accessible to a broad audience is crucial to its success in real-world applications. Moreover, partnerships with medical institutions and healthcare professionals will be vital in facilitating the widespread adoption of this technology.

In conclusion, the research presented in this thesis not only advances the technical knowledge and application of soft robotics in rehabilitation but also provides a solid platform for future innovation in this rapidly evolving field. The Cable-Driven Shoulder Exosuit represents a pioneering step towards more dynamic, user-friendly, and effective rehabilitation devices. As technology progresses, it holds the promise of significantly impacting the field of rehabilitation, offering enhanced therapeutic outcomes, and ultimately improving the quality of life for individuals with impaired mobility.

9 BLIOGRAPHY

[1] "Scopus - Analyze search results." Accessed: Sep. 07, 2020. [Online]. Available: https://www-scopus-com.salford.idm.oclc.org/term/analyzer.uri?sid=44ee6ed7f71b4aa2628c43b23addf774&origin=resultslist&src=s&s=%28TITLE-ABS-KEY%28exoskeleton+%29+AND+TITLE-ABS-KEY%28robotic%29%29&sort=plf-f&sdt=b&sot=b&sl=56&count=5520&analyzeResults=Analy

[2] "Scopus - Analyze search results," Scopus. Accessed: Sep. 07, 2020. [Online]. Available: https://www-scopus-com.salford.idm.oclc.org/term/analyzer.uri?sid=44ee6ed7f71b4aa2628c43b23addf774&origin=resultslist&src=s&s=%28TITLE-ABS-KEY%28exosuit%29+AND+TITLE-ABS-KEY%28robotic%29%29&sort=plf-f&sdt=b&sot=b&sl=51&count=103&analyzeResults=Analyze+res

[3] R. A. R. C. Gopura and K. Kiguchi, "Mechanical designs of active upper-limb exoskeleton robots state-of-the-art and design difficulties," in *2009 IEEE International Conference on Rehabilitation Robotics, ICORR 2009*, 2009, pp. 178–187. doi: 10.1109/ICORR.2009.5209630.

[4] R. J. Varghese, D. Freer, F. Deligianni, J. Liu, and G. Z. Yang, "Wearable robotics for upper-limb rehabilitation and assistance," in *Wearable Technology in Medicine and Health Care*, Elsevier, 2018, pp. 23–69. doi: 10.1016/B978-0-12-811810-8.00003-8.

[5] R. L. Drake, A. W. Vogl, and A. W. M. Mitchell, *Gray's Anatomy for Students, 4th Edition*. 2019. doi: 10.1017/CBO9781107415324.004.

[6] Z. Pang, T. Wang, Z. Wang, J. Yu, Z. Sun, and S. Liu, "Design and analysis of a wearable upper limb rehabilitation robot with characteristics of tension mechanism," *Applied Sciences (Switzerland)*, vol. 10, no. 6, Mar. 2020, doi: 10.3390/app10062101.

[7] "Sternoclavicular Joint Problems | eOrthopod.com." Accessed: Jul. 10, 2020. [Online]. Available: https://eorthopod.com/sternoclavicular-joint-problems/

[8] "Scapulothoracic - qivufuvo53.over-blog.com." Accessed: Jul. 10, 2020. [Online]. Available: http://qivufuvo53.over-blog.com/scapulothoracic

[9] N. Li *et al.*, "Bio-inspired upper limb soft exoskeleton to reduce stroke-induced complications," *Bioinspir Biomim*, vol. 13, no. 6, Aug. 2018, doi: 10.1088/1748-3190/aad8d4.

[10] F. Xiao, Y. Gao, Y. Wang, Y. Zhu, and J. Zhao, "Design of a wearable cable-driven upper limb exoskeleton based on epicyclic gear trains structure," in *Technology and Health Care*, IOS Press, Jul. 2017, pp. S3–S11. doi: 10.3233/THC-171300.

[11] D. Koo, P. H. Chang, M. K. Sohn, and J. H. Shin, "Shoulder mechanism design of an exoskeleton robot for stroke patient rehabilitation," in *IEEE International Conference on Rehabilitation Robotics*, 2011, pp. 1–6. doi: 10.1109/ICORR.2011.5975505.

[12] M. A. Ergin and V. Patoglu, "ASSISTON-SE: A self-aligning shoulder-elbow exoskeleton," in *Proceedings - IEEE International Conference on Robotics and Automation*, Institute of Electrical and Electronics Engineers Inc., 2012, pp. 2479–2485. doi: 10.1109/ICRA.2012.6225117.

[13] T. Nef, M. Guidali, and R. Riener, “ARMin III - arm therapy exoskeleton with an ergonomic shoulder actuation,” *Appl Bionics Biomech*, vol. 6, no. 2, pp. 127–142, 2009, doi: 10.1080/11762320902840179.

[14] A. Schiele and F. C. T. Van Der Helm, “Kinematic design to improve ergonomics in human machine interaction,” *IEEE Transactions on Neural Systems and Rehabilitation Engineering*, vol. 14, no. 4, pp. 456–469, Dec. 2006, doi: 10.1109/TNSRE.2006.881565.

[15] S. J. Ball, I. E. Brown, and S. H. Scott, “MEDARM: A rehabilitation robot with 5DOF at the shoulder complex,” in *IEEE/ASME International Conference on Advanced Intelligent Mechatronics, AIM*, 2007. doi: 10.1109/AIM.2007.4412446.

[16] K. Kiguchi, K. Iwami, M. Yasuda, K. Watanabe, and T. Fukuda, “An exoskeletal robot for human shoulder joint motion assist,” *IEEE/ASME Transactions on Mechatronics*, vol. 8, no. 1, pp. 125–135, Mar. 2003, doi: 10.1109/TMECH.2003.809168.

[17] M. H. Rahman, M. J. Rahman, O. L. Cristobal, M. Saad, J. P. Kenné, and P. S. Archambault, “Development of a whole arm wearable robotic exoskeleton for rehabilitation and to assist upper limb movements,” *Robotica*, vol. 33, no. 1, pp. 19–39, Jan. 2015, doi: 10.1017/S0263574714000034.

[18] “Bio-inspired Wearable Soft Upper-Limb Exoskeleton Robot for Stroke Survivors.”

[19] “Carpal bones - volar view (anatomy) - Incision Academy.” Accessed: Jul. 11, 2020. [Online]. Available: https://www.incision.care/inc_library/01-hand-volar-bones-titles/carpal-bones-labels/

[20] Kenhub, “Upper extremity: Anatomy study course |,” Kenhub. Accessed: Jun. 07, 2020. [Online]. Available: https://www.kenhub.com/en/start/upper-extremity

[21] “Anatomy of the Forearm - Muscles and Tendons,” YouTube. Accessed: Jul. 11, 2020. [Online]. Available: https://www.youtube.com/watch?v=zSjB3vEnAJ8

[22] N. Li *et al.*, “Bio-inspired upper limb soft exoskeleton to reduce stroke-induced complications,” *Bioinspir Biomim*, vol. 13, no. 6, Aug. 2018, doi: 10.1088/1748-3190/aad8d4.

[23] C. Carignan, M. Liszka, and S. Roderick, “Design of an arm exoskeleton with scapula motion for shoulder rehabilitation,” in *2005 International Conference on Advanced Robotics, ICAR ’05, Proceedings*, 2005, pp. 524–531. doi: 10.1109/ICAR.2005.1507459.

[24] M. Mihelj, T. Nef, and R. Riener, “ARMin II - 7 DoF Rehabilitation Robot: Mechanics and Kinematics,” 2007.

[25] C. Carignan and J. Tang, “A Configuration-Space Approach to Controlling a Rehabilitation Arm Exoskeleton.”

[26] N. G. Tsagarakis and D. G. Caldwell, “Development and Control of a ‘Soft-Actuated’ Exoskeleton for Use in Physiotherapy and Training,” 2003.

[27] T. G. Sugar *et al.*, “Design and control of RUPERT: A device for robotic upper extremity repetitive therapy,” *IEEE Transactions on Neural Systems and Rehabilitation Engineering*, vol. 15, no. 3, pp. 336–346, Sep. 2007, doi: 10.1109/TNSRE.2007.903903.

[28] T. Nef, M. Guidali, and R. Riener, “ARMin III - arm therapy exoskeleton with an ergonomic shoulder actuation,” *Appl Bionics Biomech*, vol. 6, no. 2, pp. 127–142, 2009, doi: 10.1080/11762320902840179.

[29] G. R. Johnson, D. A. Carus, G. Parrini, S. Scattareggia Marchese, and R. Valeggi, "The design of a five-degree-of-freedom powered orthosis for the upper limb," *Proc Inst Mech Eng H*, vol. 215, no. 3, pp. 275–284, 2001, doi: 10.1243/0954411011535867.
[30] H. Kobayashi, Y. Ishida, and H. Suzuki, "Realization of all motion for the upper limb by muscle suit," in *In RO-MAN 2004. 13th IEEE International Workshop on Robot and Human Interactive Communication (IEEE Catalog No. 04TH8759)*, 2004, pp. 631–636. doi: 10.1109/texcra.2004.1424995.
[31] R. Sanchez *et al.*, "Monitoring functional arm movement for home-based therapy after stroke," in *Annual International Conference of the IEEE Engineering in Medicine and Biology - Proceedings*, 2004, pp. 4787–4790. doi: 10.1109/iembs.2004.1404325.
[32] A. Toth, G. Fazekas, G. Arz, M. Jurak, and M. Horvath, "Passive robotic movement therapy of the spastic hemiparetic arm with REHAROB: Report of the first clinical test and the follow-up system improvement," in *Proceedings of the 2005 IEEE 9th International Conference on Rehabilitation Robotics*, 2005, pp. 127–130. doi: 10.1109/ICORR.2005.1501067.
[33] T. Nef and R. Riener, "ARMin - Design of a novel arm rehabilitation robot," *IEEE 9th International Conference on Rehabilitation Robotics*, pp. 57–60, 2005, doi: 10.1109/ICORR.2005.1501051.
[34] Q. Li, D. Wang, Z. Du, Y. Song, and L. Sun, "sEMG Based Control for 5 DOF Upper Limb Rehabilitation Robot System."
[35] E. T. Wolbrecht, J. Leavitt, D. J. Reinkensmeyer, and J. E. Bobrow, "Control of a Pneumatic Orthosis for Upper Extremity Stroke Rehabilitation."
[36] H. Kobayashi and H. Nozaki, "Development of muscle suit for supporting manual worker," in *IEEE International Conference on Intelligent Robots and Systems*, IEEE, 2007, pp. 1769–1774. doi: 10.1109/IROS.2007.4399412.
[37] M. Mihelj, T. Nef, and R. Riener, "ARMin II - 7 DoF Rehabilitation Robot: Mechanics and Kinematics," 2007.
[38] A. Frisoli *et al.*, "Arm rehabilitation with a robotic exoskeleleton in Virtual Reality," in *2007 IEEE 10th International Conference on Rehabilitation Robotics, ICORR'07*, 2007, pp. 631–642. doi: 10.1109/ICORR.2007.4428491.
[39] C. Carignan, J. Tang, S. Roderick, and M. Naylor, "A Configuration-Space Approach to Controlling a Rehabilitation Arm Exoskeleton," in *International Conference on Rehabilitation Robotics*, IEEE, 2007, pp. 1–9.
[40] J. C. Perry, J. Rosen, and S. Burns, "Upper-limb powered exoskeleton design," in *IEEE/ASME Transactions on Mechatronics*, Aug. 2007, pp. 408–417. doi: 10.1109/TMECH.2007.901934.
[41] T. Nef, M. Guidali, and R. Riener, "ARMin III - arm therapy exoskeleton with an ergonomic shoulder actuation," *Appl Bionics Biomech*, vol. 6, no. 2, pp. 127–142, 2009, doi: 10.1080/11762320902840179.
[42] S. Balasubramanian *et al.*, "Rupert: An exoskeleton robot for assisting rehabilitation of arm functions," *Virtual Rehabilitation, IWVR*, pp. 163–167, 2008, doi: 10.1109/ICVR.2008.4625154.

[43] K. Kiguchi, M. H. Rahman, M. Sasaki, and K. Teramoto, “Development of a 3DOF mobile exoskeleton robot for human upper-limb motion assist,” *Rob Auton Syst*, vol. 56, no. 8, pp. 678–691, Aug. 2008, doi: 10.1016/j.robot.2007.11.007.

[44] A. H. A. Stienen, E. E. G. Hekman, H. Ter Braak, A. M. M. Aalsma, F. C. T. Van Der Helm, and H. Van Der Kooij, “Design of a rotational hydro-elastic actuator for an active upper-extremity rehabilitation exoskeleton,” *International Conference on Biomedical Robotics and Biomechatronics*, pp. 881–888, 2008, doi: 10.1109/BIOROB.2008.4762873.

[45] S. Moubarak, M. T. Pham, T. Pajdla, and T. Redarce, “Design Results of an Upper Extremity Exoskeleton,” 2008. [Online]. Available: www.springerlink.com

[46] R. A. R. C. Gopura and K. Kiguchi, “Development of a 6DOF exoskeleton robot for human upper-limb motion assist,” in *Proceedings of the 2008 4th International Conference on Information and Automation for Sustainability, ICIAFS 2008*, 2008, pp. 13–18. doi: 10.1109/ICIAFS.2008.4783986.

[47] P. Garrec, J. P. Friconneau, Y. Méasson, and Y. Perrot, “ABLE , an Innovative Transparent Exoskeleton for the Upper-Limb,” in *International Conference on Intelligent Robots and Systems*, 2008, pp. 22–26.

[48] A. H. A. Stienen *et al.*, “Dampace: Design of an exoskeleton for force-coordination training in upper-extremity rehabilitation,” *Journal of Medical Devices, Transactions of the ASME*, vol. 3, no. 3, Sep. 2009, doi: 10.1115/1.3191727.

[49] R. Vertechy, A. Frisoli, A. Dettori, M. Solazzi, and M. Bergamasco, “Development of a new exoskeleton for upper limb rehabilitation,” in *2009 IEEE International Conference on Rehabilitation Robotics, ICORR 2009*, 2009, pp. 188–193. doi: 10.1109/ICORR.2009.5209502.

[50] R. A. R. C. Gopura, K. Kiguchi, and Y. Yi, “SUEFUL-7: A 7DOF upper-limb exoskeleton robot with muscle-model-oriented EMG-based control,” in *2009 IEEE/RSJ International Conference on Intelligent Robots and Systems, IROS 2009*, Dec. 2009, pp. 1126–1131. doi: 10.1109/IROS.2009.5353935.

[51] A. Umemura, Y. Saito, and K. Fujisaki, “A study on power-assisted rehabilitation robot arms operated by patient with upper limb disabilities,” *IEEE International Conference on Rehabilitation Robotics, ICORR*, pp. 451–456, 2009, doi: 10.1109/ICORR.2009.5209512.

[52] Y. Ren, H. S. Park, and L. Q. Zhang, “Developing a whole-arm exoskeleton robot with hand opening and closing mechanism for upper limb stroke rehabilitation,” in *2009 IEEE International Conference on Rehabilitation Robotics, ICORR 2009*, 2009, pp. 761–765. doi: 10.1109/ICORR.2009.5209482.

[53] J. Klein, S. Spencer, J. Allington, J. E. Bobrow, and D. J. Reinkensmeyer, “Optimization of a parallel shoulder mechanism to achieve a high-force, low-mass, robotic-arm exoskeleton,” *IEEE Transactions on Robotics*, vol. 26, no. 4, pp. 710–715, Aug. 2010, doi: 10.1109/TRO.2010.2052170.

[54] K. Kiguchi, Y. Kose, and Y. Hayashi, “TASK-ORIENTED PERCEPTION-ASSIST FOR AN UPPER-LIMB POWER-ASSIST EXOSKELETON ROBOT,” 2010.

[55] B. Dehez and J. Sapin, “ShouldeRO, an alignment-free two-DOF rehabilitation robot for the shoulder complex, IEEE International Conference on Rehabilitation Robotics,” in *IEEE International Conference on Rehabilitation Robotics*, 2011. doi: 10.1109/ICORR.2011.5975339.

[56] I. Galiana, F. L. Hammond III, R. D. Howe, and M. Popovic, *Wearable Soft Robotic Device for Post-Stroke Shoulder Rehabilitation: Identifying Misalignments*. 2012. doi: 10.0/Linux-x86_64.
[57] L. Pignolo, G. Dolce, G. Basta, L. F. Lucca, S. Serra, and W. G. Sannita, "Upper limb rehabilitation after stroke: ARAMIS a robo-mechatronic innovative approach and prototype," in *Proceedings of the IEEE RAS and EMBS International Conference on Biomedical Robotics and Biomechatronics*, 2012, pp. 1410–1414. doi: 10.1109/BioRob.2012.6290868.
[58] A. Pedrocchi *et al.*, "MUNDUS project: MUltimodal Neuroprosthesis for daily Upper limb Support," 2013. [Online]. Available: http://www.jneuroengrehab.com/content/10/1/66
[59] H. B. Kang and J. H. Wang, "Adaptive control of 5 DOF upper-limb exoskeleton robot with improved safety," *ISA Trans*, vol. 52, no. 6, pp. 844–852, 2013, doi: 10.1016/j.isatra.2013.05.003.
[60] Y. Ren, S. H. Kang, H. S. Park, Y. N. Wu, and L. Q. Zhang, "Developing a multi-joint upper limb exoskeleton robot for diagnosis, therapy, and outcome evaluation in neurorehabilitation," *IEEE Transactions on Neural Systems and Rehabilitation Engineering*, vol. 21, no. 3, pp. 490–499, 2013, doi: 10.1109/TNSRE.2012.2225073.
[61] K. Xu and D. Qiu, "Experimental design verification of a compliant shoulder exoskeleton," in *Proceedings - IEEE International Conference on Robotics and Automation*, 2013, pp. 3894–3901. doi: 10.1109/ICRA.2013.6631125.
[62] Y. Chen, G. Li, Y. Zhu, J. Zhao, and H. Cai, "Design of a 6-DOF upper limb rehabilitation exoskeleton with parallel actuated joints," in *Bio-Medical Materials and Engineering*, IOS Press, 2014, pp. 2527–2535. doi: 10.3233/BME-141067.
[63] W. Chonnaparamutt and W. Supsi, "SEFRE: Semiexoskeleton Rehabilitation System," *Appl Bionics Biomech*, vol. 2016, 2016, doi: 10.1155/2016/8306765.
[64] R. F. Natividad and C. H. Yeow, "Development of a soft robotic shoulder assistive device for shoulder abduction," *Proceedings of the IEEE RAS and EMBS International Conference on Biomedical Robotics and Biomechatronics*, vol. 2016-July, pp. 989–993, 2016, doi: 10.1109/BIOROB.2016.7523758.
[65] I. Gaponov, D. Popov, S. J. Lee, and J. H. Ryu, "Auxilio: A portable cable-driven exosuit for upper extremity assistance," *Int J Control Autom Syst*, vol. 15, no. 1, pp. 73–84, Feb. 2017, doi: 10.1007/s12555-016-0487-7.
[66] A. Zeiaee, R. Soltani-Zarrin, R. Langari, and R. Tafreshi, *Design and Kinematic Analysis of a Novel Upper Limb Exoskeleton for Rehabilitation of Stroke Patients*. 2017. doi: 10.0/Linux-x86_64.
[67] Ciarán T. O'Neill; Nathan S. Phipps; Leonardo Cappello; Sabrina Paganoni; Conor J. Walsh, "A Soft Wearable Robot for the Shoulder: Design, Characterization, and Preliminary Testing," in *International Conference on Rehabilitation Robotics (ICORR)*, 2017.
[68] V. W. Oguntosin, Y. Mori, H. Kim, S. J. Nasuto, S. Kawamura, and Y. Hayashi, "Design and Validation of exoskeleton actuated by soft modules toward neurorehabilitation-vision-based control for precise reaching motion of upper limb," *Front Neurosci*, vol. 11, no. JUL, Jul. 2017, doi: 10.3389/fnins.2017.00352.

[69] D. Park and K. J. Cho, "Development and evaluation of a soft wearable weight support device for reducing muscle fatigue on shoulder," *PLoS One*, vol. 12, no. 3, Mar. 2017, doi: 10.1371/journal.pone.0173730.
[70] N. Li *et al.*, "Bio-inspired Upper Limb Soft Exoskeleton to Reduce Stroke-induced Complications," *Biochemical Journal*, no. May, pp. 1–26, 2010, doi: https://doi.org/10.1088/1748-3190/aad8d4.
[71] R. F. Natividad, S. W. Hong, T. M. Miller-jackson, and C. Yeow, "The Exosleeve: A Soft Robotic Exoskeleton for Assisting in Activities of Daily Living," in *International Symposium on Wearable Robotics*, 2018, pp. 3–4.
[72] Y. G. Kiml, M. Xiloyannis, D. Accoto, and L. Masia, "Development of a Soft Exosuit for Industriale Applications," in *Proceedings of the IEEE RAS and EMBS International Conference on Biomedical Robotics and Biomechatronics*, IEEE Computer Society, Oct. 2018, pp. 324–329. doi: 10.1109/BIOROB.2018.8487907.
[73] S. Lessard, P. Pansodtee, A. Robbins, J. M. Trombadore, S. Kurniawan, and M. Teodorescu, "A Soft Exosuit for Flexible Upper-Extremity Rehabilitation," *IEEE Transactions on Neural Systems and Rehabilitation Engineering*, vol. 26, no. 8, pp. 1604–1617, Aug. 2018, doi: 10.1109/TNSRE.2018.2854219.
[74] L. Tiseni *et al.*, *On the edge between soft and rigid: an assistive shoulder exoskeleton with hyper-redundant kinematics*. 2019. doi: 10.0/Linux-x86_64.
[75] A. Carolina, D. A. Mendes, P. Kutilek, J. Hejda, P. Smrcka, and V. Havlas, "Design of Smart Orthosis of Upper Limb for Rehabilitation," in *World Congress on Medical Physics and Biomedical Engineering*, Springer Singapore, 2019, pp. 773–778. doi: 10.1007/978-981-10-9038-7.
[76] R. J. Varghese, B. P. L. Lo, and G.-Z. Yang, "Design and Prototyping of a Bio-inspired Kinematic Sensing Suit for the Shoulder Joint: Precursor to a Multi-DoF Shoulder Exosuit," Oct. 2019, [Online]. Available: http://arxiv.org/abs/1910.04787
[77] D. Pont *et al.*, "Exoflex:an upper-limb cable-driven exosuit," *Springer Nature Switzerland*, pp. 417–428, 2019.
[78] J. C. Perry, J. Rosen, and S. Burns, "Upper-limb powered exoskeleton design," *IEEE/ASME Transactions on Mechatronics*, vol. 12, no. 4, pp. 408–417, 2007, doi: 10.1109/TMECH.2007.901934.
[79] R. J. Varghese, A. Nguyen, E. Burdet, G.-Z. Yang, and B. P. L. Lo, "Nonlinearity Compensation in a Multi-DoF Shoulder Sensing Exosuit for Real-Time Teleoperation," Feb. 2020, [Online]. Available: http://arxiv.org/abs/2002.09195
[80] J. J. Chang, W. L. Tung, W. L. Wu, M. H. Huang, and F. C. Su, "Effects of Robot-Aided Bilateral Force-Induced Isokinetic Arm Training Combined With Conventional Rehabilitation on Arm Motor Function in Patients With Chronic Stroke," *Arch Phys Med Rehabil*, vol. 88, no. 10, pp. 1332–1338, Oct. 2007, doi: 10.1016/j.apmr.2007.07.016.
[81] E. Piña-Martínez, R. Roberts, S. Leal-Merlo, and E. Rodriguez-Leal, "Vision system-based design and assessment of a novel shoulder joint mechanism for an enhanced workspace upper limb exoskeleton," *Appl Bionics Biomech*, vol. 2018, 2018, doi: 10.1155/2018/6019381.

[82] R. F. Natividad, S. W. Hong, T. M. Miller-Jackson, and C. H. Yeow, “The Exosleeve: A Soft Robotic Exoskeleton for Assisting in Activities of Daily Living,” in *International Symposium on Wearable Robotics*, 2018, pp. 406–409. doi: 10.1007/978-3-030-01887-0_78.
[83] S. Micera *et al.*, “A Simple Robotic System for Neurorehabilitation,” 2005.
[84] L. Pignolo, G. Dolce, G. Basta, L. F. Lucca, S. Serra, and W. G. Sannita, “Upper limb rehabilitation after stroke: ARAMIS a robo-mechatronic innovative approach and prototype,” in *Proceedings of the IEEE RAS and EMBS International Conference on Biomedical Robotics and Biomechatronics*, 2012, pp. 1410–1414. doi: 10.1109/BioRob.2012.6290868.
[85] A. Zeiaee, R. Soltani-Zarrin, R. Langari, and R. Tafreshi, “Design and kinematic analysis of a novel upper limb exoskeleton for rehabilitation of stroke patients,” *IEEE International Conference on Rehabilitation Robotics*, pp. 759–764, 2017, doi: 10.1109/ICORR.2017.8009339.
[86] P. R. Culmer *et al.*, “A novel robotic system for quantifying arm kinematics and kinetics: Description and evaluation in therapist-assisted passive arm movements post-stroke,” *J Neurosci Methods*, vol. 197, no. 2, pp. 259–269, Apr. 2011, doi: 10.1016/j.jneumeth.2011.03.004.
[87] D. Galinski, J. Sapin, and B. Dehez, “Optimal design of an alignment-free two-DOF rehabilitation robot for the shoulder complex,” *IEEE International Conference on Rehabilitation Robotics*, 2013, doi: 10.1109/ICORR.2013.6650502.
[88] R. Bogue, “Exoskeletons and robotic prosthetics: A review of recent developments,” *Industrial Robot*, vol. 36, no. 5, pp. 421–427, 2009, doi: 10.1108/01439910910980141.
[89] P. Maciejasz, J. Eschweiler, K. Gerlach-Hahn, A. Jansen-Troy, and S. Leonhardt, “JNER JOURNAL OF NEUROENGINEERING AND REHABILITATION REVIEW Open Access A survey on robotic devices for upper limb rehabilitation,” 2014. [Online]. Available: http://www.jneuroengrehab.com/content/11/1/3
[90] M. Mihelj, T. Nef, and R. Riener, “ARMin II - 7 DoF rehabilitation robot: Mechanics and kinematics,” *Proc IEEE Int Conf Robot Autom*, no. April, pp. 4120–4125, 2007, doi: 10.1109/ROBOT.2007.364112.
[91] A. Mayr, M. Kofler, and L. Saltuari, “ARMOR: Elektromechanischer roboter für das bewegungstraining der oberen extremität nach schlaganfall. Prospektive randomisierte kontrollierte pilotstudie,” *Handchirurgie Mikrochirurgie Plastische Chirurgie*, vol. 40, no. 1, pp. 66–73, Feb. 2008, doi: 10.1055/s-2007-989425.
[92] P. Maciejasz, J. Eschweiler, K. Gerlach-Hahn, A. Jansen-Troy, and L. Leonhardt, “A survey on robotic devices for upper limb rehabilitation,” *J Neuroeng Rehabil*, vol. 11, no. 3, 2014, doi: 10.1007/s00115-003-1549-7.
[93] C. Carignan, J. Tang, S. Roderick, and M. Naylor, “A Configuration-Space Approach to Controlling a Rehabilitation Arm Exoskeleton,” in *International Conference on Rehabilitation Robotics*, IEEE, 2007, pp. 1–9.
[94] N. Jarrassé *et al.*, “Robotic exoskeletons: A perspective for the rehabilitation of arm coordination in stroke patients,” Dec. 01, 2014, *Frontiers Media S. A.* doi: 10.3389/fnhum.2014.00947.
[95] R. J. Varghese, B. P. L. Lo, and G. Z. Yang, “Design and Prototyping of a Bio-Inspired Kinematic Sensing Suit for the Shoulder Joint: Precursor to a Multi-DoF Shoulder

Exosuit," *IEEE Robot Autom Lett*, vol. 5, no. 2, pp. 540–547, 2020, doi: 10.1109/LRA.2019.2963636.

[96] D. Park and K. Cho, "Development and evaluation of a soft wearable weight support device for reducing muscle fatigue on shoulder," *PLoS One*, pp. 1–24, 2017.

[97] "ShoulderX," suitX. Accessed: Jul. 31, 2020. [Online]. Available: https://www.suitx.com/shoulderx

[98] "EksoWorks," Ekso Bionics. Accessed: Jul. 31, 2020. [Online]. Available: https://eksobionics.com/eksoworks/

[99] "Myomo -," Medical Robotics Solutions for Stroke, BPI, Upper Limb Paralysis. Accessed: Jul. 31, 2020. [Online]. Available: https://myomo.com/

[100] "Paexo Shoulder -," Ottobock Industrials. Accessed: Jul. 31, 2020. [Online]. Available: https://paexo.com/paexo-shoulder/?lang=en

[101] D. Park and K. J. Cho, "Development and evaluation of a soft wearable weight support device for reducing muscle fatigue on shoulder," *PLoS One*, vol. 12, no. 3, Mar. 2017, doi: 10.1371/journal.pone.0173730.

[102] S. Balasubramanian *et al.*, "Rupert: An exoskeleton robot for assisting rehabilitation of arm functions," *Virtual Rehabilitation, IWVR*, pp. 163–167, 2008, doi: 10.1109/ICVR.2008.4625154.

[103] A. Toth, G. Fazekas, G. Arz, M. Jurak, and M. Horvath, "Passive robotic movement therapy of the spastic hemiparetic arm with REHAROB: Report of the first clinical test and the follow-up system improvement," *IEEE 9th International Conference on Rehabilitation Robotics*, pp. 127–130, 2005, doi: 10.1109/ICORR.2005.1501067.

[104] F. Xiao, Y. Gao, Y. Wang, Y. Zhu, and J. Zhao, "Design of a wearable cable-driven upper limb exoskeleton based on epicyclic gear trains structure," in *Technology and Health Care*, IOS Press, Jul. 2017, pp. S3–S11. doi: 10.3233/THC-171300.

[105] H. Kobayashi, Y. Ishida, and H. Suzuki, "Realization of All Motion for the Upper Limb by a Muscle Suit."

[106] K. Kiguchi, Y. Kose, and Y. Hayashi, "Task-oriented perception-assist for an upper-limb power-assist exoskeleton robot," *World Automation Congress, WAC*, 2010.

[107] P. Garrec, J. P. Friconneau, Y. Méasson, and Y. Perrot, "ABLE, an innovative transparent exoskeleton for the upper-limb," in *2008 IEEE/RSJ International Conference on Intelligent Robots and Systems, IROS*, 2008, pp. 1483–1488. doi: 10.1109/IROS.2008.4651012.

[108] A. Pedrocchi *et al.*, "MUNDUS project: MUltimodal Neuroprosthesis for daily Upper limb Support," *J Neuroeng Rehabil*, vol. 10, p. 1, 2013, doi: 10.1186/1743-0003-10-66.

[109] P. Maciejasz, J. Eschweiler, K. Gerlach-Hahn, A. Jansen-Troy, and S. Leonhardt, "A survey on robotic devices for upper limb rehabilitation," 2014. [Online]. Available: http://www.jneuroengrehab.com/content/11/1/3

[110] A. Umemura, Y. Saito, and K. Fujisaki, "A study on power-assisted rehabilitation robot arms operated by patient with upper limb disabilities," in *2009 IEEE International Conference on Rehabilitation Robotics, ICORR 2009*, 2009, pp. 451–456. doi: 10.1109/ICORR.2009.5209512.

[111] R. Morales, F. J. Badesa, N. García-Aracil, J. M. Sabater, and C. Pérez-Vidal, "Pneumatic robotic systems for upper limb rehabilitation," *Med Biol Eng Comput*, vol. 49, no. 10, pp. 1145–1156, Oct. 2011, doi: 10.1007/s11517-011-0814-3.

[112] Y. G. Kim, M. Xiloyannis, D. Accoto, and L. Masia, “Development of a Soft Exosuit for Industrial Applications,” in *IEEE International Conference on Biomedical Robotics and Biomechatronics (Biorob)*, IEEE, 2018.

[113] J. Klein, S. Spencer, J. Allington, J. E. Bobrow, and D. J. Reinkensmeyer, “Optimization of a parallel shoulder mechanism to achieve a high-force, low-mass, robotic-arm exoskeleton,” *IEEE Transactions on Robotics*, vol. 26, no. 4, pp. 710–715, 2010, doi: 10.1109/TRO.2010.2052170.

[114] R. Sanchez *et al.*, “Monitoring functional arm movement for home-based therapy after stroke,” *Annual International Conference of the IEEE Engineering in Medicine and Biology - Proceedings*, vol. 26 VII, pp. 4787–4790, 2004, doi: 10.1109/iembs.2004.1404325.

[115] P. Maciejasz, J. Eschweiler, K. Gerlach-Hahn, A. Jansen-Troy, and S. Leonhardt, “JNER JOURNAL OF NEUROENGINEERING AND REHABILITATION REVIEW Open Access A survey on robotic devices for upper limb rehabilitation,” 2014. [Online]. Available: http://www.jneuroengrehab.com/content/11/1/3

[116] Q. Li, D. Wang, Z. Du, Y. Song, and L. Sun, “sEMG based control for 5 DOF upper limb rehabilitation robot system,” *IEEE International Conference on Robotics and Biomimetics, ROBIO*, pp. 1305–1310, 2006, doi: 10.1109/ROBIO.2006.340117.

[117] Y. G. Kiml, M. Xiloyannis, D. Accoto, and L. Masia, “Development of a Soft Exosuit for Industriale Applications,” in *Proceedings of the IEEE RAS and EMBS International Conference on Biomedical Robotics and Biomechatronics*, IEEE Computer Society, Oct. 2018, pp. 324–329. doi: 10.1109/BIOROB.2018.8487907.

[118] J. C. Perry, J. Rosen, and S. Burns, “Upper-limb powered exoskeleton design,” in *IEEE/ASME Transactions on Mechatronics*, Aug. 2007, pp. 408–417. doi: 10.1109/TMECH.2007.901934.

[119] M. Xiloyannis, D. Chiaradia, A. Frisoli, and L. Masia, “Characterisation of pressure distribution at the interface of a soft exosuit: Towards a more comfortable wear,” in *Biosystems and Biorobotics*, vol. 22, Springer International Publishing, 2019, pp. 35–38. doi: 10.1007/978-3-030-01887-0_7.

[120] S. Moubarak, M. T. Pham, T. Pajdla, and T. Redarce, “Design and modeling of an upper extremity exoskeleton,” *IFMBE Proc*, vol. 25, no. 9, pp. 476–479, 2009, doi: 10.1007/978-3-642-03889-1-127.

[121] E. Pirondini *et al.*, “Evaluation of the effects of the Arm Light Exoskeleton on movement execution and muscle activities: A pilot study on healthy subjects,” *J Neuroeng Rehabil*, vol. 13, no. 1, Jan. 2016, doi: 10.1186/s12984-016-0117-x.

[122] K. Kiguchi, K. Iwami, M. Yasuda, K. Watanabe, and T. Fukuda, “An exoskeletal robot for human shoulder joint motion assist,” *IEEE/ASME Transactions on Mechatronics*, vol. 8, no. 1, pp. 125–135, 2003, doi: 10.1109/TMECH.2003.809168.

[123] L. Oujamaa, I. Relave, J. Froger, D. Mottet, and J. Y. Pelissier, “Rehabilitation of arm function after stroke. Literature review,” Apr. 2009. doi: 10.1016/j.rehab.2008.10.003.

[124] M. Casadio, V. Sanguineti, P. G. Morasso, and V. Arrichiello, “Braccio di Ferro: A new haptic workstation for neuromotor rehabilitation,” IOS Press, 2006.

[125] A. Gupta, M. K. O’Malley, V. Patoglu, and C. Burgar, “Design, control and performance of RiceWrist: A force feedback wrist exoskeleton for rehabilitation and training,” in

International Journal of Robotics Research, Feb. 2008, pp. 233–251. doi: 10.1177/0278364907084261.

[126] A. Vega Ramirez and Y. Kurita, “A Soft Exoskeleton Jacket with Pneumatic Gel Muscles for Human Motion Interaction,” in *Lecture Notes in Computer Science (including subseries Lecture Notes in Artificial Intelligence and Lecture Notes in Bioinformatics)*, Springer Verlag, 2019, pp. 587–603. doi: 10.1007/978-3-030-23563-5_46.

[127] R. A. R. C. Gopura and K. Kiguchi, “Mechanical designs of active upper-limb exoskeleton robots state-of-the-art and design difficulties,” in *2009 IEEE International Conference on Rehabilitation Robotics, ICORR 2009*, 2009, pp. 178–187. doi: 10.1109/ICORR.2009.5209630.

[128] L. Masia, H. I. Krebs, P. Cappa, and N. Hogan, “Design and characterization of hand module for whole-arm rehabilitation following stroke,” in *IEEE/ASME Transactions on Mechatronics*, Aug. 2007, pp. 399–407. doi: 10.1109/TMECH.2007.901928.

[129] P. Lam *et al.*, “A haptic-robotic platform for upper-limb reaching stroke therapy: Preliminary design and evaluation results,” *J Neuroeng Rehabil*, vol. 5, 2008, doi: 10.1186/1743-0003-5-15.

[130] P. Lam *et al.*, “A haptic-robotic platform for upper-limb reaching stroke therapy: Preliminary design and evaluation results,” *J Neuroeng Rehabil*, vol. 5, 2008, doi: 10.1186/1743-0003-5-15.

[131] T. Nef, M. Guidali, V. Klamroth-Marganska, and R. Riener, “IFMBE Proceedings 2509 - ARMin - Exoskeleton Robot for Stroke Rehabilitation,” 2009. [Online]. Available: www.springerlink.com

[132] Q. Zhang, R. Liu, W. Chen, and C. Xiong, “Simultaneous and continuous estimation of shoulder and elbow kinematics from surface EMG signals,” *Front Neurosci*, vol. 11, no. MAY, May 2017, doi: 10.3389/fnins.2017.00280.

[133] A. C. Lo, “Clinical designs of recent robot rehabilitation trials,” 2012. doi: 10.1097/PHM.0b013e31826bcfa3.

[134] “Hamed Vatan - Google Scholar.” Accessed: Mar. 24, 2024. [Online]. Available: https://scholar.google.com/citations?hl=en&view_op=list_works&gmla=AJsN-F5_ZPzHX3GLmkM5H09reO4N3j8IdfN2eWg4Jd54kypQsVx9ZoZFJTwr2w7iRfZkrGKF_Kb8F_HlDIuqDdjHYslX38GRbg&user=9SR7Q80AAAAJ

[135] H. Majidi Fard Vatan, S. Nefti-Meziani, S. Davis, Z. Saffari, and H. El-Hussieny, “A review: A Comprehensive Review of Soft and Rigid Wearable Rehabilitation and Assistive Devices with a Focus on the Shoulder Joint,” May 01, 2021, *Springer Science and Business Media B.V.* doi: 10.1007/s10846-021-01353-x.

[136] S. B. Kesner, L. Jentoft, F. L. Hammond, R. D. Howe, and M. Popovic, “Design considerations for an active soft orthotic system for shoulder rehabilitation,” in *Proceedings of the Annual International Conference of the IEEE Engineering in Medicine and Biology Society, EMBS*, 2011, pp. 8130–8134. doi: 10.1109/IEMBS.2011.6092006.

[137] I. Koo *et al.*, “Development of a meal assistive exoskeleton made of soft materials for polymyositis patients,” in *IEEE International Conference on Intelligent Robots and Systems*, Institute of Electrical and Electronics Engineers Inc., Oct. 2014, pp. 542–547. doi: 10.1109/IROS.2014.6942612.

[138] Daegeun Park; Inwook Koo; Kyu-Jin Cho, “Evaluation of an Improved Soft Meal Assistive Exoskeleton with an Adjustable Weight-Bearing System for People with Disability,” IEEE 2015 IEEE International Conference on Rehabilitation Robotics (ICORR), 2015.

[139] C. S. Simpson, A. M. Okamura, and E. W. Hawkes, “Exomuscle: An inflatable device for shoulder abduction support,” in *Proceedings - IEEE International Conference on Robotics and Automation*, Institute of Electrical and Electronics Engineers Inc., Jul. 2017, pp. 6651–6657. doi: 10.1109/ICRA.2017.7989785.

[140] T. Abe *et al.*, “Fabrication of ‘18 weave’ muscles and their application to soft power support suit for upper limbs using Thin McKibben Muscle,” *IEEE Robot Autom Lett*, vol. 4, no. 3, pp. 2532–2538, Jul. 2019, doi: 10.1109/LRA.2019.2907433.

[141] Y. G. Kim, K. Little, B. Noronha, M. Xiloyannis, L. Masia, and D. Accoto, “A voice activated bi-articular exosuit for upper limb assistance during lifting tasks,” *Robot Comput Integr Manuf*, vol. 66, Dec. 2020, doi: 10.1016/j.rcim.2020.101995.

[142] R. F. Natividad, T. Miller-Jackson, and R. Y. Chen-Hua, “A 2-DOF Shoulder Exosuit Driven by Modular, Pneumatic, Fabric Actuators,” *IEEE Trans Med Robot Bionics*, vol. 3, no. 1, pp. 166–178, Feb. 2021, doi: 10.1109/TMRB.2020.3044115.

[143] M. Tschiersky, E. E. G. Hekman, D. M. Brouwer, J. L. Herder, and K. Suzumori, “A Compact McKibben Muscle Based Bending Actuator for Close-to-Body Application in Assistive Wearable Robots,” *IEEE Robot Autom Lett*, vol. 5, no. 2, pp. 3042–3049, Apr. 2020, doi: 10.1109/LRA.2020.2975732.

[144] S. Das and Y. Kurita, “ForceArm: A Wearable Pneumatic Gel Muscle (PGM)-Based Assistive Suit for the Upper Limb,” *IEEE Trans Med Robot Bionics*, vol. 2, no. 2, pp. 269–281, May 2020, doi: 10.1109/TMRB.2020.2990436.

[145] J. L. Samper-Escudero, A. Gimenez-Fernandez, M. A. Sanchez-Uran, and M. Ferre, “A Cable-Driven Exosuit for Upper Limb Flexion Based on Fibres Compliance,” *IEEE Access*, vol. 8, pp. 153297–153310, 2020, doi: 10.1109/ACCESS.2020.3018418.

[146] “Design and Performance Evaluation of a Wearable Passive Cable-driven Shoulder Exoskeleton”, doi: 10.1101/2020.05.29.096453.

[147] T. Proietti *et al.*, “Sensing and Control of a Multi-Joint Soft Wearable Robot for Upper-Limb Assistance and Rehabilitation,” *IEEE Robot Autom Lett*, vol. 6, no. 2, pp. 2381–2388, Apr. 2021, doi: 10.1109/LRA.2021.3061061.

[148] José Luis Samper-Escudero;, Sofía Coloma;, Miguel Angel Olivares-Mendez;, and Miguel Ángel Sanchez-Urán González, “A Compact and Portable Exoskeleton for Shoulder and Elbow Assistance for Workers and Prospective Use in Space,” *IEEE Trans Hum Mach Syst*, Sep. 2022, doi: 10.1109/ICHMS53169.2021.9582447.

[149] Alvin R. Tilley ; Henry Dreyfuss Associates, *THE MEASURE OF MAN AND WOMAN HUMAN FACTORS IN DESIGN*, vol. Wiley. 2002.

[150] R. Drillis, R. Contini, and M. Bluestein, “BODY SEGMENT PARAMETERS; A SURVEY OF MEASUREMENT TECHNIQUES,” *Artif Limbs. 1964;8:44-66. PMID: 14208177.*, 1964.

[151] de Leva P., “Adjustments to Zatsiorsky-Seluyanov’s segment inertia parameters.,” *J Biomech.*, vol. 1223, no. 30, p. 29, 1996, [Online]. Available: doi: 10.1016/0021-9290(95)00178-6. PMID: 8872282.

[152] M. Virmavirta and J. Isolehto, “Determining the location of the body[U+05F3]s center of mass for different groups of physically active people,” *J Biomech*, vol. 47, no. 8, pp. 1909–1913, Jun. 2014, doi: 10.1016/j.jbiomech.2014.04.001.

[153] J. W. Jeong, S. H. Kim, and Y. K. Kwak, “Kinematics and workspace analysis of a parallel wire mechanism for measuring a robot pose.”

[154] C. Author, A. Elatta, L. Pei Gen, F. Liang Zhi, Y. Daoyuan, and L. Fei, “An Overview of Robot Calibration,” *Information Technology Journal*, vol. 3, no. 1, pp. 74–78, 2004.

[155] Universitat Politècnica de Catalunya, IEEE Industrial Electronics Society, Annual IEEE Computer Conference, IEEE International Conference on Emerging Technologies and Factory Automation 19 2014.09.16-19 Barcelona, and ETFA 19 2014.09.16-19 Barcelona, “The Kautham Project: A teaching and research tool for robot motion planning”.

[156] S. Briot and I. A. Bonev, “Are parallel robots more accurate than serial robots?,” in *Transactions of the Canadian Society for Mechanical Engineering*, Canadian Society for Mechanical Engineering, 2007, pp. 445–455. doi: 10.1139/tcsme-2007-0032.

[157] M. Barghandan, A. A. Pirmohamadi, S. Mobayen, and A. Fekih, “Optimal adaptive barrier-function super-twisting nonlinear global sliding mode scheme for trajectory tracking of parallel robots,” *Heliyon*, vol. 9, no. 2, Feb. 2023, doi: 10.1016/j.heliyon.2023.e13378.

[158] D. Chen, S. Li, F. J. Lin, and Q. Wu, “New Super-Twisting Zeroing Neural-Dynamics Model for Tracking Control of Parallel Robots: A Finite-Time and Robust Solution,” *IEEE Trans Cybern*, vol. 50, no. 6, pp. 2651–2660, Jun. 2020, doi: 10.1109/TCYB.2019.2930662.

[159] H. D. Taghirad, *Parallel robots: mechanics and control*. CRC press, 2013.

[160] “Install the Simscape Multibody Link Plugin - MATLAB & Simulink - MathWorks United Kingdom.” Accessed: Mar. 29, 2024. [Online]. Available: https://uk.mathworks.com/help/smlink/ug/installing-and-linking-simmechanics-link-software.html

[161] “ReWalk - Wikipedia.” Accessed: Feb. 24, 2025. [Online]. Available: https://en.wikipedia.org/wiki/ReWalk?utm_source=chatgpt.com

[162] D. Pinto *et al.*, “Cost-effectiveness analysis of overground robotic training versus conventional locomotor training in people with spinal cord injury,” *J Neuroeng Rehabil*, vol. 20, no. 1, p. 10, Dec. 2023, doi: 10.1186/S12984-023-01134-7.

[163] “How Much Does an Exoskeleton Cost? - Cost Charts.” Accessed: Feb. 24, 2025. [Online]. Available: https://costcharts.com/exoskeleton/?utm_source=chatgpt.com

10 APPENDIXES

10.1 Detail Design Drawing

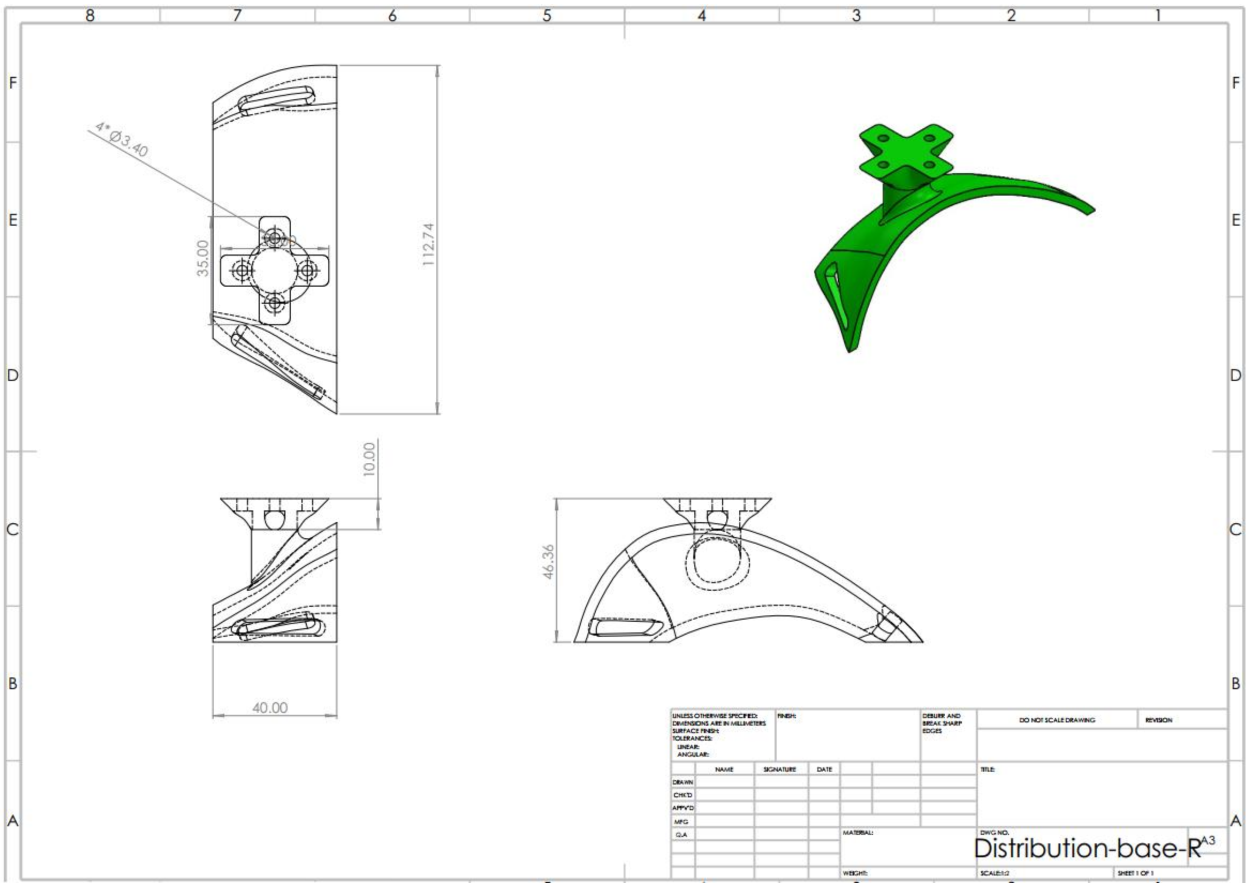

Figure 10-1: Backpack pad overall dimension.

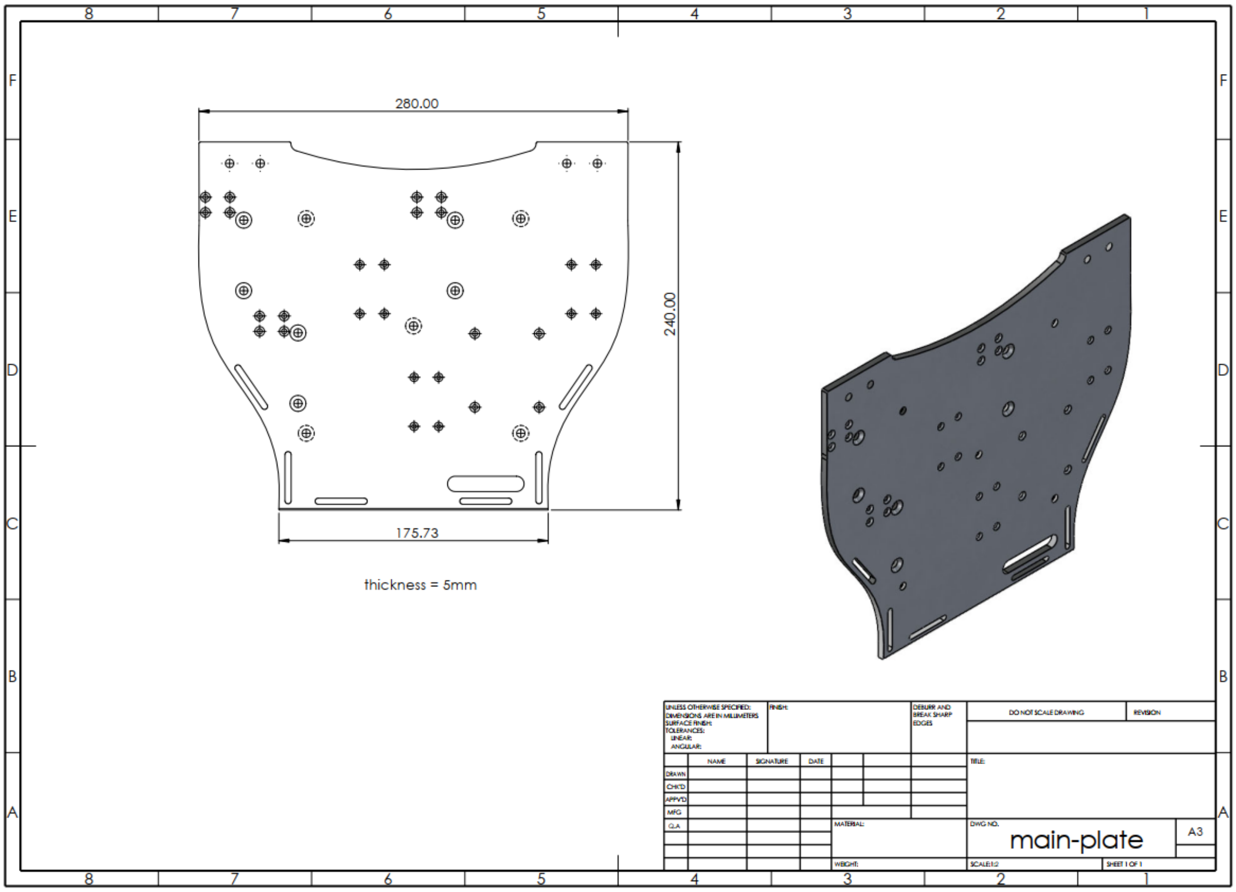

Figure 10-2: Backpack main plate's overall dimensions.

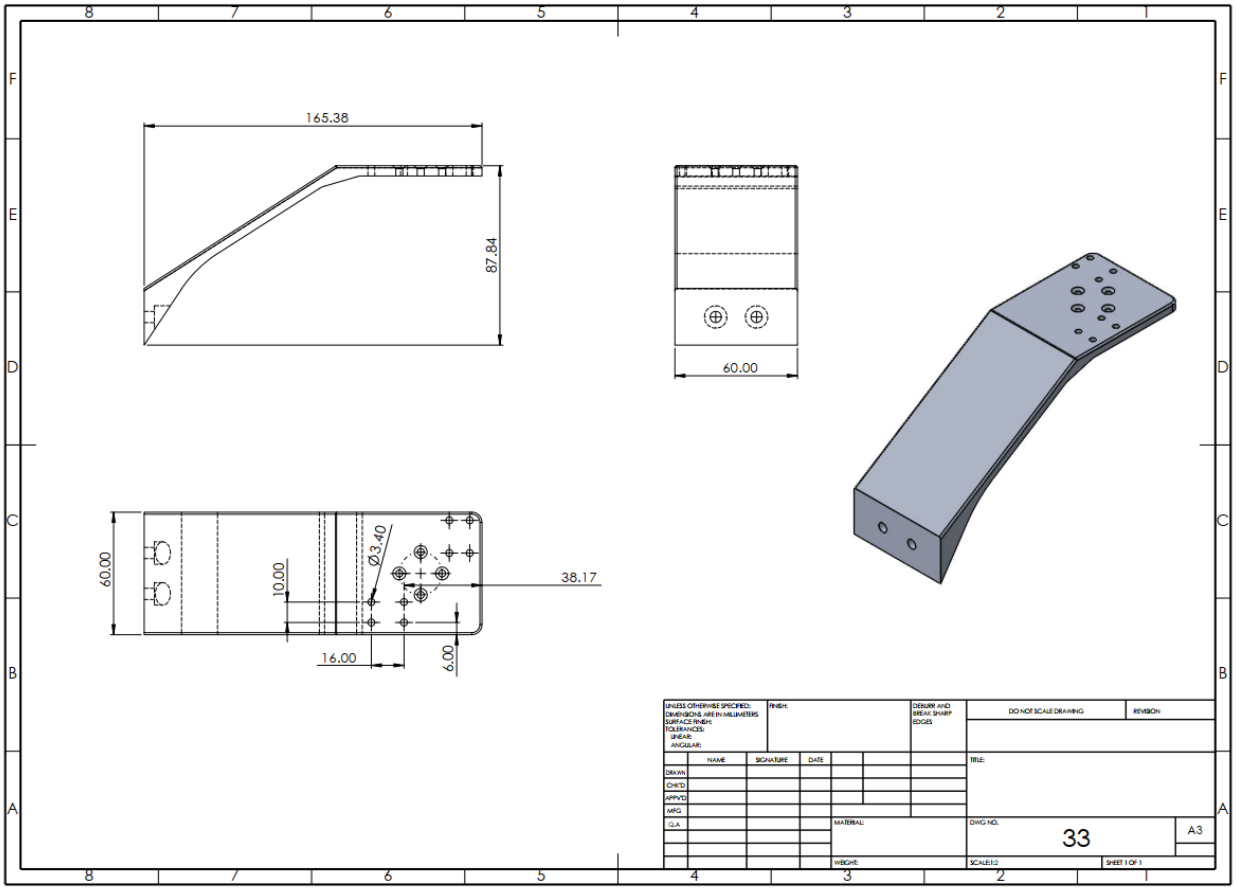

Figure 10-3: Connectors to the main plate of the backpack pad's overall dimensions.

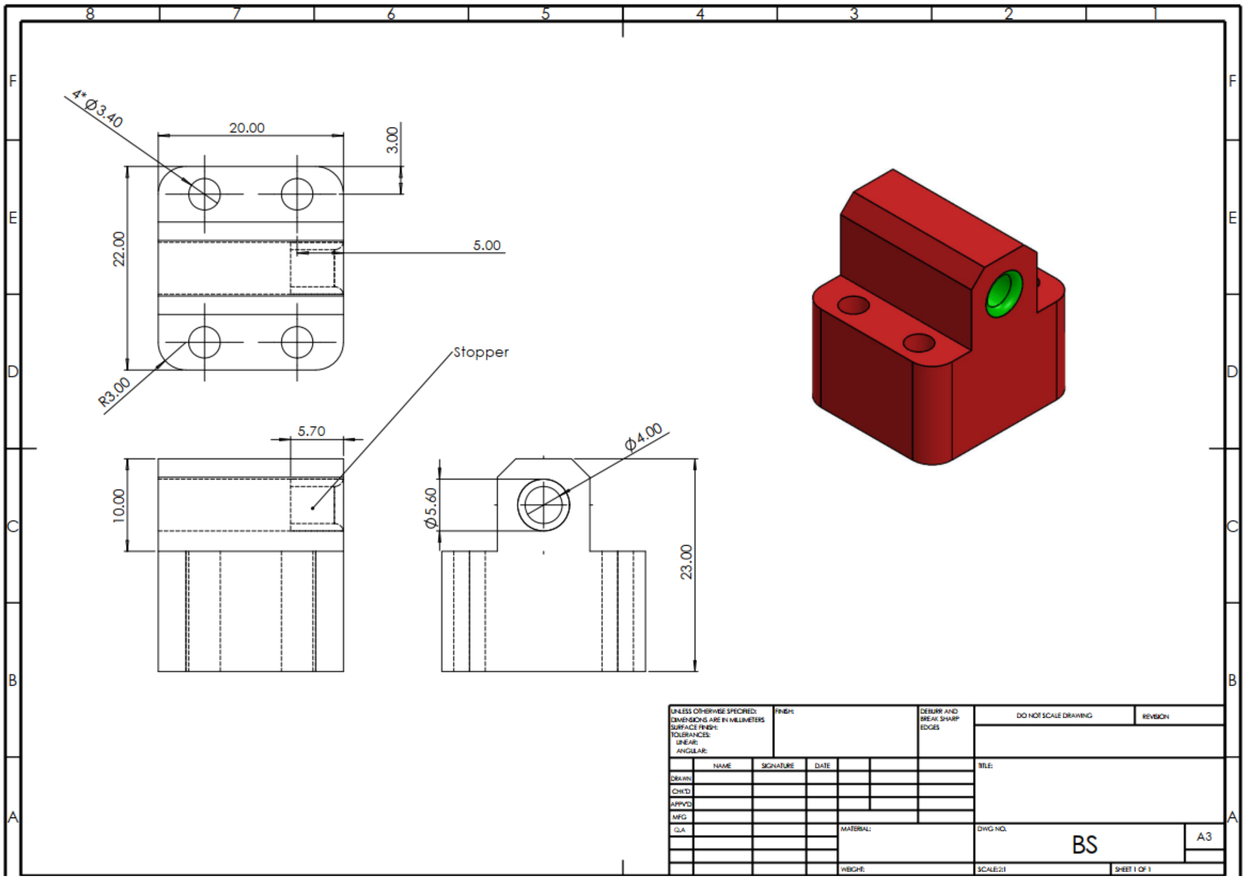

Figure 10-4: Type 1 Bowden cable housing overall dimensions.

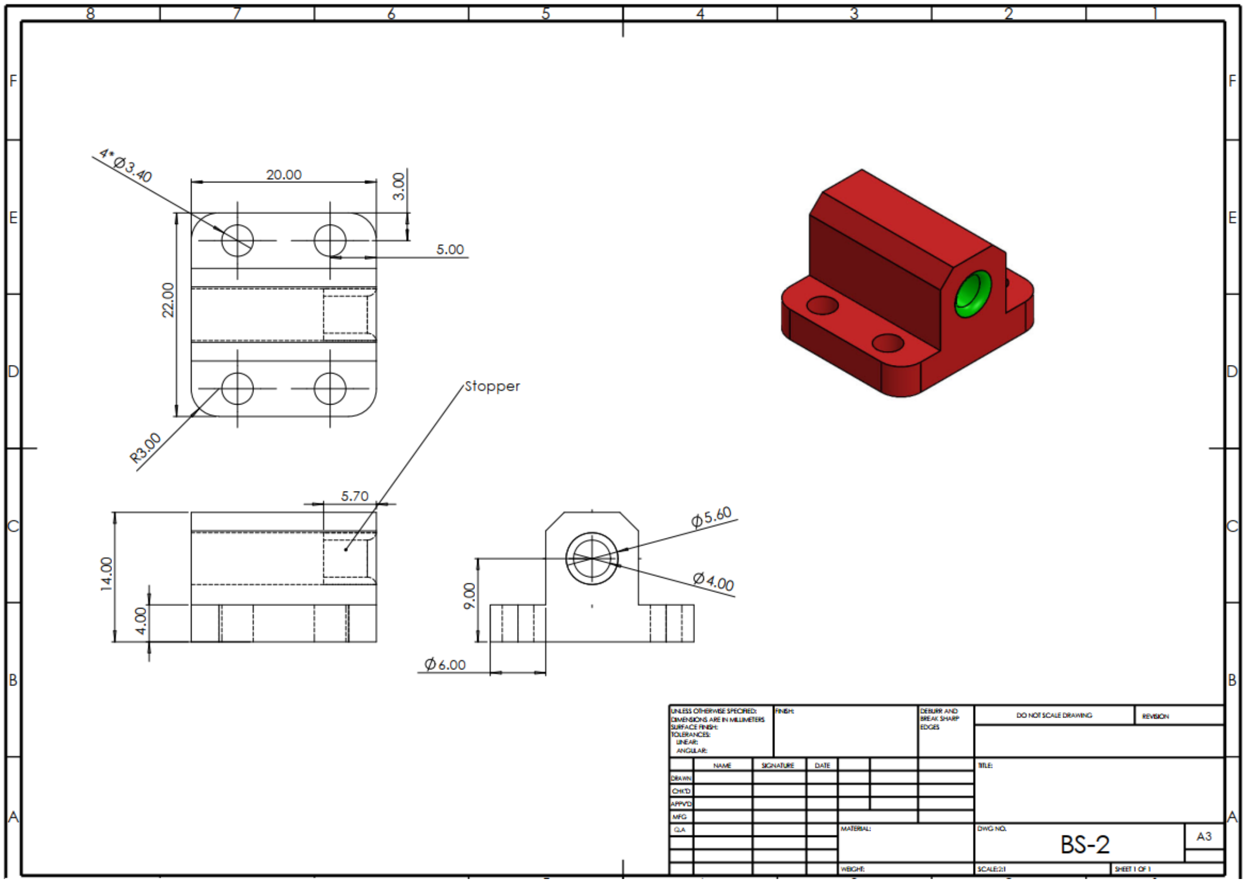

Figure 10-5: Type 2 Bowden cable housing overall dimensions.

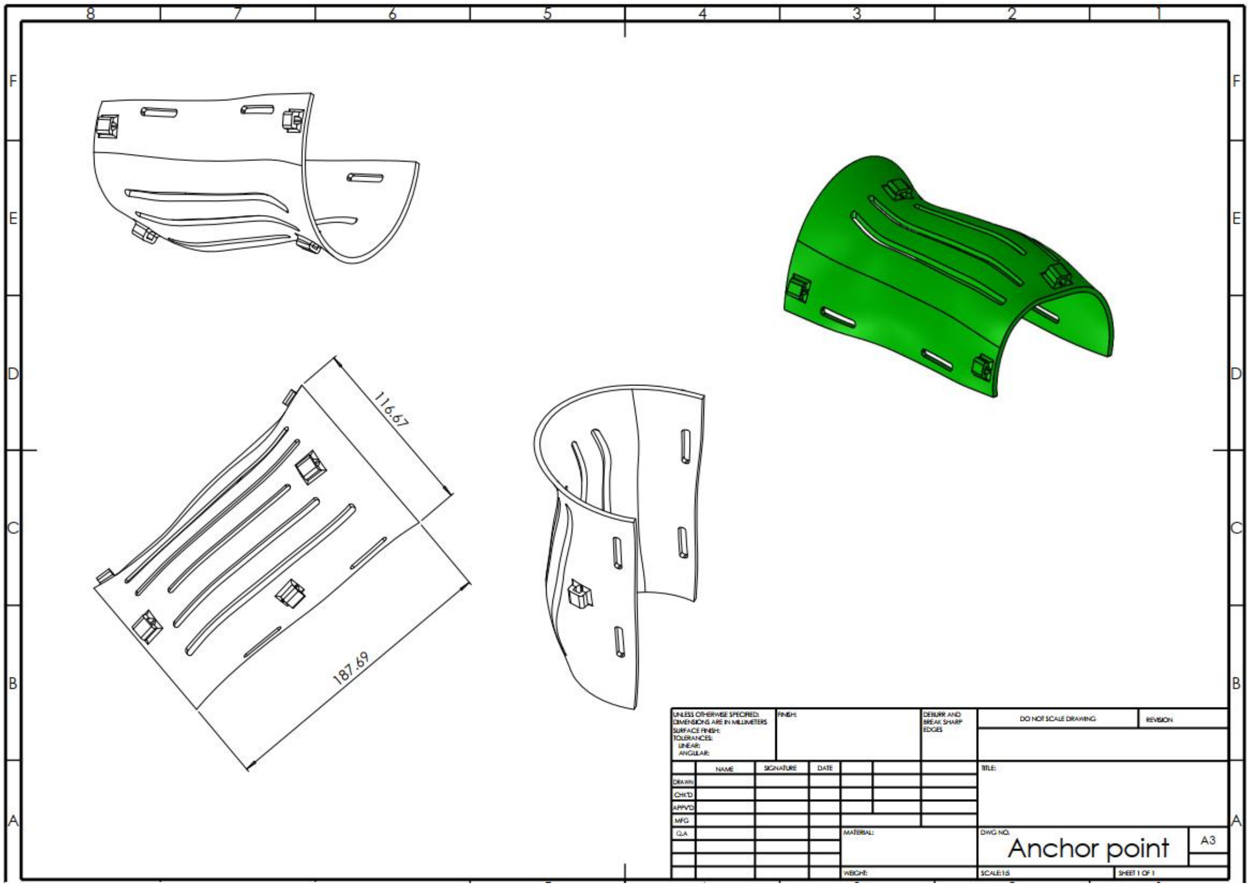

Figure 10-6: Anchor point's overall dimensions.

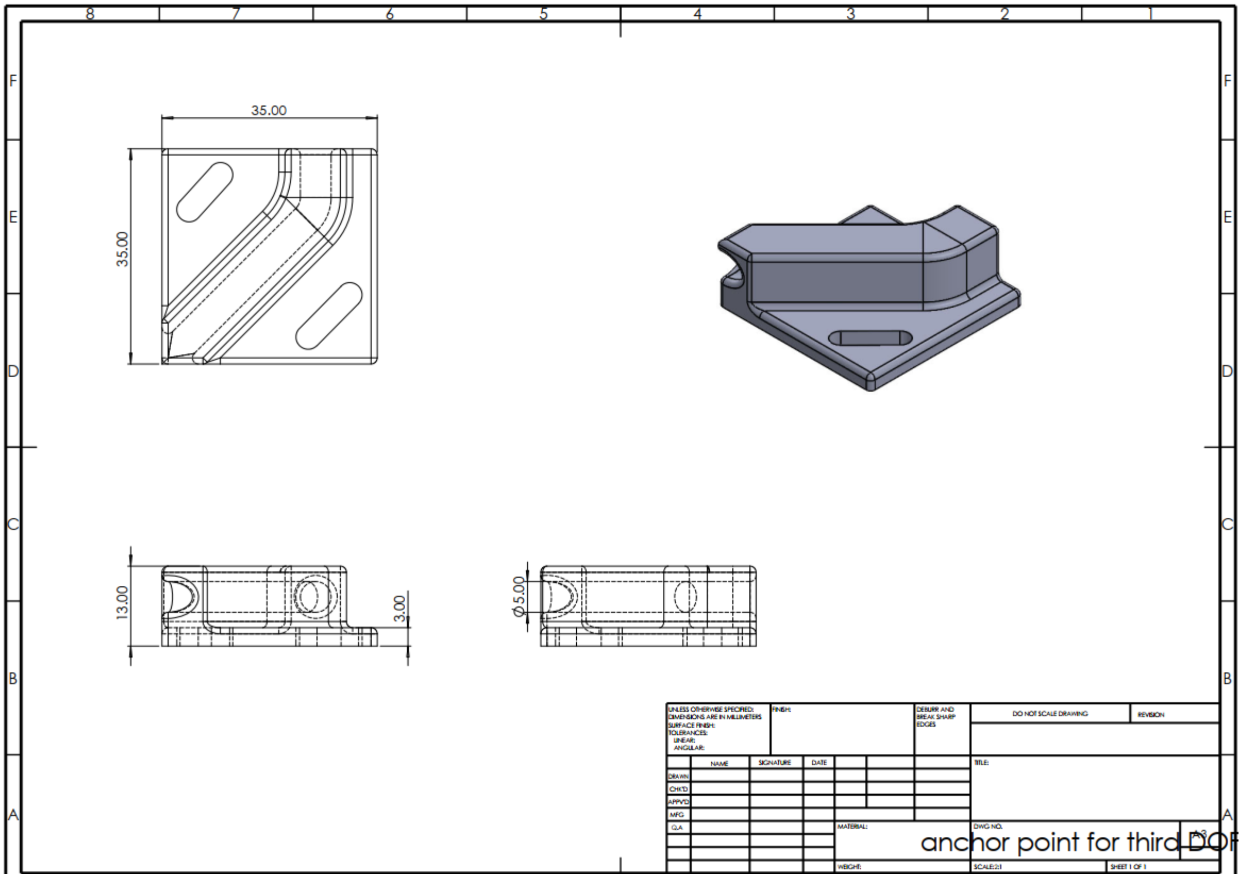

Figure 10-7: Body guiding point's overall dimensions.

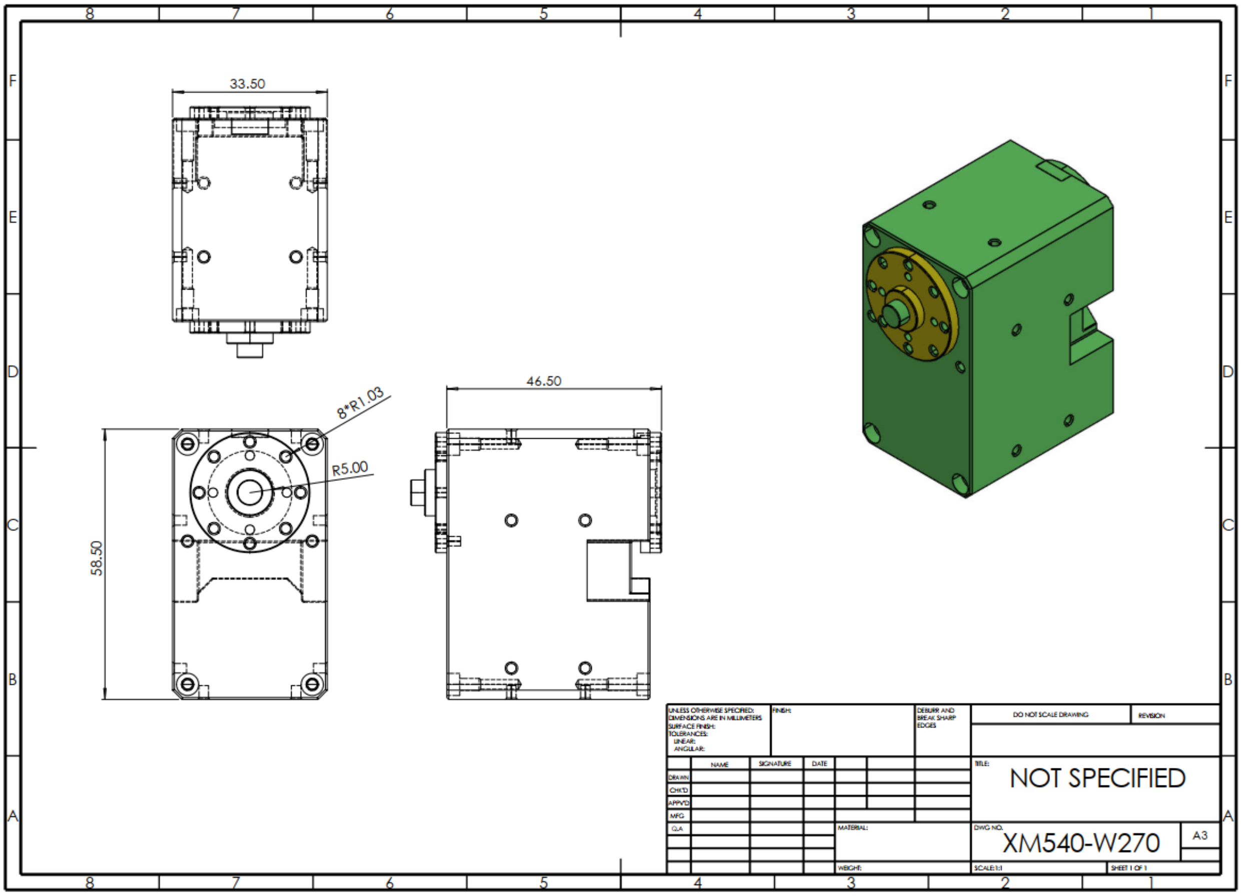

Figure 10-8: XM540-W270-R compact servomotors overall dimensions.

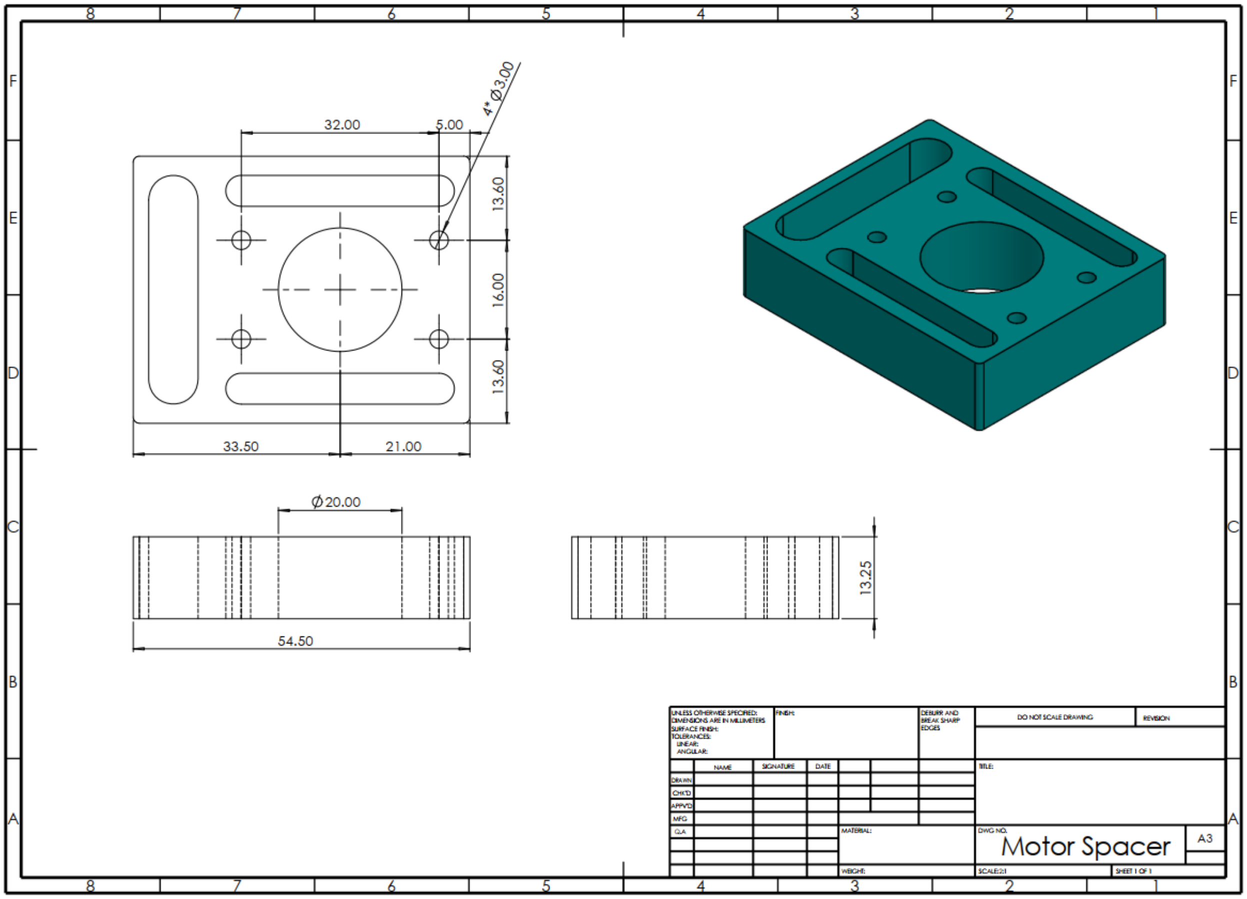

Figure 10-9: Motor-mountain plate overall dimensions.

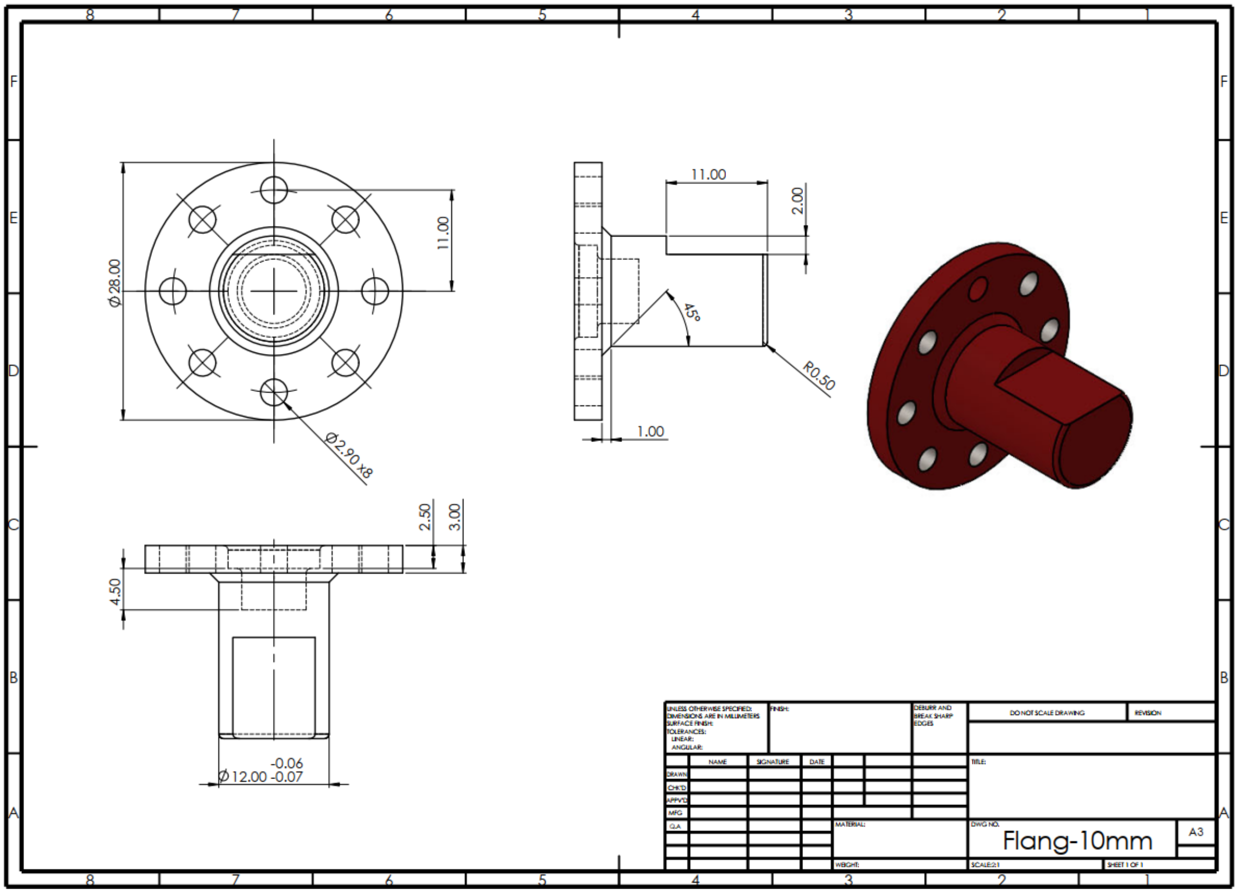

Figure 10-10: Connecting flange's overall dimensions.

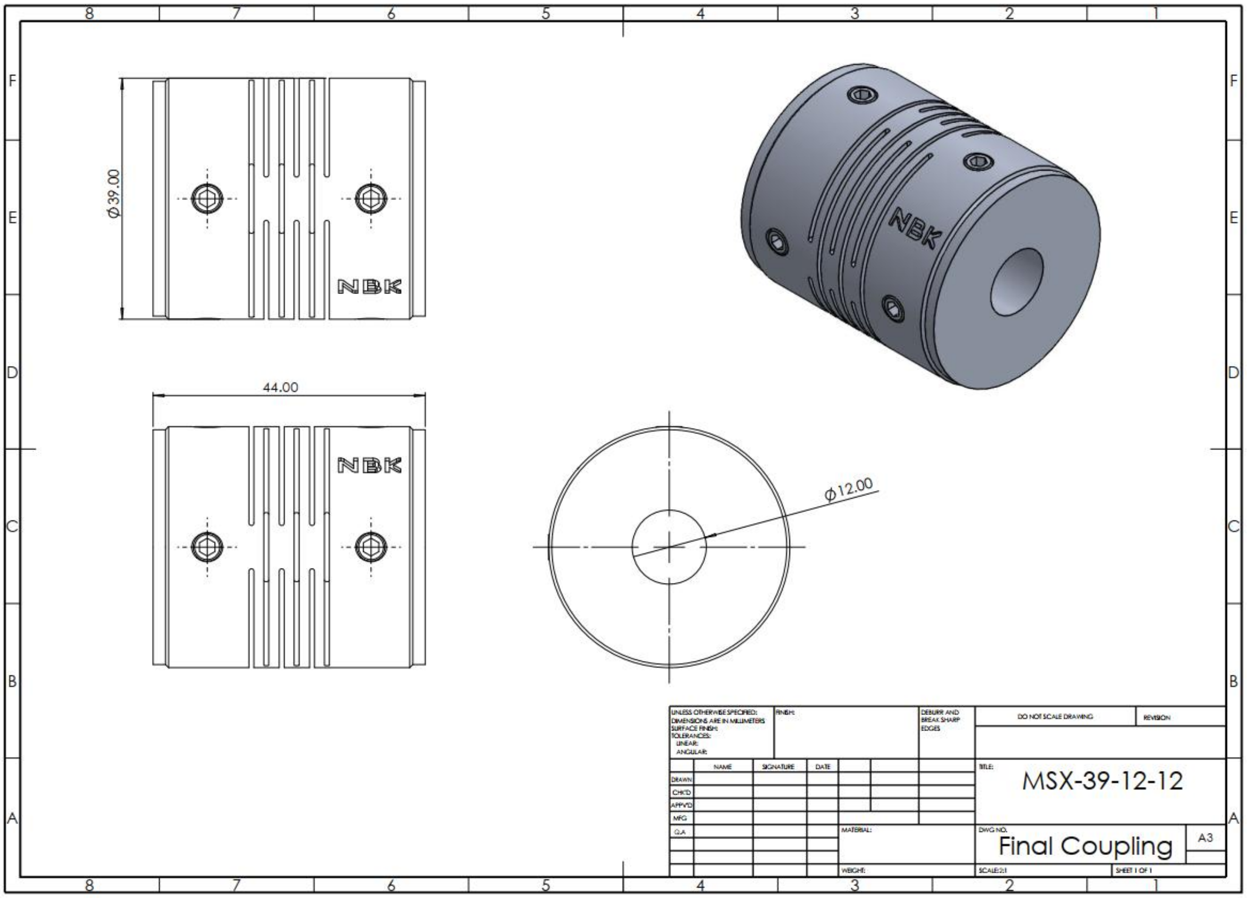

Figure 10-11: Coupling's overall dimensions.

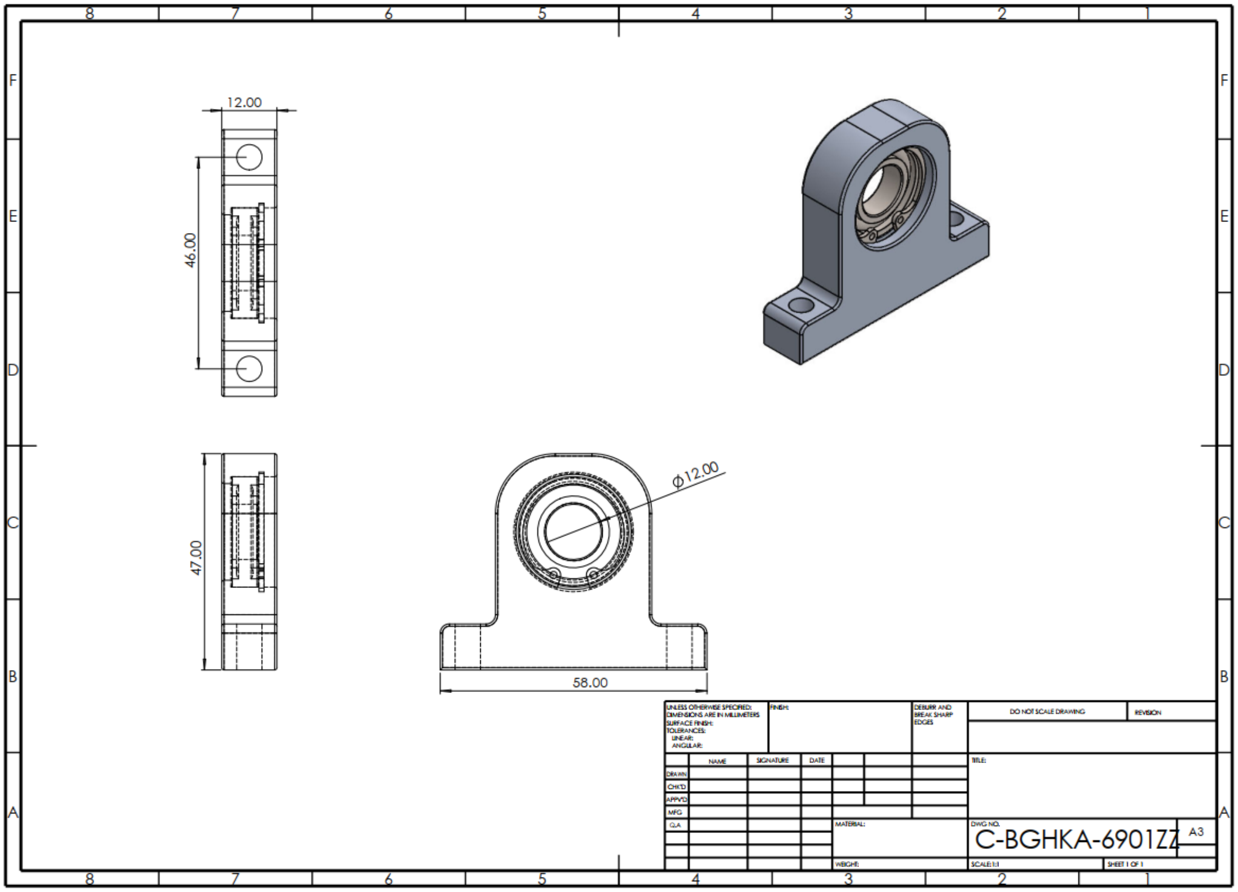

Figure 10-12: Bearing housing's overall dimensions.

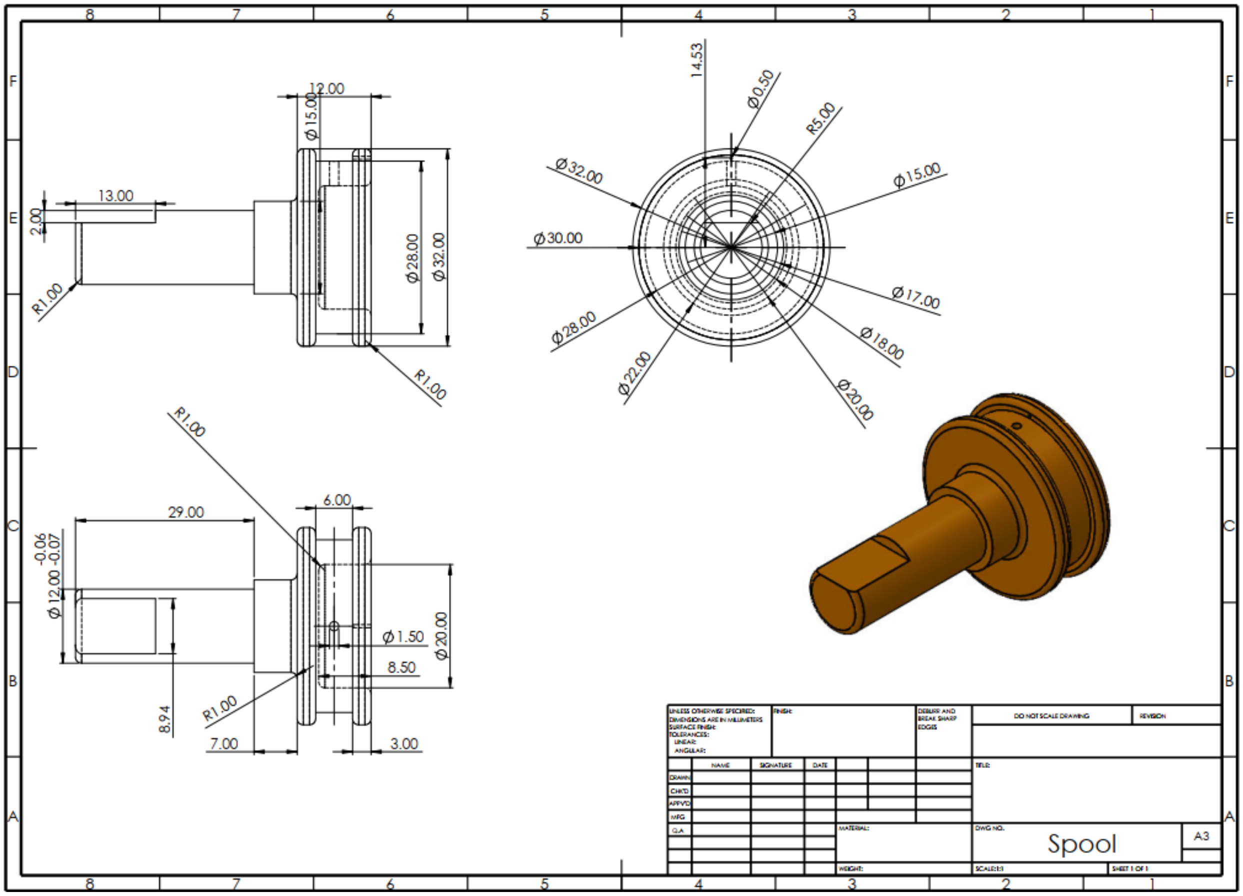

Figure 10-13: Pulley's overall dimensions.

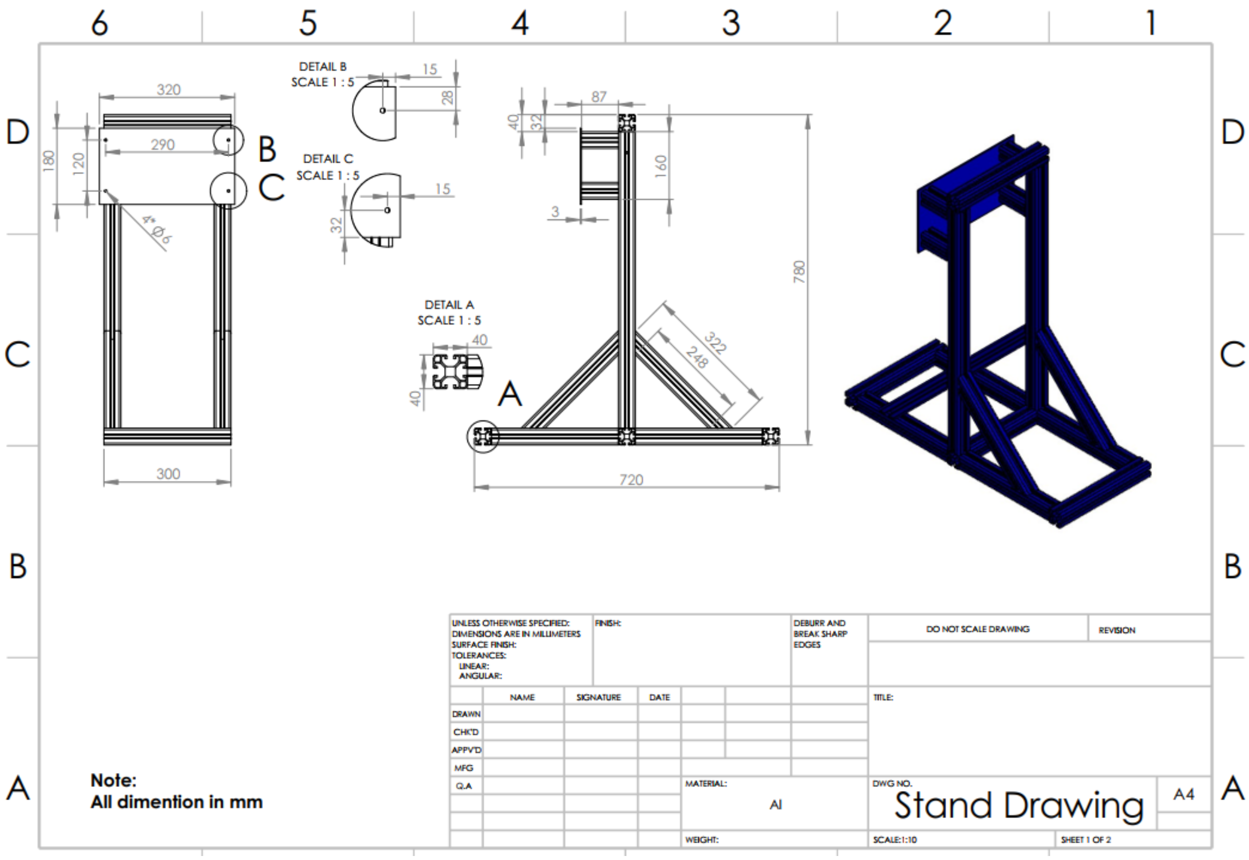

Figure 10-14: Testbench's overall dimensions.

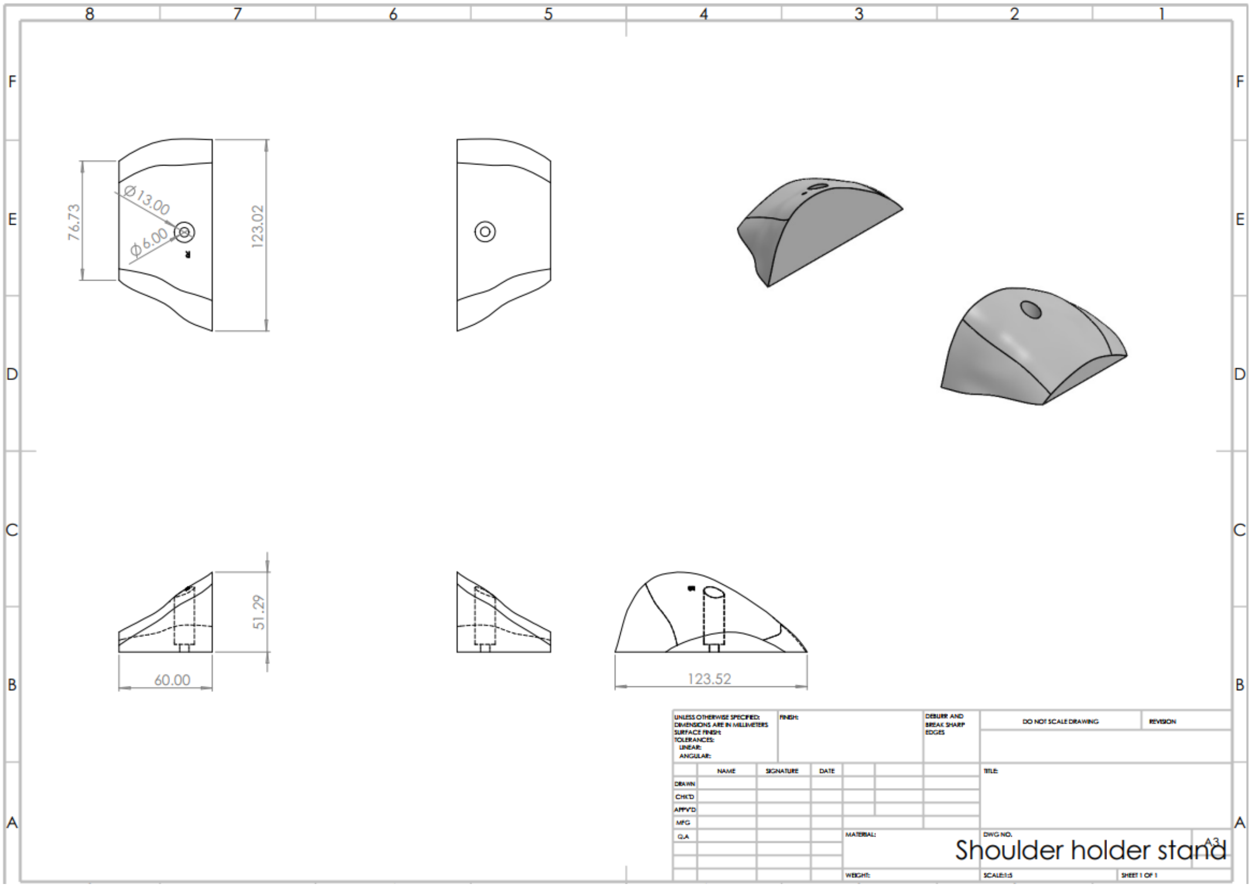

Figure 10-15: Backpack seats Drawing**.**

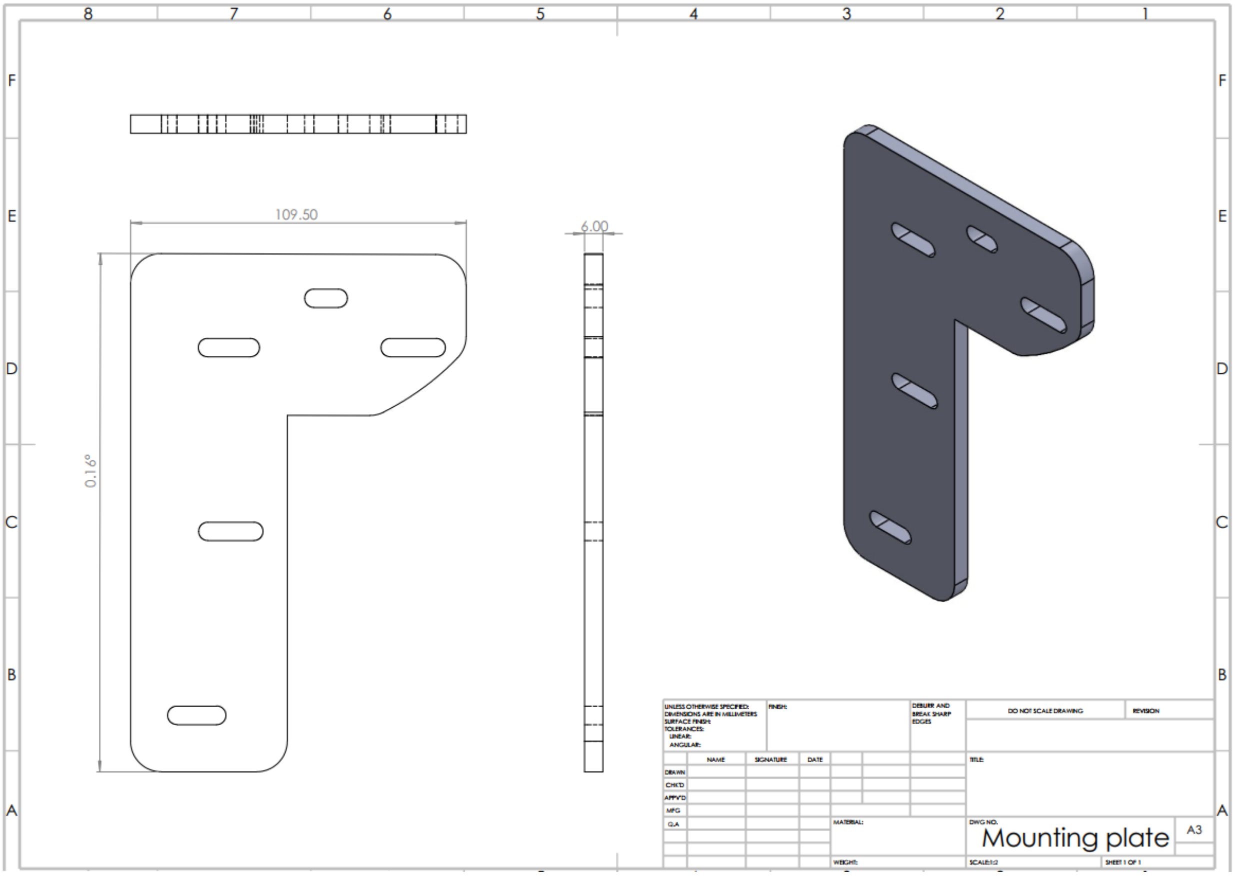

Figure 10-16: Connection plate drawing.

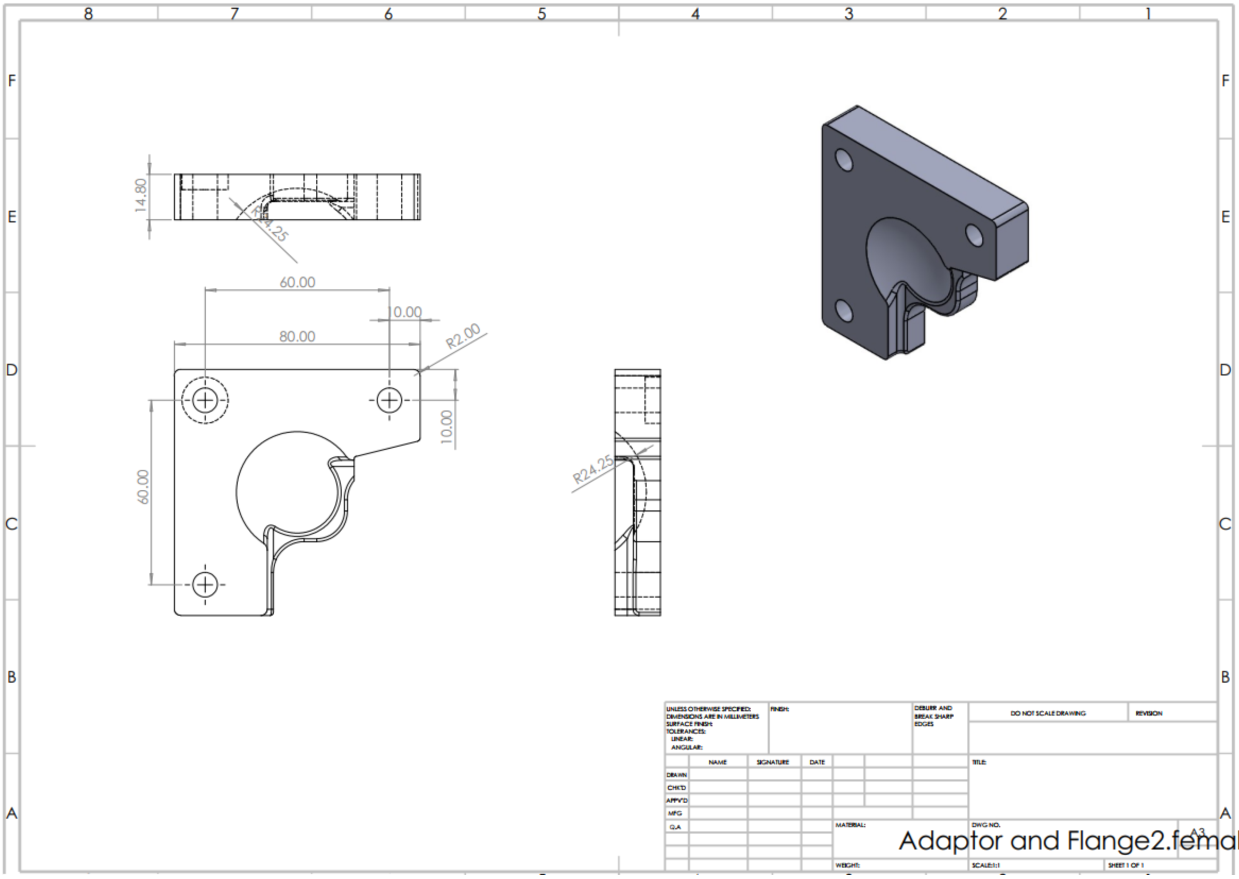

Figure 10-17: Design of the spherical joint – female part.

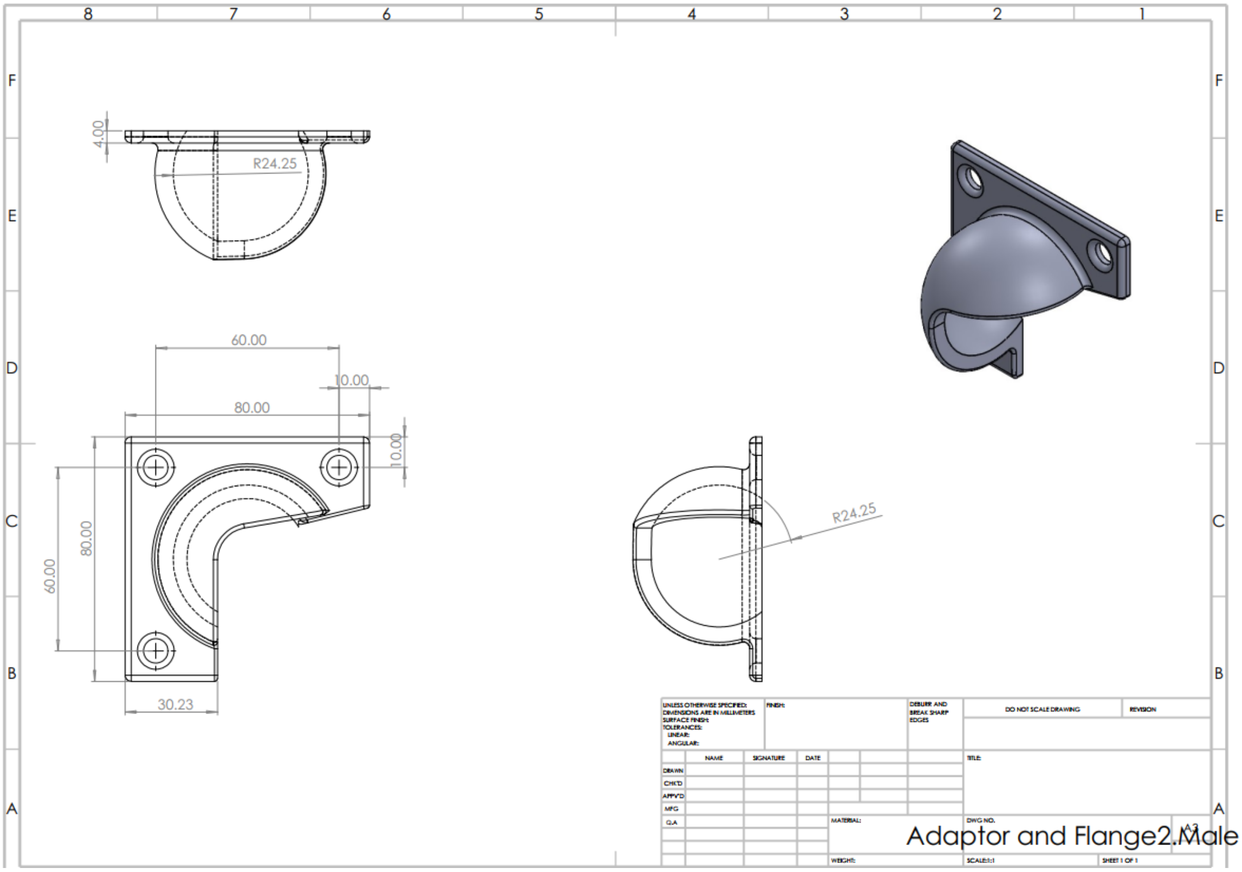

Figure 10-18: Design of the spherical joint – male part.

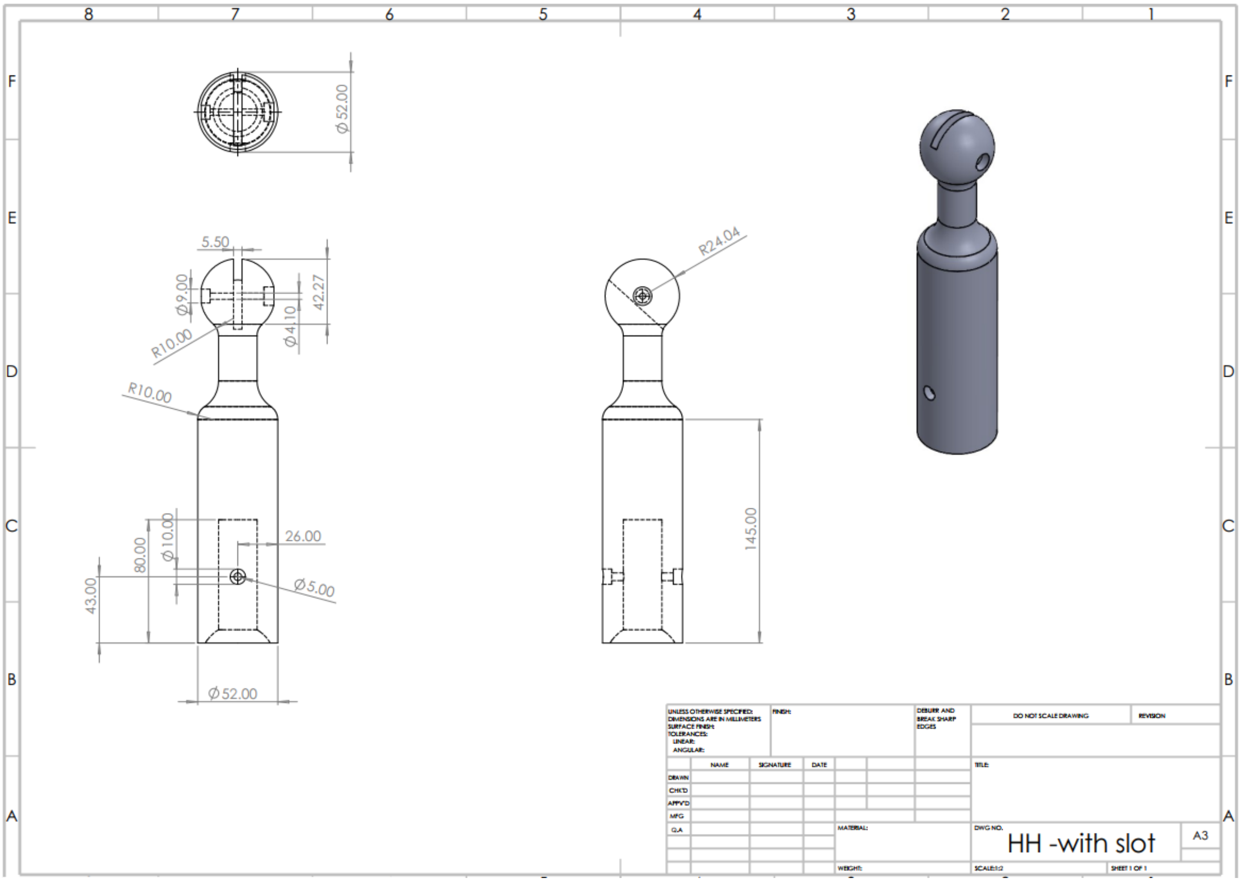

Figure 10-19: Upper arm's overall dimensions.

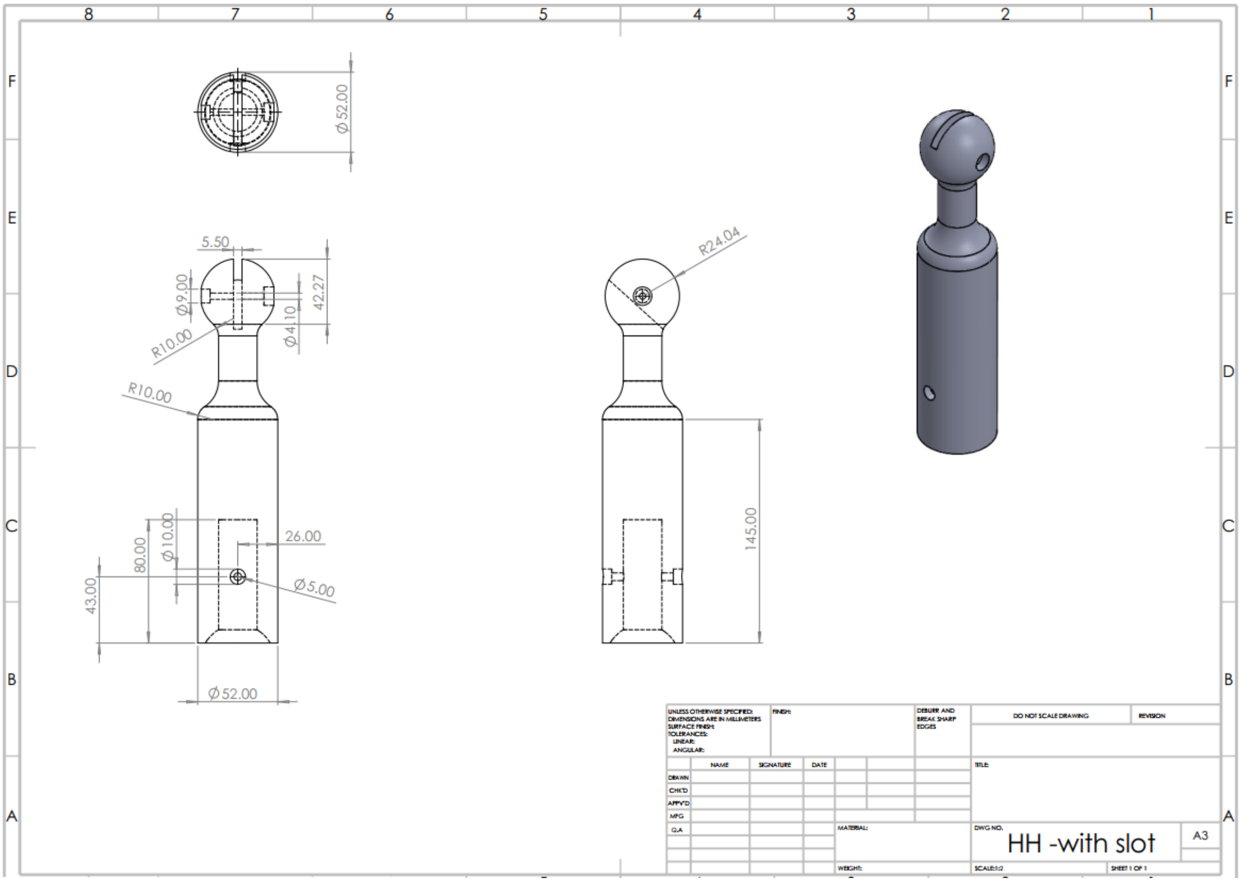

Figure 10-20: Upper arm's overall dimensions.

10.2 Dynamixel specifications (XM540-W270-T/R)

Table 10-1: Dynamixel specifications (XM540-W270-T/R)

Item	Specifications
MCU	ARM CORTEX-M3 (72 [MHz], 32Bit)
Position Sensor	Contactless absolute encoder (12Bit, 360 [°]) / Maker: AMS (www.ams.com), Part No: AS5045
Motor	Coreless
Baud Rate	9,600 [bps] ~ 4.5 [Mbps]
Control Algorithm	PID control
Resolution	4096 [pulse/rev]
Backlash	15 [arcmin] (0.25 [°])
Operating Modes	Current Control Mode, Velocity Control Mode, Position Control Mode (0 ~ 360 [°]), Extended Position Control Mode (Multi-turn), Current-based Position Control Mode, PWM Control Mode (Voltage Control Mode)
Weight	165 [g]
Dimensions (W x H x D)	33.5 x 58.5 x 44 [mm]

Gear Ratio	272.5: 1
Stall Torque	10.0 [Nm] (at 11.1 [V], 4.2 [A]) / **10.6 [Nm] (at 12.0 [V], 4.4 [A]) /** 12.9 [Nm] (at 14.8 [V], 5.5 [A])
No Load Speed	28 [rev/min] (at 11.1 [V]) / **30 [rev/min] (at 12.0 [V]) /** 37 [rev/min] (at 14.8 [V])
Radial Load	40 [N] (10 [mm] away from the horn)
Axial Load	20 [N]
Operating Temperature	-5 ~ +80 [°C]
Input Voltage	10.0 ~ 14.8 [V] (**Recommended: 12.0 [V]**)
Command Signal	Digital Packet
Physical Connection	RS485 / TTL Multidrop Bus
	TTL Half Duplex Asynchronous Serial Communication with 8bit, 1stop, No Parity
	RS485 Asynchronous Serial Communication with 8bit, 1stop, No Parity
ID	253 ID (0 ~ 252)
Feedback	Position, Velocity, Current, Realtime tick, Trajectory, Temperature, Input Voltage, etc.
Case Material	Metal (Front, Middle), Engineering Plastic (Back)
Gear Material	Full Metal Gear
Standby Current	40 [mA]

10.3 Fabrication of backpack small parts

10.3.1 Fabrication of Bowden Cable Housing

For all three backpack versions, the Bowden cable housings were fabricated from PLA material. The weight of type 1 was 3.5 grams, while type 2 weighed 2 grams. Views of both types are illustrated in Figure 10-21 and the positioning of the assembled parts on the backpack are shown in Figure 10-22.

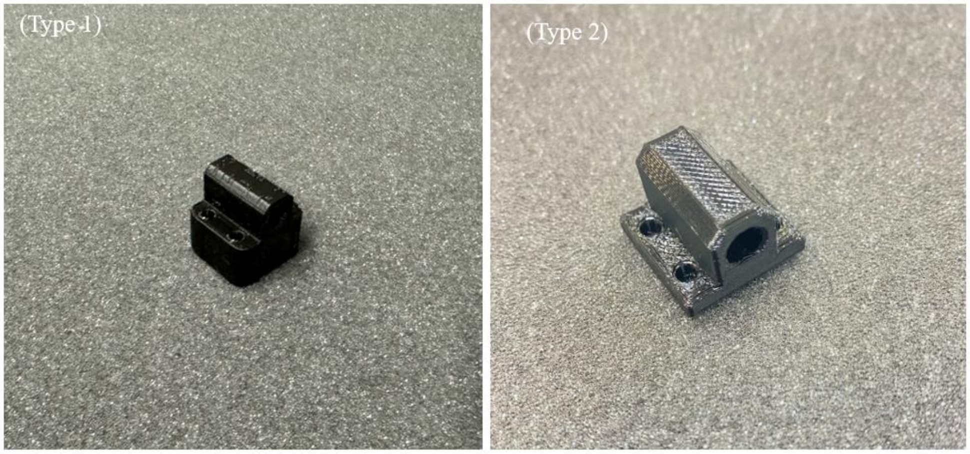

Figure 10-21: Fabricated Bowden Cables housing type 1(left) and type 2 (right).

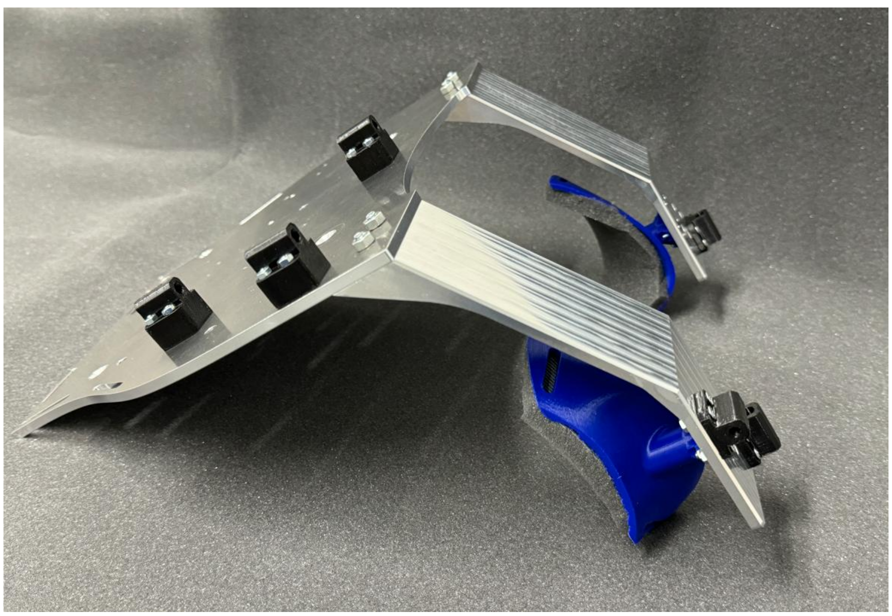

Figure 10-22: Positioning of Bowden cable housing on backpack (Type 1 and type 2).

10.3.2 Fabrication of Anchor Points

This part is fabricated from PLA and carbon fiber and weighs 90 grams. Figure 10-23 gives a view of both fabricated materials.

Figure 10-23: Fabricated anchor points. (a): PLA. (b): Carbon fiber.

As shown in Figure 10-24, 10 mm of foam was used to create a soft inner surface to this part that is in contact with the user's body, such that the user feels comfortable with this item on their arm when using it.

Figure 10-24: Anchor points with foam.

10.3.3 Fabrication of Body Guiding Point

To perform the shoulder horizontal adduction (flexion), as described in the design chapter, a point is considered as the anchor point on the arm-attached part. To complete this movement, as mentioned in the concept design section, there is a need for a guiding point on the user's body. To this end, another small part, will be used which is sewn to the backpack straps as shown in Figure 10-25 shows the body guiding point.

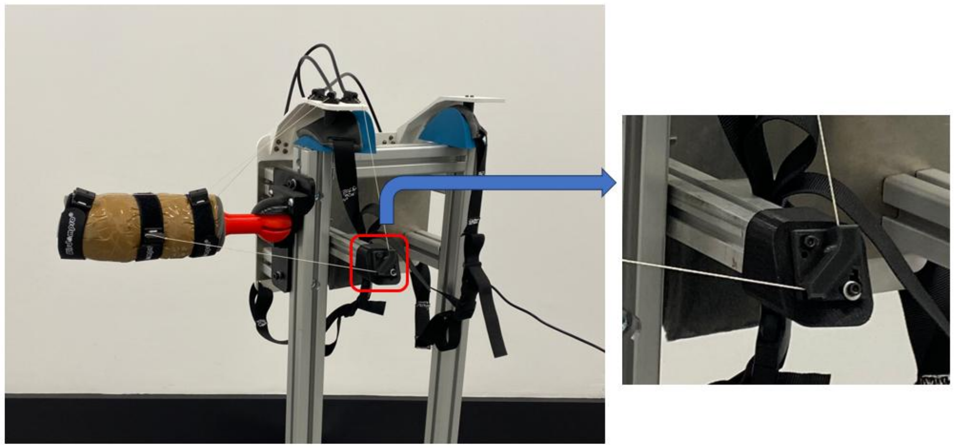

Figure 10-25: Body guiding point for third DOF.

10.3.4 Motor Pack

The motor pack includes various parts such as motor, flange connected to motor, coupling, bearing housing, and pulley related to the bearing housing and coupling. In the following, we will describe each of these parts. In the Figure 10-26, the assembled set of this motor pack is presented.

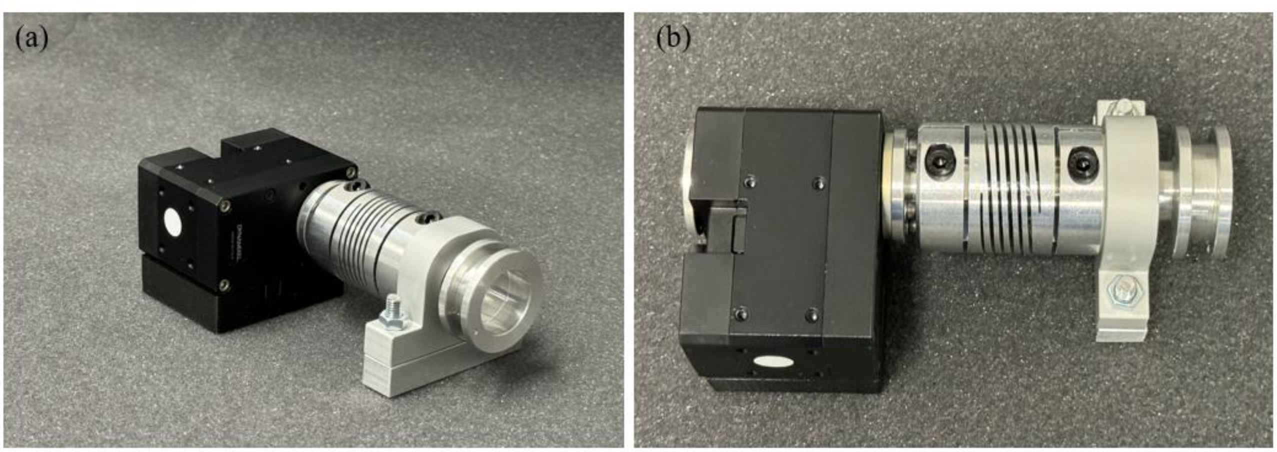

Figure 10-26: Motor Pack. (a): Isometric view. (b): Top view.

- Electric Motors

The actuator system of this project uses Dynamixel compact servomotors (XM540-W270-R). In Figure 10-27 motor pictures presented.

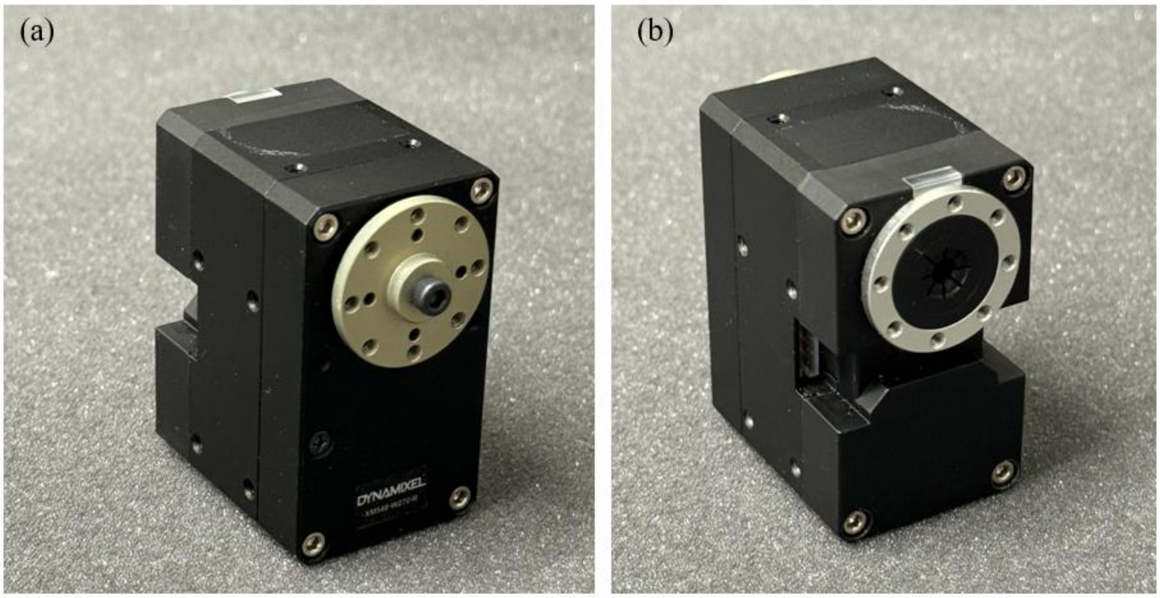

Figure 10-27: Electric motors. (a): Front view of motor. (b): Back view of motor.

- Fabrication of Motor Mountain Plate

To connect the motor to the main plate of the backpack, a motor mountain plate piece is used. In Figure 10-28 fabricated PLA motor mountain plate is presented. The weight of this part is 15grams.

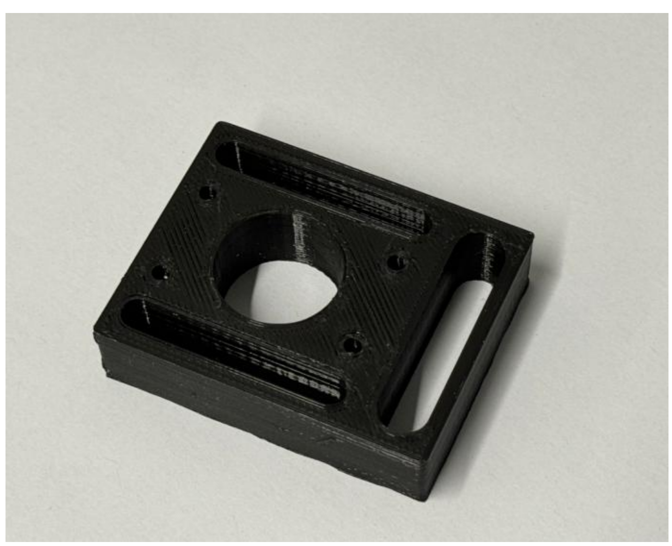

Figure 10-28: Fabricated motor mountain plate.

- Fabrication of Connection Flange

To connect the motor to the mechanical coupling, a part called the connecting flange is used. The connection flange, which is fabricated from aluminium, is shown in Figure 10-29. The weight of this part is 9 grams.

Figure 10-29: Fabricated connecting flange.

- Mechanical Coupling

Aluminium Multi-Helix Flexible 3 Beam couplings from Huco Couplings products with 8 Nm peak torque (manufacturing number: 725.19.2020) were used. Figure 10-30 shows the coupling data sheet, and Figure 10-31 the coupling shape. Machining operations were conducted on B1 and B2, increasing their dimensions to 12 mm. This adjustment was necessitated by constraints associated with the purchase order and limitations within the supply chain.

3-BEAM COUPLINGS: DIMENSIONS & ORDER CODES

	Coupling Type & Size	Set Screw Style	Clamp Type	ØD mm	L mm	① L1 mm	Bore Diameters			Mass kgx10-3	Fasteners				② Angular Offset Deg.	② Parallel Offset mm	Torsional Stiffness Nm/rad	③ Peak Torque Nm
		COUPLING REF					Min B1	Min B2	Max B1 & B2		Set Screw	Cap Screw	Torque Nm	Wrench mm				
Relieved	6	724.06	–	6.4	12.7	3.2	1.0	2.0	3.0	0.7	M2	–	0.2	0.9	3.0	0.07	1.53	0.40
	9	724.09	–	9.5	14.2	4.5	2.0	3.0	3.18	2.2	M2.5	-	0.55	1.3	3.0	0.1	5.4	0.40
		–	725.09								-	M1.6		1.5				
	13	724.13	–	12.7	19.1	6.0	3.0	4.0	5.0	5.0	M3	-	0.90	1.5	5.0	0.127	28.0	0.90
		–	725.13								-	M2		1.5				
	16	724.16	–	15.9	20.3	6.5	3.0	4.0	6.35	8.2	M4	-	2.2	2.0	5.0	0.127	38.0	1.50
		–	725.16								-	M2.5		2.0				
	19	724.19	–	19.1	22.9	6.5	4.0	4.76	8.0	12.8	M4	-	2.2	2.0	5.0	0.127	65.0	2.50
		–	725.19								-	M2.5		2.0				
	25	724.25	–	25.4	31.8	9.0	5.0	6.0	10	32.6	M5	-	4.6	2.5	5.0	0.127	121	4.0
		–	725.25								-	M3		2.5				
	32	724.32	–	31.8	44.5	12.0	6.0	8.0	14	70	M6	-	7.6	3.0	5.0	0.127	238	8.0
		–	725.32								-	M4		3.0				

Figure 10-30: Coupling data sheet.

Figure 10-31: Mechanical coupling.

- Bearing Housing

The bearing housing with the following technical information, was ordered for this project: Bearing housings / T-shape / through hole / circlip / deep groove ball bearing / aluminium / anodized (Manufacturer part number: C-BGHKA6901ZZ-30). Figure 10-32 gives an overview of this part.

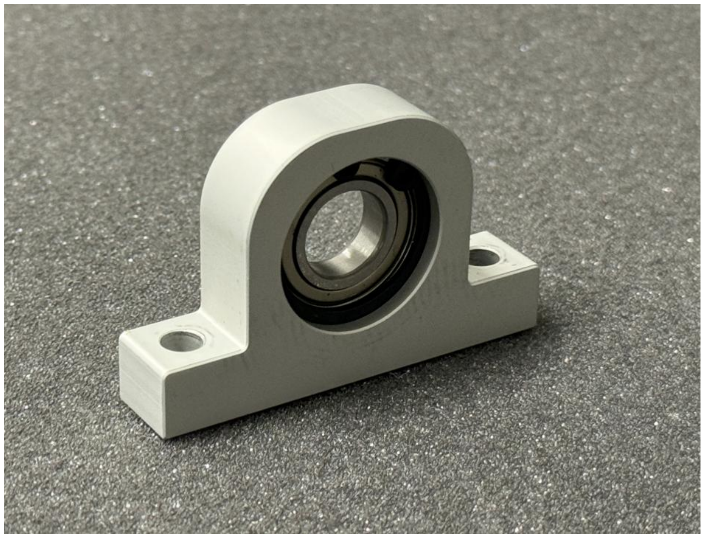

Figure 10-32: Bearing housing.

- Pulley

A pulley is required to transfer power from motors via the tendons, where Figure 10-33 shows a pulley fabricated from of aluminium.

Figure 10-33: Pulley.

10.3.5 Tendon

A braided fishing line with near-zero stretch and tough abrasion resistance has been used for this project. The diameter of these wires is 0.5 mm, as shown in Figure 10-34.

Figure 10-34: Tendon**.**

10.3.6 Arduino-UNO and U2D2 Power Hub Board (PHB)

In the preliminary testing stages of the project, U2D2 PHB Set and U2D2 were used as the interface between hardware and software. This board can be connected to a computer using a USP port and the motors can be controlled by MATLAB Simulink. The goal is to use the Arduino-UNO board to control this project after the movement cycle is finalized. These parts are shown in Figure 10-35 and Figure 10-36.

Figure 10-35: U2D2 PHB Set and U2D2.

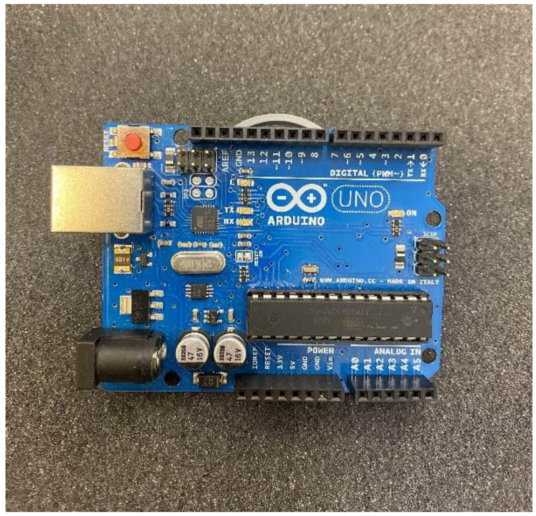

Figure 10-36: Arduino-UNO.

10.3.7 LI-PO Battery

A rechargeable 11.1 V- 1800 mAh LiPo battery has been used in this project. This battery weighs 125 grams. To place this battery on the backpack in the future, the PLA box will be used such that it can be connected to the backpack or can be placed on the waist strap and connected to the desired control system. This battery is illustrated in Figure 10-37.

Figure 10-37: LI-PO battery.

According to the selected motor and the technical specifications of the motor mentioned in chapter three, 4.2 A of current is required to supply 10 Nm torque to the motor. As mentioned on the battery, it has a capacity of 1800 mAh. This means that, generally, if a current of 1.8 A is drawn from this battery, ideally it will be discharged in about one hour. The battery capacity of

1800 milliampere-hours (mAh) is equivalent to 1.8 ampere-hours (Ah), indicating that, under ideal conditions, it can supply a current of 1.8 A for a duration of 60 minutes. Furthermore, one can approximate that this battery can deliver a higher current of 4.2 amperes for a reduced timeframe of approximately 25 minutes, which translates to 1500 seconds. This performance metric provides insight into the battery's discharge characteristics at varying loads.

According to the design, all three activities need about three seconds to perform for each of which a separate motor is provided. According to the calculations above, if a motor is running continuously for a period of 25 minutes, the battery will reach full discharge. As a result, it can be calculated that this battery has the required current to allow for several activities.

The calculation of the number of cycles a charged battery can support is derived by dividing the total operational seconds of the battery by the time required for a single action. Specifically, with a fully charged battery lasting for 1500 seconds and each action taking 3 seconds, the battery can sustain approximately 500 cycles. This metric is crucial to understanding the endurance and operational efficiency of the battery under the specified conditions.

These motors are not supposed to work permanently and turn on at the required time and turn off again after performing the desired movement, so according to the calculations performed, they can meet the user's needs. According to the estimates, the charged battery can respond to 500 cycles of movement. Still, due to being rechargeable batteries and being of very low price, a backup battery can always be made available at home, or indeed outside the home. Hence, when the backpack runs out of power, a new battery can be installed on the device and used as a backup battery with minimal inconvenience.

10.3.8 Bowden Cable Sheath

An illustration of the Bowden cable sheath is given in Figure 10-38. This item weighs 5 grams for a length of 32 cm, three lines of which are required.

Figure 10-38: Sheath wires as the Bowden cable housings.